Permian Carbonates in the Venezuelan Andes

JUAN CARLOS LAYA-PEREIRA

PERMIAN CARBONATES IN THE VENEZUELAN ANDES

Juan Carlos Laya Pereira

Doctor of Philosophy

Department of Earth Sciences

2011

A thesis submitted in partial fulfilment of the requirements for the degree of

Doctor of Philosophy at Durham University

Abstract

In northern South America, Upper Palaeozoic strata were deposited extensively over peri-cratonic areas associated with restricted seas located between Laurentia and Gondwana, in equatorial Pangea. In many places the successions are rarely exposed, and so are poorly documented; this is largely the result of extensive weathering and dense vegetation in the tropical Andes. However, these strata do contain significant information for palaeogeographic and palaeoclimatic reconstructions, and our understanding of the evolution of northern Gondwana and the finally assembly of Pangea. The main objective of this thesis is the study of Permian carbonates in the Venezuelan Andes, their sedimentology, geochemistry, diagenesis and petroleum potential.

The Palmarito sediments were deposited on a carbonate ramp that dipped basinwards towards the north facing the open ocean. The formation evolved from the underlying fluvial (Sabaneta Formation) through tidal-flat to mid-outer ramp deposits, with all facies recording a well-developed cyclicity. These strata fill an important gap in the regional palaeogeography and hence have revealed important implications for the palaeoclimate and palaeoceanography of the time.

The results of this study of Palmarito strata have significant implications for the palaeogeography of this Permian time. From the facies analysis of the Palmarito Formation, new evidence has been provided for a central Pangean seaway. Furthermore, isotope analyses have improved the time-frame for the succession from $^{87/86}Sr$ data, and in addition, the long-term stratigraphic trends in the $\delta^{13}C$ and $\delta^{18}O$ data have permitted interpretations of the climatic and oceanographic controls on Permian carbonate deposition. Moreover, metre-scale cyclicity shows the patterns of short-term controls on sedimentation, where autocyclic and allocyclic processes affected deposition and the vertical stacking of facies. An analysis of the diagenesis of the Palmarito carbonates shows several stages of cementation and alteration,

although the strata are mainly fine-grained and coarse cements are rare. Finally the elements of the petroleum system for the Palmarito have been considered for the succession and as a result, it can be proposed that, firstly, fractures in finer-grained facies have the potential to provide reservoir rocks, and secondly, that although high values of T_{max} have been obtained from rock-eval analysis from one locality, Palmarito strata do have the potential to form source rocks. Further investigation is required to ascertain the actual hydrocarbon potential of the Palmarito. The high content of finer-grained facies with low permeability provides the Palmarito strata a high potential to perform as a seal, as well as possibility to develop stratigraphic traps.

Table of contents

List of figures

List of tables

Declaration

The material contained in the thesis has not previously been submitted for a degree in this or any other institution. The work is entirely my own except where reference is made.

Acknowledgements

Many people have helped during my time in Durham, Firstly, I would like to thanks Maurice Tucker for not only being my supervisor also my mentor and friend during all this process of the PhD and in my time in Durham, specially the amazing time in castle. Also, I would like to thank to Stuart Jones and Darren Gröcke for their support throughout the research and good advice during my time here.

For my field work in Venezuela I would like to thank colleagues at Universidad de los Andes in Venezuela Patxi Viscarret, Jaime Reyes, Angel Andara, Emilio Sanchez, Rafael Aguilar and Miguel Alvarado for collaboration and assistance. In particular, I am grateful to the friendly people in the area of Mucuchachi, Mr. Neferino Noguera and Mr. Maximiliano Mesa who always offered me help during the hard times in the field.

I must also thank all my postgrad and postdoc friends of the Earth Sciences Department that have make my time here easier, especially Steve, Amelie, Katie, Mark, Dom, Aaron, Jo, Clare, Sarah, Pete, Max, Fernando, Dave and Dave, Suzi, Helen, Sam, Kathy, Kirstie and Ben for all these good moments having a pint, research reactors or just tea and cake in the coffee room; thank you so much!. The Earth Sciences Department staff have been a great help: Jo Peterkin, Alan Carr, Janice Oakes, Karen Atkinson, Stacey Firth, Chris Otley, Geff Nowell, Colin Macpherson and Graham Pearson; they were always willing to help me in all aspects during my time here. It has been a great pleasure to work with them.

Without the help of my parents, Nilder and Rafael, I would not be here; thanks to them for all the support and love during all these years.

Finally, an especial thanks goes to the woman of my life, Anto, for keeping up my motivation to carry on with this PhD; thank you so very much.

1 Introduction

1.1 General introduction

From a sedimentology-stratigraphy point of view, the Late Palaeozoic time was important in Earth history, primarily as a result of the formation of Pangea which produced extensive sedimentary basins where thick sedimentary successions were deposited. During this period several significant geological events took place including major glaciations and important orogenesis such as the Marathon-Ouachita orogeny which was responsible for uplift of the Central Pangean Mountains. However, some partly restricted seas remained between Laurentia and Gondwana, in equatorial Pangea, wherein carbonates were deposited. This is the case with the Mucuchachi Basin in Venezuela, the subject of this thesis.

The Late Palaeozoic strata in northern South America were deposited extensively over peri-cratonic areas, but in many locations they are rarely exposed and so are poorly documented. This is largely the result of extensive weathering and the dense vegetation cover in the tropical Andes. However, these strata do have a significant petroleum potential, and indeed in the southern USA and Brazil they contain important petroleum systems. This study of the Palmarito Formation in Venezuela enhances our understanding of Central Pangea during the Permian and fills a significant gap in our knowledge of Pangean palaeogeography. This research also has important implications for the palaeoclimate and palaeoceanography of the time..

Facies analysis of Palmarito strata has provided new evidence for a central Pangean seaway which necessitates revisions to the existing palaeogeographic maps of Pangea provided by Scotese (1995, 1999); Miall and Blakey (2008) and Blakey (2007). It follows from this that, the palaeoclimate models based on these maps may need to be changed to take into account the revised palaeogeographic distribution of sea, land and mountain ranges. Isotope analyses as part of this project have enabled a reliable time-frame to be proposed for

the succession from $^{87/86}Sr$ data, and in addition, the long-term stratigraphic trends in the $\delta^{13}C$ and $\delta^{18}O$ data have permitted interpretations of the climatic and oceanographic controls on Permian carbonate deposition. As a result important implications were deduced, for example, regarding the influence of nutrient supply from the carbon isotope curve. Furthermore, metre-scale cyclicity shows the behaviour of short-term controls on sedimentation, where autocyclic and allocyclic processes influenced deposition and the vertical stacking of facies. An analysis of the diagenesis of the Palmarito carbonates shows several stages of cementation and alteration, although the strata are mainly fine-grained and coarse cements are rare. Silicification and selective dolomitization has locally occurred, with the latter enhancing the porosity. The porosity in the Palmarito strata is very low, so that any reservoir potential will be dependant on the development of natural fractures. However, the few pores present, and stylolites, are often stained with bitumen, which could reflect the migration of hydrocarbon fluids through these rocks. On the other hand, the potential for source rocks has been discounted by Lugo (2008) due to high values of T_{max} (over mature) in shales from Rock-Eval analysis and low total organic carbon (TOC) figures. Nonetheless, the sampling methods that Lugo (2008) applied were restricted to one section, only in the lower-middle part of the formation and this could have biased the results. For this reason, this topic needs further investigation.

1.1.1 Aims and objectives

Venezuela has giant oil and gas reserves. However, most of the reservoirs are in Cenozoic and Mesozoic strata. In the last decade, Palaeozoic deposits have been identified as potential future oil and gas targets, not only in Venezuela but in several other countries around the world. The petroleum potential of the Upper Palaeozoic strata in Venezuela is noteworthy in view of the correlations with petroleum systems in neighbouring Brazil and the southern USA. For this reason, an understanding of palaeogeography, basin analysis, facies,

the chronostratigraphic framework, the cyclicity and its stacking patterns and diagenesis, is vital to identify the potential petroleum system in the Palmarito strata. In addition, these strata have a significant palaeogeographic location in the northern Gondwana area where there is little information available; this region is a crucial part concerning the assembly of Pangea and the nature of its palaeoclimate, palaeoceanography and palaeogeography.

Therefore the aims of this thesis are to:

Describe the facies of the Permian Palmarito Formation distributed throughout the Venezuelan Andes and discuss the palaeoenvironments of the succession. The palaeogeography reconstructed is then considered in the context of equatorial Pangea.

Discuss the stable isotope stratigraphy (carbon, oxygen and strontium) of the Palmarito Formation to improve its temporal framework, and from this, to consider the correlation with the climatic and oceanographic regimes in low latitudes during the Permian.

Analyze the metre-scale cycles and provide possible explanations of the mechanisms causing their repetition in their tropical Pangean location.

Describe and interpret the diagenetic processes that operated within the Palmarito Formation

Identify the petroleum system elements in the Palmarito succession

1.2 Locality of research

Permian carbonates crop out in the mountainous areas of western Venezuela, the so-called ‘Mérida Andes’ or ‘Venezuelan Andes’. This mountain range is a prolongation of the Colombian Eastern Cordillera and forms the northernmost part of the Andean Cordillera. The Venezuelan Andes has a complex tectonic history which has been discussed by many authors, including Audemard (1993), Pindell et al. (1998) and Audemard and Audemard (2002). The neighbouring basins are the Maracaibo to the north from which no Permian carbonates have been reported in the subsurface, and to the south a deep foreland basin (the Barinas-Apure

and Llanos basins), where although there are no publications on the topic unofficial reports do suggest that Upper Palaeozoic rocks exist in the subsurface of these basins where exploration could be a future endeavour (Figure 1.1)

Fieldwork for this project was focused in four main areas, *Carache, Bócono, Portachuelo and La Grita-El Cobre-El Zumbador*. The detailed description of these areas is provided in Chapter 3 (Description of the exposures in the Venezuelan Andes).

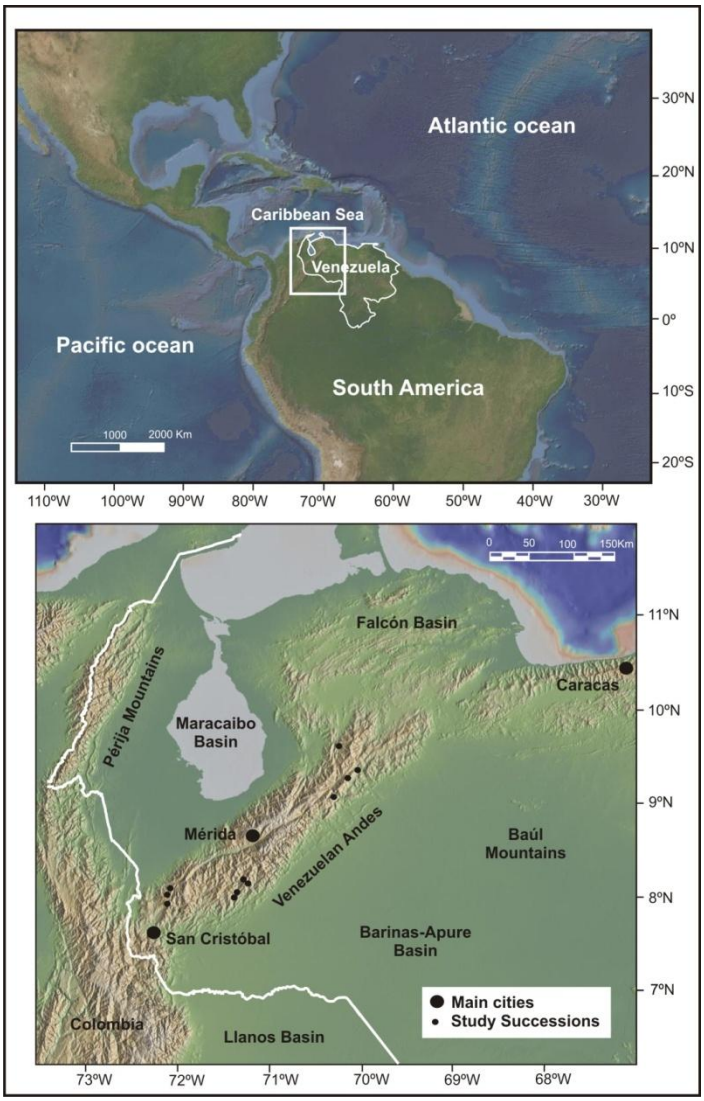

Figure 1.1. Digital relief image of South America (above) and western Venezuela (below) showing the location of the main areas of study. Modified from Ryan et al. (2009), also available in http://www.geomapapp.org.

1.3 Techniques used

1.3.1 Fieldwork

Fieldwork was undertaken on thirteen sections in four main areas located throughout the Venezuelan Andes. In the northern part, exposures in the Carache and Bócono areas are relatively easy to access, being close to roads and large towns. However, the Rio Bócono succession was extremely difficult to reach owing to poor tracks and dense forest. South of Merida City outcrops have access from the main road which connects Mucuchachi town to Santa Barbara de Barinas. This road is a 4x4 track, only accessible during the dry season. Finally, the La Grita-Zumbador outcrops are along a roadway. The Venezuelan Andes area has intense precipitation during the wet season, which is normally between April and November. Furthermore, the vegetation is very dense and almost impenetrable in places, composed of rain-forest trees and shrubs, making it difficult to access the outcrops. Thus, all fieldwork was undertaken in January, February and March (2008, 2009 and 2010).

1.3.2 Sedimentary logging techniques

Detailed field logging was undertaken on the 1:100 scale to bring out the details of the metre-scale cyclicity and to describe the sedimentary structures, textures, lithology, cycles, thickness and fossils, as well as location of samples. Dunham's textural classification was used to describe the carbonate facies, also, a facies scheme was developed for the outcrop scale (see Chapter 3). The logs were drawn in the graphical package CorelDRAW® and a compilation of the field descriptions is presented in Appendix 1.

1.3.3 Thin-section descriptions

174 thin-sections were examined for this thesis. The methodology for the petrographic analysis is presented in Appendix 2. The samples were classified using the textural scheme of Dunham (1962) and a more detailed microfacies scheme given in given in Chapter 3.

1.3.4 Carbon and oxygen isotopes

208 samples were analyzed for their carbon and oxygen isotope signatures including matrix-whole rock, brachiopods and cements. Most of the samples were analyzed at Birmingham University following the procedure described in the Chapter 4. In addition, some of the samples were analyzed in the stable isotope laboratory in NCIET (Northern Centre for Isotopic and Elemental Tracing) at Durham University with a similar procedure. The results were used to assess the controls on deposition, also the degree of digenetic alteration. The isotope variations within and through the cycles were interpreted to determine their origin. In Appendix 3, the results are presented in tables with information regarding their location in the succession.

1.3.5 Strontium isotopes

Ten samples were taken using a hand drill and micromill and the powders analyzed for their $^{87}Sr/^{86}Sr$ ratios in the Arthur Holmes Isotope Geology Laboratory (AHIGL), which forms part of NCIET. Further detailed descriptions of the technique are given in Chapter 4.

1.3.6 Trace elements

92 samples including internal layers of brachiopod shells, matrix-whole rocks and cements were drilled, crushed and analyzed for their trace elements (Ca, Si, Na, Fe, Al, Mg, K, Ba, Sr, Mn, Zn, P, Ti, and S). All analyses were carried out in the Durham University ICP laboratory under the direction of Dr C. Ottley, Senior Research Officer. The procedure is described in detail in Chapter 4

1.3.7 Cycle analysis

Once the petrographic analysis and field descriptions were completed the vertical facies stacking pattern was studied and the metre-scale cycles were identified and described. Fischer plots were drawn to identify any pattern which could be potential criteria for correlation. In addition, statistical methods were applied, runs tests and bundle testing, to

determine the degree of randomness or order in the vertical stacking patterns of the cycles, and therefore, to contribute towards an explanation for the origin of the cycles.

1.4 Thesis outline

Chapter 2: **Review and geological background of the Late Palaeozoic of Mid-Pangea.**

This chapter focuses on the description of the regional stratigraphy of the equatorial Pangean basins, which can be correlated to the Permian strata of the Palmarito Formation of the Venezuelan Andes. The possibility of there being correlative petroleum systems in the other basins is also considered

Chapter 3: **Facies analysis and depositional environments of Permian carbonates of the Venezuelan Andes: Palaeogeographic implications for Northern Gondwana**

This chapter describes and interprets the Permian strata of the Palmarito Formation distributed throughout the Venezuelan Andes and discusses the palaeoenvironments of the succession resulting from detailed field descriptions and petrographic analysis; the palaeogeography is also discussed in the context of equatorial Pangea.

Chapter 4: **Carbon, oxygen and strontium isotopic composition of low-latitude Permian carbonates: Climate proxies of tropical Pangea**

This chapter presents and discusses the stable isotope record in the context of the sedimentology of the Palmarito Formation located in western equatorial Pangea, and considers the correlation with climatic and oceanographic regimes in low latitudes during the Permian.

Chapter 5: **Metre-scale cyclicity of Permian ramp carbonates in the Venezuelan Andes: deposition under the tropical Pangean tectonic and climatic regime.**

This chapter discusses the metre-scale cycles in the Permian succession of equatorial Pangea. In addition, it provides possible explanations of the mechanisms causing Palmarito

cyclicity from the response of the facies and also the geochemical data (isotopes and trace elements).

Chapter 6: **Post-sedimentary events and petroleum potential of the Palmarito Fm.**

This chapter describes the diagenetic processes that Palmarito strata have suffered after deposition, burial and exhumation. In addition, a summary of the potential petroleum systems in Palmarito strata is presented and discussed.

Chapter 7: **Conclusion and future work.**

This chapter presents a summary, the conclusions and key findings of the chapters and their overall implications.

Appendix 1: Detailed field logging on the 1:100 scale.

Appendix 2: The methodology of the petrographic analysis and tables with all descriptions and quantitative percentages of the components.

Appendix 3: Stable isotope data (carbon, oxygen and strontium) and trace elements.

Appendix 4: Tabulation of cycle thickness data.

2 Review and geological background of the Permo-Carboniferous of Mid-Pangea: Correlations between east and west Pangea.

2.1 Introduction

Earth history has been marked by significant events and especially in the Permo-Carboniferous these played an important role with the formation of the supercontinent Pangea. Extensive sedimentary basins were created and Pangea had a major influence on global climate and the evolution and extinction of many species. There has been much documentation of some basins, such as the Delaware and Midland basins in the southern USA, whereas there are others, such as those in Colombia and Venezuela where the Permo-Carboniferous strata are poorly known. In terms of this thesis on the Permian of Venezuela the first step was to understand the stratigraphic and tectonic context of successions within the Mucuchachi basin, where deposition took place.

This chapter is focused on a description of the regional stratigraphy of the equatorial Pangean basins where the Permian successions can be correlated and compared to the equivalent strata of the Palmarito Formation. Permian carbonates are major reservoirs in the southern USA so that one aspect of this thesis is to consider the potential petroleum system of the Palmarito which could be a target for oil and gas exploration in the future, as pointed out by Audemard and Serrano (2001).

2.2 Late Palaeozoic stratigraphy

2.2.1 Carboniferous-Permian stratigraphy in Colombia.

The Permian stratigraphic record in Colombia has been poorly documented due to difficult access to exposures and the severe tectonic deformation. However, Upper Palaeozoic outcrops do exist throughout the country and these have been described by several authors (e.g. Trompy, 1943; Forero, 1967; Villarroel and Mojica, 1987) and by the Colombian

Geological Survey (INGEOMINAS) in its mapping projects (Arias and Morales, 1999; Velandria et al., 2001a; Velandria et al., 2001b; Ferreira et al., 2002; Hernandez, 2003). The location of outcrops and stratigraphic logs of the strata have been summarized by Villarroel and Mojica (1987) (Figure 2.1 and 2.2), from the two main mountain ranges in Colombia (the Eastern Cordillera and Perija Mountains). The petroleum potential of these rocks in Colombia is unknown. However, colleagues have mentioned the interest of several oil companies in exploring these horizons in the Llanos Basin (Wahlman, 2011 personal comm.).

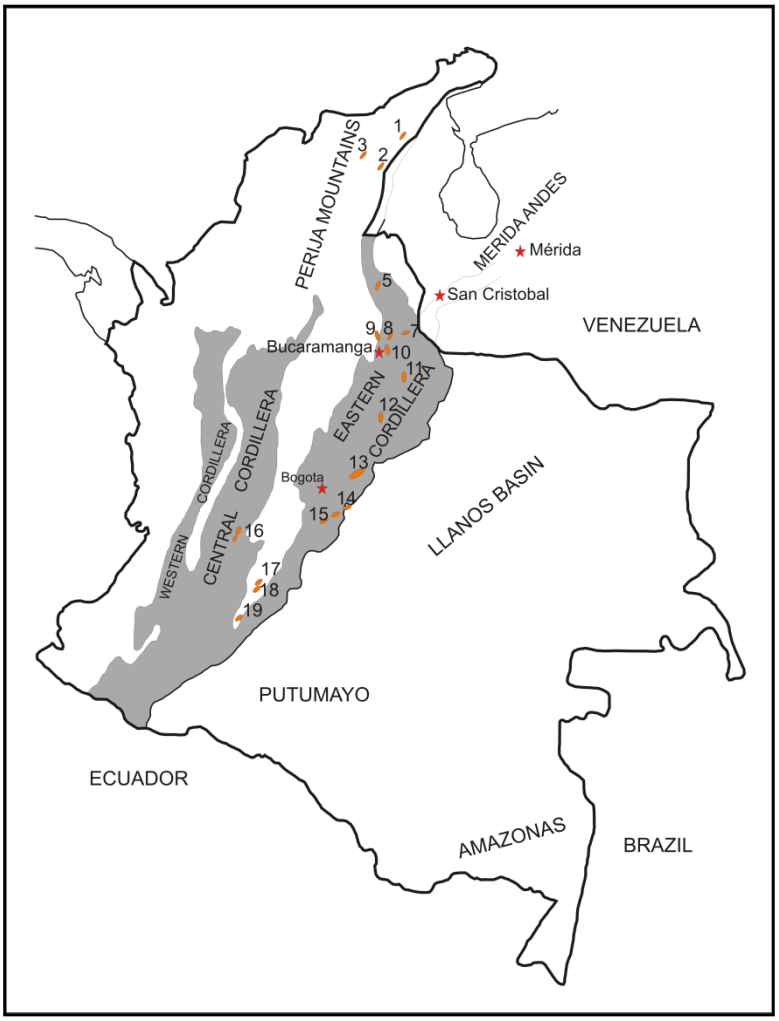

Figure 2.1. Location map of Late Palaeozoic successions in Colombia. Numbers correspond to the location of the schematic logs in Figure 2.2 After Villarroel and Mojica (1987).

According to Villarroel and Mojica's (1987) summary, the principal Upper Palaeozoic strata are represented by 10 different successions but just 3 of them correlate with Venezuelan Permian rocks; these are the sections in the Manaure area (2 on Figure 2,1),

Teorama-Calixto area (5) and Bucaramanga area (10) (Figures 2.1 and 2.2). The rest of the sections are restricted to the Devonian and Carboniferous. However, some sections, including Rio Seco, Rio Névado, Lobateca and SSE Garzón are not very well defined biostratigraphically and it appears there is some latitude for re-interpretation and potential correlation with the Venezuelan succession.

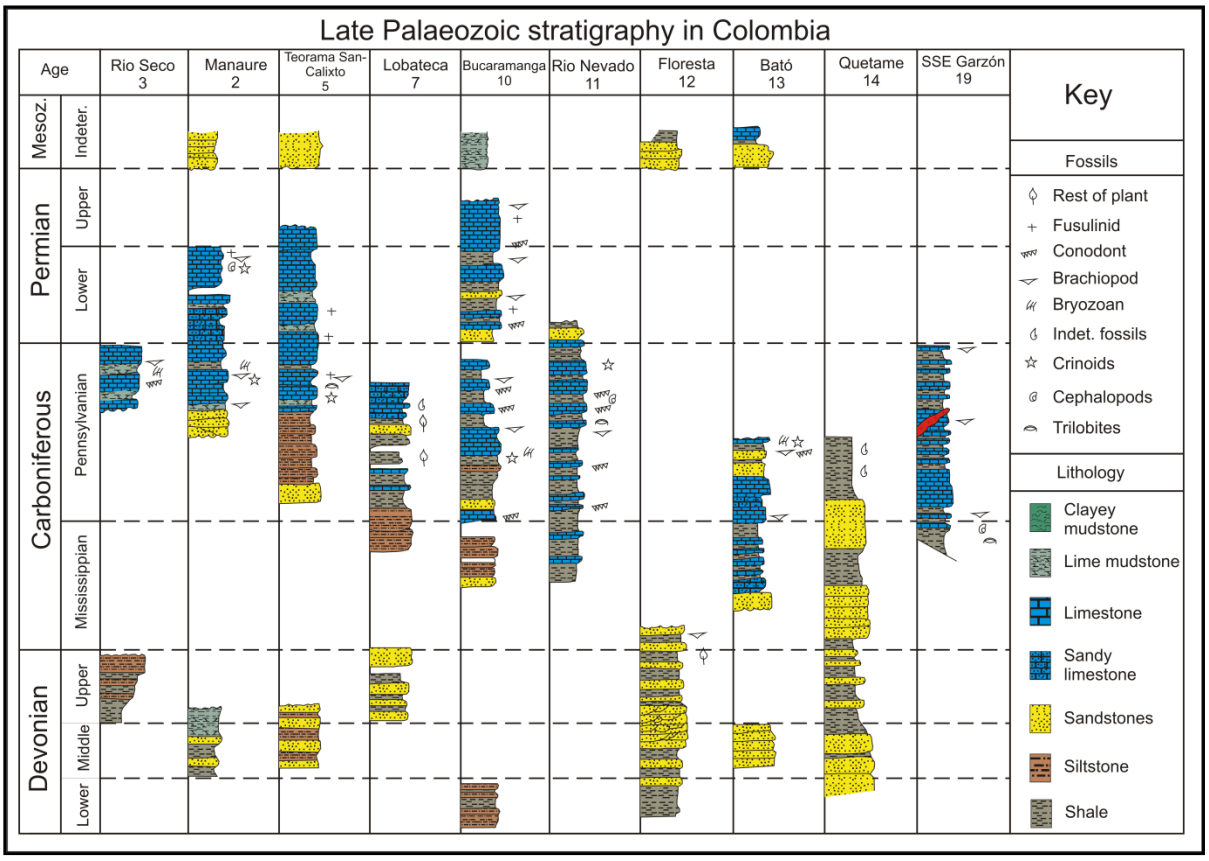

Figure 2.2. Schematic logs of Late Palaeozoic successions in Colombia. Log numbers correspond with the location map in Figure 2.1. After Villarroel and Mojica (1987).

The lithology of these successions is mixed with sandstones, siltstones, shale and thick black-greyish limestones with abundant fossils including brachiopods, bryozoans, crinoids, foraminifera and gastropods. These rocks represent a marine mixed carbonate-clastic platform, which can possibly be correlated with the same transgressive event which was responsible for the Palmarito deposits, and they were also deposited under a similar tectonic regime.

2.2.2 Late Palaeozoic stratigraphy in Brazilian basins

The Solimões and Amazonas basins are located in the middle of the Amazon rain-forest in northern Brazil. Together they comprise an impressive intracratonic basin 2500 km long, 500 km wide and up to 5000 m deep (Milani and Zalán, 1999). The boundary between the Solimões and Amazonas basins is a structural high called the Purus flexural arch that controlled deposition until the Carboniferous.

The Solimões Basin has an extent of 600,000 km^2 with 400,000 km^2 corresponding to the area of Palaeozoic deposition (Figure 2.3). The sedimentary cover occurs on the Precambrian Guyana shield and six supersequences have been described from here with four of them corresponding to the Palaeozoic, one to the Cretaceous and the most recent to early Cenozoic to Recent. The Permo-Carboniferous strata are the Jurúa, Carauri and Fonte Boa formations, which are formed of siliciclastic, carbonate and evaporitic rocks (Milani and Zalán, 1999; Azcuy et al., 2007). The Jurua Formation consists of aeolian sandstones which grade up into carbonate-evaporite cycles of the Carauri Formation (1300m thick). Finally, the Fonte Boa Formation consists of fluvial and lacustrine red-bed sandstones and siltstones.

The petroleum system for the Solimões basin is comprised of Devonian Jandiatuba, Jaraqui and Ueré formations as source rock, which contains up to 8% TOC. The aeolian sandstones of the Juruá Formation are the main reservoir with porosities reaching 22% due to primary intergranular porosity and secondary porosity from dissolution of calcite and anhydrite cements. The critical event was Triassic-Jurassic magmatism which had an important thermal influence on the maturation, expulsion and migration of the hydrocarbons (Milani and Zalán, 1999).

The Amazonas basin is 500,000 km^2 in extent with three Palaeozoic supersequences filling the basin, later covered by Cretaceous to recent continental clastics (Milani and Zalán, 1999; Azcuy et al., 2007). The lower-most Permo-Carboniferous sequence is the Monte

Alegre Formation which shows similarities to the Jurúa Fm, with aeolian deposits passing upwards to a carbonate-evaporite succession of the Itaituba and Nova Olinda formations. Finally the upper-most sequence is the Andirá Formation which shows continental red-beds in the Middle Permian (Milani and Zalán, 1999; Azcuy et al., 2007; Matsuda, 2002) (Figure 2.3 and 2.4).

The Amazonas Basin is similar to the Solimões in its petroleum system with Devonian black shales (Barreirinha Formation) interpreted as the source rock, as in the Solimões, with the main reservoirs located in the Late Carboniferous Monte Alegre and Nova Olinda formations, laterally correlative to the productive rocks in Solimões. Triassic-Jurassic magmatic events were responsible for hydrocarbon maturation, expulsion and migration in the basin (Milani and Zalán, 1999) (Figure 2.4).

Although similar Permo-Carboniferous successions are present in the Solimões and Amazonas basins, the Palmarito Formation seems to be younger than the Carauri, Itaituba and Nova Olinda formations. Probably, the upper-most Fonte Boa and Andirá formations can be correlated to the Sabaneta Formation or the base of the Palmarito, which contains tidal-flat deposits rich in siliciclastics.

The Parnaiba basin is located in eastern central Brazil with an ellipsoidal shape that covers 600,000 km^2 (Figure 2.3). This basin is limited to the northeast by the Ferrer-Urbano Santos arch which separates this depression from the open Atlantic Ocean. However, for the Palaeozoic the stratigraphic record has equivalents in West Africa basins.

The sedimentary record for the Permo-Carboniferous in the Parnaiba Basin is formed by clastics, evaporites and carbonates with four main formations within the Balsas Group. First, the Piauí Formation comprises sandstones, brown shales and several limestone units which pass upwards into rhythmites with alternating oolitic limestones and anhydrite of the Pedra de Fogo Formation. Above this, brown siltstones, sandstones and anhydrites comprise

the Motuca Formation. Finally, aeolian sandstones of the Sambaíba Formation complete the cycle (Milani and Zalán, 1999) (Figure 2.4).

The petroleum potential of this basin is restricted to the Devonian (Pimenteiras Formation) which is formed of black shale and is a potential source rock. This source rock is directly in contact with the main reservoirs of deltaic-shallow-marine sandstones of the Cabeças Formation (Milani and Zalán, 1999) (Figure 2.4).

The Paraná Basin is an extensive depositional area which covers 1,000,000 km^2; in fact, this basin is not restricted to Brazil but extends to Paraguay, Argentina and Uruguay. The strata that accumulated in this basin reached 7000 m thick. Six major supersequences have been recognized with three of them ascribed to the Palaeozoic. Gondwana Supersequence I was developed during Permo-Carboniferous time, represented by the Tubarão and Passa Dois groups, which are formed of the Itararé Subgroup and Río Bonito and Palermo formations, and the Irati, Serra Alta, Teresina and Rio do Rasto formations, respectively (Milani and Zalán, 1999; Azcuy et al., 2007; Spadini, 2008). The Tubarão Group was deposited under glacial conditions and consists of diamictites and sandstones up to 1500 m thick. The Passa Dois Group represents a major marine transgression where the most representative unit is the Irati Formation that is formed of bituminous shale, limestones and evaporites (Spadini, 2008). The Irati Formation is chronostratigraphically correlative to the Palmarito Formation. The Permo-Carboniferous supersequence ends with red-bed deposits of the Rio do Rasto Formation (Figure 2.4).

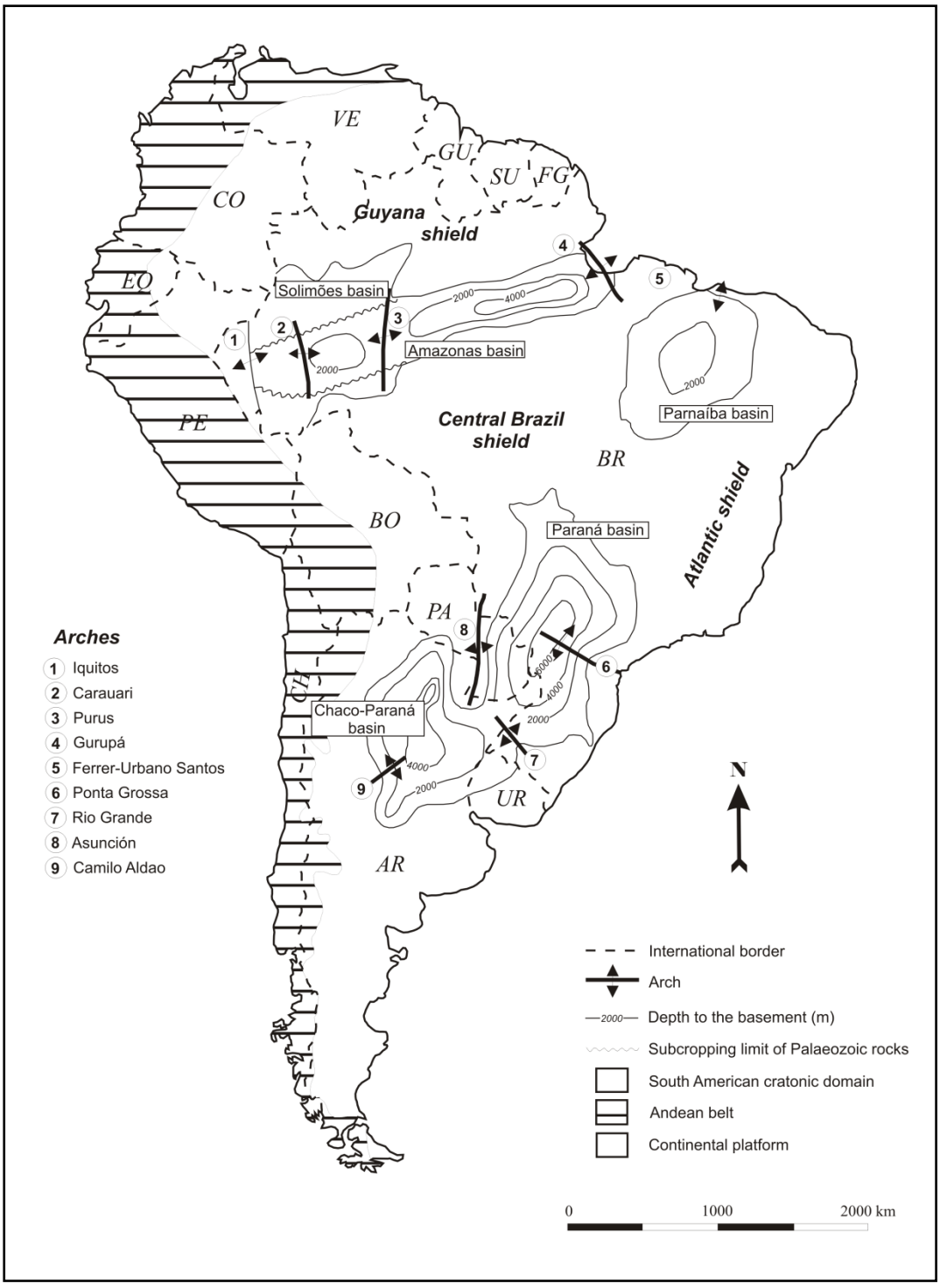

Figure 2.3. Location map of Brazilian intracratonic basins. FG–French Guyana, SU–Suriname, GU–Guyana, VE–Venezuela, CO–Colombia, EQ–Equator, PE–Perú, BO–Bolivia, CH–-Chile, AR–Argentina, PA–Paraguay, UR–Uruguay, and BR–Brazil. After Milani and Zalán (1999).

Two different petroleum systems have been distinguished. First, Devonian black shales of the Ponta Grossa Formation are source rocks which produce the hydrocarbons that later entered the glaciogenic sandstones of the Itararé Group and coastal sandstones of the

Rio Bonito Formation reservoirs (Milani and Zalán, 1999). Second, organic-rich shale of the Iratí Formation generated oil which also became reservoirs in the Rio Bonito Formation.

The Chaco-Paraná Basin is the southern-most of the Permian basins in South America occurring in Brazil, Argentina and Uruguay. The sedimentary record was directly influenced by the Gondwanan glaciation during the Late Palaeozoic. For this reason, deposits are mostly sandstones, diamictites and tillites, with some shales and siltstones, all mainly deposited under glacial-periglacial conditions with thicknesses reaching 2500 m (Milani and Zalán, 1999) (Figure 2.4).

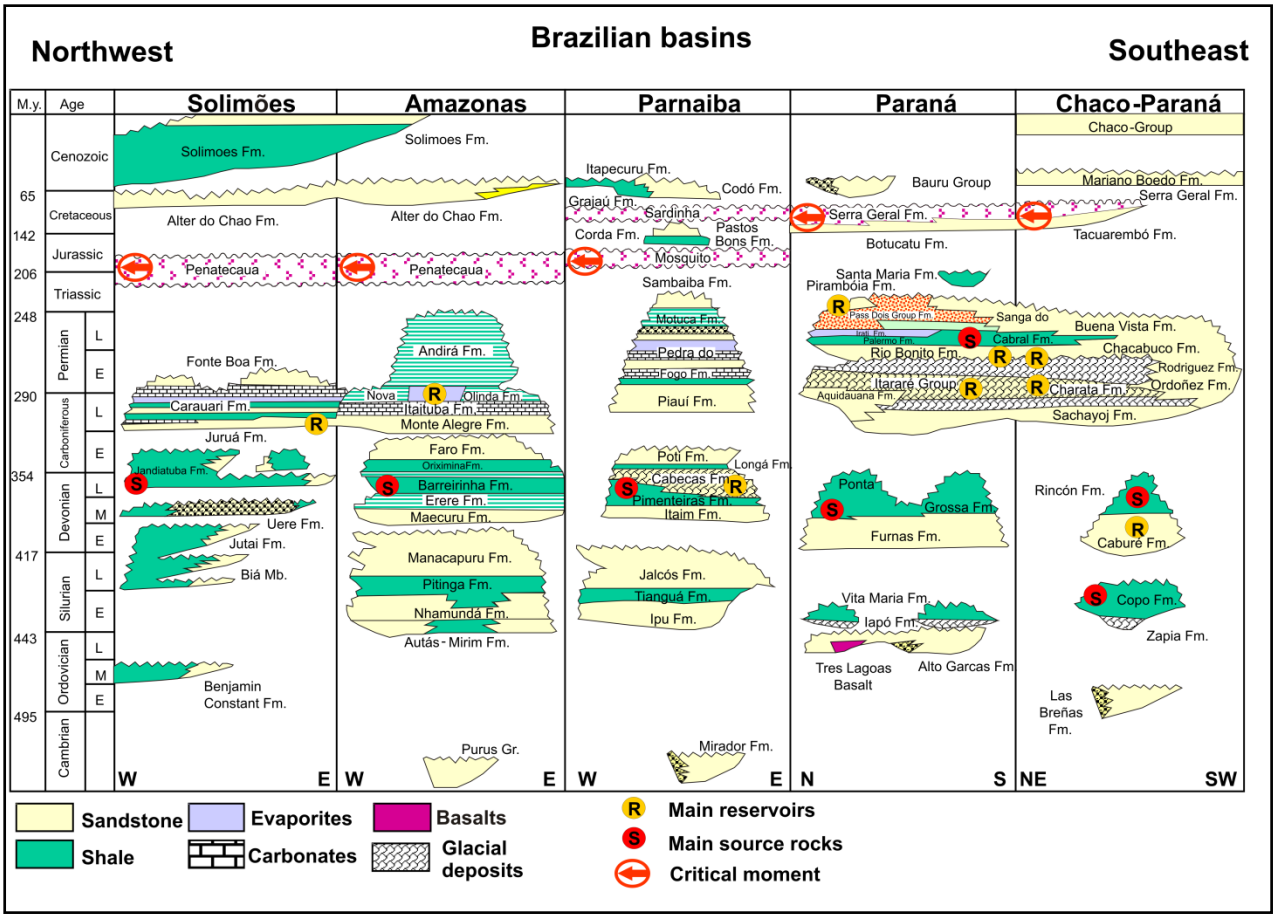

Figure 2.4. Correlation panel and lithostratigraphy of Brazilian basins. After Milani and Zalán (1999) .

2.2.3 Late Permian strata in Ecuador-Perú and Bolivia.

According to Hoover (1976), there are Upper Palaeozoic sections in south Columbia which belong to the Mucuma Formation. These successions are well-known in the mountains

of Cutucú, south of Quito, Ecuador Hoover (1976), These rocks contain a Pennsylvanian fauna that includes brachiopods, bryozoans and crinoids which have been found in the lower part of the formation; foraminifera indicate a Pennsylvanian age. In addition, in the Madre de Dios Basin there are Late Palaeozoic strata. This is a foreland basin located between southeastern Perú, northern Bolivia and Brazil which extends for 43,000 km^2 and contains 5000 m of sedimentary fill. This basin is limited by the Iquitos Arch to the northeast and the Fitzcarrald Arch to the north. One of the most important successions within the basin is the Titicaca Group or El Cuervo megasequence (Grader et al., 2003) of Permo-Carboniferous age that is comprised of the Tarma and Copacabana formations overlain by the Cangapi Formation in some regions (Figure 2.5). These stratigraphic units are formed by sandstones, siltstones and anhydrite at the base passing upwards to muddy limestones and dolomites. In addition, the Copacabana Formation contains dark organic-rich mudstones with source rock characteristics with TOC up to 9 wt% (Baby et al., 1995; Petroperú, 2002).

Grader et al. (2007) discussed the stratigraphy and palaeoclimate of the Late Palaeozoic in Bolivia and proposed a transition from cold to warm-water deposits of the Titicaca Group, based on the variation of marine limestone palaeoecology, resulting from plate movement northward of the Perú-Bolivian basins. The age of the Titicaca Group is ascribed to Bashkirian (Early Pennsylvanian) to Artinskian (Early Permian) (Wood et al., 2002). The uppermost member of the Copacabana Formation can be correlated with Palmarito strata to the north, and it may well have been connected through a seaway with a link to circulation in central Pangea (Figure 2.5).

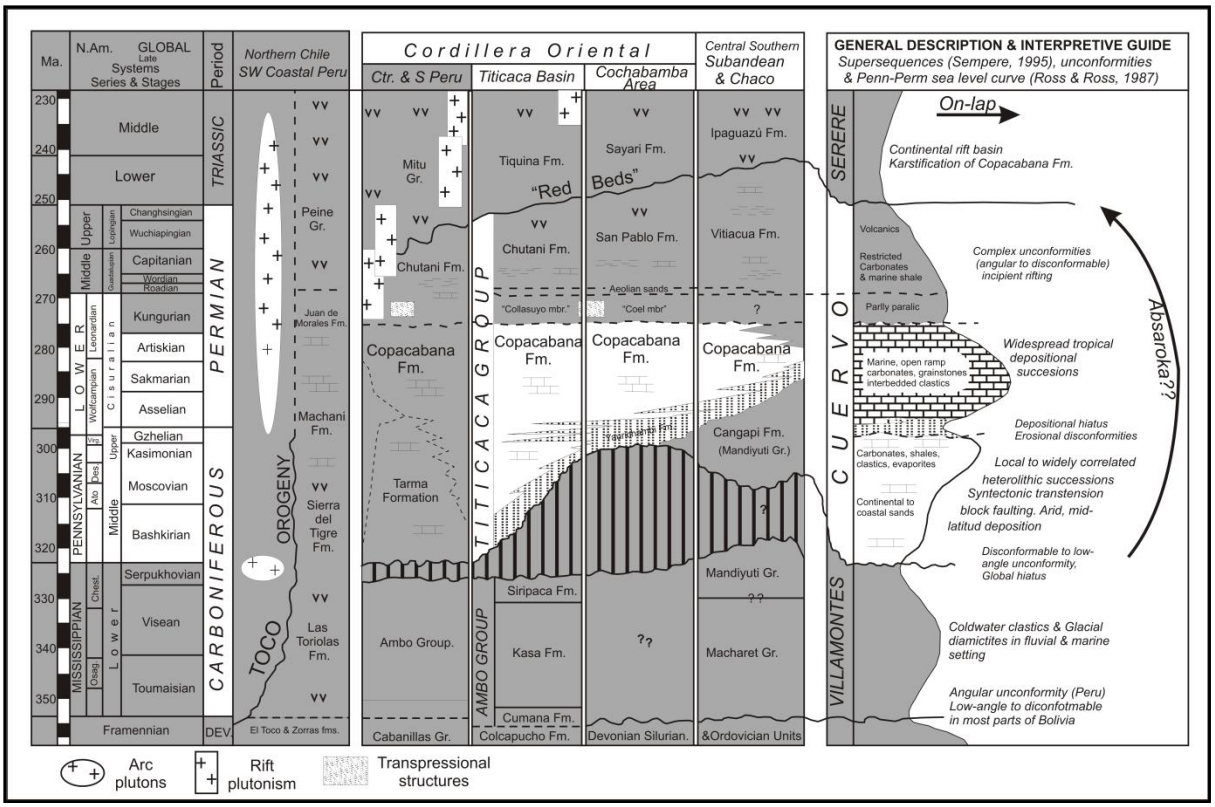

Figure 2.5. Correlation panel of the Late Palaeozoic in Bolivia and Perú areas (Grader et al., 2003).

2.2.4 México, Guatemala and Belize.

In the northwest of South America there are outcrops of Late Palaeozoic strata in Guatemala-Belize and México where the complex tectonic regime during Permian times was related to a microterrane moving with Laurentia and Gondwana to give a quite complicated stratigraphy (Figure 2.6). However, stratigraphic units can be correlated on the basis of fusulinid and other marine fossil biostratigraphy from Late Pennsylvanian to Late Permian. Marine deposits are widespread from the north of México in the Sonora area throughout the whole country, with extensive deposits especially of the period between the Kungurian and Capitanian.

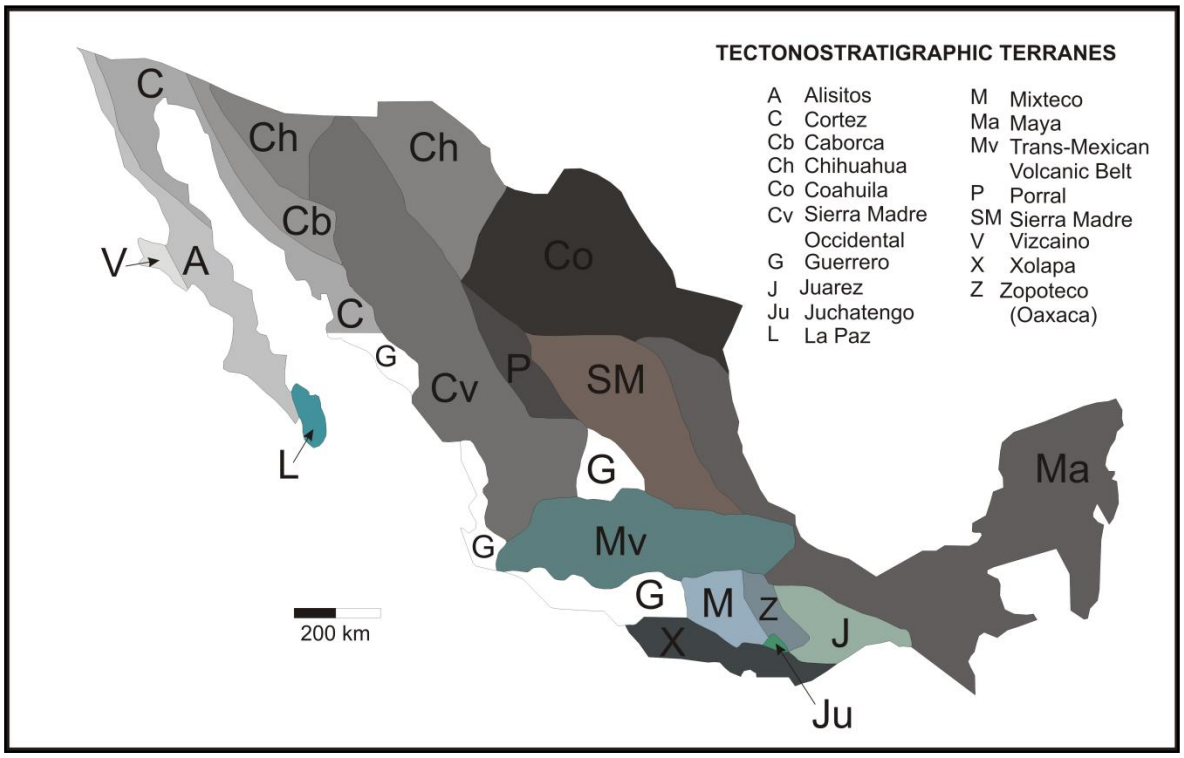

Figure 2.6. Tectonostratigraphic terranes and microplate assemblage in México. Vachard et al. (2004).

In Guatemala and Belize, Late Palaeozoic deposits comprise the Santa Rosa Group which is formed of the Tactic, Esperanza and Chochal limestone (Hoover, 1981; Vachard and Fourcade, 1996) (Figure 2.7). These units contain fossiliferous limestones and shales with brachiopods and fusulinids. The age of the successions is between the Late Pennsylvanian (Wolfcampian) and Roadian. Farther north, the stratigraphy becomes more complicated due to the distribution of the microterranes including the Mixteco and Oaxaca, where the most representative Permian strata have been recorded.

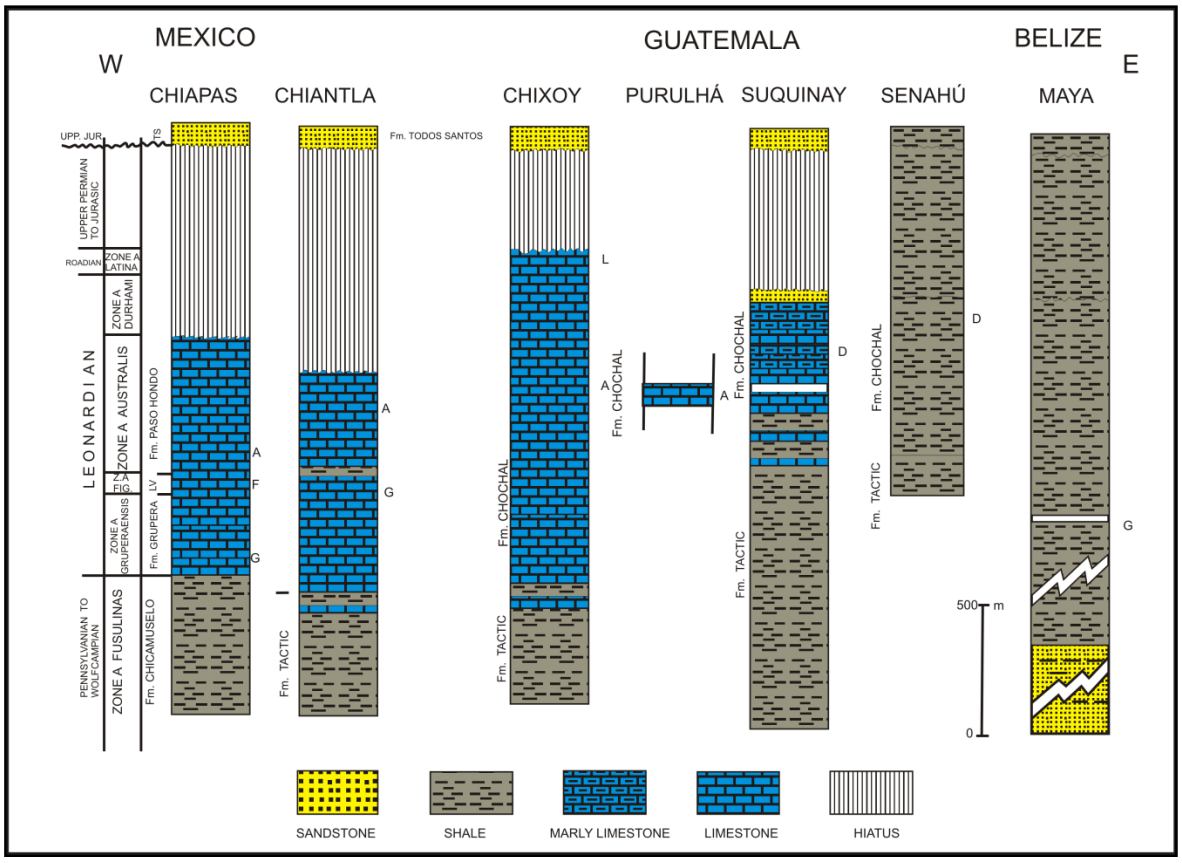

Figure 2.7. Schematic log of successions in southern México, Guatemala and Belize from Vachard and Fourcade (1996).

The Late Palaeozoic Mixteco terrane is formed of the Patlanoaya, Matzizi, Los Hornos, Ihualtepec and Olinala formations which extend from the Late Carboniferous to Late Permian (Vachard and Fourcade, 1996; Silva-Pineda et al., 2003) (Figure 2.8). The Patlanoaya Formation has the longest stratigraphic record, being deposited from the Pennsylvanian to the Middle Permian, and contains coastal sandstone, siltstone, limestone and mixed facies of clayey sandy limestone (Vasquez-Echeverria, 1986; Silva-Pineda et al., 2003). The fauna present in this stratigraphic unit includes algae, small foraminifera and fusulinids, as well as plant remains (Brummer, 1987; Vachard et al., 2000) which support the age determination. The Los Hornos Fm. can be associated with the Ihualtepec Fm. according to Vachard et al. (2004) which is formed of marine sandstones, fossiliferous limestones and black shales restricted to the Early-Middle Permian. Carbonates of the Los Hornos and Ihualtepec formations are formed of gastropods, echinoderms, bivalves, bryozoans, fusulinids

and crinoids. The Matzizi Formation consists of sandstones which interfinger with shale and conglomerate within which there is a well-preserved Late Pennsylvanian flora which was described by Silva-Pineda (1970). Finally, the Olinalá Formation contains megaconglomerate, black shales and limestones with brachiopods, ammonoids and stromatolitic buildups. According to Silva-Pineda et al. (2003) this stratigraphic unit is ascribed to the Wordian to Capitanian. However, Vachard et al. (2004) proposed a younger age, perhaps covering the P/T boundary.

The Oaxaca terrane consists of Late Palaeozoic strata comprising the Matzizi, Ixtaltepec and Guacamaya formations. These strata are correlative to units in the Mixteco terrane where the Matzizi consists of more continental clastic deposits and the Ixtaltepec and Guacamaya formations are marine carbonate successions with a similar fossiliferous content.

Late Palaeozoic strata in México and Guatemala show a general transgressive trend from the Carboniferous to Middle Permian. On the other hand, a regressive excursion towards the Upper Permian can be recognized. The transgressive trend is correlative to a similar event in the Mucuchachi Basin (Laya and Tucker, 2012) and this is probably associated with a sea-level fluctuation within the same inland sea.

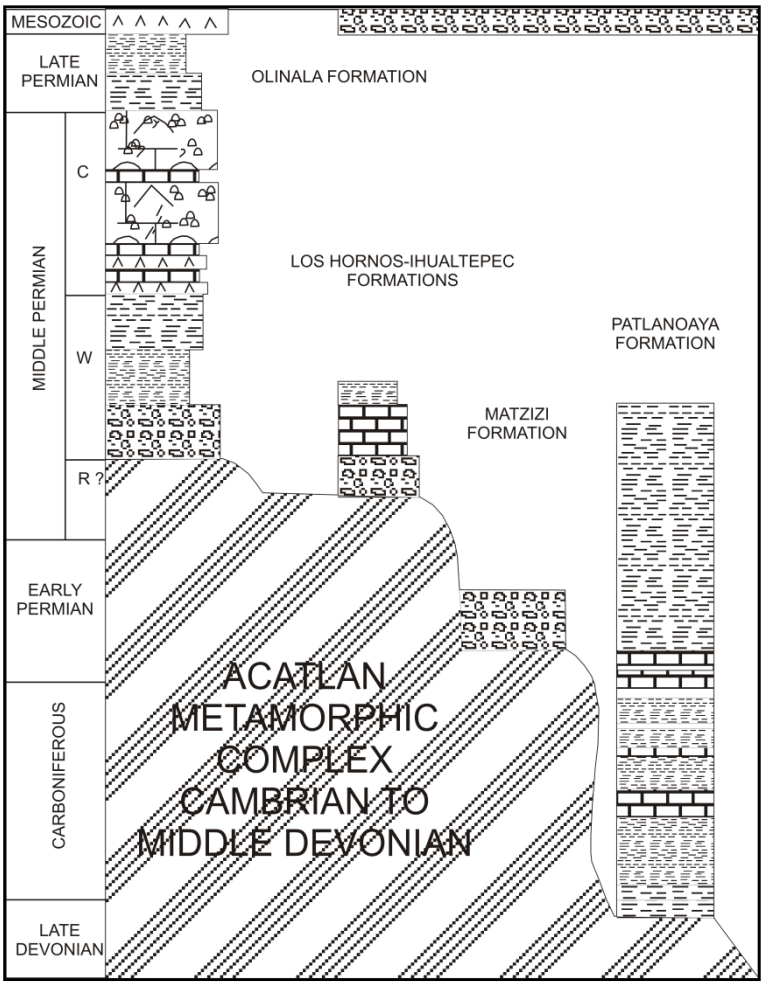

Figure 2.8 Schematic logs of Permo-Carboniferous successions of the Mixteco terrane (Vachard et al., 2004).

2.2.5 Southern basins of USA.

The Permian geological record of the southern USA has been very well studied in every aspect as a result of the highly significant petroleum production since the late 1800s. Late Palaeozoic strata in all these basins show a complex stratigraphy with vertical and lateral changes controlled by sea-level, tectonics and climate.

Blakey (2008) presented an overview of Pennsylvanian through Middle Jurassic stratigraphy and palaeogeography of basins on the Colorado Plateau and in the southern Rocky Mountains and summarized the controls on deposition in the region (Figure 2.9). Blakey's overview gave a re-interpretation of the sequence stratigraphy and identified nine sequences with clear sequence boundaries which followed the pattern established by Ross

(1973), Blakey and Knepp (1989), Blakey (1996) and Trexler et al. (2004). In terms of this Palmarito study and correlation, there are four of the nine sequences restricted to the Permian and these include the Wolfcampian, Lower Leonardian and Upper Leonardian sequences, as well as the Guadalupe sequence and younger Permian rocks (Figure 2.10).

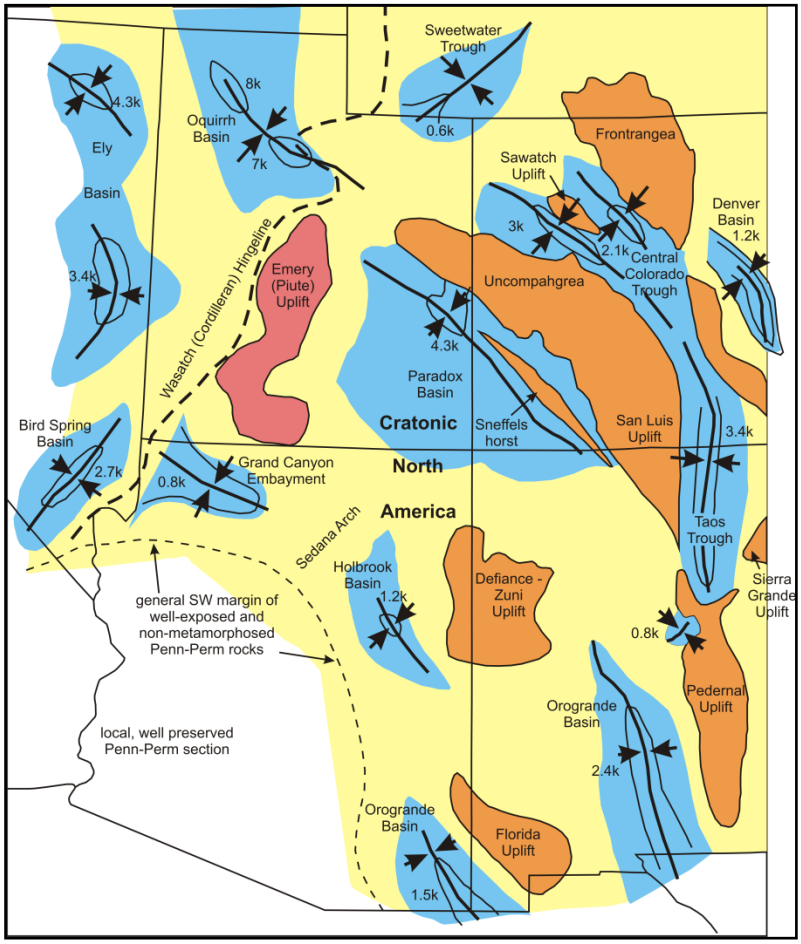

Figure 2.9 Summary map of Pennsylvanian and Permian basins and areas of uplift and other features of the Colorado Plateau and Western Interior (Blakey, 2008).

The Wolfcampian sequence is comprised of mixed lithologies that are a response to their complex tectonic and topographic setting. These strata occur upon a Virgilian sequence, separated by the Pennsylvanian-Permian boundary that is recognized as a regional unconformity.

The Wolfcampian sequence contains thick arkosic fluvial sandstones concentrated in the eastern part of the Paradox Basin (Campbell, 1980; Mack and Rasmussen, 1984); aeolian

facies are widespread through the area and in western Utah and Nevada carbonates interfinger with the last two facies.

Lower Leordanian strata are not evenly distributed but show substantial thickness variations with up to 600 m of aeolian sandstones and red mudstones, restricted marine and sabkha deposits in the Denver, Orogrande and Hallbrook basins (Blakey et al., 1988; Blakey, 1990) and 1000 m of carbonates intercalated with quartzitic sandstones located in western Utah and Nevada. Across most of the central part of the region this sequence is absent (Bissell, 1970). The uppermost part of the sequence is formed by the widespread Coconino-Glorieta aeolian complex.

The Upper Leonardian is comprised of marine deposits of the Toroweap Formation that is coeval with aeolian facies (Chan, 1989). In addition, thin evaporites appear in the Grand Canyon region (Rawson and Turner-Peterson, 1980). All of these deposits represent a general transgressive-regressive cycle across the region.

The Guadalupe sequence and younger Permian rocks are present in western and southeast parts of the Colorado Plateau and comprise shallow-marine limestones and sandy dolomites with a thickness up to 200 m. These deposits are ascribed to the last major transgressive-regressive cycle during the Permian (Blakey, 1996).

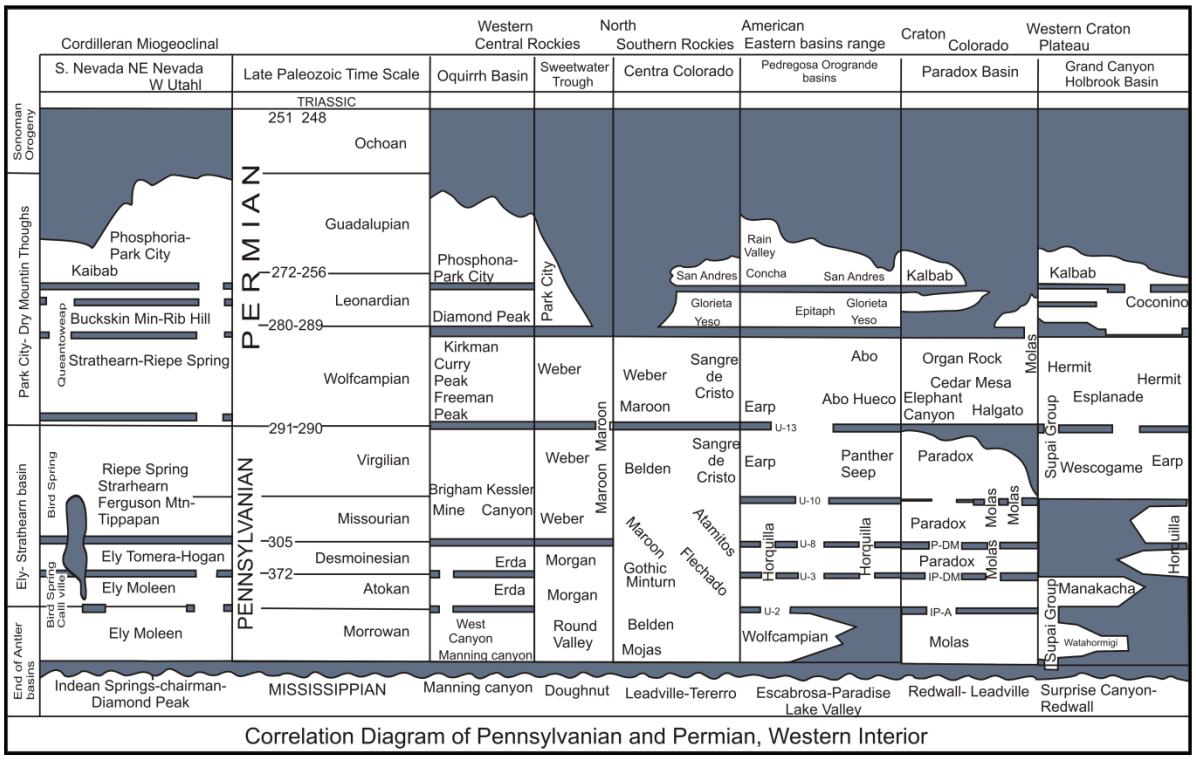

Figure 2.10. Pennsylvanian-Permian stratigraphic diagram of the US Western Interior (Blakey, 2008).

South and southeast of the Colorado plateau there are the Southern Midcontinent, Permian Basin and Ouachitas Basin and Uplift systems. This region comprises the southern margin of the Laurentian craton that was the opposite margin of Gondwana, separated only by a remnant of the Rheic Ocean. According to Scotese (1995, 1999), Blakey (2006), Miall (2008), and Miall and Blakey (2008) the collision between Gondwana and Laurentia started in the Mid-Mississippian and ended in the early Permian with a transpressive tectonic regime that lead to the Ouachita-Marathon orogeny and this closed the remnant sea-way of the Rheic Ocean. This collision resulted in a series of basins and uplifts in the area of which the best-known are the Delaware basin, Central Basin Platform, Midland Basin, as well as the Ouachitan foreland basins (Val Verde, Forth Worth and Anadarko basins, Figure 2.11). The stratigraphy can be seen in Figure 2.12.

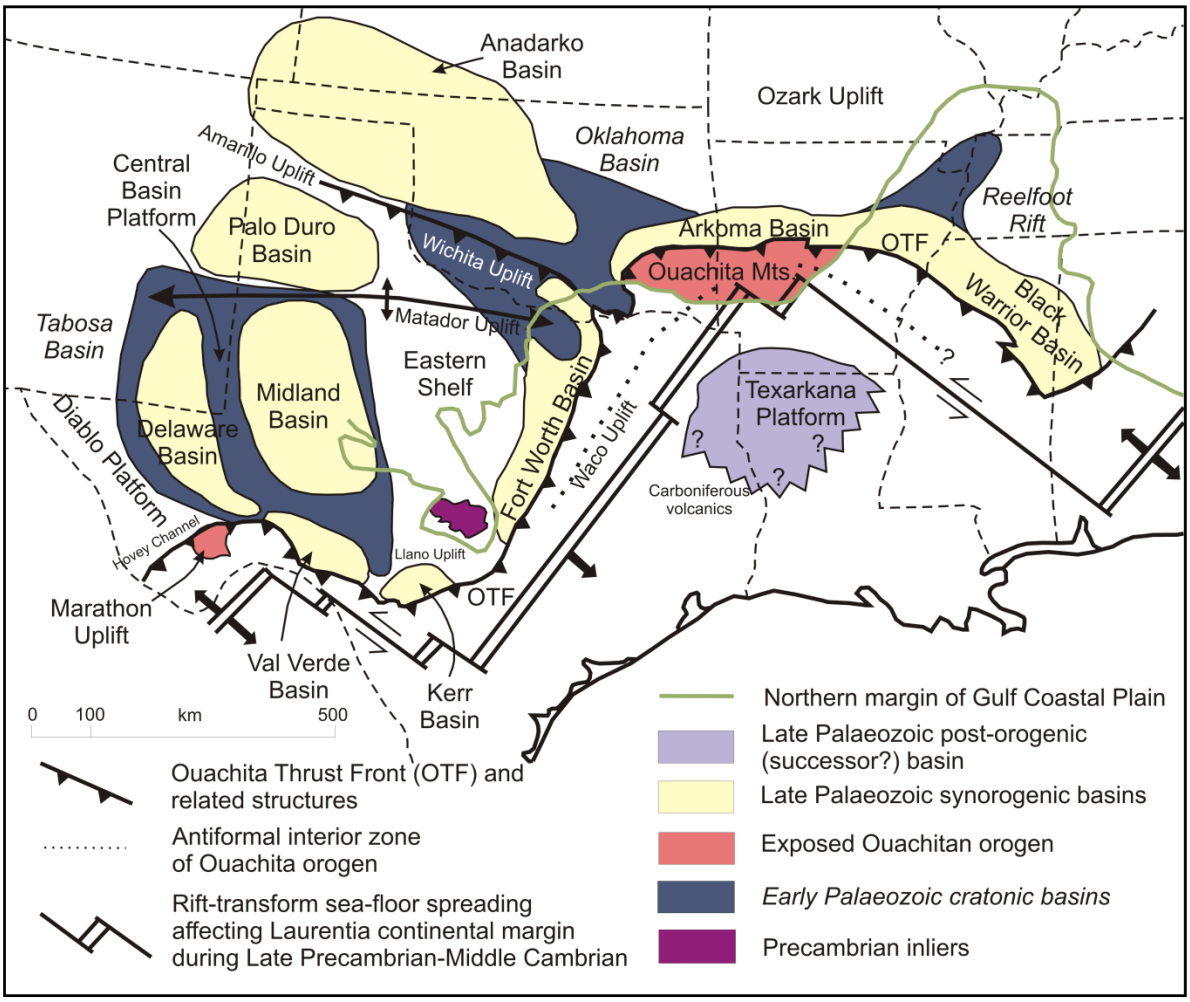

Figure 2.11 Map showing the occurrence of sedimentary basins in the Southwestern USA and their tectonic context (Miall, 2008).

The very well-developed cyclicity present in the Late Palaeozoic strata in the southern basins of the USA is a characteristic feature of depositional systems of this age. These cycles are the result of the high-frequency sea-level and climate changes of the time. The cycle types change from the northeast with repetitive clastic coastal facies to the southwest with mainly carbonates, and to distal deep-water deposits in the Delaware and Midland basins. These changes are due to the source of clastic sediments being from the active Alleghenian Orogeny.

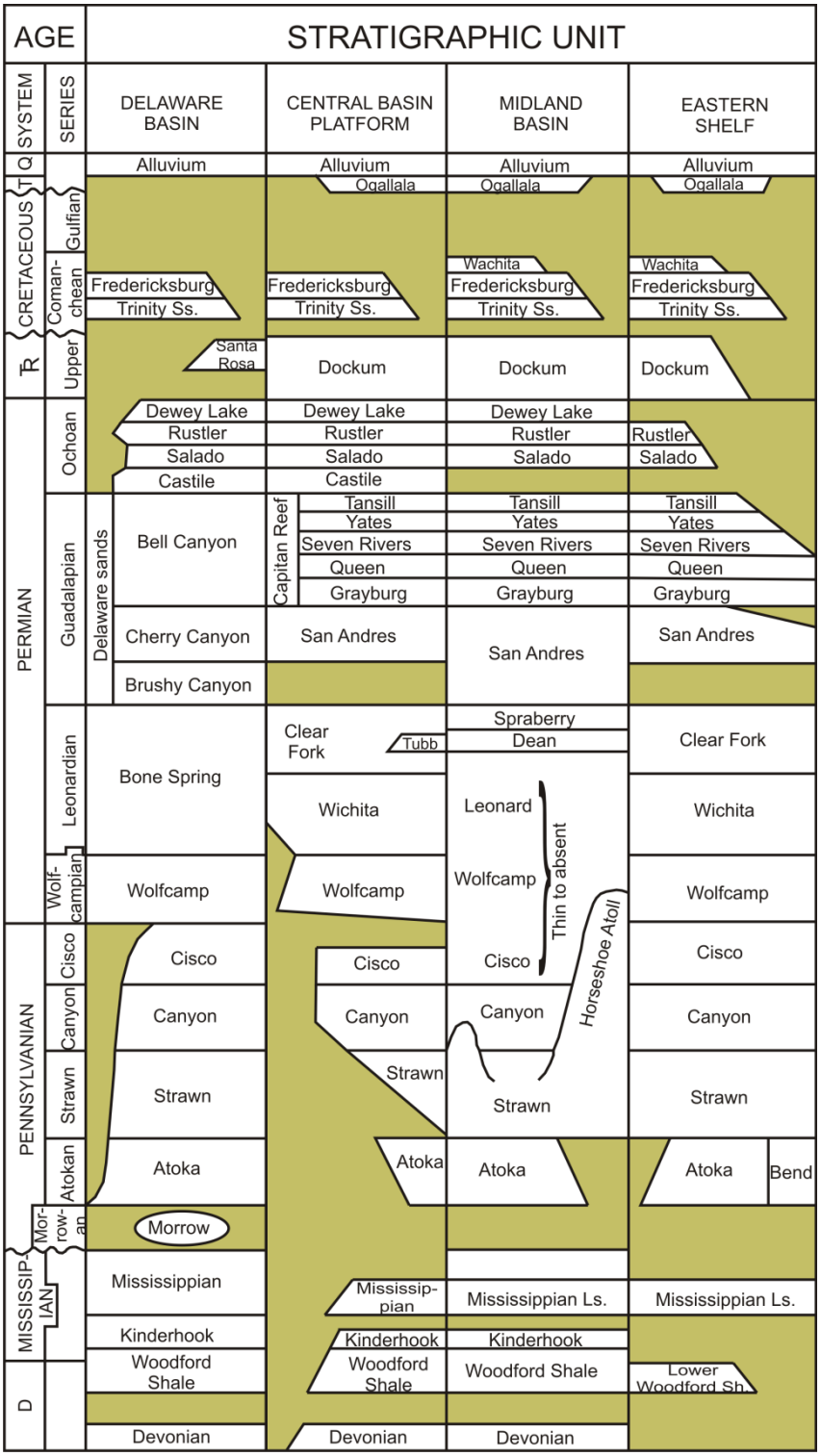

Figure 2.12. Stratigraphic columns for the main basins and platforms of the Permian basin area (Slightly modified from the U.S. Geological Survey digital data source DDS-36; 1996; see Scholle, 1996).

The Capitan Reef in the Permian Basin is the best-known part of the southern USA stratigraphy due to the superb exposures in the Guadalupe Mountains. From the north to the south the carbonate shelf was established; however the clastic influence was quite strong,

represented by coastal-fluvial red-beds of the Abo Formation that pass laterally to the south into fine-grained dolomites with peloids, oncoids, foraminifera, stromatolites and tepees that were deposited in the coastal, locally hypersaline San Andres Formation (Miall, 2008) (Figure 2.13).

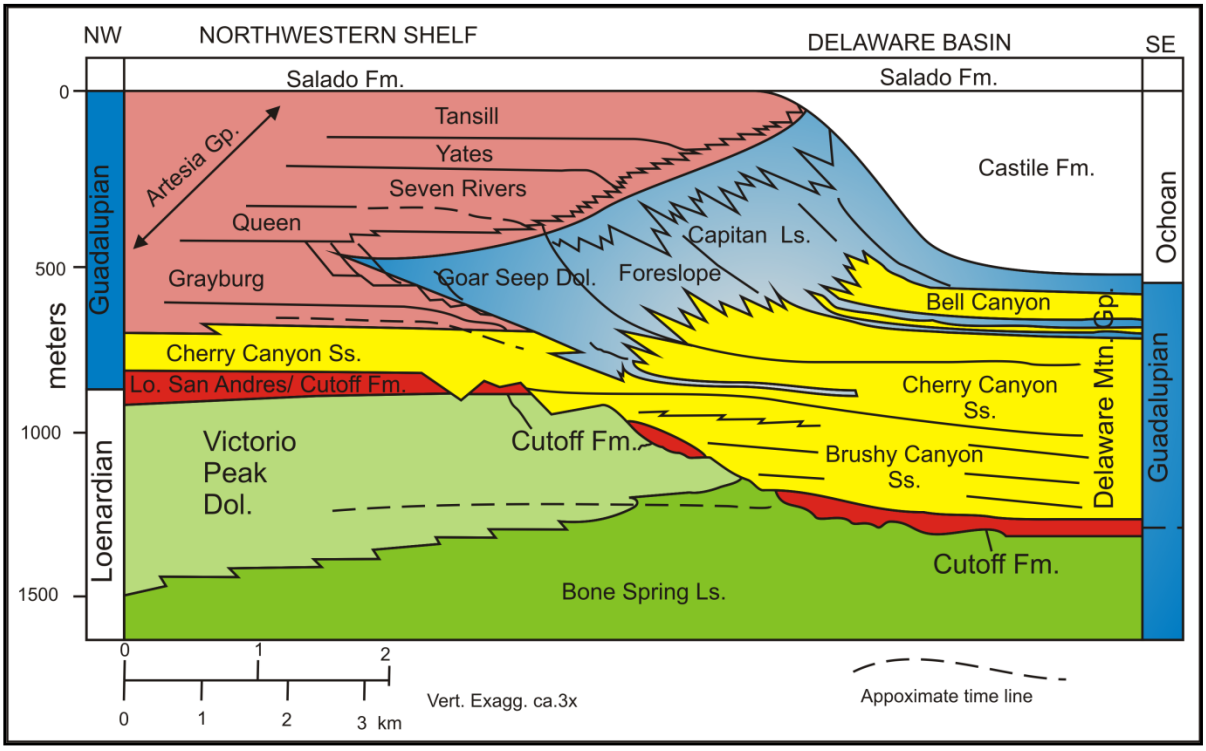

Figure 2.13. Schematic diagram of the stratigraphy in the Guadalupe Mountains (Scholle, 2006).

The platform margin and reef complex are very well developed with a range of carbonate facies including grainstone, packstone, wackestone and some algal boundstone. These rocks are formed by several bioclast types including fusulinids, gastropods and algae. The facies pass laterally basinward to the reef itself which comprises the Goat Seep Dolomite and overlying Capitan Limestone which contains an organic framework of phylloid algae, calcareous sponges, bryozoans encrusted with the red alga *Archaeolithoporella* and T*ubiphytes* (Wood et al., 1996; Wahlman, 2002.); echinoderms, brachiopods, molluscs, ostracods and solitary corals also occur. This reefal shelf margin acted as a barrier for the platform interior deposits which are formed by cyclic successions of the Seven Rivers, Yates and Tansill formations with tepees, microbialites and fenestral limestones (Mruk et al., 1993;

Tinker, 1998). The front of the reef passes to a steep slope of approximately 35°, decreasing basinward, and this is formed of carbonate debrites and turbidites, locally with clastic channel-fills with huge blocks representing different stages of landslides (Tinker, 1998; Scholle, 2006; Miall, 2008). These pass laterally to the bottom of the slope which is comprised of thin limestones (Lamar, Manzanita, McCombs, Rader, Pinery and Hegler formations), interbedded with siliciclastic deposits of channel, levee and turbidite facies, locally with synsedimentary deformation. The final clastic deposits in the basin belong to the Bell Canyon Formation and this reduces in thickness basinwards where it is succeeded by the evaporite successions of the Castile and El Salado formations, which filled the basin.

Evaporites are typical from Leonardian times (Artinskian-Kungurian) since the marine circulation in the basins was restricted through the Hovey channel; connection became more limited during the lowstands in the early Permian due to the maximum glaciation and associated sea-level fall at this time. The evaporite sediments are more frequent to the north and east in areas of very shallow-marine lagoons and sabkhas (Leonardanian-Guadalupian times). In the Delaware basin, cycles of anhydrite, halite and sandstone were common in the Yates and Tansill formations. Over the Guadalupian marine strata widespread massive evaporite units were deposited due to the global sea-level fall and dominant arid climate, and these are represented by Castile laminated gypsum-anhydrite (Figure 2.14) and El Salado Formation (halite and non-marine red beds).

Figure 2.14 Castile Formation, Guadalupe Mountains. Courtesy of Maurice Tucker .

Petroleum and gas production in these basins has been very important in the last 100 years representing significant reserves for the United States, with the discovery of 91.6 million barrels of oil and 106 trillion cubic feet of gas in the Permian Basin (Miall, 2008). Guadalupian strata represent 66% of the reservoir units and most of the rest are of Leonadian-age. The evaporites are excellent seals in many cases. In addition, traps are a combination of structural and stratigraphic with the diagenesis of the carbonates playing an essential role in porosity-permeability development. The main source rocks are the organic-rich deep-sea sediments of the Bone Spring Formation. The economic potential of this rock can be extrapolated to new frontier areas of exploration.

The Mucuchachi Basin can be correlated with the southern basins of the USA since it was located on the opposite margin of the remnant sea and would have had some ocean connection. In addition, Wood et al. (2002) and Ricardi (2008) proposed biostratigraphic similarities between the faunas of South America and the southern basins of the USA, supporting this probable marine connection.

2.2.6 Peri-Tethys successions

East from Pangea, the Palaeo-Tethys Ocean developed with a wide carbonate platform and thick deep-water deposits that left a substantial stratigraphic record for Carboniferous to Permian time. Basins developed across many countries of Europe, North-Africa, the Middle East and Asia, with well-described strata from England, Wales, northern France, Germany, Spain and Portugal, where the marine record is restricted to the Carboniferous, with the exception of England, Germany and Poland where Late Permian (Zechstein) marine deposits developed (Davydov and Leven, 2003; Izart et al., 2003; Vai, 2003). Other well documented successions for the Carboniferous-Early Permian occur in Russia (Moscow basin, Urals), Ukraine (Donets Basin), Austria-Italy (Carnic Alps), Italy (Sicily), Greece, Yugoslavia, Turkey and Tunisia. Finally in Oman carbonate platform deposits restricted to the Permian were associated with the southern margin of Palaeo-Tethys (Davydov and Leven, 2003; Izart et al., 2003; Vai, 2003) (Figure 2.15). According to Vai (2003), the Palaeo-Tethys deposits in Tunisia could have been the nearest eastern carbonate strata to western basins including the Mucuchachi (Palmarito strata), and to the west Texas depositional areas which may contain evidence of a trans-Pangean seaway, temporarily open during the Early-Middle Permian. Farther east, Chinese basins recorded Tethyan open-marine deposits which comprise carbonates and siliciclastics deposited in isolated platforms (Izart et al., 2003).

Many of the basins named above do have a significant petroleum potential, especially the Oman Basin which has large volumes of oil and gas reported in Permian carbonate reservoirs that extend towards the Arabian Gulf area (Qatar and Saudi Arabia). These arguments could support exploration in areas of similar rock, for instance the Palmarito Formation in Venezuela and Colombia.

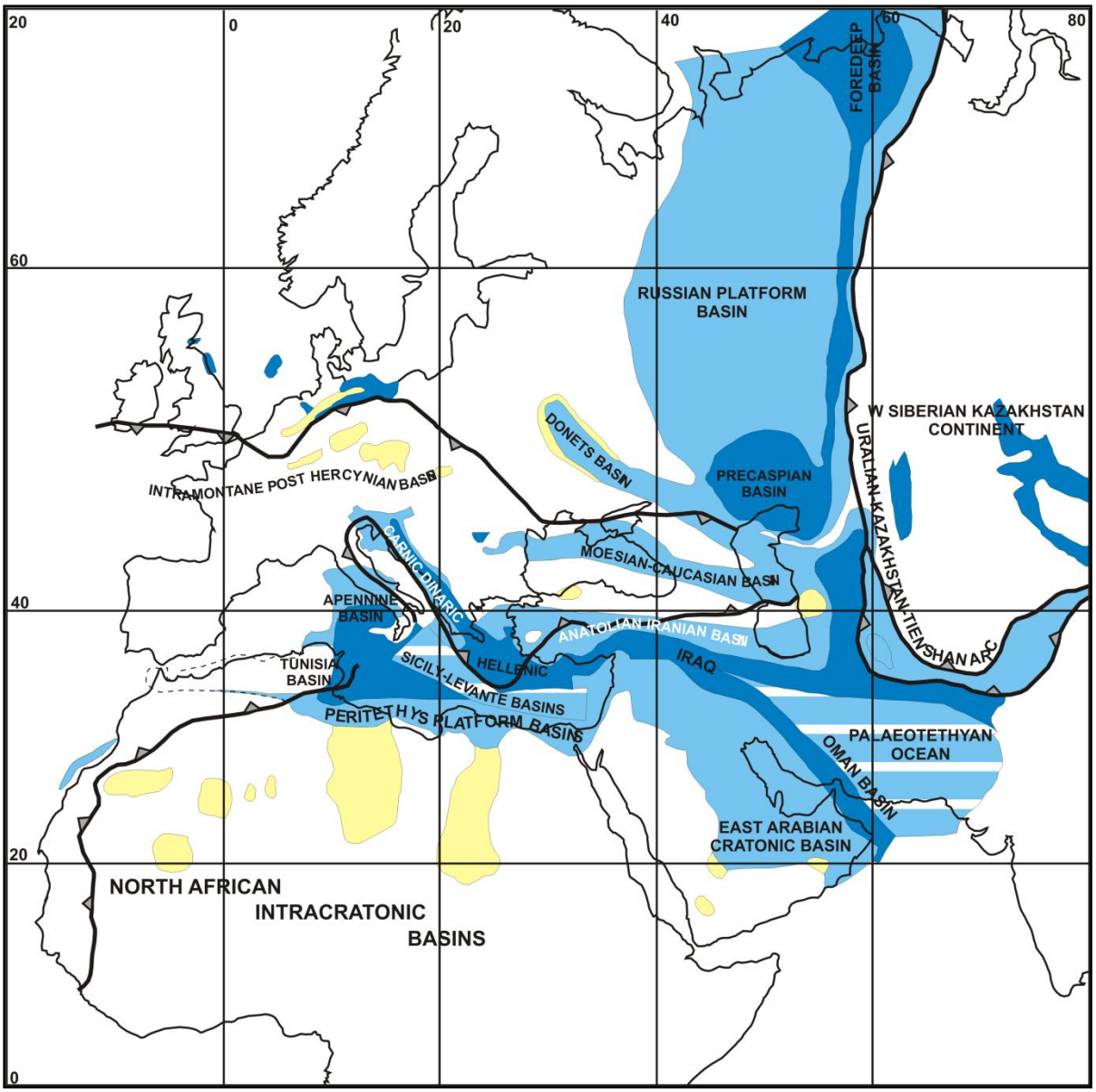

Figure 2.15 Location of the Peri-Tethyan basins in Artinskian times (modified from Vai, 2003). Continental basins (yellow), brackish and shallow-marine basins (light blue), deep marine to oceanic basins (dark blue).

2.3 Geological background of Permo-Carboniferous in Venezuela.

2.3.1 Tectono-stratigraphic setting

Bellizia (1992) proposed a tectono-stratigraphic model to explain the geological evolution of Western Venezuela during the Precambrian through Palaeozoic time. This author described 3 tectono-stratigraphic units that are: 1) an Andean igneous-metamorphic core complex that spans in age from the Precambrian to the Late Palaeozoic, 2) an igneous-metamorphic core covered by a fossiliferous Ordovician-Silurian sedimentary succession, and 3) a

Pennsylvanian-Permian sedimentary succession. These units have been defined as the Merida Terrane, Caparo Block and Supraterrane respectively. Bellizia and Pimentel (1994) recognized an additional province which they called the Chibcha Block (Figure 2.16).

The allochthonous Merida Terrane consists of the Andean igneous-metamorphic core complex (Precambrian Inglesias Complex, Tostos, Mucuchachi, Cerro Azul, Los Torres and other co-genetic metamorphic facies) (Figure 2.16). This province was highly deformed and metamorphosed during an early Hercynian orogenic phase (Early Pennsylvanian). The original position could have been close to the Appalachians or one of the Hercynian orogenic belts from Europe or African Gondwanaland. Bellizia (1992) suggested it could have been part of the Maya o Yucatán Block, although there is insufficient evidence to support this model. Thus, García (1972) considered that the Merida Terrane is not allochthonous since the metamorphic rocks can be litho-correlated with the Upper Palaeozoic sedimentary succession throughout the various tectono-stratigraphic units (the Rio Momboy and El Águila formations with the Palmarito Formation) (Figure 2.17). For this reason, García (1972) proposed an autochthonous origin for these rocks and that they were only affected by just one metamorphic event.

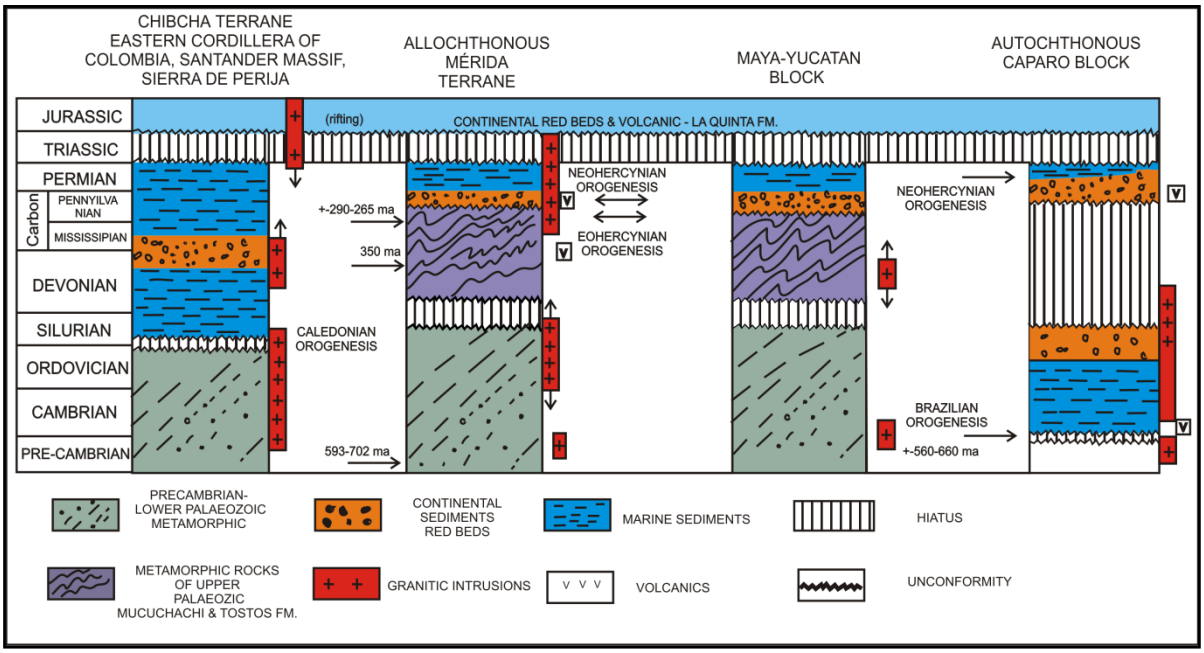

Figure 2.16. Mérida Terrane, Caparo Block, Maya Block and Chibcha Terrane (after Bellizia & Pimentel, 1994).

Even though García (1972) concluded that there was only one metamorphic event which affected the Precambrian to Upper Palaeozoic rocks, this does not provide the answer as to why these rocks are metamorphosed in some areas but not in others. The model does seem to provide an explanation of Late Palaeozoic facies distributions. However, from the results of this study (Laya and Tucker, 2012) it can be suggested that there were two different metamorphic events, the one which has been proposed by García (1972) and a second more localized one, that may have occurred during Triassic-Jurassic time or earlier, but which only affected the rocks that are now located in the central and northern areas of the Venezuela Andes**.**

The autochthonous Caparo Block is composed of Precambrian metamorphic basement, called the Bella Vista Formation, overlain by the fossiliferous Ordovician-Silurian Caparo Formation. The latter represents autochthonous deposits on the northern margin of the Guyana craton.

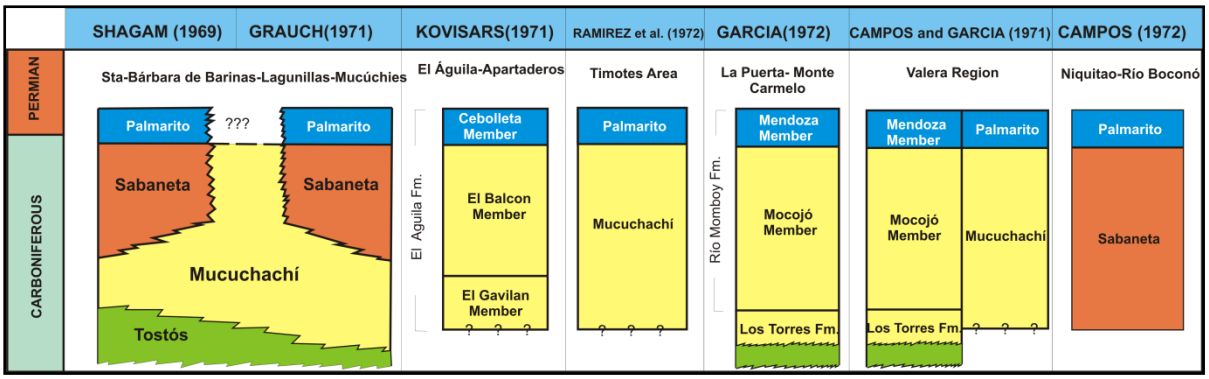

Figure 2.17 Correlation diagram of the Upper Palaeozoic rocks in the Venezuelan Andes after García (1972).

The Chibcha Terrane consists of rocks outcropping in the Perija Mountains, the Eastern Colombian Cordillera and Santander Massif (Figure 2.16). It is characterized by meta-sedimentary rocks that have been intruded by quartz-aplites and diabases and metamorphosed to greenschist facies. Overlying these is a Devonian siliciclastic succession which constitutes the Caño Grande, Caño del Oeste and Campo Chico formations.

The allochthonous Merida Terrane and autochthonous Caparo Block were sutured together to form the basement of the Mucuchachi Basin, named by Arnold (1966), wherein the Sabaneta and Palmarito formations were deposited. This basin was developed within a compressional tectonic setting related to the formation of Pangea, perhaps also to the Alleghenian orogenesis of Miall and Blakey (2008). It was also interpreted as a narrow depression oriented northeast-southwest, where the thick supraterrane succession of Upper Palaeozoic rocks was deposited.

To begin with, the supraterrane in the Andes was composed of two lithostratigraphic units, the Sabaneta and Palmarito formations, but Odreman and Wagner (1979) also included the Carache Formation which occurs in the northern Andes. In the Perija Mountains the Sabaneta Group includes the Caño Indio and Caño del Noroeste Formations, as well as the Rio Palmar and Palmarito Formations. The Supraterrane is overlain by the three further terranes previously described, which resulted from extensive transgression and deposition.

There are major contrasts of the Upper Palaeozoic succession in the Venezuelan Andes with that in the Amazonas Basin. In the latter, thick evaporites occur in a markedly cyclic succession of tidal-flat and sabkha facies. In the Delaware Basin, USA, the equivalent succession is largely carbonate, with major reefs. Moreover, during the Permo-Carboniferous carbonate deposits are widespread in many places throughout the Americas, including the USA, México, Guatemala, Bolivia, Perú, Ecuador and Brazil. However, farther south in South America (Argentina) and farther north in North America (Canada) clastic deposits dominate and these were closely influenced by the Late Palaeozoic glaciations.

2.3.2 Lithostratigraphy of the Late Palaeozoic in Venezuela

Christ (1927) was the first geologist to describe these rocks and proposed the name 'Palmarito Series' to refer to shales, marls and limestones in the Mucuchachi-Santa Barbara area on the southern flank of the Venezuelan Andes in Merida and Barinas states. This report showed for the first time that Upper Palaeozoic rocks crop out in Venezuela and he also suggested a Permian-Carboniferous age for these particular rocks.

González de Juana (1952), Pierce et al. (1961) and Shell and Creole (1964) Shagam (1972) proposed different lithostratigraphic interpretations which have been made on the basis of field observations and biostratigraphic studies, most of them as part of the search for potential petroleum systems (Figure 2.18). However, these studies did not provide an accurate chronostratigraphy to establish the age to stage level.

The oldest unit in the area is the Mucuchachi Formation which has been interpreted to range from the Upper Devonian to Lower Pennsylvanian by Pierce et al. (1961), Shell and Creole (1964) and Arnold (1966). They established the age from field stratigraphic relations with the surrounding lithostratigraphic units. However, the evidence for this interpretation is not strong. Odreman and Useche (1997) later proposed that the age is restricted to the Pennsylvanian. The formation consists of dark grey slate interlayered with fine-grained

quartzite that was affected by regional metamorphism, probably in the late Pennsylvanian. This unit constitutes the basement in the study area, being overlain by the sedimentary cover of the Sabaneta and Palmarito formations.

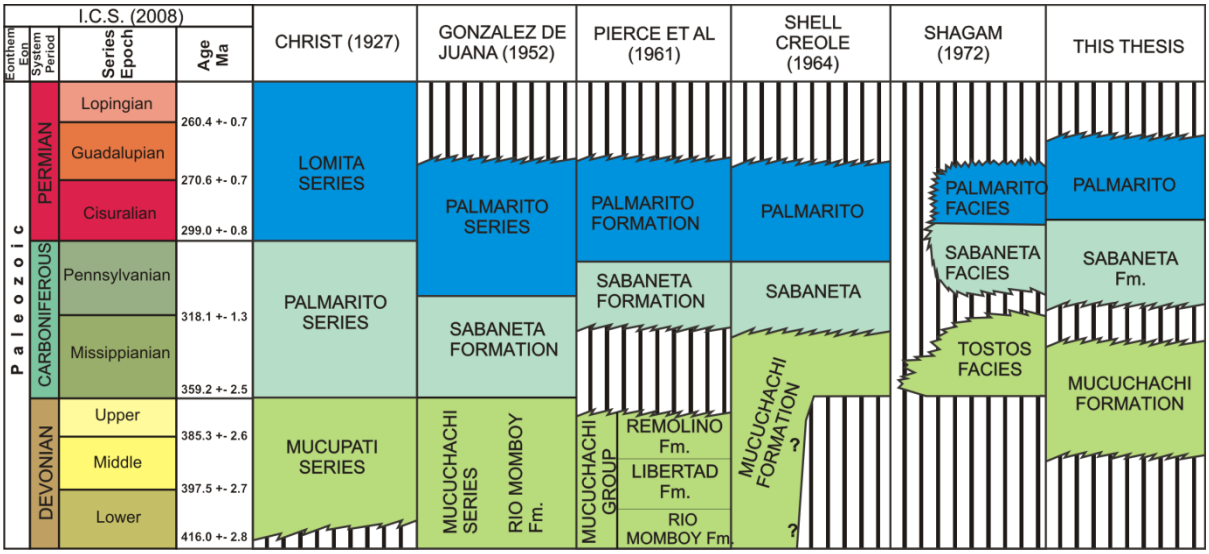

Figure 2.18 Correlation diagram of Late Palaeozoic strata in the southern Venezuelan Andes

The overlying Sabaneta Formation (Middle Pennsylvanian) consists of a fluvial succession of reddish sandstones and conglomerates with cross-bedding and channel structures. These grade into thinly-bedded red mudrocks with palaeosoils of floodplain origin (Arnold, 1966; Viscarret, 2002).

The continental deposits of the Sabaneta Formation grade up into marine sediments of the Palmarito Formation which are ascribed to the latest Carboniferous through early Middle Permian age. This formation commences with calcareous sandstone and mudstone with ostracods of a tidal-flat environment which pass upwards into dark-grey calcareous outer-ramp deposits. The succession then becomes more shallow-marine with fusulinid grainstones, calcareous algal packstones, crinoidal-bryozoan wackestones and finally dolomites interbedded with bioturbated lime mudstones with sponges. Fusulinid species identified include *Parafusulina* and *Globivalvulina* (Sellier De Civrieux, 1951; González de Juana, 1951). These species were considered characteristic of the Upper Guadalupian, probably Capitanian, in West Texas. Shell and Creole Companies (1964) provided additional

information about the rocks that contained the fusulinids and proposed one lithostratigraphic unit but split into two different members that were properly described by Arnold (1966). Furthermore, some correlation has been made by Hoover (1976, unpublished, 1981) that proposed a relationship between Venezuela, Colombia, Ecuador, Bolivia, México, Guatemala and the USA, based on a detailed study of Palmarito brachiopods from the Venezuelan Andes. However, this correlation was solely from a palaeontological point of view, since it does not have any stratigraphic information as to where those fossils were located, in fact, in most of the cases. the samples were collected from exotic blocks on a mule trail, Hoover (1976; 1981) and Rigby (1984) do not show any stratigraphic logs or the stratigraphic position of the samples.

2.4 Summary

Palmarito strata in the Mucuchachi Basin can be followed through Colombia to the west and southwest, where a few successions of limestone and shale with fusulinids occur (Villarroel and Mojica, 1987). To the northwest, correlations can be made with a marine succession in the Manaure Formation in the Perija Mountains in the border region between Venezuela and Colombia (Forero, 1967). Farther northwest the Mexican-Guatemalan microterrane (MGT) was moving northwards whilst shallow-marine sediments were being deposited on probable isolated platforms. These depositional events are represented by limestones and shales in Guatemala-Belize and México (Vachard and Foucade, 1997; Silva-Pineda et al., 2003; Vachard et al., 2004). Over the western flank of the Yucatán Block (YUC) which had collided against the northeast of Gondwana, shallow-marine carbonates were also deposited; these are the closest equivalent sediments to those in Venezuela. However, there could have been sporadic connections with basins in the southwest USA

(Delaware, Midlands), as suggested by the biostratigraphic similarities described by Wood et al. (2002).

The MB may well have been connected to the basins in Perú and Bolivia to the south, and with those in the north in the Mexican and Guatemala Terranes (MGT) and Yucatán Block (YUC), creating a remnant sea between Laurentia and Gondwana. The eastern boundary was an orogenic wedge, consisting of igneous and metamorphic rocks and continental volcanics (Feo-Codecido et al., 1984; Viscarret et al., 2009). In addition, a narrow channel through Cuba may well have existed between west and east Pangea to provide an explanation of the Tethyan fauna found within the Mucuchachi Basin (MB). Finally, the southeast border was the South American Craton (SAM), also called the Guyanan Craton which was part of continental Gondwana.

The review that has been presented above and the evidence from the Palmarito Formation suggests a new setting for northwest Gondwana in the early through late Early Permian that will be explained in detail in Chapter 3. The Mucuchachi Basin (MB) is proposed as a foreland basin within which the marine carbonates of the Palmarito Formation accumulated.

3 Facies analysis and depositional environments of Permian carbonates of the Venezuelan Andes: Palaeogeographic implications for Northern Gondwana

Abstract

Upper Palaeozoic strata in South America were deposited over cratonic areas and in intracratonic basins (e.g. Solimões, Amazonas and Paraná). However in many areas, such as Venezuela and Colombia sedimentary rocks are rarely exposed because of the dense vegetation and the nature of the terrain. As a result of this, the strata are poorly documented; nevertheless, they do have significant palaeogeographic implications. This chapter reports on a study of the Permian carbonate facies of the Palmarito Formation, exposed throughout the Venezuelan Andes, and discusses the succession of palaeoenvironments, and the palaeogeography resulting from detailed field and lab work. Deposition took place on an extensive ramp which probably dipped gently northwards towards the open ocean. Much of the Palmarito succession shows a general transgressive trend, with a few thinner and more-regressive intervals, likely a response to glaciation-deglaciation cycles. Towards the end of the Permian in the Venezuelan Andes region, a major sea-level fall led to extensive uplift and erosion, resulting in a major disconformity between the Upper Guadalupian carbonates and overlying Jurassic red beds. The early Palmarito tidal-flat facies are noteworthy for their sub-metre-scale mud-to-sand cycles with incipient palaeosoil fabrics. The mid-outer ramp carbonate facies are characterised by thin storm beds, and bioclastic lenses, arranged into metre-scale coarsening-upward cycles. Succeeding shallow-marine inner-mid ramp bioclastic grain-wacke-stones are dominated by an open-marine fauna of fusulinids, calcareous algae, crinoids, bryozoans and brachiopods. Outer-ramp facies are wacke-mud-stones with sponge spicules, radiolarians and brachiopod fragments. There are similarities between the Permian

deposits of Venezuela and those recorded from Guatemala and México to the north, and from Colombia and Perú-Bolivia to west and southwest, where carbonate systems also dominate. These facies were all part of a tropical foreland basin setting, that has been called the Mucuchachi Basin; and they contrast with the other Late Palaeozoic intracratonic basin in South American. Evidence provided here demonstrates that a seaway existed between Laurentia and Gondwana from the Early Permian through to the late Early Permian.

3.1 Introduction

The development of the supercontinent Pangea during the Permian triggered several global changes. Many sedimentary basins were created and there was also the major Gondwana glaciation which had a direct influence in high latitudes and indirect, but no less important effects, in low latitudes. The last in particular led to the formation of shallow-marine and deltaic, coal-bearing cycles that have been studied worldwide (Ross and Ross 1995; Tucker and Wright, 1990; Grader et al., 2008; Blomeier et al., 2009). In northern South America, Upper Palaeozoic strata were deposited extensively over peri-cratonic areas, but in many locations they are rarely exposed and so are poorly documented. This is largely the result of extensive weathering and dense vegetation cover in the tropical Andes, as well as the difficult access to the outcrop areas. However, these strata do have a significant petroleum potential, and indeed in the southern USA and Brazil they do contain significant source and reservoir rocks. These rocks in Venezuela have been designated as a possible future petroleum province by Audemard and Serrano (2001).

Permo-Carboniferous rocks in Venezuela have been described by only a few authors (Arnold, 1966; García, 1972; Odreman and Wagner, 1979; Bellizia, 1992; Viscarret, 2002; Laya and Reyes; 2004; Viscarret and Laya, 2007; Laya and Tucker, 2008). Permo-Carboniferous platforms and ramps have been studied in many other parts of the world (e.g. Ahr , 1998; Burchette and Wright, 1992; Tucker et al 1990a; Tucker and Wright 1990;

Wright and Burchette, 1999) and many palaeogeographic maps have been published (e.g. Pindell et al., 1985; Scotese and Langford, 1995; Scotese, 1999; Vai, 2003; Vachard et al., 2004;; Blakey, 2007 and Miall and Blakey, 2008), but there is often little information on northern South America (Venezuela and Colombia) since there have been few detailed studies there since the 1970's.

This chapter describes and interprets the Permian strata of the Palmarito Formation distributed throughout the Venezuelan Andes (Figure 3.1) and discusses the palaeoenvironments of the succession resulting from detailed field descriptions and petrographic analysis.

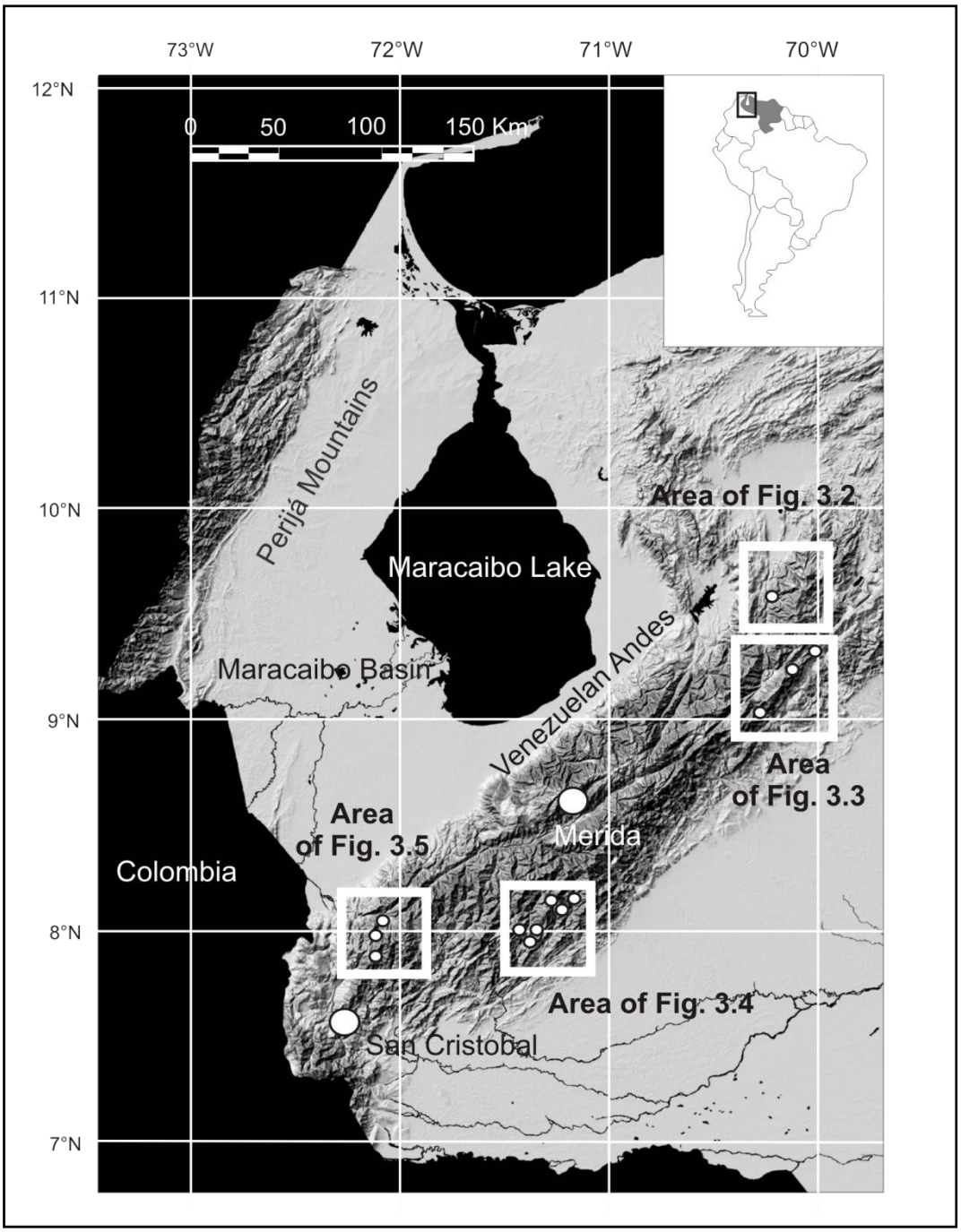

Figure. 3.1. Digital shaded relief image of western Venezuela showing the location of the main area of study. Modified from Garrity et al. 2004. (http://pubs.usgs.gov/of/2004/1322/.).

Sedimentation occurred on an extensive ramp which probably dipped basinward towards the north, towards the open ocean. The succession evolved from fluvial (Sabaneta Formation) through tidal-flat to mid-outer ramp deposits, with all facies recording a well-developed cyclicity. Although there are some references (Hoover, 1976; 1981; Scotese, and Langford, 1995; Scotese, 1999; Ricardi, 2008) the Permian successions in Venezuela provide

a new dataset and interpretations for the region between Gondwana and Laurentia, before and close to the final assembly of Pangea. The results presented here thus fill a significant gap in the regional palaeogeography.

3.2 Geological background

The Palmarito Formation is part of the sedimentary fill of a Palaeozoic basin in western Venezuela that was named by Arnold (1966) as the Mucuchachi Basin. The formation overlies the Sabaneta Formation which is comprised of a fluvial succession of reddish sandstones and conglomerates with channel structures that pass laterally into thinly-bedded red mudrocks with palaeosoils of floodplain origin (Arnold, 1966; Viscarret, 2002). The continental deposits of the Sabaneta Formation grade up into marine sediments of the Palmarito Formation which are ascribed to the Early to Middle Permian in age. For more extensive discussions of the stratigraphy of the Palmarito Formation see Chapter 2.

3.3 Methods

To achieve the objectives, this project involved detailed fieldwork (described in the Chapter 1) followed by petrography to determine microfacies and diagenetic features.

173 standard thin-sections of limestones, dolomites and sandstones have been examined for their petrographic features, to develop a microfacies scheme which is the basis of the palaeoenvironmental analysis.

3.4 Description of the exposures in the Venezuelan Andes.

3.4.1 Sections

Vertical successions are located in the 4 main areas described below (Figure 3.1). Also, complete detailed logs at the 1:100 scale can be found in the Appendix 1. Carache area

In the Carache area the ***Loma de San Juan (S1)*** section is located in the hill to the north of Carache town (Figure 3.2). These rocks are composed of greyish fusulinid

limestones and mudstones (~60 m thick), and locally weakly-stratified siltstones with poorly-preserved plant fragments. Access is from a track passing the small village of Loma de San Juan.

3.4.1.1 Bócono area

Three sections were described on the north side of Bócono: ***Campo Elías (El Morro)-Biscocuy (S2)***, ***Quebrada Segovia (S3)*** and ***Bócono River (S4)*** (Figure 3.3). The first is a succession cropping out in the main road between the towns of Campo Elías and Biscocuy. Approximately 70 m of greyish brownish limestones and mudstones are exposed, slightly metamorphosed and well-stratified. The second outcrop is located 200 m from La Laguna de Los Cedros, next to a small stream called Quebrada Segovia. This outcrop shows ~10 m of poorly-exposed strata which are formed of marls, siltstone and fine-grained sandstone, slightly metamorphosed. Finally, the largest succession within the area is located along the Río Bócono Gorge which has very difficult access through the forest on a steep slope. The section is comprised of ~200 m of sandstones and limestones, very well stratified and slightly metamorphosed.

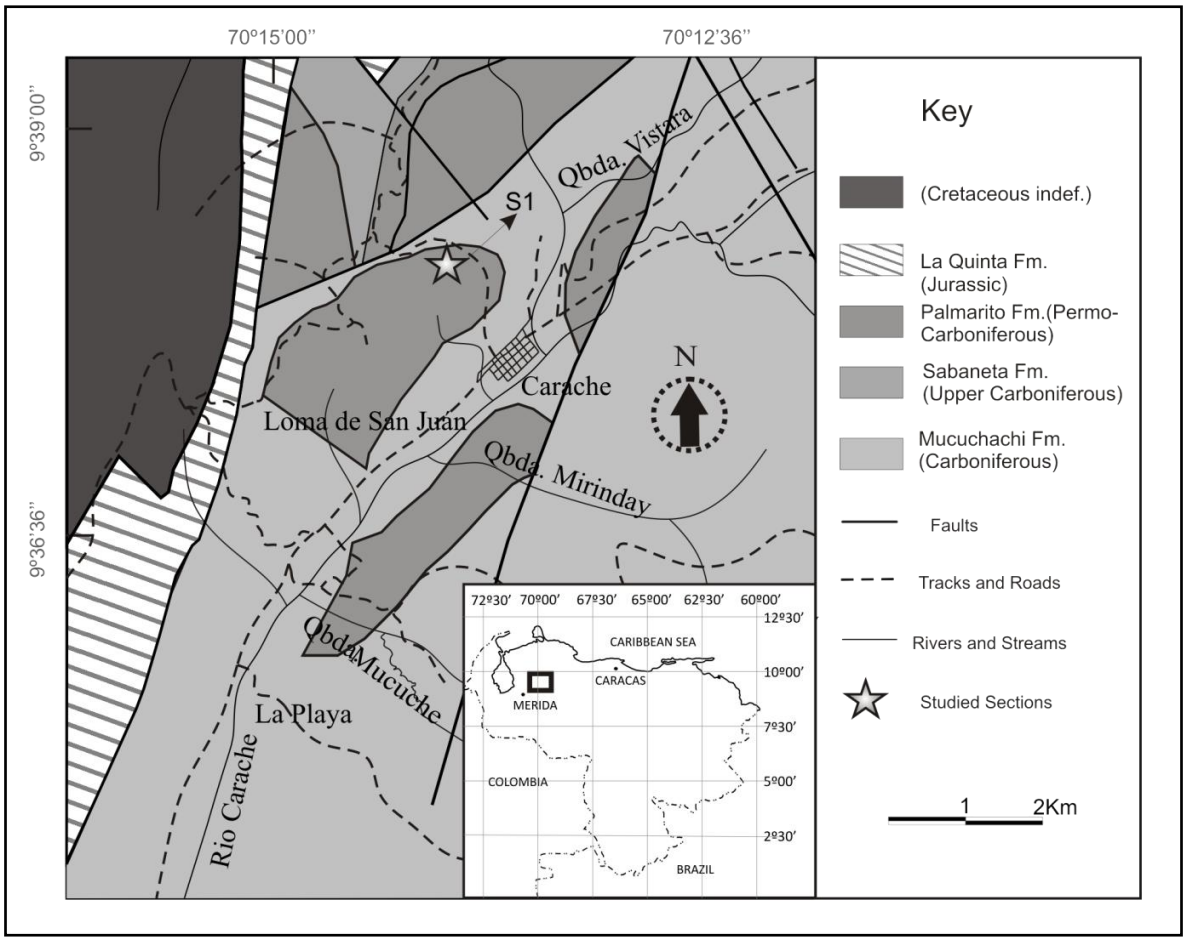

Figure. 3.2. Geological map of the Carache area modified from U.S. Geological Survey Geologic Shaded Relief Map of Venezuela Hackley et al. (2005).

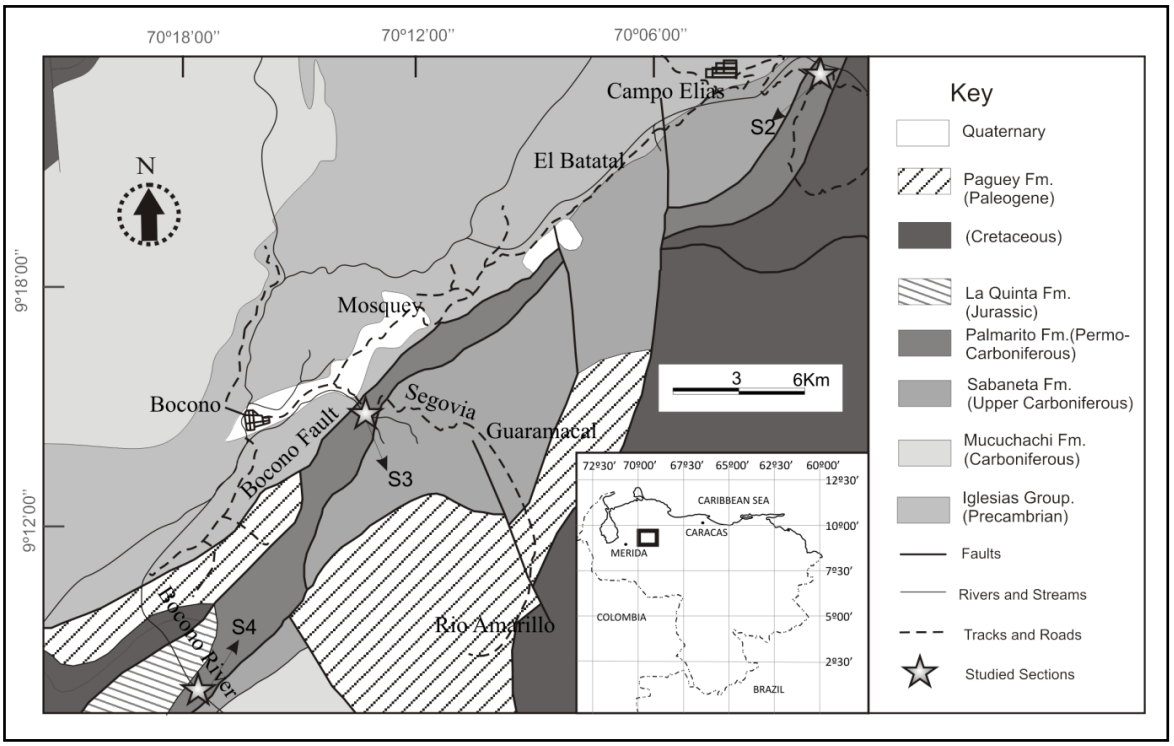

Figure. 3.3. Geological map of the Bócono area modified from U.S. Geological Survey Geologic Shaded Relief Map of Venezuela Hackley et al. (2005).

3.4.1.2 Portachuelo area

South of Merida city there are six localities for the Palmarito Formation which are the best in the Venezuelan Andes (Figure 3.4). First, ***Santa Cruz de Palmarito (S5)***, where the Palmarito Formation was first described by Christ (1927) and defined as the stratotype, is located '100 m towards the south from a small chapel called 'Santa Cruz de Palmarito' along a mule trail. However, these outcrops are not well exposed. Fortunately, in 2009 a new 4x4 track in the area was cut to reveal new outcrops that are better than those of the stratotype. The 100 m thick succession shows fossiliferous massive and nodular limestones that can be ascribed to the middle to upper part of the formation. Fusulinids and brachiopods are common in the succession here.

Second, ***Quebrada de Portachuelo 2 (S6)*** shows outcrops from the head of the stream towards the west, which are on the eastern part of a synclinal structure. The succession shows a direction that is going stratigraphically upwards in parallel to the stream flow and opposite to Quebrada de Portachuelo 1 Section. The middle and upper part of the Palmarito Formation is exposed showing massive grey-bluish, highly fossiliferous limestones and crystalline dolomite, dipping westwards. The section has been described by Arnold (1966) as Quebrada Quevada and by Hoover (1981) and Rigby (1984) as Quebrada de Portachuelo. The last two were sampled here for palaeontological reasons, but none of their articles present stratigraphic logs with the locations of the studied fauna. However, they do give excellent fossil descriptions of brachiopods, sponges, some bryozoans, corals and fusulinids.

Third***, the Quebrada de Portachuelo 1 (S7)*** section exposes rocks in the stream which are on the western flank of a syncline that is the main structural feature of the area. There is no lateral continuity of outcrop due to the thick vegetation; tufa has also formed over some outcrops. The 175 m thick section consists of Palmarito Formation that comprises of clayey

lime mudstones, sandstones which pass upwards to thick fossiliferous limestones at then top. These strata are resting on reddish sandstone and mudstone of the Sabaneta Formation.

Fourth, the ***Palmar River 1(S8)*** section reveals Palmarito strata along the river, exposing a ~400 m-thick succession of rocks which rest discordantly on the Sabaneta Formation. The latter consists of red sandstone, siltstone and mudstone with cross stratification and channel structures that have been interpreted as Upper Carboniferous fluvial deposits. The Palmarito Fm. is formed of a thick succession of calcareous sandstones and mudstones with ostracods which pass upwards to calcareous algal packstone, fusulinid grainstone, crinoidal-bryozoan wackestone and finally dolomite interbedded with boundstone with sponges. This is the most complete and best exposed section where it is possible to find the base and top of the Palmarito Formation.

Five, the ***Palmar River 2a*** section is a lateral correlative to Palmar River 1 and is composed mainly of clayey lime mudstone facies, fossiliferous nodular limestones with brachiopods, crinoids and fusulinids. The thickness of the succession is ~20 m and is probably correlated with middle part of Palmarito Formation.

Finally, the ***Palmar River 2b (S9)*** section is the southernmost outcrop located in a small tributary of the Palmar River. Mostly grey nodular fossiliferous limestone, lime mudstone and marl (60 m thick) with brachiopods, bryozoans, fusulinids and crinoids are visible. These strata are likely to be in the middle part of the Palmarito Formation.

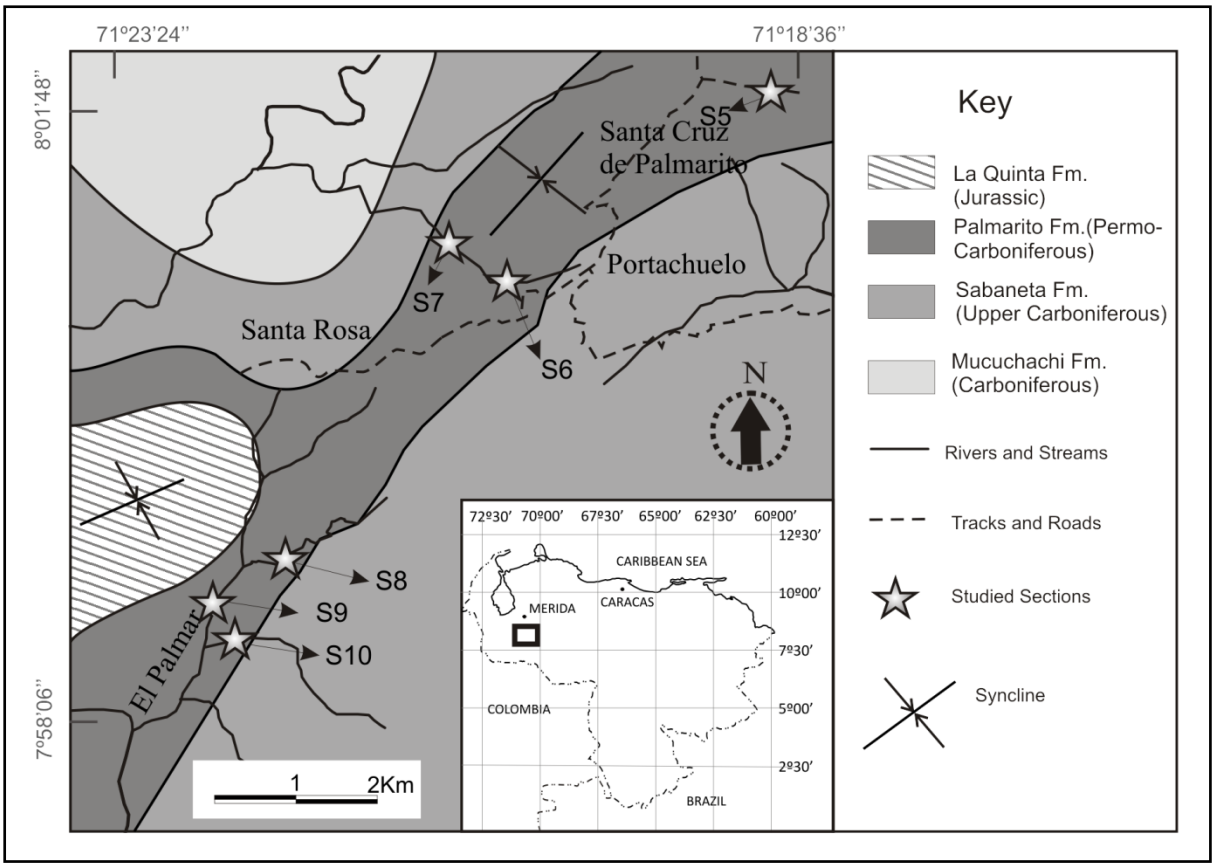

Figure. 3.4. Geological map of the Portachuelo area modified from U.S. Geological Survey Geologic Shaded Relief Map of Venezuela Hackley et al. (2005).

3.4.1.3 La Grita-El Cobre-El Zumbador area

The southernmost area of the Venezuelan Andes in Táchira state has 3 useful outcrops: ***La Grita-gypsum mine (S11), El Cobre (S12)*** and ***El Zumbador-Queniquea (S13)*** (Figure 3.5). The first outcrop is located 5 km. southwest of La Grita town in an old gypsum mine with a small gallery, but it is in a bad condition. The area is heavily overgrown with vegetation and just a few beds are exposed showing ~10 m of pink and greyish gypsum lenses interbedded with clayey lime mudstones.

The second outcrop is located on the southern hill of El Cobre town, on the slope of an off-road track. The strata are composed of ~12 metres of nodular limestone and mudstone with crinoids and brachiopods.

The third section shows ~ 40 m of massive, fossiliferous limestone, slightly metamorphosed and is located in a road-cutting between Páramo El Zumbador and Queniquea.

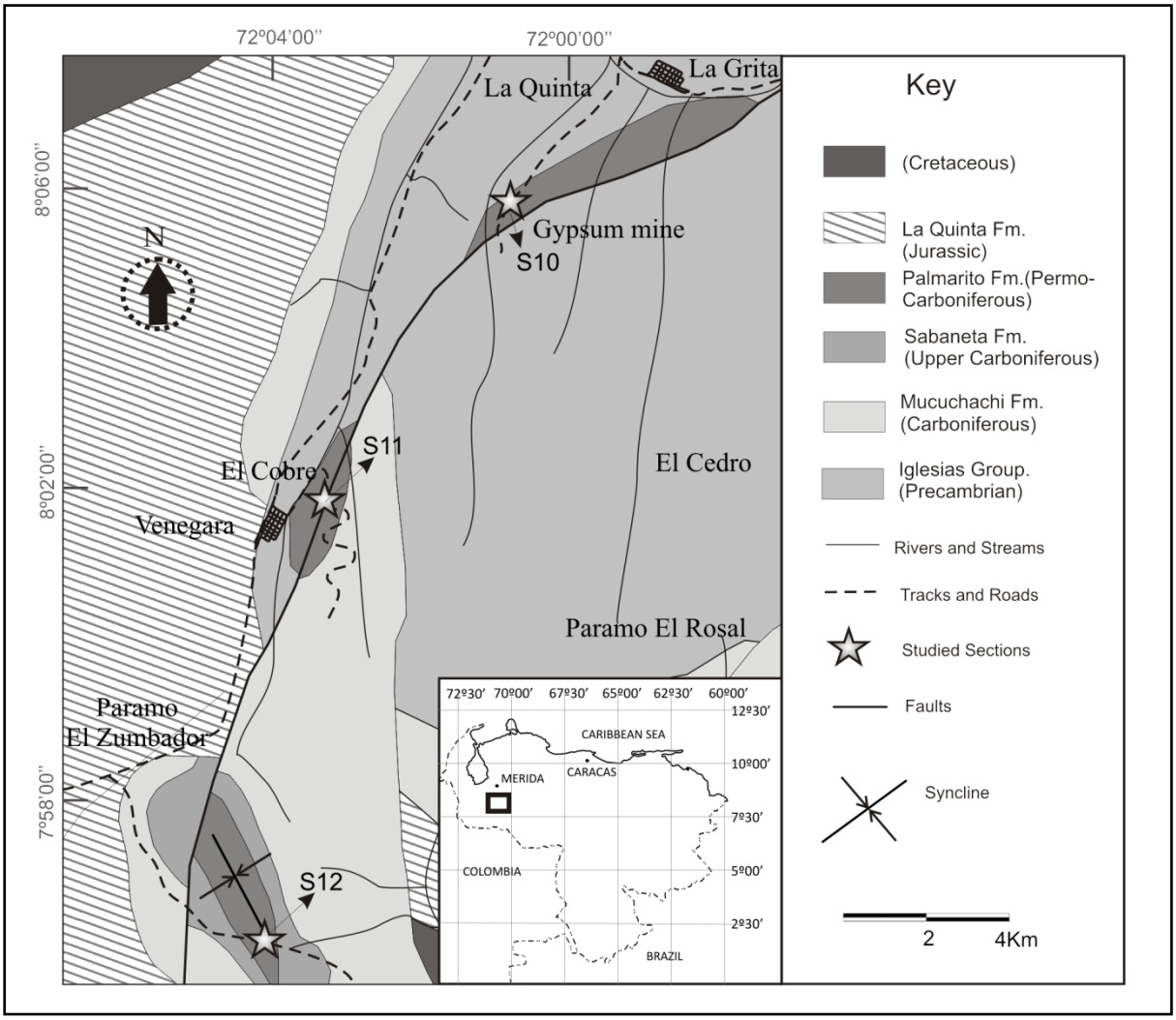

Figure 3.5. Geological map of the La Grita-El Cobre-El Zumbador area modified from U.S. Geological Survey Geologic Shaded Relief Map of Venezuela Hackley et al. (2005).

3.5 Facies Analysis

Ten macrofacies and fourteen microfacies have been identified and described from the sections of the Palmarito Formation, based on fieldwork and petrographic studies.

3.5.1 Macroscopic facies:

The macrofacies are briefly described in Table 1 and illustrated in Figs. 3.6, 3.7 and 3.8. Presented there are all the characteristics of the facies in a macro-scale which were used in the first approach to the rock descriptions.

Table 3.1. Characteristics of the macrofacies of Palmarito Formation.

Facies	Brief description
Nodular limestone	Massive lime mudstone and wackestone, mostly dark to light bluish grey with irregular stratification surfaces and no lateral continuity. Well developed nodular structures (Figure 3.6a, b).
Laminated limestone	Laminated lime mudstone and wackestone, locally floatstone, dark to light gr-y and locally black. Stratification surfaces are planar to irregular (Figure 3.6c, d).
Massive limestone	Thick limestone beds of greyish wackestone, packstone and grainstone. Planar to irregular stratification surfaces (Figure 3.6e, f)...
Crystalline dolomite	Dolomite mainly brownish, white to grey, with irregular stratification surfaces (Figure 3.6g, h)...
Boundstone with sponges	Massive lime mudstone with a framework of large branching and massive sponges (Figure 10a, b), including demosponges, heteractinid and sphinctozoan calcareous sponges (Rigby, 1984).
Calcrete	Massive lime mudstone, light to dark grey colour, associated with mud-cracks and other evidence of exposure (Figure 10c, d)...
Massive sandstone	Medium to fine-grained sandstone with planar and trough cross stratification. Brown and light grey, locally red. Irregular stratification surfaces (Figure 10e, f).
Heterolithics	Fine-grained sandstone and siltstone, very well laminated with flaser and lenticular structures, locally undulating lamination and ripples. Abundant plant remains within the fine grained material. Colour ranges from greenish grey to brown. Stratification surfaces are planar (Figure 10g, h).
Mixed carbonate-clastic	Mixed clay, lime mudrocks and calcareous sandstones (Muddy micrite and sandy allochem sandstone in Mount's (1985) classification scheme). Colour dark grey to black. Bedding surfaces from planar to irregular (Figure 11a, b).
Laminated shale	Laminated black and dark grey shale, with planar and irregular bedding surfaces (Figure 11c, d)...

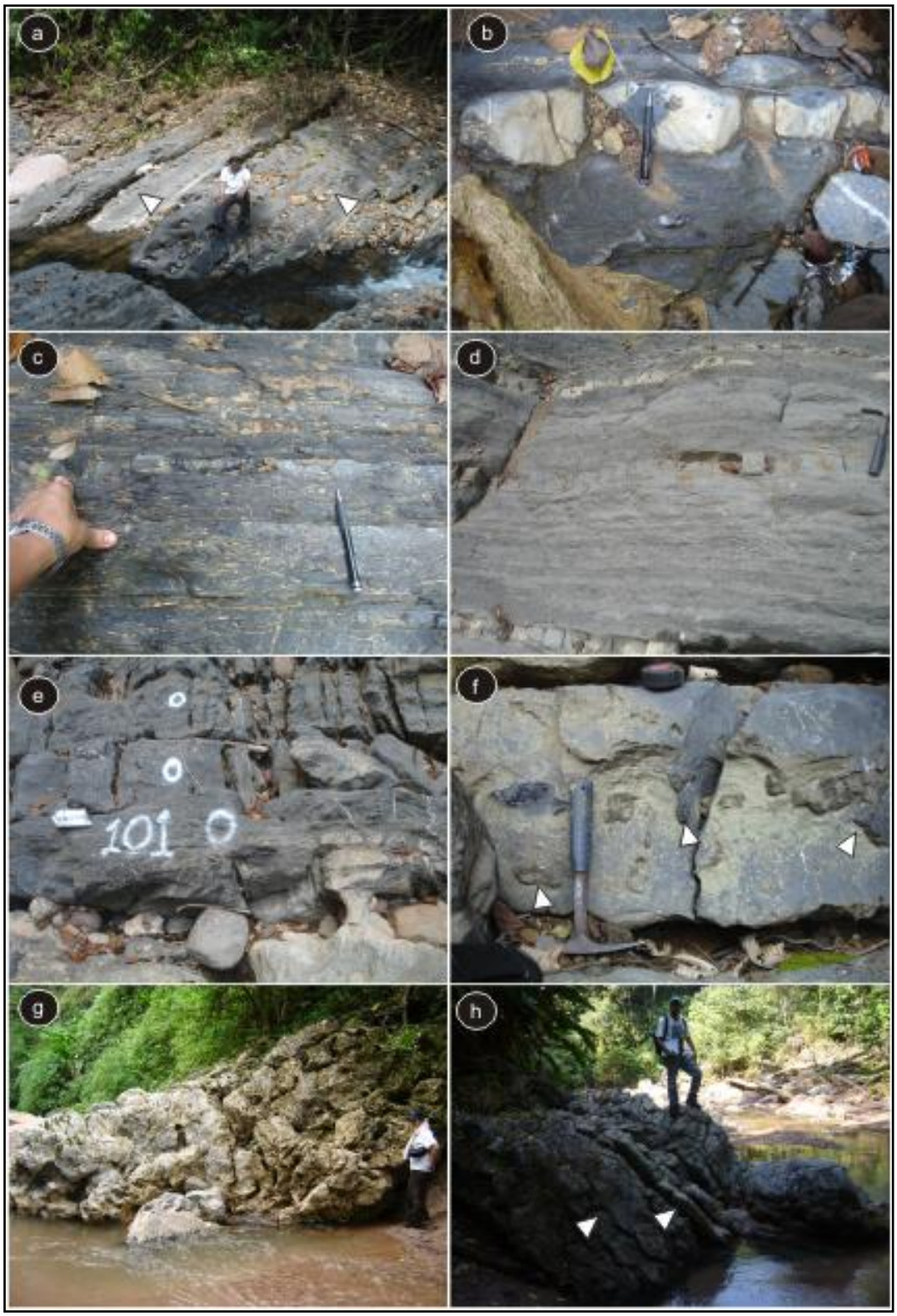

Figure 3.6. a) Nodular limestone. Note the facies is interbedded with laminar limestone (*arrows*) b) Nodular limestone. Irregular bedding planes that shows 15 cm limestone bed. c) Laminated limestone. Planar lamination locally shows a slightly wavy structure. d) Laminated limestone. Note interbedding with nodular limestone. e) Massive limestone. Metre-scale bed of bluish slightly fractured limestone. f) Massive limestone. Note silica nodules (*arrows*). g) Crystalline dolomite irregular massive beds of whitish dolomite. h) Crystalline dolomite. Note irregular bedding planes (*arrows*).

Figure 3.7 a) Boundstone of sponges. Framework of branched sponges (*arrows*). b) Boundstone of sponges. Detail of possible demosponges. c) Calcrete. Note coalesced nodules with laminated dark material between interstitial areas. d) Calcrete. Note sharp upper surface to the hard concretion of cemented material (*arrows*). e) Massive sandstone. Note the interbedding between red and greyish massive sandstone f) Massive sandstone with irregular bedding planes. g) Heterolithics. Meter-scale bed of silty-fine grained heterolithic facies interbedded with massive limestones. h) Heterolithics. Note flaser and lenticular bedding in an organic-rich sediment.

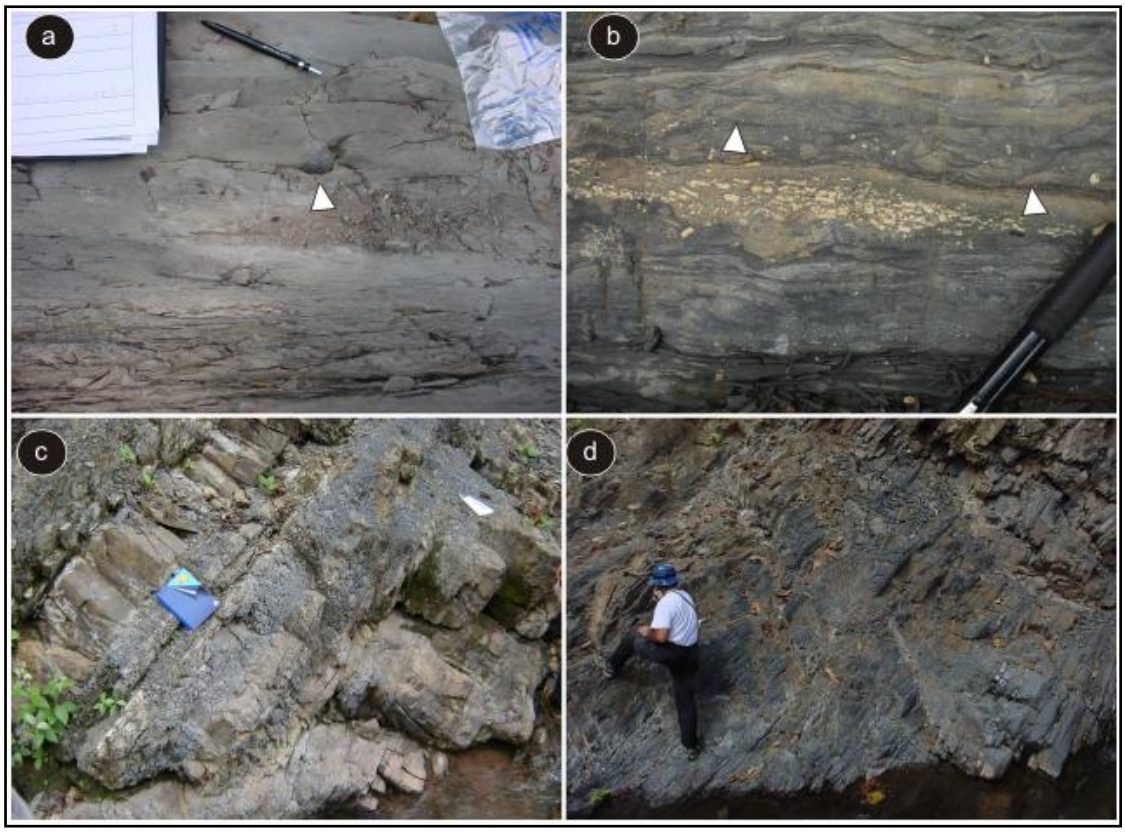

Figure 3.8 a) Mixed carbonate-clastics. Note irregular lamination; locally large brachiopod shells in living position (*arrows*). b) Mixed carbonate-clastics. Sandy-bioclastic facies with wavy and cross lamination (*arrows*). c) Laminated shale. Black and dark grey shale interbedded with calcrete and nodular limestone, locally with heterolithic and mixed carbonate-clastic facies d) Laminated shale. Outcrop of dark shale.

3.5.2 Microfacies:

3.5.2.1 Spiculite wackestone-packstone

This microfacies consists of mud-supported wacke/pack-stone rich in sponge spicules, small bioclasts and organic matter (Figure 3.9a). The common skeletal fragments are sponge spicules that seem to be monoaxon type, locally triaxon (Figure 3.9b). The small foraminifera *Endothyra* sp.and *Archeodiscus* sp. are present, as well as brachiopod bioclasts which show an impunctate and pseudopunctate microstructure. Also, crinoids and small bryozoan fragments (Fistuliporid, Fenestellid and Trepostome*)*. Bioclasts may have been derived from the shallower areas reworked by bottom currents and some of these deposits could be related to mud-mound structures

The microfacies is poorly sorted, has low porosity and shows dark grey and black colours due to the organic content. The deposits are mainly massive, but locally laminated or with a nodular fabric. Calcite cements are patchy, but silica cements are more common, probably due to the large volume of siliceous (opaline) sponge spicules that were likely dissolved and reprecipitated as microquartz during diagenesis.

The assemblage suggests a heterozoan association, specifically a transition between the hyalosponge and brynoderm grain association types of Flügel (2004). Therefore, it is interpreted as deposition from suspension under quiet-water conditions in a deeper-water environment, rich in sponges. This facies would correspond to SMF 1 and RMF 1 of Flügel (2004).

3.5.2.2 Neomorphic wackestone

Lime mudstone with brachiopod shells and spines is characteristic of this facies. The shells mostly have a pseudopunctate microstructure and are broken, and small foraminifera *Endothyra* sp., and *Archeodiscus* sp.are present, probably the result of reworking by bottom currents (Figure 3.9c).

This microfacies is mud supported and grains are poorly sorted. The beds are generally massive, but locally they have a nodular fabric and bioturbation is common. The fine-grained carbonate is commonly replaced by calcite microsparite where almost the only skeletal grains remaining unaltered are brachiopods. This probably relates to the composition of the shell, which is formed of the more stable low-Mg calcite (Figure 3.9d). This could indicate early cementation-neomorphism, perhaps related to the formation of firmgrounds at a time of reduced sediment supply.

The skeletal association is dominantly heterozoan which implies a deep subtidal environment. This microfacies would correspond to RMF 9 of Flügel (2004).

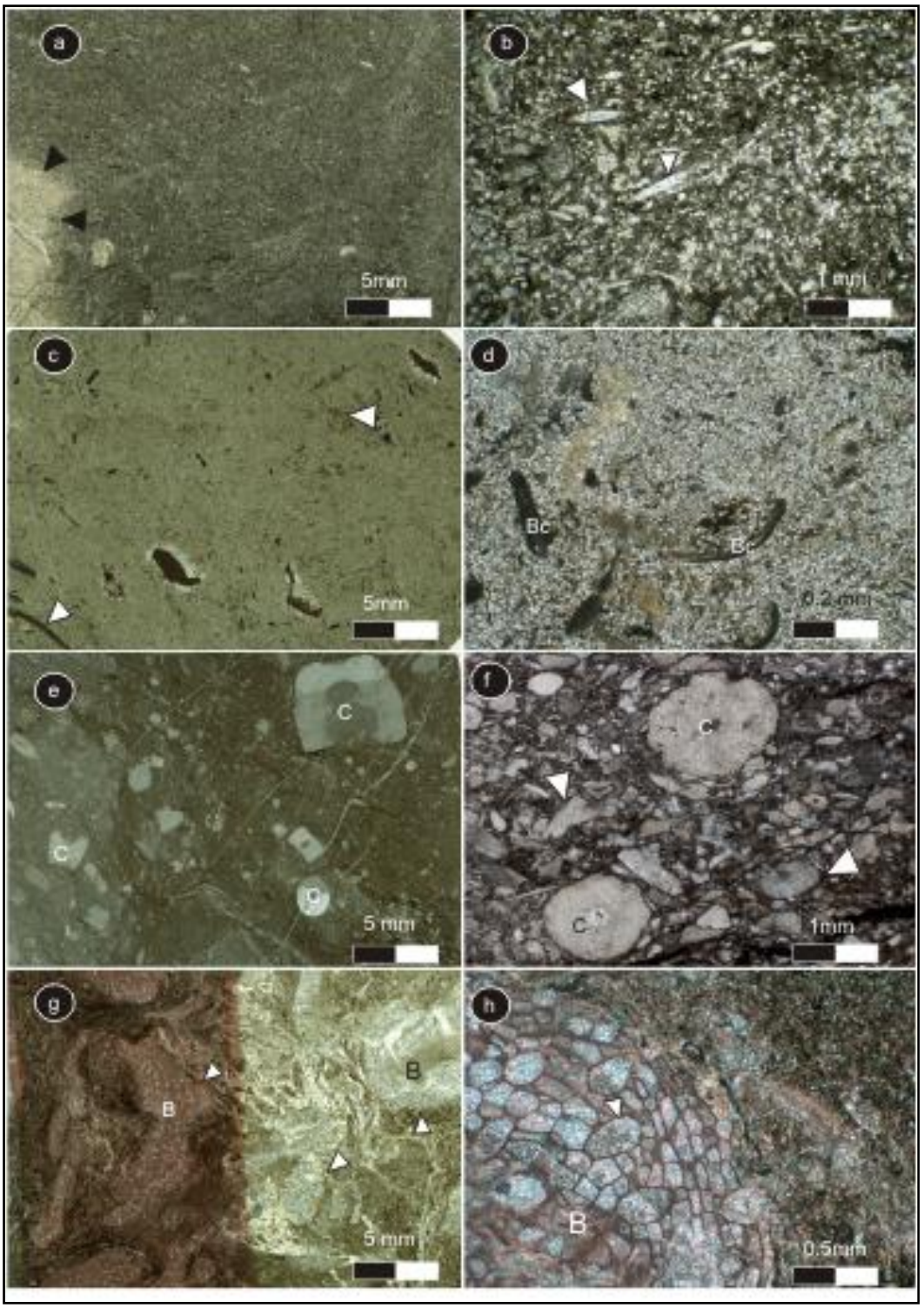

Figure 3.9 a) Spiculite wackestone-packstone. Note silicification front (*arrow*) which is replacing all sponge spicules and matrix. b) Spiculite wackestone-packstone. Monaxon spicules usually formed by silica but now recrystallized to calcite (*arrows*). c) Neomorphic wackestone. Note fine microcrystalline calcite is replacing the matrix and unstable cemented bioclasts; just the low-Mg calcite of the brachiopods are well preserved (*arrows*) (Bc). d). Neomorphic wackestone. Brachiopod fragments of low-Mg calcite which remain unaltered. e) Bioclastic crinoidal-bryozoan wackestone-packstone. Large fragments of crinoids (C) and matrix with mechanical compaction. f) Bioclastic crinoidal-bryozoan wackestone-packstone. Note poorly-sorted bioclastic distribution with some fractured crinoids (C) and bryozoan fragments (*arrows*). g) Bryozoan boundstone. Several generations of encrusting bryozoans (B), probably *Fistulipora sp*. f) Bryozoan boundstone. Detail of fistuliporids (B), with zoecia filled by drusy calcite (*arrows*).

3.5.2.3 Bioclastic crinoidal-bryozoan wackestone-packstone

This microfacies is comprised of light to dark-grey wackestone-packstone that contains abundant large bioclasts of crinoids, bryozoans (Fistuliporid, Fenestellid and Trepostome) and brachiopods. In addition, small foraminifera such as *Endothyra* sp. and gastropods are commonly present, as well as rare trilobite and green algal fragments (Figure 3.9e).

The beds are mostly massive and coarse grained. The texture is mud and grain-supported with evidence of mechanical compaction (Figure 3.9f) in the form of sutured skeletal grains, stylolites and dissolution seams. Calcite has replaced original aragonitic bioclasts with equant textures and fibrous silica occurs within calcitic bioclasts.

The skeletal association is dominated by heterozoan organisms but most of them are broken due to the high energy of the environment, which was broadly mid-ramp affected by storms. This sediment may have been deposited close to a crinoidal-bryozoan mud-mound. It may correspond to facies RMF 7-9 or SMF 12 of Flügel (2004).

3.5.2.4 Bryozoan boundstone

Abundant well-preserved bryozoans include mostly encrusting fistuliporid, fenestellids and *Archimedes*-like helicoidal forms, and less common trepostome types. The matrix is comprised of lime-mud and bioclastic debris of crinoids, sponge spicules and fragments of brachiopod shells (Figure 3.9g). The strata show massive structure-less beds with irregular bedding planes and a common grey-bluish colour.

The cavities of the bryozoans are filled by lime-mud in some cases but also locally radial fibrous cements from marine diagenesis, and sparry calcite cement precipitated during burial (Figure 3.9h). In addition, the silicification has locally affected calcitic skeletal grains.

The skeletal content of this facies is largely of the heterozoan association which is likely an autochthonous community formed in a mud mound –type buildup which probably

developed in a deep-subtidal location. This facies would correspond with SMF 7 or RMF 12 of Flügel (2004).

3.5.2.5 Fusulinid grainstone-packstone

Large fusulinid foraminifera, algae and crinoids characterize this microfacies which has a grain-support fabric. It is commonly associated with green algal packstone. The main bioclasts are fusulinid foraminifera (e.g., *Parafusulina* sp., *Pseudofusulina* sp., and possibly *Triticites sp*.) (Figure 3.10a). The phylloid alga *Achaeolithophylum* and green alga *Gymnocodiacea* are also present. This microfacies also contains large amounts of broken fragments of crinoids, bryozoans and brachiopods. Normally, it is characterized by a massive structure and a bluish-grey colour.

Chemical compaction has produced stylolites and pressure dissolution seams. Marine radial fibrous cements are locally present. However, sparry calcite has replaced original aragonite in phylloid algae and gastropod shells (Figure 3.10b).

The fusulinid-algal assemblage is generally assumed to reflect a symbiosis between foraminifera, algae and cyanobacteria (Vachard et al., 2004) in warm, shallow-marine waters and is typical of a photozoan association (chloroforam). This facies would correspond to SMF 18-For or RMF 13 of Flügel (2004).

3.5.2.6 Calcareous green algal packstone

This facies is mainly composed of green algae *Gymnocodiacea*, as well as phylloid algae *Achaeolithophylum* and gastropods (Figure 3.10c). The fauna is of very low diversity and bioclasts are poorly sorted. There is a packstone -grainstone texture, with a sparse muddy matrix probably derived from the disintegration of the green algae (Figure 3.10d). The common cements are sparry cements replacing the original aragonite of the green algae. In addition, there are marine fibrous calcite cements.

The skeletal association is dominated by photozoan organisms (chloroforam) which probably lived in a regime of low nutrient supply since it is characteristic of an oligotrophic environment.

This microfacies is ascribed to a very shallow-marine environment of the inner ramp within a regime of low energy. It could correspond with facies SMF 18-Gymno or RMF 20 of Flügel (2004).

3.5.2.7 Dolomite

This microfacies is formed mainly of equigranular dolomite and shows light grey, whitish and yellowish colours (Figure 3.10e). Some crystals are saddle dolomite (Figure 3.10f). All primary components such as echinoderms, algae and peloids have been replaced and the suggestion is that the original limestone was bioclastic grainstone-packstone. The dolomites are mostly massive with little intercrystalline porosity. The crystals show subhedral and anhedral shapes ranging from 50-200 microns in size.

Dolomitization probably occurred in the shallow subsurface during the early stages of burial. It may have been connected to sea-level fluctuations and seawater circulation within the sediment. Continued dolomite precipitation during burial is likely for the formation of the saddle dolomite. This facies corresponds to RMF 22 of Flügel (2004).

3.5.2.8 Massive gypsum

This facies forms structureless beds interlaminated with wavy laminated clayey lime mudstone. The microfacies shows euhedral to subhedral elongate gypsum crystals (0.3-0.05 mm in size), in single, twin and crystal clusters (Figure 3.10g, h). The most likely depositional environment is a hypersaline sabkha and this facies would correspond to SMF 25 or RMF 25 of Flügel (2004).

3.5.2.9 Mixed bioclastic rudstone-packstone

This microfacies shows a mixture of broken bioclastic elements from different organisms such as brachiopods, bivalves, ostracods and crinoids (Figure 3.11a). The angular shape could indicate reworking in a high-energy regime. This facies has a light grey colour and is usually massive. The common bioclasts are pseudopunctate brachiopods and ostracods.

Marine fibrous cements occur as crusts on brachiopod and bivalve shells, and later sparry and bladed calcite crystals are also present. Pyrite replaces calcite in some skeletal fragments. Mechanical compaction has affected bioclasts and matrix, stylolites and pressure dissolution seams are also present (Figure 3.11b).

This facies was most likely deposited in a brackish lagoon or tidal area with storm influences controlled by climatic process. It could correspond to RMF 12 of Flügel (2004).

3.5.2.10 Calcareous sandstone

This is characterized by mixed clastic-carbonate sediment, a dark grey colour and a wavy lamination too. The sediments contain abundant brachiopods, crinoids and sand-size quartz, but are poorly sorted and closely packed. The bioclasts are highly fractured but punctate brachiopod shells, bivalves and minor small foraminifera and crinoids can be recognized (Figure 3.11c,d).

Radiaxial fibrous calcite is present between brachiopod fragments as well as bladed cements. In addition, dissolution seam and stylolites affect bioclasts and matrix.

This microfacies reflects high energy within the subtidal zone where there was also an important clastic input, probably from storms. There is no corresponding microfacies in Flügel (2004) due to that classification being only concerned with pure carbonate sediment.

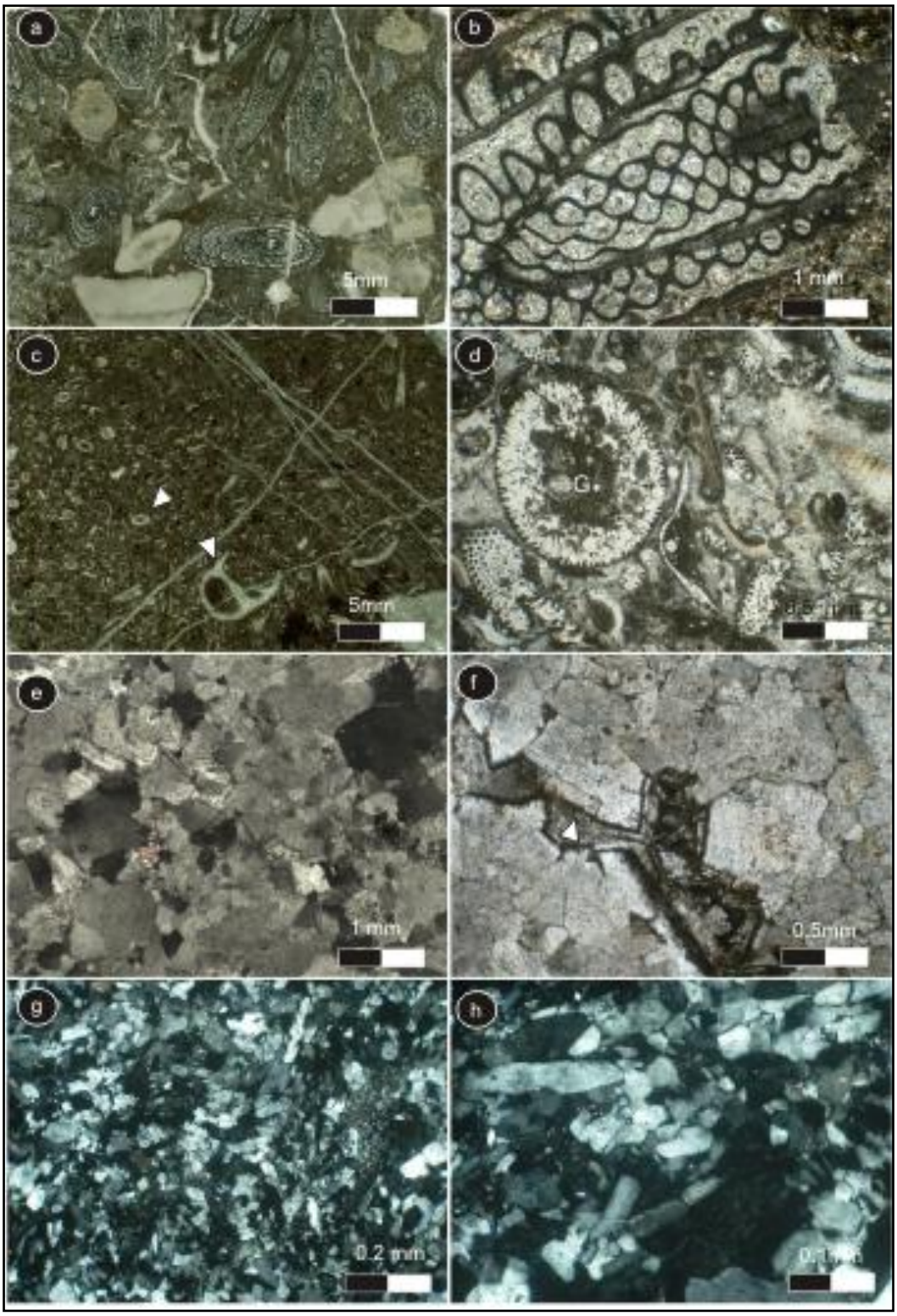

Figure 3.10. a) Fusulinid grainstone-packstone. Note different sections through the fusulinids (F) probably *Triticites sp*.and *Parafusulina* sp. b) Fusulinid grainstone-packstone. Note microgranular wall of fusulinid as well as sparry cement filling chambers. c). Calcareous green algal packstone. Green algae *Gymnocodiacea* (G) and gastropod fragments (*arrows*) embedded in a muddy matrix. d) Calcareous green algal packstone. Details of green alga *Gymnocodiacea* (*arrows*) surrounded by bryozoan and brachiopod fragments. e) Dolomite. General view of dolomitized facies. f) Dolomite. Note saddle dolomite (*arrows*) and intercrystalline porosity probably filled by bitumen. g) Massive gypsum. Note euhedral and subhedral shapes of the crystals. h) Massive gypsum with elongate crystals.

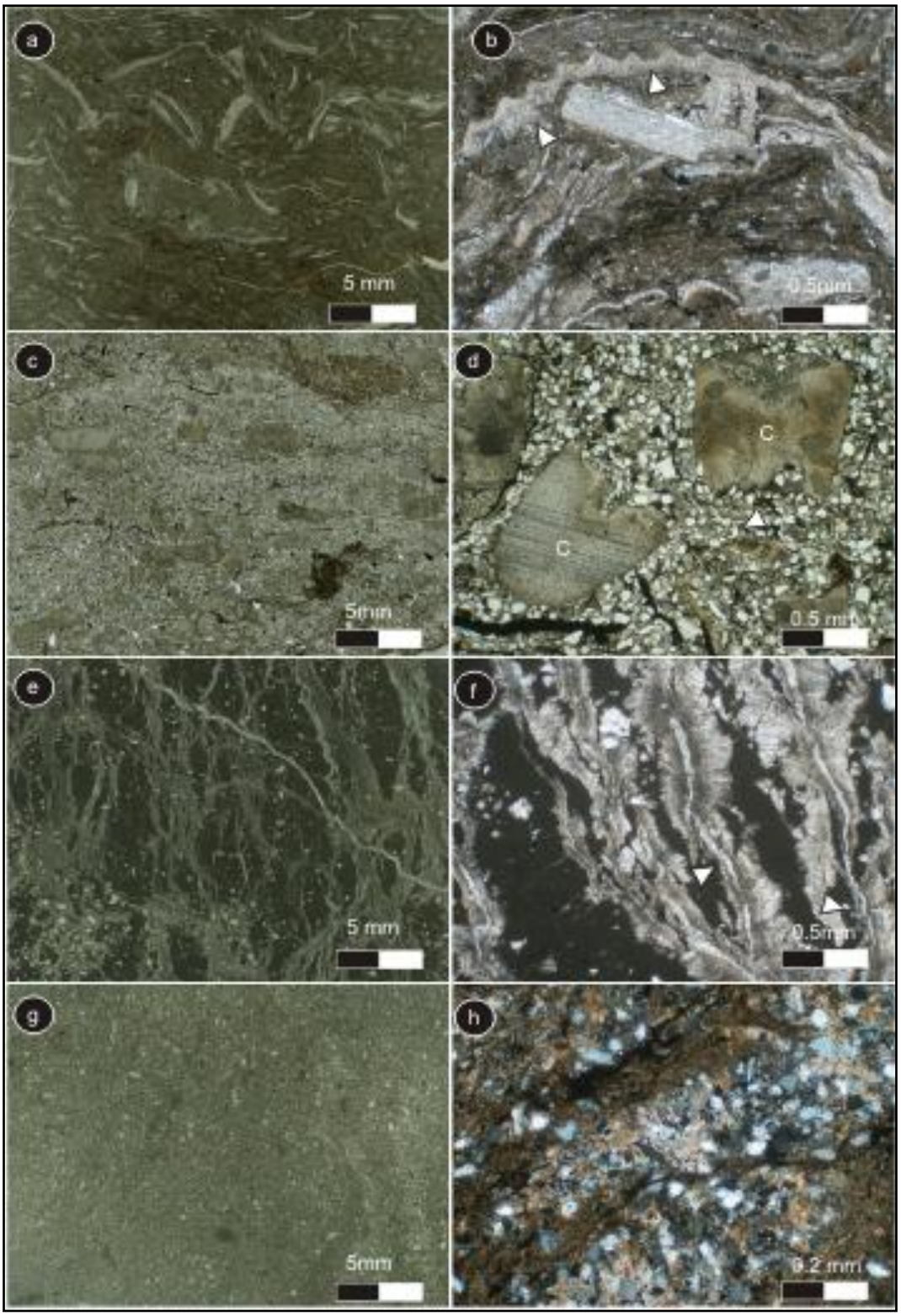

Figure 3.11. a) Mixed bioclastic rudstone-packstone. Sparse brachiopod fragments embedded in muddy silty matrix. b) Mixed bioclastic rudstone-packstone. Brachiopod fragment broken and coated by fibrous cements (*arrows*). c) Calcareous sandstone. Crinoid-rich debris mixed with sandy silty quartz. d) Calcareous sandstone. Broken crinoid fragments (C) within fine sandy matrix (*arrows*). e) Clayey lime mudstones. General view of fine bioclasts with silt-size quartz grains. f) Clayey lime mudstones. Slightly laminated clay mixed with microcrystalline calcite cements and fine quartz grains. g) Calcrete. Brownish lime mud mixed with clay and fine grained quartz. h) Calcrete. Syn-sedimentary fractures filled by fibrous cements (*arrows*).

3.5.2.11 Calcrete

This microfacies is mostly composed of lime mud mixed with clay and quartz. There are few carbonate grains, although peloids occur which show irregular to nearly spherical shapes. Bioclast diversity is low, with just ostracods and fragments of bivalve shells (Figure 3.11e).

This facies has a brownish colour, possibly due to Fe-staining or organic matter impregnation. There are vertical-subvertical fenestrae and elongate micritic zones which could be rootlets or rhizoliths. In addition, there appear to be calcite crystal aggregates that are reminiscent of *Microcodium*. However, this is not 100% convincing but nevertheless it is thought to be related to subaerial exposure in view of the association with mud-cracks and fibrous (feathery) cements (Figure 3.11f).

This facies is interpreted as a supratidal deposit that has been affected by pedogenesis and subaerial exposure that resulted in a palaeosoil of calcrete type. It probably corresponds to SMF 23 of Flügel (2004).

3.5.2.12 Clayey lime mudstone

This facies comprises a mixture of clay, silt-size quartz and lime mud, as well as organic matter (Figure 3.11g, h). It often has a laminated or flaser structure. There is a lack of bioclasts, but it is highly bioturbated. This microfacies can be interpreted as mixed clastic-carbonate mudflat associated with lagoons in a low-energy zone. There is no corresponding facies in the Flügel (2004) scheme.

3.5.2.13 Quartz siltstone

This microfacies is mainly composed of detrital silt-size quartz, with finer-grained sediments, partly lime mud and partly terrigenous clay, also kaolinite and illite (Figure 15a, b). This facies has a light to dark brown colour with lamination, mud cracks, ripples and bioturbation. It is also locally enriched in organic matter. A tidal flat of medium to low

energy is the most likely depositional environment. There is no corresponding microfacies in the Flügel (2004) scheme.

3.5.2.14 Arkosic sandstone

This is well-sorted massive sandstone with a light to dark brown colour and cross stratification, locally planar and wavy, with ripples. The sediments are characterized by fine sand-size feldspar and quartz grains, and also present are muscovite, illite and smectite (Figure 3.12c, d). This facies can be interpreted as an estuarine deposit from a coastal area, perhaps with tidal channels and sand flats. There are no fossils present. There is no corresponding microfacies in the Flügel (2004) scheme.

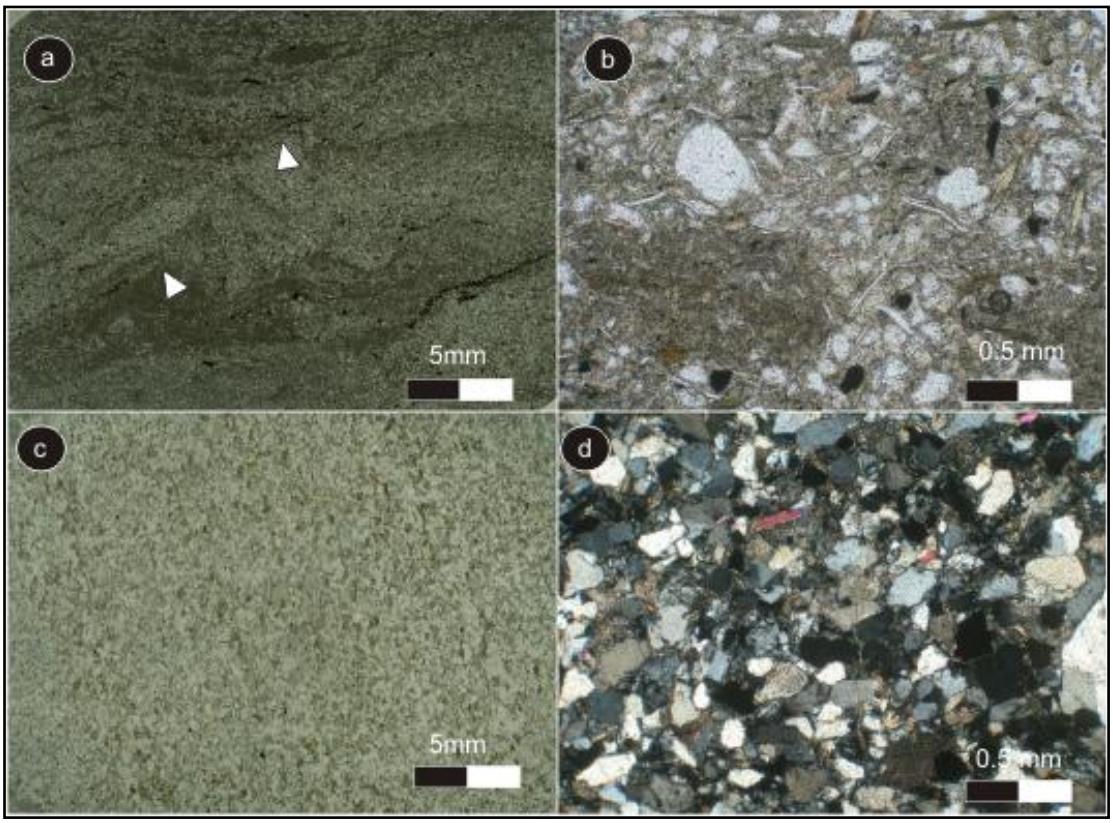

Figure 3.12. a) Quartz siltstone. Note bioturbation modifying the original lamination (*arrows*). b) Quartz siltstone. Fine-grain quartz embedded in a silty-muddy matrix composed of micas and clay minerals. c) Arkosic sandstone. General view of homogeneous sandstone. d) Arkosic sandstone. Note quartz and feldspar grains closely packed.

3.6 Discussion

3.6.1 Depositional environment.

From the facies described above and the fact that the succession shows no evidence of slope deposits, the most likely interpretation of the Palmarito Formation is that it was deposited on a homoclinal ramp, as described by Read (1982, 1985, 1989) Tucker et al. (1990); Tucker and Wright (1990), Burchette and Wright (1992), Jones and Desrochers (1992), Wright and Burchette (1996) and Flügel (2004). The model shows different sub-environments from the *inner to mid to outer ramp* with distinctive sub- and micro-facies. The *inner-ramp* is characterized by areas of exposure with calcrete, tidal-flats and evaporites, and shallow lagoons and inner shoreface sand shoals. A photozoan association with calcareous algae and large foraminifera is typical of a clear warm shallow-marine environment. Also, the inner/mid-ramp may well have been under the strong influence of storms. The *mid-ramp* is an area from the shoreface offshore, with skeletal packstones and wackestones formed of a heterozoan association of crinoid and bryozoan fragments and possibly with a crinoid-fenestrate bryozoan buildups (mud mounds). The *outer ramp* of deeper subtidal sediments consists of muddy facies with different types of sponge spicule and bryozoans (Figure 3.13).

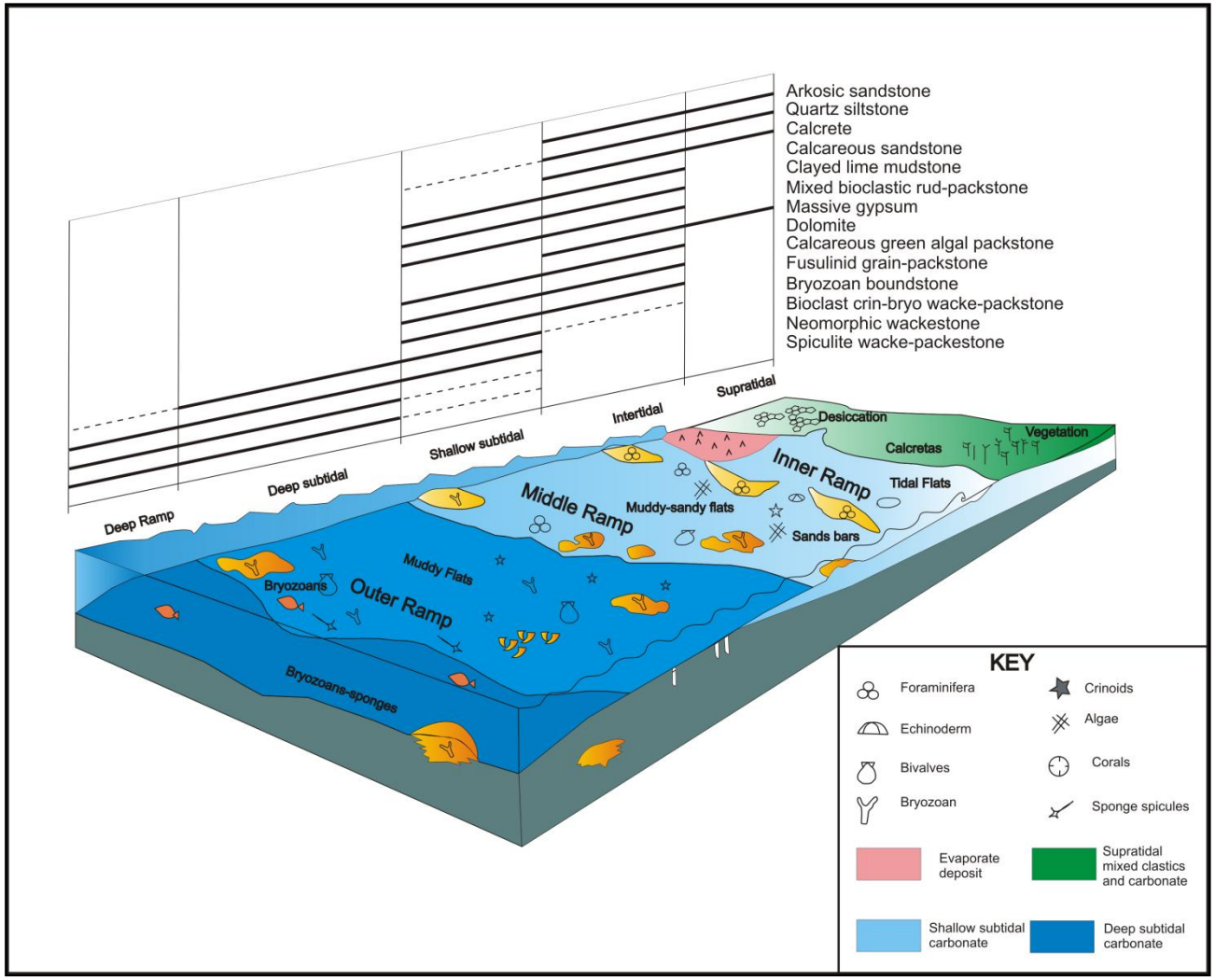

Figure 3.13. Schematic model showing the location of the defined microfacies types within the carbonate ramp model. After Blomeier et al. (2009).

3.6.2 Carbonate ramp evolution.

The succession through the Palmarito Formation can be divided into 6 broad facies units reflecting various phases of deposition during the long-term evolution of the carbonate ramp, and a response to long-term changes in sea-level and / or the effects of tectonics. The early part of the Palmarito Formation (depositional phase 1, ~70 metres thick) consists of peritidal facies that are noteworthy for their sub-metre-scale mud-to-sand cycles. Within the first part of the succession there occur the heterolithic, muddy micrite, massive sandstone, calcrete and laminated shale facies. The lack of fossils is a feature with just some remains of plants, rare ostracods and small bivalves, which overall suggests a high degree of exposure and low nutrient availability, within an area influenced by continental sediment input. Supra- and inter-tidal flat deposits of mixed sediments show evidence of exposure with calcretes and mud-cracks. Although the palaeosoils are not very well developed they still indicate pedogenesis; occasionally the tidal flats were flooded and shallow brackish lagoons established. Thus, this first part of the succession represents the shallowest part of the Formation and overall belongs to an inner ramp setting (Figure 3.13 and light grey colour in Figure 3.14).

The tidal-flat facies grade upwards to shallow subtidal mixed clastic-carbonate facies (phase 2; ~30 metres thick) that are characterized by thin storm beds and bioclastic lenses, arranged into metre-scale coarsening-upward cycles (green in Figure 3.14, details of the cycles are presented in Chapter 5 and Appendix 1). The facies associated are calcareous sandstone, clayey lime mudstone, mixed bioclastic rudstone-grainstone and calcrete. Bioclasts become more common up through the section but they are usually broken and mixed with important amounts of siliciclastic material as a result of reworking by storms. The incipient nature of the calcretes suggests short-term subaerial exposure.

Thin silty-sandy beds which coarsen and thicken upwards are interbedded with the phase 2 carbonates. With some poor biotubation structures, they can be interpreted as tidal heterolithic sand-bar facies. These deposits also occur higher up within the unit and they probably represent episodic events of clastic influx; they could be related to tropical climate changes (e.g. increased intensity of a monsoonal climate). The clastic influx could be the result of sea-level falls although there is little evidence for water depth change or associated tectonic movements.

Upwards the overall transgressive trend is evident with the occurrence of deep subtidal facies (depositional phase 3, ~50 metres thick; dark blue on Figure 3.14); this includes Spiculite wacke-packstone, Neomorphic wackestone, and Bioclastic crinoidal-bryozoan wackestone-packstone. The diversity of the marine biota increases dramatically and remarkably well-preserved brachiopods are found in their living position within the laminated clayey lime mudstones that form the deepest parts of the shallowing-upward subtidal cycles (Chapter 5). The main components are brachiopods, crinoids, bryozoans, small foraminifera, gastropods and sponge spicules; these represent an open-marine fauna (heterozoan association), probably of the middle to outer ramp (dark blue on Figure 3.14).

Above the deep subtidal facies, the succession passes up sharply into shallow-marine facies (depositional phase 4, ~200 metres thick) with Calcareous algal packstone, Fusulinid grainstone-packstone, and Bioclastic crinoidal-bryozoan wackestone-packstone; these are all photozoan associations. The bedding within this part of the succession shows a thickening upwards that suggests prograding and shallowing upwards. There appears to be an upward increase in dominance of oligotrophic organisms, and this could be the result of a decrease in nutrient supply to the environment. The highly productive carbonate factory of this time lead to the filling of available accommodation space in the basin.

The shallow-marine facies are interbedded with several packages of poorly-bedded massive limestones, composed of bryozoans, crinoids, sponges, brachiopods and foraminifera. There are three microfacies within the massive limestones, namely Spiculite wackestone-packstone, Bioclastic crinoidal-bryozoan wackestone-packstone and Bryozoan boundstone. It is noteworthy that there are encrustations between sponges, bryozoans and rugose corals, and fibrous calcite cements are commonly present. Although there are no clear field indications of a mound geometry due to the quality of the outcrops, the thick beds of massive limestone and the particular fauna, along with the fibrous calcite cements, do suggest a mud-mound type buildup (see review of Bridges et al., 1995) . Bridges et al. (1995) recognized 5 different mud-mound facies types and the three Palmarito microfacies are very similar to Bridges et al. (1995)'s type 1 Fenestrate bryozoan-sponge facies, type 2 Crinoidal-bryozoan facies, and type 3 Crinoidal-brachiopod-fenestrate bryozoan facies. These likely mud mound carbonates would have been deposited in the middle to outer ramp setting.

The uppermost part of the Palmarito Formation (phase 5, ~100 metres thick) consists of cyclic deeper-ramp facies that include Spiculite wackestone-packstone alternating with bioclastic crinoidal-bryozoan wackestone-packstone. Farther upwards carbonate buildups re-appear and are interbedded with thick dolomites. They pass upwards into thin peritidal facies (phase 6, ~20 metres thick; light blue on Figure 3.14) and massive gypsum (pink on Figure 3.14) and these are in unconformable contact with red beds belonging to the Jurassic La Quinta Formation. However, the unconformity cannot be seen in all of the sections, just those on the Palmar River.

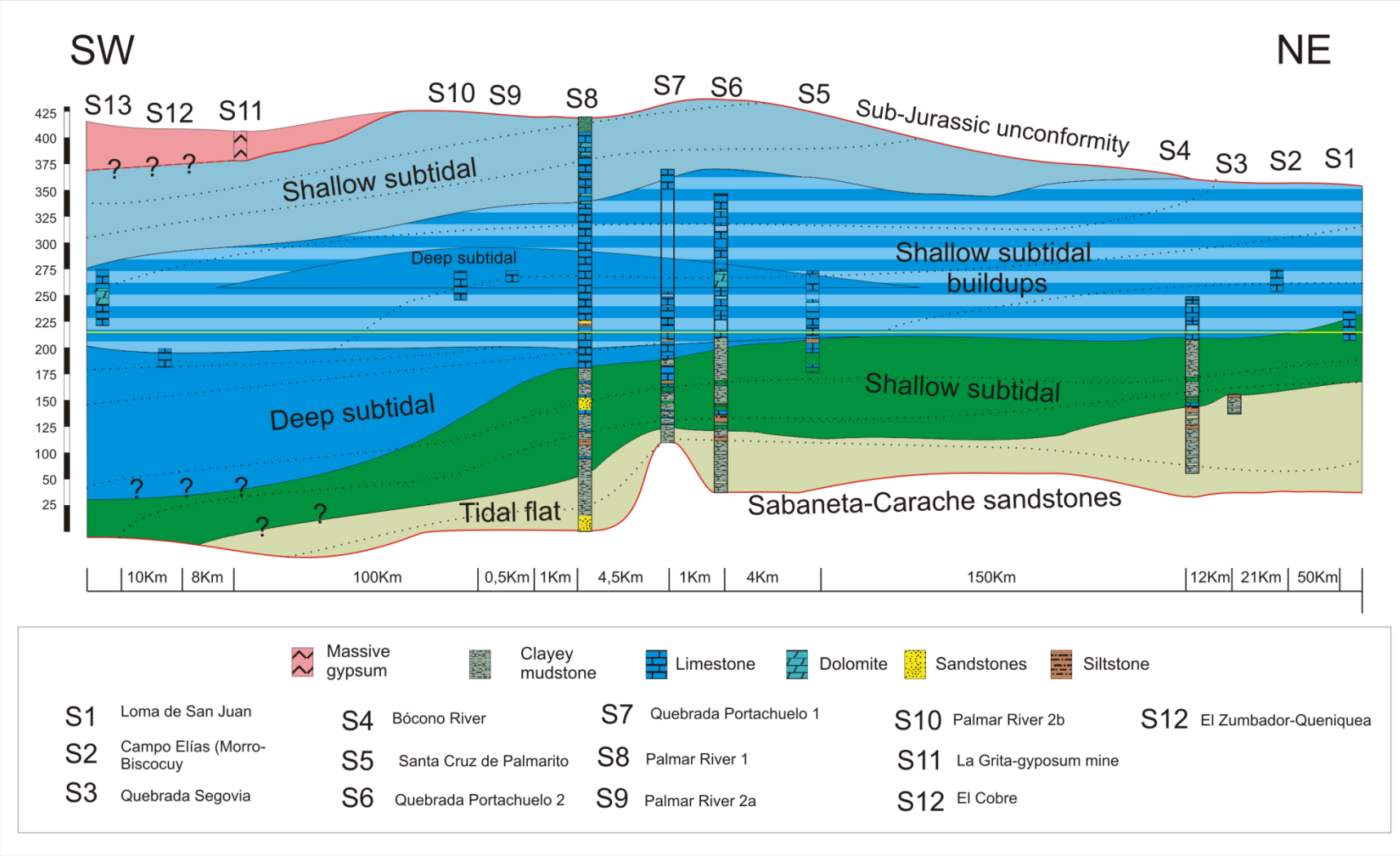

Figure 3.14. Schematic correlation panel of the 12 successions from the Venezuelan Andes.

3.6.3 Palaeogeographic implications

The Permian was an important time in Earth history since it was then that the Pangea supercontinent was formed and this enormous landmass significantly affected many global processes including tectonics, climate and ocean circulation, as well as evolution. Several authors have constructed maps of Pangea for the Permian including Pindell et al. (1985), Scotese and Langford, 1995; Scotese, 1999, Vai (2003), Vachard et al. (2004), Blakey (2006) and Miall and Blakey (2008).

Different interpretations have been made for the equatorial Pangean region, where Venezuela was located at this time. These interpretations can be divided in two groups. First, the group which supports the model of Pangea as formed during the Permo- Carboniferous through the collision between Laurentia and Gondwana (Scotese and Langford, 1995; Scotese, 1999; Blakey, 2007; Tabor and Poulsen, 2008) which is represented by the Alleghenian orogeny and the Marathon-Ouachita orogeny in North America. The implication of these tectonic events is the closing of the seaway between Palaeo-Tethys and the Panthalassa Ocean during the Early Permian. The second group supports the existence of a seaway connecting Palaeo-Tethys and Panthalassa which lasted until the late-Early Permian (Davydov and Leven, 2003; Izart et al., 2003 and Vai, 2003). This interpretation has been based on palaeontological evidence such as Tethyan brachiopods and fusulinid distribution. The second interpretation accounts for shallow-marine environments over western Venezuela during the Permian. Nevertheless, none of these publications have described the depositional setting of this Venezuelan basin nor how it was connected and related to neighbouring oceans.

The Palmarito Formation can be correlated thought Colombia to the west and southwest, where a few outcrops of limestone and shale with fusulinids can be found in the Teorama-Calixto area and nearby Bucaramanga City (Villarroel and Mojica, 1987). To the

northwest, a marine succession can be followed with the Manaure Formation in the Perijá Mountains, close to the border between Venezuela and Colombia (Forero, 1967). Farther northwest the Mexican and Guatemalan microterrane (MGT) was moving northwards whilst shallow-marine sediments were being deposited on probable isolated platforms. These depositional events are represented by the Tactic, Esperanza and Chochal Formations in Guatemala-Belize and México (Vachard and Foucade, 1997; Vachard et al., 2004). Over the western flank of the Yucatán Block (YUC), which had collided against the northeast of Gondwana, shallow-marine carbonates were also deposited.

The evidence that has been presented above and the new data from the Palmarito Formation suggest a new setting for northwest Gondwana (Figure 3.15) in the Early -Middle Permian. The Mucuchachi Basin (MB) is proposed as a foreland basin within which the marine carbonates of the Palmarito Formation and their equivalents in Colombia were deposited. The MB may well have been connected to the basins in Perú and Bolivia to the south, and with those in the north in the Mexican and Guatemala Terranes (MGT) and Yucatán Block (YUC), creating a remnant sea between Laurentia and Gondwana. The eastern boundary was an orogenic wedge, comprising igneous and metamorphic rocks and continental volcanics (Feo-Codecido et al., 1984; Viscarret et al., 2009). In addition, a narrow channel may well have existed between west and east Pangea to provide an explanation of the Tethyan fauna found within the Mucuchachi Basin (MB). Finally, the southeast border was the South American Craton (SAM), also called the Guyana Craton which was part of continental Gondwana (Figure 3.15).

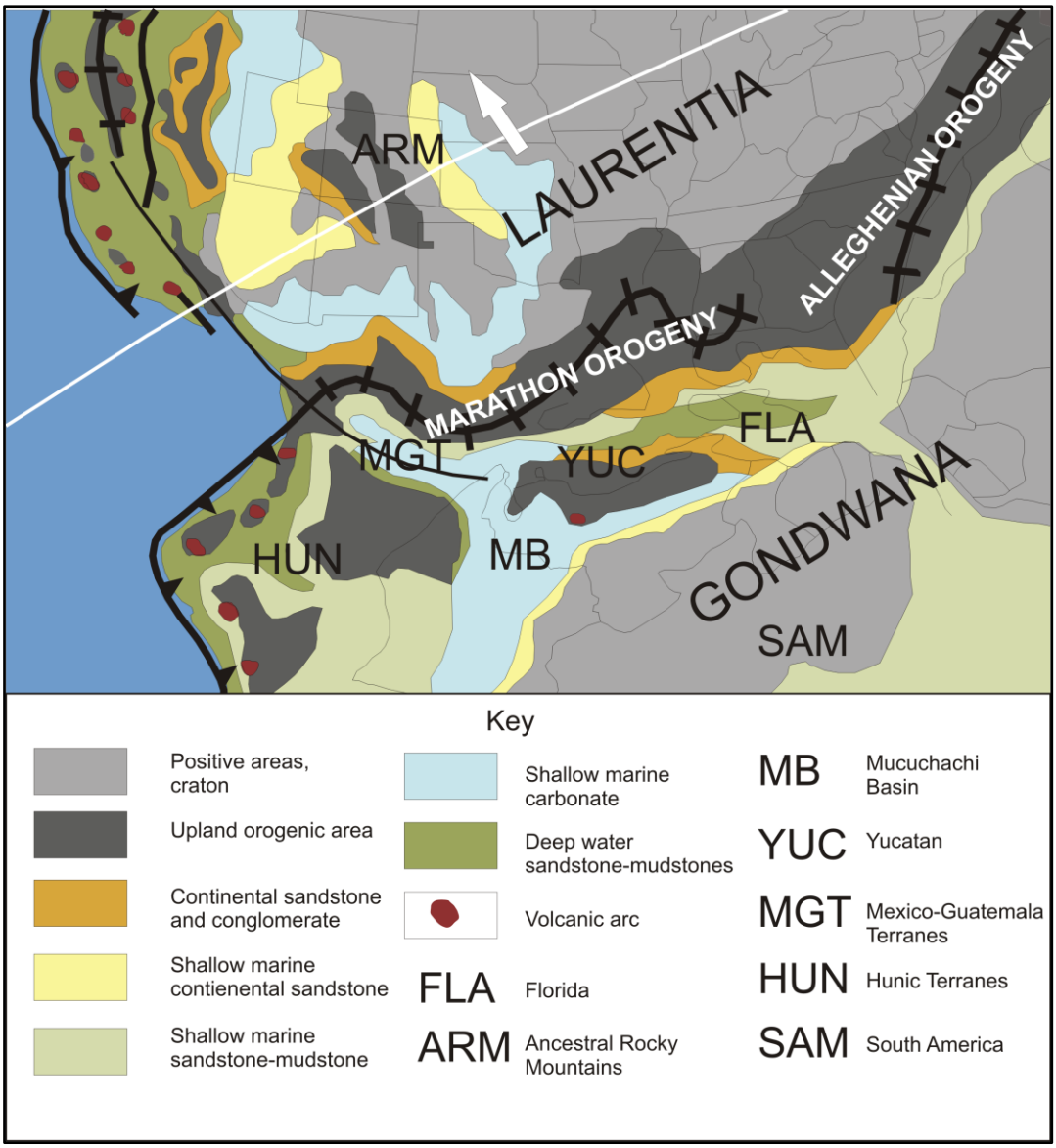

Figure 3.15. Palaeogeographic map of northern Gondwanaland and southern Laurentia during the Early to Middle Permian. Modified from Miall and Blakey (2008) and Blakey (2007); also available in (http://cpgeosystems.com/gallery.html).

The internal facies distribution of the Mucuchachi Basin (MB) in Western Venezuela for the Sakmarian-Artinskian (295-275 Ma) is not easy to define (Figure 3.16). The basin appears to have deepened towards the northwest, away from the Guyana craton, where continental environments covered a large part of southwestern Venezuela. These passed gradually to tidal-flat facies and, moving to the west, increasingly to marine carbonates. Finally, the deepest part of the basin was located to the northwest of Lake Maracaibo.

The transgression which flooded the ramp during the Artinskian-Roadian (275-268 Ma) (Figure 3.17) came from the northwest towards the southeast, and almost covered the

whole of the eastern part of the basin. Most of the area was covered by shallow to deep subtidal carbonates with a predominance of the heterozoan skeletal association. The sea-level was rising, probably due to melting of the ice caps during the post-glacial period after Glaciation III, according to Isbell et al. (2003) or during the interglacial period between the P2 and P3 glaciations, according to Fielding et al. (2008). The main depocentre seems to have been located in Colombia by this time. However, there is no strong evidence for this, except for the reference to a very thick succession from the Perijá Mountains recorded by Villarroel and Mojica (1987). The deepening trend recorded in the Palmarito succession is consistent with deposition in a foreland basin (e.g. Bosence 2005) In addition, the orogenic wedge appears to have been moving progressively from the east to west (Feo-Codecido et al., 1984; Viscarret et al., 2009), generating the flexural subsidence that created the high accommodation space for the Palmarito.

Finally, during Roadian to probably Early Capitanian times (Figure 3.18), relative sea-level was falling; this may well have been the result of developing glaciation P3, as suggested by Fielding et al. (2008). Also, aridification was developing in the region (Grossman et al., 2008), leading to evaporite facies. A large part of the Palmarito ramp was exposed and eroded at this time. Meanwhile, the orogenic wedge continued moving southwards; this probably caused the closure of the sea-way with Palaeotethys, so that from this time Pangea was completely formed.

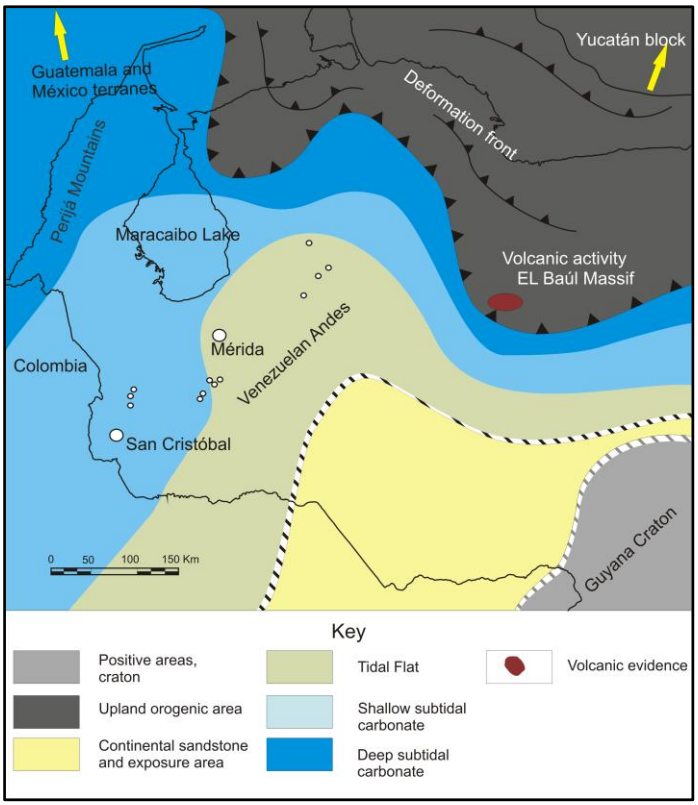

Figure 3.16. Palaeogeographic map of Western Venezuela during the Sakmarian- Artinskian (295-275 Ma).

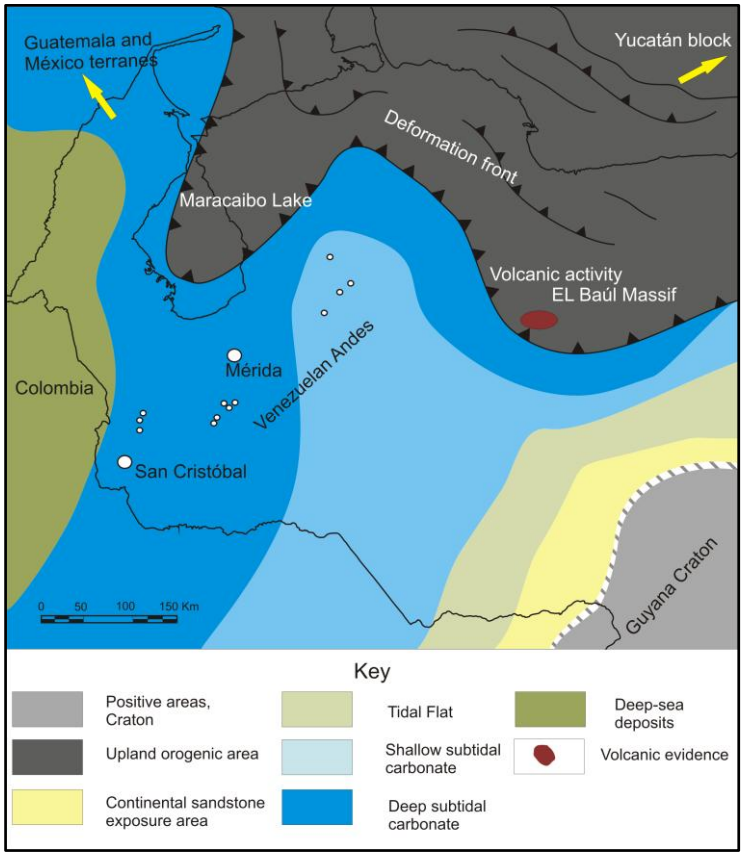

Figure 3.17. Palaeogeographic map of Western Venezuela during the Kungurian-Wordian (275-265 Ma).

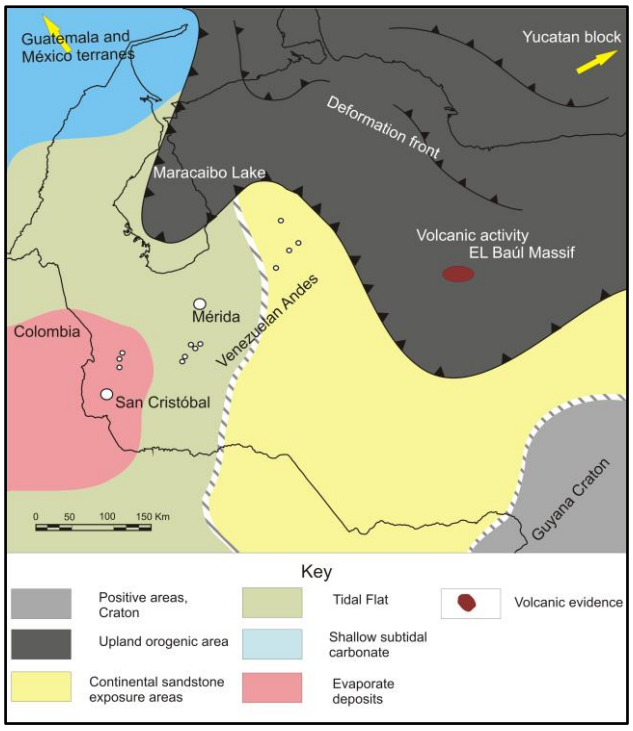

Figure 3.18. Palaeogeographic map of Western Venezuela during the Wordian-Capitanian (265-260 Ma).

3.6.4 Controls

3.6.4.1 Climate

The Permian carbonates in the Venezuelan Andes were strongly influenced by climatic factors in this low latitude tropical Gondwanaland, with dominant humid conditions in the lower part of the Palmarito, giving way to a more arid climate in the upper part of the succession. Tabor and Poulsen (2008) discussed climate change in equatorial Pangea from humid conditions during the Late Carboniferous passing through a transitional period to a more arid climate in the Late Permian. The Palmarito Formation shows evidence of humid conditions in the lower part with facies rich in plant remains and an estuarine flora (e.g. *Lobatopteris vestita*, *Annularia stellata*, *Delnortea* cf. *D. abbottiae*) that has been studied by Ricardi (2008) and this shows a trend to aridification upwards. The neighbouring basins to Venezuela, such as the Solimões Basin in Brazil (e.g.the Jurúa, Carauri and Fonte Boa formations) and the Delaware Basin in the southern USA (e.g. the Castille, El Salado, Yates

and Tansill formations), all record extremely arid conditions with thick evaporite successions during the Middle to Late Permian.

3.6.4.2 Sea-level changes

Overall, much of the Palmarito succession shows a general transgressive trend, with several thinner, more regressive units. This contrasts with the long-term regressive trend through the Permian documented by Haq and Shutter (2008). The difference probably relates to the strong, long-term, underlying regional tectonic subsidence history of this northern area of South America, creating the additional accommodation space. There are similarities between the Permian deposits of Venezuela and those recorded from Guatemala, Belize and southern México, for instance the Chochal and Tactic formation, where carbonate systems also dominate. These facies were all part of an ancient tropical Caribbean or Proto-Caribbean setting that has not been recognized in many palaeogeographic interpretations. After Palmarito Formation deposition, probably in the Late Permian in the Venezuelan Andes region, a major relative sea-level fall, probably tectonically induced, led to extensive uplift and erosion, resulting in the major disconformity between the Guadalupian carbonates and overlying Jurassic red beds.

3.6.4.3 Tectonics

Upper Palaeozoic tectonics in northern Gondwanaland were dominated by a compressive tectonic regime as a result of the collision between Gondwana and Laurentia during the Permo-Carboniferous, which involved Alleghenian and Marathon-Ouachita orogenesis (Miall and Blakey, 2008; Pindell et al., 1985). These processes were complicated as a result of the irregular nature of the plate boundaries involved in the collision, which left a remnant sea between these two continents. This can be regarded as an ancient tropical Caribbean or Proto-Caribbean sea, where the Palmarito Formation was deposited on the margins. Furthermore, subsidence in the area could have been affected by the existing

compressive regime and associated increasing flexural effects, which would have increased the accommodation space available for sedimentation within the basin.

3.6.4.4 Carbonate factory

Jones and Desrochers (1992) have defined the carbonate factory as the area of carbonate sediment production that is controlled by oceanographic and biological processes, nutrient supply, and clastic input. The nature of the carbonate factory and degree of sediment transport are direct controls on the development of a carbonate ramp and its growth rate. In this case, it can be suggested that increasing productivity in the carbonate factory is evident up through the succession as a result of the reduction in clastic input, probably related to the development of a more arid climate during the Middle to Late Permian. In addition, according to Martin (1996), there was a global increase in nutrient supply to the oceans, reaching a mesotrophic stage during the Permian, which again allowed a decrease in productivity of the carbonate factory. Although the area where the Palmarito Formation was deposited seems have been a restricted basin, the deposits seem to follow the global trend. This argument is supported by the microfacies which have been described above; they show an increasing faunal diversity, a dominance of heterozoan organisms, increasing thickness of massive limestones and the presence of a mud-mound heterozoan association. According to Bridges et al. (1995) the latter are related to upwelling currents which could have brought substantial nutrients to the carbonate ramp. However, continental run-off could also have been the cause of increased nutrient supply to the carbonate factory of heterozoan organism.

3.7 Summary and conclusions

The Palmarito Formation is part of the supraterrane, tectonostratigraphic unit defined by Bellizia (1992) that is the sedimentary cover of all Palaeozoic terranes in western Venezuela; it was deposited in the Mucuchachi Basin, as named by Arnold (1966). The Palmarito Formation can be correlated with the Río Momboy and El Aguila formations which

occur throughout the Venezuelan Andes but were metamorphosed as a result of Mesozoic to Cenozoic regional events. Thus, sedimentation of the Permian carbonates is a widespread phenomenon in northwest Venezuela, with possible extensions and correlations through Colombia to the southwest, then to Perú and Bolivia, but also northward to Guatemala, México and also to the southern USA.

The succession of the Palmarito Formation has been ascribed to a homoclinal ramp model in tropical northern Gondwanaland. This interpretation is supported by the features of the 10 macrofacies and 14 microfacies that have been identified. Broadly, the succession begins with heterolithic calcareous sandstone, mudstone and siltstone with ostracods and plant debris of a tidal-flat environment (phase 1); these grade upwards to dark-grey calcareous deeper-ramp deposits (phase 2). Farther up, the succession becomes more shallow-marine with calcareous algal packstone and fusulinid grainstone (phase 3), that represent inner ramp deposits and sand bars, and then crinoidal-bryozoan wackestone of the middle to deep ramp with some buildups (phase 4), also deep ramp facies interbedded with dolomites (phase 5) and finally lime mudstones and evaporites (phase 6). Evidence presented from the Palmarito Formation indicates a new setting for northwest Gondwana in the Early to Middle Permian with the Mucuchachi Basin interpreted as a foreland basin.

Deposition of the Palmarito Formation was largely controlled by climate, sea-level, tectonics and the nature of the carbonate factory. Through the succession, climate in this low-latitude region changed from humid through to a more arid climate in the upper part. Along with this the Palmarito succession shows a general overall transgressive trend until the end of the Permian. A major sea-level fall in this Venezuelan Andean region lead to extensive uplift and erosion, resulting in a major disconformity between these rocks and overlying Jurassic red-beds. Furthermore, Upper Palaeozoic tectonics in northern Gondwana was dominated by a compressional regime due to the collision between Gondwana and Laurentia. This resulted

in flexural effects leading to increased subsidence and creation of accommodation space within the developing foreland basin. Finally, the nature of the carbonate factory changed with the upwards decrease in clastic input, that was associated with the aridification towards the late Permian time. Related to this, Martin (1996) proposed a global increase in nutrient supply to the oceans, reaching a mesotrophic stage during the Permian which allowed the dominance of heterotrophic organisms in the carbonate factory (Wright and Burchette, 1996).

4 Carbon, oxygen and strontium isotopes of the Permian carbonates in the Venezuelan Andes. Climatic proxy of tropical Pangea.

Abstract

The Late Palaeozoic period was an important time in Earth history, primarily as a result of the formation of Pangea and the Gondwana glaciations that had direct influences in high latitudes and indirect, but no less important effects in low latitudes. The main aims of this chapter are to document and interpret the isotopic record for the Early-Middle Permian in Northern Gondwana. Detailed fieldwork in the Venezuelan Andes has been supplemented by petrographic studies and stable isotope analyses ($\delta^{13}C$ and $\delta^{18}O$), as well as dating using $^{87}Sr/^{86}Sr$ in brachiopod shells.

Sr-isotope dating of well-preserved brachiopod shells suggests a Kungurian age from samples located within the middle part of the Palmarito Formation. This is supported by biostratigraphy, which indicates that deposition started during the Sakmarian–Artinskian, and continued up until the early Capitanian in the Middle Permian. Carbon isotope ratios (expressed as $\delta^{13}C$) show a long-term trend through the section towards more positive values. However, in the lower part of the studied succession the very negative $\delta^{13}C$ values of the carbonates suggest they have undergone pedogenic and/or diagenetic groundwater alteration. In the middle part of the succession, major excursions in $\delta^{13}C$ show a strong connection with glacial/deglacial events during the Early to Middle Permian. Although oxygen isotope values (expressed as $\delta^{18}O$) are prone to diagenetic alteration, there are similarities between low-Mg calcite bioclasts (which are resistant to alteration). The relative trends through the succession suggest cooler periods are coincident with glaciations P3 and P4 proposed by Fielding (2008). The results presented here then fill an important gap in the regional palaeogeography and therefore have important implications for the palaeoclimate and palaeoceanography of the time.

4.1 Introduction

The assembly of Pangea during the Permian triggered important geological, oceanographic and climatic events, which had a direct influence on the geological record. Many isotope studies of Permian rocks from the equatorial region of Pangea have been undertaken during the last two decades, primarily focusing on specifically understanding palaeoceanography and palaeoclimate (e.g. Tabor and Montañez, 2002; Isbell et al., 2003; Brant, 2004; Korte, 2006; Montañez et al., 2007; Tabor and Poulsen, 2008; Fielding et al., 2008; Peyser and Poulsen, 2008). As a result, palaeoclimate models have been developed which show reconstructions of palaeoprecipitation, palaeotemperature and the variation in position of the inter-tropical convergence zone (ITCZ) during the Permian. However, there is still insufficient information about regions around northern Gondwana, particularly for Central and South America.

In northern South America, Upper Palaeozoic strata were deposited extensively over peri-cratonic areas, but in many places they are rarely exposed, and so poorly documented. This is largely the result of extensive weathering and dense vegetation in the tropical Andes, as well as the remoteness of the outcrop areas. However, these strata do contain significant information for palaeogeographic and palaeoclimatic reconstructions and the evolution of northern Gondwana, and it is shown here that a seaway existed between Gondwana and Laurentia until middle Permian. In fact, few authors support the existence of a seaway connecting Palaeotethys with Panthalassa, suggesting after the late-Early Permian (Davydov and Leven, 2003; Izart et al., 2003 and Vai, 2003). This interpretation has been based on palaeontological evidence such as Tethyan brachiopods and fusulinid distribution. re-interpretation of the palaeogeography accounts for shallow-marine environments over western Venezuela during the Permian. Nevertheless, none of these publications have

described the depositional setting of this Venezuelan basin, nor how it was connected and related to neighbouring oceans (Figure 4.1).

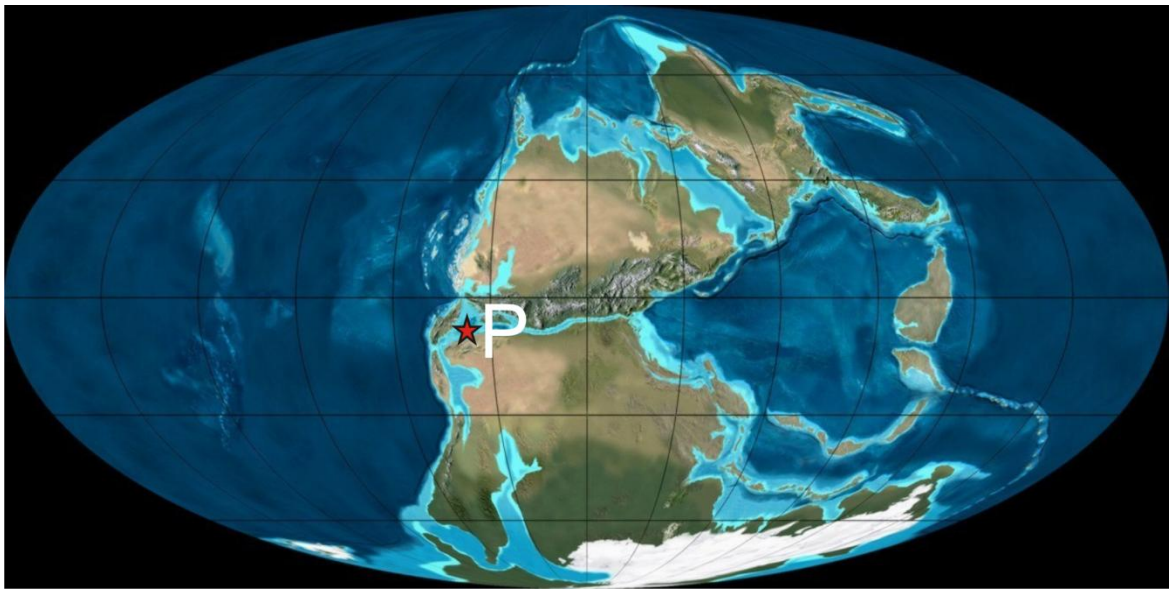

Figure 4.1 Mollweide projections of Early Permian Artinskian (280 Ma) modified from Blakey (2007). Red star represent palaeogeographic location of Palmarito Formation (P).

Permian rocks in Venezuela have been described by Bellizia, (1992), Garcia (1972), Odreman and Wagner (1979), Arnold (1966), Viscarret (2002) and Viscarret and Laya (2007). However, the description of the facies and microfacies of the Palmarito Formation which crops out throughout the Venezuelan Andes and the depositional environments suggest that there was seaway connecting central Pangea with basins to the northwest and also a connection to the southwest with basins in the Bolivian-Peruvian region. This would have implications for the regional climate in terms of land-sea distribution, supercontinentality, uplift/collapse of the Central Pangean Mountains and the source of moisture.

The Palmarito sediments were deposited on a carbonate ramp that dipped basinwards towards the north facing the open ocean. The formation evolved from the underlying fluvial (Sabaneta Formation) through tidal-flat to mid-outer ramp deposits, with all facies recording a well-developed cyclicity. The aims of this study are to present and discuss the stable isotope record in the context of the sedimentology of the Palmarito Formation located in western

equatorial Pangea, and to consider this data in terms with climatic and oceanographic regimes in low latitudes during the Permian. The Permian succession in Venezuela covers the poorly known region between Gondwana and Laurentia, before the final assembly of Pangea. The results presented have important implications for understanding the palaeoclimate and palaeoceanography of the time.

4.2 Methods

Samples of whole rock and brachiopods were taken from the successions recorded in sections located in the Portachuelo area in the southern Venezuelan Andes (Figure 4.2). Carbonate powder was collected using a hand-drill on brachiopods and pestle and mortar for matrix-whole rock samples. Strontium, carbon and oxygen isotopes were determined on unaltered brachiopod shells of low-Mg calcite that could retain original seawater signatures. For matrix-whole rock material only carbon and oxygen isotopes were determined.

4.2.1 Sections

For this study, four sections in the Portachuelo area were sampled. These are located to the south of Merida city (Figure 4.2).

1) ***Santa Cruz de Palmarito*** is located 100 m southwards from a small chapel called 'Santa Cruz de Palmarito' along a mule trail. The section has been described by Arnold (1961) and Hoover (1981). The succession is formed of ~100 m of fossiliferous massive and nodular limestones that are assigned to the middle to upper part of the formation.

2) ***Quebrada de Portachuelo 2*** comprises outcrops from the head of the stream towards the west, which is located on the eastern flank of a syncline. The succession shows a younging-direction that is parallel to the stream flow and opposite to that in the Quebrada de Portachuelo 1 Section. The middle and upper part of the Palmarito Formation is exposed showing massive grey-bluish, highly fossiliferous limestones and crystalline dolomite, dipping westwards.

3) ***Quebrada de Portachuelo 1*** exposes rocks in the stream which are on the western flank of a syncline that is the main structural feature of the area. The 175 m thick section consists of lime mudstones and sandstones which grade into thick massive limestones of the Palmarito Formation, resting on reddish sandstone and mudstone of the Sabaneta Formation.

4) The ***Palmar River*** exposes Palmarito strata consisting of a thick succession of calcareous sandstones and mudstones with ostracods which pass upwards to calcareous algal packstone, fusulinid grainstone, crinoidal-bryozoan wackestone and finally dolomites interbedded with boundstone containing sponges. This is the most complete and best exposed section where it is possible to find the base and top of the Palmarito Formation.

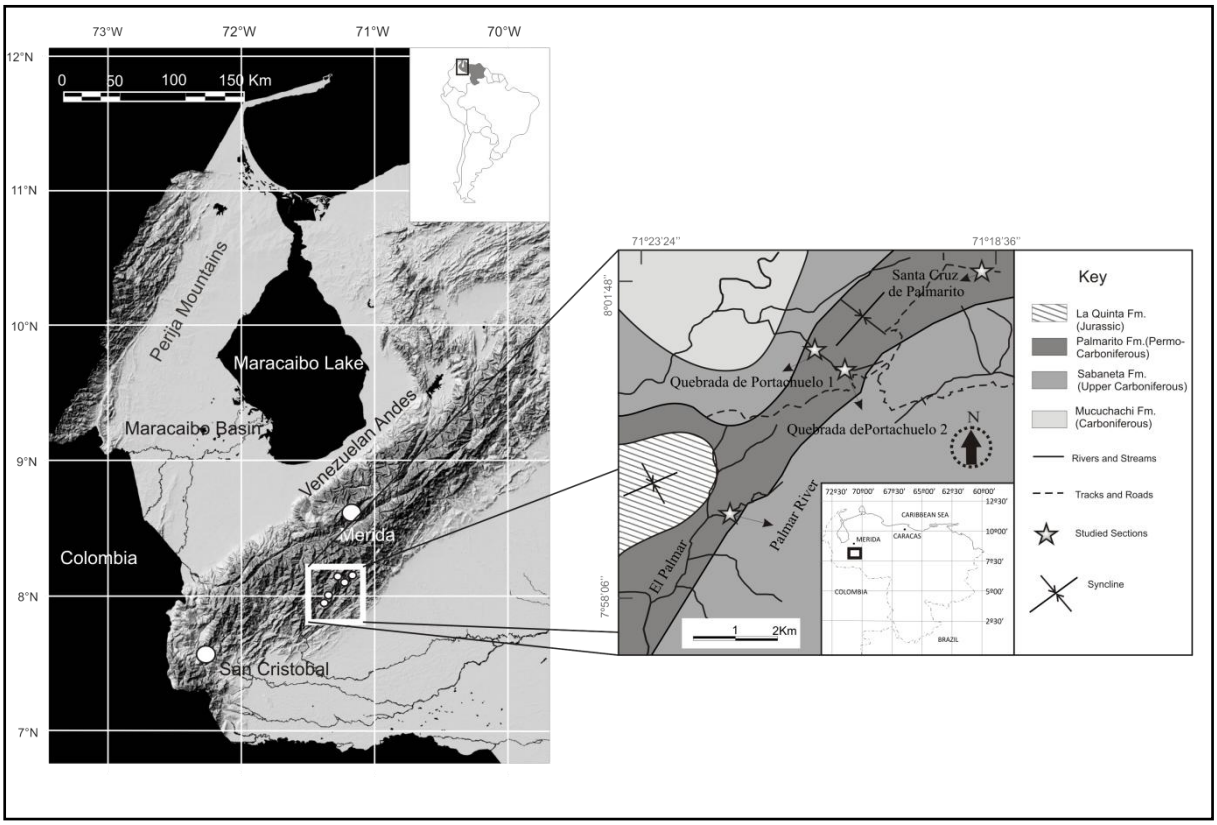

Figure 4.2 Digital shaded relief image of western Venezuela showing the location of the main area of study. Modified from Garrity et al. 2004. (http://pubs.usgs.gov/of/2004/1322/.). And detailed geological map of the Portachuelo are south area of Venezuelan Andes.

4.2.2 Sample screening

Brachiopod shells are composed of low-Mg calcite which is normally stable and resistant to diagenetic alteration. According to Brand (2004), brachiopod shell material is the

most suitable for the study of ancient sea-water composition. However, a suite of tests was undertaken to discard material that had been altered; these included microtextural analyses using petrography, scanning electron microscope (SEM), cathodoluminescence (CL) and trace element analyses.

4.2.2.1 Trace element contents

The internal layers of fifteen brachiopod shells were drilled and analyzed for trace elements (Ca, Si, Na, Fe, Al, Mg, K, Ba, Sr, Mn, Zn, P, Ti and S). 10 mg powders were weighed and placed in vials of 20 ml together with 10 ml (5%) HNO_3. The solution was left reacting for at least 2 hours. 20 ml beakers (samples and blanks) were spiked with 10 ppm yttrium, to act as an internal standard. Three different groups of standards were made: first, Ca (75 ppm, 150 ppm, 300 ppm and 600 ppm) and then a second group of 10 ppm, 20 ppm, 30 ppm and 60 ppm for Si, Na, Fe, Al and K. A final group contained 5 ppm, 2.5 ppm, 1.25 ppm, 0.625 ppm, 0.313 ppm and 0.156 ppm of Mg, K, Ba, Sr, Mn, Zn, P, Ti and S. Samples, blanks and standards were analyzed in a Perkin Elmer Optima 3300RL ICP OES (Inductively Coupled Plasma Optical Emission Spectrometer). This and the previous stage were carried out under the direction of Dr C. Ottley (Senior Research Officer) Durham University.

4.2.3 Carbon and oxygen isotopes

The carbon and oxygen analyses were performed at Birmingham University using the following procedure:

100 -140 μg of powdered carbonate were placed into 4 ml glass vials then sealed by a lid and pierceable septum. The vials were placed in a heated sample rack (90°C) where the vial head space was replaced by pure helium via an automated needle system as part of an Isoprime Multiflow preparation system. Samples were then manually injected with approximately 200μl of phosphoric acid and left to react for at least 1 hour before the headspace gas was sampled by automated needle and introduced into a continuous-flow

Isoprime mass-spectrometer. Duplicate samples were extracted from each vial and a mean value obtained for both $\delta^{13}C$ and $\delta^{18}O$. Samples were calibrated using IAEA standards NBS-18 and NBS-19 and reported as ‰ on the VPDB scale. An external precision of better than 0.1‰ is typically achieved for both $\delta^{13}C$ and $\delta^{18}O$ (Boomer, 2011, Pers. comm.).

Additionally, some of the samples were analyzed in the Stable Isotope Biogeochemistry Laboratory in NCIET (Northern Centre for Isotopic and Elemental Tracing) at Durham University. The procedure was the same but it was carried out using an Isotope Ratio Mass Spectrometer Thermo Finnigan Gasbench II connected to a Thermo Finnigan MAT 253.

4.2.4 Strontium isotopes

Using hand-drill and micromill techniques, powders were collected and analyzed for their $^{87}Sr/^{86}Sr$ isotope ratios in the Arthur Holmes Isotope Geology Laboratory in NCIET. Samples were extracted from low-Mg calcite shells by micro-mill sampling using a New Wave Instruments™ Micromill™ system. This technique was developed by Charlier et al. (2006) and used by Deegan et al. (2010) and Font et al. (2008). The New Wave Instruments™ Micromill™ system comprises a stage, drill and binocular microscope connected to a computer work-station. The system is driven by software which projects a microscopic image of a thick section of the sample, in this case the brachiopod shells. The drilling point location can be placed in an X-Y coordinate system with accuracy up to 1 µm. A hand-drill was also used directly on fragments of the brachiopod shells with less accuracy using a drill-bit up to 1 mm in diameter. Afterwards, all powders were placed in 3 ml beakers and subjected to a dissolution procedure which consisted of dissolving powders in ultra-pure distilled acid. The strontium fraction was then separated by micro-Sr column chemistry described by Charlier et al. (2006). Finally, samples from the micro-mill technique were place in a thermal ionization mass spectrometer, (TIMS) and the samples from the hand-

drilling procedure were put in a plasma ionization multi-collector mass spectrometry,MC-PCP-MS PIMMS (Neptune). Results were reported in ratios with a range of standard deviation of ±0.000016 to ±0.000012 (2σ). The samples were analyzed in a single session during which the average $^{87}Sr/^{86}Sr$ value for NBS 987 was 0.710262 ± 0.000016 (2σ) (n=4) for the TIMS which agrees extremely well with the accepted NBS 987 $^{87}Sr/^{86}Sr$ value reported by Thirlwall et al. (1991) of 0.710248±0.000023 (2 σ) (n=427) and the average $^{87}Sr/^{86}Sr$ value for NBS 987 was 0.710259 ± 0.000012 (2σ) (n=8) for the PIMMS.

4.3 Geological background

The Palmarito Formation is part of the Palaeozoic tectonostratigraphic unit in western Venezuela that has been referred to as a supraterrane Bellizia (1992); the sediments were deposited within the Mucuchachi Basin a name introduced by Arnold (1966). Sedimentation of Permian carbonates seems to be a widespread phenomenon in northwest Venezuela, with likely extensions and correlations through Colombia to the southwest, then to Peru and Bolivia farther south, but also northward to Guatemala, Mexico and also to the southern USA.

Palmarito Formation strata have been ascribed to a carbonate ramp model within northern Gondwanaland. This formation overlies the Sabaneta Formation and is unconformably in contact at the top with the La Quinta Formation of Jurassic age. The deposits begin with clastic heterolithic calcareous sandstone, mudstone and siltstone with ostracods and plant debris of a tidal-flat environment, these grade upwards to dark-grey calcareous deeper-ramp deposits. Further up, the succession becomes more typical of a shallow-marine sediment with calcareous algal packstone and fusulinid grainstone, that represent inner ramp deposits and sand bars, and then crinoidal-bryozoan wackestone of the middle to deep ramp with some buildups. Some dolomites are interbedded in the deeper ramp facies and finally lime mudstones and evaporites terminate the succession.

4.4 Results

4.4.1 Results from screening samples.

4.4.1.1 Microtextural preservation

The primary, outer layer of brachiopod shells is commonly altered and for this reason the secondary internal layer was sampled (Scholle and Ullmer-Scholle, 2003) after examination with the scanning electron microscope, as Korte et al. (2005) proposed, for any sign of alteration. In thin-section, samples are composed of fibrous calcite crystals with no signs of recrystallization (Figure 4.3). However, some of the shells do have punctate that seem to be recrystallized; in other cases the punctate are holes filled by diagenetic cements (Scholle and Ullmer-Scholle, 2003). For this reason, these areas were avoided. Under the SEM, the fibrous structure is again well preserved with no micro- or nano-scale evidence of neomorphism or borings.

4.4.1.2 Cathodoluminescence (CL)

With cathodoluminescence (CL), all samples show very dull or almost no luminescence (Figure 4.3). Nevertheless, (Gröcke et al., 2007) have proposed that this technique has to be complemented with other tests.

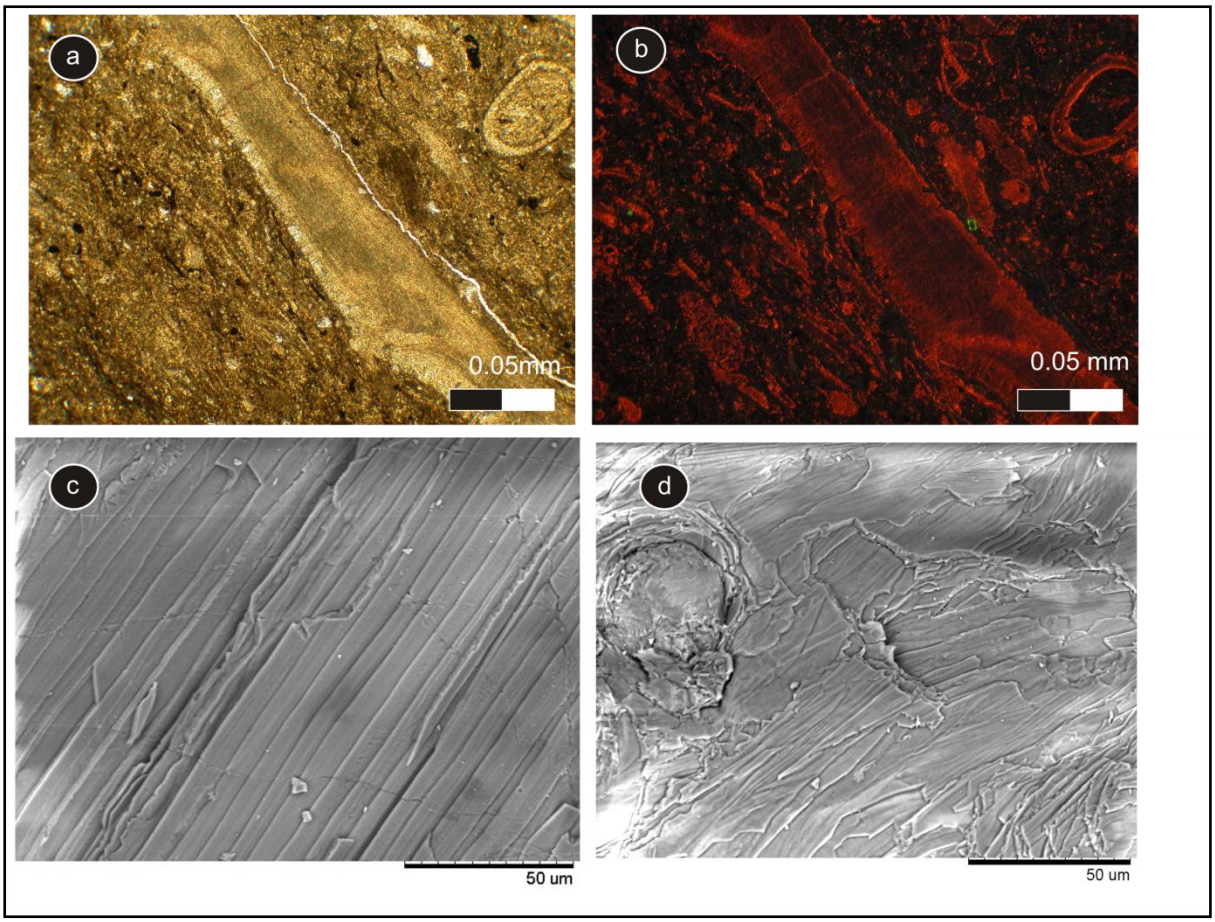

Figure 4.3 a) Petrography, b) Cathodoluminscence (CL), c) SEM analysis showing well preserved brachiopods shells and d) SEM analysis showing punctate of the brachiopods shells which were avoided for this analysis.

4.4.1.3 Trace element contents

Different authors have established cut-off values above which the shell material is considered to have been affected by diagenesis. Brand (2004) followed the values proposed by Denison et al. (1994), namely suitable material less than 300 ppm Mn and 3000 ppm Fe. Korte et al. (2005) considered concentrations no greater than 250 ppm Mn and 300 to 3400 ppm strontium as acceptable and Popp et al. (1986) supported this. With the Palmarito secondary layer of shells, the concentration of Mn is slightly high (average 283 ppm) and Fe is quite high too (9589 ppm) (Table 2.1), but they do show very good preservation in cathodoluminiscence petrography and SEM (Figure 4.3). For these reasons, the shells are

considered acceptable for Sr isotope analysis and it is believed that the values should reflect the composition of Permian sea-water.

Table 4.1. Trace elements of secondary layer of brachiopods

Sample	Fe (ppm)	Sr(ppm)	Mn(ppm)
67-A	9351	903	287
N1-A	13120	978	405
N1-B	7322	1423	578
BQ-1	967	927	130
BQ-2	26154	869	323
BQ-3	12398	867	212
BQ-4	5080	874	526
BQ-5	25633	896	386
BQ-6	3361	750	116
BQ-7	9129	747	118
BQ-8	16902	532	130
BQ-9	9746	826	92
BQ-10	4050	1704	110
129	-	-	-
138-A	-	-	-
141-shell	3171	740	610
143-shell	6442	1085	488
144	-	-	-
152	-	-	-
154-shell	367	970	22
109-B	-	-	-
109-A	-	-	-

4.4.2 Strontium isotopes

Ten seemingly unaltered brachiopods from the Portachuelo and Palmar sections were analyzed for their strontium isotopes. The values vary between 0.707223 and 0.707435. However, sample 138-A shows a much higher value, up 0.708537; this could have been the result of contamination from clay-rich matrix during the micro-drilling process; clay minerals can be enriched in more radiogenic strontium thus increasing the value (Table 4.2)

Table 4.2 $^{87}Sr/^{86}Sr$ values and ages in M.y. based in GTS (2004)

Sample	$^{87}Sr/^{86}Sr$	Age (My)
67-A	0.707286	271.00
N1-B	0.707223	270.44
N1-A	0.707324	271.72
138-A	0.708537	-
109-B	0.707435	273.32
109-A	0.707331	271.88
152	0.707272	270.50
144	0.707319	271.60
143	0.707325	271.71
129	0.707366	272.00

4.4.3 Long-term trends in carbon isotope values

There is a long-term trend through the succession in $\delta^{13}C$ of progressively increasingly negative and then increasingly positive values from -9‰ to +5.3‰ (see appendix 3). The negative values of the carbon isotopes are present in the pedogenic facies within the tidal-flat facies of the lowest part of the carbonate ramp succession. The long-term positive trend is typical of the Permian and it has been attributed to several factors including a long-term increase in nutrient supply to the ocean leading to a sub-mesotrophic to mesotrophic regime during the upper part of the Permian (Martin, 1996). The common interpretation for this increase in positive $\delta^{13}C$ values is through elevated organic productivity and burial which would have led to an ocean carbon reservoir that is more ^{13}C enriched. Cardenas and Harries (2010) suggested that this phenomenon triggered evolutionary opportunities due to the improvement of the food-web complexity created by an increased abundance of primary producers.

The first part of the Palmarito succession is attributed to the Artinskian stage and this is where the $\delta^{13}C$ values of the palaeosoil facies are very negative as a result of the decomposition of organic matter and light soil CO_2 being incorporated into the pedogenic carbonate. Light $\delta^{13}C$ signatures are characteristic of early diagenesis in a subaerial / pedogenic environment. The succeeding strata are more open-marine deposits and here the

$\delta^{13}C_{carb}$ rises to positive values reaching +2‰; this is a typical open-marine signal (Tucker & Wright, 1990). The increasingly positive trend continues through the Kungurian and then there is a zone where the data show much scatter, with values varying from -1‰ to +5‰ (Figure 4.4). During the Roadian to Capitanian the general pattern is one of less scatter and values varying between +3‰ to +5‰.

In terms of comparison of this isotopic record with strata that have been deposited in similar environments in other basins, the intervals with tidal-flat facies reflect local early diagenesis/pedogenesis and so need to be separated off from the higher, more normal-marine facies which may reflect a more global oceanic signature.

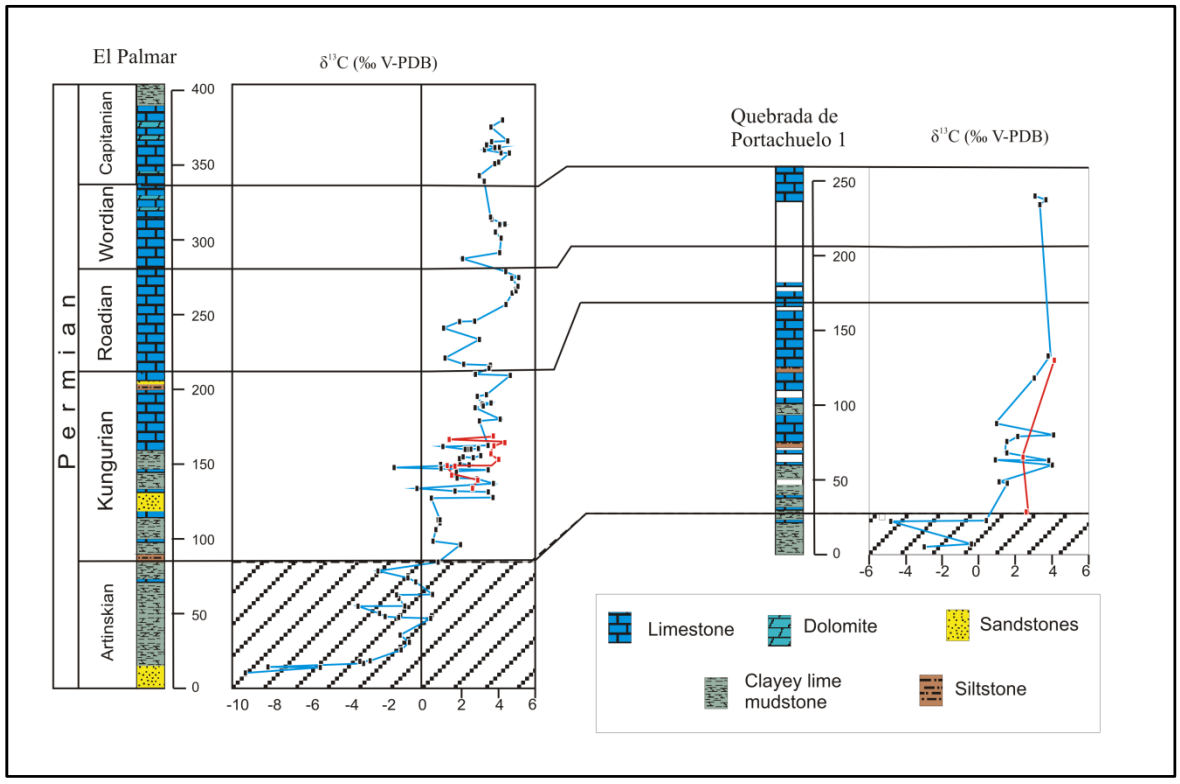

Figure 4.4 Carbon isotopes of whole-rock carbonate(blue line) and well-preserved brachiopods (red line) from Palmar River and Quebrada de Portachuelo 1 successions.

4.4.4 Marine carbon isotope trends

Four localities of the Palmarito Formation have been analyzed and each shows the same broad overall positive trend. However, each succession presents its own particular pattern of which the most common feature is a strong scatter of data-points from the cyclic

deep subtidal strata. In contrast, the data from the Portachuelo 2 section shows a smooth, increasingly positive pattern from +1.6‰ to +5.6‰. A total of 103 samples were collected from different facies of the ***Palmar*** succession of which 82 correspond to marine carbonate strata (see Figure 4.5). The vertical pattern shows up to 5‰ of scatter. The curve starts with values slightly below zero to +1‰ and a range of variation smaller than ~1‰ during the first 50 m of the succession in the marine facies (85.5-127.8 m above the base) (mean $\delta^{13}C$ = +1‰). Upwards an intense scatter in the curve is present with a dispersion of 5‰. Within the interval 127-162 m above the base, it is noteworthy to highlight the negative values in the deep subtidal facies that reach -1.4‰ (mean $\delta^{13}C$ = +2.24‰). Above this part, the $\delta^{13}C$ values become heavier and vary between +2.8‰ to +4.7‰ for the next 50 m (mean = +3.4‰). Values for the next interval of 35 m reveal a decrease in $\delta^{13}C$ with a scatter of 2 per mil (mean = +2.4‰). For the next 40 m above (heights 210-250 m), the isotopes become heavier to the maximum values for the whole succession, increasing from +1 and reaching +5.1‰ (mean = +4.4). Continuing up, there is a less positive excursion with values that fall almost to 3 per mil. Above this, there is an upwards increase with values showing a variation of 1 per mil (mean = +3.92) in the next 100 m, up to the top of the succession.

Seventeen samples were analyzed in the marine carbonate facies from the ***Portachuelo 1*** section (Figure 4.5). The succession starts with low positive values close to 0‰ and they increase to 1‰ in first 25 m of the section (27.8 - 58.8 m above the base). Subsequently, the interval of 58.8 m to 109.5 m exhibits much scatter towards more positive values where the variation is between +0.7‰ to +3.1 ‰. Upwards $\delta^{13}C$ becomes a little more positive, reaching above +4‰ for last part of the succession.

A total of 33 samples were taken from the ***Portachuelo 2*** section (Figure 4.5). In contrast to the last two sections, the data show less scatter, rising smoothly from values higher than +2‰ with a small variation of no more than 0.5‰, except for one sample at 39.4

m above the base which exhibits a signature of +1.6‰. This trend keeps constant to 108.5 m where the values increase dramatically to +5.6‰ in the 100 m above. Afterwards, a less positive excursion is present, with values decreasing to +3.8‰. Subsequently, another interval shows $\delta^{13}C$ values increasing to +5‰. Finally, a drop from +5‰ to +3‰ occurs in the last part of the section.

Twenty-six samples of marine carbonate were collected from the ***Cruz de Palmarito*** section (Figure 4.5). The first values recorded in this succession exhibit near to +4 ‰ and in the initial 10 m above the base a less positive excursion is seen. Afterwards, a heavier isotopic composition is present and this stays relatively constant between +4‰ and +5‰ for the next 45 m above the base. Then, the curve shows a dramatic drop from +4‰ to 0 at 55.5 m above the base. Subsequently, the values show a moderate scatter between +3‰ and +5‰ for the next 30 m. (All data can be consulted in the Appendix 3).

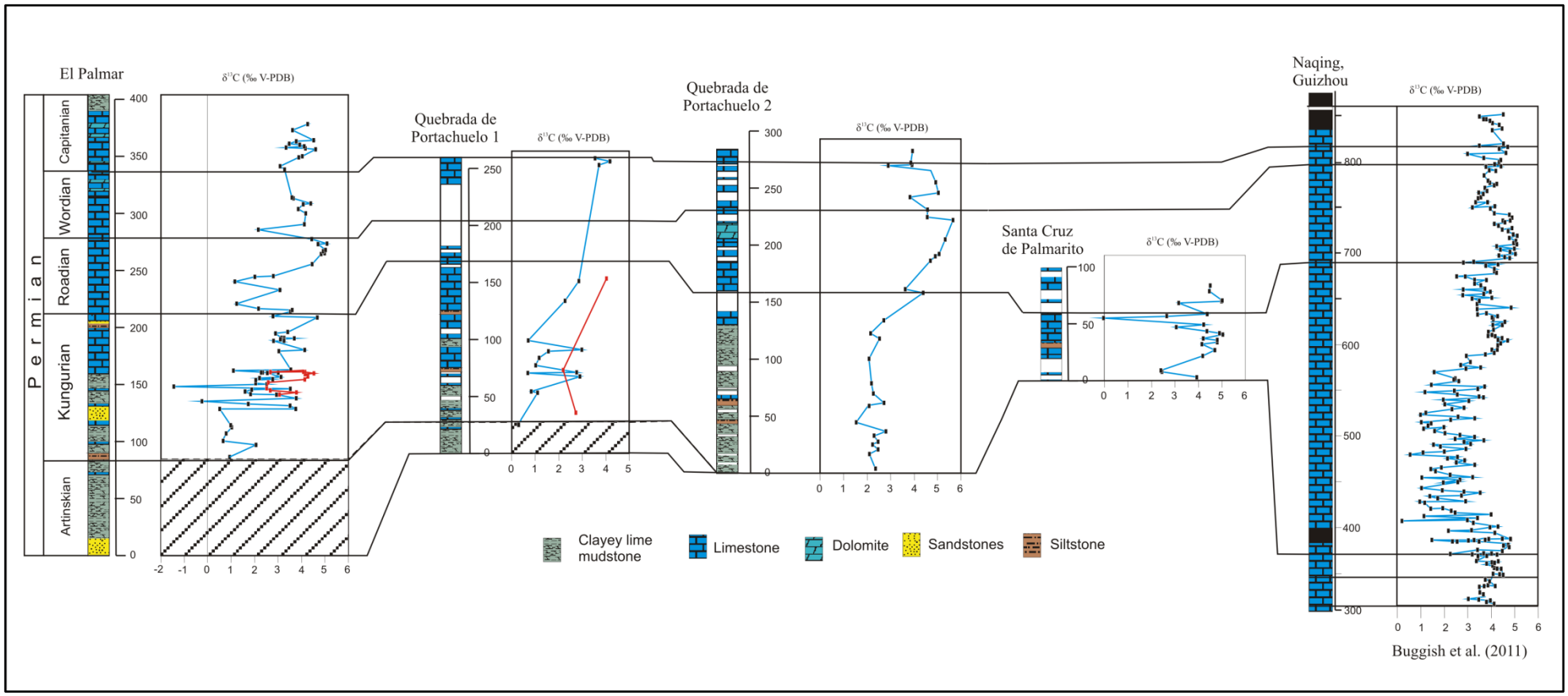

Figure 4.5 Carbon isotopes of whole-rock carbonate from 4 successions in the Portachuelo area, Venezuelan Andes and the Niqing succession from China (Buggisch et al., 2011)

4.4.5 Oxygen isotopes

In general, values of $\delta^{18}O$ in the matrix-whole rock carbonates from the Palmarito strata show a wide scatter and range from -11.8‰ to -2.1‰ with an overall average of -6.3‰. However, the oxygen isotopic signatures from the tidal-flat facies exhibit lighter values with an average of -8‰. In addition, these facies preserve a $\delta^{18}O$ isotopic signal with a high dispersion which includes the maximum and minimum values of the whole succession. Following this, oxygen isotope values of the marine facies lie between -2.9‰ and -9.4‰ (mean = -5.8‰). The range of scatter is smaller than the tidal-flat facies. The last two groups of values exhibit a slightly lighter isotopic composition than the well-preserved low-Mg calcite brachiopod shells. However, the average for brachiopods shows values a little higher than the others, reaching -6.24 ‰.

Fifteen low-Mg calcite brachiopod shells were collected from two sections, namely the Palmar River (n =13), and the Portachuelo 1 sections since only part of the successions contains brachiopods. Values vary between -7.3‰ and -4‰ throughout both sections. These occur within the deeper subtidal facies so that their isotopic signatures may reflect the seawater of the Mucuchachi Basin. (All data can be consulted in Appendix 3)

4.5 Discussion

4.5.1 Age determination from strontium isotopes and chronostratigraphy

The trend of the $^{87}Sr/^{86}Sr$ ratios from Asselian to Capitanian in the mid-Permian is a decreasing pattern that has been related to the decline of continental input as a result of the gradual aridification of Gondwana associated to deglaciation of the southern polar region; this reduced the continental run-off from central and northern Pangea (Korte et al., 2006; Grossman et al., 2008). Sedimentological evidence of the inferred aridification trend can be seen in the Palmarito strata in the form of decreasing clastic input up through the succession and evaporite precipitation towards the top. Since this is a global phenomenon, it would be

expected that the $^{87}Sr/^{86}Sr$ ratios from the Palmarito should show the same behaviour as that of the global trend proposed by Korte et al. (2006) for the Permian. Thus, although, brachiopods are restricted to one part of the Palmarito Formation, their $^{87}Sr/^{86}Sr$ values should lie upon the global Sr curve.

The strong change in the strontium isotope curve does allow the Palmarito values to be used for absolute dating for the horizons where the brachiopods are located. $^{87}Sr/^{86}Sr$ ratios for the Permian have been refined by Korte el al. (2006) (see Figure 4.6).

The ages obtained from the $^{87}Sr/^{86}Sr$ data (see Table 2.2) occur between 270.5 to 273.5 Ma and these correspond to the Kungurian stage according to Gradstein et al. (2004). However, there is an inconsistency with the stratigraphic position of one sample which provided an older date than expected. The sample is from a higher stratigraphic horizon and since the curve at this Permian time is showing a sharp decrease in values, the sample should be showing a lower value. The higher $^{87}Sr/^{86}Sr$ ratio could be due to reworking of the brachiopod shell into a younger horizon or, more likely, it could be an effect of diagenetic alteration, which commonly leads to a higher value since radiogenic Sr is released as a result of low-grade heating.

Brachiopods (Hoover, 1981) and sponges (Rigby, 1984) have been well studied for the time-frame of the Palmarito Formation; however, there is poor biostratigraphic control on the horizons where these fossils are located. Thus, the precise age-range of these fossils has not been easy to determine.

Localities 1, 2, 3 and 4 studied by Hoover (1976, 1981) were included in the succession at Quebrada de Portachuelo 2 for this study. These localities are stratigraphically located in middle and upper part of the formation and were assigned to a Roadian-Wordian age by Hoover (1976; 1981). The Sr analysis reported here does indicate a Kungurian age for the strata below the horizons studied by Hoover (1976, 1981). In addition, cephalopods

appear in the Quebrada de Portachuelo which the same author suggested belong to the late Artinskian. However, the vertical range of the cephalopods is not known, and they could be associated with a level below that from where the samples for strontium dating were collected.

The evidence suggests that the Palmarito Formation could be restricted to the Sakmarian-Artinskian, but possibly it could extend up to the early Capitanian. However, this time-frame needs further investigation. In addition, the Palmarito Formation has great potential for biostratigraphic studies since it does contain several highly fossiliferous horizons.

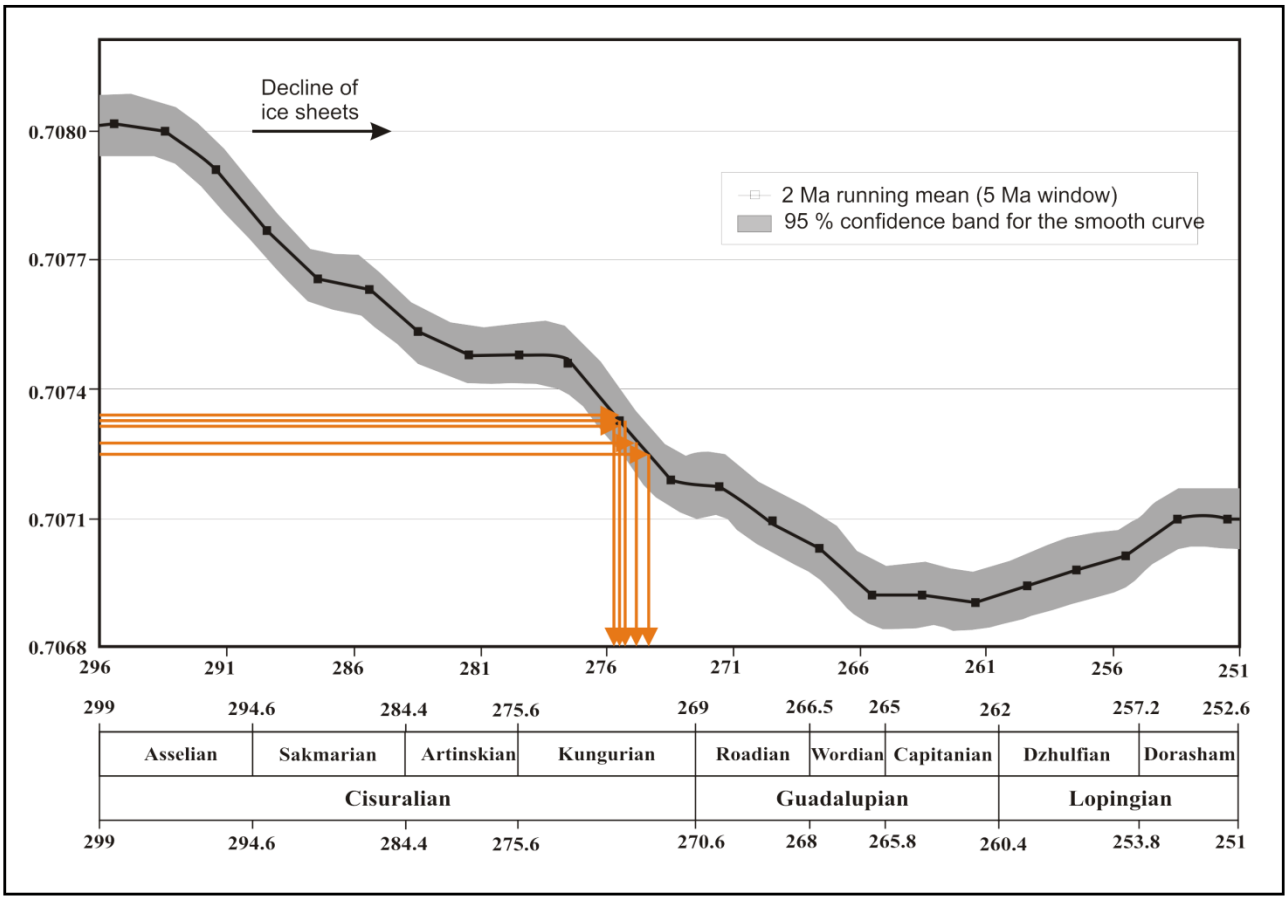

Figure 4.6 $^{87}Sr/^{86}Sr$ mean (2 Ma steps, 5 Ma windows) for well-preserved Permian brachiopod shells from Korte (2006). Orange lines represent Palmarito $^{87}Sr/^{86}Sr$ signatures from well-preserved brachiopods.

4.5.2 Carbon isotopes in Palmarito strata

Carbonate deposits are directly or indirectly affected by climatic factors and sea-level variations. The lowermost part of the formation is probably Artinskian or possibly Sakmarian in age, and is composed of inner-ramp deposits which were subjected to exposure and early meteoric diagenesis. Thus, the carbon isotope values show very low positive or negative values. Upwards, the general trend in the marine record exhibits low positive values closer to 0‰ and these could be the result of weathering and the influx of carbon from terrestrial organic matter which has a much lighter isotopic composition. An increase in continental organic matter input into the basin, with its negative carbon isotopic composition, could be expected during this late phase of deglaciation. This assumption is supported by the interpretation of relatively humid conditions for this period proposed by Ricardi (2008). Also, it is likely that vegetation was relatively dense in terrestrial areas of Venezuela at this time. Within the succeeding marine facies, the data are quite scattered and this is probably due to the influx not only of terrestrial organic matter but also of carbon from marine carbonates composed of brachiopods, crinoids and bryozoans, which generally have a heavier isotopic composition due to the vital effect (Tucker and Wright, 1990). The strong seasonality of humid and arid climate at this stage due to the deglaciation would be a time when the Intertropical convergence zone had a strong north-south migration. However, low positive values are dominant until the middle Kungurian and this could be a reflection of the last phase of deglaciation. This excursion can be correlated with the isotope stratigraphy from the Naqing section in China (Buggisch et al., 2011) that shows a similar fall to lower values. In addition, the same trend can be seen in the $\delta^{13}C$ data from brachiopods collected from the U.S. craton, compiled by Grossman et al. (2008). For the late Kungurian, the curve exhibits strong dispersion but with a dominance of high positive values of around 5‰. This phenomenon is perhaps related to high primary productivity resulting from an increased

influx of nutrients to the carbonate ramp. Furthermore, the increased deposition of organic matter could have led to a reduction in atmospheric pCO_2 and this could have triggered a fall in temperature. As a result, ice caps may have increased in size during this period. In association with this phenomenon, Fielding et al. (2008) have suggested a short period of glaciation during the late Kungurian and also in the Capitanian (glacial phases P3 and P4); these could correspond to the positive excursions that are repeated twice in the four successions. Finally, the trend shows stabilization to values around +4 ‰ during the Capitanian stage. A similar trend is seen in values from brachiopods reported by Grossman et al. (2008) from the Guadalupe Mountains and Buggisch et al. (2011) from the Naqing section in China. Although in general carbon isotope values are much more stable and less prone to alteration by diagenesis compared with oxygen isotope data, some effects of diagenesis cannot be discounted (Figure 4.7).

4.5.3 Oxygen isotopes

Original oxygen isotope signatures in limestones are susceptible to alteration by diagenesis. For this reason, grains and cements originally (and usually still) of low-Mg calcite are preferred in isotope studies seeking the isotopic composition of sea-water since they are the most stable form of the $CaCO_3$ minerals. Well-preserved low-Mg calcite brachiopods in the Palmarito Formation were analyzed as well as matrix-whole rock samples; in general their results exhibit close similarities. Thus, there are two possibilities: First, the values could be reflecting sea-water composition and temperature, or, secondly, if ratios have been affected by diagenesis then it is possible that all components, fossils and matrix could have been shifted uniformly (normally to more negative values) by the alteration, such that the original relative stratigraphic trend is preserved.

During the early-middle Kungurian the oxygen values decreasing towards to more negative ones could indicate development of a warmer period that is probably associated

with the deglaciation interval between glacial stages P2 and P3 of Fielding et al. (2008) (Figure 4.8). After this, the values increase during the late Kungurian-early Roadian and this trend coincides with the positive excursion of carbon isotopes as has been mentioned before; the enhanced deposition of organic matter would have resulted in a reduction of atmospheric pCO_2 and this could have triggered the temperature fall recorded by the oxygen isotope signatures. Fielding et al. (2008) proposed a smaller glaciation (P3) at about this time. Subsequently, for the Roadian stage the results from oxygen isotopes show evidence of a warming which could correlate with a deglaciation. Although it is known from the Quaternary record that the temperature variation between glaciation and deglaciation in low latitudes is really quite small, Grossman et al. (2008) showed a quite large range of oxygen isotope signatures for low-latitude Permian samples; this could be a diagenetic effect or simply large temperature variations during this time of unstable climate.

During the Wordian, the $\delta^{18}O$ values of the limestones become less negative in a quite smooth trend, and this could be the result of a developing glacial period, correlating with stage P4 of Fielding et al. (2008). However, Grossman et al. (2008) have interpreted the heavier composition of $\delta^{18}O$ as related to the aridification process, inferred from facies analysis, based on data from Russia and the USA. Finally, the more negative trend in the $\delta^{18}O$ in the limestones in the top part of the succession could indicate a temperature rise towards the early Capitanian.

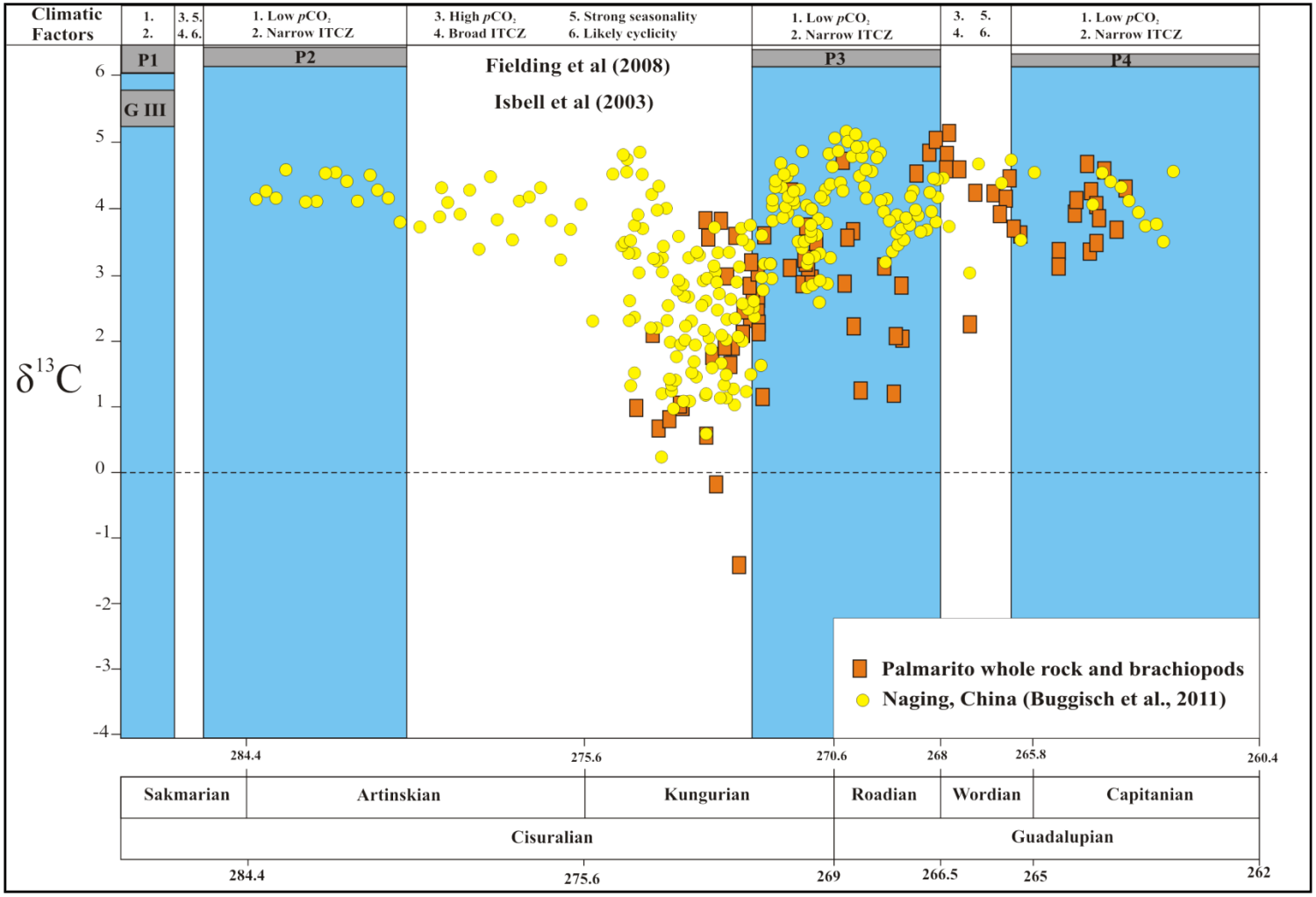

Figure 4.7 Whole-rock and brachiopod carbon isotope values from Permian carbonates in the Palmar succession, Venezuelan Andes (orange squares) and Whole-rock carbon isotopes of Permian carbonates from the Naqing succession in China (yellow circles). The blue areas represent periods of glaciation proposed by Fielding et al. (2008) and Isbell et al. (2003, 2008).

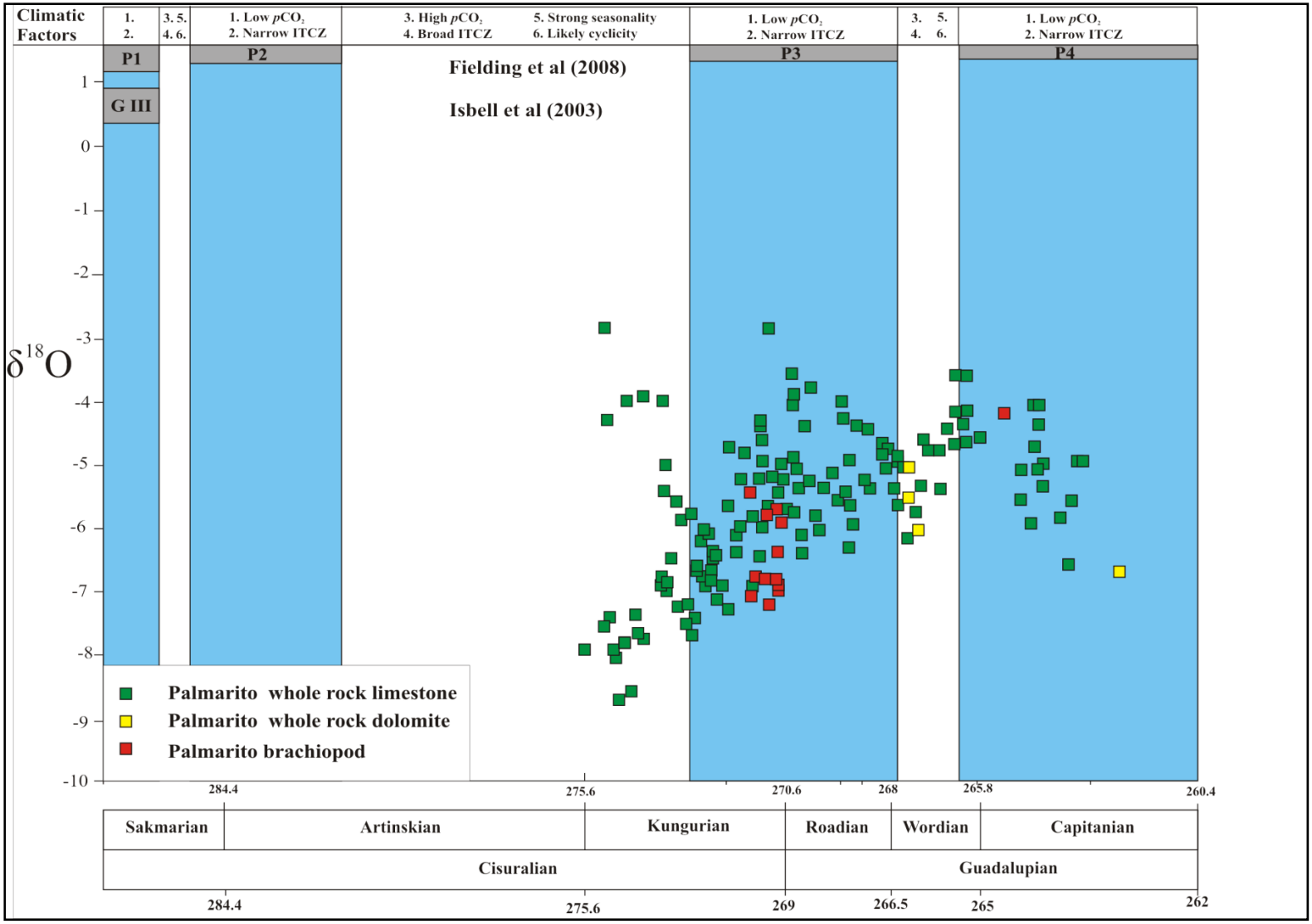

Figure 4.8 Oxygen isotope data from brachiopods and whole-rock limestones and dolomites from the Palmarito Formation, Venezuelan Andes.

4.5.4 Relationship of the Palmarito strata with palaeoclimatic factors

Plate movements (tectonic drift of Tabor and Poulsen, 2008) have been considered one of the factors that could have brought about climate change in the Late Palaeozoic. Western and central Pangean plate movements were modeled for this thesis using the Point Tracker software developed by Scotese and the results show that the huge Pangean land-mass gradually moved northwards from 10° to 14° north (Tabor and Poulsen, 2008). A consequence of this was the migration of the Pennsylvanian equatorial basins from the humid climate associated with the Intertropical Convergence Zone (ITCZ) (high precipitation conditions) into the adjacent northern subtropical arid zone (Witzke, 1990; Gibbs et al., 2002; Ress et al., 2002; Tabor et al., 2008). If this is correct, then the long term aridification of Pangea could be caused by plate movement rather than a change of atmospheric conditions. However, palaeomagnetic studies (Steiner, 1983, 2003; May and Butler; 1986; Bazard and Butler, 1991; Steiner and Lucas, 2000) have suggested that western Pangea remained at the same latitude until the Late Triassic. The rapid change from humid to arid conditions and the persistent humid climate in eastern tropical Pangea are arguments against this hypothesis of the plate movements. Therefore, plate movements can be disregarded as an important control on climate change of low-latitude Pangea during the Permian. Tropical humid conditions during deposition of the Palmarito have been suggested by Ricardi (2008) for the early Permian. Venezuelan carbonates were located slightly south of the equator within central Pangea and could have remained stable as well.

Land-sea distribution seems to have been an important factor that could have had a significant influence on the Permian climate (Tabor and Poulsen, 2008). For Pennsylvanian-Permian times an increase in land area over equatorial Pangea has been suggested by Blakey (2007) in his palaeogeographic maps, due to the withdrawal of the inland epeiric sea. However, the different land-sea distributions deduced on the basis of the occurrence of

Permian transgressive carbonates over central Pangea extended until the middle Permian, and perhaps up to the Capitanian. The increase in continentality could have pushed away the source of moisture and triggered the aridification process. Nevertheless, the Palmarito strata do show evidence for humid conditions in the early Permian. In addition, the climate models of Tabor and Poulsen (2008) and Peyser and Poulsen (2008) show a decrease of precipitation, but still remaining quite high, during the early Permian, and this matches with the Palmarito evidence (e.g. presence of horizons with high content carbonaceous material). In addition, from the Palmarito carbon isotope curve, the humid conditions could have controlled the input of carbon into the basin; this is also the case in the North China and Turpan basins located in eastern equatorial Pangea (Ress et al., 2002; Ziegler et al., 2003; Tabor and Poulsen, 2008)

The climate of tropical Pangea was characterized by monsoonal circulation (Tabor and Montañez, 2002; Tabor and Poulsen, 2008; Peyser and Poulsen, 2008). Tabor and Poulsen (2008) and Perlmutter and Plotnick (2003) proposed that monsoon intensity over equatorial Pangea might have changed over shorter periods of time than a tectonic timescale. In addition, monsoon intensity was more significant during glacial periods and lower during interglacial stages, as a result of the change in temperature difference between the poles and equator (Perlmutter and Plotnick, 2003).

Moist tropical air-masses of the Intertropical Convergence Zone (ITCZ) which came from the Panthalassa Ocean and inland seas were diverted away from the equator due to the effects of the Central Pangean Mountains (Tabor and Poulsen, 2008; Peyser and Poulsen, 2008; Parrish, 1993). The Palmarito area was located south of this physiographic high where the ITCZ could migrate freely during the seasons. Then, the migrations of the ITCZ were strong in the interglacial periods and extended in a broad band over the tropics, in contrast to times of maximum glaciation when the ITCZ was quite narrow and focused around the

equator according to Tabor and Poulsen (2008), However in a unipolar glaciation model that is the case for the Late Palaeozoic, it would have been expected that the ITCZ moved farther north. But in any case, strong seasonality during interglacial periods, as shown by the strong scatter of $\delta^{18}O$ values in the Palmarito pedogenic facies can be interpreted, according to Tabor and Montañez (2002), as a proxy of palaeo-precipitation in equatorial Pangea. These results suggest that there could have been an alternating near and far source of rainfall for this region due to the wide movements of the ITCZ which could have triggered arid and sub-arid conditions alternating with a humid climate. In addition, during the deposition of the tidal-flat facies (first part of Palmarito Formation) evidence of exposure was found, including calcrete and thin coal horizons. These facies indicate an alternation of humid and arid climates. Furthermore, intense cyclicity in the marine facies of Palmarito strata was mainly developed during the period when seasonality was strongly expressed as a result of a high-frequency climatic control on sedimentation on the Venezuelan carbonate ramp.

According to Peyser and Poulsen (2008), atmospheric pCO_2 concentrations are the most important climatic factor to explain long-term aridification. However, Tabor and Poulsen (2008) supported the thesis that not only atmospheric pCO_2 was responsible for climate change during the Late Palaeozoic but also latitudinal plate movements, the assembly of Pangea and orogenesis. Yet, the evidence for these processes is weak. Furthermore, atmospheric pCO_2 variations during the Late Palaeozoic have been discussed by many authors (e.g. Saltzman, 2003; Tabor and Montañez, 2002; Montañez et al., 2007; Peyser and Poulsen, 2008; Tabor and Poulsen, 2008; Parrish, 1993). All of them suggested that pCO_2 was a significant control on surface temperature, evapotranspiration and palaeo-precipitation in the short and long term. In addition, the effect on expansion and contraction of the ice caps, which controlled the migration of the ITCZ, caused strong seasonality and so affected sedimentation and the geochemical signals.

Although, the long-term trend towards aridity in western and central Pangea was the dominant process, short-lived wet periods were present, associated with possible intensification of monsoonal circulation during the periods of glaciation. In the Palmarito strata these were associated with the P3 and P4 glaciations proposed by Fielding et al. (2008) (Figures 4.7 and 4.8).

4.5.5 Marine circulation

Permian ocean circulation has been studied by several authors (Winguth et al., 2002; Winguth and Maier-Reimer, 2005; Grossman et al., 2002). Their models suggest that there were strong global changes in atmospheric circulation, pCO_2 levels and carbon sequestration at this time. However, Grossman et al. (2008) have emphasized the potential danger in misinterpreting regional changes as being on a global scale. As an example, they noted the misconception of seawater ^{18}O enrichment being only due to glaciation and they suggested that excess evaporation was an equally plausible alternative explanation.

Palmarito strata were deposited in an epicontinental sea that could potentially have been restricted as a result of the partly enclosed palaeogeography; this may have given rise to distinctive geochemical signals. However, the carbon and oxygen isotope data from the Venezuelan Permian carbonates exhibit similar trends to those from other areas, such as the Niqing section in China (Buggisch et al., 2011), where deposition took place in the open Tethys Ocean. This argument supports the suggestion that the area of Palmarito deposition had free circulation with the open-ocean, so that the isotopic data from there reflect global isotopic trends (Figure 4.9).

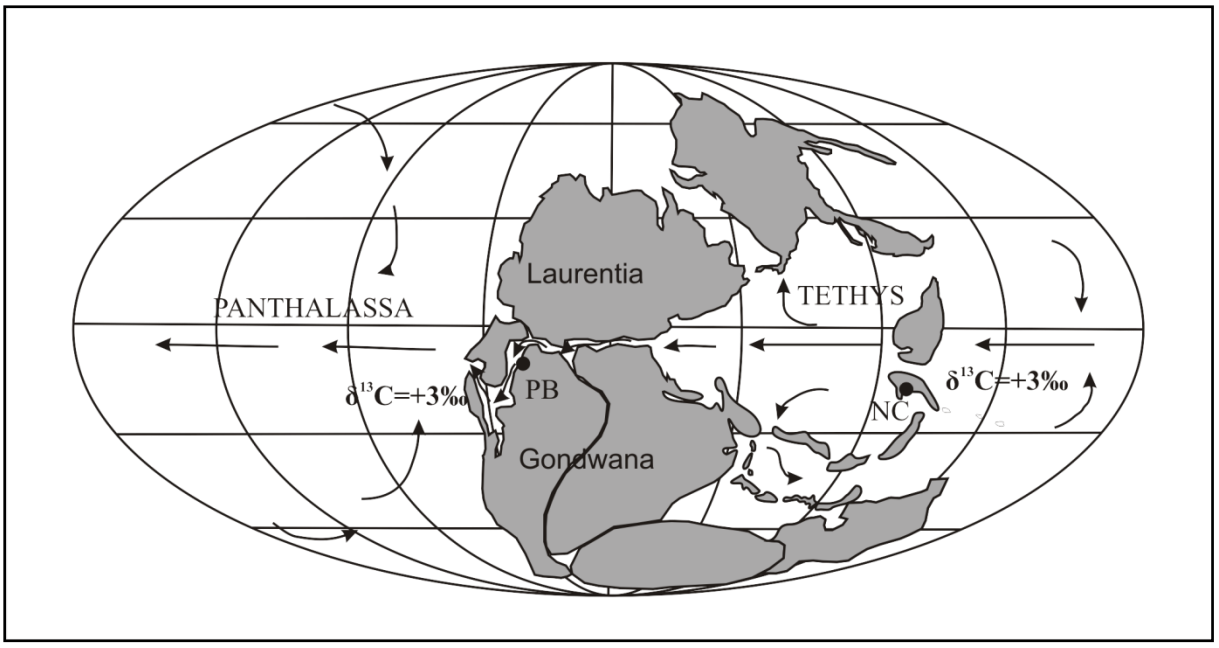

Figure 4.9 Schematic palaeogeographic projection showing simplified ocean circulation and mean carbon values of the Palmarito Formation in the Venezuelan Andes (PB) and carbonates of the Niqing succession in China (Buggisch et al., 2011) (NC)

Summary and conclusions

The Palmarito strata in Venezuela are located in the west-central Pangean region which is a poorly known area between Gondwana and Laurentia, at a time just before the final assembly of Pangea. The data presented here thus fill an important gap in the regional palaeogeography and also have significant implications for the palaeoclimate and palaeoceanography over equatorial Pangea at that time.

Values of $^{87}Sr/^{86}Sr$ ratios from low-Mg calcite brachiopod shells in the central part of the Palmarito Formation have provided useful dates for the strata, placing them within the Kungurian stage at 270.5 to 273.5 M.y. The improvement of the dating has allowed better correlations and comparison with global climate and palaeoceanographic changes at the time.

Carbon isotope data show a long-term trend towards more positive values. However, values in the lower part of the succession are more negative and this is attributed to the affects of pedogenesis and weathering during early diagenesis. Excursions of $\delta^{13}C$ higher up in the formation show a strong relationship to the inferred glaciation-deglaciation events that

have been described by Isbell et al. (2003, 2008) and Fielding et al. (2008) for the early and middle Permian.

Although original oxygen isotope signatures of limestones are prone to diagenetic alteration, the similarities of the results from low-Mg calcite brachiopods (generally resistant to alteration) and whole-rock samples, and from different sections, allow the interpretation of the relative trends within the strata. The trends of oxygen were correlated with glacial events, P3 and P4, proposed by Fielding et al. (2008). Changes in Permian climate related to plate movements, land-sea distributions, monsoonal circulation, the Intertropical Convergence Zone and atmospheric pCO_2 levels have been discussed with reference to the Palmarito succession in central Pangea. As a result, it has been concluded that pCO_2 was the most significant factor that controlled not only long-term climate change but also short-term variations.

Marine circulation within the Mucuchachí Basin potentially could have been restricted as a result of which distinctive geochemical signals might have been expected. However, carbon and oxygen isotope data from the Venezuelan Permian carbonates exhibit trends similar to those from other successions, such as the Niqing section in China, which was deposited in an open-marine realm of the Panthalassa Ocean. Thus an open-marine basin was likely established in northern Venezuela at this time.

5 Metre-scale cyclicity of Permian ramp carbonates in the Venezuelan Andes: deposition under the tropical climate and tectonic regime of Pangea.

Abstract

Metre-scale cycles have been a controversial topic for the last few decades. There has been no complete agreement over the origin of the cycles and the consensus has been split between three major controls: orbital forcing, tectonics and sedimentary processes (autocyclicity). Palmarito strata show three different types of cycle: Type A cycles are mixed clastic-carbonate, shallowing-upward peritidal cycles. The upper boundaries of the cycles are exposure surfaces with calcrete. The origin of the cycles is attributed to tidal-flat progradation, variations in carbonate productivity and clastic input to the depositional area. Type B cycles consist entirely of subtidal facies and show shallowing-upward facies arrangements, but without exposure. They commonly show an alternation between heterozoan and photozoan assemblages, Type C cycles were deposited in a middle to outer ramp setting and are characterized by heterozoan assemblages and shallowing-upward trends that include spiculitic wackestone-packstone passing up to neomorphic wackestone or bioclastic crinoidal-bryozoan wackestone-packstone. The cycles are interpreted as 4^{th}-5^{th} order (10^4 to 10^5 years) in duration and some can be linked to Milankovitch orbital rhythms, notably short eccentricity (~100,000 years). Overall, the origin of the Palmarito cycles was a complex combination of autocyclic and allocyclic controls; however, the evidence suggests that cycles in the lower part of the succession were dominated by autocyclic process whereas those in the upper part were more the result of allocyclic processes. Climate-driven processes, such as migration of the ITCZ and the waxing and waning of polar ice-caps had significant effects on deposition of the Palmarito succession and the cycles therein, controlling the

clastic sediment supply, nutrient availability and thus carbonate production and sea-level change, which determined the vertical stacking pattern of the cycles.

5.1 Introduction

Carbonate ramps show a broad variety of facies and their features are the key to understanding changes in environmental conditions which at the same time are the product of changes of local and regional tectonic, climatic and oceanographic processes. Mostly in the Permian strata here, the facies show a vertical repetition in an ordered stacking pattern which can be used to define the cycles; these occur on different scales from several 10s centimeters to a few metres in thickness.

Permian times were important on the global scene with the formation of Pangea which led to significant tectonic, sedimentary and stratigraphic developments, global changes in climate, and biotic evolutionary events. For these reasons, the Palmarito strata consist of well-developed metre-scale cycles. The nature of the high-frequency cycles was influenced by climatic and tectonic factors in this low latitude region. The dominant humid conditions give way to a more arid climate in the uppermost part of the succession and this was taking place under a compressive tectonic regime that was dominant during the Permian collision between Gondwana and Laurentia.

The aim of this chapter is to discuss these metre-scale cycles in the context of Permian equatorial Pangea and provide possible explanations of the mechanisms causing their repetition. The fieldwork and facies studies have been augmented by geochemical data (isotopes and trace elements).

5.2 Cycle analysis

5.2.1 Stratigraphic context of metre-scale cycles

Small-scale cycles in carbonates are most typical of shallow-marine (peritidal) depositional systems but they do occur in all environments from lacustrine to open-

shelf/ramp and even pelagic successions (Tucker and Garland, 2010). Many authors have used the concept of metre-scale cycles in sequence stratigraphic models, referring to them as "parasequences" (Van Wagoner, 1988), or 4^{th}-5^{th} order depositional units. The stacking patterns of parasequences are used to define systems tracts within a 3^{rd}-order sequence (Lehrmann & Goldhammer 1999).

Parasequences typically shallow- upwards but there can also be a deepening up and symmetrical (transgressive-regressive) facies arrangement (Tinker, 1998; Spence and Tucker, 2007; Tucker and Garland,2010). The bounding surfaces which limit each parasequence are usually a clear, sharp contact. However, this does not mean that it always has to be a flooding surface as Van Wagoner (1988) described; instead it can be an exposure horizon or shallower-water facies, but an abrupt change in grain assemblage or facies is typical (Spence and Tucker, 2007). The boundaries in shallowing-upward cycles are commonly related to the position of sea-level and the accommodation space available. However, if the seafloor above fair weather wave base has enough energy to keep sediments moving rather than allowing them to be deposited, then wave-base can act as base level to produce the cycle boundary, rather than sea-level itself which is the usual mechanism (Tucker and Garland, 2010). More complex scenarios have been proposed by authors including Soreghan and Dickinson (1994) and Jones and Desrochers (1992) who have described cycle types related to the record of changes in accommodation space and carbonate production based on the facies arrangement within the cycles.

Stacking patterns of cycles/parasequences have been described by many authors for different sedimentary environments where changes in accommodation space and sediment supply have given rise to thickening-up, thinning-up and aggradational patterns. Commonly, in cycles that shallow upwards to sea-level, a thinning-upward package of cycles develops where there is long-term decrease (3^{rd} order) in accommodation space, that is a

progradational or regressive cycle package. Thickening-upward cycle packages suggest long-term decrease in accommodation space that is retrogadational or transgressive. However, with wholly subtidal cycles the opposite pattern can result since the main control in this situation is the sediment available rather that the accommodation space. The stacking pattern of cycles can be useful as a correlation tool, especially in areas with poor exposure (Tucker and Garland, 2010), like the Andes here, where the lateral tracking of the cycles is difficult.

The origin of small-scale cycles is a significant issue. Local processes can control the development of the cycles through autocyclic mechanisms that are intrinsic processes within the depositional system and basin, for instance, lateral migration of tidal islands or channels, and the effect of hydrographic factors. In contrast, allocyclic mechanisms are external processes such as sea-level change, tectonic subsidence and orbital forcing. These mechanisms mainly have an indirect control on the autocyclic factors (Pratt et al., 1992; Pratt, 2010; Tucker, 2011). The duration of some allocyclic processes, notably orbital forcing, is periodic and therefore in statistical analyses non-random, ordered responses should be obtained, rather than purely random as would be the case for cycles produced by autocyclicity that reflect a more erratic control on deposition.

Allocyclic periodicity has commonly been ascribed to Milankovitch orbital rhythms with durations of 20,000 years (precession), 40,000-years (obliquity) or 100,000-years (eccentricity) (Pratt, 2010; Tucker and Garland, 2010), but then the rhythms often are overlapped by local tectonic effects to confuse the stratigraphic record and cause more random variations of the cycle thickness. One useful technique to analyse this thickness variation is the Fischer plot which was used in this study.

5.2.2 Fischer plots

A Fischer plot is a method to illustrate the deviation of cycle thickness through a succession of cycles from the average cycle thickness (Fischer, 1964; Sadler et al., 1993; Diecchio et al., 1995; Tucker and Garland, 2010). In the plot, 'cumulative departure from the mean thickness' is plotted against 'cycle number'; a series of cycles that is thicker than the average will develop a positive inclination, and a series thinner than the average cycles will show a negative slope (Figure 5.1). This technique provides a visual tool to identify a higher hierarchy of cycles within a succession, such as third order, that may be difficult to observe in areas where the outcrop has limited lateral and vertical continuity (Figure 5.2).

The interpretation of a Fischer plot can be related to long-term change of accommodation space and relative sea-level variations through time. However, detailed interpretations have been criticised for being too subjective as a result of various assumptions, such as that each cycle represents the same length of time or that every cycle corresponds to a complete record of change in accommodation space. For example, subtidal cycles normally do not record the complete filling of accommodation space due to the fact that they do not reach sea-level. Cycles which do show exposure surfaces within the facies succession should mark the sea-atmosphere limit, which is a definition of the upper boundary of the accommodation space. In the case of a succession composed only of subtidal cycles the interpretation of the Fischer plot as reflecting the long-term trend in accommodation space would be incorrect.

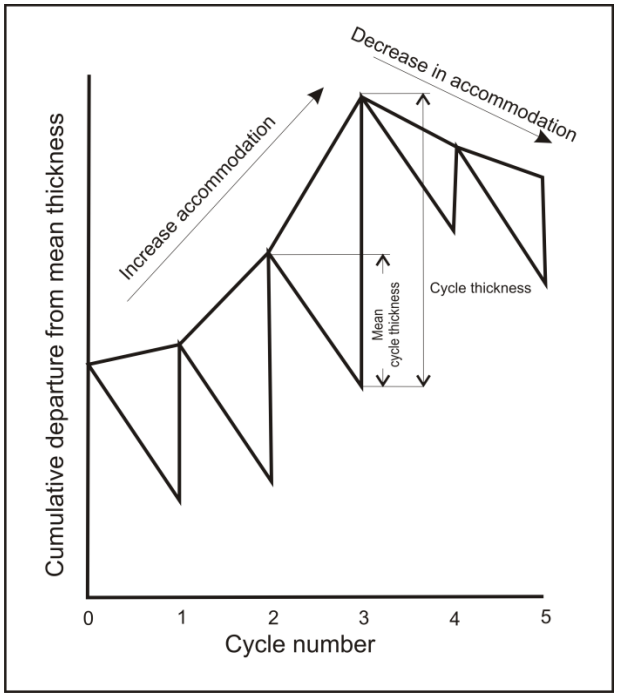

Figure 5.1 Schematic Fischer plot showing the thickness of each cycle against cumulative departure from the mean thickness (Husinec et al., 2008). (Discussed in the text).

Statistical methods should be used to determine the level of randomness and to assist in the interpretation of the origin of these cycles (Sadler et al., 1993; Tucker, 2011). Fischer plots with less than 50 cycles may not be sufficiently long for the robust calculation of statistical parameters. However, in some cases the outcrops or exposures simply do not show enough cycles to meet this condition. On the other hand, Fischer plots can still be useful in correlation of platform sections, especially when combined with facies analysis (Tucker and Garland, 2010).

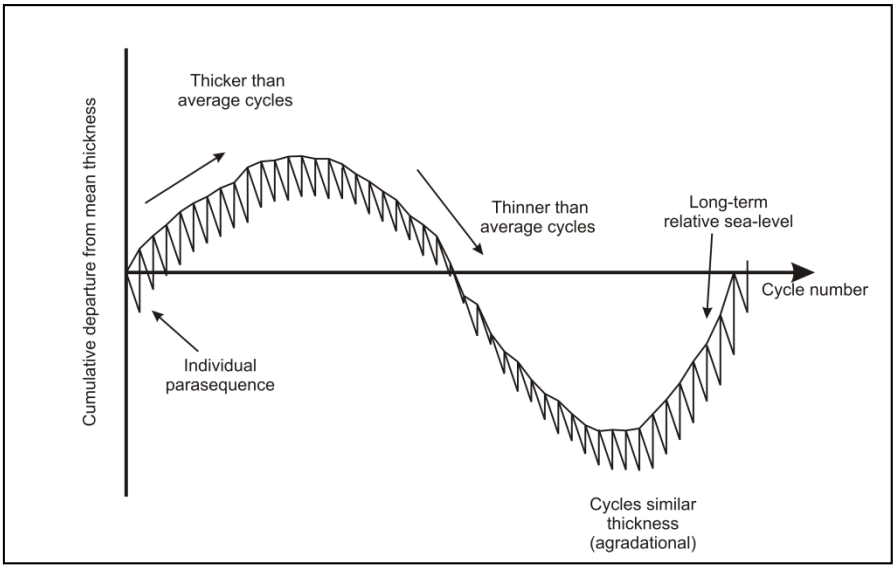

Figure. 5.2. Hypothetical Fischer plot showing how long-term cycles can be interpreted from short-term cyclicity (Garland, 1997).

Fischer plots can contribute to the interpretation of the origin of the cycles. For instance, if a succession of cycles is well-ordered it would be expected that this pattern reflects an allocyclic mechanism, such as orbital forcing. However, Fischer plots will also be affected by noise produced by autocyclic processes which might overprint eustatic signals associated with Milankovitch rhythms or other global control. (Burgess 2006; Bosence et al., 2009; Tucker and Garland, 2010).

5.2.3 Geochemical data (carbon and oxygen isotopes and trace elements)

Samples of whole rock/matrix were collected from representative cycles and analyzed for carbon and oxygen stable isotopes and for trace elements using the same methods that were described in Chapter 4 for brachiopods. The objectives here were to contribute to an understanding of the controls of the cyclicity.

5.3 Metre-scale cyclicity in Palmarito strata.

Permian carbonates in the Venezuelan Andes exhibit well developed metre-scale cycles in most of the sections and these are described in the follow sections.

5.3.1 Cycles types in Venezuelan Permian carbonates.

Three main groups of cycle type have been recognized in the study area with various subtypes; these are mixed clastic-carbonate peritidal cycles (Type A), shallow-subtidal cycles (Type B) and deep-subtidal cycles (Type C), all of which have mainly shallowing-upward facies arrangements. Cycle thickness and stacking patterns were used to indentify longer-term cycles and Fischer plots were useful in this respect. In appendix 4 all information from this study is presented in tables.

5.3.1.1 Mixed clastic-carbonate peritidal cycles (Type A)

Peritidal deposits are typically deposited in very shallow to subaerial marine areas where the dominant hydrodynamic processes are the tides. These deposits are subdivided into three main zones. First, the supratidal zone is characterized by exposure surfaces (with calcrete, palaeosoils) and mud cracks; rhizoliths may also be present. Second, the intertidal zone is an area of intermittent flooding and there may be a brackish fauna preserved, with much bioturbation. Finally, the subtidal zone is below sea-level and fine-grained sediments with an open-marine to restricted fauna are common, possibly with evidence of storms (Pratt et al., 1992, 2010). For the Palmarito peritidal cycles, there are three slightly different facies associations. Although, mostly facies are clastic-rich they do correspond to the facies associations proposed by Pratt et al. (1992), Pratt (2010), Tucker and Wright (1990) and Tucker (2010) for the tidal flat (cycle types A1 and A2), or a mix between carbonate peritidal and clastic tidal-flat facies described by Dalrymple (1992, 2010), which can be ascribed to A3 cycles.

Type A1 cycles

These cycles are formed of facies that cover the range from subtidal to supratidal deposits. These facies are described in detail in Chapter 3. Macrofacies include *laminated shale* in the lower part of the cycle. This facies passes up to fine-grained *mixed carbonate-*

clastic and *clayey lime mudstone*.. In the upper part of the cycles there is *nodular or laminated limestone,* in some cases with mud cracks, bioturbation and calcrete texture, with the last indicating exposure and pedogenesis. There are few fossils, just some bivalves and ostracods in the fine-grain laminated limestones. This cycle type has a thickness average of 2.2 m with a range from 0.5 to 7.6 m and is common in the Palmar River and Quebrada de Portachuelo 1 sections (Figure 5.3). In the studied sections, 37 of this type of cycle have been recognised, mainly occurring in the basal part of the Palmarito Formation.

Type A2 cycles

These cycles exhibit a coarsening-upwards trend from clay-grade to medium grained sand. The thickness of the cycles ranges from 2.6 to 7 m with an average of 4.70 m. The bottom of the cycle is formed of *laminated shale* that represents subtidal facies and this passes upwards into silt-dominated *heterolithic* horizons. The *quartz siltstone* facies grades upwards to fine-grained *arkosic sandstone*. Type A2 cycles are capped by a *clayey lime mudstone* and *calcrete*. This cycle is relatively rare in the Palmarito succession, just 7 have been identified, and they are mainly found in the basal part of the formation where the clastics are dominant (Figure 5.3 and 5.4). A characteristic feature of the A2 cycles is that fossils are rarely present, just a few bivalves in the carbonate facies towards the top

Type A3 cycles

These cycles are extremely rare within the successions, just 6 cycles of this type were recognized. They are formed of heterolithic facies, silty and sandy clastics which pass up to fine-grained laminated sandstone. They can be ascribed to tidal heterolithic sand-bar deposits. Flaser and lenticular lamination is common with a brownish-greenish colour The average thickness of this cycle type is 3.50 m with a range from 0.6 to 7.4 m (Figure 5.3). These cycles occur higher up within the formation.

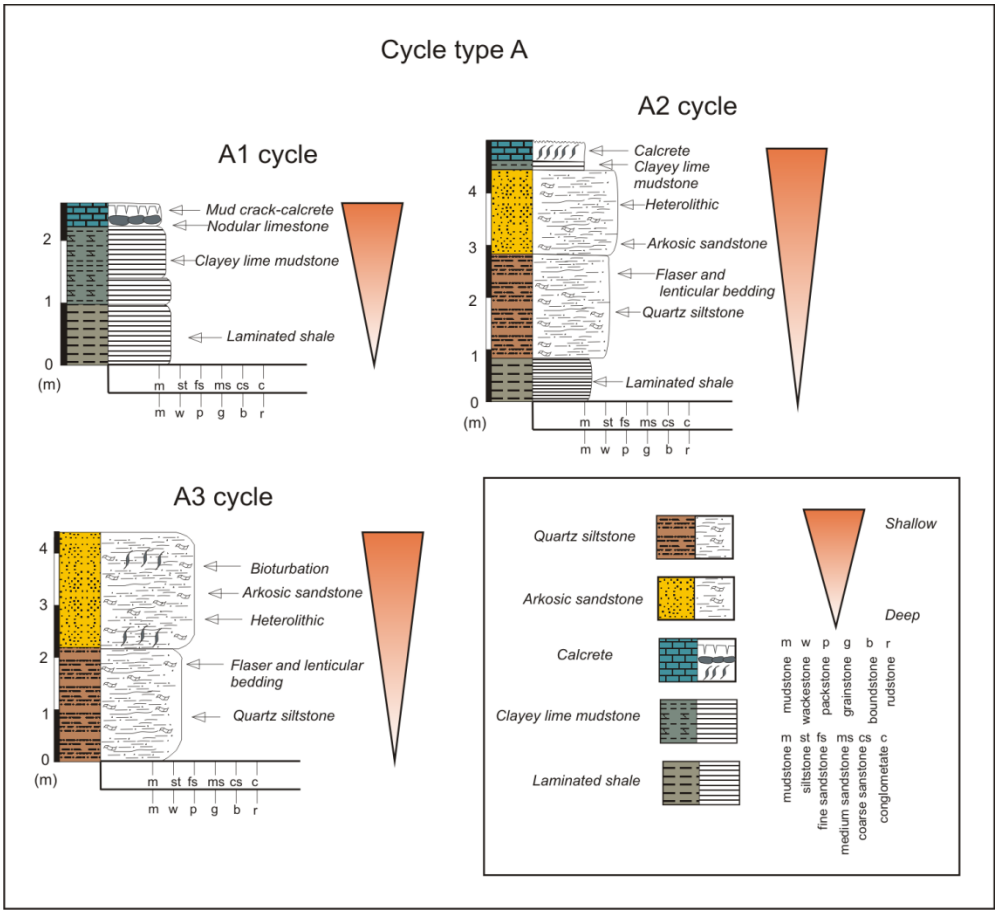

Figure 5.3. Schematic illustration of cycle-type A.

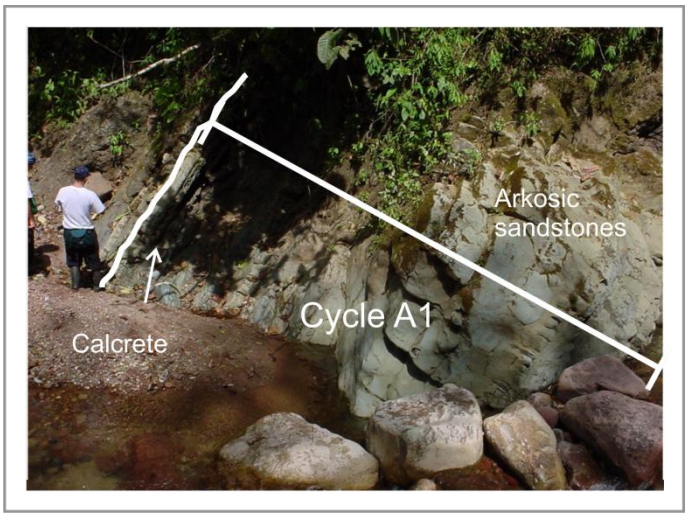

Figure 5.4. Cycle-type A2 with laminated shale followed by arkosic sandstone and calcrete on top.

5.3.1.2 Shallow subtidal cycles (Type B)

Type B cycles consist entirely of sutidal facies and show a shallowing-upward facies arrangement. Four different subtypes are recognized (Figure 5.5).

Type B1 cycles

The cycles are formed of *laminated limestone* or *clayey lime mudstone* with a heterozoan assemblage. Brachiopods, sponge spicules, crinoids and bryozoans (*spiculitic wackestone-packstone*) towards the base pass up into massive limestone characterized by photozoan grain-types (*green algae and fusulinid microfacies*). Thirty-six cycles of this type have been identified with a range in thickness from 0.25 to 5.90 m and an average of 1.8 m (Figure 5.5). The photozoan microfacies represents a very shallow-marine environment; however, there are no exposure surfaces at the top of these cycles.

Type B2 cycles

These cycles are similar to type B1 cycles with massive heterozoan-rich bioclast horizons which pass upwards to photozoan facies, but in this case both are massive (Figure 5.5). These cycles are typical of the middle to upper part of the Palmarito succession with an average thickness of 4.72 m (11 cycles ranging between 0.5 and 10.5 m). Type B2 cycles represent phase 4, as explained in Chapter 3.

Type B3 cycles

These cycles consist of thick *massive limestones* which show internally *bryozoan boundstone* and *bioclastic crinoidal-bryozoan wackestone-packstone*, located at the base of the cycle. These facies grade upward to crystalline dolomite that normally occurs in metre-thick beds. Original components such as fusulinids and crinoids can be recognized. The fauna suggests a possible photozoan association and shallowing-upward trend (Figure 5.5). Nineteen of these B3 cycles are present in the Palmarito Formation and they only appear in the upper part of the succession with a range of thickness from 2 to 14 m and an average of 7.73 m. Some authors (e.g. Jones and Desrochers, 1992) would categorize these cycles as diagenetic cycles

Type B4 cycles

These cycles are composed *of laminated clayey lime mudstone* with brachiopods at the base followed by *bioclast rudstone-grainstone* and *calcareous sandstones* with brachiopods which cap the cycle. Ten cycles of this type occur, with an average thickness of 3.14 m (range from 1.5 to 6 m) (Figure 5.4). The coarse bioclastic facies with hummocky cross stratification is interpreted as a storm wave facies, with deposition just below fair-weather wave-base (FWWB). Overall these cycles show a regressive trend through the succession and they also are located preferentially in the lower part of the succession. These cycles are limited to the lower-middle part of the Palmar River section (Figure 5.7).

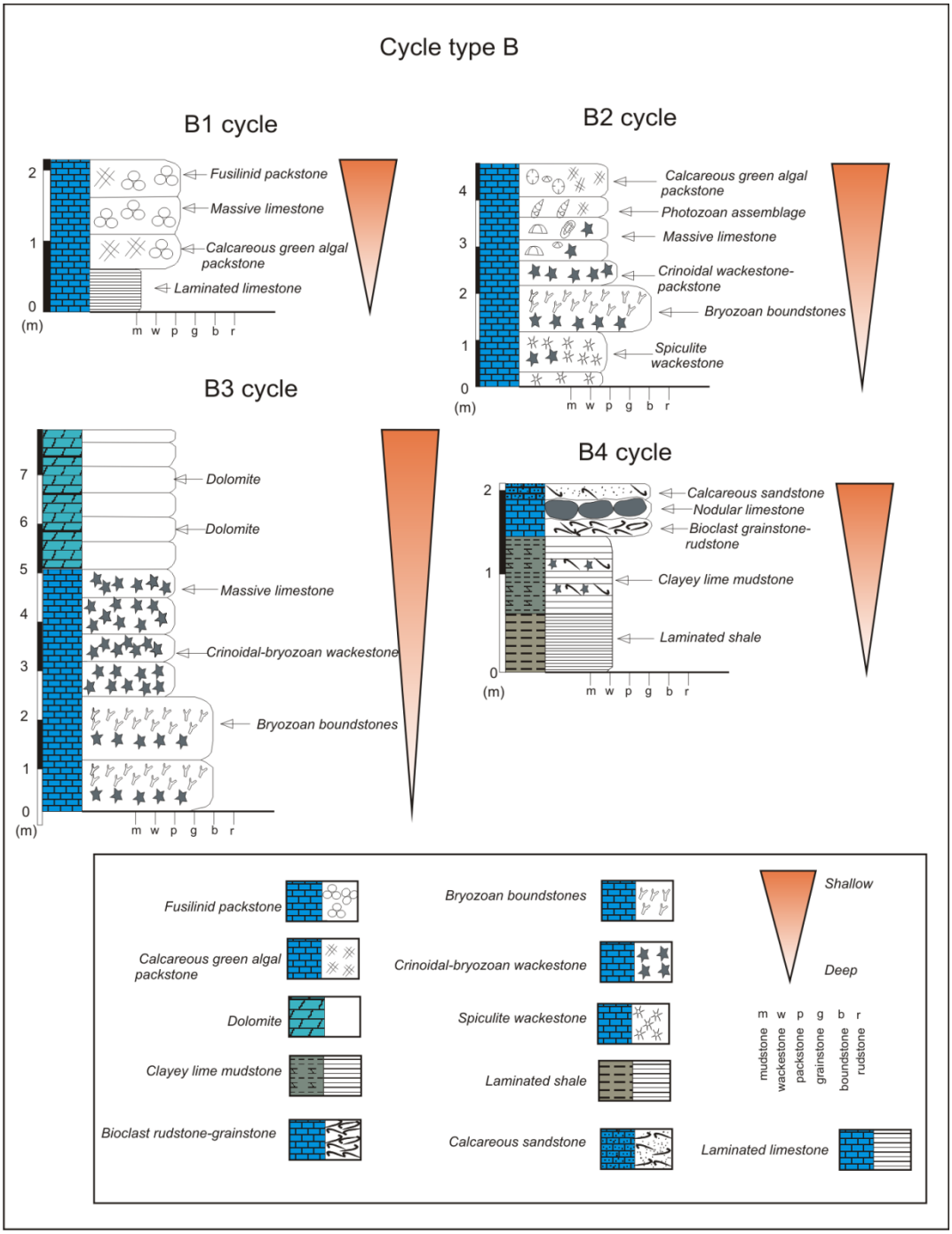

Figure 5.5 Schematic illustration of type B cycles.

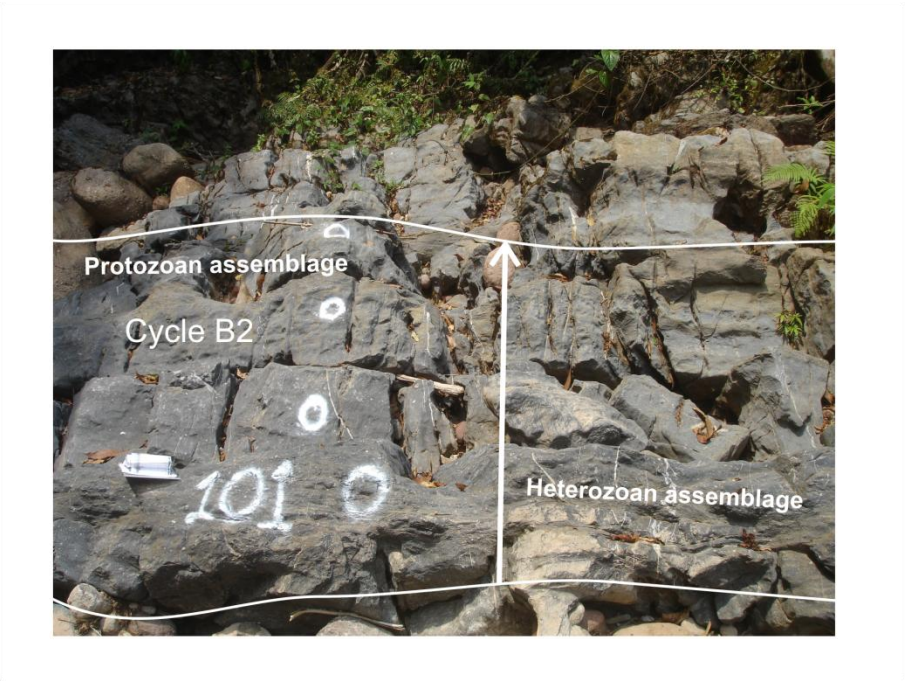

Figure 5.6 Cycles of type B2 showing massive limestone formed of a heterozoan assemblage followed by a calcareous green algal photozoan assemblage towards the top.

Figure 5.7 Cycle-type B4 with laminated shale followed by bioclastic rudstone and calcareous sandstones at the top.

5.3.1.3 Deep subtidal cycles (Type C).

These cycles occur in the middle-outer ramp characterized by heterozoan assemblages and a shallowing-upward trend. They are interpreted from the clear variation of bioclast associations that include *spiculitic wackestone-packestone* to *neomorphic wackestone* or *bioclastic crinoidal-bryozoan wackestone-packstone*. They have been subdivided into 2 groups (Figure 5.8).

Type C1 cycles

The cycles in the lower part are composed of *laminated shale* which passes up to *spiculitic wackestone-packstone* and eventually into *clayey lime mudstone*. The cycles are capped by *nodular neomorphic wackestone* (Figure 5.8). At the top of cycles, the bioturbated nodular neomorphic wackestone is interpreted as a firmground (Figure 5.9). 150 cycles have been identified in total and cycle-type C1 is the most common, occurring throughout the whole Palmarito Formation. They occur in the middle and upper part of the successions with a thickness average of 1.74 m (range between 0.2 and 15 m).

Type C2 cycles

These cycles are composed of laminated *spiculitic wackestone-packstone* which grades upwards into massive *bioclastic crinoidal-bryozoan wackestone-packstone* (average 1.39 m with a range between 0.15 to 6.6 m). There have been recognized 142 cycles of this type. Although, they do not show a clear shallowing-upward trend, they do display an increasing bioclastic diversity upwards but this is limited to the heterozoan association (Figure 5.8).

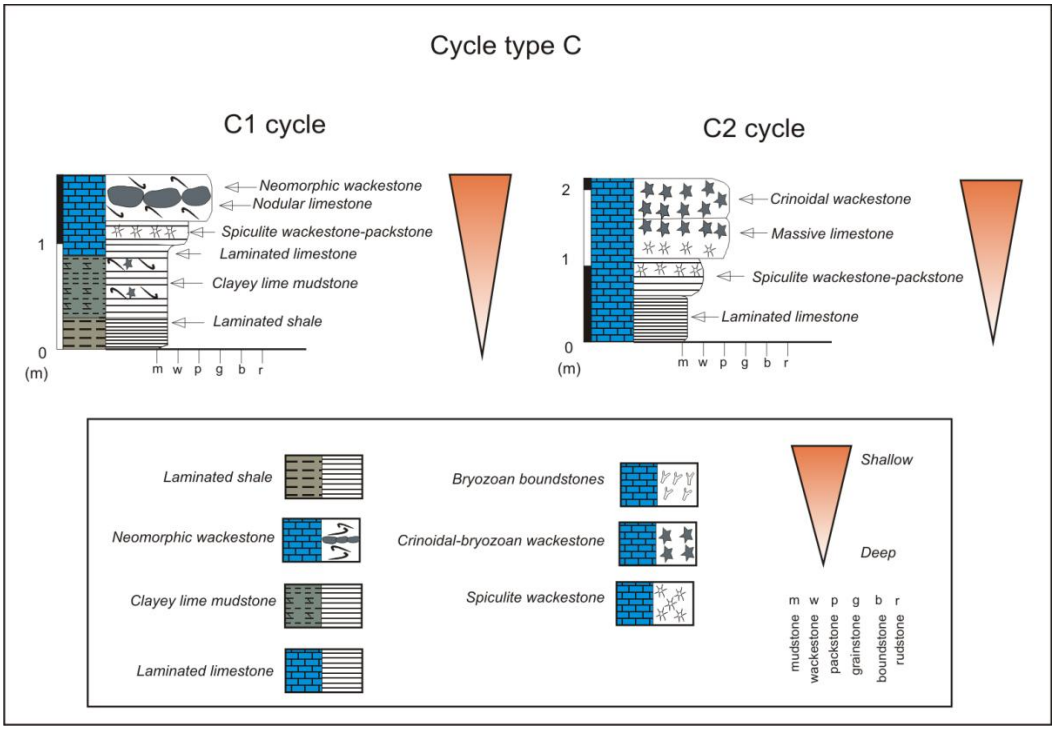

Figure 5.8 Schematic illustration of cycle-types C.

Figure 5.9 a). General view of subtidal cycles C1 showing constant repetition of the facies. b) L*aminated shale* passes up to *clayey lime mudstone* at its base. The cycles are capped by *nodular neomorphic wackestone.*

5.3.2 Isotopic and geochemical variations within the Palmarito cycles.

Samples from the cycles in the Palmarito Formation have been examined for their isotope and trace element contents. However, only the most representative cycles were analyzed (A1, B1 and C1). The geochemical data linked with the facies interpretations provide much information for the interpretation of the origin of the cycles. The variation of

the carbon isotope signature in matrix-whole rock (calcite) has been analyzed for most of the cycles; but for cycle type A1, carbon isotope values of the organic matter and total organic carbon (TOC) have also been determined. All signatures show important changes with regard to interpreted depth of deposition within the cycles. In addition, P/Al and Fe/Al ratios were calculated just for the fully marine cycles (B1 and C1) as a proxy of nutrient level which stimulated the organic productivity (Brasier, 1995; Soreghan and Soreghan, 2002; Perez-Huerta and Sheldon, 2006).

Cycle-type A1 displays a decrease upwards in the carbon isotope values. The carbon isotope signature of the organic matter shows a similar trend towards more negative values up through the cycle. The concentrations of TOC are relative low; however, there is an increasing-decreasing pattern whereby the lowest values are associated with calcrete facies (Figure 5.10).

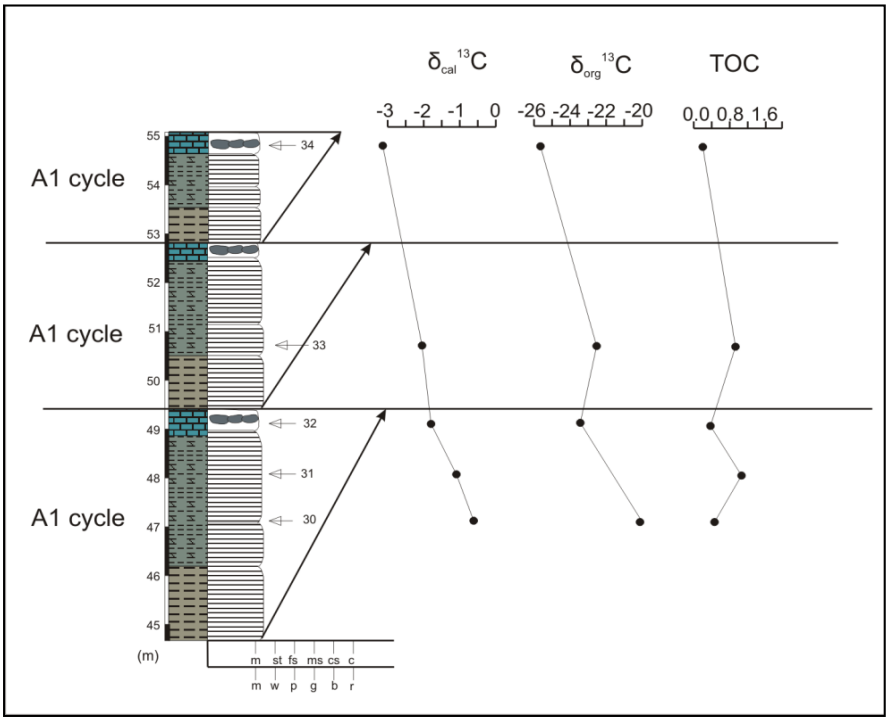

Figure 5.10 Stratigraphic log from the Palmar River section showing the cycle-type A1 and the values of carbon isotopes in calcite and organic matter, and in addition, the total organic carbon (TOC).

Cycles B1 consist of an alternation of heterozoan and photozoan assemblages, deposited in a shallow subtidal environment. However, the variation of $\delta^{13}C$ is not significant

within the cycles, which fluctuates around high positive values of +3. In addition, the ratios P/Al and Fe/Al do not show any particular pattern; rather they have a high variability (Figure 5.11).

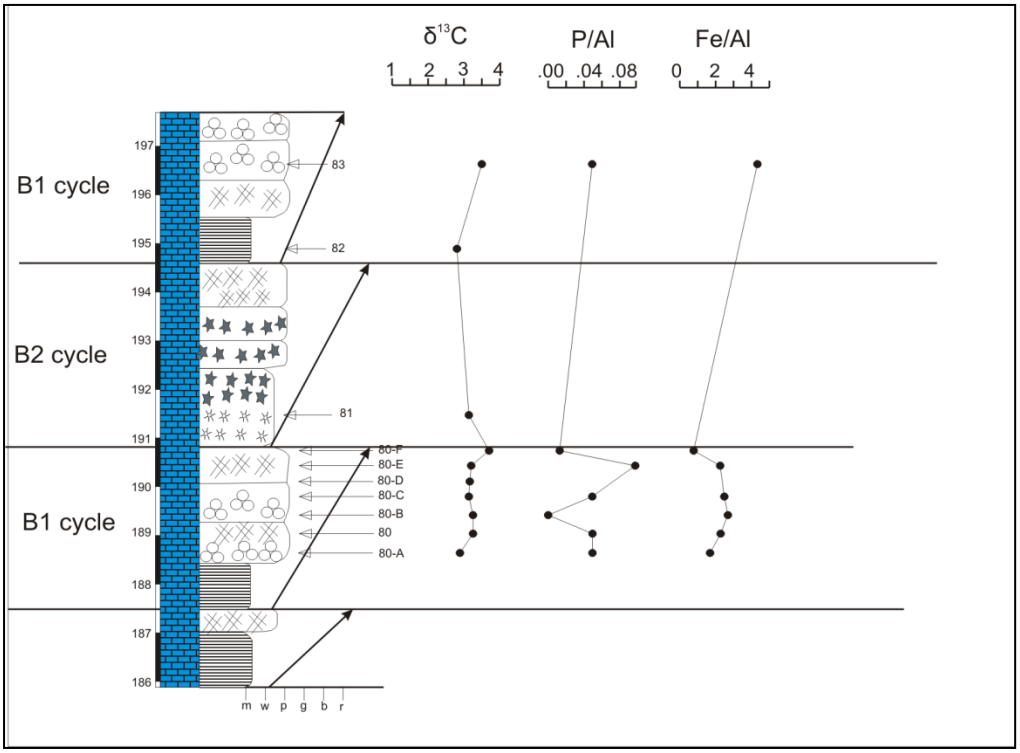

Figure 5.11. Stratigraphic log of the section in the Palmar River showing the type B1 cycles and the values of carbon isotopes in the matrix-whole-rock, as well as the ratios P/Al and Fe/Al.

Cycles C1 were deposited in a deep subtidal setting and are dominated by heterozoan assemblages. The carbon isotope signal shows a strong upward increase, as does the ratio P/Al and also the content of $CaCO_3$ (Figure 5.12). In contrast, the ratio Fe/Al shows a decrease.

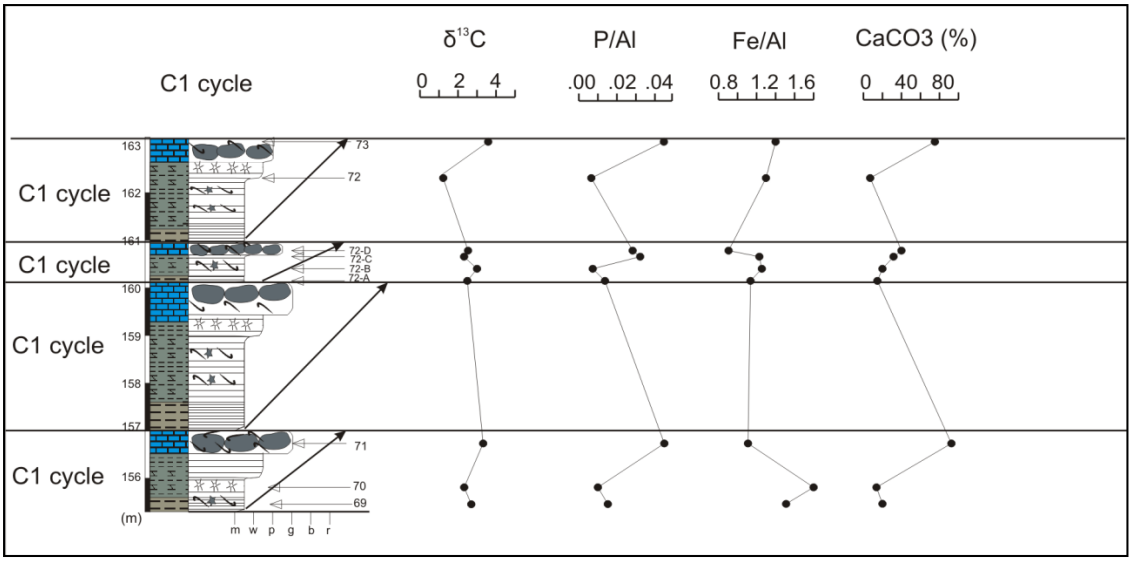

Figure 5.12 Stratigraphic log of the Palmar River section showing the C1-type cycles and the values of carbon isotopes of the matrix-whole-rock, $CaCO_3$ and the ratios P/Al and Fe/Al.

5.3.3 Interpretations of cycle types

With information from the fieldwork, facies and microfacies, trace elements and isotopes, the processes and controls involved in cycle deposition and repetition can be deduced. Different factors appear to have been involved with the different cycle types.

Cycle types A1 and A2 show shallowing-upward trends and are dominated by clastic facies in the lower part which could be ascribed to intertidal or very shallow subtidal environments. The *calcrete* facies at top indicates exposure and pedogenesis, taking place above sea-level in the supratidal zone. In these cases, therefore, tidal-flat progradation took place and completely filled the accommodation space. The cycle type A1 also shows an upward decrease in the carbon isotope values. This is most likely the result of decomposition of organic matter in the soil-zone which produces negative CO_2/HCO_3, which can then be incorporated into the calcite of the calcrete. The carbon isotope signature of the organic matter can be interpreted in a similar way, related to pedogenic alteration of organic matter. Finally, the concentrations of TOC are relative low in these sediments; this could be due to oxidizing conditions within the soil-zone and the near-complete destruction of organic matter there.

The main difference between the cycle sub-types is the grain-size trend. In A1 cycles, it is fining-upwards and in A2 it is coarsening-upwards. These different trends are a reflection of the different energy levels in the depositional system. Both cycle types A1 and A2 have an exposure surface (calcrete, mud-cracked horizon or peloidal intraclast layer) at the top of each cycle. Cycle type A3 does show a coarsening-upward trend, but there is no exposure surface; this is probably due to the creation of accommodation space faster than the sediment supply. In this case, clastic input could have reduced the carbonate production rate at this time; there may well have been episodic events of clastic influx

The B cycle types can be interpreted along similar lines, associated with the shallow subtidal zone. For the B1 cycle type, the environment was quite restricted in terms of circulation and a warm-water, shallow-marine environment is suggested by the green algae *Gymnocodiacea*, as well as the phylloid algae *Achaeolithophylum*, a delicate fossil which can be preserved only in a low energy zone and oligotrophic conditions.

These B1 cycles can be compared with the interpretation of the cycles in the Upper Carboniferous of Austria (Samankassou, 2002) who included the phylloid alga *Achaeolithophylum* as part of the heterozoan association, although there is some controversy here of heterozoan organisms occurring in shallow water of low-latitude areas. The Palmarito type B1 cycles could fit this model, which would suggest that the rapid change in the grain types from heterozoan to photozoan, with little change in water depth, was caused by a rapid change in nutrient supply or temperature.

Although the geochemical and isotopic patterns do not show a particular trend, they can suggest that primary productivity and the carbon sequestration in the facies were high (Cárdenas and Harris, 2010). The B2 cycles formed in a similar depositional setting but the laminated limestone is replaced by massive beds. These massive limestones with heterozoan organisms may represent small buildups or intermound sediment within the middle-outer

ramp that has been described in Chapter 3. For the cycles B3 the dolomites cap the cycles, although the original components such as fusulinids and crinoids can be recognized, and these suggest a possible photozoan association and shallowing-upward trend. Dolomitization may have occurred during early diagenesis in the shallow subsurface during the early stages of burial. It may have been connected to sea-level fluctuations and seawater circulation within the sediment. For the type B4 as with all the type B cycles, there is no evidence of exposure, and therefore they did not reach sea-level at any point. On the other hand, the FWWB could have worked as base level where all sediments above were re-mobilized and eroded.

The C type cycles have been interpreted as deep subtidal cycles. Type C1 cycles show a regressive trend and this was likely controlled by the carbonate factory, although not enough sediment was provided to fill the accommodation space.

The neomorphic wackestone is interpreted as a firmground; these are usually the result of reduced or lack of sediment input. This could have been the result of a decrease in output from the carbonate factory or an increase in current activity (Figure 5.9).

James and Bone (1991) and Jones and Desrochers (1992) have described similar cycles in the Oligocene-Miocene Abrakurrie Limestone of southern Australia as deep-shelf cycles with well-cemented firmgrounds at the top. They are explained as the result of deposition when storm wave base (SWB) was located above the sea floor (high sea-level), and lithification and erosion when SWB reworked sediment on the sea-floor (low sea-level) (Figure 5.13). As a result, this can be linked to short-term sea-level changes, probably under the influence of Milankovich rhythms and orbital forcing.

These patterns would suggest that there is an increasing supply of nutrients (ratio P/Al), probably due to increased continental run-off (Perez-Huerta and Sheldon 2006). With increased nutrient supply, primary productivity would have increased and the larger biomass

would have extracted the ^{12}C preferentially, so leaving the heavy carbon isotope in seawater CO_2/HCO_3, which would have made $\delta^{13}C$ marine carbonate more positive (Brasier, 1995). This phenomenon could be a response to increased chemical weathering; this is a direct response to the intensity of rainfall. Increased precipitation could also be related to migration of the intertropical convergence zone (ITCZ). The ITCZ does move in its latitudinal position, driven especially by contraction and expansion of the polar ice-caps during periods of glaciation. During the time of deposition of the Palmarito strata, a glaciation (P3 of Fielding et al., 2008) was affecting the Earth, and it is very likely that this promoted the migration of the ICTZ through the operation of the Milankovitch rhythms which also controlled facies arrangements.

The decrease of the Fe/Al ratio could have been the result of the expansion of phytoplankton activity, which would have consumed the available iron (Brasier, 1995). C2 type cycles can be ascribed to an outer ramp setting and restricted to deep subtidal depositional areas.

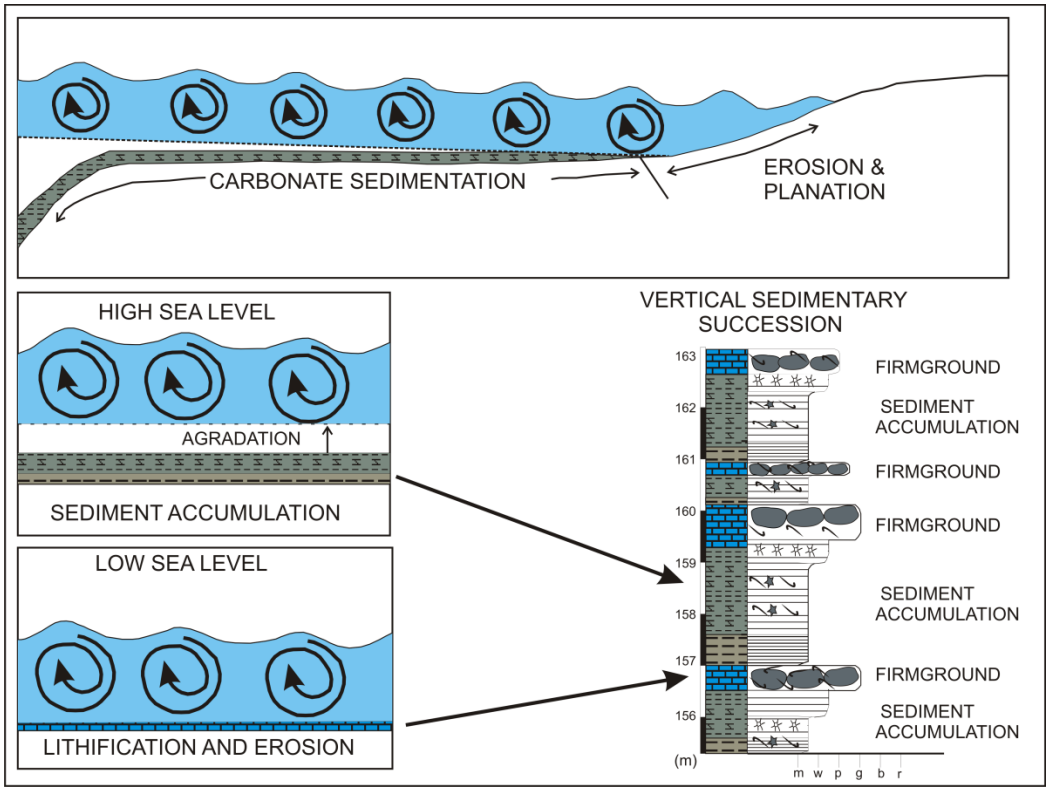

Figure. 5.13 Diagram showing the effect of sea-level change to form the cycles C1 (adapted from Jones and Desrochers, 1992). Example from the Great Australian Bight Shelf (James and Bone, 1991).

5.3.4 Cyclicity in Palmarito strata.

For this study of cyclicity, six sections (Palmar River, Quebrada de Portachuelo 1, Quebrada de Portachuelo 2, Cruz de Palmarito, Palmar River 2a and Palmar River 2b) have been examined in the Portachuelo area since they are the best preserved outcrops from which the most reliable field data could be obtained. Across all of the sections the most common cycles are the deep subtidal C group, followed by B-type cycles, which are shallow subtidal in origin. Less common are the fully regressive cycles, types A1 andA2, which are capped by supratidal facies (calcrete); these are only present in two sections, Palmar River and Quebrada de Portachuelo 1. Fischer plots were used to correlate and interpret possible long-term trends in cycle thickness patterns (Figure 5.14). Although, individual cycles cannot be correlated from one section to another, the overall cycle thickness trends are clearly correlatable on a local and regional scale.

The Palmar River succession has a well-developed and exposed cyclicity with 158 cycles and an average thickness of 2.51 m. The Fischer plot for this succession starts with a positive slope composed of A1 and A2-type cycles that are followed by a smooth negative slope for a few cycles (Phase 1, Section 3.6.2). This would suggest that accommodation space was increasing rapidly in the early part of deposition of this formation. This could have been the result of flexural deformation due to the active tectonism to the north. In addition, sea-level was rising, probably as a result of deglaciation, as shown by the passage from tidal-flat to shallow subtidal cycles. The rising relative sea-level trend continued and shallow subtidal B4-type cycles with storm influence and a high input of clastics were deposited (Phase 2, Section 3.6.2); one A3-type regressive cycle is present (cycle 41, Figure 5.14). Continuing, the Fischer plot shows a thickening-thinning pattern above 10 m of cumulative thickness which then passes to a gentle negative slope of cycles thinner than the average.

Deep subtidal C-type cycles, mainly of C1 type, now follow, with less common shallow subtidal type B1 cycles (Phase 3, Section 3.6.2). The thicknesses of C-type cycles are mostly below the average and so there is a negative slope. In fact, all the facies in these cycles are subtidal, both shallow and deep-water facies, without any evidence of subaerial exposure Thus these cycles do not record the pattern of change of accommodation space. This would suggest that the carbonate factory is the main control in the thickness of the cycles. However, there is no clear ordered pattern in these cycles which would be part of a longer term cycle. This would imply an influence of autocyclic processes controlling the environmental conditions responsible for carbonate production.

Higher in the succession, on the Fischer plot between cycles 78 to 118, a steep negative slope is particularly evident. This is a section of deep subtidal cycles, mainly C1 type and less common C2 (Phase 4, Section 3.6.2). The thinning pattern can be interpreted as a reduction in production of the carbonate factory. In addition, strong subsidence produced by

the flexural deformation triggered by an advance of the deformation front could have contributed (Section 3.6.3).

A subsequent package of shallow subtidal cycles shows a thickening-up pattern composed mainly of B2 cycle (Phase 4, Section 3.6.2). The facies are incomplete, only deep and shallow subtidal cycles appear, so these cycles do not record changes in accommodation space. However, they did reach closer to sea-level than the C-type cycles. This would suggest that the carbonate factory was increasing in production. In addition, a cycle-set of C types, mainly C2, is recorded which shows a negative slope (Phase 5, Section 3.6.2).

The uppermost package of this succession shows a positive slope formed of shallow subtidal cycles, generally B3, associated with heterozoan organisms and dolomitized shallow-water facies. The thickening-upward stacking pattern could have been produced by increasing production of the carbonate factory, with substantial accommodation space in the basin. Finally, peritidal cycles A1 (Phase 6, Section 3.6.2) display a negative slope due to a long-term sea-level fall causing the withdrawal of the epicontinental sea and exposure of the ramp, resulting in a major unconformity.

The Quebrada de Portachuelo 1 succession exhibits a well developed cyclicity that is represented by 75 cycles with an average thickness of 2.1 m; it is formed of most of the cycle types described above with the most common cycle being type C1. The Fischer plot illustrates a similar pattern to that from the Palmar River, with a thickening-upward section in the early part, followed by a thinning-upward section which drops the plot into the negative part of the graph. This package comprises cycle types A, mainly A1 and fewer A2 (Phase 1, Section 3.6.2). This would suggest that in the early stages of Palmarito deposition accommodation space was being created rapidly and the supply of clastic sediment was significant as well. However, it decreased quite suddenly, suggesting perhaps that it was associated with local tectonic uplift.

After this, there is no clear pattern; cycles thicken and thin upwards and they are located in the negative area of the plot. This section is composed of C1-type cycles and ends with an A3 clastic cycle that is followed by a set of 14 cycles, mainly C1 and C2 and one B1 cycle. There is an upward trend on the Fischer plot, reaching a maximum peak in the positive area (Phase 3, Section 3.6.2).

Subsequently, the graph shows a steep negative slope characterized by C1 and C2 cycle types with locally a B1 cycle present (Phase 4, Section 3.6.2). This package can be correlated broadly between every locality and represents an increase of accommodation space and/or decrease of carbonate production/sediment supply that can be ascribed to allocyclic processes. This was likely corresponding to the time of glaciation P3 of Fielding et al. (2008), when there could have been a high input of nutrients to the equatorial basins due to localized high precipitation. This phenomenon could have been triggered by migration of the intertropical convergence zone (ITCZ) close to the equator, which produced high continental run-off and monsoonal conditions, but not enough to produce large rivers or at least not in this area.

Finally in the Quebrada de Portachuelo 1 section, the mainly B3 cycles are thicker than the average and they can be correlated with those in the Palmar River section. This would suggest a similar interpretation of this interval as given above.

The Quebrada de Portachuelo 2 section exposes 83 cycles with a thickness average of 2.21m. C1 and C2-type cycles are most common with fewer B1, B2 and B3 cycles. The Fischer plot starts with a steep positive trend mainly composed of C1 cycles and one A3 (cycle 13) (Phase 3, Section 3.6.2). This pattern differs from that in the Palmar River section; however, it can be partly correlated with other measured sections. This trend is probably the result of local controls that increased the thickness of the cycles in this particular package.

Afterwards, the diagram show a very abrupt negative (downward) slope that represents the thinning upwards of mainly C1 and C2 cycles with one incursion of B1 cycles (cycles 54-56) (Phase 4, Section 3.6.2). This bundle is clearly correlatable to the other sections; thus it is likely that just allocyclic processes were responsible for the deposition of this part of the succession, and that deposition was controlled by similar processes.

Subsequently, a bundle of thick B2 and B3 cycles appears, and there is an upward RISE in the Fischer plot into the positive area of the graph. It can also be correlated with the Palmar River and Quebrada de Portachuelo 1 sections. Thus, similar controls can be postulated. This package is followed by a thinner-than-average cycle set of C2 cycles that is also similar to the Palmar River trend; this part finishes with one thick B2 cycle.

The Cruz de Palmarito section is formed of 30 cycles with an average thickness of 2.09 m where the dominant cycle is C2 type. The Fischer plot displays a thinner-than-average cycle package which contains B2 and C1 and C2 cycle types in the early part; these were probably influenced by autocyclic processes. This package is followed by a positive slope with a cycle-set which is formed mainly of B1-type cycles and less frequent C2 cycles; these pass up into a short steep section formed by a bundle of C2 cycles. This package could be correlated to the beginning of the steep slope that is present in every other succession. The same interpretation is likely for all of these cycles. Finally, the last package of C2 cycles keeps a relatively constant thickness until the end of the exposure.

The Palmar River 2a section is a lateral correlative to the Palmar River and is composed of 18 cycles (average = 1.10 m), mainly of C1 type and one cycle B1 (cycle 7). The Fischer plot shows a trend of relatively constant thickness, slightly less than the average, and then a small thickening-thinning trend. This pattern shows similarities with a peak just before the steep negative slope (Figure 5.14), which is the boundary between the Kungurian and Roadian stages.

The Palmar River 2b section is characterized of 32 cycles with an average thickness of 1.62 m; the most common cycles are C2, with 2 cycles of A3 (cycle 12, 14). The Fischer plot shows a thicker-than-average package followed by a thinner-than-average package, and this is correlatable to the inflection on the Fischer plot that matches with the boundary between the Kungurian and Roadian stages. Therefore, this can be interpreted as the product of the same events.

5.4 Discussion

5.4.1 Duration of the cycles

Although the duration of the whole Palmarito succession cannot be very well defined, it is also likely to be incomplete, with several or many stratigraphic gaps. These pose a difficulty in terms of elucidating the cycle hierarchy and determining the duration of cycles. With regard to the metre-scale cycles with an average thickness between 1-3 m, this scale of cycle has been related to 4^{th}-5^{th} order sea-level cycles (Goldhammer et al., 1990); they are also referred to as parasequences (Van Wagoner, 1988). These have been linked to the Milankovitch orbital rhythms, with durations of 20,000 years (precession), 40,000-years (obliquity) and 100,000-years (eccentricity) (Pratt, 2010; Tucker and Garland, 2010). For the Palmarito Formation in the Portachuelo area, the combination of Sr-isotope dating, the long-term trend in carbon isotope signatures (discussed in Chapter 4) and the biostratigraphy (from Hoover, 1981; Rigby, 1984), it can be suggested that many of the cycles are related to the short eccentricity (~100,000 years) rhythm. If this is the case, then from the total thickness (401.5 m) of the Palmarito and the total number (158) of cycles, the sedimentation rate can be calculated as approximately 0.021 m $1000yr^{-1}$. This figure is similar to the value of 0.037 m $1000yr^{-1}$ for the succession of Devonian cycles in Belgium (Tucker and Garland, 2010), which is comparable with other ancient carbonate platforms (e.g. 0.05 m $1000yr^{-1}$ for the Upper Permian of West Texas, and 0.04 m $1000yr^{-1}$ for the Upper Cretaceous of the Bahamas

subsurface (Tucker and Wright, 1990). Sedimentation rates do vary of course, from one formation to another, depending on the facies, lithology, tectonic regime and biota, and accommodation space.

5.4.2 Origin of the metre-scale cyclicity in Palmarito strata.

The origin of metre-scale cycles has been a controversial issue over the last 50 years with many papers addressing the cause of cyclic facies repetition in the geological record (e.g. Fischer, 1964; Goldhammer et al., 1990; Lehrmann and Goldhammer, 1999; Bosence et al., 2009; Tucker and Garland, 2010). Three basic mechanisms have been proposed for the repetitive vertical stacking of facies: tectonics, eustasy (Milankovich rhythms / orbital forcing), which can be grouped together as allocyclic processes, and autocyclic sedimentary processes (Lehrmann and Goldhammer, 1999; Schlager, 2005; Bosence et al., 2009; Tucker and Garland, 2010). Many techniques have been used to assess cycle thickness data and interpret cycle origin (e.g. Fischer plots, statistical tests, forward modelling, e.g. Wilkinson et al., 1998; Weedon, 2003; Burgess et al., 2001, Burgess, 2006).

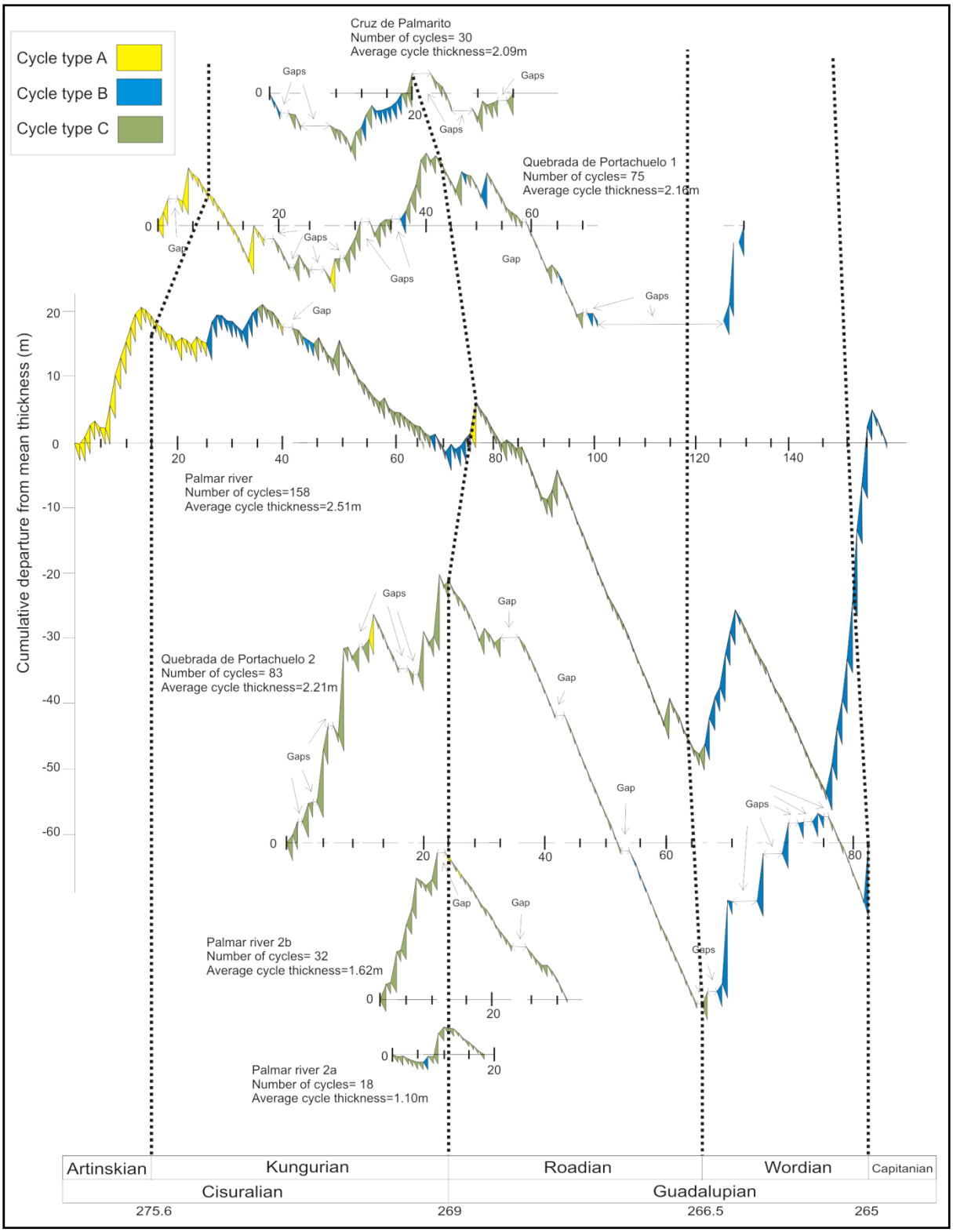

Figure 5.14. Fischer plots of six sections in the Portachuelo area of the Venezuelan Andes. Palmar River, Quebrada de Portachuelo 1, Quebrada de Portachuelo 2, Cruz de Palmarito, Palmar River 2a, Palmar River 2b.

The Fischer plots offer a graphical way to contrast the variation of thickness in different successions (qualitative evaluation) (Bosence et al., 2009). A visual assessment of

the Fischer plots for the Palmarito Formation suggests two main groups (Figure 5.14). First, an interval of cycles from the middle Artinskian to the Kungurian-Roadian boundary shows no common long-term trend of cycle thickness variation between sections. In the Palmar River 2b and Quebrada de Portachuelo 2 sections, both start with a rising trend for the initial 10 cycles. However, the other time-equivalent plots do not display any similar trends. In addition, the 3 cycle types, A, B and C, interfinger with each other, suggesting variable controls on deposition; this contrasts with the upper part of the succession. Here, from the Kungurian-Roadian boundary to the Capitanian, there is a very clear correlation between sections, with a steep slope in every plot; in addition, there is a rising-falling-rising pattern in the most complete successions. Above this, the dominant cycles are C types which are mainly thinner-than-average and quite continuous, just interrupted by several B-type cycles, thicker-than-average, grouped into bundles. This arrangement could indicate the operation of composite eustasy, i.e. two Milankovitch rhythms superimposed on each other, or the effect of a longer-term, 3rd-order relative sea-level pattern.

Statistical tests were used to assess the degree of order in the succession of cycles in the Palmarito (quantitative assessment) (see Sadler et al., 1993; Lehrman and Goldhammer 1999; Bosence et al., 2009). A runs test was applied and the z-values calculated for every section (Table1). The z-scores show values between -2.53 to -5.39, which, according to Sadler et al. (1993) and Burgess (2006) places the cycle patterns in the non-random area of the graph (Figure 5.15; Table 1). However, there is one exception in the succession from Palmar River 2b, which presents a z-value of -0.48. This would indicate a random succession of cycles. It is possible this is due to the fact that this is the shortest succession of cycles (only 18 cycles), so that it may not be statistically valid to use this section. Lehrman and Goldhammer (1999) noted that successions with more cycles generally tend to give more negative (i.e. ordered) z-values compared with successions with far fewer cycles.

Table 5.1 Z-scores for the successions of metre-scale cycles from 6 localities in the Palmarito Formation

Locality	No.Cycles	AvThick	n1>	n2<	r (runs)	Z score
Palmar River	158	2.54	106	52	41	-5.39
Portachuelo 1	75	2.16	49	26	25	-2.56
Portachuelo 2	83	2.21	58	25	21	-3.93
Cruz de Palmarito	30	2.09	15	15	8	-2.97
Palmar River 2a	18	1.1	13	5	9	0.48
Palmar River 2b	32	1.62	22	10	7	-3.26
Palmar River lower part	75	2.7	46	29	28	-2.10
Palmar River upper part	83	2.44	62	21	13	-5.68
Quebrada de Portachuelo 1 lower part	43	2.38	26	17	17	-1.47
Quebrada de Portachuelo 1 upper part	32	1.86	23	9	11	-1.32
Quebrada de Portachuelo 2 lower part	25	3.76	17	8	13	0.53
Quebrada de Portachuelo 2 upper part	58	1.54	46	12	9	-4.50

Although, most of the successions have generated z-scores which indicate very-well ordered vertical stacking of cycles, this did involve including all the cycles in a section. A close visual assessment of the Fischer plots in Figure 5.14 invites further consideration: the successions can actually be divided into two packages. For this assessment, only the longest and statistically more representative successions were used, namely Palmar River, Quebrada de Portachuelo 1 and Quebrada de Portachuelo 2. For the lower part of the plots (Artinskian to the Kungurian-Roadian boundary) from the three sections, random values are obtained (using Burgess, 2006, z-score boundaries of randomness values are between +2.4 and -2.4): -2.1 for Palmar River, -1.47 for Quebrada de Portachuelo 1 and 0.53 for Quebrada de Portachuelo 2. In contrast, for the upper part of the Fischer plot (Kungurian-Roadian boundary to Capitanian), two of the successions show very-well ordered z-scores of -5.58 for the Palmar River and -4.50 for the Quebrada de Portachuelo 2, and they display a good graphical correlation between the Fischer plots too. However, Quebrada de Portachuelo 1 shows a random vertical stacking pattern. This is probably due to this succession not having

enough exposed cycles for the upper part to be statistically representative (Figure 5.15; Table 1). In summary, it would seem that the lower part of the cyclic succession has a random stack of cycles and so is controlled mainly by autocyclic processes, whereas the upper part has a more ordered pattern of cycles, indicating that depositional processes were controlled more by allocyclic, probably Milankovich rhythms and orbital forcing. However, there may well have been some overprinting from other controls, namely tectonics and movement on faults.

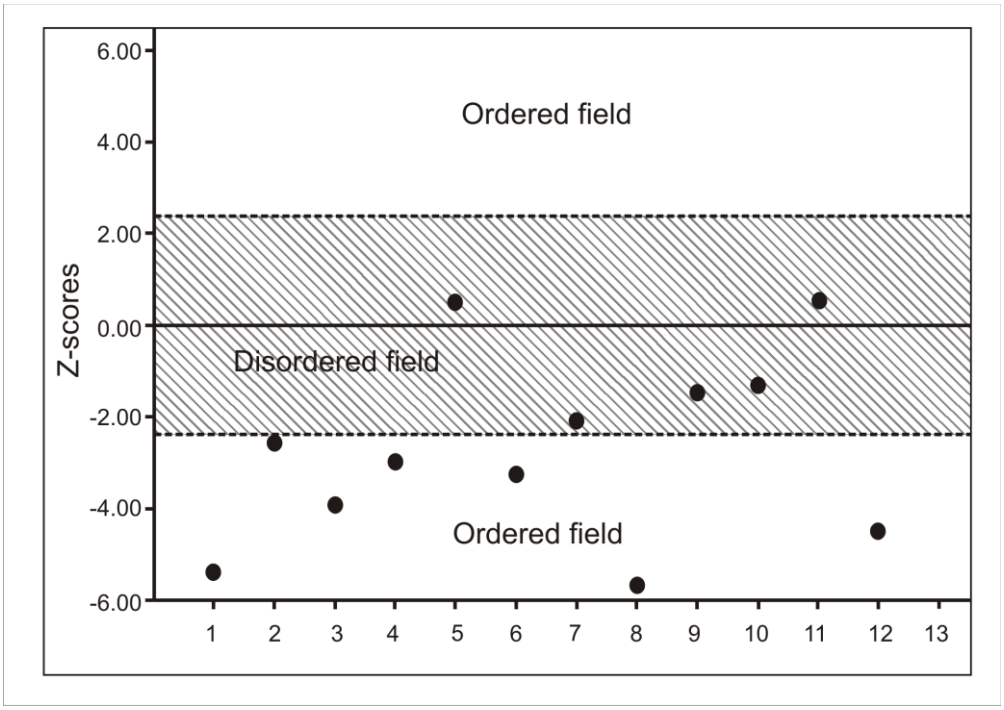

Figure 5.15. Z-scores of six whole successions and three successions divided into 2 packages. (1) Palmar River, (2) Quebrada de Portachuelo 1, (3) Quebrada de Portachuelo 2, (4) Cruz de Palmarito, (5) Palmar River 2a, (6) Palmar River 2b. In addition, (7) Palmar River lower part, (8) Palmar River upper part, (9) Quebrada de Portachuelo 1 lower part, (10) Quebrada de Portachuelo 1 upper part, (11) Quebrada de Portachuelo 2 lower part , (12) Quebrada de Portachuelo 2 upper part.

The bundling of cycles into packages in Palmarito strata is unlikely to be associated to Milankovich rhythms in the lower part, Artinskian to the Kungurian-Roadian boundary, due to the overprinting by autocyclic processes. However, in the upper part (Kungurian-Roadian boundary to Capitanian) the cycles might show some bundling of cycles into packages if two Milankovitch rhythms were controlling sea-level and so sedimentation, as described in the literature with of bundles of 4 or 5 cycles (Goldhammer et al., 1990; Satterley, 1996; Chen & Tucker, 2004; Bosence et al., 2009). In contrast, they reflect bundles of 1:2 or 1:3 In fact the

Palmarito cycles do not show 1:4 or 1:5 bundling related to short-eccentricity + precession rhythms but there is a suggestion of 2 or 3 cycles forming packages (see Figure 5.14). This could be ascribed to short-eccentricity + long-eccentricity rhythms

5.4.2.1 Autocyclic controls

Autocyclic processes are the result of sedimentary mechanisms that are a normal part of the depositional environment. These processes are restricted to localized areas and can vary through the basin producing irregular signals in the cycles. Statistical analysis and graphical tools (Fischer plots) presented above have suggested that the lower part of the Palmarito cyclic succession is dominated by autocyclic processess. James (1984), Pratt, James and Cowan (1992) and Pratt (2010) have described the tidal-flat progradation model, which in this study could only be applied to A-type cycles which have been interpreted as shallowing-upwards peritidal cycles capped by calcrete through subaerial exposure . In the tidal-flat interval of the Palmarito Formation, the clastic input is quite significant; therefore, clastic models can be applied as well (e.g. Dalrymple, 1992; 2010). For B-type cycles that are entirely subtidal, the autocyclic processes are less important but definitely had an influence in the lower part of the formation. Jones and Desrochers (1992) have proposed the influence of storms as the critical element in fully shallow subtidal cycles due to the increase of carbonate production attempting to grow above storm wave base, but the energy of the storms rework and redistribute the sediments and limit vertical accretion. In this way, therefore, the seafloor is kept below or close to storm wave base. In cycle type B4, storm beds are common with a mixed clastic-carbonate composition and also sedimentary structures typical of storms, including hummocky cross stratification (HCS). In addition, B4 cycles do not appear in the upper part of the succession. Finally, type C cycles are more difficult to explain through autocyclic mechanisms.

5.4.2.2 Allocyclic controls

Tectonics

In Chapter 3 the general tectonic context has been discussed where it was suggested that this was dominated by a compressive tectonic regime as a result of the collision between Gondwana and Laurentia during the Permo-Carboniferous, which involved Alleghenian and Marathon-Ouachita orogenesis (Miall and Blakey, 2008; Pindell, 1985). The subsidence in the area could have been affected by the compressive regime and associated increasing flexural effects, which would have generated the accommodation space available for sedimentation within the basin. This process is not easy to demonstrate on a short time-scale; however, in the long-term, tectonics seems to be responsible for the creation of accommodation space, since long-term global sea-level was falling according to the Haq and Schutter (2009) sea-level curve. The deformation front that is described in Chapter 3 could be an explanation for the increased subsidence that was higher than the global sea-level fall. The accommodation space generated for the type A cycles is directly a major control. On the other hand, the other cycle types are subtidal and the accommodation space in these deposits is not the major control on their origin, or thickness either. Sediment supply and carbonate factory production were the major controls on cycle types B and C.

Carbonate factory

Jones and Desrochers (1992) have defined the carbonate factory as the area of carbonate sediment production and this is controlled by oceanographic and biological processes, nutrient supply, and clastic input. Carbonate factory production and sediment transport are direct controls on the development of carbonate cycles and carbonate platforms themselves (Williams et al., 2011). Expansion (or reduction) of the carbonate factory is normally assumed to be related to the production of photozoan assemblage carbonates, which are favored by warm, shallow water and oligotrophic conditions. Photozoans have a higher

rate of carbonate production than heterozoans (Schlager, 2005). However, during the Late Palaeozoic, and especially in the Permian, heterozoan organisms were generally dominant (Wright and Burchette, 1996) and this has been ascribed to the widespread development of eutrophic-mesotrophic oceans and warm to cool sea-water (Wright and Burchette, 1996). Although, the rate of carbonate production is an intrinsic control on deposition within a basin, this is largely driven by external factors such as climate

Nutrient supply

According to Martin (1996), over the long-term during the Palaeozoic there was a global increase in nutrient supply to the oceans, reaching a mesotrophic stage during the Permian. This resulted in a general increase in organic productivity and therefore, an expansion of the carbonate factory. With the high level of nutrient supply, the biotic community was dominated by heterotrophic organisms. Variations in nutrient supply on a shorter time-scale have been invoked here for the cycle types C1 and C2 (see Section 5.3.3), from the increasing heterozoan bioclast content and faunal diversity up through the cycles, along with their P/Al ratio and more positive $\delta^{13}C$. These features were interpreted as reflecting an increase in organic productivity as a result of the increased input of nutrients to the basin. This could have been related to enhanced chemical weathering during a period of heavy precipitation and a more humid climate, controlled by migration of the intertropical convergence zone (ITCZ) According to Bridges et al. (1995), Halfar et al. (2004), Samankassou (2002) and James and Lukasik (2010), an alternative explanation for the heterozoan assemblage could be nutrients derived from upwelling currents. However, for the Palmarito Formation, a continental run-off control is more likely. Although, the setting of the basin is poorly known there is no evidence of a deep, offshore environment from which cool, nutrient-rich waters could have been derived. Another less probable option is coastal upwelling which was suggested by Samankassou (2002) for Pennsylvanian heterozoan

carbonates in Austria-Italy. However, the location of Austria-Italy at the time, on the margins of the opening Tethys ocean, was near to potential sources of upwelling; this is an argument that cannot be used in the Palmarito case.

Climate, Milankovich rhythms and orbital forcing

Variation of sea-level due to changes in ice volume is a classic explanation that has been used in the last 30 years for the deposition of cycles. This theory is related to changes in the distance between the Earth and the Sun, and variations in the angle that these electromagnetic radiations (or sun's rays) reach the Earth's surface. These variations or changes were calculated by Milankovich who proposed that the Earth´s orbit is affected by three components; eccentricity, obliquity and precision. The Milankovich theory is based on the idea that these three components are cyclical and quasi-periodic and they are very closely connected to the history of climate change over geological time giving warm and cold periods which are driven by changes in glacial ice volumes, and therefore changes in sea-level (e.g. see Drake, 2000; De Boer & Smith, 1994; Schwarzacher, 2000; Einsele 1991).. Sedimentary cycles have also been recognized to support this variation (De Boer & Smith 1994) and have assumed similar time-bands of 20,000 years (precession), 40,000-years (obliquity) and 100,000-years (eccentricity).

The climate of equatorial Pangea was characterized by monsoonal circulation (Tabor and Montañez, 2002; Tabor and Poulsen, 2008; Peyser and Poulsen, 2008). Tabor and Poulsen (2008) and Perlmutter and Plotnick (2003) proposed that monsoon intensity over equatorial Pangea might have changed over shorter periods of time than a tectonic timescale. In addition, monsoon intensity was higher during periods of glacial maximum and lower during glacial minima, as a result of the changes in temperature between the poles and equator (Perlmutter and Plotnick, 2003). The seasonal migration of the ITCZ moved in a broad zone in the glacial minimum periods and extended over a wide zone of the tropics; in

contrast, at times of maximum glaciations, the ITCZ was quite narrow. However, in the case of the Permo-Carboniferous the glaciations were developed almost entirely around the south pole, therefore, it would have driven the ITCZ to the north (Figure 5.16). This would have resulted in intense rainfall and a more humid climate during the time of maximum glaciation for this region due to the narrow movements of the ITCZ in the north; the opposite would have been the case during times of glacial minimum when the climate would have been driven to more arid conditions. These fluctuations in climate, driven by orbital forcing and so on a periodic time-frame, would have driven continental chemical weathering and input of nutrients to the basin from the north. These arguments support the initial idea of the intensification of rainfall which increases chemical weathering and the flux of nutrients to the basin. This process could have varied in intensity on different scales, from short-term Milankovich rhythms to long-term glacial periods (i.e. the P3 (4 My) and P4 (7 My) glaciations proposed by Fielding et al., 2008).

Atmospheric pCO_2 variations during the Late Palaeozoic have been discussed by many authors (e.g. Saltzman, 2003; Tabor and Montañez, 2002; Montañez et al., 2007; Peyser and Poulsen, 2008; Tabor and Poulsen, 2008; Parrish, 1993); all of them have suggested that CO_2 was a significant control on surface temperature, evapotranspiration and palaeo-precipitation in the short and long term. In addition, the effect on expansion and contraction of the ice caps in high latitudes, which were likely driven by orbital forcing, would simultaneously have controlled the migration of the ITCZ in low latitudes. This would have caused strong seasonality during times of deglaciation and long periods of humid climate during the glaciations from a narrow zone of the ITCZ. It is suggested that these effects were recorded in the Palmarito sedimentary cycles through the biota, facies and geochemical signals. These processes may have been effective throughout the successions but only in the upper part can they be recognized, since the cycles in lower part of the formation

were more affected by autocyclic processes which overprinted the allocyclic controls, such as the regional climatic system.

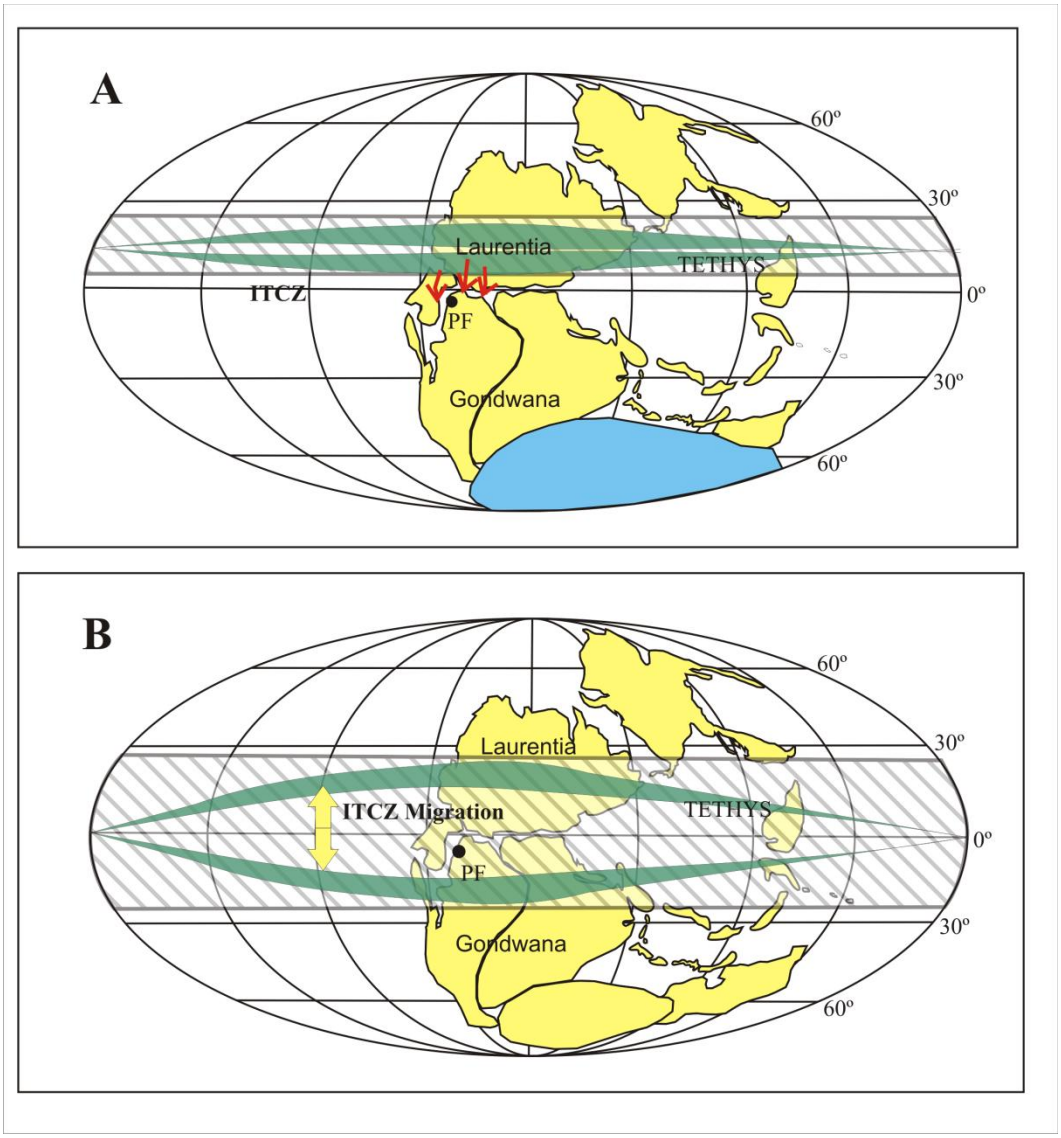

Figure 5.16. Schematic palaeogeography for the Kungurian. (PF) Palmarito Formation area (A) For glacial maxima the ITCZ migration band was narrow and focused in tropical area; (B) For glacial minima the ITCZ migration band was wide and moved away from the equatorial area. (Modified from Tabor and Montañez, 2008). Red arrows indicate potential continental run-off from the north.

Summary and conclusions

In the Venezuelan Permian carbonate succession 3 major types of metre-scale cycle, with various subtypes, can be recognized; these are mixed clastic-carbonate peritidal cycles (Type A), shallow subtidal cycles (Type B) and deep subtidal cycles (Type C). Most of these show mainly shallowing-upward facies arrangements.

Type A cycles are mixed clastic-carbonate, shallowing-upward peritidal cycles. The upper boundaries of the cycles are exposure surfaces with calcrete. The origin of the cycles is attributed to tidal- flat progradation, variations in carbonate productivity and clastic input to the depositional area.

Type B cycles consist entirely of subtidal facies and show shallowing-upward facies arrangements, but without exposure. These cycles are normally thicker than the average and show an alternation between heterozoan and photozoan assemblages, but with little indication of any water depth change. They could reflect rapid variations in nutrient supply or temperature, possibly due to upwelling as suggested by Samankassou (2002) for similar-aged cycles in Austria. However, long-term fluctuation in continental run-off is another possible control; changes in rain-fall and chemical weathering could lead to variations in nutrient supply to the sea, and changes in trace element contents of the limestones may be reflecting this. Although, geochemical signatures of carbonates are not conclusive evidence one way or the other, the regional setting of the basin does suggest continental run-off as a cause rather than upwelling.

Type C cycles were deposited in the middle to outer ramp setting and are characterized by heterozoan assemblages and shallowing-upward trends. The model proposed by James and Bone (1991) and Jones and Desrochers (1992) seems to explain the origin of cycle type C1, with deposition taking place when storm wave base (SWB) was located above the sea floor (highstand of sea-level), and lithification and erosion were acting when the SWB was reworking sediment at the sea-floor (lowstand of sea-level). Probably the same model can be applied to cycle type C2 but instead of lithification there was just erosion and reworking of the more abundant heterozoan bioclasts. This can be linked to short-term sea-level changes, probably under the influence of orbital forcing. In addition, the carbon isotope signal shows a strong positive increase through a cycle, and, coupled with this, the P/Al ratio

and also the $CaCO_3$ content increase upwards. These patterns would suggest that the increase in nutrient supply (as indicated by the P/Al ratio) was probably due to continental run-off; primary productivity would have been enhanced, leading to an increase in the biomass. This process could be explained by the migration of the ITCZ which was broad at the time of reduced glaciations, extending in a wide band over the tropics. By way of contrast, at times of maximum glaciation the ITCZ was quite narrow, but, in this Permo-Carboniferous case, the glaciation was developed almost entirely in the south pole region, therefore, expansions of the polar ice-cap would have driven the ITCZ farther to the north. Thus there could have been times of intense rainfall during the maximum glacial periods for this northwestern region due to the narrow movements of the ITCZ. These would have created a humid climate, and during times of minimal glaciation, the climate could have become more arid. An increase and decrease in this ITCZ behaviour in a cyclic pattern would have affected chemical weathering in continental areas, and resulted in variations in nutrient supply to the basin.

For the 4^{th}-5^{th} order cycles / parasequences in the Palmarito strata, the combination of Sr-isotope dating, long-term trends in carbon isotope values and the biostratigraphy of Hoover (1981) and Rigby (1984) have permitted the duration of an average cycle to be ascribed to the short eccentricity (~100,000 years) rhythm. In addition, the deduced sedimentation rate is similar to other ancient carbonate platforms in the geological record.

In summary, the cycles of the Palmarito Formation were formed through the operation of different controls with autocyclic processes more dominant in the lower part of the succession and allocyclic processes, most likely orbital forcing, more important in the upper part.

6 Post-sedimentary events and petroleum potential of the Palmarito Formation.

6.1 Introduction

After deposition, Palmarito strata were affected by a range of diagenetic processes, taking place at different stages in the burial history. For the most part Palmarito strata are fine-grained, and there are few grainstones or cavity structures where coarse cements can be observed. The main post-depositional processes were compaction and cementation, as well as silicification and selective dolomitization. The latter has in some cases enhanced the porosity although elsewhere the most common primary intraskeletal porosity has been reduced. The Palmarito succession in the central and northeast part of the Andes has been affected by low-grade regional metamorphism; this is probably the result of intense tectonic activity in some regions and deep burial. However, in the south-western Venezuelan Andes the sediments are unmetamorphosed and this suggests a differential burial history for the basin here or a lower heat flow associated with the tectonic activity.

In the last decade, Palaeozoic deposits have been identified as potential future oil and gas reserves, not only in Venezuela but in several other countries around the world. The petroleum potential of the Upper Palaeozoic strata in Venezuela is noteworthy in view of the correlations with hydrocarbon-bearing strata and source rocks in neighbouring Brazil and the southern USA.

The aim of this chapter is to provide a description of the post sedimentary processes that have affected the Palmarito strata using petrographic analysis, cathodoluminescence, trace elements and stable isotopes. In addition, this chapter summarizes the features of the potential petroleum system in these rocks, which may well be hydrocarbon-bearing in the Barinas-Apure and Llanos basins.

6.2 Methods

For this chapter conventional petrography was carried out (the methodology is presented in Appendix 2). The samples were classified using the textural scheme of Dunham (1962) and the diagenetic features were identified including compaction, cementation and dissolution. The stable isotopes $\delta^{13}C$ and $\delta^{18}O$ are useful for understanding the evolution of these rocks from subaerial exposure through to burial and subsequent uplift. Matrix-whole rock and cements were analyzed using the methodology explained in Chapter 4. In addition trace elements were determined: iron (Fe), manganese (Mn), magnesium (Mg) and strontium (Sr), with a view to providing information on the diagenetic processes and fluids involved. Cathodoluminescence was used to identify the different stages of cementation. However, there were few cements to study since most of the facies were lime-mud rich which limited the use of this practical tool.

The identification of the elements of the petroleum systems was carried out based on the information in the previous chapters relating to facies distribution, enhanced time frame, palaeogeography, climatic pattern and cyclicity, as well as, the model for diagenesis presented in this chapter.

6.3 Diagenetic processes in Palmarito strata

The diagenesis of Palmarito strata can be separated into early and late stages, and involves near-surface to burial cementation, and compaction and dolomitization. The following section will provide the description of the cements and compaction features, supplemented by stable isotope and trace element data in the whole rock and the cements.

6.3.1 Early marine diagenesis

Marine cements have been identified in the Palmarito strata associated with bioclastic crinoidal-bryozoan wackestone-packstones, bryozoan boundstones, and fusulind grainstone-packstones, as well as mixed bioclast rudstone-packstones and calcareous sandstones.

Radiaxial-fibrous and bladed calcites are the common shallow-marine cements here and are present mainly as crusts attached to brachiopod and bivalve shells, as well as filling the internal cavities of brachiopods and bryozoans (Figure 6.1). The fibrous cements show the typical undulose extinction pattern and curved twin planes. Crystal lengths reach several millimetres. These types of cement typically occur within ancient reefs and buildups, also mud-mounds, and they are now generally regarded as primary marine cement (Kendall, 1985).

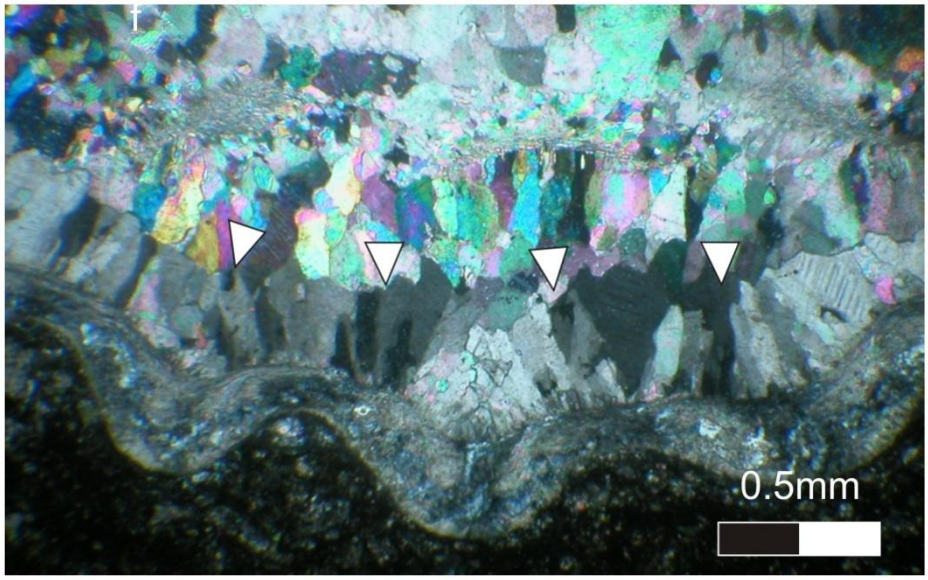

Figure 6.1 Marine radiaxial fibrous calcite cement (arrows). The first stage of cementation from brachiopod shell. Sample 166 Quebrada de Portachuelo 2 section.

Neomorphism has been described by many authors (Folk, 1965; Scoffin, 1987; Tucker and Wright, 1990; Flügel, 2004) as a process of transformation of one mineral to itself or a polymorph. The term aggrading neomorphism is commonly used in lime mud diagenesis to describe the enlargement of mosaics to microspar (generally 5-10 μm) or to a coarser pseudospar (>30 μm). In Palmarito strata, neomorphic wackestones are common in the succession; this facies is characterized by floating bioclasts in a coarse microspar, with irregular intercrystalline boundaries, irregular crystal sizes and locally patchy areas with very coarse crystals (several mm in diameter). In addition, the pseudospar crystals are rich in

inclusions, and clay minerals occur between the crystals as well (Figure 6.2). All these features suggest that aggrading neomorphism is the dominant diagenetic process of this facies. Micritization (or degrading neomorphism) is present in a few samples and it is usually associated with crinoid, bryozoan and green algal bioclasts.

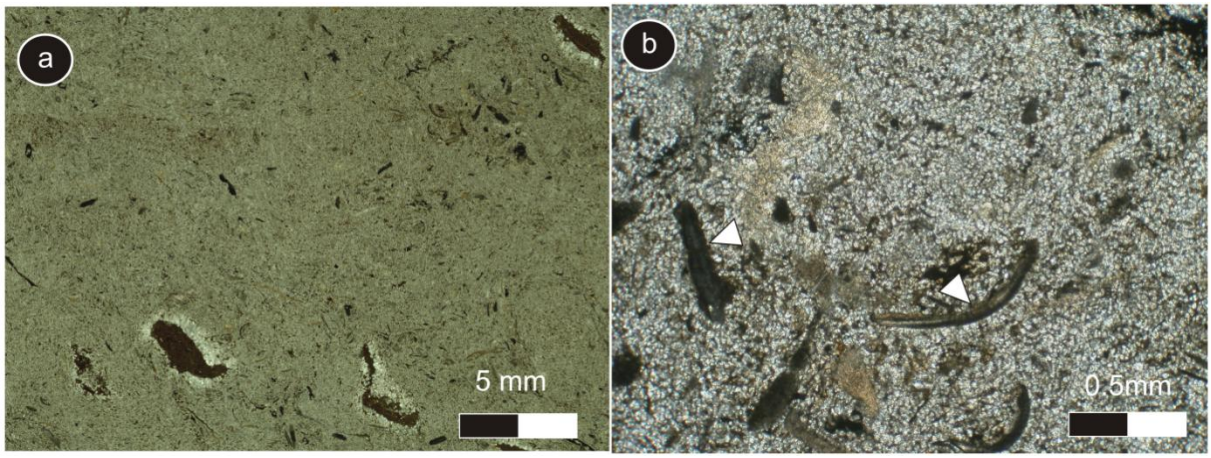

Figure 6.2 a) General view of the neomorphic facies showing patches of coarse microspar mosaic. b) Floating bioclasts in microspar. Sample 60 Palmar River section.

6.3.2 Early meteoric diagenesis

Pedogenetic features have been found that were directly associated with meteoric diagenesis; they are normally located at the top of the A-type cycles in the tidal-flat facies. These calcretes are a clayey lime mudstone and have a brownish-greyish colour. Vertical-subvertical fenestrae and elongate micritic zones are present, and these could be rootlets or rhizoliths. There are also calcite crystal aggregates that are reminiscent of *Microcodium*. This identification is not completely conclusive, however; the association with mud-cracks and fibrous (feathered) cements does support a meteoric diagenetic environment. In addition, other features can be found in the facies such as complex irregular cracks, cemented cracks, abundant inclusions of detrital siliciclastic grains (silt and sand) as well as neomorphic textures in some of these horizons. The calcretes also have a bright luminescence in CL; this could be related to the transformation from an original microcrystalline aragonite or high-Mg calcite to low-Mg calcite in the phreatic zone under reducing conditions (Figure 6.3). In terms

of the genetic classification of calcretes of Esteban and Klappa (1983) alpha and beta calcrete fabric types can be identified (Figure 6.3). Their presence could be the result of alternations of environmental conditions through the succession.

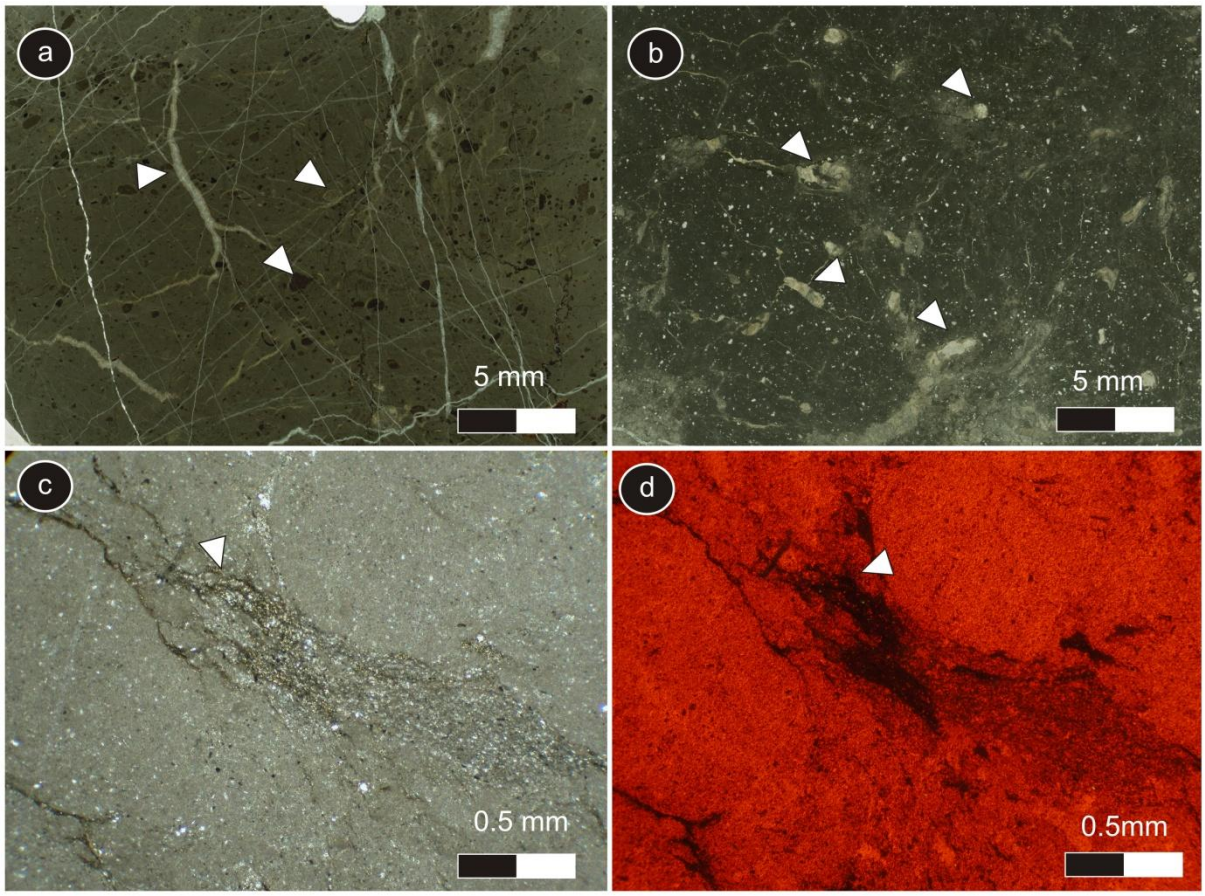

Figure 6.3 a) General view of calcrete showing complex irregular cracks and cemented cracks (arrows), also, irregular peloids. Sample 43 Palmar River. b) Rhizolith structures in lime mudstone facies. Sample p56-m36b2 Palmar River. c) Irregular crack of lime mudstone facies with abundant inclusions of detrital siliciclastic material. Sample 133 Quebrada de Portachuelo 1 section. d) Highly-luminescent microspar of calcrete. Sample 133 Quebrada de Portachuelo 1 section

6.3.3 Burial diagenesis

Drusy, equant calcite spar cements are present in Palmarito strata with a post-compaction timing providing evidence of their burial diagenetic origin. In most of the examples drusy cements are present filling the cavities in bryozoans and brachiopod shells. Calcite spar is also seen replacing pre-existing cements in bioclasts. This represents another kind of neomorphism (i.e. calcitization). Phylloid algae, originally composed of aragonite,

have also been replaced (Figure 6.4). Most of the calcite spar cements show a dull or non-luminescent appearance in cathodoluminescence (CL). *Poikilotopic* and *peloidal* cements also appear filling cavities of corals and bryozoans with non-luminescence in CL.

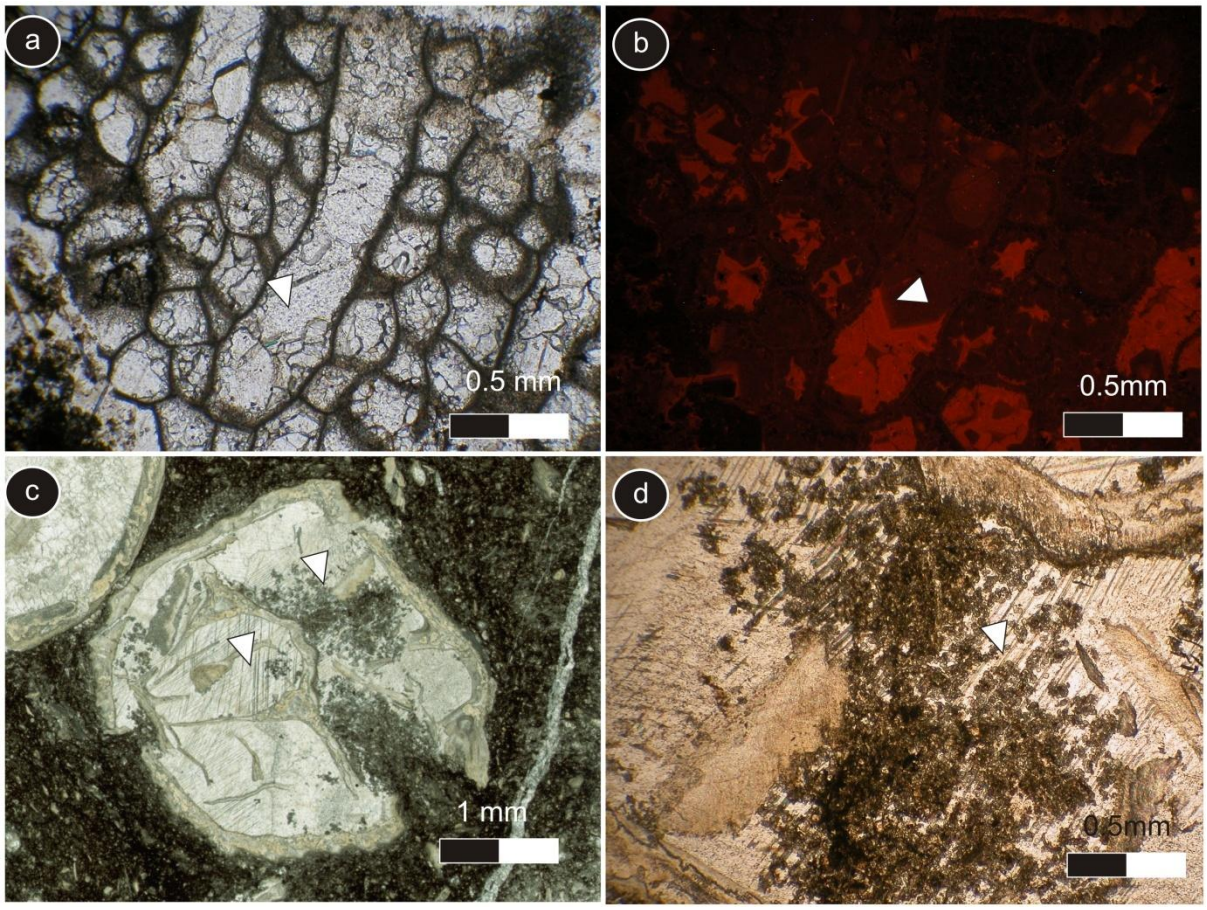

Figure 6.4 a) Zooecia of bryozoan filled with sparry drusy cement. Sample 166 Quebrada de Portachuelo 2 section b) Cathodoluminescence image of a bryozoan showing different stages of cementation. Sample 166 Quebrada de Portachuelo 2 section. c) Poikilotopic and peloidal cements filling intraskeletal void (arrows). Sample 166 Quebrada de Portachuelo 2 section. d) Detail of peloidal cements (arrows). Sample 166 Quebrada de Portachuelo 2 section.

Compaction is a common process during burial diagenesis and it is described as any process that reduces the volume of the rock. Many limestones lose their porosity by compaction during burial (Tucker and Wright, 1990; Flügel, 2004). This process generally affects facies where there has been little early cementation. Compaction is one of the most common processes in Palmarito sediments since only a few horizons have been affected by early cementation. Features of both mechanical and chemical compaction are developed and

include fitted or condensed fabric, broken bioclasts and a variety of stylolites that are present chiefly in the muddy and bioclastic facies. Broken and deformed fusulinids are common in the Palmarito strata as a result of *mechanical (physical) compaction*. Fusulinids show broken walls that normally are in contact with other or more rigid bioclasts, such as crinoids. In other examples they are completely deformed, probably due to their ductile state during burial (Figure 6.5 a, b). The bioclasts appear to have a preferred orientation and they normally have a grain-to-grain contact. These can be found in the mixed bioclastic crinoidal-bryozoan microfacies and in the fusulinid packstones. However, these features are difficult to observe in the more muddy facies.

With increasing burial, *chemical compaction* takes over from mechanical processes, leading to pressure dissolution within the rock. This process drives the dissolution of grains, matrix and cements and is an important source of $CaCO_3$ that contributes to cementation in other horizons in the basin. Logan and Seminiuk (1976), Wanless (1979) and Choquette and James (1987) have all developed terminologies to describe pressure dissolution features that include stylolite geometry, distribution, orientation and the nature of the material involved, as well as the insoluble residue (stylocumulate). Chemical compaction is quite remarkable throughout the Palmarito facies where it is possible to identify irregular anastomosed sutured seams (microstylolite sets) with black insoluble reside (stylocumulate) that includes clay minerals and bitumen. Also, a condensed fabric in the crinoidal facies is frequently present and is the product of densely packed irregular anastomosing microstylolites (Figure 6.5 c,d). In addition, non-sutured wispy parallel and irregular seams (‘horse tails’) to small and large amplitude stylolites can be found showing the importance of pressure-dissolution processes during burial diagenesis of Palmarito strata. It is noteworthy to report that there is porosity developed along the stylolites, specifically in the form of irregular open pores along high amplitude seams. In addition, residues of bitumen can be recognized partly filling these

spaces. Pressure-dissolution processes have a significant impact on carbonate reservoirs, in providing pathways for fluid migration. Stylolites in Palmarito strata seem to have acted as pathways for hydrocarbon migration.

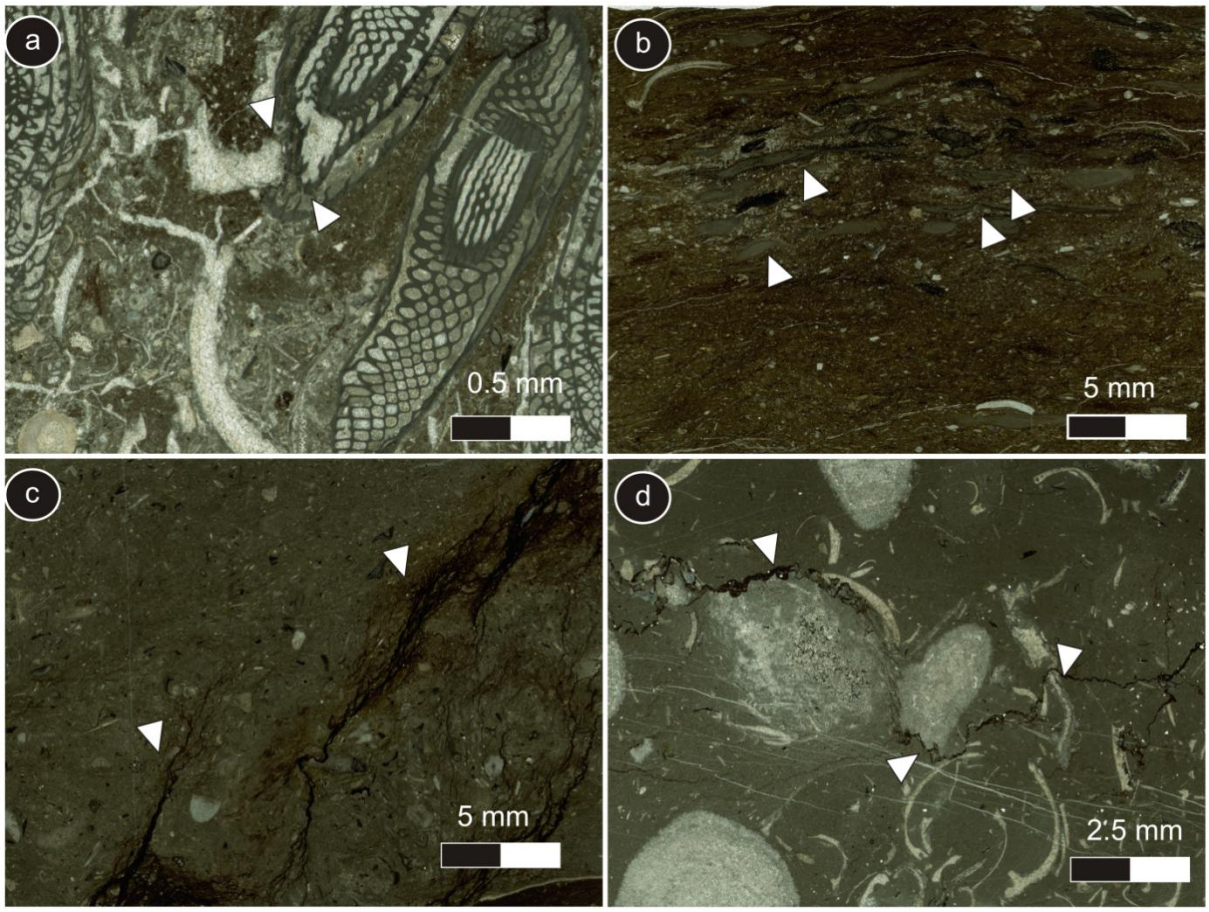

Figure 6.5 a) Broken *Parafusulina* result from mechanical compaction. Sample 80-a Palmar River section b) Highly deformed fusulinids, the product of mechanical compaction. Sample 151 Quebrada de Portachuelo 1 section. c) Non-sutured wispy parallel and irregular seams ('horse tails') (arrows). Sample 109 Palmar River section. d) Irregular anastomosing microstylolites (arrows). Sample 129-G Palmar River section.

Autogenic *pyrite* crystals have been recognized in Palmarito mudstone and wackestone with a framboidal habit. It occurs in the residual clays of the stylolites. Pyrite is also a common replacement of bioclasts such as bryozoans, fusulinids and brachiopods in Palmarito strata. The origin of this authigenic cement is related to reducing conditions and presence of organic matter and associated presence of bacterial activity (Flügel, 2004) (Figure 6.6 a, b).

Silicification is a common feature in the Palmarito facies that normally appearing as a replacement of crinoid and brachiopod bioclasts, less commonly green algae *Gymnocodiacea*. The silicification process has been described by Maliva and Siever (1988) and Mu and Riding (1988). In addition, silica cements occur in the internal void of brachiopods. The typical silica fabrics found in Palmarito strata are amorphous quartz (opal), drusy megaquartz, microquartz and chalcedony (fibrous) (Flügel, 2004) (Figure 6.6 c, d). The degree of silicification varies throughout the succession; in some of the facies, such as crinoidal bioclastic microfacies, the process is selective, whereas in other facies it can be pervasive, replacing the entire bed (e.g. spiculitic wackestones).

The timing of silica cementation seems to have been during late diagenesis, since original calcite bioclast have been replaced as well as secondary cements such as drusy calcite. Additionally, silica cement appears as a filling of the centre of the voids nucleating upon the early calcite and dolomite cements; therefore, this suggests that the silica cements were the last to precipitate in this sequence. However, the silica nodules could have had an early origin but it is difficult to be certain. The source of the silica is commonly ascribed to the dissolution of sponge spicules which are quite abundant in the deep subtidal facies of the Palmarito.

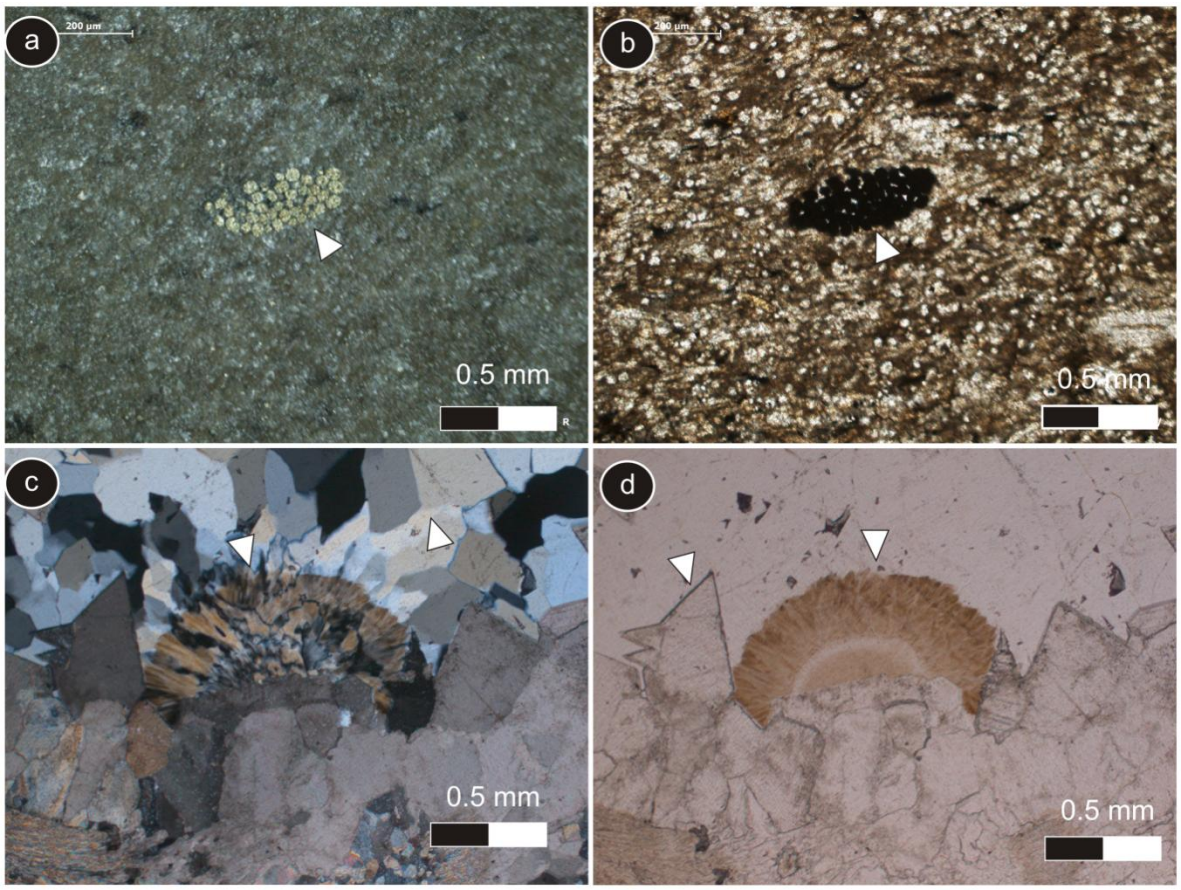

Figure 6.6 a) Framboidal pyrite (arrows) reflected light showing the golden framboidal habit. Sample 53 Palmar River. b) Framboidal pyrite PPL. Sample 53 Palmar River. c) Chalcedony and drusy megaquartz XPL(arrows). Sample 166 Quebrada de Portachuelo 2 section. d) Chalcedony and drusy megaquartz PPL (arrows). Sample 129-G Palmar River section.

Finally, a few samples from north-eastern Venezuelan Andes show evidence of low-grade metamorphism with a phylitic aspect for the lime-mud facies and highly deformed fusulinids, as well as interlocked calcite cements. This process is perhaps associated with regional tectonic events that the Venezuelan Andes suffered from the Late Palaeozoic to Recent.

6.3.4 Dolomitization

The fabric of the dolomite is equigranular and some crystals are saddle dolomite (Figure 6.7). The dolomites are mostly massive with little intercrystalline porosity, and little or no preservation of the original textures. The crystals show subhedral and anhedral shapes

ranging from 50-200 microns in size. The typical fabric is a xenotopic mosaic of anhedral crystals. A less common type of dolomite is a dolomitized bioclastic facies with fusulinids or crinoids. The dolomite crystals show a zoned character that can be seen in cathodoluminescence with several well-defined dull, luminescent and non-luminescent growth bands (Figure 6.7).

Pervasive dolomitization may have occurred in the shallow subsurface during the early stages of burial. It may have been connected to sea-level fluctuations and seawater circulation within the sediment. Continued dolomite precipitation during deep burial probably accounts for the formation of the saddle dolomite (Figure 6.7). This process enhances the intercrystalline porosity which is impregnated with residual bitumen; however, it does not contribute significantly to increasing the potential of the Palmarito as a reservoir rock.

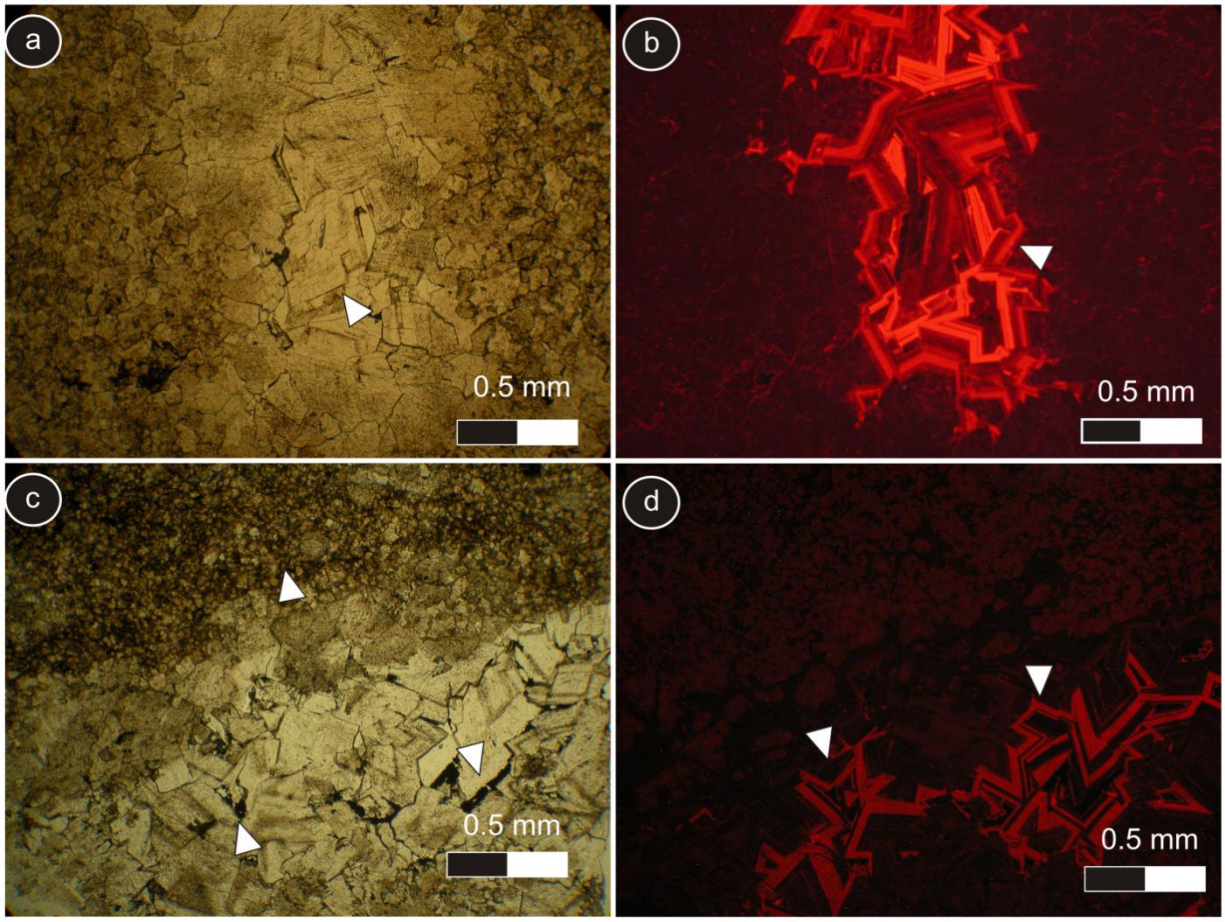

Figure 6.7 a) Saddle dolomite filling a void (arrows) PPL. Sample 165 Quebrada de Portachuelo 2 section. b)) Saddle dolomite filling a void (arrows) CL. Sample 165 Quebrada de Portachuelo 2 section. c) Saddle

dolomite filling a void and remnant bitumen filling porosity (arrows), also dolomitic microspar PPL(arrows). Sample 165 Quebrada de Portachuelo 2 section. d) Saddle dolomite filling a void (arrows) CL Sample 165 Quebrada de Portachuelo 2 section.

6.4 Geochemistry of the Palmarito Formation

6.4.1 Trace elements

Trace elements have been a useful tool for the interpretation of diagenetic modifications to carbonates. Variations of iron, manganese, magnesium and strontium contents of the acid–soluble fraction have been used to determine mineralogical and compositional changes in comparison with modern and other ancient carbonates. However, through time the original composition of sea water has changed to an extent and therefore the composition of diagenetic fluids are likely to have been affected as well. For this reason, a comparison with the composition of modern sea water has been questioned (Gröcke et al., 2001).

Different authors have suggested different ranges of values above which the shell or carbonate material is considered to have been affected by diagenesis; this has mainly been by way of comparison with modern carbonates. Brand (2004) and Denison et al. (1994) agreed that carbonate material has been little altered during diagenesis if it contains less than 300 ppm Mn and 3000 ppm Fe. However, Korte et al. (2005) considered concentrations no greater than 250 ppm Mn and between 300 to 3400 ppm strontium as acceptable and Popp et al. (1986) supported this.

Concentrations of iron (Fe) and manganese (Mn) of modern marine carbonates are very low, in the range of a few tens of ppm (Tucker, 1986). These values are a reflection of the very low content of these elements in sea water, largely because seawater is oxygenated and Fe and Mn are not in solution in such a fluid. However, in diagenetic fluids principally in shallow to deep burial environments these elements can be present in higher concentrations since the waters are normally suboxic to anoxic (Tucker, 1983; 1986). In Palmarito strata the

values of Fe are higher than modern marine carbonates with values of 7940 ppm on average for the whole rock marine facies with a maximum of 36,496 ppm and a minimum of 915 ppm. For meteoric (calcrete) facies the values of Fe are high too with figures up to 26,530 ppm and a minimum of 8150 ppm with a mean of 17,340 ppm. However, the marine cements, for instance the radiaxial fibrous cement, have a low value of 147 ppm that is quite different from the drusy burial cements with an average of 2363 ppm (minimum of 271 ppm and maximum of 3927 ppm). The dolomite has a quite high value of 7759 ppm. The concentrations of Mn are also slightly higher that the values proposed for diagenetic alteration by Popp et al. (1986), Denison et al. (1994), Brand (2004) and Korte et al. (2005) with values for whole-rock marine facies of 201 ppm average, which match with the modern sea-water composition; however, the maximum value reaches 877 ppm, which is way above the range for modern carbonates. The calcretes and cements in the calcrete present very high values of manganese up to 12,692 ppm with an average of 7000 ppm. This is very high for meteoric diagenetic precipitates and suggests Fe and Mn derived from clay minerals during shallow burial For the marine cements the value is very low at 22 ppm; this contrasts with the burial cements at 189 ppm on average, with a maximum of 344 ppm and minimum of 74 ppm. Finally, the figures for dolomite cement are higher than the average with 802 ppm of Mn. The cross plot of Fe and Mn show a trend of high variability in Fe values in contrast to the Mn that is present in quite a narrow range. One exception is the cement in sample 14 that displays of 12,692 ppm in Mn and 26,530 ppm in Fe; the calcrete also has high values of Mn. In general, the Fe-Mn values do show very little relation between each other and R^2= 0.15.

Jenking et al. (2002) suggested that Fe and Mn can come from associated clay minerals or organic matter. These elements can be released during burial and incorporated into the calcite lattice in reducing environments with negative Eh (Tucker and Wright, 1990). In Palmarito strata the concentration of Fe and Mn can be generally associated with clay

minerals in different stages of the burial history due to the facies comprising a high content of clay material.

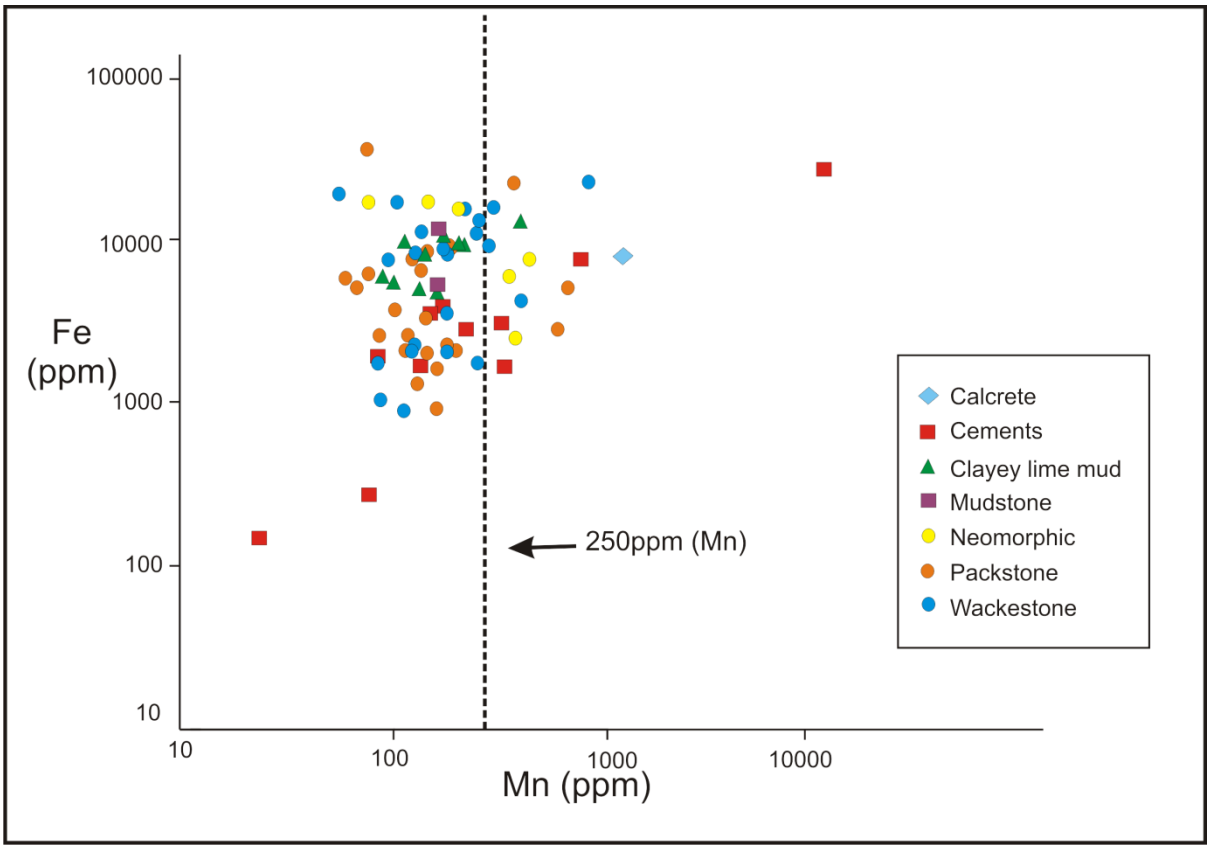

Figure 6.8 Cross-plot of Fe against Mn.

Denison et al. (1994), Bruckschen et al. (1999), Brand (2004) and Korte et al. (2005) suggested that well-preserved brachiopods would have values of Mn between 200 and 300 ppm and these would be acceptable for investigation of original isotopic signatures, having suffered little diagenetic alteration. Although, it would not be pretended that a whole-rock analysis, which would include a combination of aragonite, low- and high- Mg calcite from matrix, grains and cements, would be comparable with low-Mg calcite of brachiopods, the concept is useful and supports the discussion in the Chapter 4, especially if a cut-off value of 300 ppm is used. Based on this concept, the majority of the samples (85%) of whole rock display values below 300 ppm suggesting that severe burial diagenetic alteration has not taken place.

The strontium (Sr) is mainly provided to the ocean by hydrothermal systems and rivers (Jenking et al., 2002) and is incorporated into carbonate minerals. In modern carbonate sediments the Sr content depends of the mineralogy; aragonite usually has a high concentration of Sr (10,000 ppm) compared with calcite (high-Mg calcite 1000-1500 ppm) (Tucker, 1986; Moore, 1989; Tucker and Wright, 1990). However, during diagenesis the concentration normally decreases to reach equilibrium of less than 100 ppm in burial environments. There usually remains a 'memory' of the original high Sr in calcitized aragonite grains however. In Palmarito strata whole-rock values have a large range between 1666 ppm and 23 ppm, with an average of 667 ppm. These values are similar to those of Popp et al. (1986) and Korte et al. (2005), between 300 ppm and 3000 ppm, for well-preserved brachiopods. However, 33% of the Palmarito samples have Sr below 300ppm, suggesting a loss of strontium during burial diagenesis. In addition, the drusy cements have a range of 245 ppm to 1388ppm; this is quite high for sparry calcite cements. The fibrous calcites display high values as expected for this kind of marine cement.

Plotting Fe+Mn against Sr provided a useful diagram to interpret the trend of Sr evolution (Tucker, 1986). A positive correlation suggest an addition of Sr during diagenesis, in contrast, a negative correlation implies that Sr was being lost during burial. The Palmarito samples show a general negative correlation that confirms the general decrease of Sr with time and burial. However, the values show a high dispersion in the diagram which suggests a variable degree of diagenetic alteration and Sr loss and/or Fe/Mn availability.

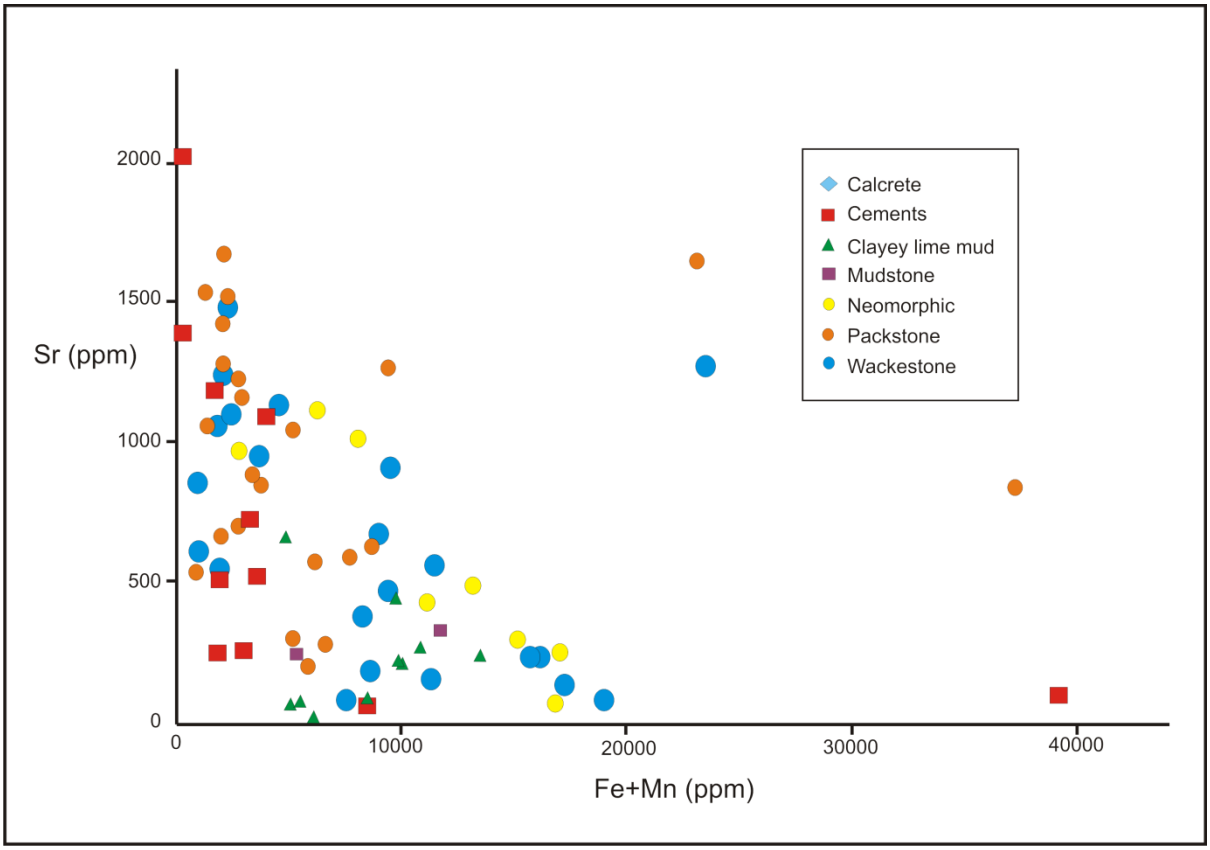

Figure 6.9 Cross-plot of Sr against Fe+Mn.

Ancient limestones were formed originally of aragonite, high-Mg calcite and low-Mg calcite. The metastable minerals such as aragonite, high-Mg calcite normally are replaced by more stable low-Mg calcite during diagenesis. This process involving aragonite transforming to calcite is called calcitization (Scoffin, 1987; Tucker and Wright, 1990; Tucker, 1986). The diagram Sr against Mg illustrates the distribution of the Palmarito values and areas of stability of ancient limestone, marine aragonite and marine high-Mg calcite. The plot presents values of whole rock which match with the ancient limestone values proposed by Tucker (1986). In addition just a few values are located closer than the Mg-calcite area but with high Sr; these would suggest a possible aragonitic origin after diagenesis. High contents of Mg are expected in dolomite, which is present as a cement in some cases. In general the reduction of Mg and Sr during diagenesis is normally expected.

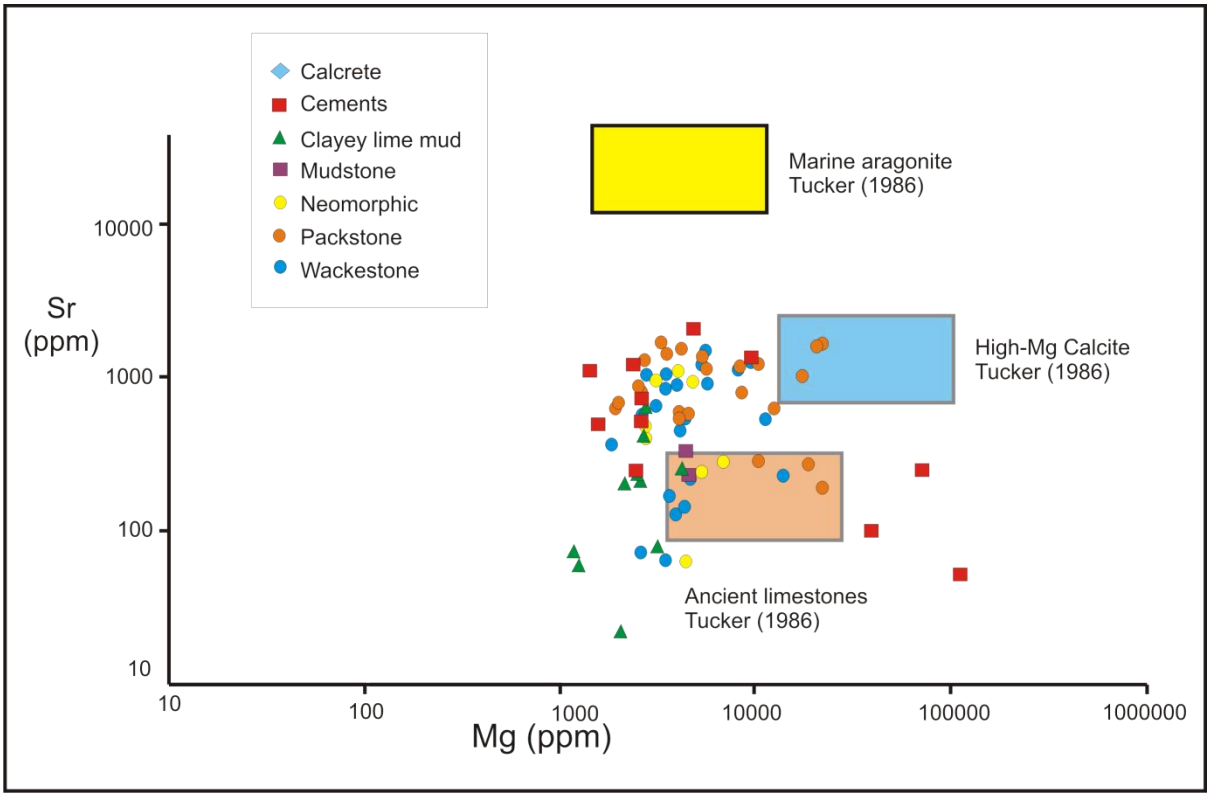

Figure 6.10 Cross-plot of Sr against Mg.

6.4.2 Carbon and oxygen isotopes

The oxygen and carbon stable isotopes were discussed in detail in Chapter 4 in term of stratigraphic trends. In this chapter the isotopic variation will be considered in terms of diagenetic evolution. Modern carbonates have carbon and oxygen stable isotope values in the range between 0‰ and +4‰ in carbon and -2‰ and +1‰ in oxygen; the average for ancient limestones is normally between -2‰ and +2‰ $\delta^{13}C$ and -10‰ and -2‰ for $\delta^{18}O$ (Tucker, 1986). Brand (2004), Grossman et al. (2008) and Brand et al. (2009) and Buggisch et al. (2011) presented carbon and oxygen data from brachiopods and whole rock from USA, Russia and China, where they showed values of $\delta^{18}O$ between -13‰ and +2‰, but the whole rock showed lower values of $\delta^{18}O$ between -13‰ and -5‰ than the well-preserved brachiopods that had figures between -6‰ and +2‰. In carbon isotope the values for well preserved brachiopods vary between -4‰ to +7‰ $\delta^{13}C$ and for the whole-rock 0 and +6‰ $\delta^{13}C$ for whole-rock data from China. Carbon isotopes are more resistant to diagenetic

alteration; in contrast, oxygen shows a susceptibility to diagenetic alteration due to its association with the temperature of precipitation. These data imply that the well-preserved brachiopods have the least negative values as the original marine fibrous calcite was precipitated in low temperature, and more negative figures indicate higher temperature of crystallization that may have occurred during burial diagenesis processes. As it has been argued above, whole rock includes a combination of aragonite, low and high Mg calcite from matrix, grains and cements, and this can be affected by diagenesis; burial cements either filling voids or replacing original skeletal material will give rise to an isotopic signal with more negative oxygen values.

For Palmarito strata, the values of $\delta^{13}C$ of -9‰ to +5.3‰ and of $\delta^{18}O$ -11.8‰ to -2.1‰ partly match the compilation of data from well-preserved brachiopods from the Late Palaeozoic presented by Grossman et al. (2008). These suggest that intense burial diagenetic alteration has not occurred (Figure 6.11). However, there are some whole rock samples that present more negative values of oxygen that could likely imply early burial diagenetic alteration, by comparing with the data of whole rock presented by Buggisch et al. (2011) and partly with the range of ancient limestones proposed by Tucker (1986).

The facies described petrographically as calcrete and clayey lime mudstone and associated with tidal-flat facies display negative $\delta^{13}C$ and quite negative $\delta^{18}O$; these suggest fresh water and decomposition of organic matter affecting these isotopic signals. Also early burial diagenesis could be responsible for very negative oxygen values in some samples. The cements, apart of the one associated with calcrete, have marine signals with a trend from less negative in oxygen ~ -4‰ for radiaxial fibrous cements to more negative to -9‰ for the drusy early burial cements. In addition, the carbon isotope values for the cements decrease from +5‰ to +2‰. This would suggest the typical diagenetic trend from marine diagenesis to early burial and possibly later burial too. In addition, $\delta^{13}C$ values of dolomites are quite

high at +5‰ to +4‰ and for $\delta^{18}O$ the values are not too depleted from -6‰ to -5‰. These are quite typical isotopic signals for dolomites presented by Tucker (1983)

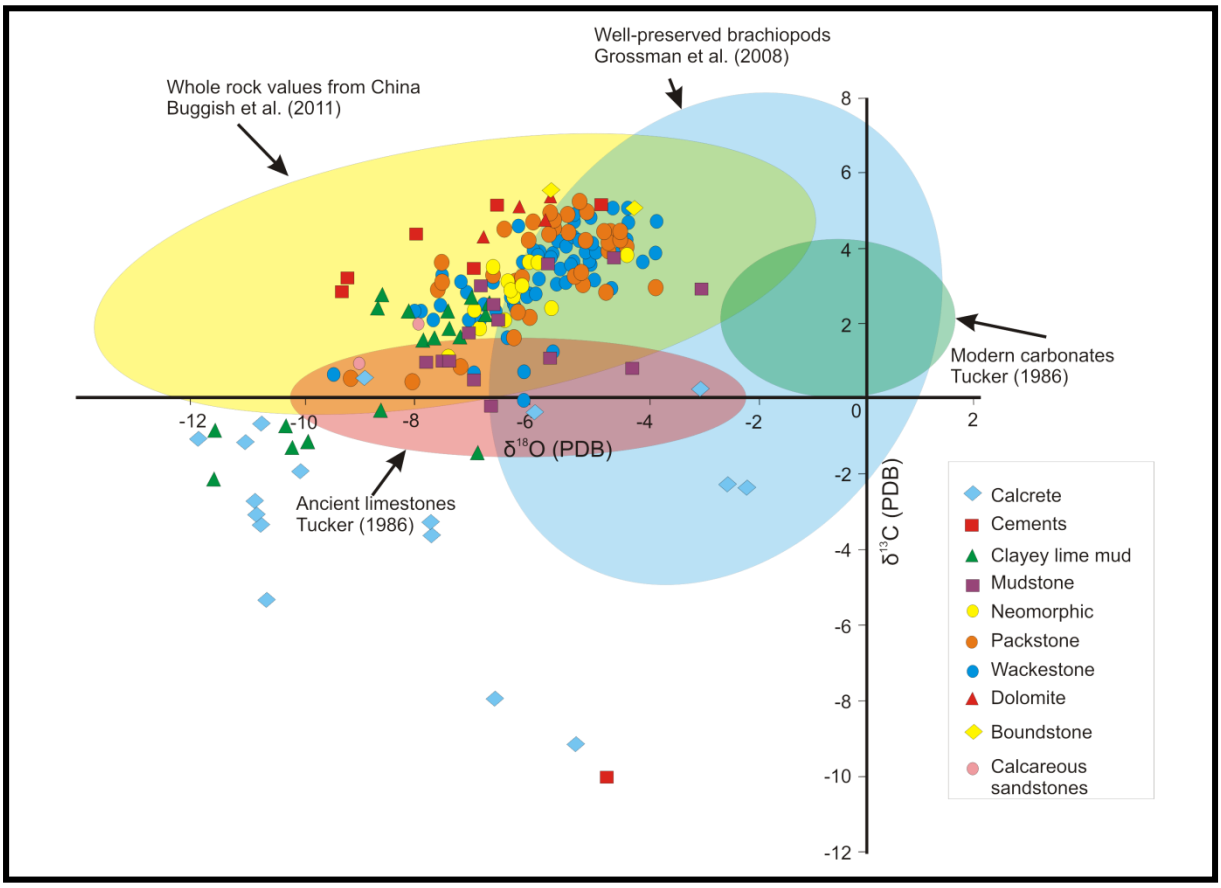

Figure 6.11 Cross-plot of stable isotopes $\delta^{13}C$ against $\delta^{18}O$. The areas in colour show the distribution of data from whole-rock values of limestones from China (Buggisch et al., 2011), well-preserved brachiopods from USA, Russia and China (Grossman et al., 2008), and values of ancient limestones and marine carbonates (Tucker, 1986).

6.5 Diagenetic interpretations

Palmarito strata have been affected by different processes during their deposition and burial which has led to a range of petrographic features and geochemical signals. The results obtained from petrography, cathodoluminescence, trace elements and stable isotopes support the evolution of Palmarito strata from deposition on a carbonate ramp to deep burial. (Figure 6.12)

The early diagenesis in the marine facies is not extensive, due to the fine-grained nature of the carbonates and relative paucity of cements in the Palmarito strata. Evidence of marine cements includes radiaxial fibrous and bladed calcite filling voids or attached to

brachiopod shells. These fibrous cements have low contents of Fe and Mn, and high Sr; these signatures are consistent with precipitation in the marine phreatic environment (Kendall, 1985). In addition, neomorphic processes associated very early marine diagenesis are supported by geochemical data with moderate concentrations of Mn and Fe, and positive values of $\delta^{13}C$ between +1‰ to +3‰ and low negative $\delta^{18}O$ between -7‰ to -4‰. Early cementation is implicated, probably in the marine phreatic zone not far from the sea floor. A similar model was put forward for the Eucla Platform in South Australia described by James and Bone (1991).

The calcretes provide petrographic evidence of exposure that includes calcite crystal aggregates that could be ascribed to *Microcodium* as well as complex irregular cracks, and cemented cracks, abundant inclusions of detrital siliciclastic material (silt and sand), and sign of neomorphism. Additionally, the isotopic signal displays negative values of $\delta^{13}C$ that suggest fresh water passing through the soil, carrying the light ^{12}C from decomposition of organic matter, which was then incorporated into the calcite lattice. However, very negative values of $\delta^{18}O$ and high concentration of Fe and Mn is unclear, but the most likely explanation is that this facies may have been affected by late diagenetic process in burial environment and incorporate the Mn and Fe and also the light ^{16}O in reducing burial zone.

The burial diagenesis has effects on Palmarito strata that are evidenced by burial cements such as drusy and equant calcite cements as well as poikilotopic and peloidal. This cements show increasing of the Mn and Fe also decreasing Sr in their composition typical of burial cognate pore waters (Tucker and Wright, 1990), also much negative values of $\delta^{18}O$. The compaction is very important in the Palmarito diagenesis perhaps due to the poor early cementation in the strata mechanical and chemical evidences of compaction are present as is described above deforming bioclast and dissolving grains, matrix and cements as a result of this compaction the porosity was severe reduced. Others cements in the late stages of

diagenesis that includes silica precipitation and pyrite that imply changes of pore water chemistry during the burial period in reducing environment.

Dolomitization is present in Palmarito strata that may have occurred in the shallow subsurface during the early stages of burial. It may have been connected to sea-level fluctuations and phreatic mixed zone. In addition, dolomite precipitation during deep burial can have occurred due to evidence of the saddle dolomite can be found in few horizons. Finally the saddle dolomite is present filling fracture with rusty appearance that suggest that have been replace for calcite with iron oxide inclusions probably during the exhumation and cropping out. Saddle dolomite is prone to alteration for meteoric waters during telogenesis, this process probably have occurred during the uplift of Venezuelan Andes.

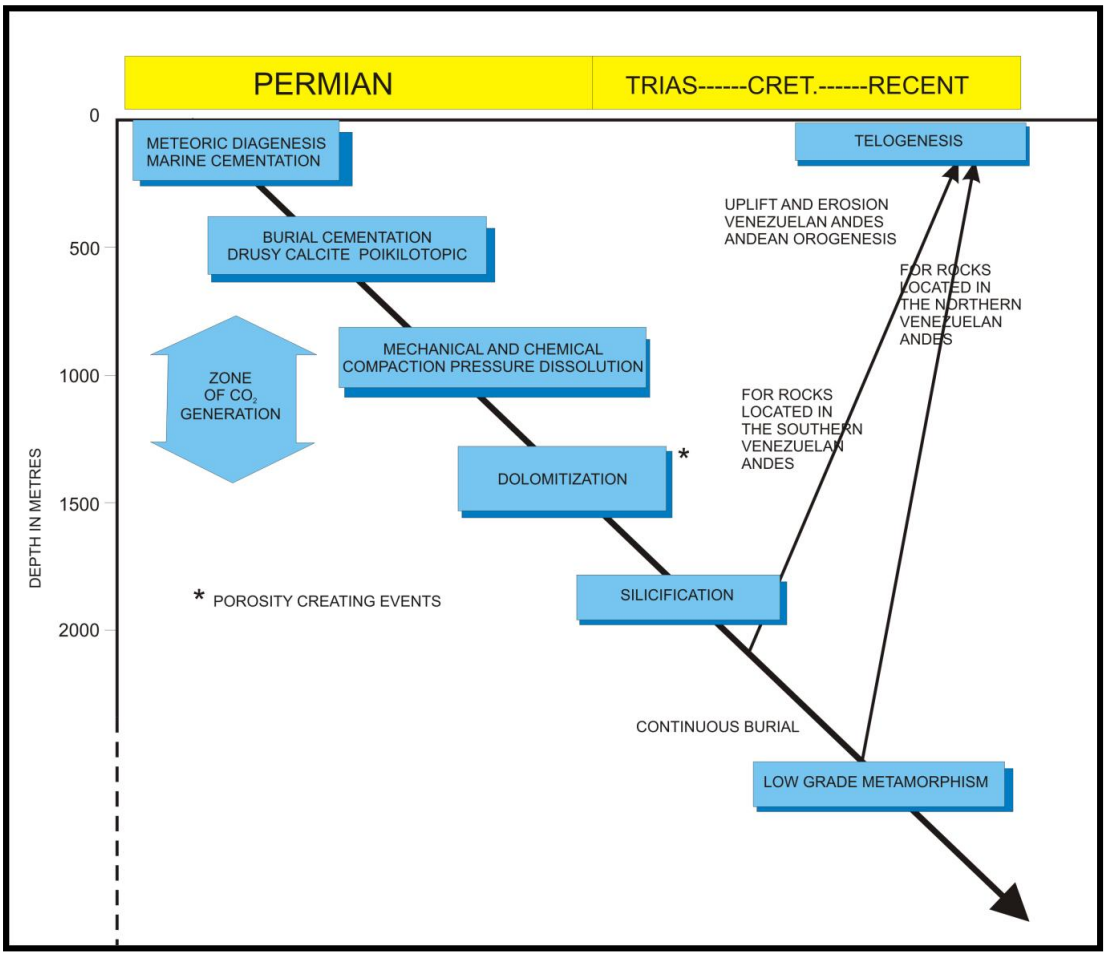

Figure 6.12 Schematic burial diagram of Palmarito Formation adapting from Clark (1980).

6.6 Fractures in carbonates

Natural fractures are features of many carbonate reservoirs and are significant in creating secondary porosity and permeability which enhance their potential. In some cases it appears there is a control on fracture development from the facies and bedding of a succession, but this has only been explored in detail in a few formations. An understanding of the development of fractures in sedimentary formations is important in considering their potential for hydrocarbon reservoirs or aquifers (Di Naccio, 2005). Mostly fractures have been examined from a structural point of view but in most cases there is a strong control from the sediments themselves in terms of their mineralogy, texture, facies, internal heterogeneity and sedimentary structures. An analysis of fractures more from a sedimentological point of view will help in predicting the density and continuity of fractures. In terms of comparison with the Palmarito Formation, some outcrops of the Permian (Zechstein) carbonates in Northeast England have been analyzed for their fracture development.

The Zechstein carbonates of Northeast England are the onshore equivalents of reservoir rocks in the North Sea and Poland especially, and they exhibit a wide range of facies from reefal boundstones, through shelf oolites to slope lime mudstones and turbidite packstones, arranged in various stratal geometries and bed thicknesses (Tucker 1991). The Zechstein was also subjected to regional stress patterns as well as localized major faults. Dissolution of interbedded evaporites has also given rise to extensive fracturing, as well as collapse breccias.

Using the methodology proposed by Eyssautier-Chuine et al. (2002) fractures in the Zechstein carbonates were measured in terms of density (fracture/metre) and spacing (average of distance between the fractures), and the bed thickness was measured and the facies noted. As a result, the fracture density within the Roker and Raisby dolomites shows values between 0.7 and 18.2 (fractures/metre) with higher densities typical of finer-grained

dolomite rather than dedolomite or oolitic facies (Figure 6.13 and 6.14). The bed thickness varies between 1 cm and 3 m and there is a clear increase of fracture density in the thinner-bedded facies, which are typical of outer ramp and slope carbonates. Most fractures are perpendicular or subvertical to bedding planes, with some containing fracture-filling dolomite or calcite cements.

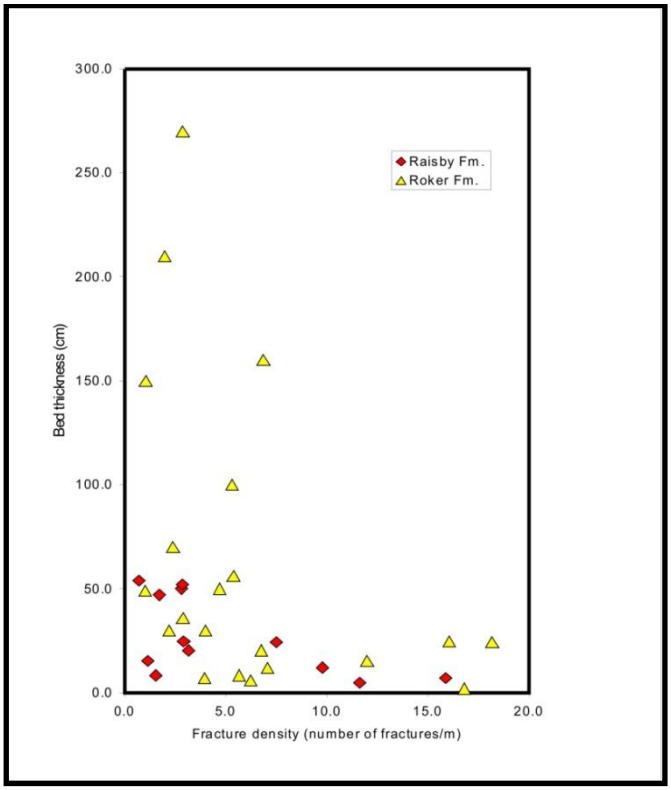

Figure 6.13. Diagram showing relationship between bed thickness and fracture density in Raisby and Roker formations, Zechstein, North-East England.

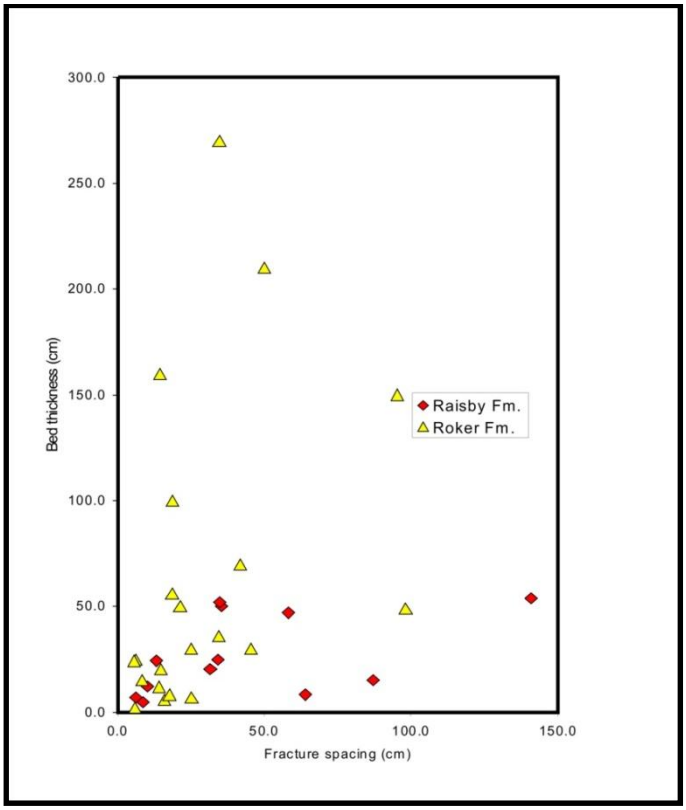

Figure 6.14 Diagram showing relationship between bed thickness and fracture spacing in Raisby and Roker formations. Zechstein, North-East England.

In Palmarito strata, some representative beds were analyzed to provide a rough idea as to how the Palmarito facies responded to fracturing. Although the tectonics in the Venezuelan Andes is quite complex, the outcrops are barely deformed, therefore, the rheology of the facies does have a significant control. The thickness of the sampled beds varies between 20 to 400 cm and the fracture density between 0.3 to 10 (frac/m); the fracture spacing is between 27 to 395 cm (Table 6.1). It can be seen that in general the thinner beds have higher values of fracture density than the thicker beds, with one exception, a bed which is formed of fusulinid packstone. This bed shows a high fracture density, in spite of it being a relatively thick bed (Figures 6.15, 6.16). However, there is not a strong relationship between the fracture density and the facies in this case; packstone and wackestone seem to be more affected by fracturing than mudstones in the Palmarito strata; this is probably due to the ductility on the clay-rich

facies also. It seems that thickness was a slightly more significant control than the clay content.

Table 6.1 Fracture data from Palmarito Fm.

Sec.	Palmar River						
Bed	**Average spacing**	**Density (frac/m)**	**Thickness (cm)**	**n (fractures)**	**Lithology**	**Microfacies**	**m above base**
Bed 1	34,7	2,9	55	10	Calcareous Sst.	Carbonate sandstone	97 m
Bed 2	46,9	2,1	20	10	Calcareous Sst.	Carbonate sandstone	99 m
Bed 3	62,6	1,6	300	10	Mudstone	Clayey lime mudstone	103m
Bed 4	395,0	0,3	30	2	Wackestone	Neomorphic wackestone	157 m
Bed 5	14,1	7,1	20	10	Wackestone	Neomorphic wackestone	160 m
Bed 6	10,0	10,0	270	10	Packstone	Fusulinid packstone	188 m
Bed 7	28,2	3,5	75	10	Packstone	Bioclast Crin-Bry packstone	266 m
Bed 8	31,1	3,2	75	10	Packstone	Bioclast Crin-Bry packstone	267 m
Bed 9	25,6	3,9	100	10	Packstone	Bioclast Crin-Bry packstone	268 m
Bed 10	22,2	4,5	60	10	Packstone	Calcareous algal packstone	269 m
Sec.	**Santa Cruz de Palmarito**						
Bed	**Average spacing**	**Density (frac/m)**	**Thickness (cm)**	**n (fractures)**	**Lithology**	**Microfacies**	**m above base**
Bed 11	106,3	0,9	150	10	Packstone	Calcareous algal packstone	35 m
Bed 12	68,7	1,5	200	6	Packstone	Bioclast Crin-Bry packstone	37 m
Bed 13	62,6	1,6	200	7	Packstone	Fusulinid packstone	41.5 m
Bed 14	20,7	4,8	60	9	Mudstone	Clayey lime mudstone	43 m
Bed 15	58,8	1,7	100	6	Packstone	Calcareous algal packstone	43.5 m
Bed 16	34,7	2,9	400	6	Mudstone	Clayey lime mudstone	47.5 m
Bed 17	23,8	4,2	90	9	Wackestone	Spiculitic wackestone	69.5 m
Bed 18	30,4	3,3	40	9	Wackestone	Spiculitic wackestone	71 m

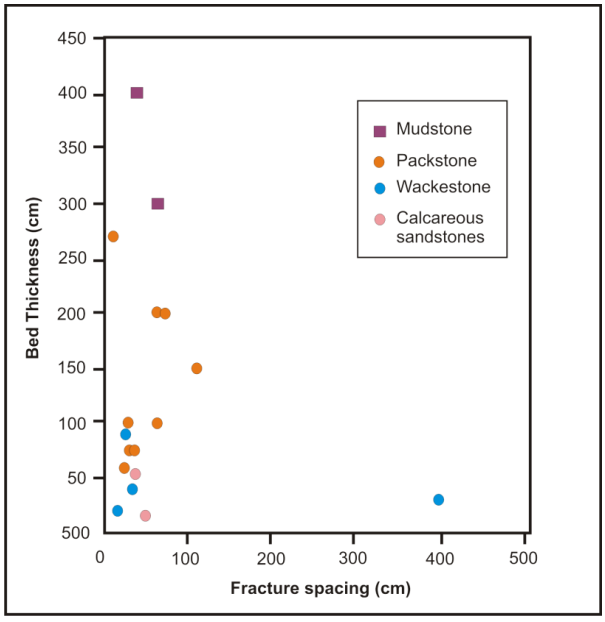

Figure 6.15. Diagram showing relationship between bed thickness and fracture spacing in the Palmarito Formation, Venezuelan Andes.

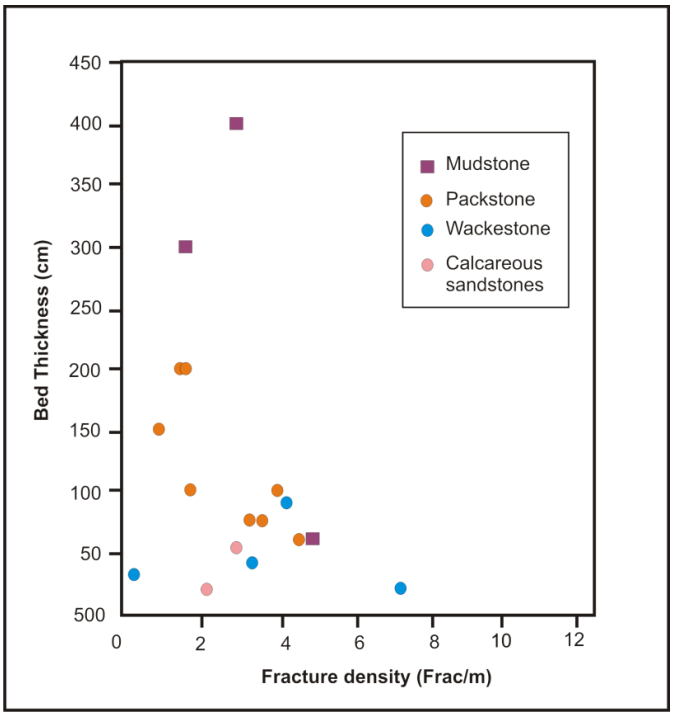

Figure 6.16 Diagram showing relationship between bed thickness and fracture density in Palmarito Formation Venezuelan Andes.

In general, the finer-grained facies are more prone to develop fractures than the coarser ones, and the content of clay affects the rheology of the rock in terms of response to deformation. In the case of the Zechstein, the major control is the bed thicknesses, and this is a similar situation with the Palmarito strata. It would suggest that thinner beds and fine-grained clay-free lime mudstones would be the facies most prone to fracturing; therefore, they would have the higher potential as a natural fracture reservoir.

6.7 Petroleum system in Palmarito strata

In the last decade, it has been suggested that Palaeozoic deposits could be future oil and gas reserves in Venezuela. For this reason, this project will be one of the first to assess the facies distribution, reservoir and source rock potential and vertical stratigraphic evolution, with a view to developing models for basin analysis. Furthermore, the correlation of these rocks with the North American Permian basins and others basins is crucial to understand the

possible petroleum system and their context. In addition, the understanding of the petroleum system elements is a key to provide an approach of the potential of these rocks as petroleum reservoirs.

6.7.1 Seals and traps

The Palmarito Formation contains a high volume of fine-grained clay-rich sediment with low permeability, which would be less prone to fracturing. This could act as an impermeable horizon, dependent on the hydrocarbon migration pattern and the potential reservoir units. The latter could be within Palmarito Formation itself or in the fluvial sandstones of the Sabaneta Formation that are located beneath. The heterogeneous lithologies of the Palmarito strata could provide an important range of permeabilities and porosities that are likely to create a migration barrier within the formation and generate stratigraphic traps.

Regional tectonic structures (anticlines and synclines) were described by Audemard and Serrano (2001). These have the potential to form structural traps (Figure 6.16) in the Barinas-Apure Basin. This basin extends to the Los Llanos Basin in Colombia so that this could increase the interest in the Palmarito as an exploration play in the near future.

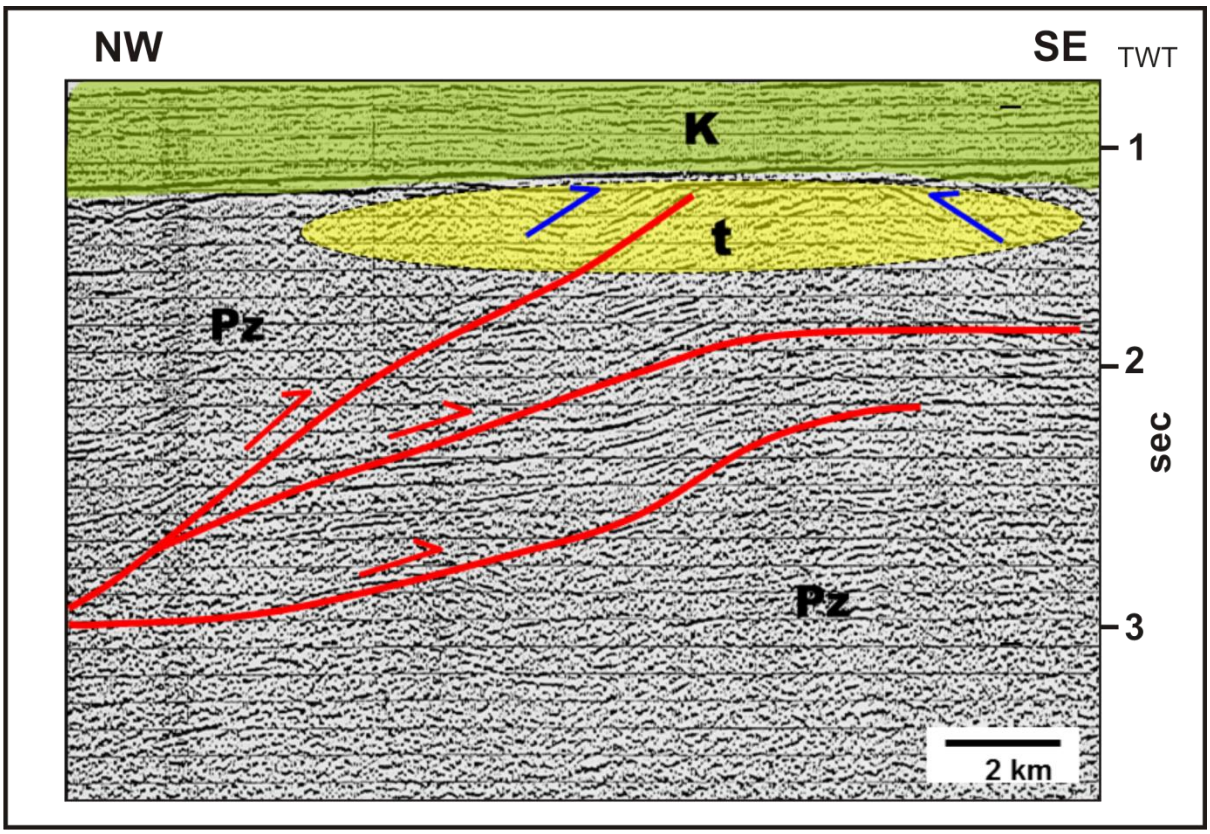

Figure 6.17. Seismic line located in the Barinas-Apure Basin showing potential structural traps (Audemard and Serrano, 2001). Pz: Palaeozic rocks, t: traps, K: Cretaceous.

6.7.2 Source rock

Lugo (2008) presented values of total organic carbon (TOC) from the Palmarito Formation between 0.28 to 1.48 % and bitumen concentrations between 68 ppm and 223 ppm. In spite of the values being acceptable for a potential source rock, this was discounted by Lugo (2008) because of the high values of T_{max} (over mature) in the rocks from Rock-Eval analysis which gave a range between 518 ºC to 353 ºC with an average of 490 ºC. On the other hand, the sampling methods that Lugo (2008) applied were restricted to one section, only in the lower-middle part of the formation and this could have biased the results. For this reason, this topic needs further investigation.

6.7.3 Reservoir rocks

The lack of early cementation in the Palmarito Formation has meant that the sediments have been highly compacted and that most of the primary porosity has been lost.

However, a secondary porosity has been developed as a result of the dolomitization in the upper part of the formation, giving an intercrystalline porosity, and there is also the development of fractures. The latter offers the most likely option for potential reservoirs. In addition, there are many examples of naturally fractured reservoirs around the world in Permian carbonates, including the Yates and Seven Rivers formations in the Delaware Basin and the Zechstein in the North Sea. The discussion above suggests that the Palmarito Formation could have a potential as naturally fractured reservoir in the middle-upper part of the succession and also in the upper part where thick dolomites are located. Additionally, bitumen has been identified in the stylolites and dolomite porosity, providing evidence of hydrocarbon migration through these rocks. If the volumes of these facies throughout the basin could be determined, it would be possible to calculate the possible potential reservoir.

6.8 Summary and conclusions

Palmarito strata do contain evidence of early marine and meteoric diagenesis through to burial diagenesis with few stages of cementation. However, mechanical and chemical compaction are the most significant processes that have affected the formation, and as a result of these, most of the primary porosity has been lost. Silicification and dolomitization has also affected Palmarito strata, replacing original or secondary calcite in later diagenesis. The succession in the central and northeast parts of the Andes have suffered low-grade regional metamorphism, that is probably related to more intense tectonic activity there with higher heat flow or a thermal event and deeper burial. However, in the south-western Venezuelan Andes there was no metamorphism, suggesting lower heat flow associated with minor tectonic activity.

A high density of fractures is more likely to be related to finer-grained facies (lime/dolo- mudstones, than to the coarse ones (grainstones). In addition, the content of clay in a limestone does affect the rheology of the rock in terms of response to deformation,

showing a more ductile response for those facies with a high content of clay. In the case of the Zechstein dolomites, one major control on fracture development appears to be bed thickness; it is likely that a similar effect would be found with Palmarito strata. It would suggest that thinner beds and lime / dolo- mudstones with little clay would be the facies most prone to fracturing. Thus, this facies type would have the higher potential as a natural fractured reservoir.

The elements for a petroleum systems that can be identified in Palmarito strata include potential source rock that according to Lugo (2008) show high values of T_{max} from Rock-Eval analysis and quite low total organic carbon (TOC) figures that suggest an over-mature stage has been reached and that there is not enough organic material to generate hydrocarbons . However, the sampling was restricted to one section, only in the lower-middle part of the formation and this could have biased the results. For this reason, these results are not completely conclusive and it would seem premature to dismiss the Palmarito Formation as a potential source rock. In addition, the high content of finer-grain facies with low permeability give the Palmarito a high potential to act as a seal, as well as possibility to develop stratigraphic traps. Also, structural traps could be found in folds that have been described by Audemard and Serrano (2001) in the Barinas-Apure Basin. Finally, the reservoir potential would have to depend on fractures since the primary porosity has been destroyed by the mechanical and chemical compaction. In addition, the most common Palmarito facies are finer-grained lithologies that typically can develop a significant fracture network. As a result the Palmarito has the potential to be a good reservoir in Palaeozoic prospects in Venezuela.

7 Conclusions and future work

This chapter compiles all the key findings and main interpretations of the research following this investigation into the microfacies, sedimentary environments, palaeogeography, geochemistry as well as diagenesis and petroleum potential of the Palmarito Formation and its relationship with similar successions in equatorial Pangea.

7.1 Key results and interpretations

In *Chapter 2* the regional context of the Palmarito Formation, deposited in the Mucuchachi Basin (MB) was presented. The Palmarito strata extend through Colombia to the west and southwest (Villarroel and Mojica, 1987). To the northwest, the formation can be correlated with marine limestones of the Manaure Formation in the Perija Mountains in the border region between Venezuela and Colombia (Forero, 1967). Farther northwest the Mexican-Guatemalan microterranes (MGT) were moving northwards at this time and limestones and shales were deposited in Guatemala-Belize and México (Vachard and Foucade, 1997; Silva-Pineda et al., 2003; Vachard et al., 2004). Continuing to the north, there could have been sporadic connections with basins in the southwest USA (Delaware, Midlands), as suggested by the biostratigraphic similarities described by Wood et al. (2002). In this chapter evidence from the Palmarito Formation is presented which suggests a new setting for northwest Gondwana in the early through middle Permian. Also, the Mucuchachi Basin (MB) is proposed as a foreland basin within which the marine carbonates of the Palmarito Formation accumulated.

For *Chapter 3* the sedimentary environments of Palmarito strata were reconstructed from facies description and analysis and a homoclinal ramp model was proposed for this tropical area of northern Gondwanaland. This interpretation is supported by the characteristics of the 10 macrofacies and 14 microfacies, recognised from fieldwork and petrographic study. Generally, the succession begins with a unit of heterolithic calcareous

sandstone, mudstone and siltstone with ostracods and plant debris of a tidal-flat environment. This grades upwards to dark-grey calcareous deeper-ramp deposits. Farther up, the succession becomes more shallow-marine with calcareous algal packstone and fusulinid grainstone, that represent inner-ramp deposits, and then crinoidal-bryozoan wackestone of the middle to deep ramp with some buildups. Deeper- ramp facies are interbedded with dolomites and the formation finishes with lime mudstones and evaporites. In the long term the deposition of the Palmarito Formation was largely controlled by climate, sea-level, tectonics and the nature of the carbonate factory.

The results of isotope analyses presented in *Chapter 4* include the $^{87}Sr/^{86}Sr$ ratios and the long-term trend of the carbon and oxygen isotope data which have given an enhanced time-frame of Palmarito strata. Values of $^{87}Sr/^{86}Sr$ ratios from low-Mg calcite brachiopod shells in the central part of the Palmarito Formation have provided useful dates for the strata, placing them within the Kungurian stage at 270.5 to 273.5 M.y. Furthermore, carbon isotope data show a long-term trend towards more positive values. Excursions of $\delta^{13}C$ higher up in the formation show a strong relationship to the inferred glaciation-deglaciation events that have been described by Isbell et al. (2003, 2008) and Fielding et al. (2008) for the early and middle Permian.

Although original oxygen isotope signatures of limestones are prone to diagenetic alteration, the similarities of the results from low-Mg calcite brachiopods (generally resistant to alteration) and whole-rock samples allow the interpretation of the relative trends within the strata. The trends of oxygen were correlated with glacial events, P3 and P4, proposed by Fielding et al. (2008). Also the climatic controls were discussed and as a result of this, it has been concluded that pCO_2 was the most significant factor that controlled not only long-term climate change but also short-term variations. Finally, an open-marine basin was likely established in northern Venezuela at this time since the carbon and oxygen isotope data from

the Venezuelan Permian carbonates exhibit similar trends to those from other successions, such as the Niqing section in China, which was deposited in an open-marine section of the Panthalassa Ocean.

Cyclicity in the Venezuelan Permian carbonate succession was described in the *Chapter 5*. Three major types of metre-scale cycle were recognized, with various subtypes; Type A cycles are mixed clastic-carbonate peritidal cycles. Calcrete or an exposure surface is present at the upper boundaries of these cycles. The cycles are ascribed to tidal-flat progradation, variations in carbonate productivity and clastic input to the depositional area for their origin. Shallow subtidal cycles (Type B) consist entirely of subtidal facies and show shallowing-upward facies arrangements, but without exposure. These cycles are normally thicker than the others and show an alternation between heterozoan and photozoan assemblages, but with little indication of any change in water depth. Therefore, variation in nutrient supply or temperature is most likely, possibly due to upwelling as suggested by Samankassou (2002) for similar-aged cycles in Austria. Nevertheless, long-term fluctuation in continental run-off is another possible control; changes in rain-fall and chemical weathering could lead to variations in nutrient supply to the sea, and changes in trace element contents of the limestones may be reflecting this. Even though geochemical signatures of carbonates are not conclusive evidence one way or the other, the regional setting of the basin does suggest continental run-off as a cause rather than upwelling. Deep subtidal cycles (Type C) mostly show shallowing-upward facies arrangements and are characterized by heterozoan assemblages. The model proposed by James and Bone (1991) and Jones and Desrochers (1992) seems to explain the origin of cycle type C1, with deposition taking place when storm wave base (SWB) was located above the sea floor (highstand of sea-level), and lithification and erosion were acting when the SWB was reworking sediment at the sea-floor (lowstand of sea-level). Probably the same model can be applied to cycle type C2 but instead of

lithification there was just erosion and reworking of the more abundant heterozoan bioclasts. Facies and geochemical signals can be linked to climatic variations which could have been triggered by migration of the Intertropical Convergence Zone (ITCZ), driven by variations in the extent of polar ice.

For the 4^{th}-5^{th} order cycles / parasequences in the Palmarito strata, the combination of Sr-isotope dating, long-term trends in carbon isotope values and the biostratigraphy of Hoover (1981) and Rigby (1984) have permitted the duration of an average cycle to be ascribed to the short eccentricity (~100,000 years) rhythm. In addition, the deduced sedimentation rate is similar to other ancient platform carbonates in the geological record.

In summary, the cycles of the Palmarito Formation were formed through the operation of different controls with autocyclic processes more dominant in the lower part of the succession and allocyclic processes, most likely orbital forcing, more important in the upper part.

The post-sedimentary processes were described in *Chapter 6* including diagenesis, fracture formation and petroleum potential. First, Palmarito strata do contain evidence of early marine and meteoric diagenesis through to burial diagenesis with few stages of cementation. However, mechanical compaction and chemical compaction are the most significant processes that have affected the formation, and as a result of these, most of the primary porosity has been lost. Silicification and dolomitization have also affected Palmarito strata, replacing original or secondary calcite in later diagenesis. The succession in the central and northeastern parts of the Andes have suffered low-grade regional metamorphism, that is probably related to more intense tectonic activity there with higher heat flow or a thermal event; there was probably also deeper burial in this area. However, in the south-western Venezuelan Andes there was no metamorphism, suggesting lower heat flow associated with minor tectonic activity.

In considering the development of fractures , a high density of fractures is more likely to be related to finer-grained facies (lime/dolo- mudstones, than to the coarser lithologies (grainstones). In addition, the content of clay in a limestone does affect the rheology of the rock in terms of response to deformation, showing a more ductile response for those facies with a high content of clay. In the case of the Zechstein dolomites (and others), one major control on fracture development appears to be bed thickness; it is likely that a similar effect would be found with Palmarito strata. It would suggest that thinner beds and lime / dolo-mudstones with little clay would be the facies most prone to fracturing. Thus, this facies type would have the higher potential as a natural fractured reservoir.

The elements for a petroleum system that can be identified in Palmarito strata include potential source rocks that according to Lugo (2008) show high values of T_{max} from Rock-Eval analysis and quite low total organic carbon (TOC) figures. These figures would suggest an over-mature stage had been reached and that there is not enough organic material to generate hydrocarbons . However, Lugo's sampling was restricted to one section, only in the lower-middle part of the formation and this could have biased the results. For this reason, these results are not completely conclusive and it would seem premature to dismiss the Palmarito Formation as a potential source rock. In addition, the high content of finer-grain facies with low permeability gives the Palmarito a high potential to act as a seal, as well as the possibility of developing stratigraphic traps. Also, structural traps could be found in folds that have been described by Audemard and Serrano (2001) in the Barinas-Apure Basin. Finally, the reservoir potential would have to depend on fractures since the primary porosity has been destroyed by the mechanical and chemical compaction. In addition, the most common Palmarito facies are finer-grained lithologies that typically can develop a significant fracture network. As a result the Palmarito has the potential to be a good reservoir among the Palaeozoic prospects in Venezuela.

7.2 Overall implications

The results presented in this thesis should be of broad interest to those studying Permian palaeogeography and palaeoclimate, which are a consequence of the dynamics of the supercontinent of Pangea, which has been a significant topic of research in last decade. In addition, the results provide a new dataset for central Pangea during the Permian which has implications for palaeotectonics, palaeoclimate and palaeoceanography of the basin and its connections with Panthalassa and Tethys oceans. The research presented here should be of wide interest to the scientific community, but, in addition some of this research has implications for the reservoir potential of the Palmarito Formation and its equivalents in the subsurface in the Barinas-Apure Basin in southern Venezuela and the Llanos Basin in Colombia.

Overall the Palmarito strata can be ascribed to the homoclinal ramp model with deposition in the equatorial Pangean basin called the Mucuchachi Basin. The facies analysis of Palmarito strata in this basin provides evidence of a possible sea-way connection between Tethys and Panthalassa Oceans for early-middle Permian time. This necessitates a revision to the existing palaeogeographic maps of Pangea provided by Scotese (1995, 1999); Miall and Blakey (2008) and Blakey (2006). As a consequence of this, the palaeoclimate models based on these maps may need to be improved to take into account the revised palaeogeographic distribution of sea, land and mountain ranges.

Isotope analyses have provided an enhanced time-frame for the succession from $^{87/86}Sr$ data, In addition, the long-term stratigraphic trends in the $\delta^{13}C$ and $\delta^{18}O$ data have permitted interpretations of the climatic and oceanographic controls on the deposition of Permian carbonates.

As a result important implications were deduced, for example, regarding the influence of nutrient supply from the carbon isotope curve. Furthermore, metre-scale cyclicity shows

the behaviour of short-term controls on sedimentation, where autocyclic and allocyclic processes influenced deposition and the vertical stacking of facies. An analysis of the diagenesis of the Palmarito carbonates shows several stages of cementation and alteration, although the strata are mainly fine-grained and coarse cements are rare. Silicification and selective dolomitization have locally occurred, with the latter enhancing the porosity. The porosity in the Palmarito strata is very low, so that any reservoir potential will be reliant on the development of natural fractures. However, the few pores present, and stylolites, are often stained with bitumen, which could reflect the migration of hydrocarbon-rich fluids through these rocks. On the other hand, the potential for source rocks has been discounted by Lugo (2008) due to high values of T_{max} (over mature) in the rocks from Rock-Eval analysis and low total organic carbon (TOC) figures. Nonetheless, the sampling methods that Lugo (2008) applied were restricted to one section, only in the lower-middle part of the formation and this could have biased the results. For this reason, this topic needs further investigation.

7.3 Future Work

In term of Pangean palaeogeography, a palaeomagnetic study could prove very useful and would improve our knowledge of the relative position of Palmarito strata during the Permian. This could provide a useful data set in the search for a resolution of the several models which have been put forward for the amalgamation of the tectonic plates that formed Pangea and its subsequent break-up, as Rakotosolofo et al. (2006) and other authors including Morel and Irving (1981) and Smith et al. (1981) have pointed out. Furthermore, high resolution biostratigraphy is required to improve the vertical resolution in the succession. This could increase the confidence of the correlations that have been proposed in this thesis.

This thesis provides significant evidence of a strong petroleum potential within the Palmarito Formation. However, more detailed organic geochemical studies are required to ascertain its source-rock potential. Nonetheless, it will not be until the acquisition of

subsurface data (seismic and well data) that the real potential can be ascertained for oil and gas in the Permian carbonates in the Barinas-Apure Basin or in the Llanos Basin in Colombia.

References

A

Ahr, W.M., 1998. Carbonate ramps, 1973-1996: a historical review. *In:* Wright, V.P., Burchette, T.P., (eds) *Carbonate Ramps*. Geological Society of London Special Publication. **149**, 7-14.

Arias, A., Morales, C.J., 1999. Mapa Geologico generalizado del Departamento del Cesar. *Ingeominas*. Bogota

Arnold, H. C., 1966. Upper Paleozoic Sabaneta-Palmarito sequence of Mérida Andes, Venezuela. *American Association of Petroleum Geologist Bulletin*, **50**, 2366-2387.

Arthur, M.A., Anderson, T.F., 1983. Stable isotopes of oxygen and carbon and their application to sedimentologic and paleoenvironmental problems: Society of Economic Paleontologists and Mineralogists Short Course 1011–1151.

Audemard, F.A., 2003. Geomorphic and geologic evidence of ongoing uplift and deformation in the Mérida Andes, Venezuela. *Quaternary International* 101-102, 43–65.

Audemard, F.E., Audemard, F.A., 2002. Structure of the Mérida Andes, Venezuela: relations with the South America–Caribbean geodynamic interaction. *Tectonophisics*, **345**, 299-327.

Audemard, F.E., Serrano I.C., 2001. Future petroliferous province of Venezuela. *In*: Downey, N.W., Threet, J.C., Morgan, W.A., (eds) Petroleum Provinces of the Twenty-First Century: *American Association of Petroleum Geologists Memoir*, **74**, 353-372.

Azcuy, C., Beri, Á., Bernardes-de-Oliveira, M. E. C, Carrizo, H. A., di Pasquo, M., Díaz Saravia, P., González, C, Iannuzzi, R., Lemos, V. B., Henrique, G., Melo, J., Pagani, A., Rohn, R., Amenábar, C. R, Sabattini, N., Souza, P. A, Taboada, A. y Vergel, M. M., 2007. *Bioestratigrafía del Paleozoico Superior de América del Sur:*

Primera Etapa de Trabajo hacia una nueva propuesta cronoestratigráfica. Asociación Geológica Argentina, Serie D: Publicación especial, **11,** 09-65. 64.

B

Baby, P., Moretti, I., Guillier, B., Limachi, R., Mendez, E., Oller, J., Specht, M., 1995. Petroleum system of the northern and central Bolivian Sub-Andean zone. Petroleum basins of South America. *American Association of Petroleum Geologists, Memoir*, **62**. 445-445.

Bazard, D.R., Butler, R.F., 1991. Palaeomagnetism of the Chinle and Kayenta Formations, New Mexico and Arizona. *Journal of Geophysical Research*, **96**, 9,847-9,871.

Bebout, D.G., Kerans, C., 1993. Guide to the Permian Reef Geology Trail, McKittrick Canyon, *Guadalupe Mountains National Park, West Texas*. Texas Bureau of Economic Geology, Guidebook **26**, 14-22.

Bellizia, A., Pimentel, N., 1994. Terreno Mérida: Un cinturón alóctono herciniano en la Cordillera de Los Andes de Venezuela. *V Simposio Bolivariano: Exploración Petrolera en las Cuencas Subandinas, Memoria, Sociedad Venezolano de Geólogos*, Puerto la Cruz, Venezuela, 271-290.

Bellizia, A., 1992 Terreno Mérida y Bloque Caparo. Cordillera de Los Andes de Venezuela. *III Congreso Geológico de España*, **4.**, (resumen de actas), 112-116.

Benedetto, G., Odreman, O., 1977. Nuevas evidencias paleontológicas en la Formación La Quinta. Su edad y correlación con las unidades aflorantes en la Sierra de Perijá y Cordillera Oriental de Colombia. *V Congreso Geológico Venezolano Memoria*, 1, 87-106.

Benedetto, J., 1982. Las unidades tectono-estratigráficas paleozoicas del norte de Sudamérica, Apalaches del Sur y noroeste de África: Comparación y Discusión. *Quinto Congreso Latinoamericano de Geología, Argentina. Actas I*, 469-488.

Bissell, H., 1970. Realms of Permian tectonism and sedimentation in western Utah and eastern Nevada. *American Association of Petroleum Geologist Bulletin*, 54, 285-312.

Blakey, R.C., Knepp, R., 1989. Pennsylvanian and Permian Geology of Arizona. In: Reynolds S.J., Jenney, J.P., (eds), *Geological evolution of Arizona Geology*. Arizona Geological Society Digest, **17**, 313-347.

Blakey, R.C., 1990. Stratigraphy and geologic history of Pennsylvanian and Permian rocks, Mogollon Rim region, central Arizona and vicinity. *Geological Society of America Bulletin*, **102**, 1189-1217.

Blakey, R.C., 2007. Carboniferous–Permian palaeogeography of the Assembly of Pangae. *In:* Wong, T. E. (eds) *Proceedings of the XVth International Congress on Carboniferous and Permian Stratigraphy*. Utrecht, 10–16 August 2003. Royal Dutch Academy of Arts and Sciences, (Amsterdam), 443–456.

Blakey, R.C., 2008. Pennsylvanian-Jurassic Sedimentary Basins of Colorado Plateau and Southern Rocky Mountains. *In:* Miall A. (eds) The *Sedimentary Basins of the United States and Canada.* Sedimentary Basins of the World, N° 5. Elsevier, Amsterdam, 245-296.

Blakey, R.C., Havholm, K.G., Jones, L.S., 1996. Stratigraphic analysis of eolian interactions with marine and fluvial deposits, Middle Jurassic Page Sandstone and Carmel Formation, Colorado Plateau, USA. *Journal of Sedimentary Research,* 66, 324-342.

Blakey, R.C., Peterson, F., Kocurek, G., 1988. Synthesis of late Paleozoic and Mesozoic eolian deposits of the Western Interior of the United States. *Sedimentary Geology* 56: 3-126.

Blomeier, D., Scheibner C., Forke H., 2009. Facies arrangement and cyclostratigraphic architecture of a shallow-marine, warm-water carbonate platform: the Late Carboniferous Ny Friesland Platform in eastern Spitsbergen (Pyefjellet Beds, Wordiekammen Formation, Gipsdalen Group). *Facies*, **55**, 291–324.

Bosence, D., 2005. A genetic classification of carbonate platforms based on. their basinal and tectonic setting in the Cenozoic. *Sedimentary Geology*, **175**, 49-72.

Bosence, D., Procter, E., Aurell, M., Bel Kahla, A., Boudagher-Fadel, M., Casaglia, F., Cirilli, S., Mehdie, M., Nieto, L., Rey, J., 2009. A dominant tectonic signal in high-

frequency, peritidal carbonate cycles? A regional analysis of Liassic platforms from Western Tethys. *Journal of Sedimentary Research*, **79**, 389-415.

Brand, U., 2004. Carbon, oxygen and strontium isotopes in Paleozoic carbonate components: an evaluation of original seawater-chemistry proxies. *Chemical Geology*, **204**, 23-44.

Brasier, M., 1995. Fossil indicators of nutrient levels. 1: Eutrophication and climate change. *Geological Society, London, Special Publications*, 83, 113-132.

Bridges, P. H., Gutteridge P., Pickard N.A.H., 1995. The environmental setting of early Carboniferous mud-mounds. *In*: Monty, C.L.V., Bosence, D.W.J., Bridges P. H., Pratt B.R. *Carbonate Mud Mound Origin and their Evolution*. Special Publication International Association of Sedimentologist, **23**, 171-190.

Bruckschen, P., Oesmann, S., Veizer, J., 1999. Isotope stratigraphy of the European Carboniferous: proxy signals for ocean chemistry, climate and tectonics. Chemical Geology, **161**, 127-163.

Brunner, P., 1987, Microfacies y microfósiles de las rocas carbonatadas del Paleozoico de San Salvador Patlanoaya, Puebla, México: *Revista de la Sociedad Mexicana de Paleontología*, **1,** 98-112.

Buggisch, W., Wang, X., Alekseev, A.S., Joachimski, M.M., 2011. Carboniferous-Permian carbon isotope stratigraphy of successions from China (Yangtze platform), USA (Kansas) and Russia (Moscow Basin and Urals). *Palaeogeography, Palaeoclimatology, Palaeoecology*, **301**, 18-38.

Burchette, T.P., Wright V.P., 1992. Carbonate ramps depositional systems. *Sedimentary Geology*, **79**, 3-57.

Burgess, P.M., 2006. The signal and the noise: forward modeling of allocyclic and autocyclic processes influencing peritidal carbonate stacking patterns. *Journal of Sedimentary Research*, **76**, 962-977.

Burgess, P., Wright, V., Emery, D., 2001. Numerical forward modelling of peritidal carbonate parasequence development: implications for outcrop interpretation. *Basin Research*, 13, 1-16.

C

Campbell, J.A., 1980. Lower Permian depositional systems and Wolfcampian paleogeography, Uncompahgre basin, eastern Utah and southwestern Colorado. *In:* Fouch, T.D., Magathan, E.R. (eds) *Paleozoic Palaeogeography of the West-Central United States; Rocky Mountains Paleogeography Symposium* . Society of Economic Palaeontologist and Mineralogist. 327–340.

Campos, V., 1972. Geología de la región de Calderas Estados Trujillo, Portiguesa y Barinas. Internal report. *División de exploraciones. Ministerio de Minas e Hidrocarburos*. Caracas

Campos, V., García, R., 1971. Geología de la región de Valera, Estados Trujillo y Zulia. Internal report. *División de exploraciones Ministerio de Minas e Hidrocarburos*. Caracas

Cárdenas, A.L., Harries, P.J., 2010. Effect of nutrient availability on marine origination rates throughout the Phanerozoic eon. *Nature Geoscience*, **3**, 430-434.

Chan, M., 1989. Erg margin of the Permian White Rim Sandstone. SE Utah: *Sedimentology*, 36, 235–250.

Charlier, B. L. A., Ginibre, C., Morgan, D., Nowell, G. M.,Pearson, D. G., Davidson, J. P. & Ottley, C. J., 2006. Methods for microsampling and high-precision analysis of strontium and rubidium isotopes at single crystal scale for petrological and geochronological applications. *Chemical Geology*, **232**, 114-133.

Christ, P., 1927 La Coupe Geologique le long du chemin de Mucuchachí a Santa Bárbara dans les andes Venezueliennes. *Ecologae Geologica Levetiae*, **20**, 397- 414.

Choquette, P.W., James, N.P., 1987. Diagenesis in Limestones. The deep burial environment. Geoscience Canada 14. 4-35.

Clark, D., 1980. The diagenesis of Zechstein carbonate sediments. *Contributions to Sedimentology*, **9**, 167-203.

D

Dalrymple, R.W., 1992. Tidal depositional system. *In:* Walker R.G., James N.G. (eds) *Facies Models: response to sea level change*. Geological Association of Canada, 195-218.

Dalrymple, R.W., 2010. Tidal depositional system. *In:* James, N.P., Dalrymple, R.W., (eds) *Facies Models 4*. Geological Association of Canada, 201-232.

Davydov, V.I., Leven, E.Y., 2003. Correlation of Upper Carboniferous (Pennsylvanian) and Lower Permian (Cisuralian) marine deposits of the peri-Tethys. Palaeogeogreography, *Palaeoclimatology, Palaeoecology*, **196**, 125-155.

De Boer, P & Smith, D., 1994. Orbital Forcing and Cyclic Sequence. *In*: Boer, P. D., Smith, D., (eds) *Orbital Forcing and Cyclic Sequence*. International Association of Sedimentologists, Special Publication, **19**, 1-14.

Deegan, F.M., Troll, V.R., Freda, C., Misiti, V., Chadwick, J.P., McLead, C.L., Davidson, J. P., 2010. Magma Carbonate Interaction Processes and Associated CO2 Release at Merapi Volcano, Indonesia: Insights from Experimental Petrology. *Journal of Petrology*, **51**, 1027-1051.

Denison, R.E., Koepnick, R.B., Fletcher, A., Howell, M.W., Calloway, W.S., 1994. Criteria for the retention of original seawater $^{87}Sr/^{86}Sr$ in ancient limestones. *Chemical Geology*, **112**, 132–143.

Di Naccio, D., Boncio P., Cirilli S., Casaglia F., Morettini E., Lavecchia G. & Brozzetti F. 2005 Role of mechanical stratigraphy on fracture development in carbonate reservoirs: Insights from outcropping shallow-water carbonates in the Umbria-Marche Apennines, Italy. *Journal of Vulcanology and Geothermal Research*, **148**, 98-115.

Drake, F., **2000.** *Global warming - The science of climate changes*, Oxford University Press **,** London. 1-288.

Dunham, R.J., 1962. Classification of carbonate rocks according to depositional texture. *In:* Ham, W.E., (eds) Classification of carbonate rocks. *Association of Petroleum Geologist Bulletin. Memoir,* **1**, 108-171

E

Einsele, G., Seilacher, A. (eds) 1991, *Cyclic and event stratification*, Springer–Verlag, Berlin.

Esteban, M., Klappa, C.F., 1983. Subaerial exposure environment. *In: Carbonate Depositional Environments* (eds). Scholle, P. A., Bebout, D. G.,. Moore, C. H.. Association of Petroleum Geologist Bulletin. Memoir , **33**, 1–54.

Eyssautier-Chuine, S., Odonne, F., Massonnat, G., 2002. Control of bioclast abundance on natural joint density in carbonate rocks: data from Oman, Provence and Languedoc (France). *Terra Nova*, **14**, 198-204.

F

Feo-Codecido, G., Smith, F., Aboud, N., Di Giacomo, E., 1984. Basament and Paleozoic rocks of the Venezuelan Llanos basins. *Geological Society of America Memoir* **162**, 175-187.

Ferreira, P., Nuñez, A., Rodriguez, M. A., 2002. Levantamiento Geologico de la Plancha 323 Neiva. *Ingeominas*. Bogota.

Fielding, C.R., Frank, T.D., Birgenheier, L.P., Rygel, M.C., Jones, A.T., Roberts, J., 2008. Stratigraphic imprint of the Late Palaeozoic Ice Age in eastern Australia: a record of alternating glacial and non-glacial climate regime. *Journal of Geological Society, London*, **165**, 129-140.

Fierro, I., 1979. Geología de la Región de Caparo. *Ministerio de Minas e Hidrocarburos*, Internal Report, Caracas**.**

Fisher, A.G., 1964. The Lofer cyclothems of Alpine Triassic. *Geological Survey of Kansas Bulletin*. **169**, 107-149.

Flügel, E., 2004. *Microfacies of Carbonate Rocks, Analysis, Interpretation and Application*. Springer and Verlag, Berlin, 1-921.

Folk, R.L., 1974. The natural history of crystalline calcium carbonate; effect of magnesium content and salinity. *Journal of Sedimentary Research*, **44**, 40-53.

Font, L., Davidson, J. P., Pearson, D. G., Nowell, G. M., Jerram, D. A. & Ottley, C. J., 2008. Sr and Pb isotope micro-analysis of plagioclase crystals from Skye lavas: an insight into open-system processes in a flood basalt province. *Journal of Petrology*, **49**, 1449-1471.

Forero, S., 1967. Estratigrafía del Precámbrico en el flaco occidental de la Sierra de Perijá. *Geología Colombiana*, **7**, 7-78.

G

García, R., 1972. El Permo-Carbonífero en Venezuela. *Boletín de la Sociedad Venezolana de Geólogos*, **VII**, 203-214

Garland, J., 1997. Middle to Upper Devonian(Givetian and Frasnian) shallow-water carbonates of Western Europe: facies analysis and cyclicity. *PhD Thesis, Durham University*, 1-484.

Garrity, C.P., Hackley, P.C., Urbani, Franco, 2010, Digital shaded relief map of Venezuela (v. 2.0): *U.S. Geological Survey Open-File Report 2004–1322*, 1 p. text, plus metadata. (Also available at http://pubs.usgs.gov/of/2004/1322/.)

Gibbs, M.T., Rees, P.M., Kutzbach, J.E., Ziegler, A.M., Behling, P.J., Rowley, D.B., 2002. Simulations of Permian climate and comparisons with climate-sensitive sediments. *Journal of Geology*, **110,** 33-55.

Goldhammer, R., Dunn, P., Hardie, L., 1990. Depositional cycles, composite sea-level changes, cycle stacking patterns, and the hierarchy of stratigraphic forcing: examples from Alpine Triassic platform carbonates. *Geological Society of America Bulletin*, **102**, 535-562.

González de Juana, C., 1951. Introducción al estudio de la geología en Venezuela. *Boletín de Geología*., Caracas, **1,** 117-139**.**

Grader, G. W., Isaacson, P.E., Diaz-Martínez, E., Pope, M.C., 2008. Pennsylvanian and Permian sequences in Bolivia: Direct response to the Gondwana glaciation. *In*: Fielding, C.R, Frank, T.D., Isbell, J.L., (eds) *Resolving the Late Paleozoic Ice Age in Time and Space*, Geological Society of America Special Publication **441,** 143-159**.**

Gradstein, F., Ogg, J., Smith, A., 2004. *A Geologic Time Scale*. Cambridge University Press. United Kingdom. 1-589 .

Grauch R.I., 1971. Geology of the Sierra Nevada south of Mucuchies, Venezuelan Andes. PhD. *Thesis. University of Pennsylvania.*

Gröcke, D. E., Hesselbo, S. P., Duncan , J. F., 2007. Atypical diagenetic effect on strontium-isotope composition of Early Jurassic belemnites, Queen Charlotte Islands, British Columbia, Canada. *Canadian Journal of Earth Sciences*, **44.** 181-197

Grossman, E.L., Bruckschen, P., Mii, H., Chuvashov, B.I., Yancey, T.E., Veizer, J., 2002. Carboniferous paleoclimate and global change: isotopic evidence from the Russian Platform. *Carboniferous stratigraphy and Paleogeography in Eurasia*, 61-71. Also available at http://geoweb1.tamu.edu/faculty/grossman/Grossman02.pdf

Grossman, E.L., Yancey, T.E., Jones, T. E., Bruckschen, P., Chuvashov, B., Mazzullo, S.J., Mii, H., 2008. Glaciation, aridification, and carbon sequestration in the Permo-Carboniferous: The isotopic record from low latitudes. *Palaeogeography, Palaeoclimatology, Palaeoecology*, **268,** 222–233.

H

Hackley P.C., Urbani F., Karlsen A. W., Garrity C. P., 2005. Geologic Shaded Relief Map of Venezuela. *U.S. Geological Survey, Open File Report 2005-1038*. (htpp://pubs.usgs.gov/of/2005/1038). Download at 15/03/2010.

Halfar, J., Godinez-Orta, L., Mutti, M., Valdez-Holguín, J.E., Borges, J.M., 2004. Nutrient and temperature controls on modern carbonate production: an example from the Gulf of California, Mexico. *Geology* **32,** 213-216.

Haq, B.U.,Shutter, S.R., 2008. A chronology of Paleozoic sea-level changes. *Science*, **322,** 64-68.

Hernandez , M., 2003. Geología de la Plancha 48 La Jagua de Ibirico. Internal report, *Ingeominas*. Bogota D.C. 99.

Hoover, P. R. 1981 Paleontology, taphonomy and paleoecology of the Palmarito Formation (Permian of Venezuela). *Bulletin of American Paleontology***, 80,** 0-128

Hoover, P.R., 1976. The paleontology, taphonomy and paleogeology of the Palmarito Formation (Permian) of the Mérida Andes. Venezuela. *Thesis PhD. Dept. Earth Sciences. Case Western University*, 1-632**.**

Husinec, A., Basch, D., Rose, B., Read F.J., 2008. FISCHERPLOTS: An Excel spreadsheet for computing Fischer plots of accommodation change in cyclic carbonate successions in both the time and depth domains. *Computers & Geosciences,* **34,** 269–277.

I

Isbell, J.L., Cole, D.I., Catuneanu, O., 2008. Carboniferous-Permian glaciation in the main Karoo Basin, South Africa: Stratigraphy, depositional controls, and glacial dynamics. *In:* Fielding, C.R., Frank, T.D., Isbell, J.L (eds) *Resolving the Late Paleozoic Ice Age in Time and Space*. Geological Society of America Special Paper, **441,** 71-82.

Isbell, J.L., Miller, M.F., Wolfe, K.L., Lenaker, P.A., 2003. Timing of late Paleozoic glaciation in Gondwana: was glaciation responsible for the development of northern hemisphere cyclothems? *In*: Chan, M.A., Archer, A.W. (eds), *Extreme Depositional Environments: Mega End Members in Geologic Time*, Geological Society of America Special Paper, **370,** Boulder, Colorado, 5-24.

Izart, A., Stephenson, R., Vai, G.B., Vachard, D., Le Nindre, Y., Vaslet, D., Fauvel, P.J., Suss, P., Kossovaya, O., Chen, Z., 2003. Sequence stratigraphy and correlation of late Carboniferous and Permian in the CIS, Europe, Tethyan area, North Africa, Arabia, China, Gondwanaland and the USA. *Palaeogeography, Palaeoclimatology, Palaeoecology*, **196,** 59-84.

J

James N. P., 1984. Shallowing-upward sequences in carbonates. *In*: (eds) Walker. R. G. *Facies Models* Geoscience Canada. 213-228.

James N.P., Lukasik, J.J., 2010. Cool and Cold-Water Neritic Carbonates . *In:* James N.P., Dalrymple R.W. (eds) *Facies Models 4*. Geological Association of Canada, 371-400.

James, N.P., Bone, Y.B., 1991. Origin of a cool-water Oligo-Miocene deep-shelf limestone, Eucla Platform, southern Australia. *Sedimentology***, 60,** 323-341.

Jenkyns, H, C., Jones, C, E., Gröcke, D, R., Hesselbo, S, P., Parkinson, D, N., 2002. Chemostratigraphy of the Jurassic System: applications, limitations and implications for palaeoceanography. *Journal of the Geological Society, London,***159,** 351-378.

Jones, B., Desrochers, A., 1992. Shallow Platform Carbonates. *In*: Walker R.G., James N.G. (eds) *Facies Models: response to sea level change*. Geological Association of Canada, 277-301.

K

Kendall, A.C., 1985, Radiaxial fibrous calcite: a reappraisal. *In* Schneidermann, H., Harris, P.M., (eds) *Carbonate Cements*: Society of Economic Palaeontologists and Mineralogists Special Publication, **36**, 59-77.

Korte, C., Jasper, T., Kozur, H., Veizer, J., 2005. $\delta^{18}O$ and $\delta^{13}C$ of Permian brachiopods: a record of seawater evolution and continental glaciation. *Palaeogeography, Palaeoclimatology, Palaeoecology*, **224,** 333-351.

Korte, C., Jasper, T., Kozur, H.W., Veizer, J., 2006. $^{87}Sr/^{86}Sr$ record of Permian seawater. *Palaeogeography, Palaeoclimatology, Palaeoecology*, **240,** 89-107.

Kovisars, L., 1971. Geology of a portion of the North-Central Venezuelan Andes. *Geological Society of America Bulletin,* **82,** 3111-3138.

L

Laya, J. C., Tucker, M.E., 2012. Facies analysis and depositional environments of Permian carbonates of the Venezuelan Andes: Palaeogeographic implications for Northern Gondwana. *Palaeogeography, Palaeoclimatology, Palaeoecology.*

Laya, J. C., Reyes, J., 2004. Facies relationship of Carboniferous-Permian sedimentary sequence, paleogeographic implications, Venezuelan Andes. *23th International Association of Sedimentologist meeting*, Abstracts.

Lehrmann, D.J., Goldhammer, R.K., 1999. Secular variation in parasequence and facies stacking patterns of platform carbonates: a guide to application of stacking-patterns analysis in strata of diverse ages and settings. *Society of Economic Palaeontologists and Mineralogists Special Publication*, **63,** 187-226.

Logan, B.W., Semeniuk, V., 1976. Dynamic metamorphism; process and products in Devonian carbonate rocks: Canning Basin, Eastern Australia. *Western Australia. Geological Society of Australia special Publication*, **6**, 138

Lugo, P.M., 2008. Cuantificación y caracterización de la material orgánica en rocas Pre-Cretácicas de los Andes Venezolanos. *PhD Disertation. Universidad Central de Venezuela*. 1-152.

M

Mack, G.H., Rasmussen, K.A., 1984. Alluvial-fan sedimentation of the Cutler Formation (Permo-pennsylvanian) near Gateway, Colorado. *Geological Society of America Bulletin*, **95,** 109-116

Maliva, R.G., Siever, R., 1988. Diagenetic replacement controlled by force of crystallization. *Geology*, **16**, 688-691.

Martin, R.E., 1996. Secular increase in nutrients levels through the Phanerozoic: Implications for productivity, biomass, and diversity of the marine biosphere. *PALAIOS Society of Economic Palaeontologists and Mineralogists*, **11,** 209-219.

Matsuda, N. S., 2002. Carbonate sedimentation cycle and origin of dolomite in the Lower Pennsylvanian intracratonic Amazon Basin, *Dissertation Thesis, Department of Earth & Planetary Science, University of Tokyo*.

May, S.R., Butler, R.F., 1986. North American Jurassic apparent polar wander implications for plate motions, palaeogeography and Cordilleran tectonics. *Journal of Geophysical Research*, **91,** 11519-11544.

Miall, A.D., Blakey, R.C., 2008. Phanerozoic tectonic and sedimentary evolution of North America. *In*: Miall A. (eds) *Sedimentary Basins of the United States and Canada*. Sedimentary Basins of the World N° 5, Elsevier, Amsterdam, 1-30.

Miall, A.D., 2008. Southern Midcontinent, Permian Basin, and Ouachitas. *In*: Miall A. (eds) *Sedimentary Basins of the United States and Canada*. Sedimentary Basins of the World, N° 5, Elsevier, Amsterdam, 297-325.

Milani, E. J., Zalán, P.V., 1999. An outline in the geology and prtroluem systems of the Paleozoic interior basins of South America, *Episodes***, 23,** 199-205

Montañez, I.P., Tabor, N.J., Niemeier, D., DiMichele, W.A., Frank, T.D., Fielding, C.R., Isbell, J.L., Birgenheier, L.P., Rygel, M.C., 2007. CO2-forced climate and vegetation instability during Late Paleozoic deglaciation. *Science*, **315,** 87-91

Moore, C.M., 1989. *Carbonate diagenesis and porosity*. Elsevier. 1-317.

Mount, J., 1985. Mixed siliciclastic and carbonate sediments: a proposed first-order textural and compositional classification. *Sedimentology***, 32,** 435-442.

Mruk, D., Bebout, D.G., 1993. Slope. *In:* Bebout, D.G., Kerans, C. (eds), *Guide to the Permian Reef Geology Trail, McKittrick Canyon, Guadalupe Mountains National Park, West Texas,* Texas. Boreau Economics. Geology, Guidebook, **26**, 14–22.

Mu, X., Riding, R., 1988. Silicification of Permian calcareous algae from Nanjing, China. *Geological Magazine.* **125,** 123-139.

O

Odreman, O., Useche A., 1997. Formación Palmarito. Léxico Estratigráfico de Venezuela. *Ministerio de energía y minas*. Comisión de Estratigrafía y Terminología. Caracas.

Odreman, O., Wagner, Y. R., 1979. Precisiones sobre algunas floras carboníferas y pérmicas se los Andes venezolanos. *Boletín de Geología Ministerio de Energía y Minas*, Caracas, **13,** 77-81.

P

Parrish, J.T., 1993. Climate of the supercontinent Pangaea. *Journal of Geology*, **101,** 215-233.

Perlmutter, M.A., Plotnick, R.E., 2003. Hemispheric asymmetry of the marine stratigraphic record: conceptual proof of a unipolar ice cap. *In:* Cecil, C.B., Edgar, T.N. (eds) *Climate Controls on Stratigraphy*. Society of Economic Paleontologists and Mineralogists Special Publication, **77,** 51-66.

Peyser, C.E., Poulsen, C.J., 2008. Controls on Permo-Carboniferous precipitation over tropical Pangaea: a GCM sensitivity study. *Palaeogeography, Palaeoclimatology, Palaeoecology*, **268,** 181-192**.**

Pierce, G. R., Jefferson, C. C.,Smith, W. R., 1961. Fossiliferous Paleozoic localities in Mérida Andes, Venezuela. *American Association of Petroleum Geologist Bulletin*, **45,** 342-375.

Pindell, J. L, Cande, S.C.; Pitman, W.C.; Rowley, D. B.; Dewey, J. F.; Labrecque, J.,Haxby, W., 1985. A plate-kinematic framework for models of Caribbean evolution. *Tectonophysics*, **155,** 121-138.

Pindell, J.L., Higgs, R., Dewey, J.F., 1998. Cenozoic palinspastic reconstruction, paleogeographic evolution and hydrocarbon setting of the northern margin of South America. *In*: Pindell, J.L., Drake, C.L. *Paleogeography evolution and non-glacial eustasy, northern South America*. Society of Economic Paleontologists and Mineralogists Special Publication, **58,** 45-86

Pérez-Huerta A., Sheldon, N., 2006. Pennsylvanian sea level cycles, nutrient availability and brachiopod paleoecology. *Palaeogeography, Palaeoclimatology, Palaeoecology*, 230, 264-279

Popp, B.N., Anderson, T.F., Sandberg, P.A., 1986, Brachiopods as indicators of original isotopic compositions in some Paleozoic limestones. *Geological Society of America Bulletin*, **97,** 1262-1269.

Pratt, B. R., James, N.P., Cowan, C.A., 1992. Peritidal carbonates. *In*: Walker, R.G., James, N.G. (eds) *Facies Models: response to sea level change*. Geological Association of Canada, 277-301.

Pratt, B.R., 2010. Peritidal Carbonates. *In*: James N.P., R.W. Dalrymple (eds) *Facies Models 4*. Geological Association of Canada, 401-420.

R

Ramirez, C., Garcia, R., Campos, V., 1972. Geología de la Región de Timotes, Estados Mérida, Barinas y Trujillo. *Boletín de Geología publicación especial* **5,** 898-934.

Ryan, W.B.F., Carbotte, S.M., Coplan, J.O., O'Hara, S., Melkonian, A., Arko, R., Weissel, R.A., Ferrini, V., Goodwillie, A., Nitsche, F., 2009. Global multi-resolution topography synthesis. *Geochemestry. Geophysiscs Geosystems*, **10**, Q03014.

Rawson, R.R., Turner-Peterson, C.E., 1980. Paleogeography of northern Arizona during the deposition of the Permian Toroweap Formation, *In:* Fouch, T.D., Magathan, E.R. (eds) *Paleozoic Palaeogeography of the West-Central United States; Rocky Mountains Paleogeography Symposium* . Society of Economic Palaeontologist and Mineralogist Rocky Mountains section. 341-352.

Read, J.F, 1982. Carbonate Platforms of Passive (extensional) Continental Margin: Types, Characteristics and Evolution. *Tectonophysics.* **81,** 195-212.

Read, J.F., 1985. Carbonate Platforms Facies models. *American Association of Petroleum Geologist Bulletin*, **69,** 1-21.

Read, J.F., 1989. Controls on evolution of Cambrian-Ordovician passive margin, US Appalachians. *In*: Crevello, P.D., Wilson, J.L., Sarg, J.F., Read, J.F. (eds) *Controls on Carbonate Platform and Basin Development*. Society of Economic Palaeontologists and Mineralogists, Special Publication **44,** 147–185.

Rees, P.M., Ziegler, A.M., Gibbs, M.T., Kutzbach, J.E., Behling, P.J., Rowley, D.B., 2002. Permian phytogeographic patterns and climate data/model comparisons. *Journal of Geology*, **110,** 1-31.

Ricardi, T. F., 2008. Venezuelan paleoflora of the Pennsylvanian-Early Permian: Paleobiogeographical relationships to central and western equatorial Pangea. *Gondwana Research*, **14,** 297-305.

Rigby, J.K., 1984. Permian Sponges from Western Venezuela. *Journal of Paleontology*, **58,** 1436-1462.

Ross, C. A., 1973. Pennsylvanian and Early Permian depositional history, southwestern Arizona. *American Association of Petroleum Geologists Bulletin*, **57,** 887-912.

Ross, C., J. Ross., 1995. Permian sequence stratigraphy. *In:* Scholle P.A., Tadeusz M.P., Ulmer-Scholle D., (eds). *The Permian of Northern Pangea: Paleogeography, paleoclimates, stratigraphy*. Springer-Verlag, Berlin, 98-123.

S

Sadler, P.M., Osleger, D.A., Montañez, P. (1993) On the labeling, length, and objective basis of Fischer plots. *Journal of Sedimentary Research,* **63,** 360-368.

Saltzman,M.R., 2003. Late Paleozoic ice age: ocean gateway or pCO2? *Geology* **31,** 151-154.

Samankassou, E., 2002. Cool-water carbonates in a paleoequatorial shallow-water environment: The paradox of the Auernig cyclic sediments (Upper Pennsylvanian, Carnic Alps, Austria-Italy) and its implications. *Geology* **30,** 655-658.

Satterley, A.K., 1996. Cyclic carbonate sedimentation in the Upper Triassic Dachstein Limestone, Austria; the role of patterns of sediment supply and tectonics in a platform-reef-basin system. *Journal of Sedimentary Research*. **66,** 307-326**.**

Schlager, W., 2005. Carbonate sedimentology and sequence stratigraphy. *Society of Economic Paleontologists and Mineralogists Concepts of Sedimentology and Paleontology*, **8.** 1-198

Scholle, P., 2006. An Introduction and Virtual Geologic Field Trip to the Permian Reef Complex, Guadalupe and Delaware Mountains, New Mexico-West Texas. Downloaded on 10 of december 2008 *in:* http://geoinfo.nmt.edu/staff/scholle/guadalupe.html.

Scholle, P., Ulmer-Scholle, D., 2003: A color guide to the petrography of carbonate rocks, grains, textures, porosity, diagenesis. *American Association of Petroleum Geologist Memoir*, **77**, 0-460

Schwarzacher, W 2000. Repetitions and cycles in stratigraphy. *Earth-Science Reviews***, 50,** 51-75.

Scoffin, T.P., 1987. *Introduction to carbonate sediments and rocks*. Chapman and Hall and Methuen. 1-274

Scotese, C.R., 1999. *PALEOMAP Animations Paleogeography*. PALEOMAP Project. Department of Geology, University of Texas, Arlington, TX.

Scotese, C.R., Langford, R., 1995. Pangaea and the Palaeogeography of the Permian. *In:* Scholle, P.A., Peryt, T.M., Ilmer-Scholle, D.S. (eds), *The Permian of Northern Pangaea: Paleogeography, paleoclimates, stratigraphy,* **1.** Springer-Verlag, Berlin, 3-19.

Sellier De Civrieux, J., 1951. Ocurrencia del género Glovobalbulina en el Permiano de Venezuela. *Boletín de Geología,* **1,** 141-146.

Shagam, R., 1969. Geología de los Andes Centrales de Venezuela. Internal report. *División de exploraciones. Ministerio de Minas e Hidrocarburos*. Caracas

Shagam, R., 1972. Geología de los Andes Venezolanos. (resum.) Bol. Geol. Rb. Esp. **5,** 935-938.

Shell de Venezuela, Creole Petroleum Corporation, 1964. Paleozoic rocks of Mérida Andes, Venezuela. *American Association of Petroleum Geologist Bulletin,* **48,** 70-84.

Silva-Pineda, A., 1970, Plantas del Pensilvánico de Tehuacán, Puebla: Universidad Nacional Autónoma de México, *Instituto de Geología, Paleontología Mexicana***, 29,** 49-108

Silva-Pineda, A., Buitrón-Sánchez, B., Arellano-Gil, J., Vachard, D., Ramírez, J., 2003. Permian Continental and Marine Biota of South-Central Mexico: A Synthesis. *In* Bartolini, C., Buffler, R. T., Blickwede, J., (eds) The Circum-Gulf of Mexico and the Caribbean: Hydrocarbon habitats,basin formation, and plate tectonics: *American Association of Petroleum Geologist Memoir***, 79,** 462–475**.**

Soreghan, G., Soreghan, M.J., 2002. Atmospheric dust and algal dominance in the late Paleozoic: a hypothesis. *Journal of Sedimentary Research*, **72,** 457-461**.**

Soreghan, G.S., Dickinson, W.R., 1994. Generic types of stratigraphic cycles controlled by eustasy. *Geology* **22,** 759-761**.**

Spadini, A. R., 2008. Carbonate reservoirs in Brazilian sedementary basins. *19th World Petrolem Congress, Spain*. Abstracts.

Spence, G.H., Tucker, M.E., 2007. A proposed integrated multi-signature model for peritidal cycles in carbonates. *Journal of Sedimentary Research*, **77,** 797-808**.**

Steiner, M.B., 1983. Mesozoic apparent polar wander and plate motions of North America. *In:* Fouch, T.D., Magathan, E.R. (eds) *Paleozoic Palaeogeography of the West-Central United States; Rocky Mountains Paleogeography Symposium* . Society of Economic Palaeontologist and Mineralogist 1–11.

Steiner, M.B., 2003. A cratonic middle Jurassic palaeopole: Callovian–Oxfordian pole stillstand (J-2 cusp), rotation of the Colorado Platea, and Jurassic North American apparent polar wander, *Tectonics*, **22,** 1020.

Steiner, M.B., Lucas, S.G., 2000. Palaeomagnetism of the Late Triassic Petrified Forest Formation, Chinle Group, western United States: further evidence of 'large' rotation of the Colorado Plateau. *Journal of Geophysical Research*, **105,** 25,791–25,808.

T

Tabor, N.J., Montanez, I.P., 2002. Shifts in late Paleozoic atmospheric circulation over western equatorial Pangea: Insights from pedogenic mineral $\delta^{18}O$ compositions. *Geology* ,**30,** 363-366.

Tabor, N.J., Montañez, I.P., Scotese, C.R., Poulsen, C.J., Mack, G.H., 2008. Paleosol archives of environmental and climatic history in paleotropical western Pangea during the latest Pennsylvanian through Early Permian. *In:* Fielding, C.R., Frank, T.D., Isbell, J.L., (eds) *Resolving the Late Paleozoic Ice Age in Time and Space*. Geological Society of America Special Paper, **441,** 291-304**.**

Tabor, N.J., Poulsen, C.J., 2008. Palaeoclimate across the Late Pennsylvanian-Early Permian tropical palaeolatitudes: A review of climate indicators, their distribution, and relation to palaeophysiographic climate factors. *Palaeogeography, Palaeoclimatology, Palaeoecology*, **268,** 293-310.

Thirlwall, M., 1991. High-precision multicollector isotopic analysis of low levels of Nd as oxide. *Chemical Geology*, **94**, 13-22.

Tinker, S.W., 1998. Shelf-to-basin facies distribution and sequence stratigraphy of a steep-rimmed carbonate margin: Capitan depositional system, McKittrick Canyon, New Mexico and Texas. *Journal of Sedimentary Research*, **68,** 1146-1174.

Trexler, J.H., Cashman, P.H., Snyder, W.S., Davydov, V.I., 2004. Late Paleozoic tectonism in Nevada: Timing, kinematics, and tectonic significance. *Geological Society of America Bulletin*, **116,** 525-538

Trompy, D., 1943. Pre-Cretaceus of Colombia. *Geological Society of America Bulletin*, **54,** 1281-1304**.**

Tucker, M. E. Garland, J., 2010. High-frecuency Ccycles and their sequence stratigraphic context: Orbital forcing and tectonc controls on Devonian cyclicity, Belgium. *Geologica Belgica*, **13,** 213-240**.**

Tucker, M. E., 2011. *Sedimentary rocks in the field*. Wiley.

Tucker, M. E., 1983. Diagenesis, geochemistry, and origin of a Precambrian dolomite; the Beck Spring Dolomite of eastern California. *Journal of Sedimentary Research*, **53**, 1097.

Tucker, M. E., 1986. Formerly aragonitic limestones associated with tillites in the late Proterozoic of Death Valley, California. *Journal of Sedimentary Petrology*, **56**, 818-830.

Tucker, M. E., 1991. Sequence stratigraphy of carbonate-evaporite successions: Models and application to the Upper Permian (Zechstein) of northeast England and adjoining North Sea. *Journal of the Geological Society London*, **148**, 1019-1036.

Tucker, M.E., Wilson, J.L., Crevello, P.D., Sarg, J.R., Read, J.F., 1990: Carbonate platforms. Facies, sequences and evolution. *Intentional Association of Sedimentologists Special Publication*, **9,** 1-328.

Tucker, M.E., Wright, V.P., 1990. Carbonate sedimentology. Oxford (Blackwell), 0-482

V

Vachard, D., Fourcade, E., 1996. Foraminifères y otrosgues du Permien du Guatémala. *GEOBIOS*, **30,** 745-784.

Vachard, D., Flores de Dios, A., Buitrón-Sánchez, B. E., Grajales, M., 2000. Biostratigraphie par fusulines del calcaires Carboniferes et Permiens de San Salvador Patlanoaya (Puebla, Mexique): *GEOBIOS***, 33,** 5-33.

Vachard, D., Buitrón, B., Flores de Dios, A., 2004. Guadalupian and Lopingian (Middle and Late Permian) deposits from Mexico and Guatemala, a review with new data. *GEOBIOS*, **37,** 99-115.

Vai, G.B., 2003. Development of the palaeogeography of Pangaea from Late Carboniferous to Early Permian. *Palaeogeography*, *Palaeoclimatology*, *Palaeoecology*, **196,** 125-155.

Van Wagoner, J., Posamentier, H., Mitchum, R., Vail, P., Sarg, J., Loutit, T., Hardenbol, J., 1988. An overview of the fundamentals of sequence stratigraphy and key definitions. *Sea-Level Changes: An Integrated Approach*. Society of Economic Palaeontologist and Mineralogist Special Publication **42,** 39–45**.**

Vázquez-Echeverría, A., 1986, Descubrimiento de una nueva localidad de rocas marinas del Paleozoico al suroeste del Estado de Puebla: *XXIV Congreso Nacional de la Asociación de Geólogos Petroleros Mexicanos*, Petróleos Mexicanos, Departamento Exploración Zona Centro, Veracruz, México, 19.

Velandria, F., Nuñez, A., Marquinez, G., 2001. Mapa Geologico del Departamento de Huila. *Ingeominas*. Bogota.

Velandria, F., Ferreira, P., Rodríguez, G., Nuñez, A., 2001. Levantamiento Geológico de la Plancha 366 Garzon. *Ingeominas*. Bogota.

Villarroel, C., Mojica, J., 1987. El Paleozoico Superior(Carbonifero-Permico) sedimentario de Colombia. Afloramintos conocidos y características generales. *Geología Colombiana*. **16,** 81-87.

Viscarret P., Wright, J., Urbani, F., 2009. New U-pb zircon ages of El Baul Massif, Cojedes State, Venezuela. *Revista Técnica de Ingeniería Universidad del Zulia.* **32,** 210-221.

Viscarret, P., Laya, J., 2007. Facies sedimentarias del pérmico en el flanco surandino de Venezuela. *Ciencia e Ingeniería***, 28,** 55-60.

Viscarret, P. J., 2002. Estudio integral del Paleozoico no metamorfizado (formaciones Caparo, el Horno, Sabaneta y Palmarito) en los Andes de Mérida. Venezuela. *Disertation. Universidad de Los Andes*. 1-135.

W

Wanless, H.R., 1979. Limestone response to stress; pressure solution and dolomitization. *Journal of Sedimentary Research*, **49**, 437-462.

Wahlman, G.P., 2002. Upper Carboniferous-Lower Permian (Bashkirian-Kungarian) mounds and reefs. . In Kiessling, W., Flügel, E., Golonka, J.e., 2002. *Phanerozoic reef patterns*. Society of Economic Palaeontologist and Mineralogist Special Publication, **72,** 271-338

Weedon, G.P., 2003. *Time-series analysis and cyclostratigraphy: examining stratigraphic records of environmental cycles*. Cambridge University Press. 1- 252**.**

Williams, H. D., Burgess, P.M., Wright, V. P., Della Porta, G., Granjeon, D., 2011. Investigating carbonate platform types: multiple controls and a continuum of geometries. *Journal of Sedimentary Research***, 81,** 18-37.

Wilkinson, B.H., Diedrich, N.W., Drummond, C.N., Rothman, E.D., 1998. Michigan hockey, meteoric precipitation, and rhythmicity of accumulation on peritidal carbonate platforms. *Geological Society of America Bulletin*, **110**, 1075-1093.

Winguth, A.M.E., Heinze, C., Kutzbach, J., Maier-Reimer, E., Mikolajewicz, U., Rowley, D., Rees, A., Ziegler, A., 2002. Simulated warm polar currents during the middle Permian**.** *Paleoceanography*, **17,** 1057.

Winguth, A. M. E., Maier-Reimer, E., 2005. Causes of the marine productivity and oxygen changes associated with the Permian-Triassic boundary: A reevaluation with ocean general circulation models**.** ***Marine Geology*****, 217,** 283-304.

Witzke, B. J., 1990. Palaeoclimatic constraints for Palaeozoic palaeolatitudes of Laurentia and Euramerica. In: McKerrow, W.S., Scotese, C.R. (eds) Palaeozoic Palaeogeography and Biogeography. *Geological Society, London, Memoir*, **12,** 57-74.

Wood, G., Groves, J., Wahlman, G., Breckle, P., Alemán, A., 2002. The paleogeographic and biogeographic significance of fusulinaceans, smaller foraminifers and palynomorphs from the Copacabana Formation (Pennsylvanian–Permian), Madre de Dios Basin, Peru. Carboniferous of the World: *Canadian Society of Petroleum Geologists Memoir* **19,** 630–664.

Wood, R., Dickson, J.A.D., Kirkland, B.L., 1996. New observation on the ecology of the Permian Capitan reef, Texas and New Mexico. *Paleontology*, **39,** 733-762.

Wright V.P., Burchette, T.P, 1996. Shallow-water carbonates environment. *In:* Reading, H.G. (eds): *Sedimentary environments: processes, facies, stratigraphy*, 325-394.

Wright, V.R., Burchette, T.P., 1999: Carbonate ramps. *Geological Society of London Special Publication*. **149,** 1-465.

Z

Ziegler, A.M., Eshel, G., Rees, P.McA., Rothfus, T.A., Rowley, D.B., Sunderlin, D., 2003. Tracing the tropics across land and sea: Permian to present. *Lethaia*, **36,** 227-254.

Appendix 1. Detailed sedimentary logs

The following appendix shows the sedimentary logs of the sections that have been studied in this thesis. All logs are presented in 1:100 scale and include all information collected in the field, petrography and cycles studies. All samples numbers are placed in the stratigraphic position where they were collected, also, rock texture using Dunham's textural classification and the grain-size table of Wentworth (1922) modified by Blair and McPherson (1999). In addition, sedimentary structures, cyclicity and microfacies are presented in the logs. Figure A1.1 shows the Key of all the symbols used in the logs.

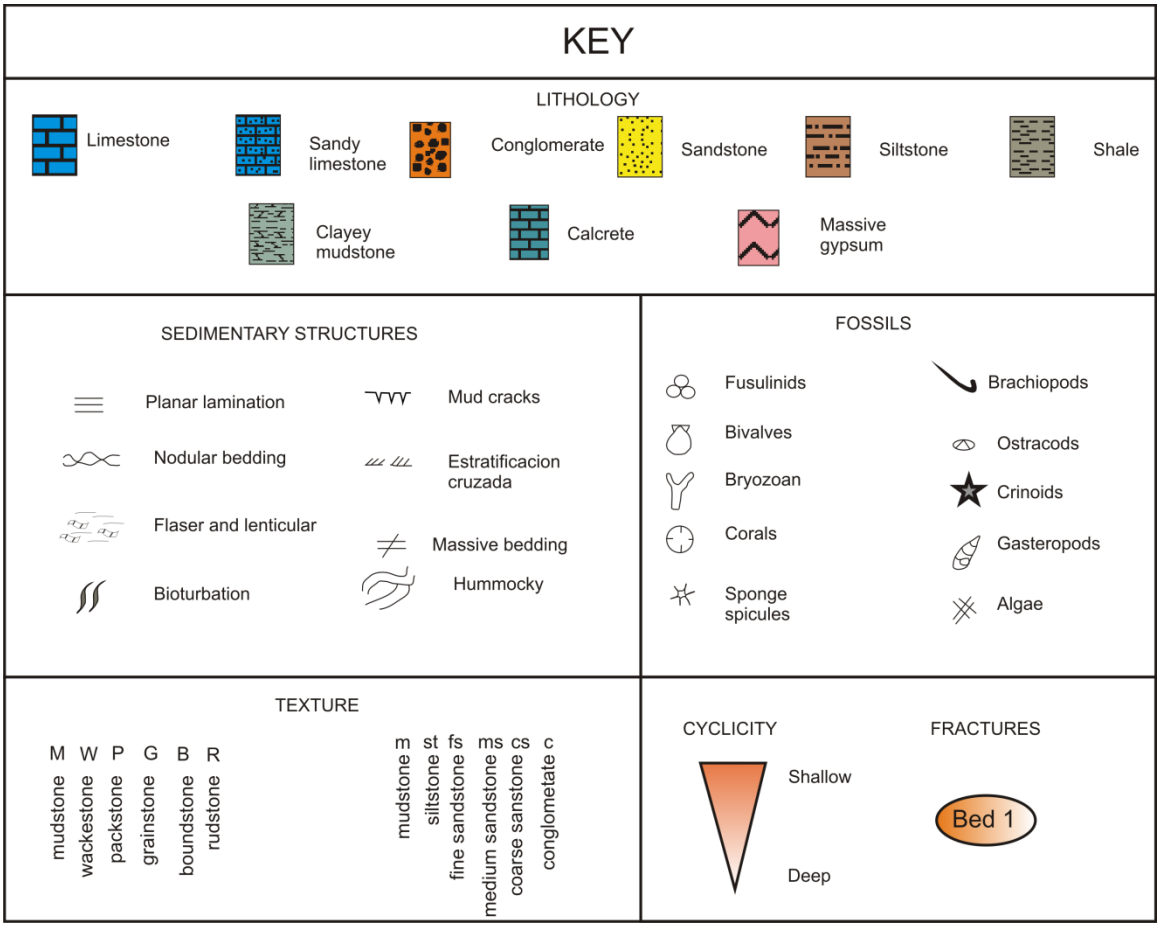

Figure A1.1Key to symbols used in the logs.

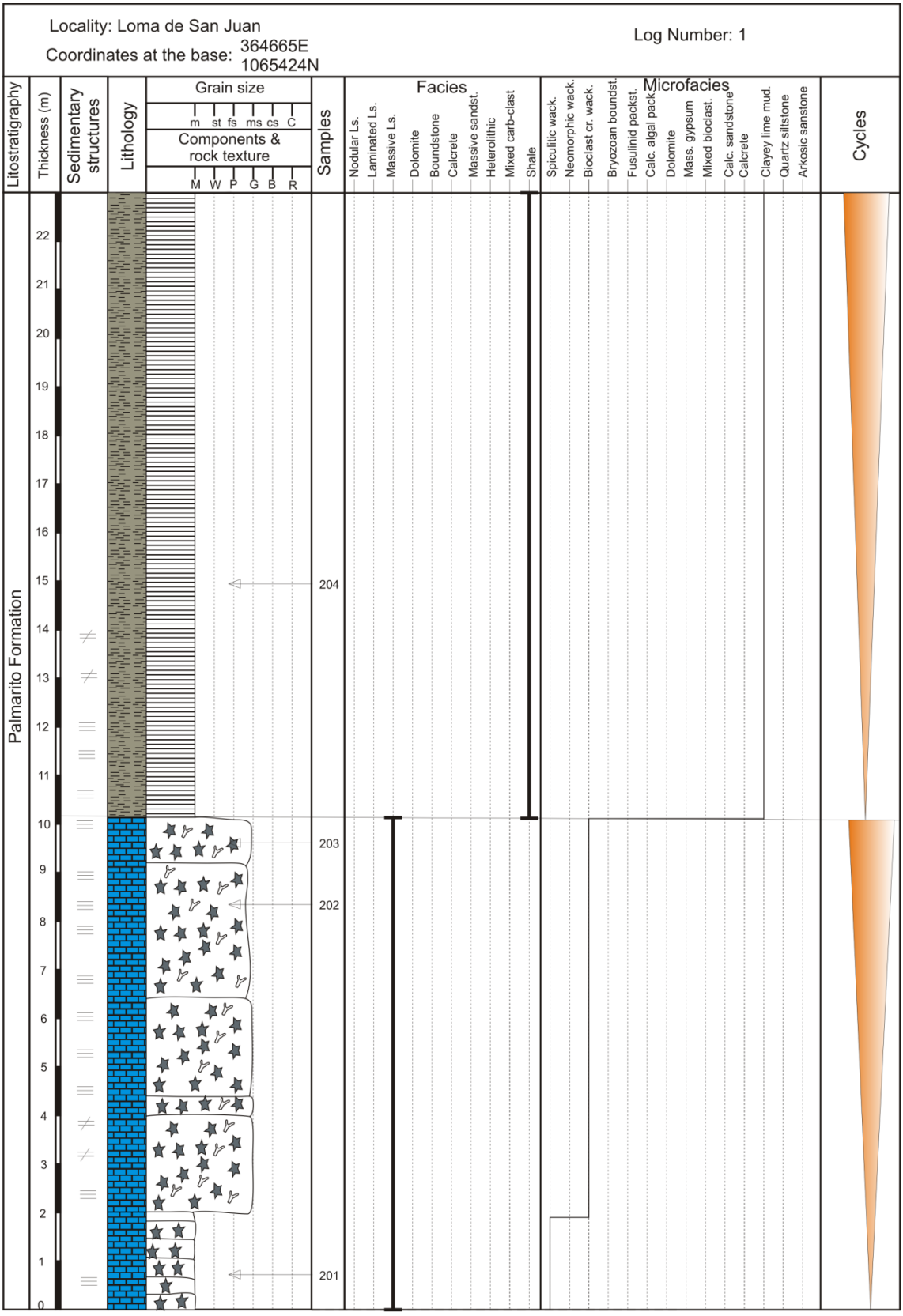
Locality: Loma de San Juan
Coordinates at the base: 364665E 1065424N
Log Number: 1
Litostratigraphy
Thickness (m)
Sedimentary structures
Lithology
Grain size
m st fs ms cs C
Components & rock texture
M W P G B R
Samples
Facies
Nodular Ls.
Laminated Ls.
Massive Ls.
Dolomite
Boundstone
Calcrete
Massive sandst.
Heterolithic
Mixed carb-clast
Shale
Microfacies
Spiculitic wack.
Neomorphic wack.
Bioclast cr. wack.
Bryozoan boundst.
Fusulinid packst.
Calc. algal pack.
Dolomite
Mass. gypsum
Mixed bioclast.
Calc. sandstone
Calcrete
Clayey lime mud.
Quartz siltstone
Arkosic sanstone
Cycles
Palmarito Formation
0
1
2
3
4
5
6
7
8
9
10
11
12
13
14
15
16
17
18
19
20
21
22
201
202
203
204

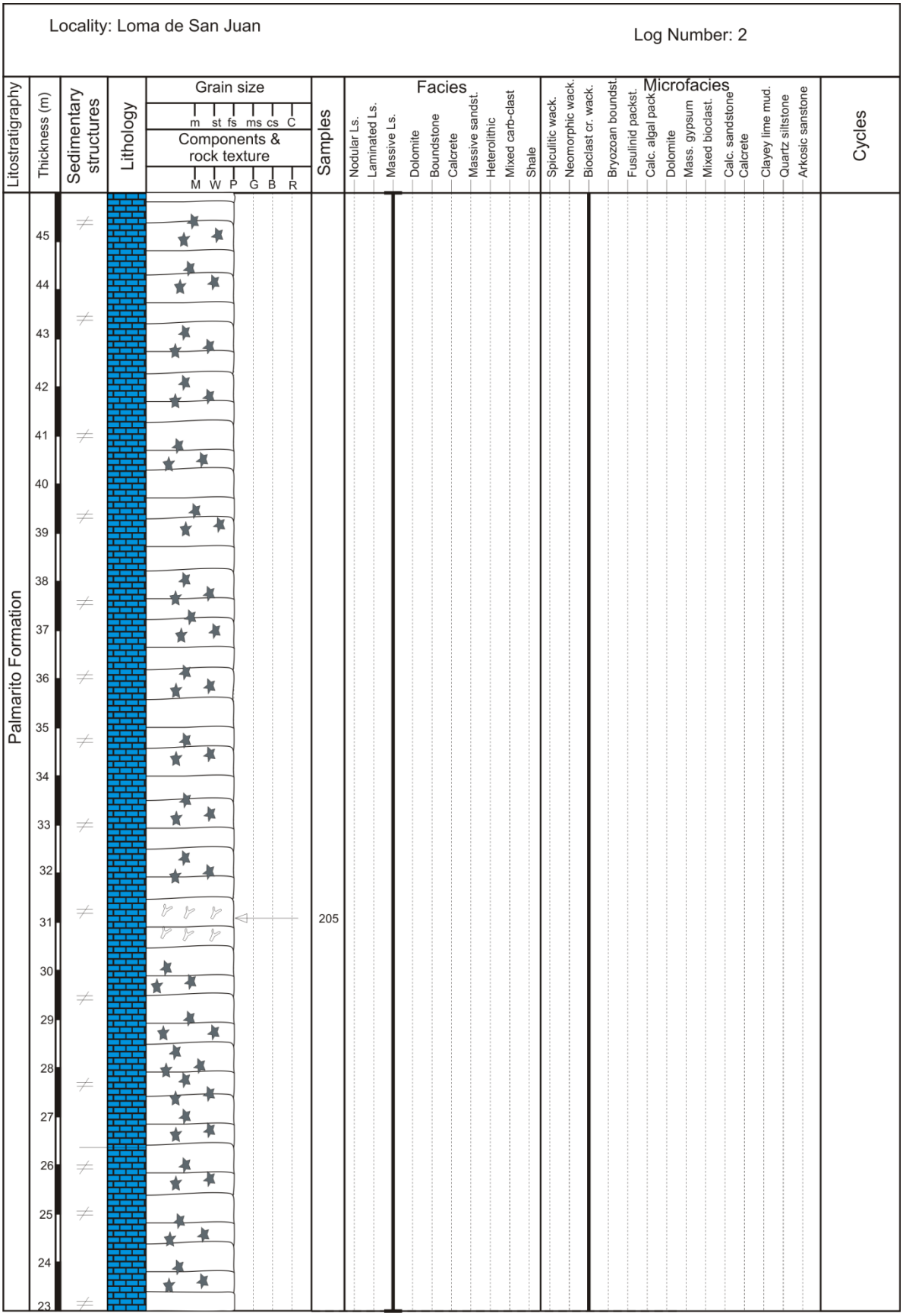
Locality: Loma de San Juan
Log Number: 2
Litostratigraphy
Thickness (m)
Sedimentary structures
Lithology
Grain size
m st fs ms cs C
Components & rock texture
M W P G B R
Samples
Facies
Nodular Ls.
Laminated Ls.
Massive Ls.
Dolomite
Boundstone
Calcrete
Massive sandst.
Heterolithic
Mixed carb-clast
Shale
Microfacies
Spiculitic wack.
Neomorphic wack.
Bioclast cr. wack.
Bryozoan boundst.
Fusulinid packst.
Calc. algal pack.
Dolomite
Mass. gypsum
Mixed bioclast.
Calc. sandstone
Calcrete
Clayey lime mud.
Quartz siltstone
Arkosic sanstone
Cycles
Palmarito Formation
45
44
43
42
41
40
39
38
37
36
35
34
33
32
31
30
29
28
27
26
25
24
23
205

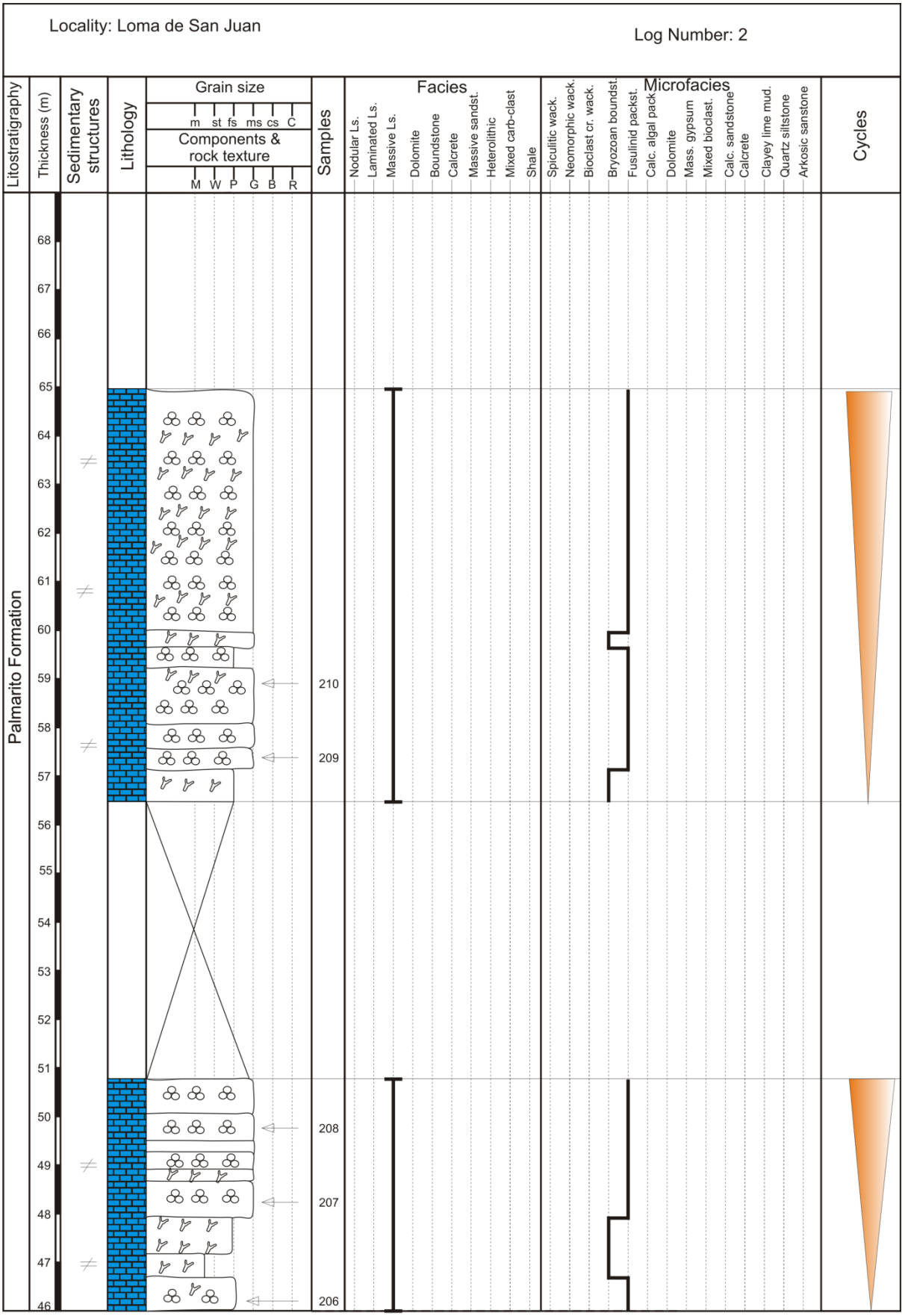
Locality: Loma de San Juan
Log Number: 2
Litostratigraphy
Thickness (m)
Sedimentary structures
Lithology
Grain size
m st fs ms cs C
Components & rock texture
M W P G B R
Samples
Facies
Nodular Ls.
Laminated Ls.
Massive Ls.
Dolomite
Boundstone
Calcrete
Massive sandst.
Heterolithic
Mixed carb-clast
Shale
Microfacies
Spiculitic wack.
Neomorphic wack.
Bioclast cr. wack.
Bryozoan boundst.
Fusulinid packst.
Calc. algal pack.
Dolomite
Mass. gypsum
Mixed bioclast.
Calc. sandstone
Calcrete
Clayey lime mud.
Quartz siltstone
Arkosic sanstone
Cycles
Palmarito Formation
68
67
66
65
64
63
62
61
60
59
58
57
56
55
54
53
52
51
50
49
48
47
46
210
209
208
207
206

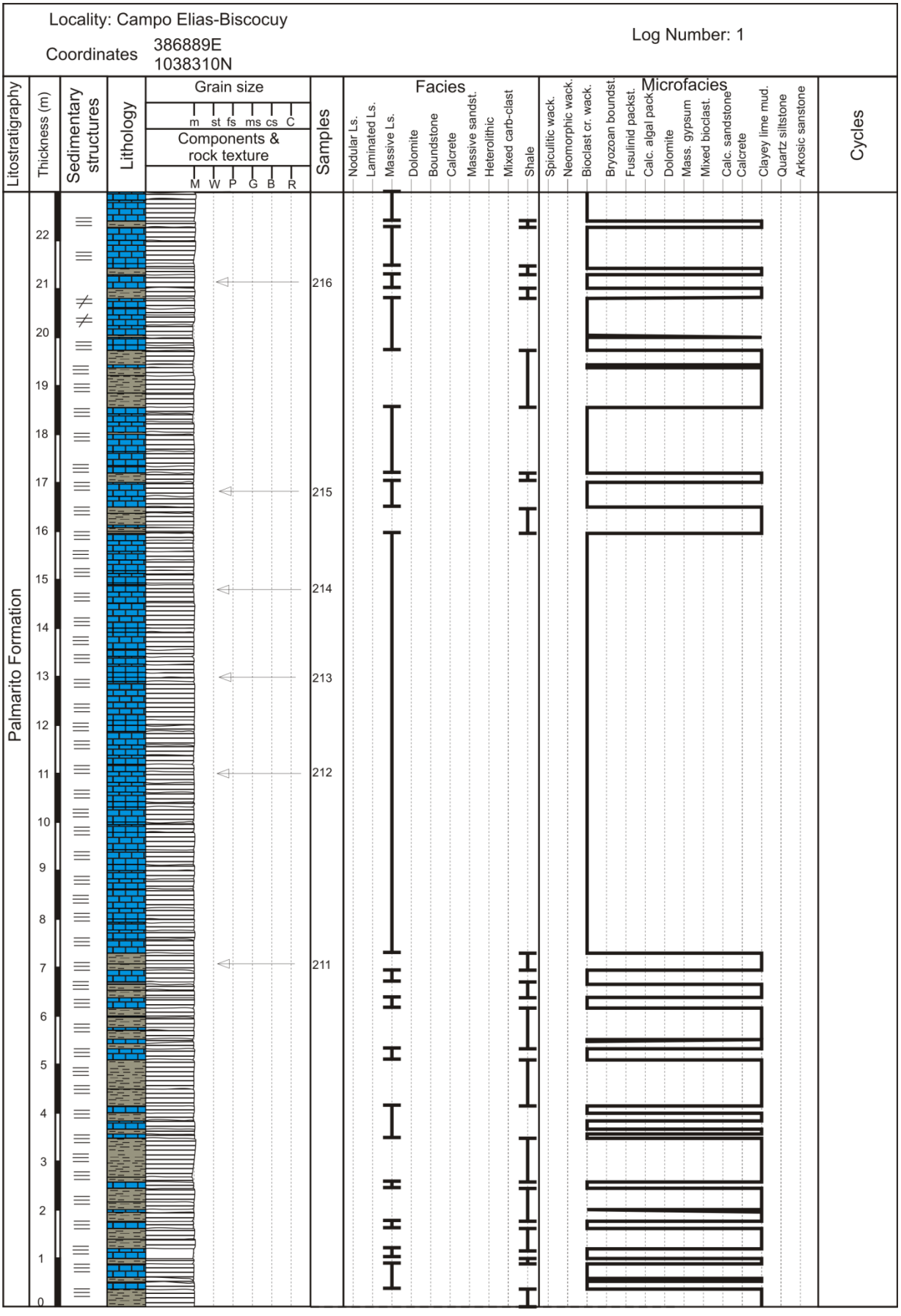
Locality: Campo Elias-Biscocuy
Coordinates 386889E 1038310N
Log Number: 1
Litostratigraphy
Thickness (m)
Sedimentary structures
Lithology
Grain size
m st fs ms cs C
Components & rock texture
M W P G B R
Samples
Facies
Nodular Ls.
Laminated Ls.
Massive Ls.
Dolomite
Boundstone
Calcrete
Massive sandst.
Heterolithic
Mixed carb-clast
Shale
Microfacies
Spiculitic wack.
Neomorphic wack.
Bioclast cr. wack.
Bryozoan boundst.
Fusulinid packst.
Calc. algal pack.
Dolomite
Mass. gypsum
Mixed bioclast.
Calc. sandstone
Calcrete
Clayey lime mud.
Quartz siltstone
Arkosic sanstone
Cycles
Palmarito Formation
0
1
2
3
4
5
6
7
8
9
10
11
12
13
14
15
16
17
18
19
20
21
22
211
212
213
214
215
216

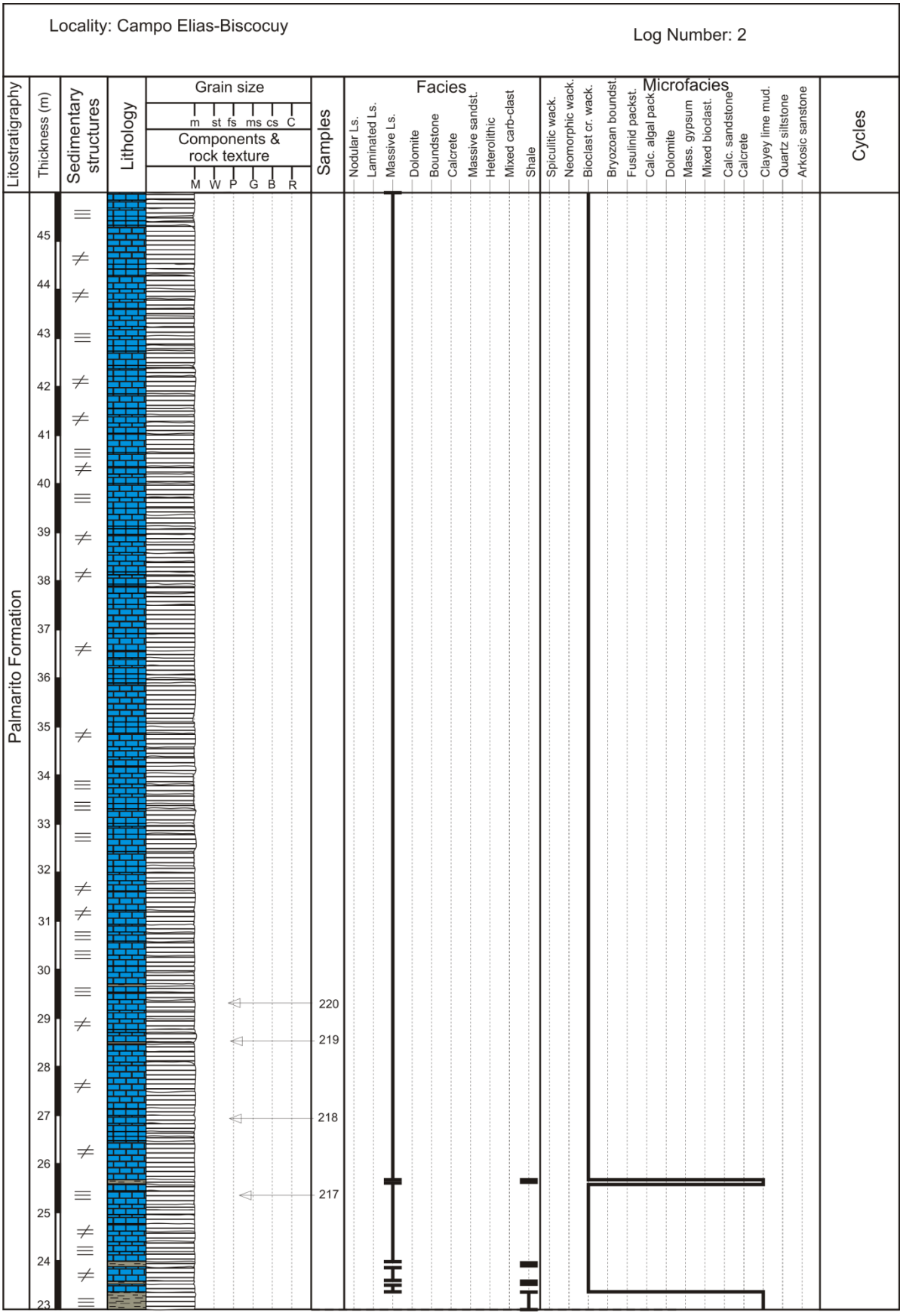
Locality: Campo Elias-Biscocuy
Log Number: 2
Litostratigraphy
Thickness (m)
Sedimentary structures
Lithology
Grain size
m st fs ms cs C
Components & rock texture
M W P G B R
Samples
Facies
Nodular Ls.
Laminated Ls.
Massive Ls.
Dolomite
Boundstone
Calcrete
Massive sandst.
Heterolithic
Mixed carb-clast
Shale
Microfacies
Spiculitic wack.
Neomorphic wack.
Bioclast cr. wack.
Bryozoan boundst.
Fusulinid packst.
Calc. algal pack.
Dolomite
Mass. gypsum
Mixed bioclast.
Calc. sandstone
Calcrete
Clayey lime mud.
Quartz siltstone
Arkosic sanstone
Cycles
Palmarito Formation
45
44
43
42
41
40
39
38
37
36
35
34
33
32
31
30
29
28
27
26
25
24
23
220
219
218
217

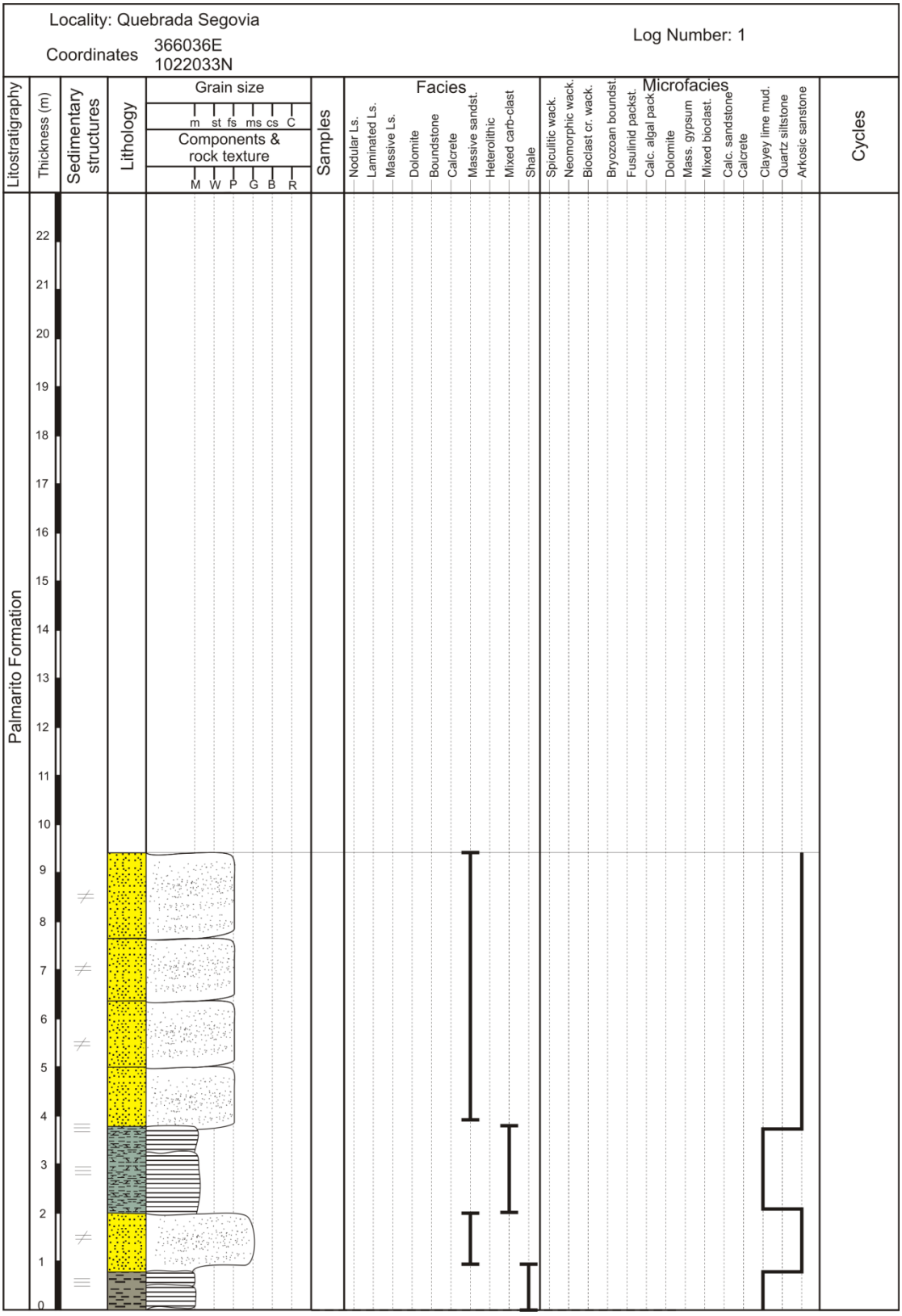
Locality: Quebrada Segovia
Coordinates 366036E 1022033N
Log Number: 1
Litostratigraphy
Thickness (m)
Sedimentary structures
Lithology
Grain size
m st fs ms cs C
Components & rock texture
M W P G B R
Samples
Facies
Nodular Ls.
Laminated Ls.
Massive Ls.
Dolomite
Boundstone
Calcrete
Massive sandst.
Heterolithic
Mixed carb-clast
Shale
Microfacies
Spiculitic wack.
Neomorphic wack.
Bioclast cr. wack.
Bryozoan boundst.
Fusulinid packst.
Calc. algal pack
Dolomite
Mass. gypsum
Mixed bioclast.
Calc. sandstone
Calcrete
Clayey lime mud.
Quartz siltstone
Arkosic sanstone
Cycles
Palmarito Formation
0
1
2
3
4
5
6
7
8
9
10
11
12
13
14
15
16
17
18
19
20
21
22

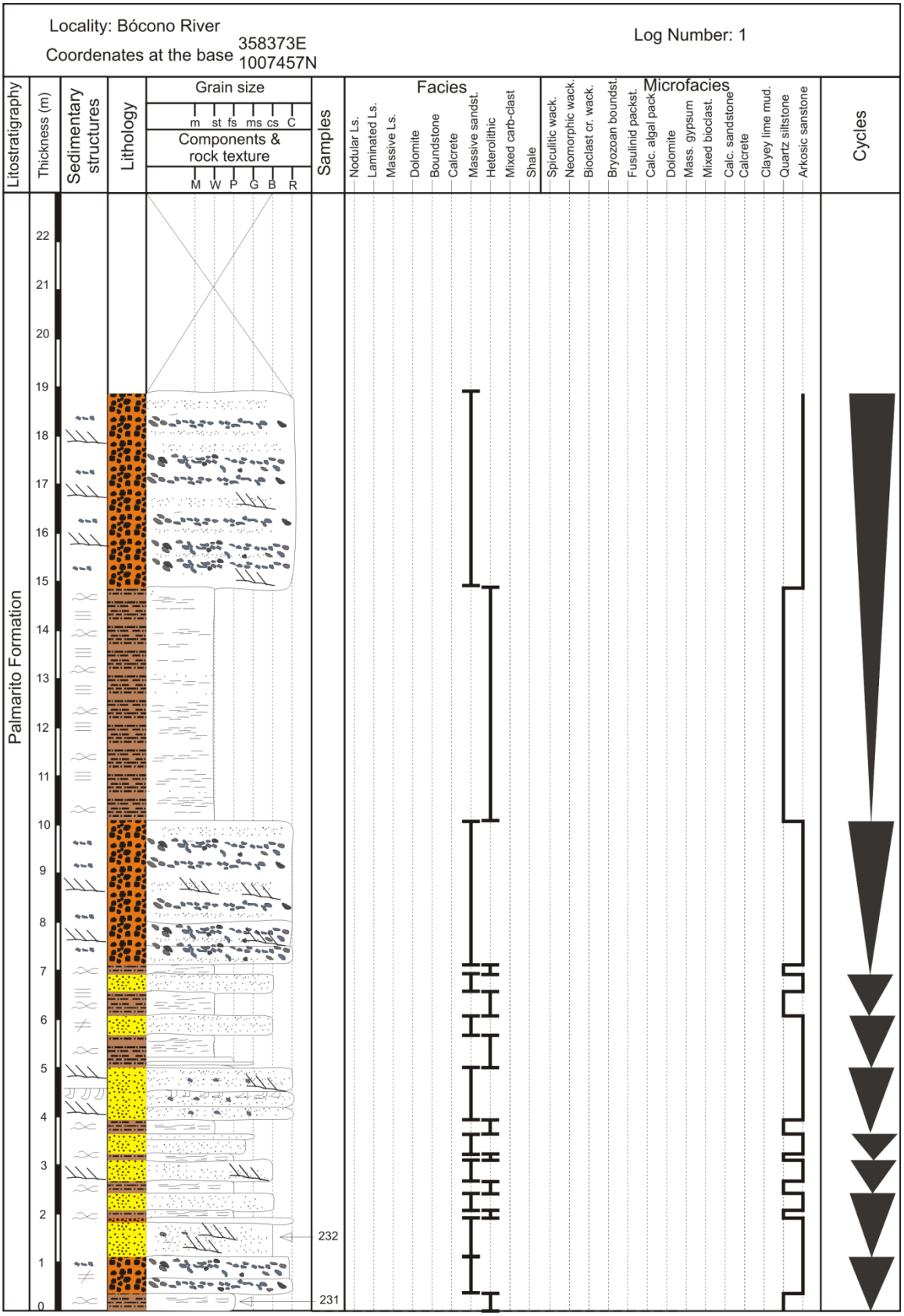
Locality: Bócono River
Coordenates at the base 358373E 1007457N
Log Number: 1
Litostratigraphy
Thickness (m)
Sedimentary structures
Lithology
Grain size
m st fs ms cs C
Components & rock texture
M W P G B R
Samples
Facies
Nodular Ls.
Laminated Ls.
Massive Ls.
Dolomite
Boundstone
Calcrete
Massive sandst.
Heterolithic
Mixed carb-clast
Shale
Microfacies
Spiculitic wack.
Neomorphic wack.
Bioclast cr. wack.
Bryozoan boundst.
Fusulinid packst.
Calc. algal pack
Dolomite
Mass. gypsum
Mixed bioclast.
Calc. sandstone
Calcrete
Clayey lime mud.
Quartz siltstone
Arkosic sanstone
Cycles
Palmarito Formation
0
1
2
3
4
5
6
7
8
9
10
11
12
13
14
15
16
17
18
19
20
21
22
232
231

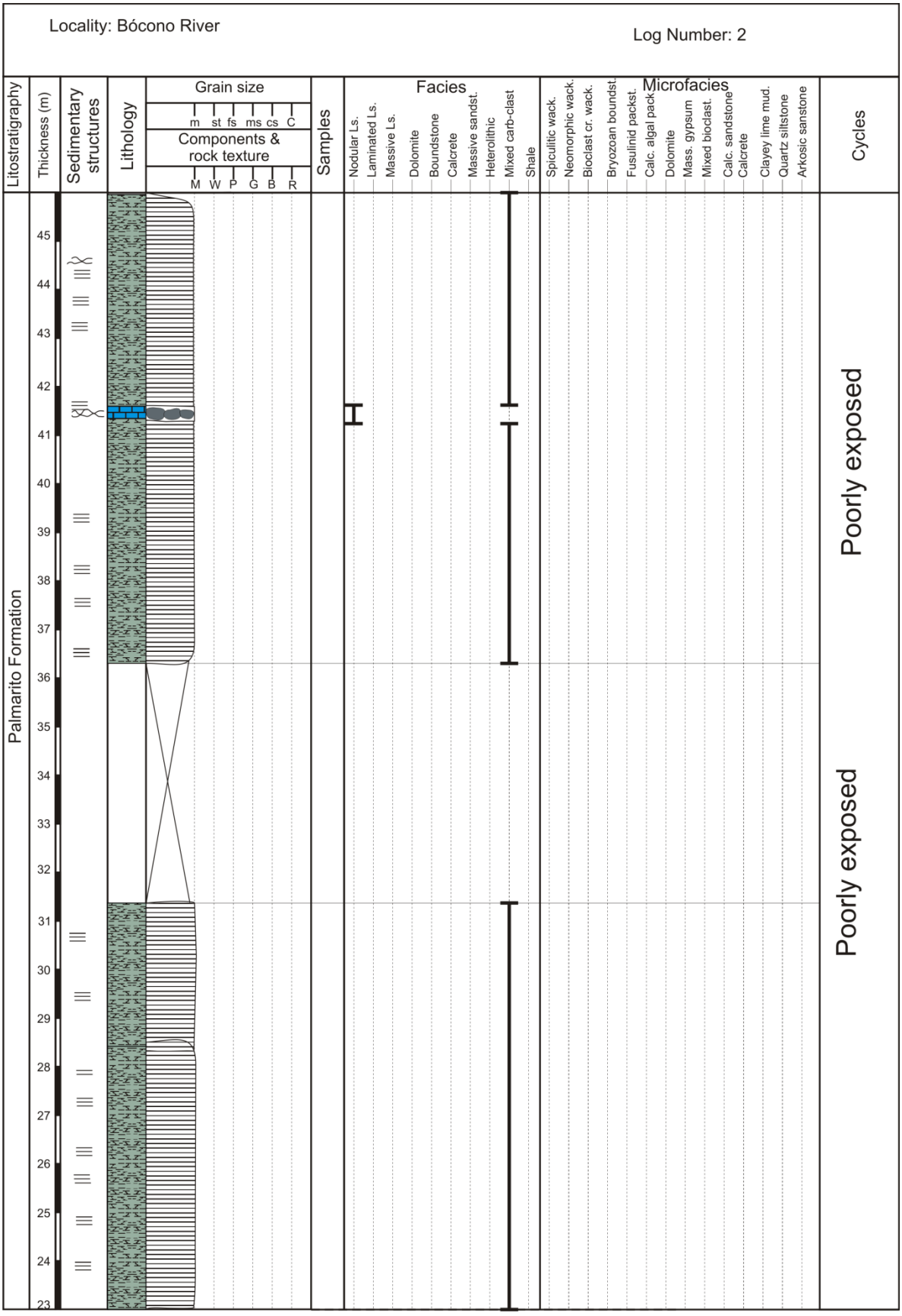
Locality: Bócono River
Log Number: 2
Litostratigraphy
Thickness (m)
Sedimentary structures
Lithology
Grain size
m st fs ms cs C
Components & rock texture
M W P G B R
Samples
Facies
Nodular Ls.
Laminated Ls.
Massive Ls.
Dolomite
Boundstone
Calcrete
Massive sandst.
Heterolithic
Mixed carb-clast
Shale
Microfacies
Spiculitic wack.
Neomorphic wack.
Bioclast cr. wack.
Bryozoan boundst.
Fusulinid packst.
Calc. algal pack.
Dolomite
Mass. gypsum
Mixed bioclast.
Calc. sandstone
Calcrete
Clayey lime mud.
Quartz siltstone
Arkosic sanstone
Cycles
Palmarito Formation
45
44
43
42
41
40
39
38
37
36
35
34
33
32
31
30
29
28
27
26
25
24
23
Poorly exposed
Poorly exposed

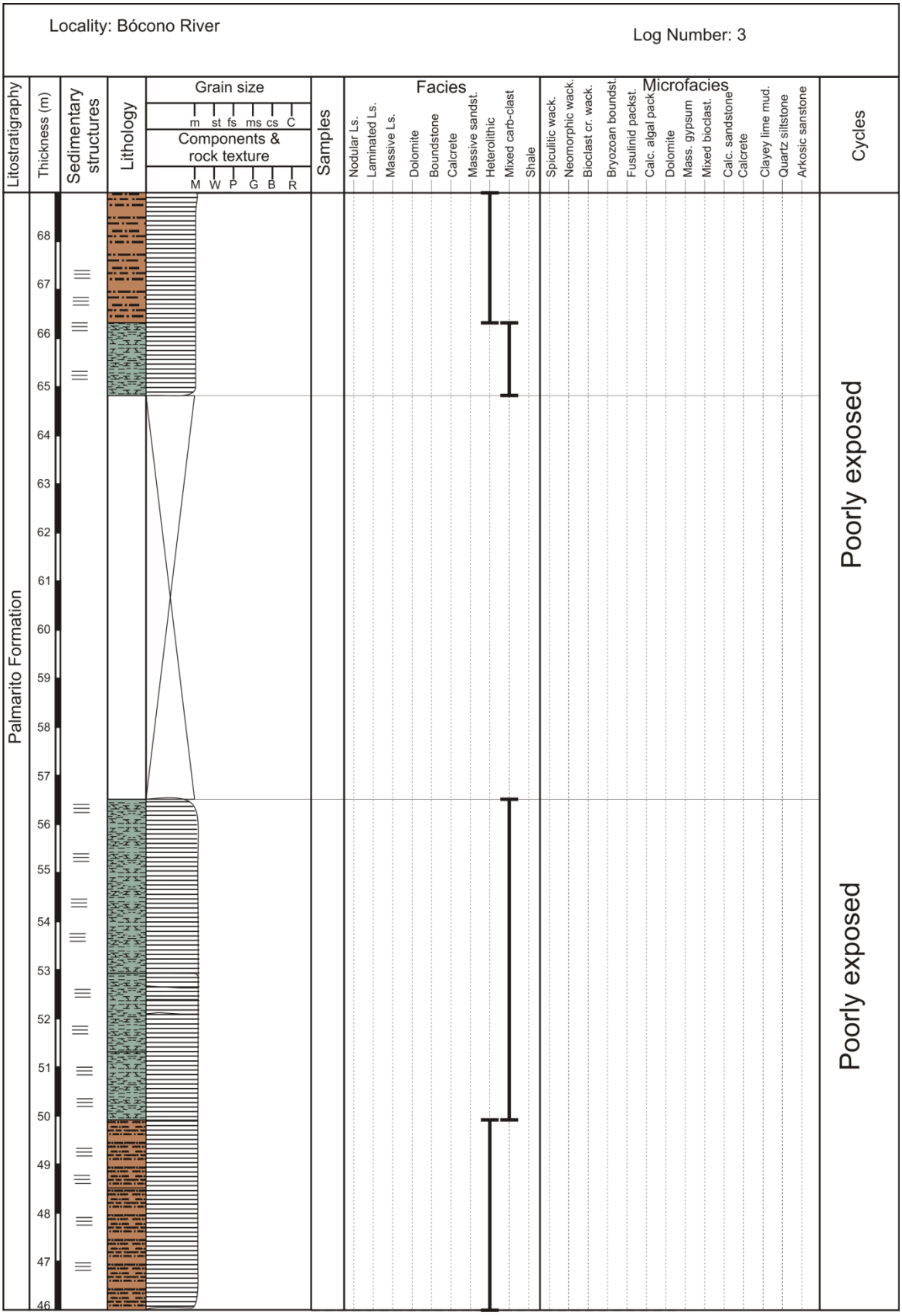
Locality: Bócono River
Log Number: 3
Litostratigraphy
Thickness (m)
Sedimentary structures
Lithology
Grain size
m st fs ms cs C
Components & rock texture
M W P G B R
Samples
Facies
Nodular Ls.
Laminated Ls.
Massive Ls.
Dolomite
Boundstone
Calcrete
Massive sandst.
Heterolithic
Mixed carb-clast
Shale
Microfacies
Spiculitic wack.
Neomorphic wack.
Bioclast cr. wack.
Bryozoan boundst.
Fusulinid packst.
Calc. algal pack.
Dolomite
Mass. gypsum
Mixed bioclast.
Calc. sandstone
Calcrete
Clayey lime mud.
Quartz siltstone
Arkosic sanstone
Cycles
Palmarito Formation
68
67
66
65
64
63
62
61
60
59
58
57
56
55
54
53
52
51
50
49
48
47
46
Poorly exposed
Poorly exposed

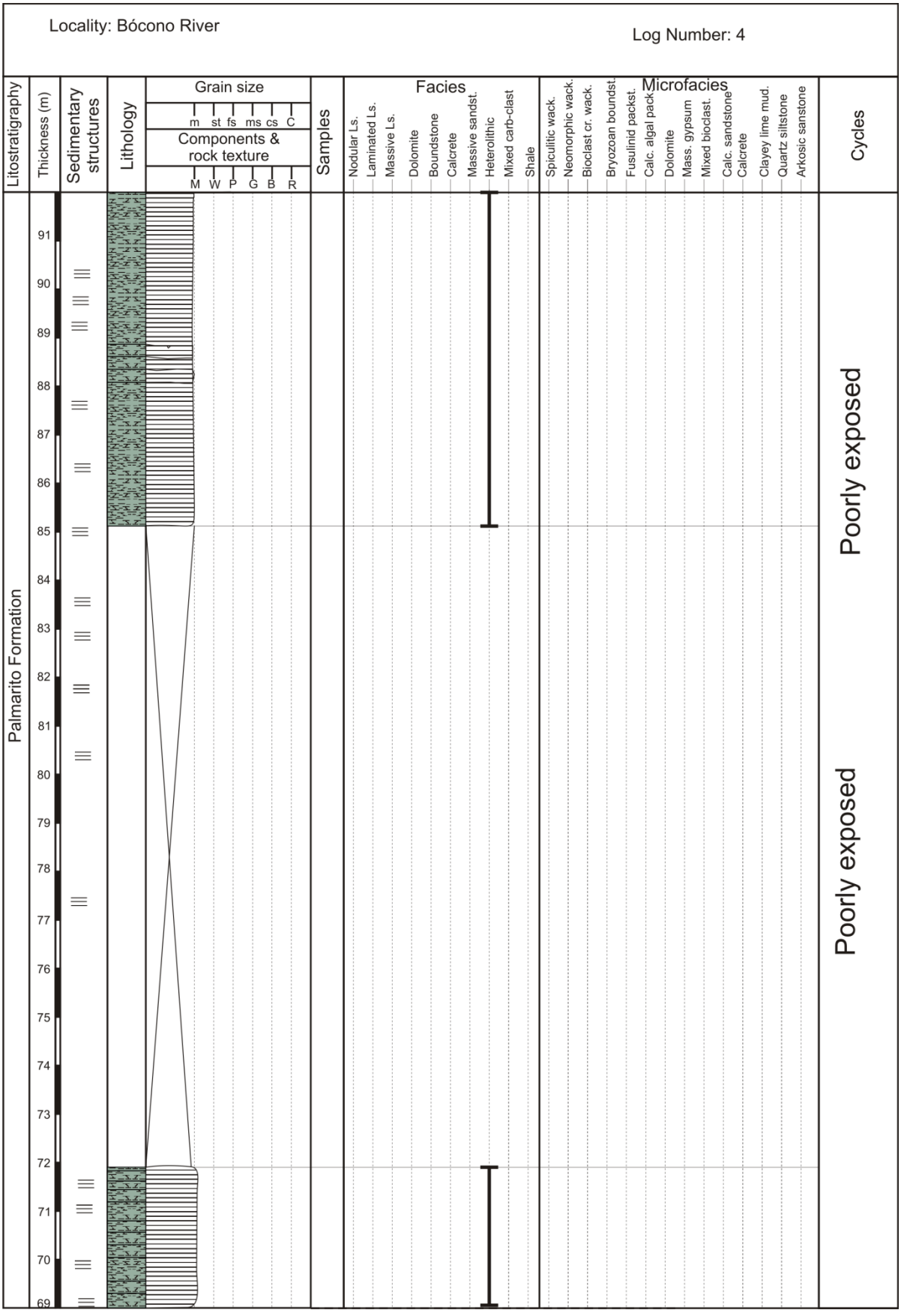
Locality: Bócono River
Log Number: 4
Litostratigraphy
Thickness (m)
Sedimentary structures
Lithology
Grain size
m st fs ms cs C
Components & rock texture
M W P G B R
Samples
Facies
Nodular Ls.
Laminated Ls.
Massive Ls.
Dolomite
Boundstone
Calcrete
Massive sandst.
Heterolithic
Mixed carb-clast
Shale
Microfacies
Spiculitic wack.
Neomorphic wack.
Bioclast cr. wack.
Bryozoan boundst.
Fusulinid packst.
Calc. algal packst.
Dolomite
Mass. gypsum
Mixed bioclast.
Calc. sandstone
Calcrete
Clayey lime mud.
Quartz siltstone
Arkosic sanstone
Cycles
Palmarito Formation
91
90
89
88
87
86
85
84
83
82
81
80
79
78
77
76
75
74
73
72
71
70
69
Poorly exposed
Poorly exposed

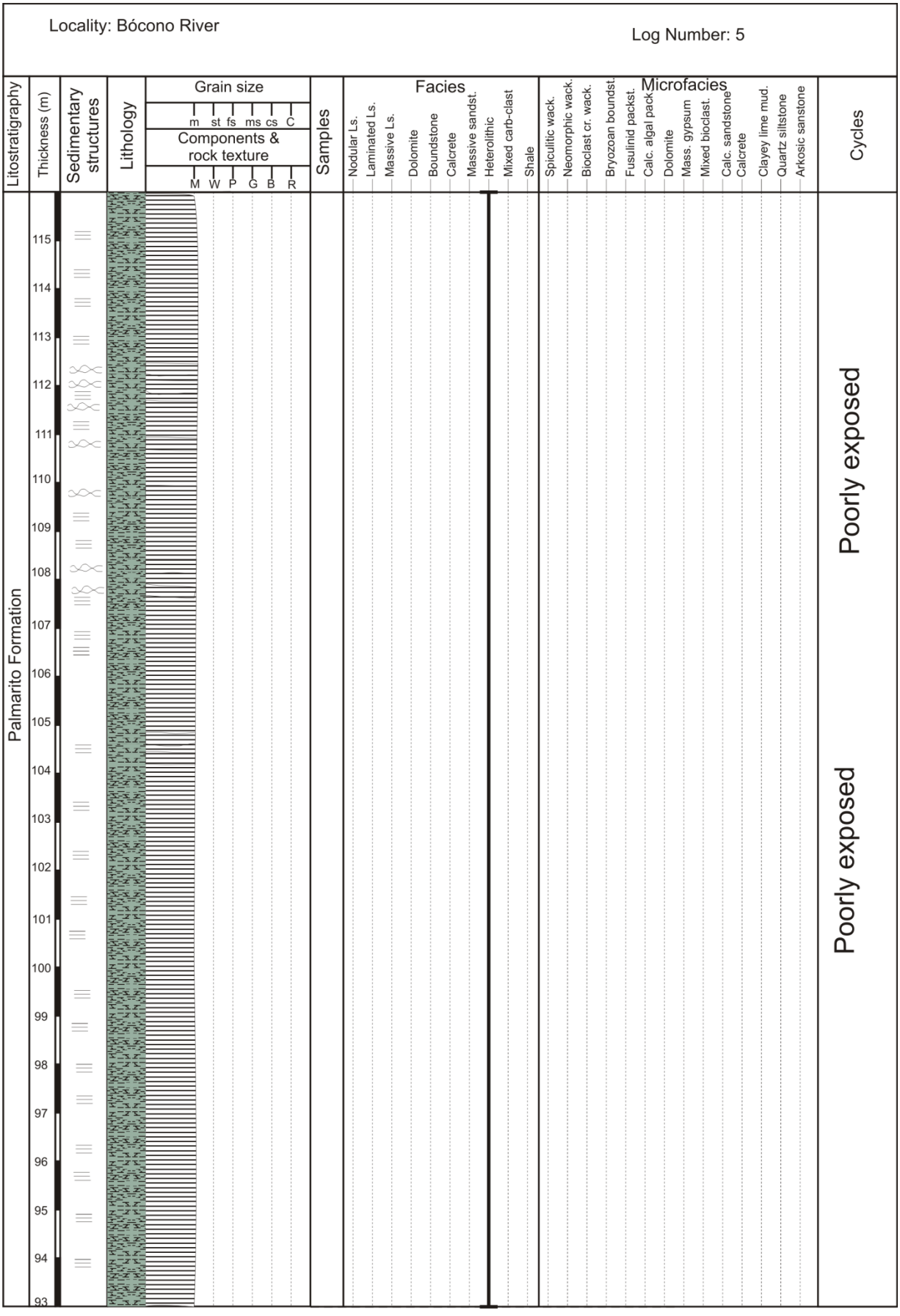
Locality: Bócono River
Log Number: 5
Litostratigraphy
Thickness (m)
Sedimentary structures
Lithology
Grain size
m st fs ms cs C
Components & rock texture
M W P G B R
Samples
Facies
Nodular Ls.
Laminated Ls.
Massive Ls.
Dolomite
Boundstone
Calcrete
Massive sandst.
Heterolithic
Mixed carb-clast
Shale
Microfacies
Spiculitic wack.
Neomorphic wack.
Bioclast cr. wack.
Bryozoan boundst.
Fusulinid packst.
Calc. algal pack.
Dolomite
Mass. gypsum
Mixed bioclast.
Calc. sandstone
Calcrete
Clayey lime mud.
Quartz siltstone
Arkosic sanstone
Cycles
Palmarito Formation
115
114
113
112
111
110
109
108
107
106
105
104
103
102
101
100
99
98
97
96
95
94
93
Poorly exposed
Poorly exposed

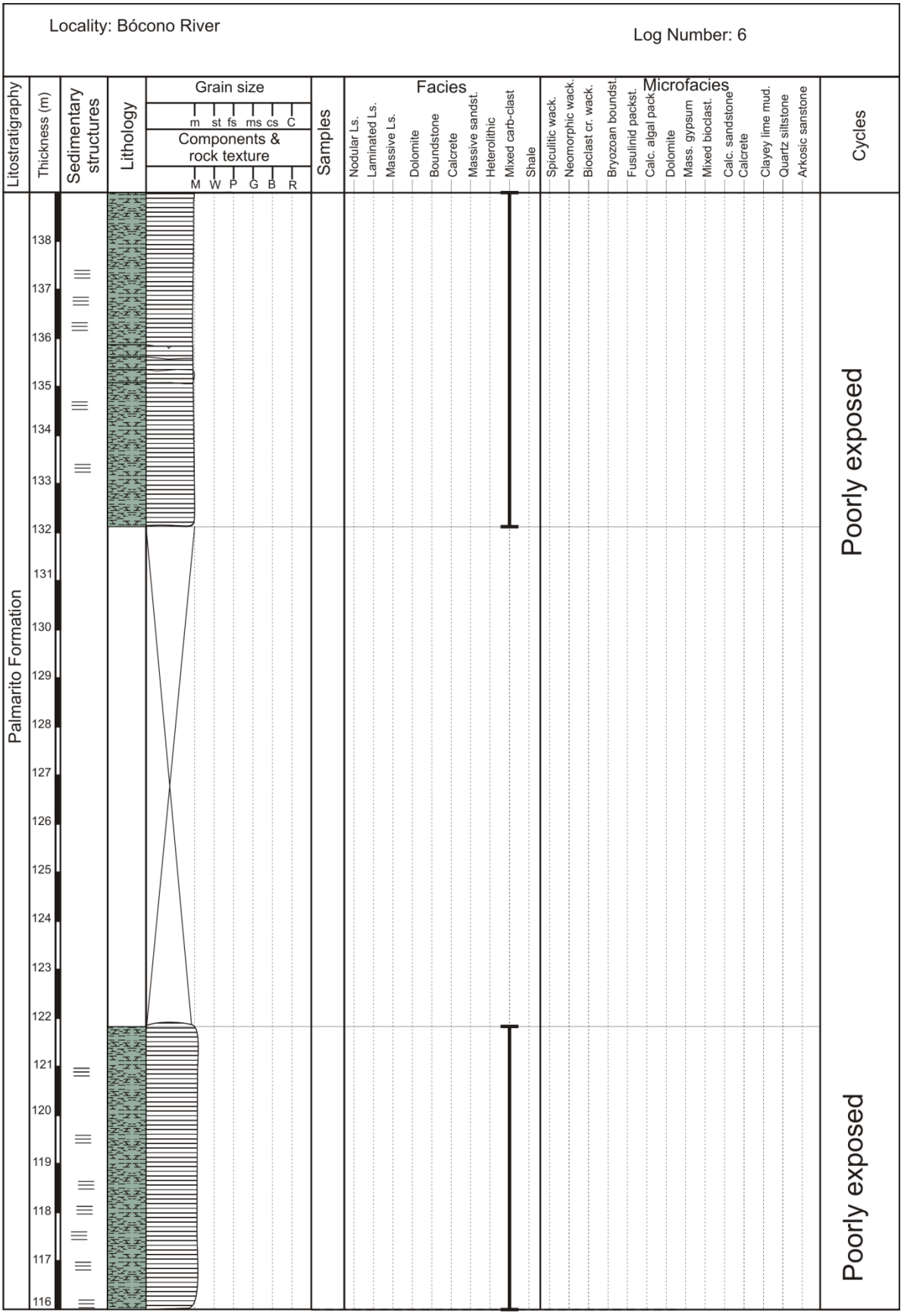
Locality: Bócono River
Log Number: 6
Litostratigraphy
Thickness (m)
Sedimentary structures
Lithology
Grain size
m st fs ms cs C
Components & rock texture
M W P G B R
Samples
Facies
Nodular Ls.
Laminated Ls.
Massive Ls.
Dolomite
Boundstone
Calcrete
Massive sandst.
Heterolithic
Mixed carb-clast
Shale
Microfacies
Spiculitic wack.
Neomorphic wack.
Bioclast cr. wack.
Bryozoan boundst.
Fusulinid packst.
Calc. algal pack.
Dolomite
Mass. gypsum
Mixed bioclast.
Calc. sandstone
Calcrete
Clayey lime mud.
Quartz siltstone
Arkosic sanstone
Cycles
Palmarito Formation
138
137
136
135
134
133
132
131
130
129
128
127
126
125
124
123
122
121
120
119
118
117
116
Poorly exposed
Poorly exposed

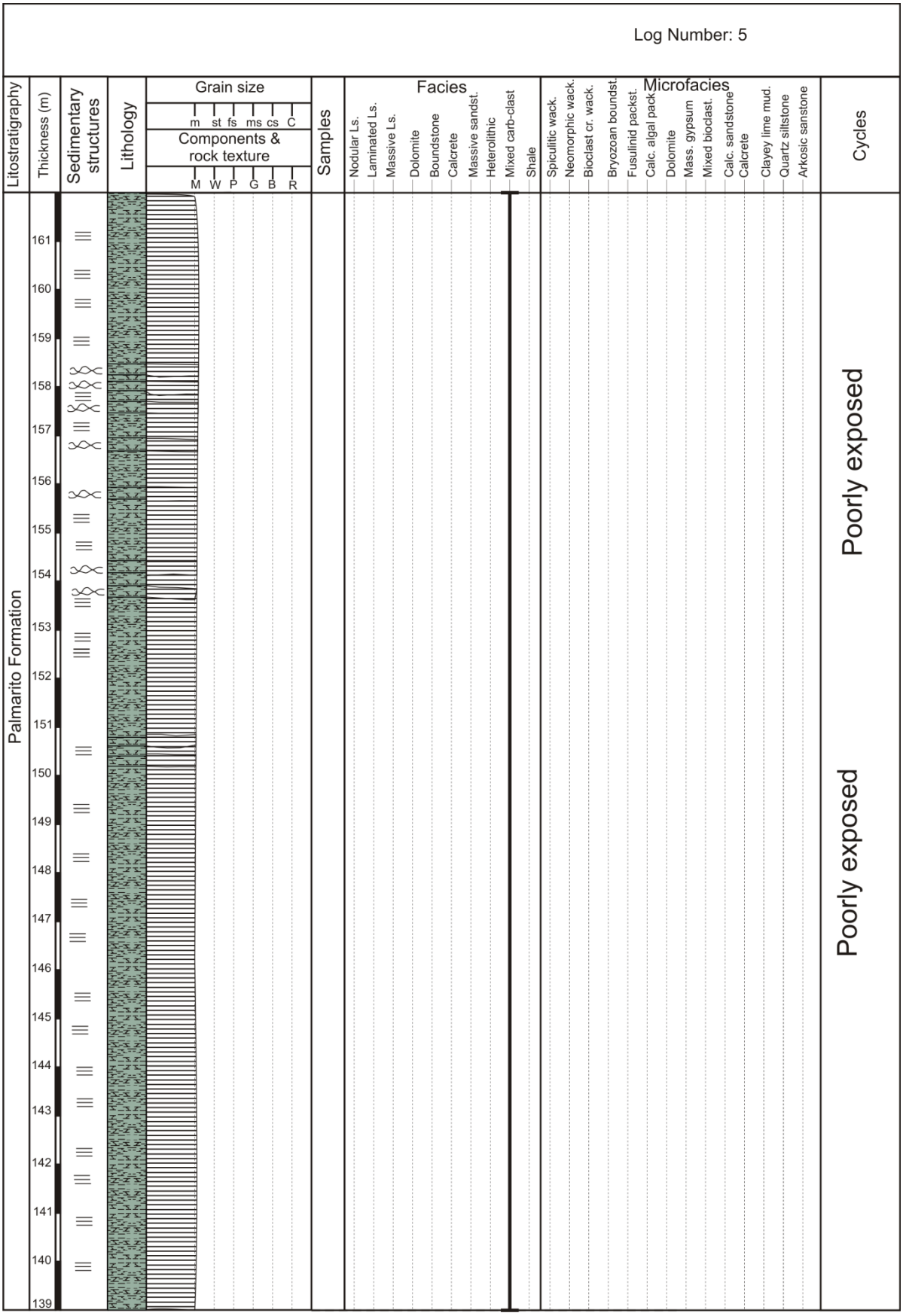
Log Number: 5
Litostratigraphy
Thickness (m)
Sedimentary structures
Lithology
Grain size
m st fs ms cs C
Components & rock texture
M W P G B R
Samples
Facies
Nodular Ls.
Laminated Ls.
Massive Ls.
Dolomite
Boundstone
Calcrete
Massive sandst.
Heterolithic
Mixed carb-clast
Shale
Microfacies
Spiculitic wack.
Neomorphic wack.
Bioclast cr. wack.
Bryozoan boundst.
Fusulinid packst.
Calc. algal pack
Dolomite
Mass. gypsum
Mixed bioclast.
Calc. sandstone
Calcrete
Clayey lime mud.
Quartz siltstone
Arkosic sanstone
Cycles
Palmarito Formation
161
160
159
158
157
156
155
154
153
152
151
150
149
148
147
146
145
144
143
142
141
140
139
Poorly exposed
Poorly exposed

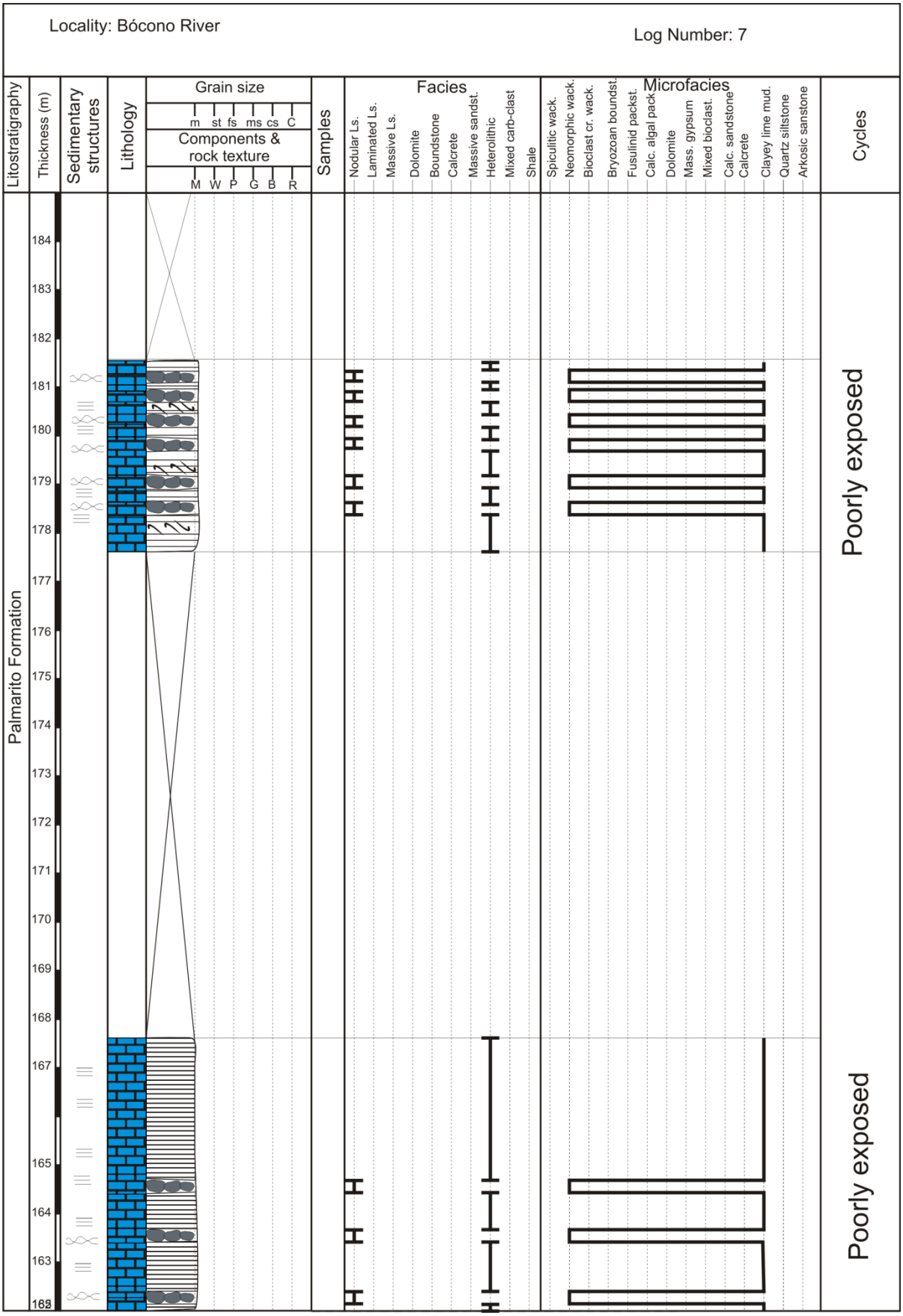
Locality: Bócono River
Log Number: 7
Litostratigraphy
Thickness (m)
Sedimentary structures
Lithology
Grain size
m st fs ms cs C
Components & rock texture
M W P G B R
Samples
Facies
Nodular Ls.
Laminated Ls.
Massive Ls.
Dolomite
Boundstone
Calcrete
Massive sandst.
Heterolithic
Mixed carb-clast
Shale
Microfacies
Spiculitic wack.
Neomorphic wack.
Bioclast cr. wack.
Bryozoan boundst.
Fusulinid packst.
Calc. algal pack.
Dolomite
Mass. gypsum
Mixed bioclast.
Calc. sandstone
Calcrete
Clayey lime mud.
Quartz siltstone
Arkosic sanstone
Cycles
Palmarito Formation
184
183
182
181
180
179
178
177
176
175
174
173
172
171
170
169
168
167
165
164
163
Poorly exposed
Poorly exposed

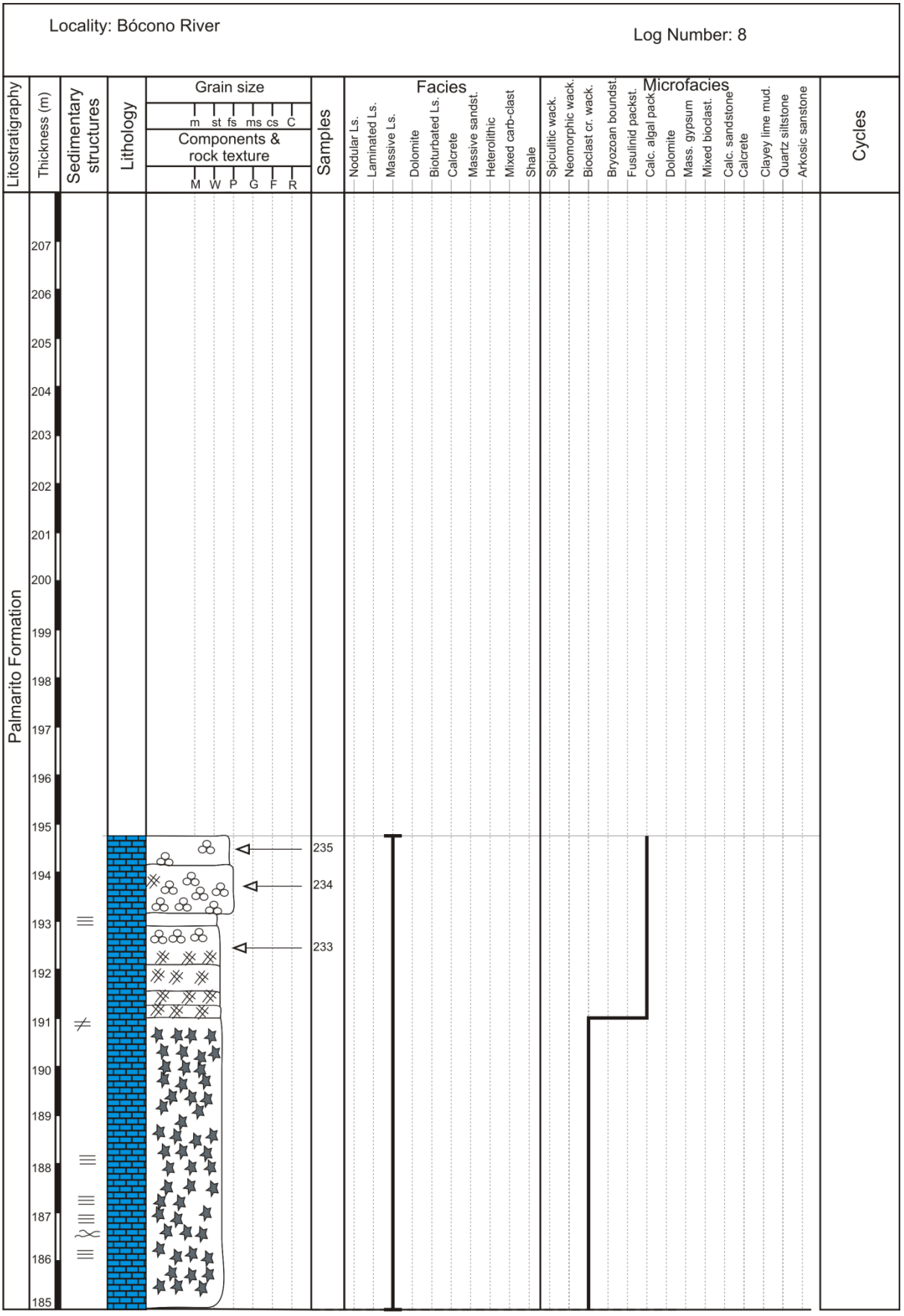
Locality: Bócono River
Log Number: 8
Litostratigraphy
Thickness (m)
Sedimentary structures
Lithology
Grain size
m st fs ms cs C
Components & rock texture
M W P G F R
Samples
Facies
Nodular Ls.
Laminated Ls.
Massive Ls.
Dolomite
Bioturbated Ls.
Calcrete
Massive sandst.
Heterolithic
Mixed carb-clast
Shale
Microfacies
Spiculitic wack.
Neomorphic wack.
Bioclast cr. wack.
Bryozoan boundst.
Fusulinid packst.
Calc. algal pack.
Dolomite
Mass. gypsum
Mixed bioclast.
Calc. sandstone
Calcrete
Clayey lime mud.
Quartz siltstone
Arkosic sanstone
Cycles
Palmarito Formation
207
206
205
204
203
202
201
200
199
198
197
196
195
194
193
192
191
190
189
188
187
186
185
235
234
233

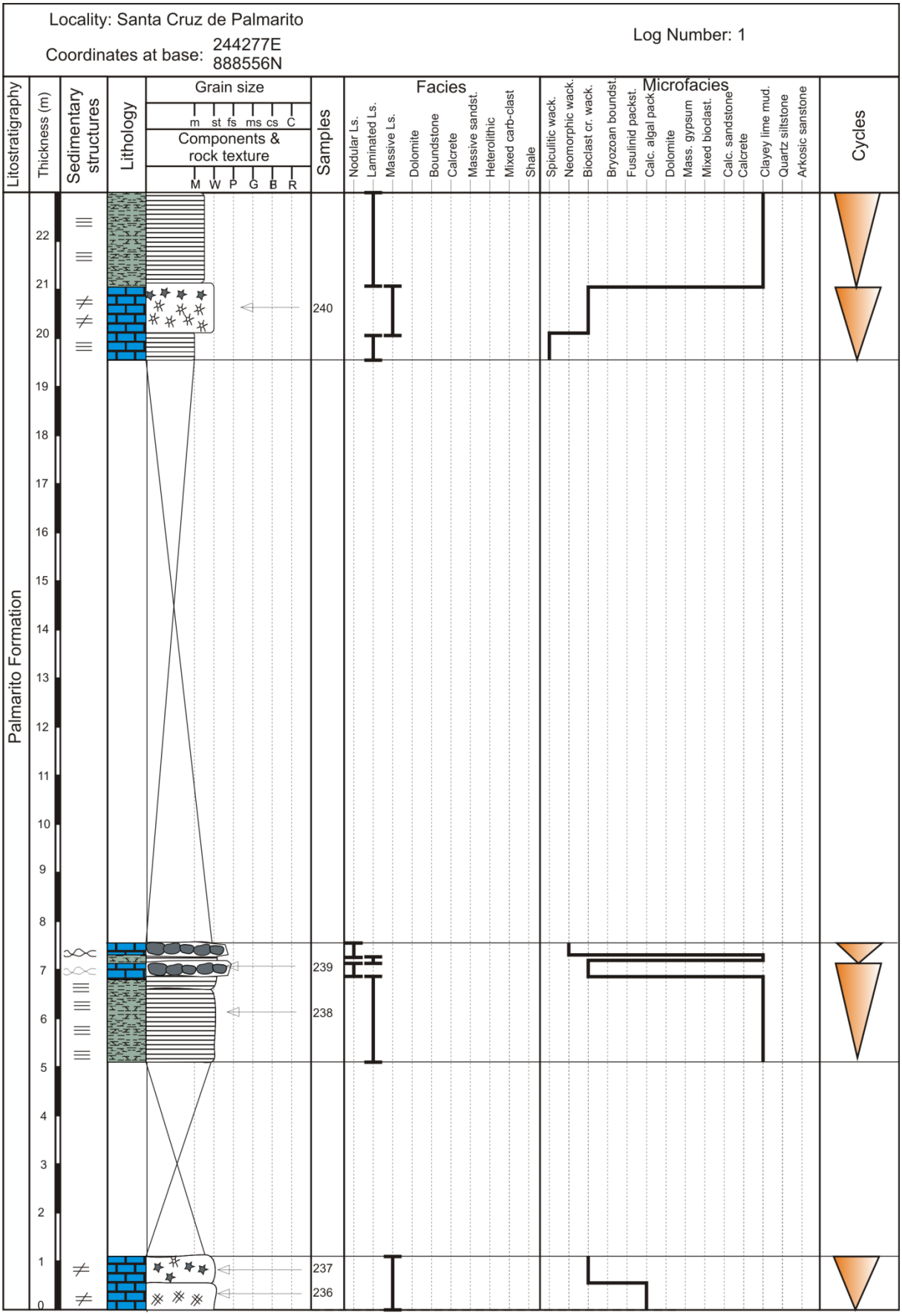
Locality: Santa Cruz de Palmarito
Coordinates at base: 244277E 888556N
Log Number: 1
Litostratigraphy
Thickness (m)
Sedimentary structures
Lithology
Grain size
m st fs ms cs C
Components & rock texture
M W P G B R
Samples
Facies
Nodular Ls.
Laminated Ls.
Massive Ls.
Dolomite
Boundstone
Calcrete
Massive sandst.
Heterolithic
Mixed carb-clast
Shale
Microfacies
Spiculitic wack.
Neomorphic wack.
Bioclast cr. wack.
Bryozoan boundst.
Fusulinid packst.
Calc. algal pack.
Dolomite
Mass. gypsum
Mixed bioclast.
Calc. sandstone
Calcrete
Clayey lime mud.
Quartz siltstone
Arkosic sanstone
Cycles
Palmarito Formation
240
239
238
237
236

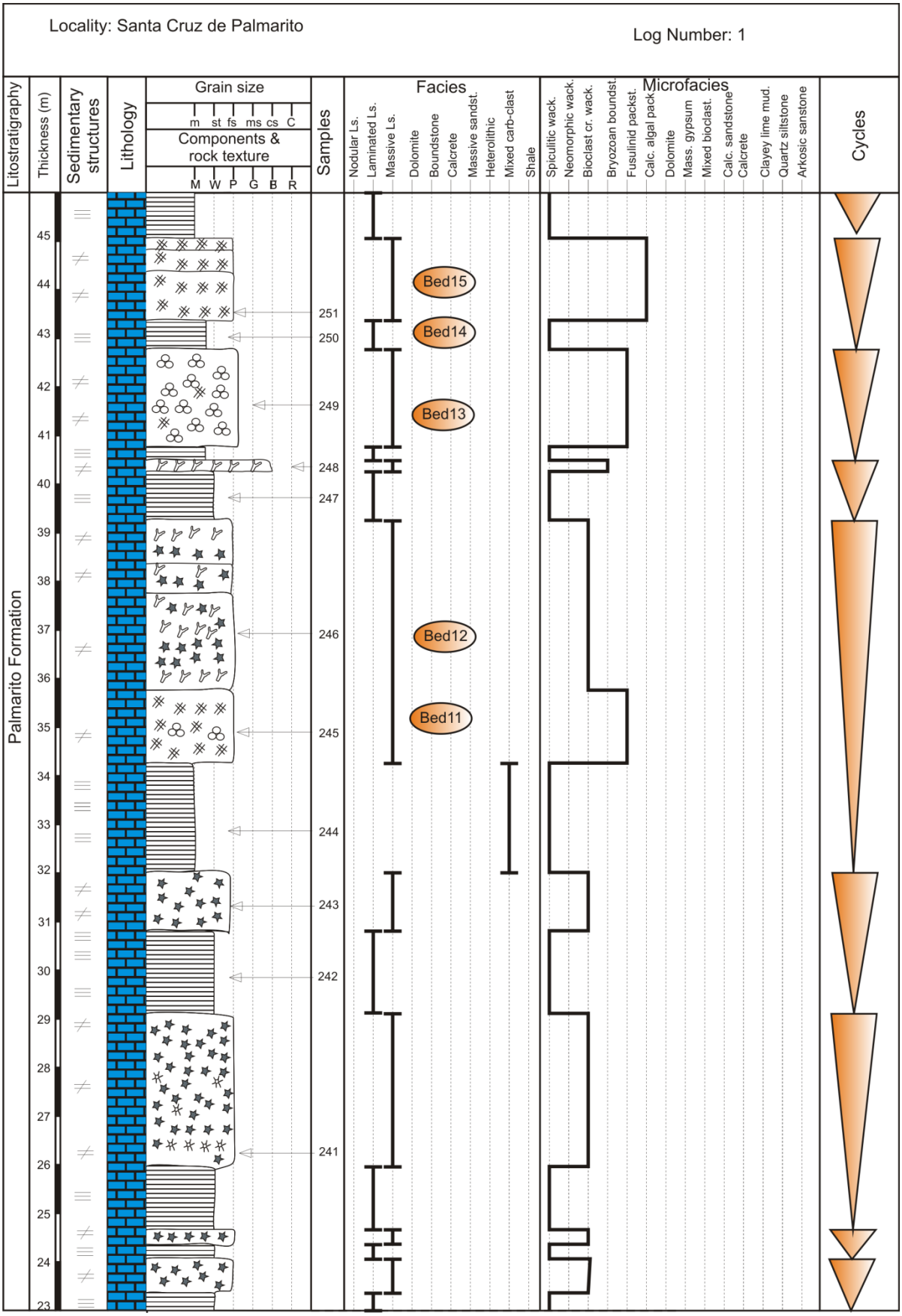
Locality: Santa Cruz de Palmarito
Log Number: 1
Litostratigraphy
Thickness (m)
Sedimentary structures
Lithology
Grain size
m st fs ms cs C
Components & rock texture
M W P G B R
Samples
Facies
Nodular Ls.
Laminated Ls.
Massive Ls.
Dolomite
Boundstone
Calcrete
Massive sandst.
Heterolithic
Mixed carb-clast
Shale
Microfacies
Spiculitic wack.
Neomorphic wack.
Bioclast cr. wack.
Bryozoan boundst.
Fusulinid packst.
Calc. algal pack.
Dolomite
Mass. gypsum
Mixed bioclast.
Calc. sandstone
Calcrete
Clayey lime mud.
Quartz siltstone
Arkosic sanstone
Cycles
Palmarito Formation
45
44
43
42
41
40
39
38
37
36
35
34
33
32
31
30
29
28
27
26
25
24
23
251
250
249
248
247
246
245
244
243
242
241
Bed15
Bed14
Bed13
Bed12
Bed11

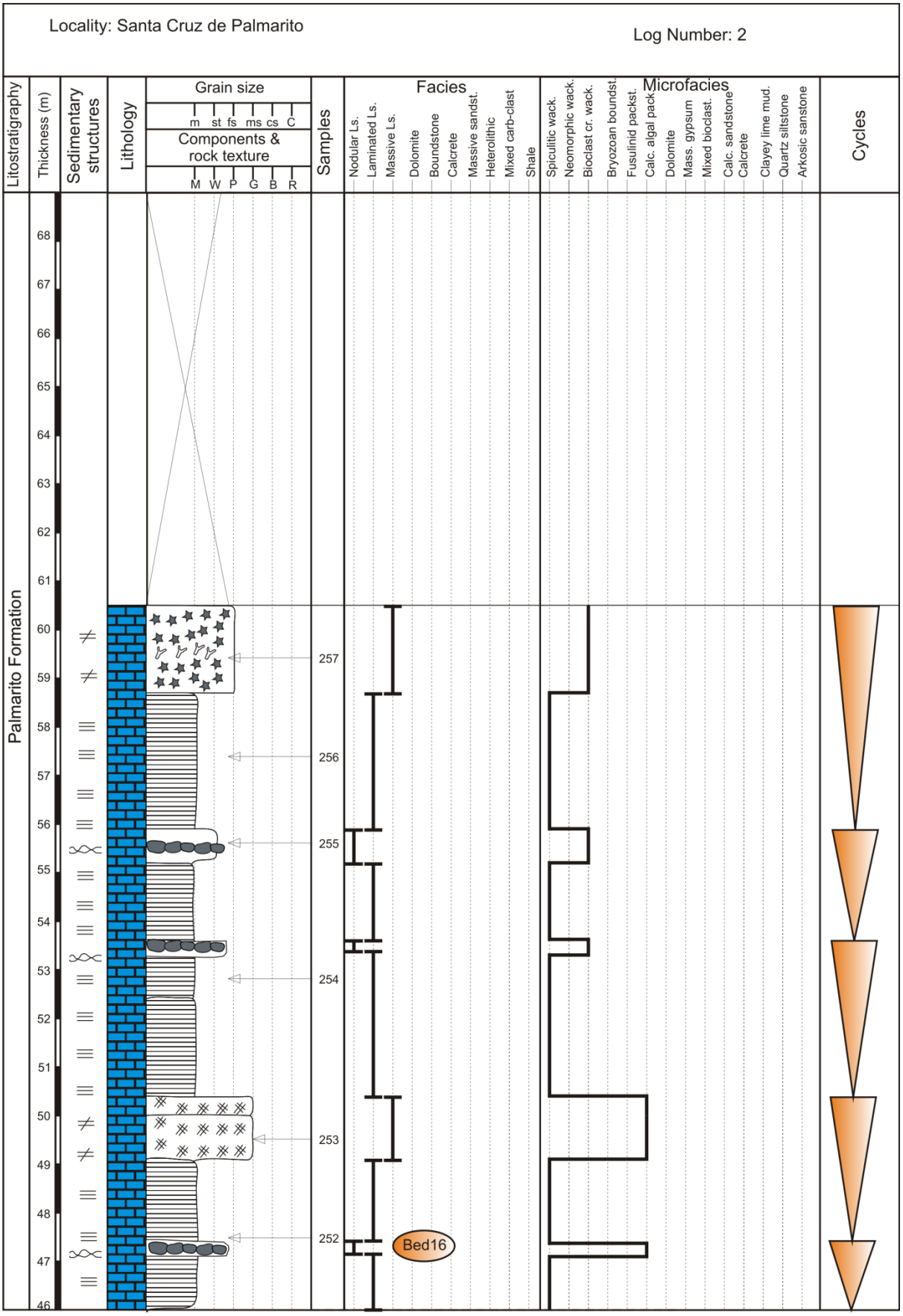
Locality: Santa Cruz de Palmarito
Log Number: 2
Litostratigraphy
Thickness (m)
Sedimentary structures
Lithology
Grain size
m st fs ms cs C
Components & rock texture
M W P G B R
Samples
Facies
Nodular Ls.
Laminated Ls.
Massive Ls.
Dolomite
Boundstone
Calcrete
Massive sandst.
Heterolithic
Mixed carb-clast
Shale
Microfacies
Spiculitic wack.
Neomorphic wack.
Bioclast cr. wack.
Bryozoan boundst.
Fusulinid packst.
Calc. algal pack.
Dolomite
Mass. gypsum
Mixed bioclast.
Calc. sandstone
Calcrete
Clayey lime mud.
Quartz siltstone
Arkosic sanstone
Cycles
Palmarito Formation
68
67
66
65
64
63
62
61
60
59
58
57
56
55
54
53
52
51
50
49
48
47
46
257
256
255
254
253
252
Bed16

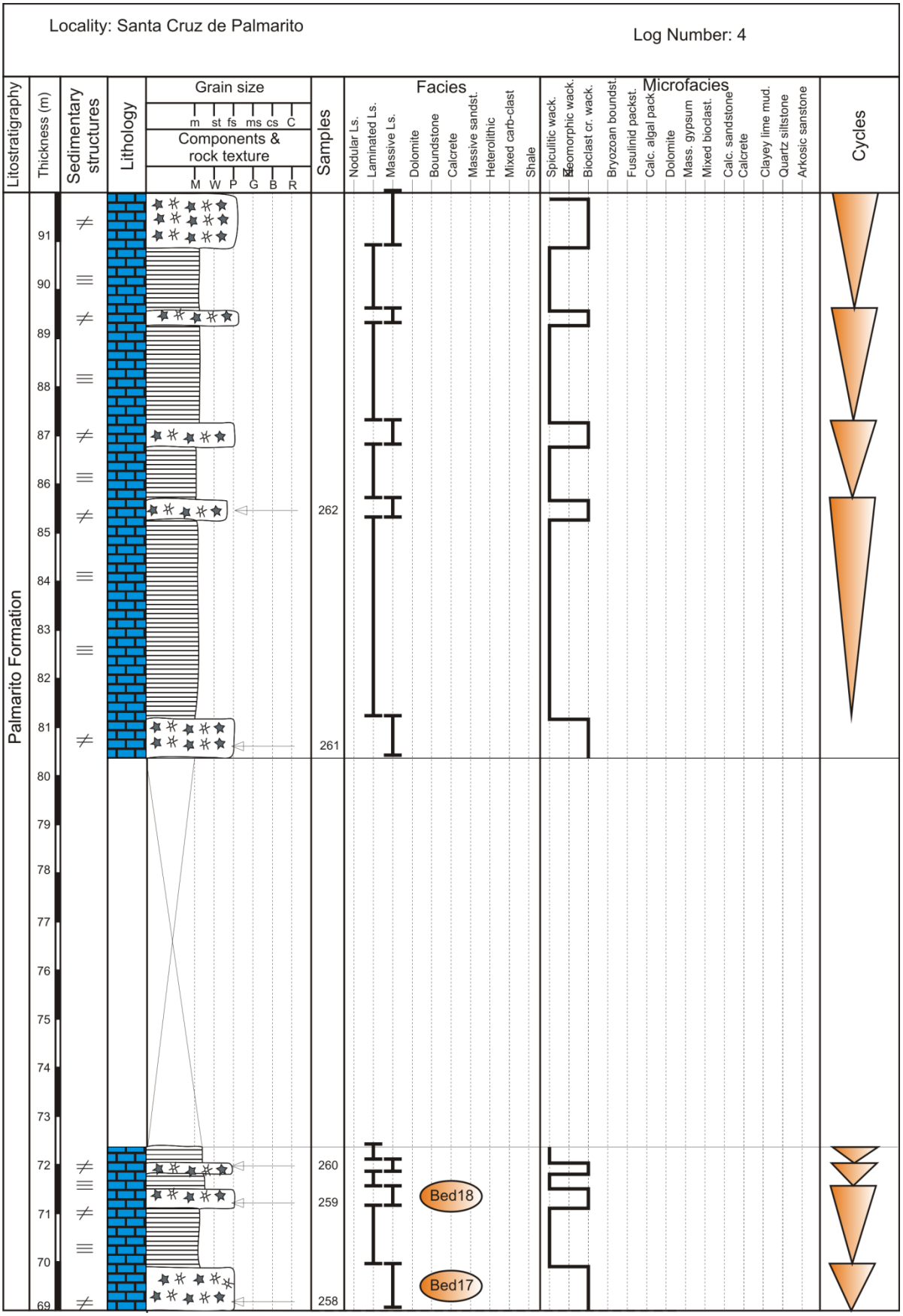
Locality: Santa Cruz de Palmarito
Log Number: 4
Litostratigraphy
Thickness (m)
Sedimentary structures
Lithology
Grain size
m st fs ms cs C
Components & rock texture
M W P G B R
Samples
Facies
Nodular Ls.
Laminated Ls.
Massive Ls.
Dolomite
Boundstone
Calcrete
Massive sandst.
Heterolithic
Mixed carb-clast
Shale
Microfacies
Spiculitic wack.
Recrystallized wack.
Bioclast cr. wack.
Bryozoan boundst.
Fusulinid packst.
Calc. algal pack.
Dolomite
Mass. gypsum
Mixed bioclast.
Calc. sandstone
Calcrete
Clayey lime mud.
Quartz siltstone
Arkosic sanstone
Cycles
Palmarito Formation
91
90
89
88
87
86
85
84
83
82
81
80
79
78
77
76
75
74
73
72
71
70
69
262
261
260
259
258
Bed18
Bed17

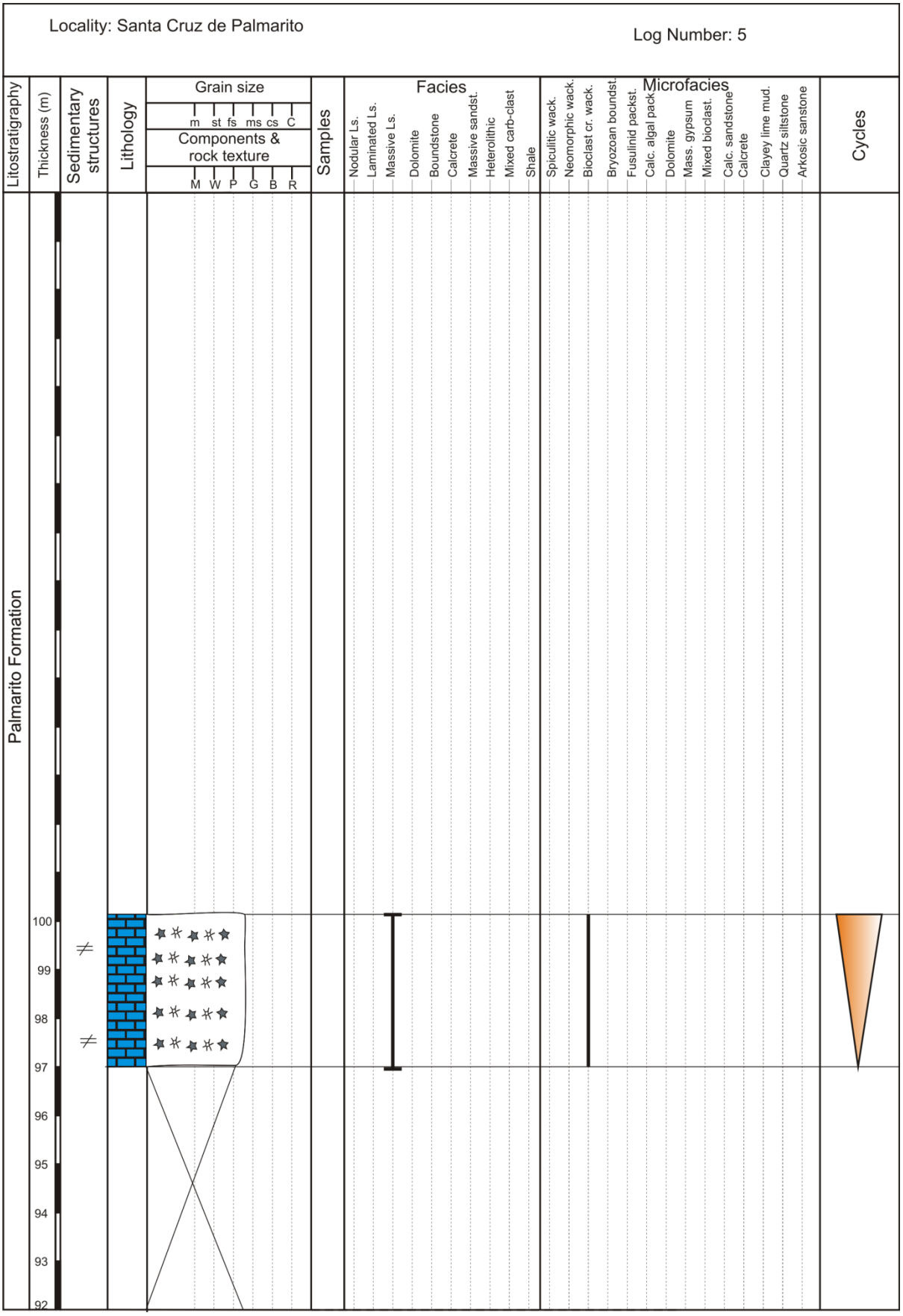
Locality: Santa Cruz de Palmarito
Log Number: 5
Litostratigraphy
Thickness (m)
Sedimentary structures
Lithology
Grain size
m st fs ms cs C
Components & rock texture
M W P G B R
Samples
Facies
Nodular Ls.
Laminated Ls.
Massive Ls.
Dolomite
Boundstone
Calcrete
Massive sandst.
Heterolithic
Mixed carb-clast
Shale
Microfacies
Spiculitic wack.
Neomorphic wack.
Bioclast cr. wack.
Bryozoan boundst.
Fusulinid packst.
Calc. algal pack.
Dolomite
Mass. gypsum
Mixed bioclast.
Calc. sandstone
Calcrete
Clayey lime mud.
Quartz siltstone
Arkosic sanstone
Cycles
Palmarito Formation
100
99
98
97
96
95
94
93
92

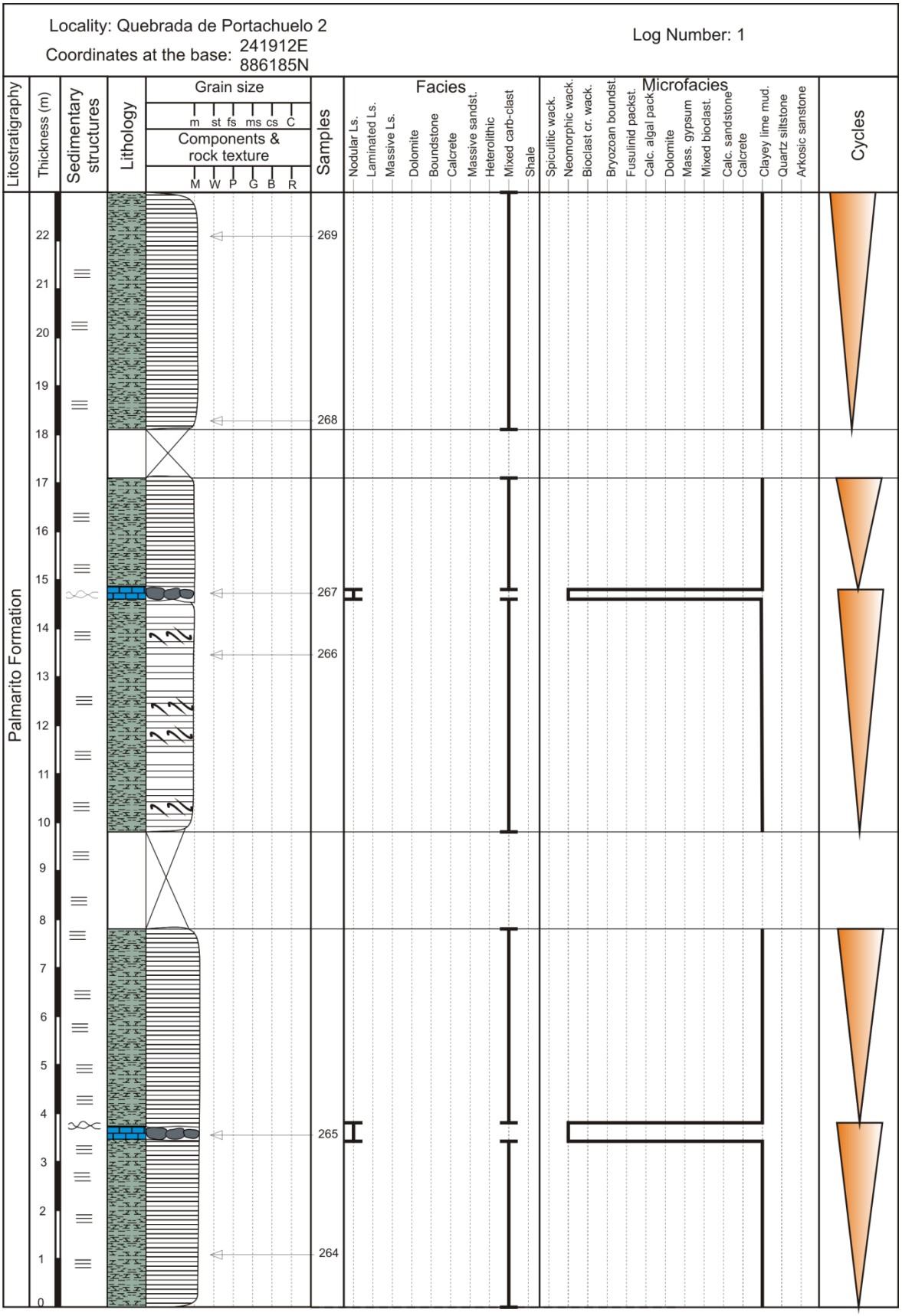
Locality: Quebrada de Portachuelo 2
Coordinates at the base: 241912E 886185N
Log Number: 1
Litostratigraphy
Thickness (m)
Sedimentary structures
Lithology
Grain size
m st fs ms cs C
Components & rock texture
M W P G B R
Samples
Facies
Nodular Ls.
Laminated Ls.
Massive Ls.
Dolomite
Boundstone
Calcrete
Massive sandst.
Heterolithic
Mixed carb-clast
Shale
Microfacies
Spiculitic wack.
Neomorphic wack.
Bioclast cr. wack.
Bryozoan boundst.
Fusulinid packst.
Calc. algal pack.
Dolomite
Mass. gypsum
Mixed bioclast.
Calc. sandstone
Calcrete
Clayey lime mud.
Quartz siltstone
Arkosic sanstone
Cycles
Palmarito Formation
269
268
267
266
265
264

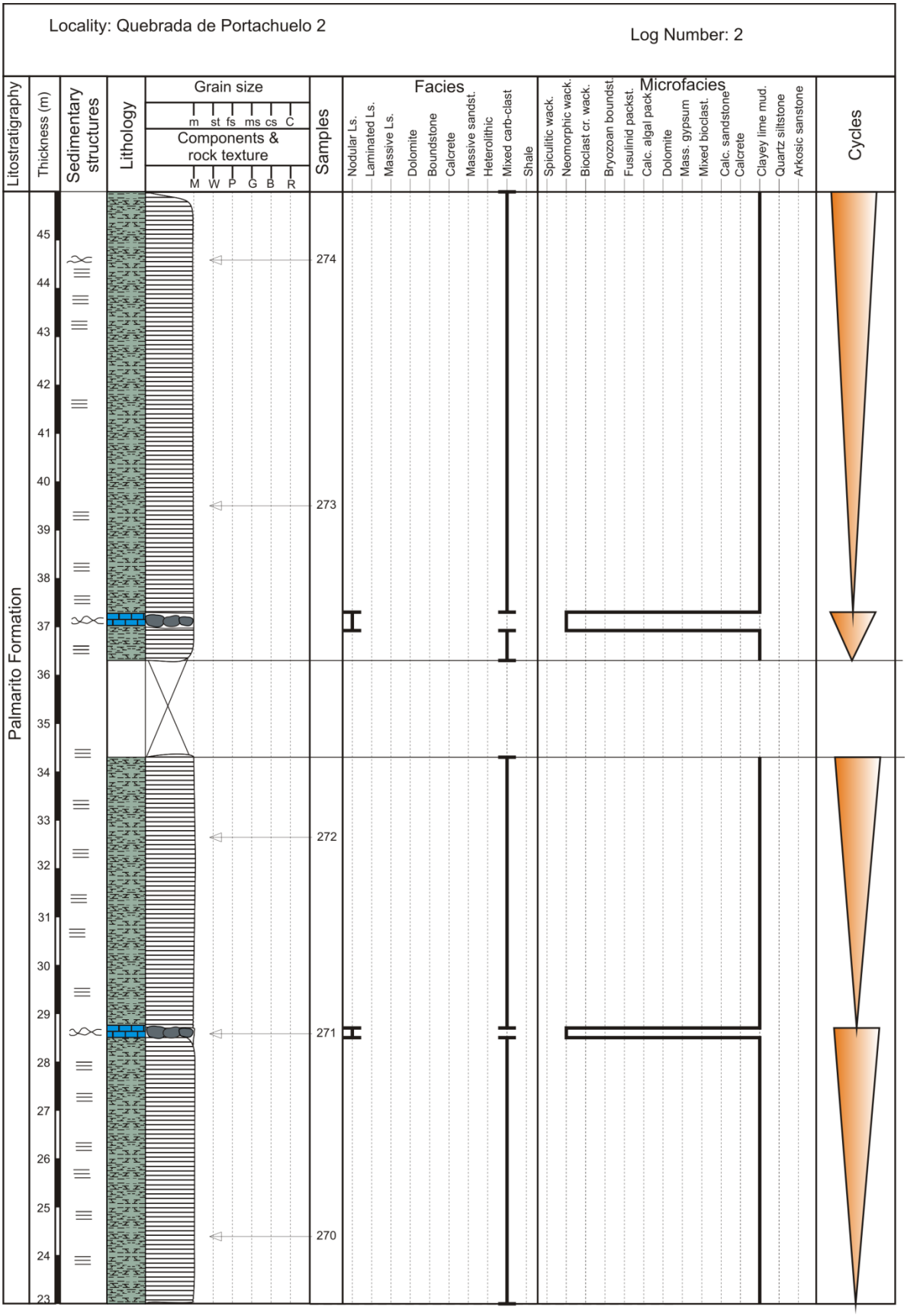
Locality: Quebrada de Portachuelo 2
Log Number: 2
Litostratigraphy
Thickness (m)
Sedimentary structures
Lithology
Grain size
m st fs ms cs C
Components & rock texture
M W P G B R
Samples
Facies
Nodular Ls.
Laminated Ls.
Massive Ls.
Dolomite
Boundstone
Calcrete
Massive sandst.
Heterolithic
Mixed carb-clast
Shale
Microfacies
Spiculitic wack.
Neomorphic wack.
Bioclast cr. wack.
Bryozoan boundst.
Fusulinid packst.
Calc. algal pack
Dolomite
Mass. gypsum
Mixed bioclast.
Calc. sandstone
Calcrete
Clayey lime mud.
Quartz siltstone
Arkosic sanstone
Cycles
Palmarito Formation
45
44
43
42
41
40
39
38
37
36
35
34
33
32
31
30
29
28
27
26
25
24
23
274
273
272
271
270

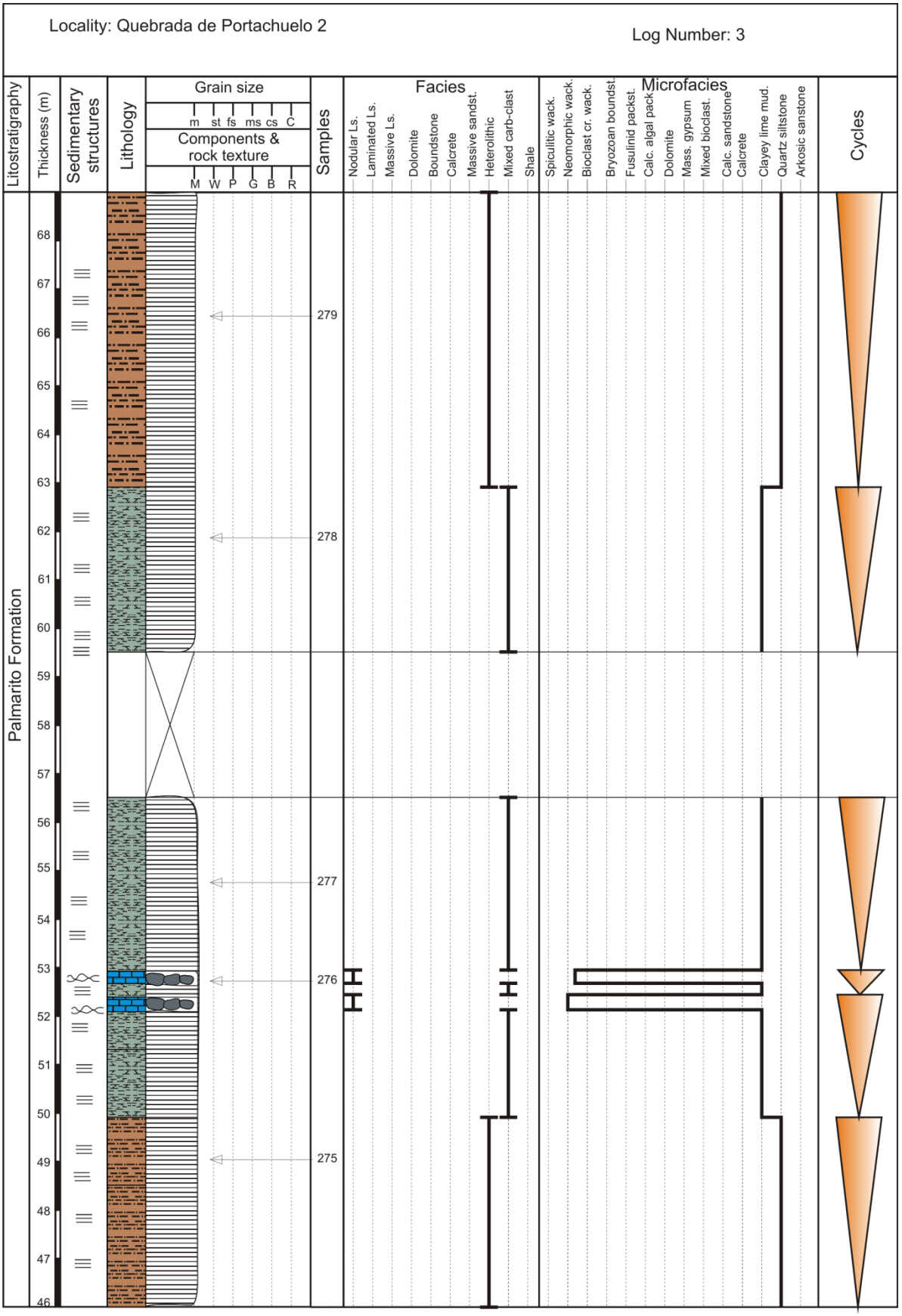
Locality: Quebrada de Portachuelo 2
Log Number: 3
Litostratigraphy
Thickness (m)
Sedimentary structures
Lithology
Grain size
m st fs ms cs C
Components & rock texture
M W P G B R
Samples
Facies
Nodular Ls.
Laminated Ls.
Massive Ls.
Dolomite
Boundstone
Calcrete
Massive sandst.
Heterolithic
Mixed carb-clast
Shale
Microfacies
Spiculitic wack.
Neomorphic wack.
Bioclast cr. wack.
Bryozoan boundst.
Fusulinid packst.
Calc. algal pack.
Dolomite
Mass. gypsum
Mixed bioclast.
Calc. sandstone
Calcrete
Clayey lime mud.
Quartz siltstone
Arkosic sanstone
Cycles
Palmarito Formation
68
67
66
65
64
63
62
61
60
59
58
57
56
55
54
53
52
51
50
49
48
47
46
279
278
277
276
275

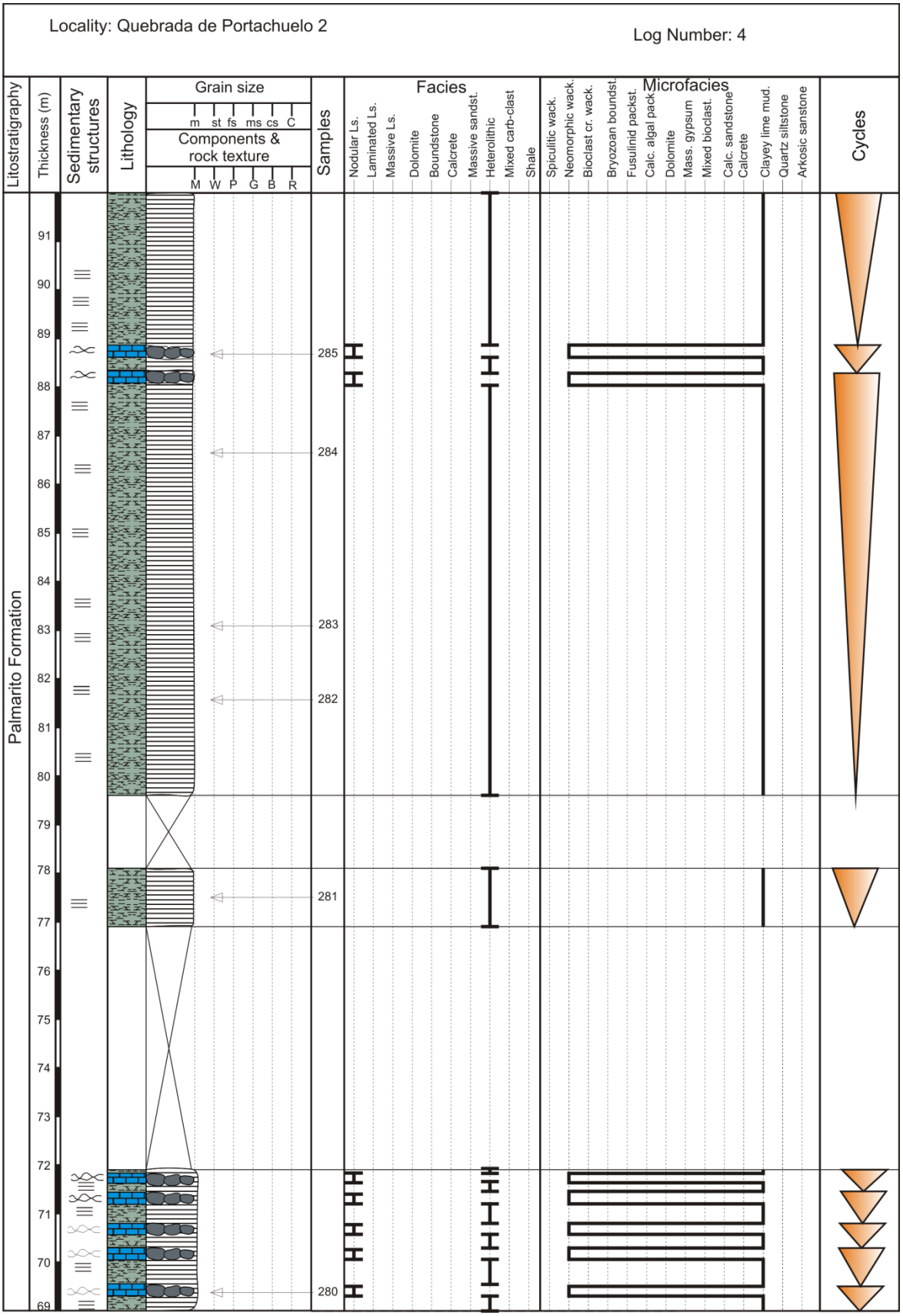
Locality: Quebrada de Portachuelo 2
Log Number: 4
Litostratigraphy
Thickness (m)
Sedimentary structures
Lithology
Grain size
m st fs ms cs C
Components & rock texture
M W P G B R
Samples
Facies
Nodular Ls.
Laminated Ls.
Massive Ls.
Dolomite
Boundstone
Calcrete
Massive sandst.
Heterolithic
Mixed carb-clast
Shale
Microfacies
Spiculitic wack.
Neomorphic wack.
Bioclast cr. wack.
Bryozoan boundst.
Fusulinid packst.
Calc. algal pack.
Dolomite
Mass. gypsum
Mixed bioclast.
Calc. sandstone
Calcrete
Clayey lime mud.
Quartz siltstone
Arkosic sanstone
Cycles
Palmarito Formation
91
90
89
88
87
86
85
84
83
82
81
80
79
78
77
76
75
74
73
72
71
70
69
285
284
283
282
281
280

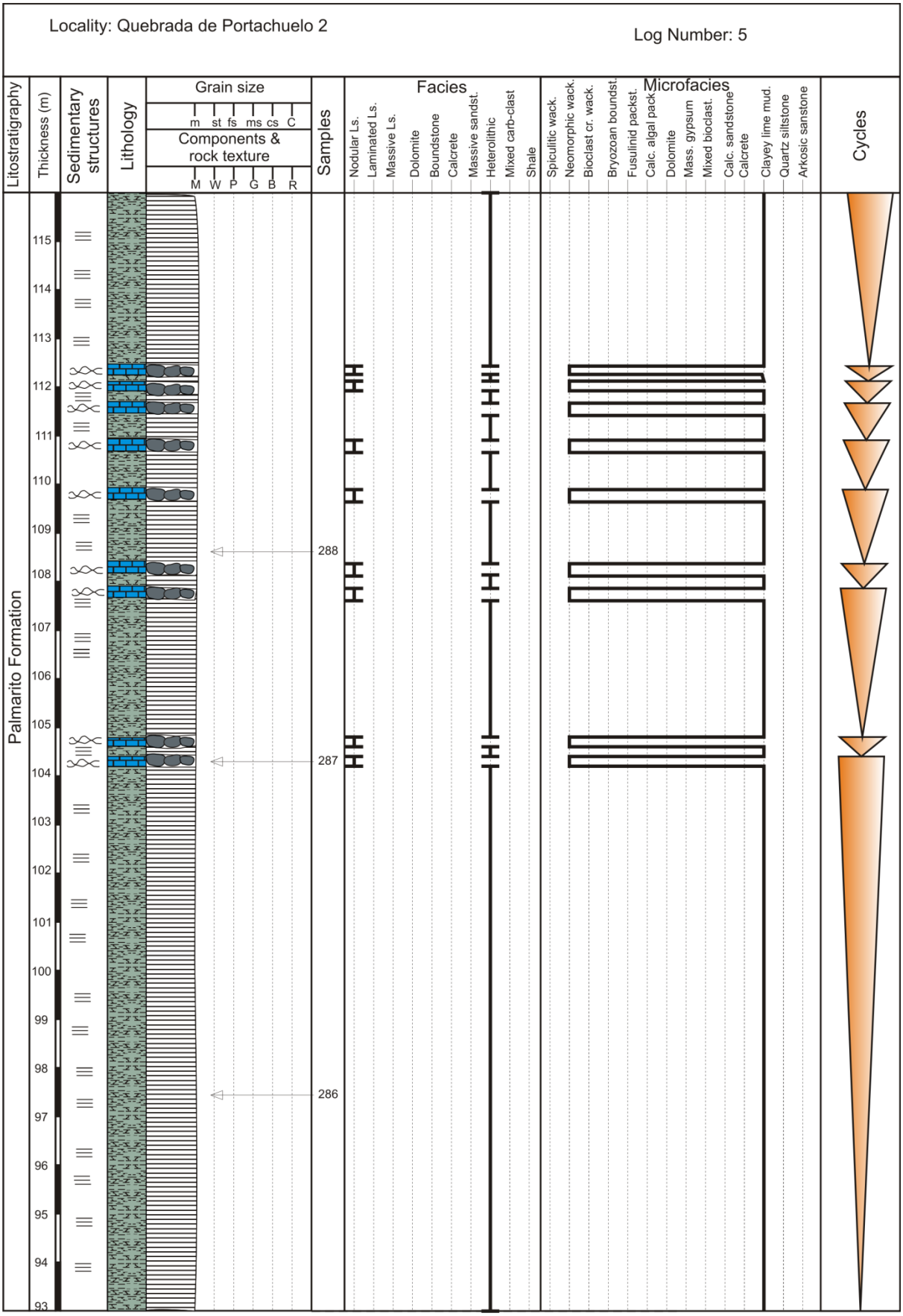
Locality: Quebrada de Portachuelo 2
Log Number: 5
Litostratigraphy
Thickness (m)
Sedimentary structures
Lithology
Grain size
m st fs ms cs C
Components & rock texture
M W P G B R
Samples
Facies
Nodular Ls.
Laminated Ls.
Massive Ls.
Dolomite
Boundstone
Calcrete
Massive sandst.
Heterolithic
Mixed carb-clast
Shale
Microfacies
Spiculitic wack.
Neomorphic wack.
Bioclast cr. wack.
Bryozoan boundst.
Fusulinid packst.
Calc. algal pack.
Dolomite
Mass. gypsum
Mixed bioclast.
Calc. sandstone
Calcrete
Clayey lime mud.
Quartz siltstone
Arkosic sanstone
Cycles
Palmarito Formation
115
114
113
112
111
110
109
108
107
106
105
104
103
102
101
100
99
98
97
96
95
94
93
288
287
286

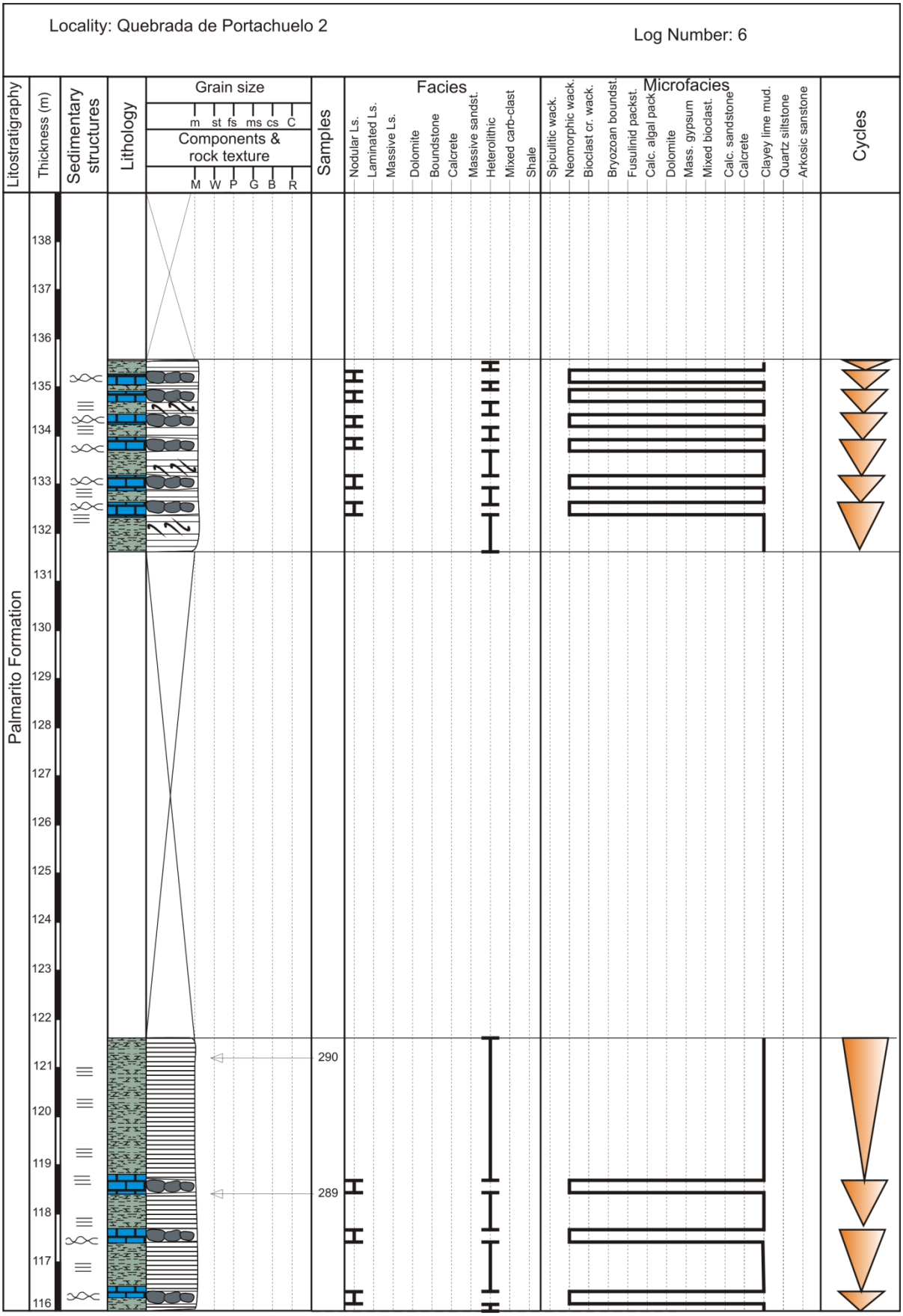
Locality: Quebrada de Portachuelo 2
Log Number: 6
Litostratigraphy
Thickness (m)
Sedimentary structures
Lithology
Grain size
m st fs ms cs C
Components & rock texture
M W P G B R
Samples
Facies
Nodular Ls.
Laminated Ls.
Massive Ls.
Dolomite
Boundstone
Calcrete
Massive sandst.
Heterolithic
Mixed carb-clast
Shale
Microfacies
Spiculitic wack.
Neomorphic wack.
Bioclast cr. wack.
Bryozoan boundst.
Fusulinid packst.
Calc. algal pack.
Dolomite
Mass. gypsum
Mixed bioclast.
Calc. sandstone
Calcrete
Clayey lime mud.
Quartz siltstone
Arkosic sanstone
Cycles
Palmarito Formation
138
137
136
135
134
133
132
131
130
129
128
127
126
125
124
123
122
121
120
119
118
117
116
290
289

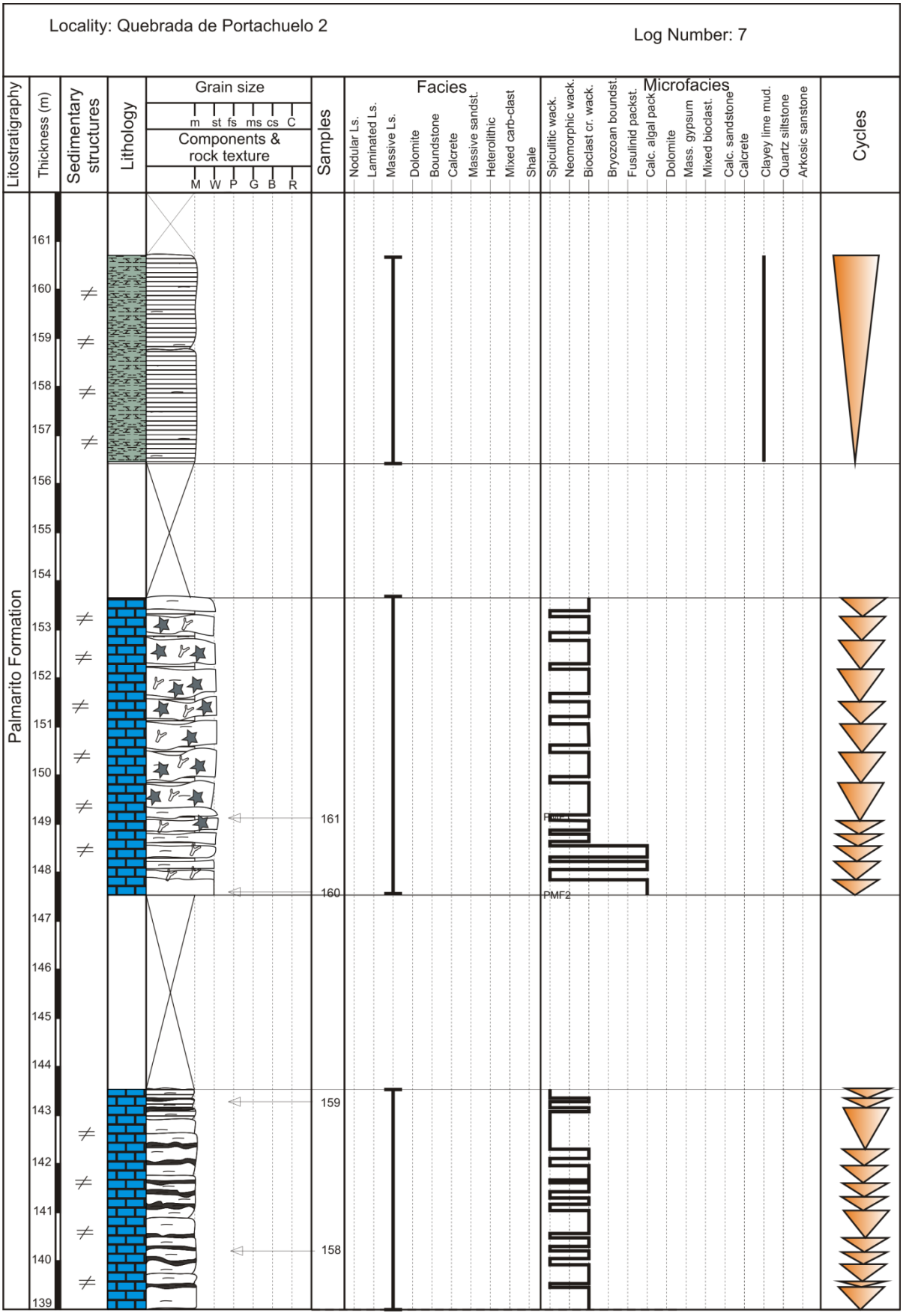
Locality: Quebrada de Portachuelo 2
Log Number: 7
Litostratigraphy
Thickness (m)
Sedimentary structures
Lithology
Grain size
m st fs ms cs C
Components & rock texture
M W P G B R
Samples
Facies
Nodular Ls.
Laminated Ls.
Massive Ls.
Dolomite
Boundstone
Calcrete
Massive sandst.
Heterolithic
Mixed carb-clast
Shale
Microfacies
Spiculitic wack.
Neomorphic wack.
Bioclast cr. wack.
Bryozoan boundst.
Fusulinid packst.
Calc. algal pack.
Dolomite
Mass. gypsum
Mixed bioclast.
Calc. sandstone
Calcrete
Clayey lime mud.
Quartz siltstone
Arkosic sanstone
Cycles
Palmarito Formation
161
160
159
158
157
156
155
154
153
152
151
150
149
148
147
146
145
144
143
142
141
140
139
161
160
159
158
PMF1
PMF2

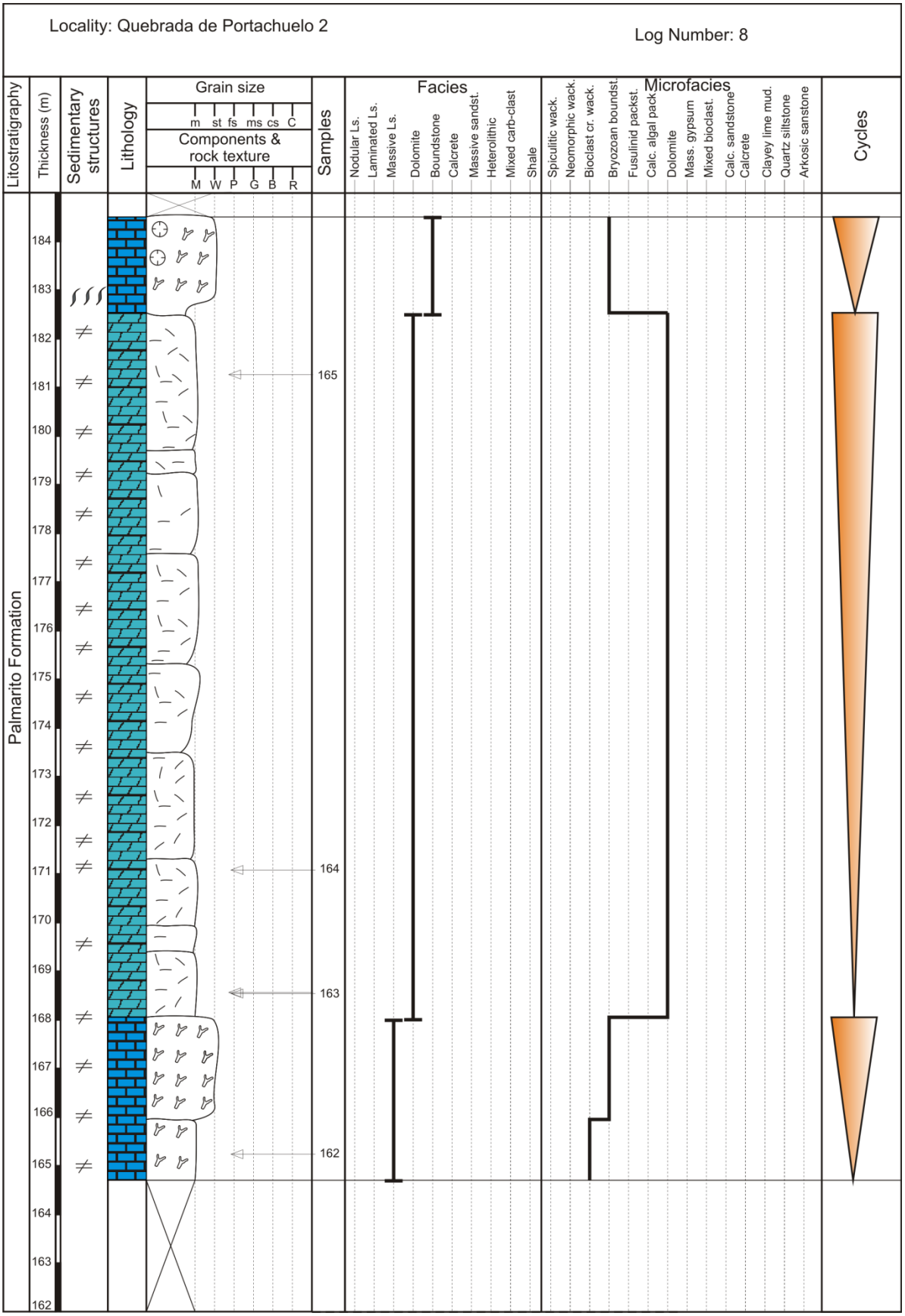
Locality: Quebrada de Portachuelo 2
Log Number: 8
Litostratigraphy
Thickness (m)
Sedimentary structures
Lithology
Grain size
m st fs ms cs C
Components & rock texture
M W P G B R
Samples
Facies
Nodular Ls.
Laminated Ls.
Massive Ls.
Dolomite
Boundstone
Calcrete
Massive sandst.
Heterolithic
Mixed carb-clast
Shale
Microfacies
Spiculitic wack.
Neomorphic wack.
Bioclast cr. wack.
Bryozoan boundst.
Fusulinid packst.
Calc. algal pack.
Dolomite
Mass. gypsum
Mixed bioclast.
Calc. sandstone
Calcrete
Clayey lime mud.
Quartz siltstone
Arkosic sanstone
Cycles
Palmarito Formation
184
183
182
181
180
179
178
177
176
175
174
173
172
171
170
169
168
167
166
165
164
163
162
165
164
163
162

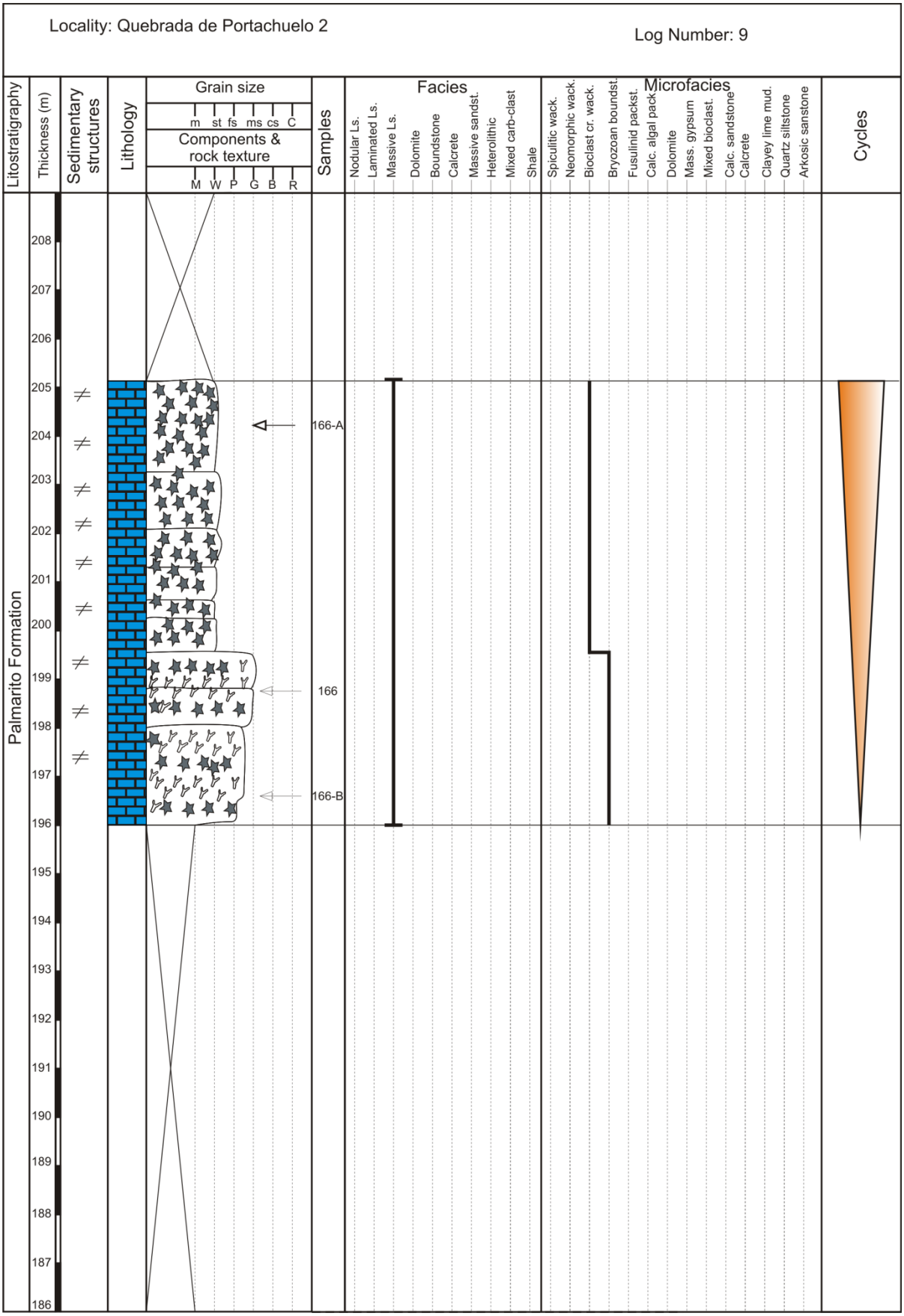
Locality: Quebrada de Portachuelo 2
Log Number: 9
Litostratigraphy
Thickness (m)
Sedimentary structures
Lithology
Grain size
m st fs ms cs C
Components & rock texture
M W P G B R
Samples
Facies
Nodular Ls.
Laminated Ls.
Massive Ls.
Dolomite
Boundstone
Calcrete
Massive sandst.
Heterolithic
Mixed carb-clast
Shale
Microfacies
Spiculitic wack.
Neomorphic wack.
Bioclast cr. wack.
Bryozoan boundst.
Fusulinid packst.
Calc. algal pack.
Dolomite
Mass. gypsum
Mixed bioclast.
Calc. sandstone
Calcrete
Clayey lime mud.
Quartz siltstone
Arkosic sanstone
Cycles
Palmarito Formation
208
207
206
205
204
203
202
201
200
199
198
197
196
195
194
193
192
191
190
189
188
187
186
166-A
166
166-B

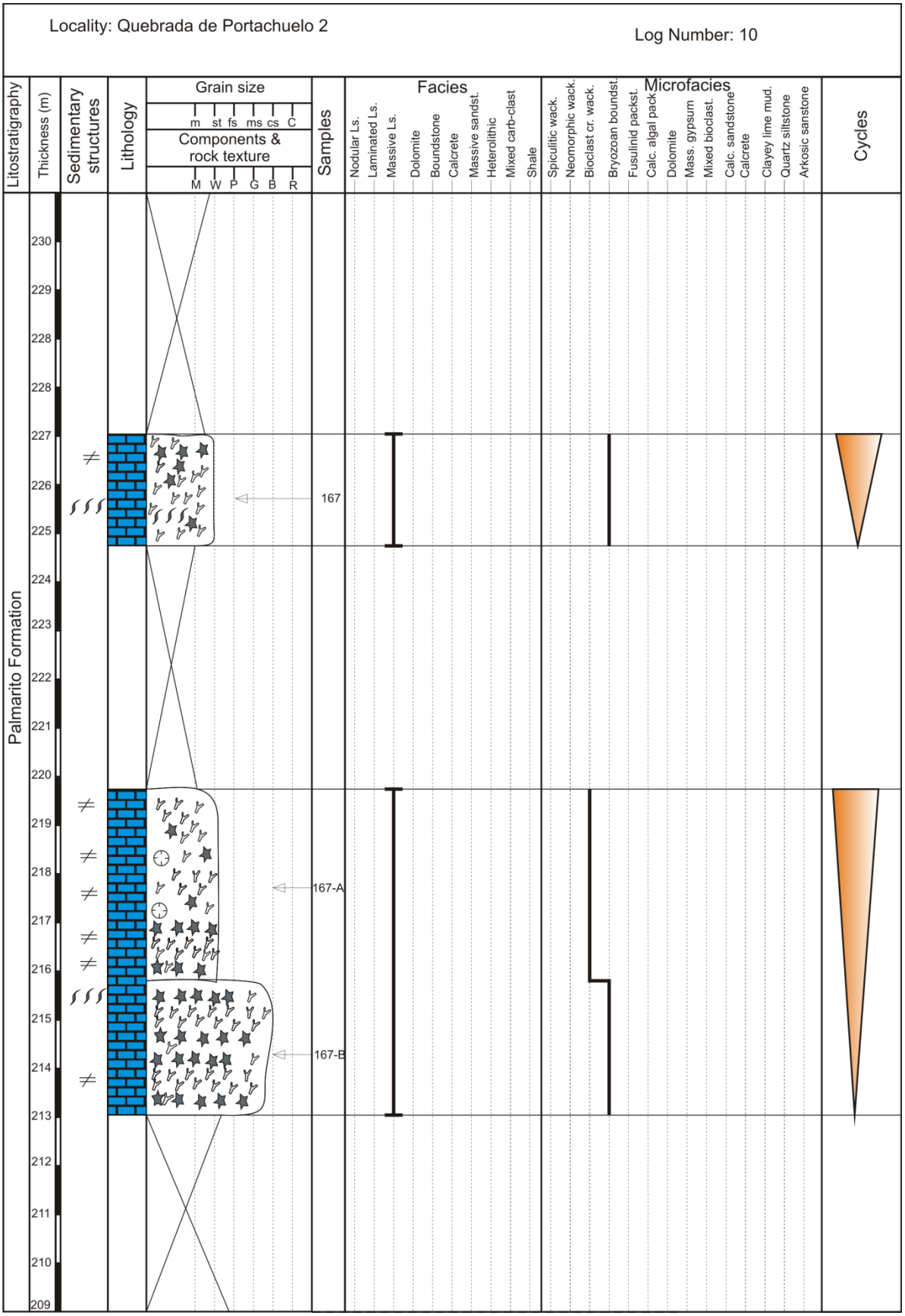
Locality: Quebrada de Portachuelo 2
Log Number: 10
Litostratigraphy
Thickness (m)
Sedimentary structures
Lithology
Grain size
m st fs ms cs C
Components & rock texture
M W P G B R
Samples
Facies
Nodular Ls.
Laminated Ls.
Massive Ls.
Dolomite
Boundstone
Calcrete
Massive sandst.
Heterolithic
Mixed carb-clast
Shale
Microfacies
Spiculitic wack.
Neomorphic wack.
Bioclast cr. wack.
Bryozoan boundst.
Fusulinid packst.
Calc. algal pack
Dolomite
Mass. gypsum
Mixed bioclast.
Calc. sandstone
Calcrete
Clayey lime mud.
Quartz siltstone
Arkosic sanstone
Cycles
Palmarito Formation
230
229
228
228
227
226
225
224
223
222
221
220
219
218
217
216
215
214
213
212
211
210
209
167
167-A
167-B

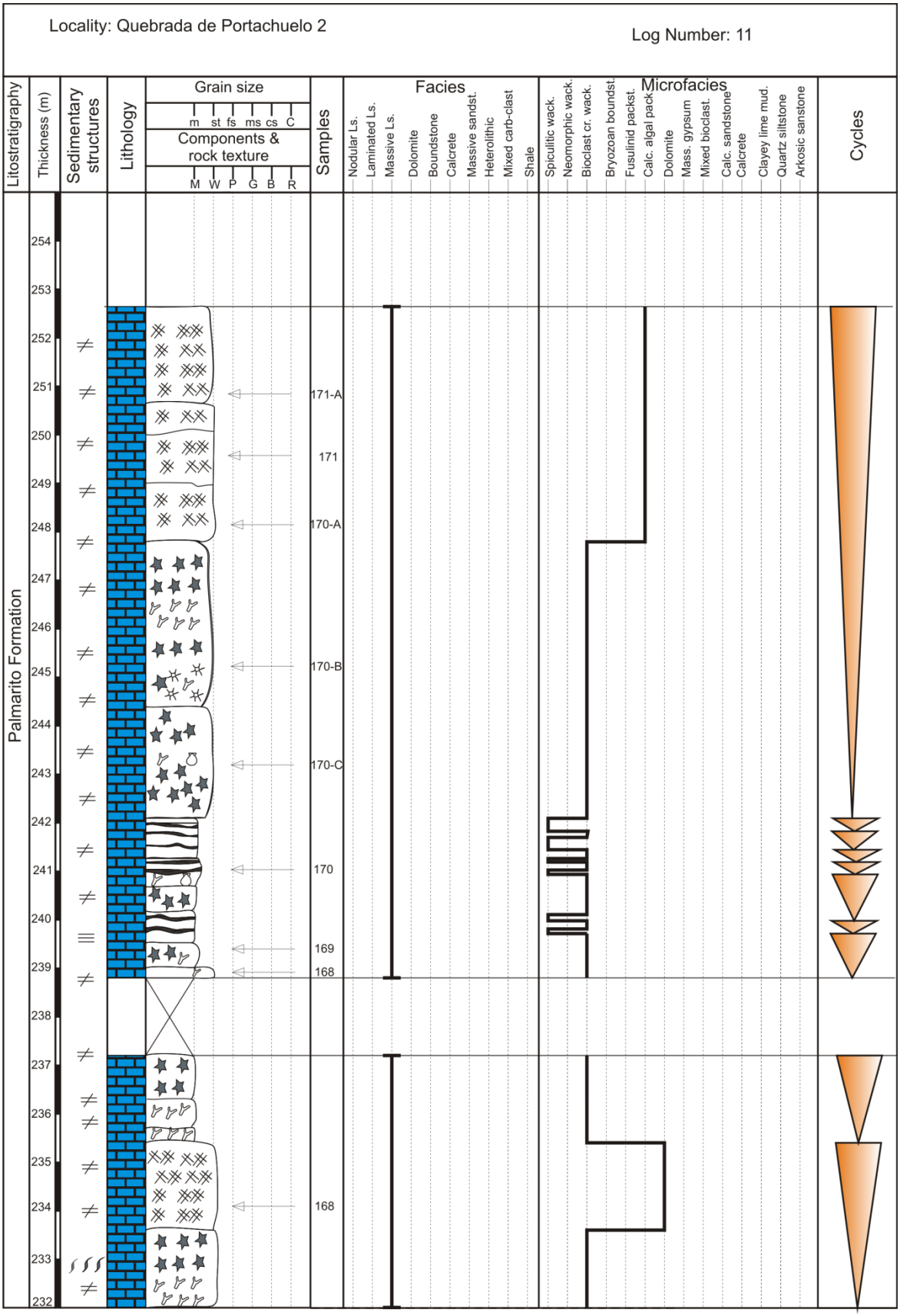
Locality: Quebrada de Portachuelo 2
Log Number: 11
Litostratigraphy
Thickness (m)
Sedimentary structures
Lithology
Grain size
m st fs ms cs C
Components & rock texture
M W P G B R
Samples
Facies
Nodular Ls.
Laminated Ls.
Massive Ls.
Dolomite
Boundstone
Calcrete
Massive sandst.
Heterolithic
Mixed carb-clast
Shale
Microfacies
Spiculitic wack.
Neomorphic wack.
Bioclast cr. wack.
Bryozoan boundst.
Fusulinid packst.
Calc. algal pack
Dolomite
Mass. gypsum
Mixed bioclast.
Calc. sandstone
Calcrete
Clayey lime mud.
Quartz siltstone
Arkosic sanstone
Cycles
Palmarito Formation
254
253
252
251
250
249
248
247
246
245
244
243
242
241
240
239
238
237
236
235
234
233
232
171-A
171
170-A
170-B
170-C
170
169
168
168

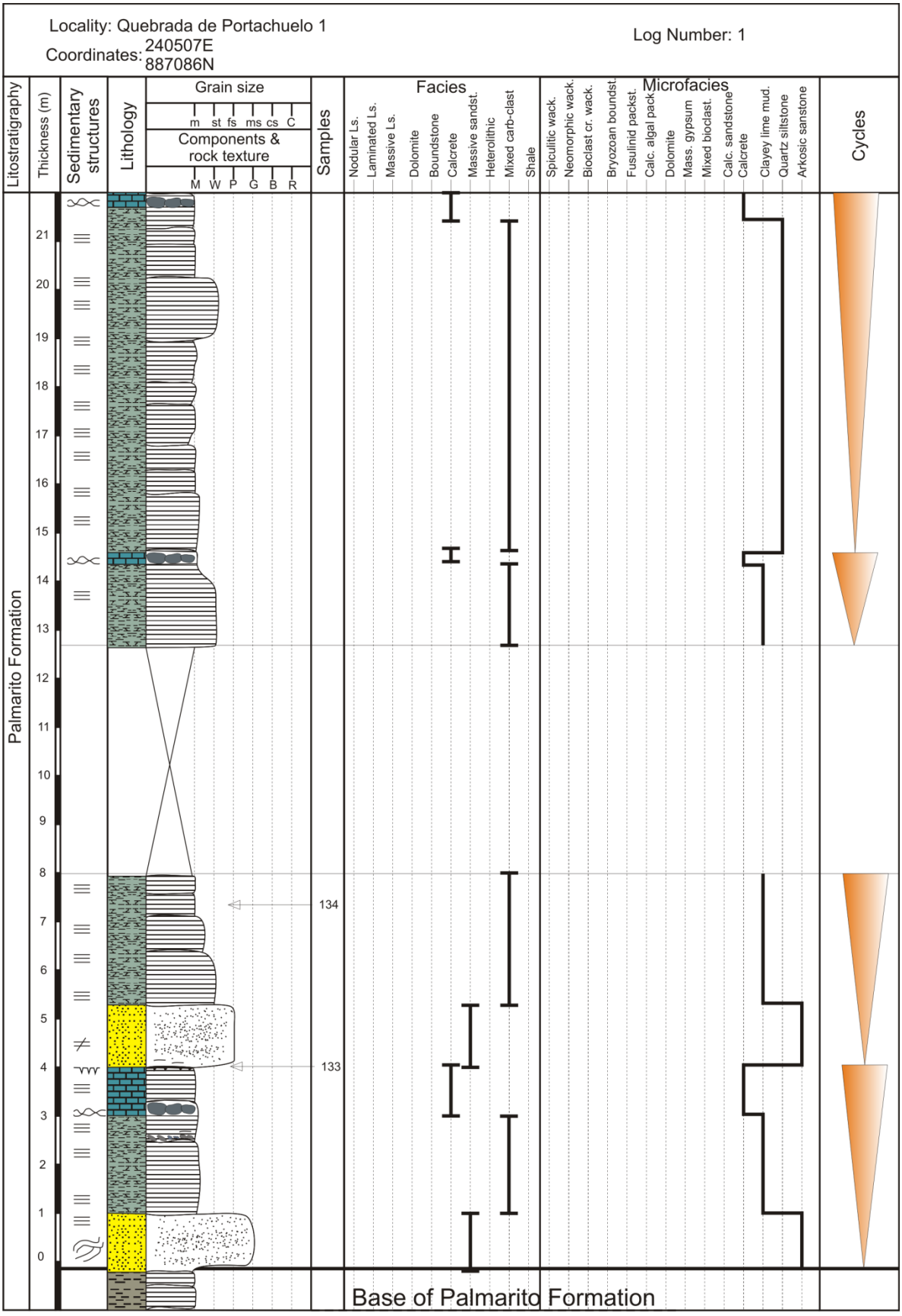
Locality: Quebrada de Portachuelo 1
Coordinates: 240507E 887086N
Log Number: 1
Litostratigraphy
Thickness (m)
Sedimentary structures
Lithology
Grain size
m st fs ms cs C
Components & rock texture
M W P G B R
Samples
Facies
Nodular Ls.
Laminated Ls.
Massive Ls.
Dolomite
Boundstone
Calcrete
Massive sandst.
Heterolithic
Mixed carb-clast
Shale
Microfacies
Spiculitic wack.
Neomorphic wack.
Bioclast cr. wack.
Bryozoan boundst.
Fusulinid packst.
Calc. algal pack.
Dolomite
Mass. gypsum
Mixed bioclast.
Calc. sandstone
Calcrete
Clayey lime mud.
Quartz siltstone
Arkosic sanstone
Cycles
Palmarito Formation
134
133
Base of Palmarito Formation

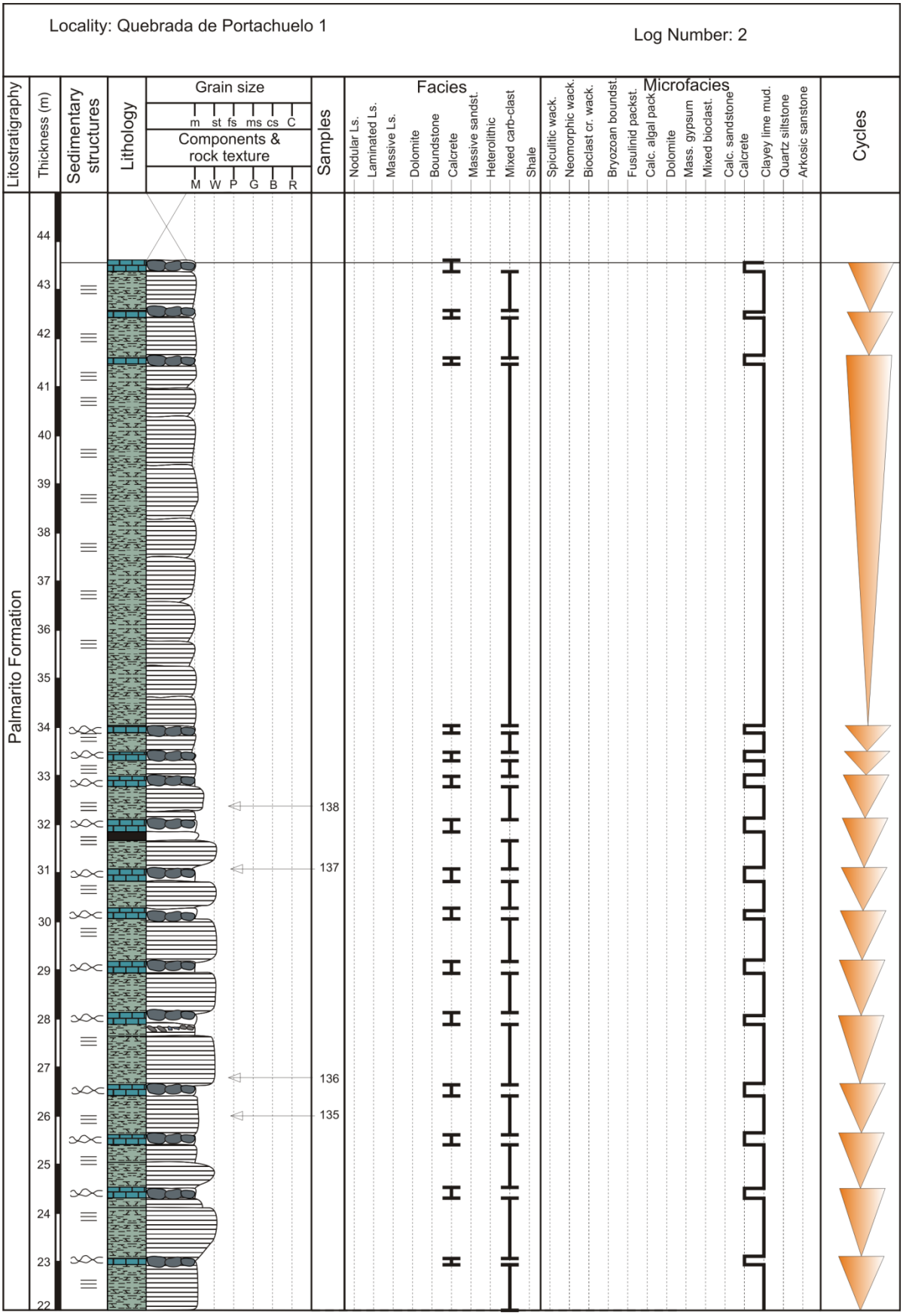
Locality: Quebrada de Portachuelo 1
Log Number: 2
Litostratigraphy
Thickness (m)
Sedimentary structures
Lithology
Grain size
m st fs ms cs C
Components & rock texture
M W P G B R
Samples
Facies
Nodular Ls.
Laminated Ls.
Massive Ls.
Dolomite
Boundstone
Calcrete
Massive sandst.
Heterolithic
Mixed carb-clast
Shale
Microfacies
Spiculitic wack.
Neomorphic wack.
Bioclast cr. wack.
Bryozoan boundst.
Fusulinid packst.
Calc. algal pack.
Dolomite
Mass. gypsum
Mixed bioclast.
Calc. sandstone
Calcrete
Clayey lime mud.
Quartz siltstone
Arkosic sanstone
Cycles
Palmarito Formation
44
43
42
41
40
39
38
37
36
35
34
33
32
31
30
29
28
27
26
25
24
23
22
138
137
136
135

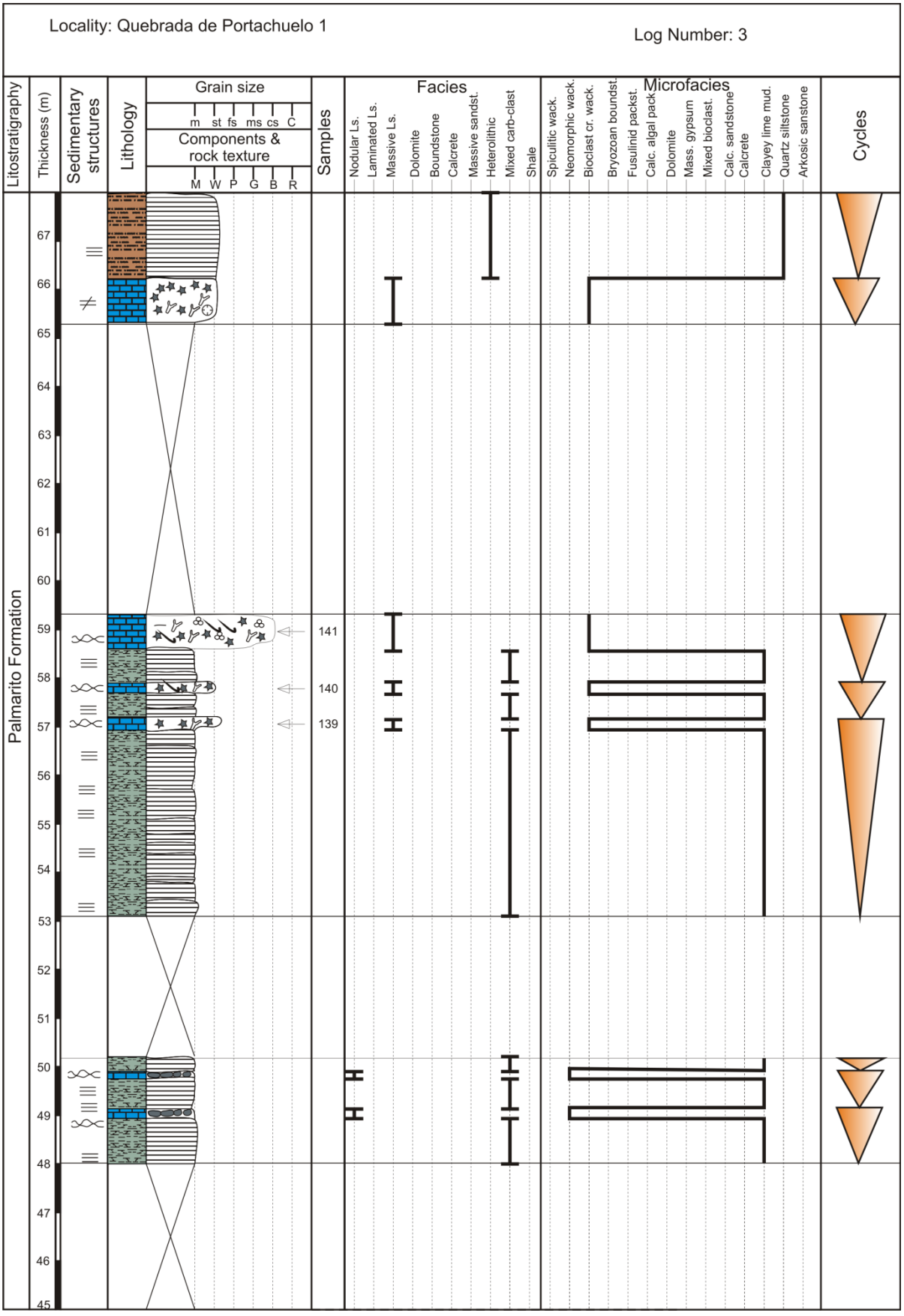
Locality: Quebrada de Portachuelo 1
Log Number: 3
Litostratigraphy
Thickness (m)
Sedimentary structures
Lithology
Grain size
m st fs ms cs C
Components & rock texture
M W P G B R
Samples
Facies
Nodular Ls.
Laminated Ls.
Massive Ls.
Dolomite
Boundstone
Calcrete
Massive sandst.
Heterolithic
Mixed carb-clast
Shale
Microfacies
Spiculitic wack.
Neomorphic wack.
Bioclast cr. wack.
Bryozoan boundst.
Fusulinid packst.
Calc. algal pack.
Dolomite
Mass. gypsum
Mixed bioclast.
Calc. sandstone
Calcrete
Clayey lime mud.
Quartz siltstone
Arkosic sanstone
Cycles
Palmarito Formation
67
66
65
64
63
62
61
60
59
58
57
56
55
54
53
52
51
50
49
48
47
46
45
141
140
139

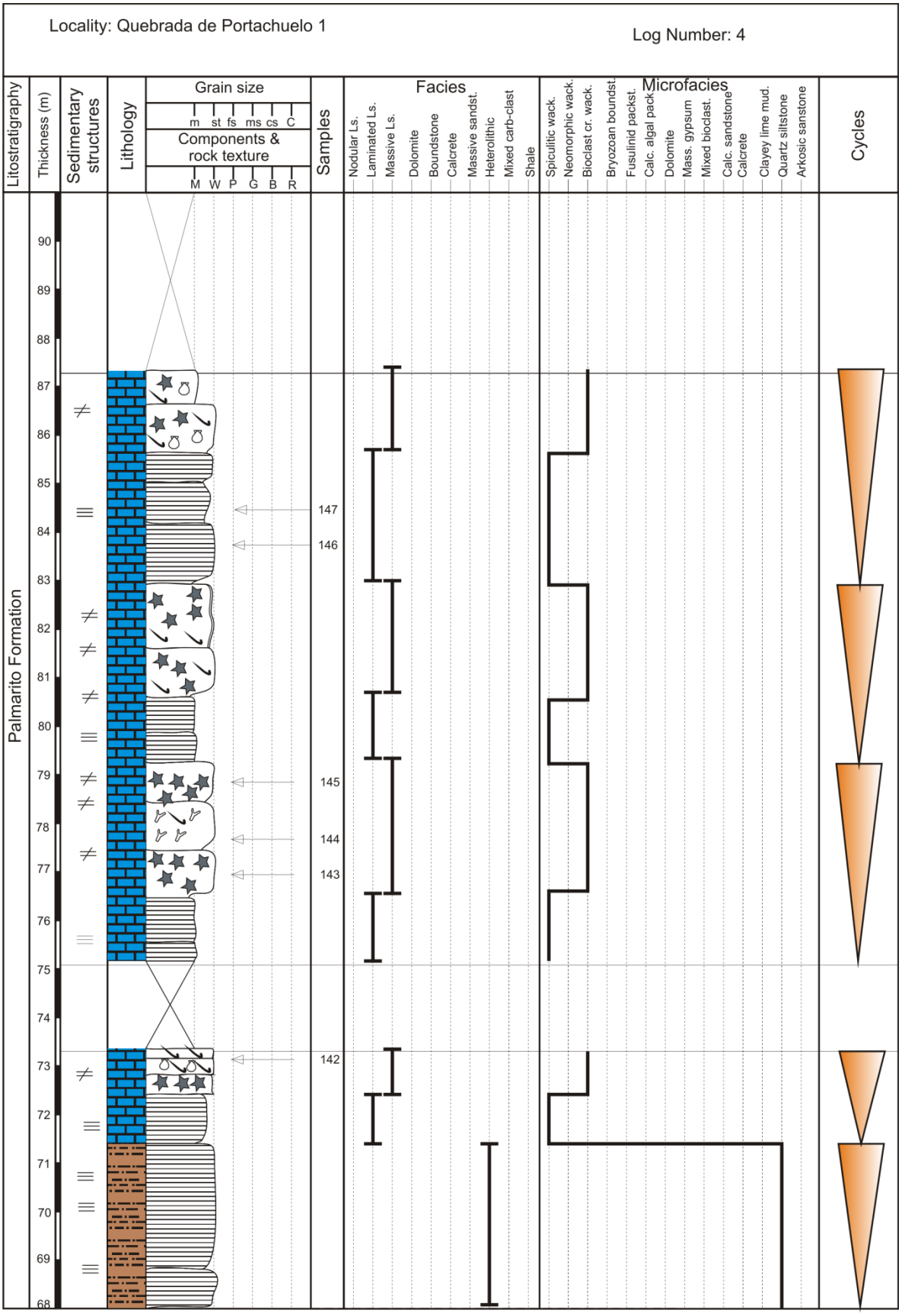
Locality: Quebrada de Portachuelo 1
Log Number: 4
Litostratigraphy
Thickness (m)
Sedimentary structures
Lithology
Grain size
m st fs ms cs C
Components & rock texture
M W P G B R
Samples
Facies
Nodular Ls.
Laminated Ls.
Massive Ls.
Dolomite
Boundstone
Calcrete
Massive sandst.
Heterolithic
Mixed carb-clast
Shale
Microfacies
Spiculitic wack.
Neomorphic wack.
Bioclast cr. wack.
Bryozoan boundst.
Fusulinid packst.
Calc. algal pack.
Dolomite
Mass. gypsum
Mixed bioclast.
Calc. sandstone
Calcrete
Clayey lime mud.
Quartz siltstone
Arkosic sanstone
Cycles
Palmarito Formation
90
89
88
87
86
85
84
83
82
81
80
79
78
77
76
75
74
73
72
71
70
69
68
147
146
145
144
143
142

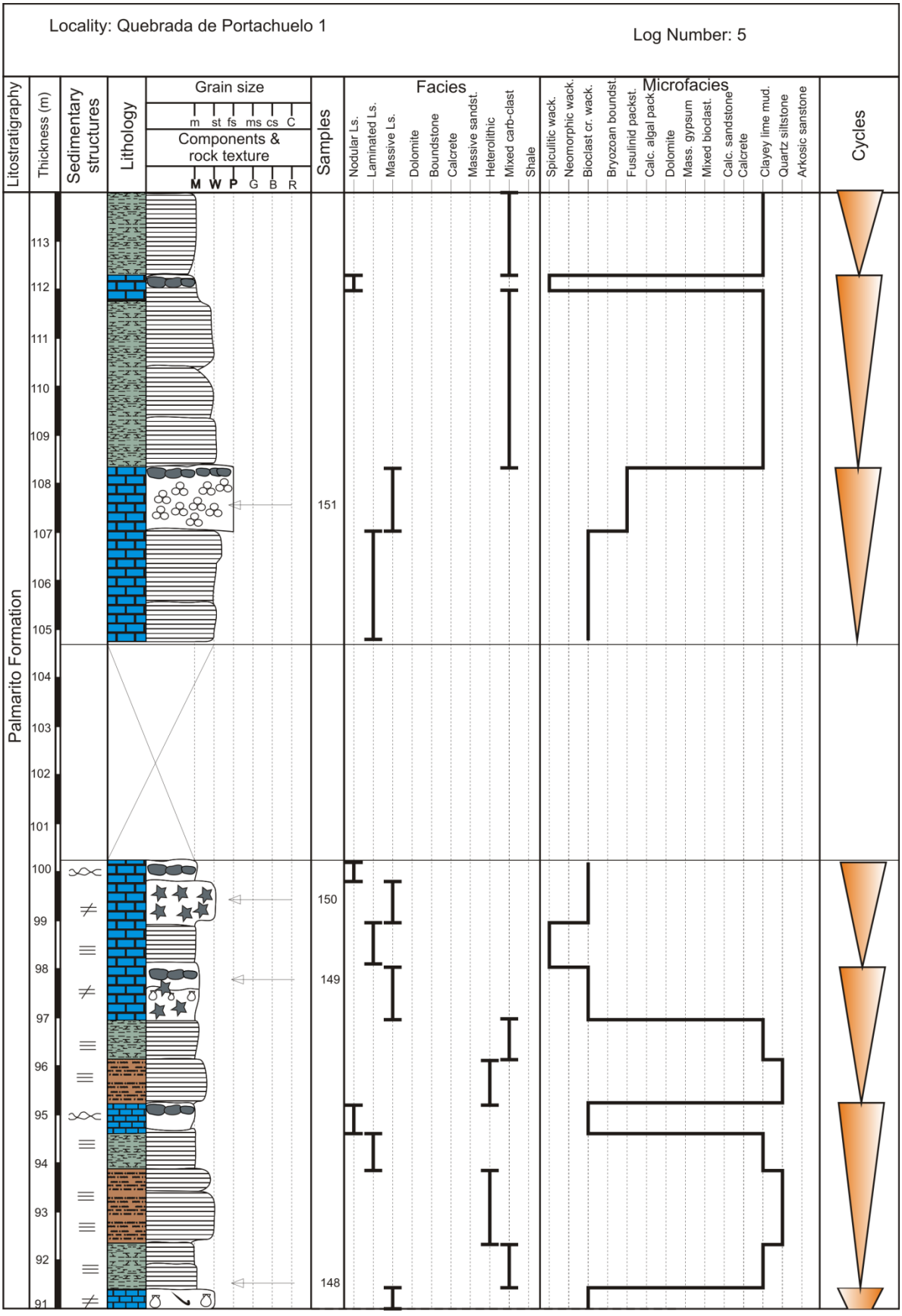
Locality: Quebrada de Portachuelo 1
Log Number: 5
Litostratigraphy
Thickness (m)
Sedimentary structures
Lithology
Grain size
m st fs ms cs C
Components & rock texture
M W P G B R
Samples
Facies
Nodular Ls.
Laminated Ls.
Massive Ls.
Dolomite
Boundstone
Calcrete
Massive sandst.
Heterolithic
Mixed carb-clast
Shale
Microfacies
Spiculitic wack.
Neomorphic wack.
Bioclast cr. wack.
Bryozoan boundst.
Fusulinid packst.
Calc. algal pack.
Dolomite
Mass. gypsum
Mixed bioclast.
Calc. sandstone
Calcrete
Clayey lime mud.
Quartz siltstone
Arkosic sanstone
Cycles
Palmarito Formation
113
112
111
110
109
108
107
106
105
104
103
102
101
100
99
98
97
96
95
94
93
92
91
151
150
149
148

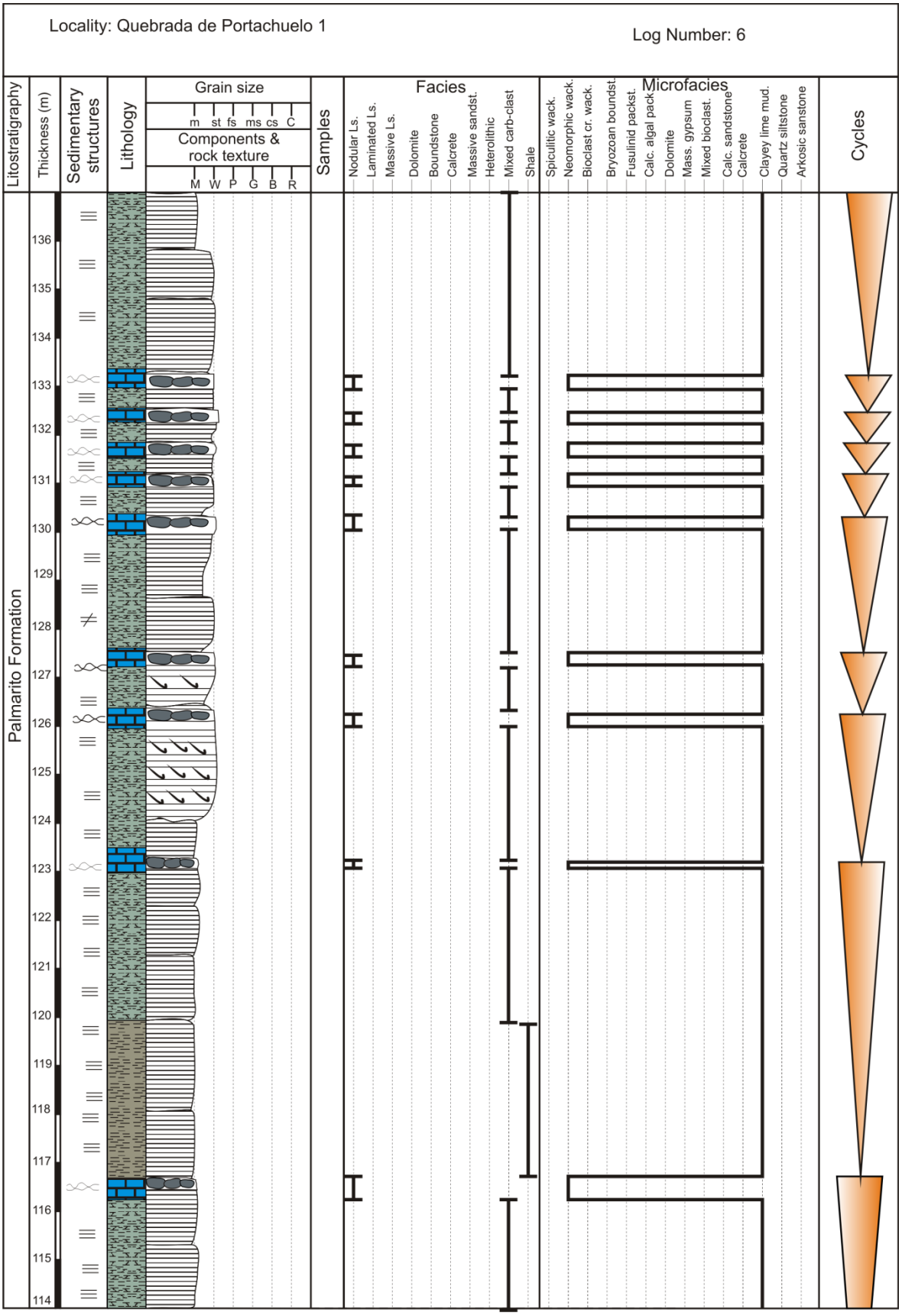
Locality: Quebrada de Portachuelo 1
Log Number: 6
Litostratigraphy
Thickness (m)
Sedimentary structures
Lithology
Grain size
m st fs ms cs C
Components & rock texture
M W P G B R
Samples
Facies
Nodular Ls.
Laminated Ls.
Massive Ls.
Dolomite
Boundstone
Calcrete
Massive sandst.
Heterolithic
Mixed carb-clast
Shale
Microfacies
Spiculitic wack.
Neomorphic wack.
Bioclast cr. wack.
Bryozoan boundst.
Fusulinid packst.
Calc. algal pack.
Dolomite
Mass. gypsum
Mixed bioclast.
Calc. sandstone
Calcrete
Clayey lime mud.
Quartz siltstone
Arkosic sanstone
Cycles
Palmarito Formation
136
135
134
133
132
131
130
129
128
127
126
125
124
123
122
121
120
119
118
117
116
115
114

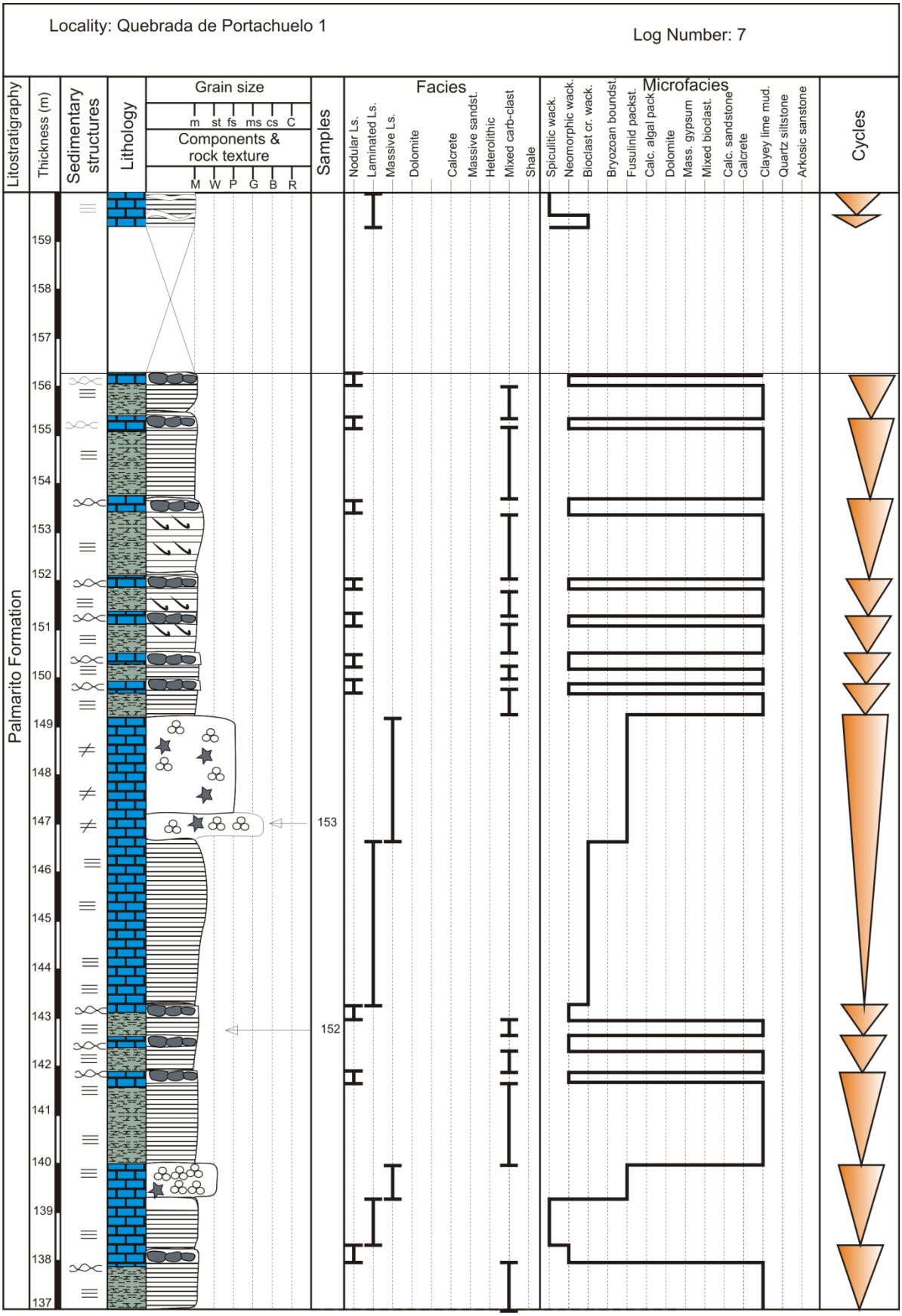
Locality: Quebrada de Portachuelo 1
Log Number: 7
Litostratigraphy
Thickness (m)
Sedimentary structures
Lithology
Grain size
m st fs ms cs C
Components & rock texture
M W P G B R
Samples
Facies
Nodular Ls.
Laminated Ls.
Massive Ls.
Dolomite
Calcrete
Massive sandst.
Heterolithic
Mixed carb-clast
Shale
Microfacies
Spiculitic wack.
Neomorphic wack.
Bioclast cr. wack.
Bryozoan boundst.
Fusulinid packst.
Calc. algal pack
Dolomite
Mass. gypsum
Mixed bioclast.
Calc. sandstone
Calcrete
Clayey lime mud.
Quartz siltstone
Arkosic sanstone
Cycles
Palmarito Formation
159
158
157
156
155
154
153
152
151
150
149
148
147
146
145
144
143
142
141
140
139
138
137
153
152

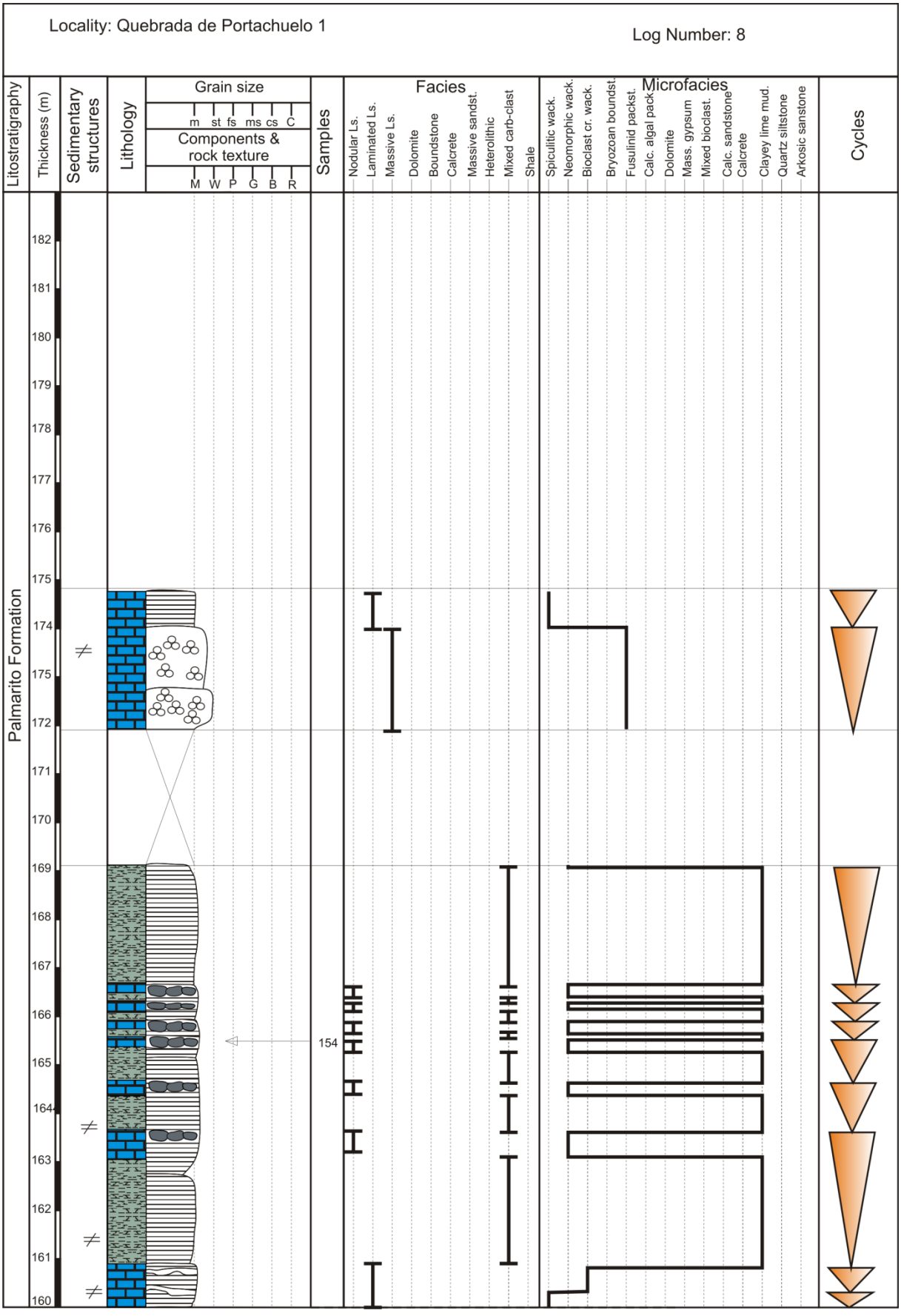
Locality: Quebrada de Portachuelo 1
Log Number: 8
Litostratigraphy
Thickness (m)
Sedimentary structures
Lithology
Grain size
m st fs ms cs C
Components & rock texture
M W P G B R
Samples
Facies
Nodular Ls.
Laminated Ls.
Massive Ls.
Dolomite
Boundstone
Calcrete
Massive sandst.
Heterolithic
Mixed carb-clast
Shale
Microfacies
Spiculitic wack.
Neomorphic wack.
Bioclast cr. wack.
Bryozoan boundst.
Fusulinid packst.
Calc. algal pack.
Dolomite
Mass. gypsum
Mixed bioclast.
Calc. sandstone
Calcrete
Clayey lime mud.
Quartz siltstone
Arkosic sanstone
Cycles
Palmarito Formation
182
181
180
179
178
177
176
175
174
175
172
171
170
169
168
167
166
165
164
163
162
161
160
154

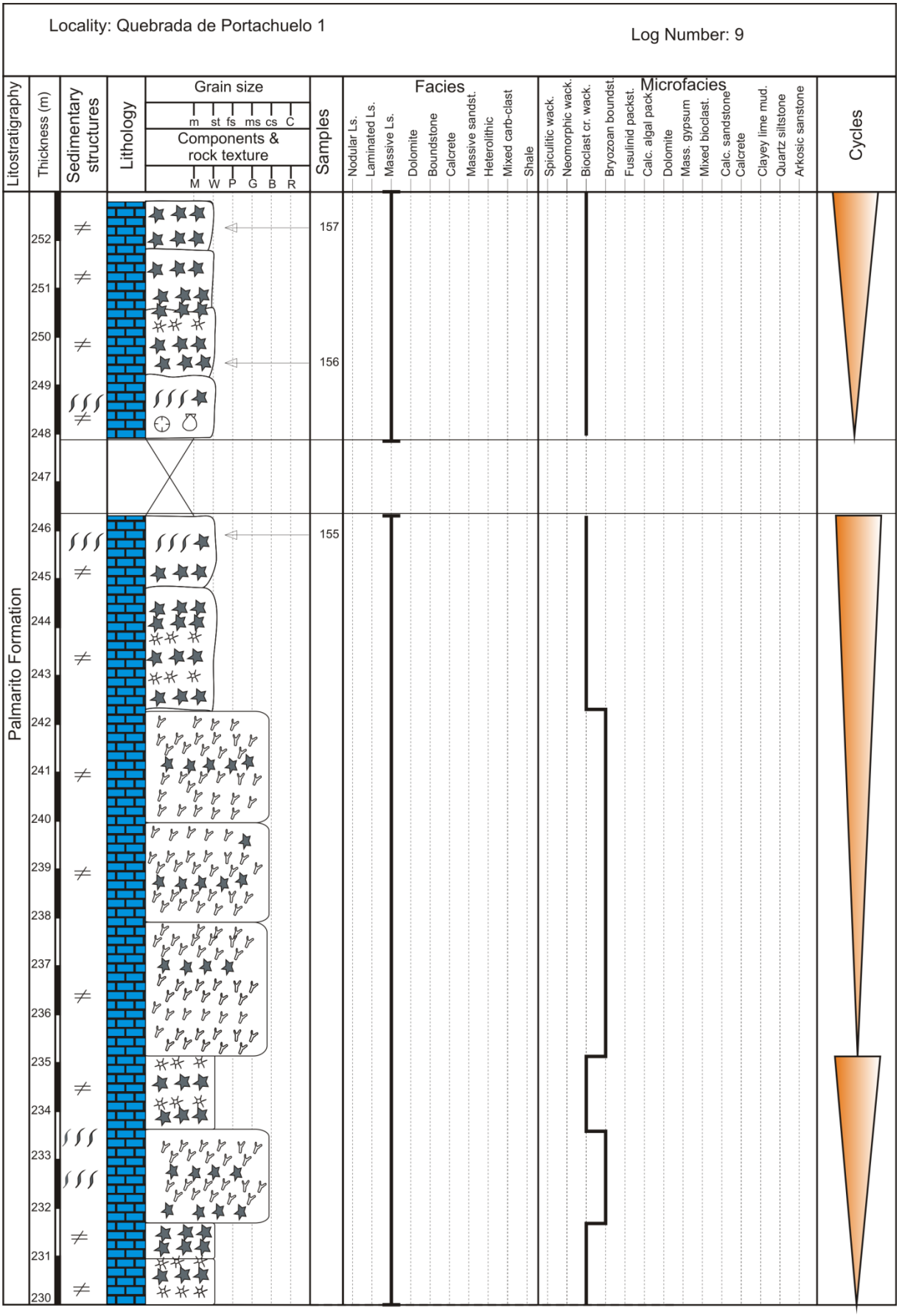
Locality: Quebrada de Portachuelo 1
Log Number: 9
Litostratigraphy
Thickness (m)
Sedimentary structures
Lithology
Grain size
m st fs ms cs C
Components & rock texture
M W P G B R
Samples
Facies
Nodular Ls.
Laminated Ls.
Massive Ls.
Dolomite
Boundstone
Calcrete
Massive sandst.
Heterolithic
Mixed carb-clast
Shale
Microfacies
Spiculitic wack.
Neomorphic wack.
Bioclast cr. wack.
Bryozoan boundst.
Fusulinid packst.
Calc. algal pack.
Dolomite
Mass. gypsum
Mixed bioclast.
Calc. sandstone
Calcrete
Clayey lime mud.
Quartz siltstone
Arkosic sanstone
Cycles
Palmarito Formation
252
251
250
249
248
247
246
245
244
243
242
241
240
239
238
237
236
235
234
233
232
231
230
157
156
155

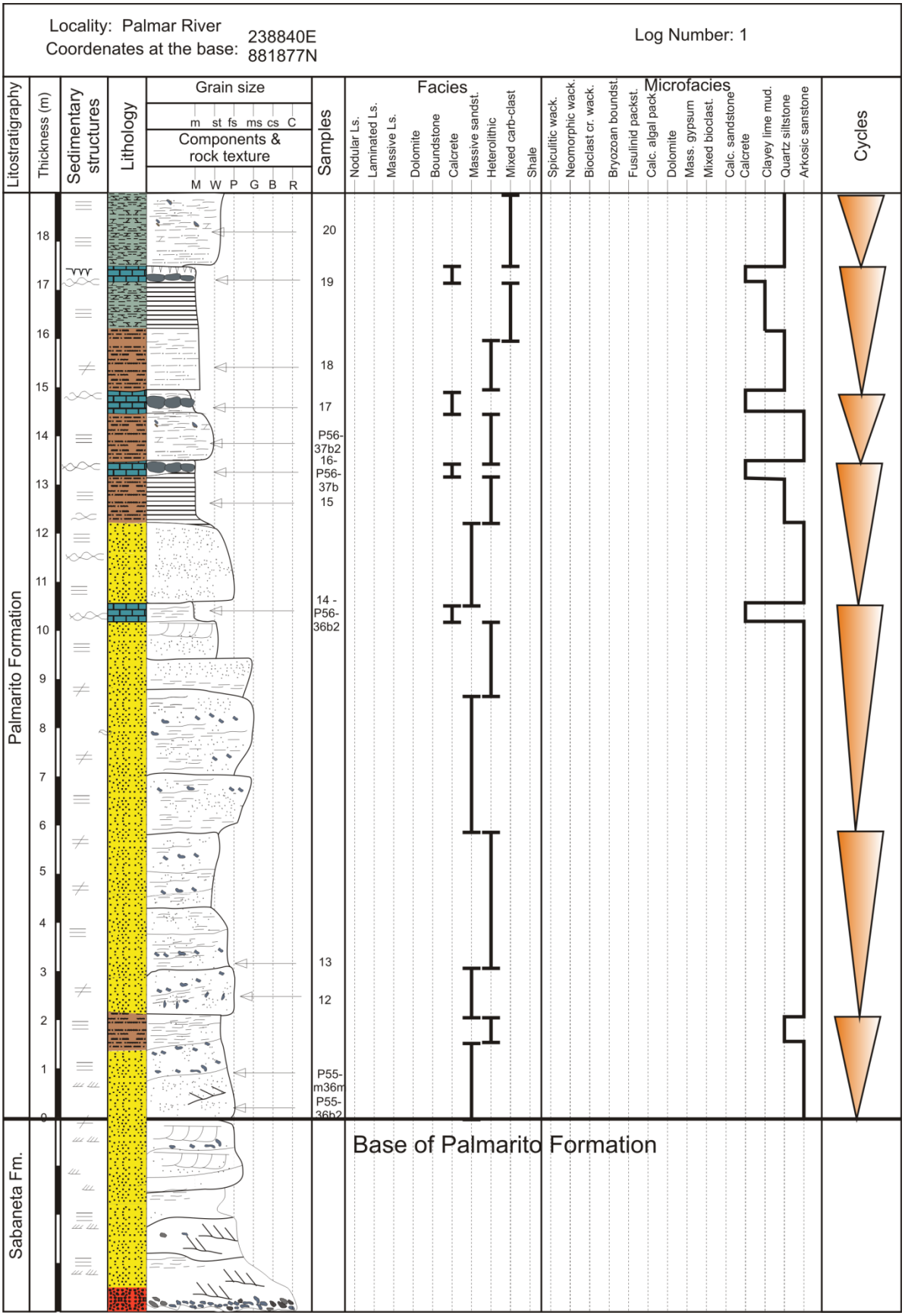
Locality: Palmar River
Coordenates at the base: 238840E 881877N
Log Number: 1
Litostratigraphy
Thickness (m)
Sedimentary structures
Lithology
Grain size
m st fs ms cs C
Components & rock texture
M W P G B R
Samples
Facies
Nodular Ls.
Laminated Ls.
Massive Ls.
Dolomite
Boundstone
Calcrete
Massive sandst.
Heterolithic
Mixed carb-clast
Shale
Microfacies
Spiculitic wack.
Neomorphic wack.
Bioclast cr. wack.
Bryozoan boundst.
Fusulinid packst.
Calc. algal pack
Dolomite
Mass. gypsum
Mixed bioclast.
Calc. sandstone
Calcrete
Clayey lime mud.
Quartz siltstone
Arkosic sanstone
Cycles
Palmarito Formation
Sabaneta Fm.
20
19
18
17
P56-37b2
16-P56-37b
15
14 - P56-36b2
13
12
P55-m36m
P55-36b2
Base of Palmarito Formation

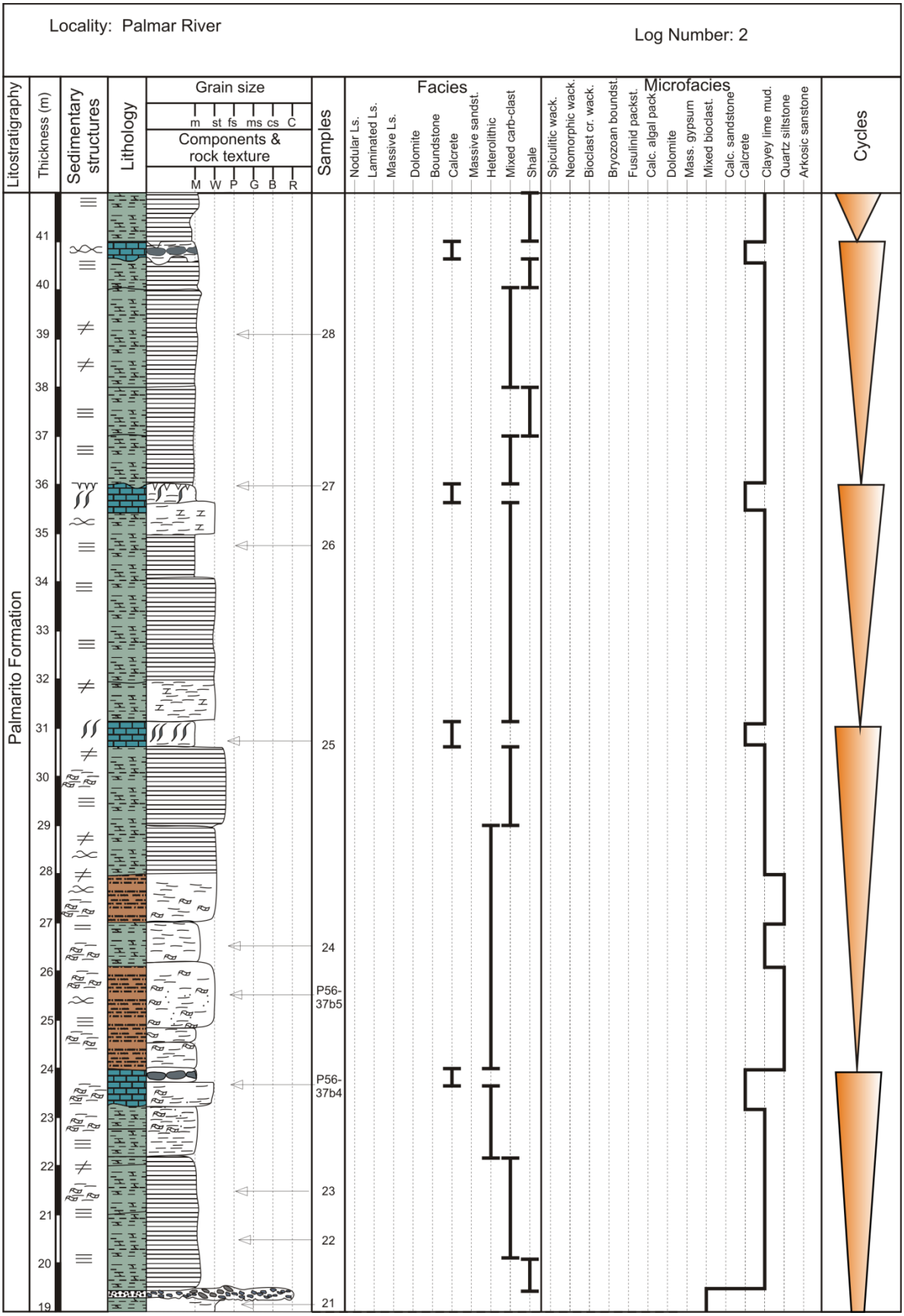
Locality: Palmar River
Log Number: 2
Litostratigraphy
Thickness (m)
Sedimentary structures
Lithology
Grain size
m st fs ms cs C
Components & rock texture
M W P G B R
Samples
Facies
Nodular Ls.
Laminated Ls.
Massive Ls.
Dolomite
Boundstone
Calcrete
Massive sandst.
Heterolithic
Mixed carb-clast
Shale
Microfacies
Spiculitic wack.
Neomorphic wack.
Bioclast cr. wack.
Bryozoan boundst.
Fusulinid packst.
Calc. algal pack.
Dolomite
Mass. gypsum
Mixed bioclast.
Calc. sandstone
Calcrete
Clayey lime mud.
Quartz siltstone
Arkosic sanstone
Cycles
Palmarito Formation
19
20
21
22
23
24
25
26
27
28
29
30
31
32
33
34
35
36
37
38
39
40
41
21
22
23
24
25
26
27
28
P56-37b4
P56-37b5

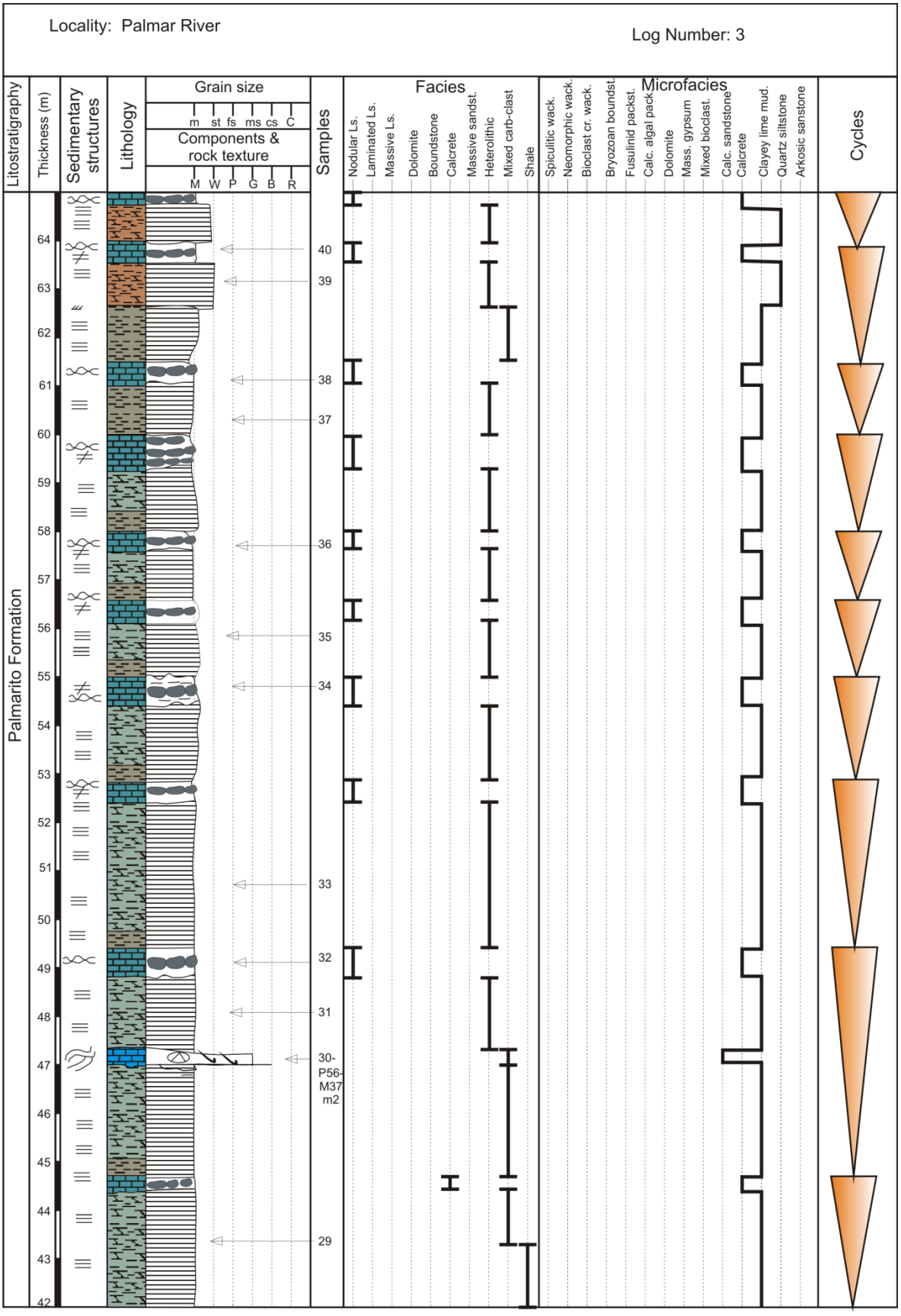
Locality: Palmar River
Log Number: 3
Litostratigraphy
Thickness (m)
Sedimentary structures
Lithology
Grain size
m st fs ms cs C
Components & rock texture
M W P G B R
Samples
Facies
Nodular Ls.
Laminated Ls.
Massive Ls.
Dolomite
Boundstone
Calcrete
Massive sandst.
Heterolithic
Mixed carb-clast
Shale
Microfacies
Spiculitic wack.
Neomorphic wack.
Bioclast cr. wack.
Bryozoan boundst.
Fusulinid packst.
Calc. algal pack.
Dolomite
Mass. gypsum
Mixed bioclast.
Calc. sandstone
Calcrete
Clayey lime mud.
Quartz siltstone
Arkosic sanstone
Cycles
Palmarito Formation
64
63
62
61
60
59
58
57
56
55
54
53
52
51
50
49
48
47
46
45
44
43
42
40
39
38
37
36
35
34
33
32
31
30-
P56-
M37
m2
29

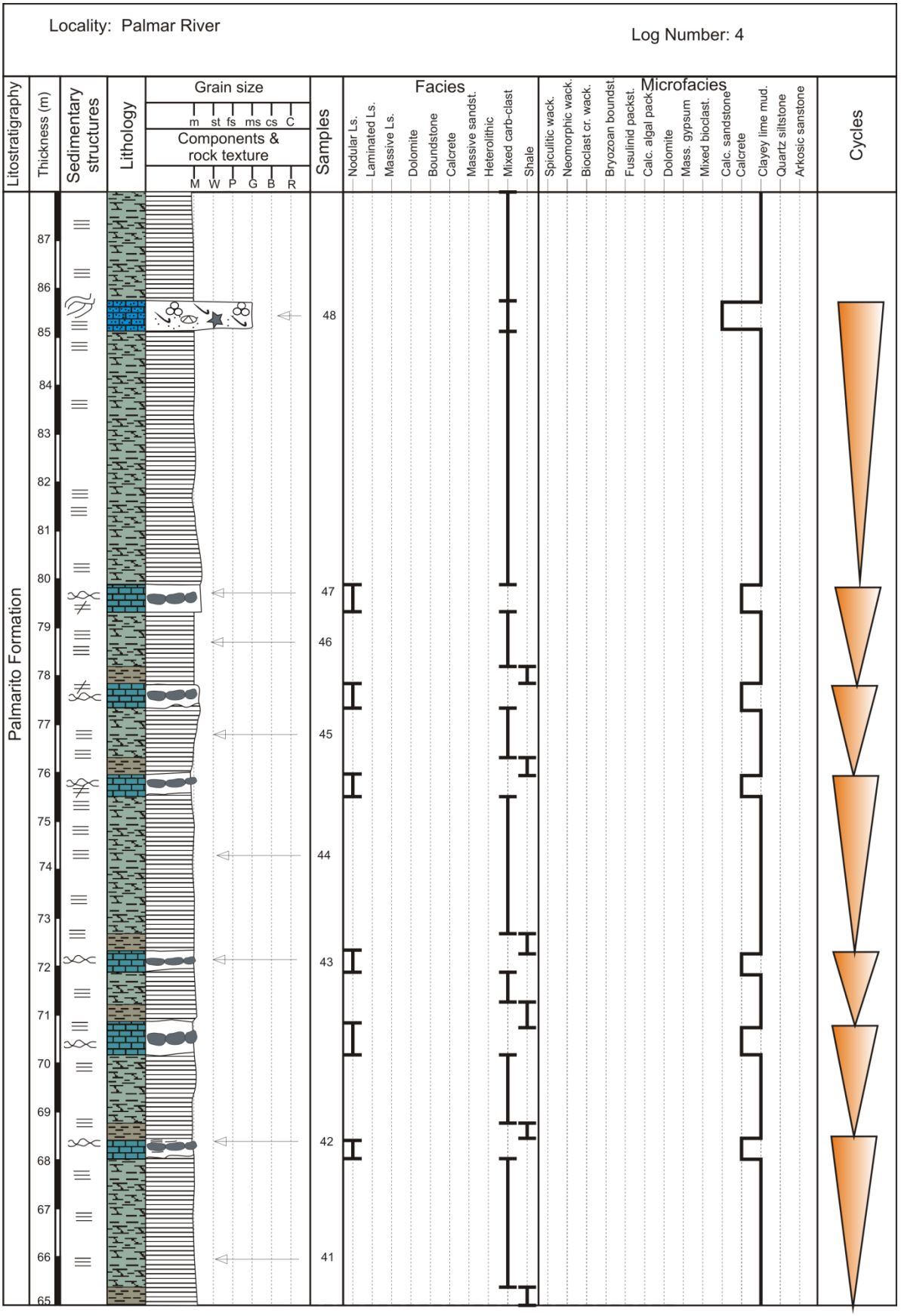
Locality: Palmar River
Log Number: 4
Litostratigraphy
Thickness (m)
Sedimentary structures
Lithology
Grain size
m st fs ms cs C
Components & rock texture
M W P G B R
Samples
Facies
Nodular Ls.
Laminated Ls.
Massive Ls.
Dolomite
Boundstone
Calcrete
Massive sandst.
Heterolithic
Mixed carb-clast
Shale
Microfacies
Spiculitic wack.
Neomorphic wack.
Bioclast cr. wack.
Bryozoan boundst.
Fusulinid packst.
Calc. algal pack.
Dolomite
Mass. gypsum
Mixed bioclast.
Calc. sandstone
Calcrete
Clayey lime mud.
Quartz siltstone
Arkosic sanstone
Cycles
Palmarito Formation
87
86
85
84
83
82
81
80
79
78
77
76
75
74
73
72
71
70
69
68
67
66
65
48
47
46
45
44
43
42
41

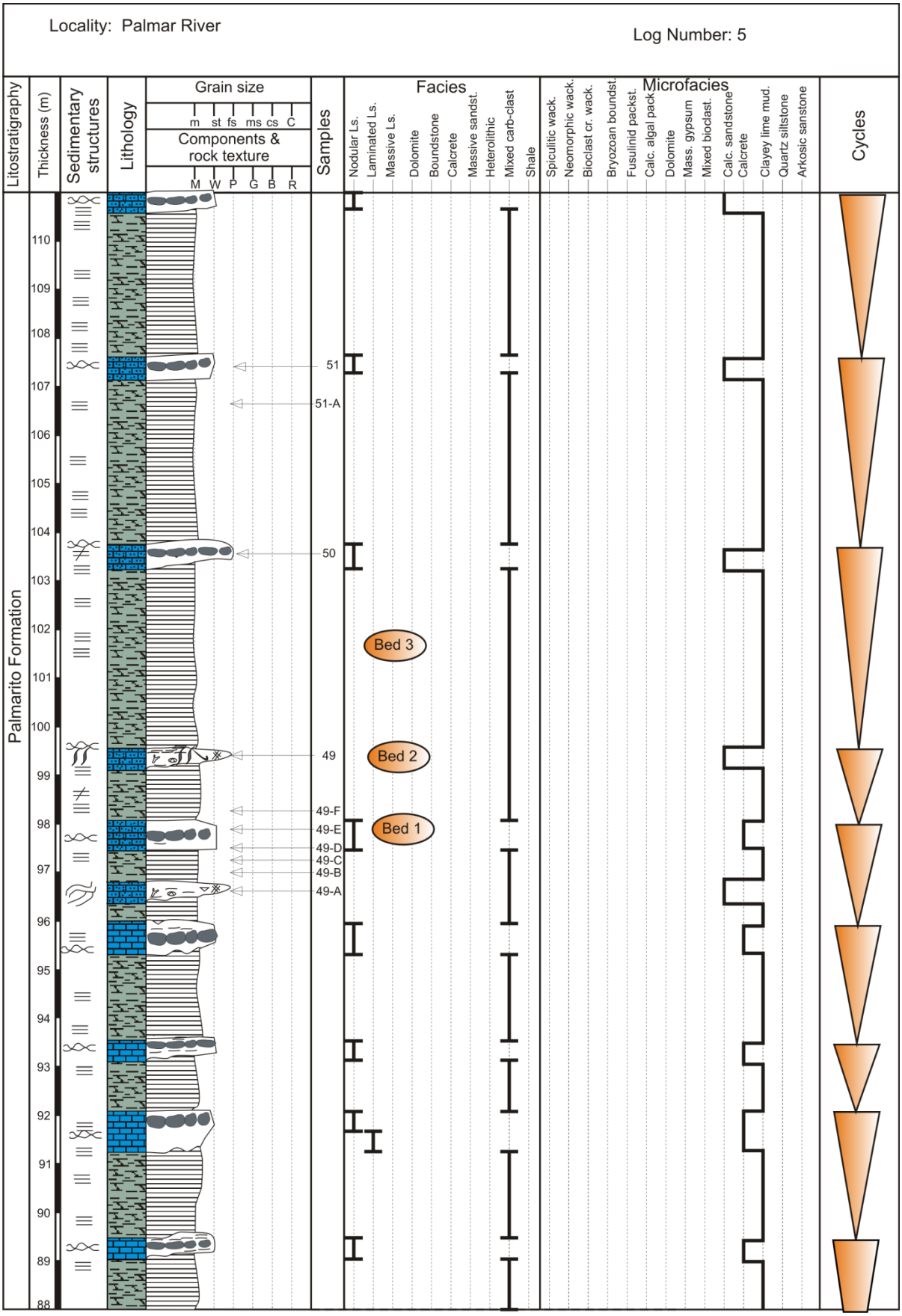
Locality: Palmar River
Log Number: 5
Litostratigraphy
Thickness (m)
Sedimentary structures
Lithology
Grain size
m st fs ms cs C
Components & rock texture
M W P G B R
Samples
Facies
Nodular Ls.
Laminated Ls.
Massive Ls.
Dolomite
Boundstone
Calcrete
Massive sandst.
Heterolithic
Mixed carb-clast
Shale
Microfacies
Spiculitic wack.
Neomorphic wack.
Bioclast cr. wack.
Bryozoan boundst.
Fusulinid packst.
Calc. algal pack.
Dolomite
Mass. gypsum
Mixed bioclast.
Calc. sandstone
Calcrete
Clayey lime mud.
Quartz siltstone
Arkosic sanstone
Cycles
Palmarito Formation
110
109
108
107
106
105
104
103
102
101
100
99
98
97
96
95
94
93
92
91
90
89
88
51
51-A
50
49
49-F
49-E
49-D
49-C
49-B
49-A
Bed 3
Bed 2
Bed 1

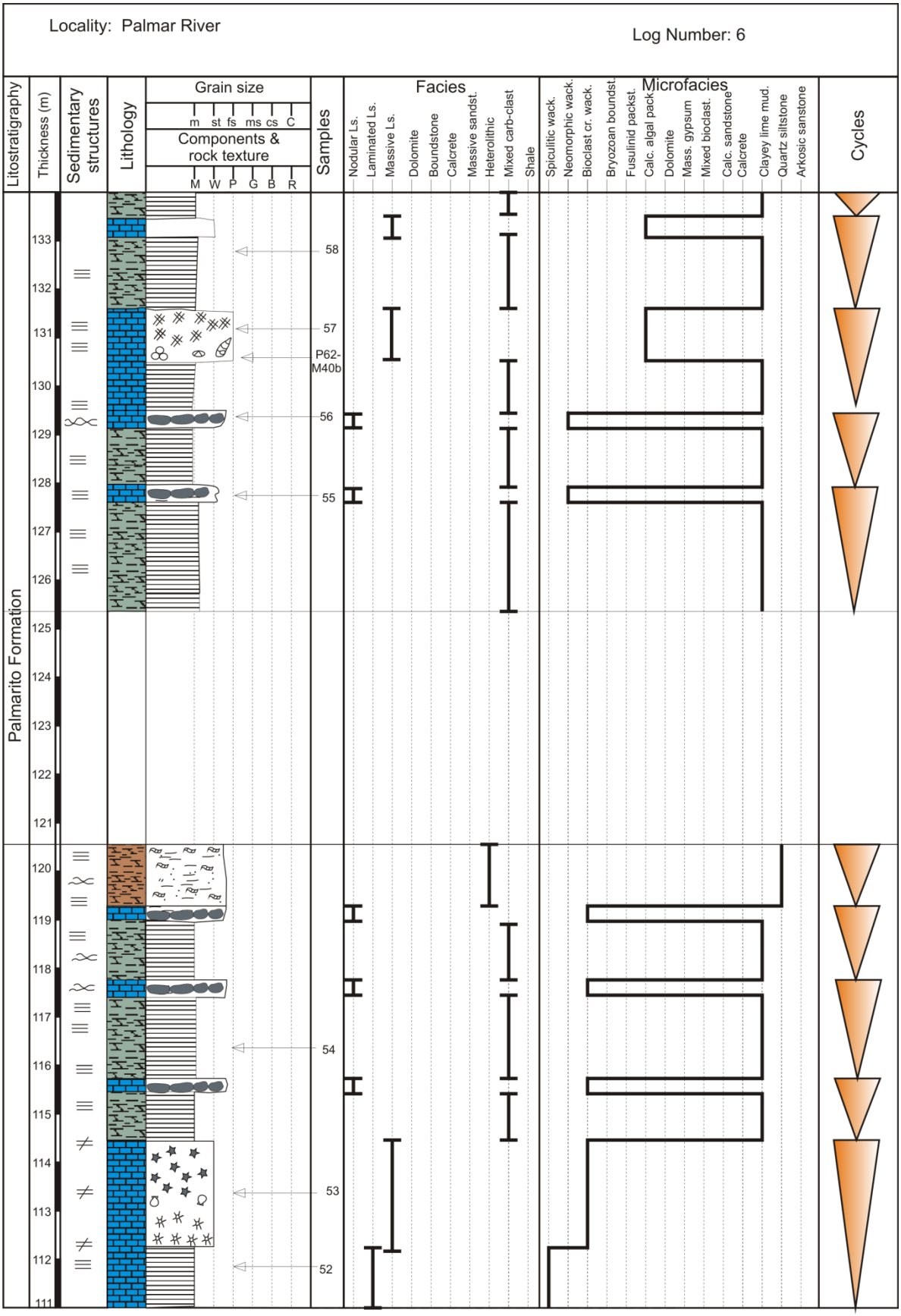
Locality: Palmar River
Log Number: 6
Litostratigraphy
Thickness (m)
Sedimentary structures
Lithology
Grain size
m st fs ms cs C
Components & rock texture
M W P G B R
Samples
Facies
Nodular Ls.
Laminated Ls.
Massive Ls.
Dolomite
Boundstone
Calcrete
Massive sandst.
Heterolithic
Mixed carb-clast
Shale
Microfacies
Spiculitic wack.
Neomorphic wack.
Bioclast cr. wack.
Bryozoan boundst.
Fusulinid packst.
Calc. algal pack.
Dolomite
Mass. gypsum
Mixed bioclast.
Calc. sandstone
Calcrete
Clayey lime mud.
Quartz siltstone
Arkosic sanstone
Cycles
Palmarito Formation
58
57
P62-M40b
56
55
54
53
52

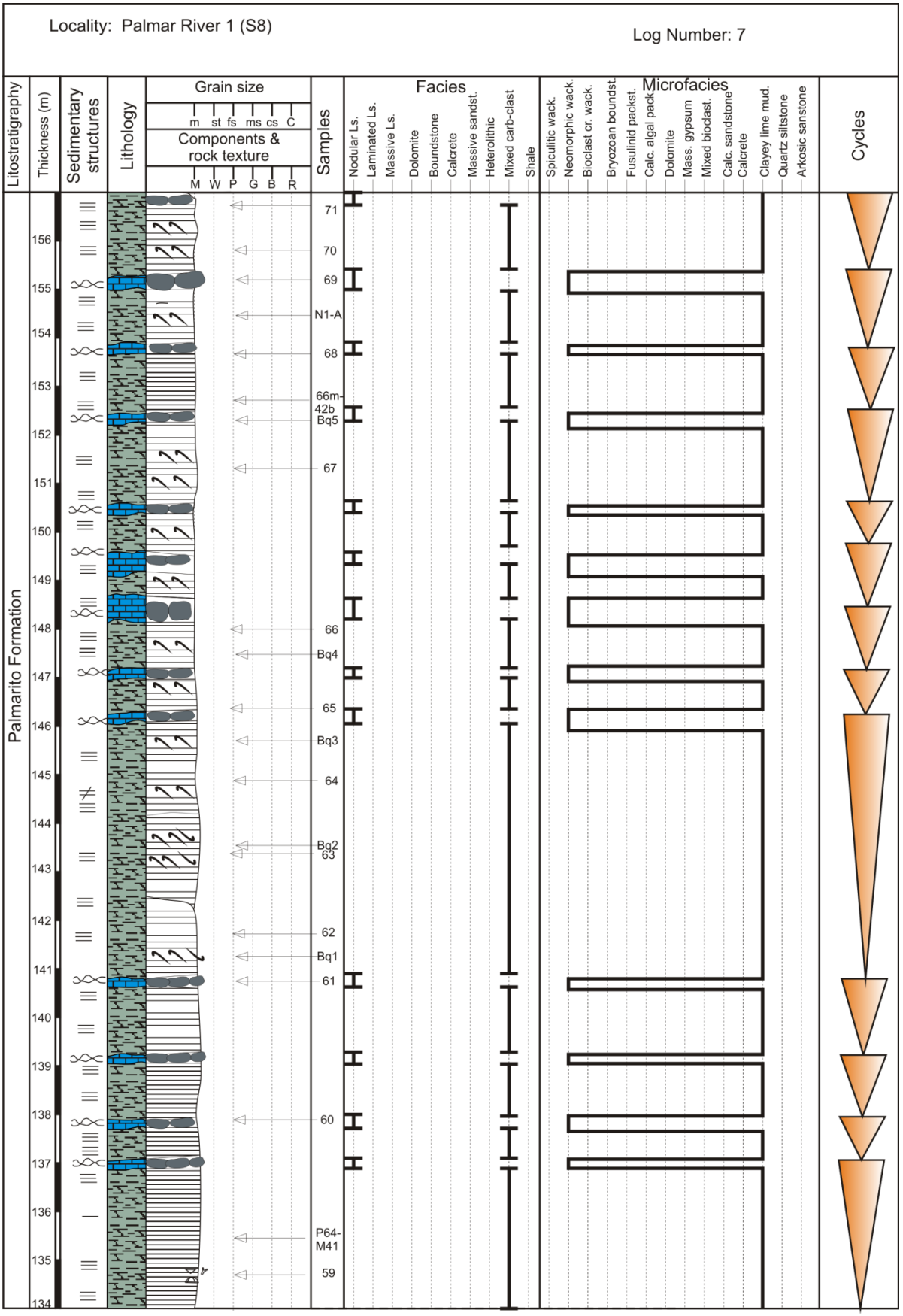
Locality: Palmar River 1 (S8)
Log Number: 7
Litostratigraphy
Thickness (m)
Sedimentary structures
Lithology
Grain size
m st fs ms cs C
Components & rock texture
M W P G B R
Samples
Facies
Nodular Ls.
Laminated Ls.
Massive Ls.
Dolomite
Boundstone
Calcrete
Massive sandst.
Heterolithic
Mixed carb-clast
Shale
Microfacies
Spiculitic wack.
Neomorphic wack.
Bioclast cr. wack.
Bryozoan boundst.
Fusulinid packst.
Calc. algal pack.
Dolomite
Mass. gypsum
Mixed bioclast.
Calc. sandstone
Calcrete
Clayey lime mud.
Quartz siltstone
Arkosic sanstone
Cycles
Palmarito Formation
156
155
154
153
152
151
150
149
148
147
146
145
144
143
142
141
140
139
138
137
136
135
134
71
70
69
N1-A
68
66m-42b
Bq5
67
66
Bq4
65
Bq3
64
Bq2
63
62
Bq1
61
60
P64-M41
59

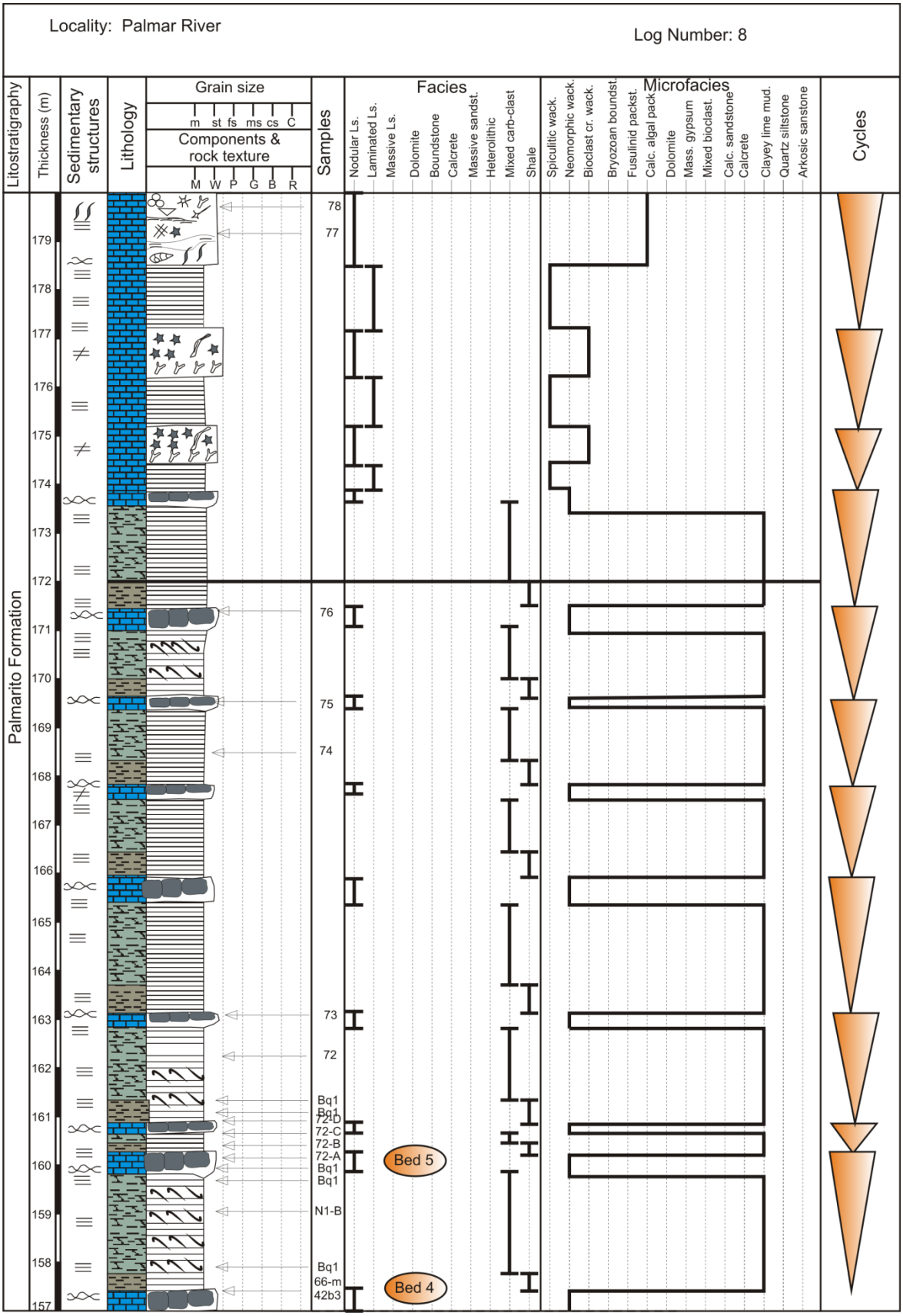
Locality: Palmar River
Log Number: 8
Litostratigraphy
Thickness (m)
Sedimentary structures
Lithology
Grain size
m st fs ms cs C
Components & rock texture
M W P G B R
Samples
Facies
Nodular Ls.
Laminated Ls.
Massive Ls.
Dolomite
Boundstone
Calcrete
Massive sandst.
Heterolithic
Mixed carb-clast
Shale
Microfacies
Spiculitic wack.
Neomorphic wack.
Bioclast cr. wack.
Bryozoan boundst.
Fusulinid packst.
Calc. algal pack
Dolomite
Mass. gypsum
Mixed bioclast.
Calc. sandstone
Calcrete
Clayey lime mud.
Quartz siltstone
Arkosic sanstone
Cycles
Palmarito Formation
179
178
177
176
175
174
173
172
171
170
169
168
167
166
165
164
163
162
161
160
159
158
157
78
77
76
75
74
73
72
Bq1
Bq1
72-D
72-C
72-B
72-A
Bq1
Bq1
N1-B
Bq1
66-m
42b3
Bed 5
Bed 4

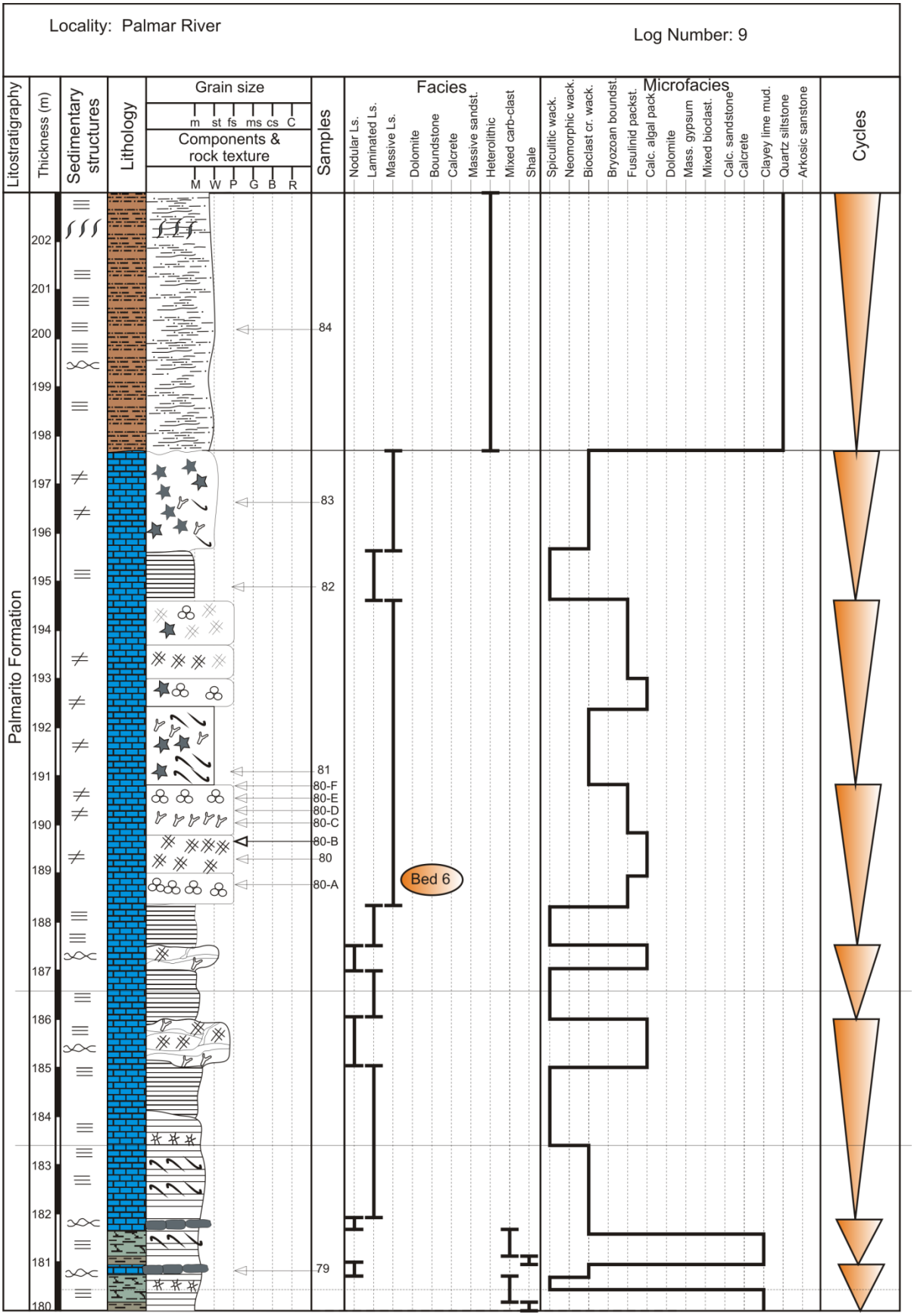
Locality: Palmar River
Log Number: 9
Litostratigraphy
Thickness (m)
Sedimentary structures
Lithology
Grain size
m st fs ms cs C
Components & rock texture
M W P G B R
Samples
Facies
Nodular Ls.
Laminated Ls.
Massive Ls.
Dolomite
Boundstone
Calcrete
Massive sandst.
Heterolithic
Mixed carb-clast
Shale
Microfacies
Spiculitic wack.
Neomorphic wack.
Bioclast cr. wack.
Bryozoan boundst.
Fusulinid packst.
Calc. algal pack.
Dolomite
Mass. gypsum
Mixed bioclast.
Calc. sandstone
Calcrete
Clayey lime mud.
Quartz siltstone
Arkosic sanstone
Cycles
Palmarito Formation
202
201
200
199
198
197
196
195
194
193
192
191
190
189
188
187
186
185
184
183
182
181
180
84
83
82
81
80-F
80-E
80-D
80-C
80-B
80
80-A
79
Bed 6

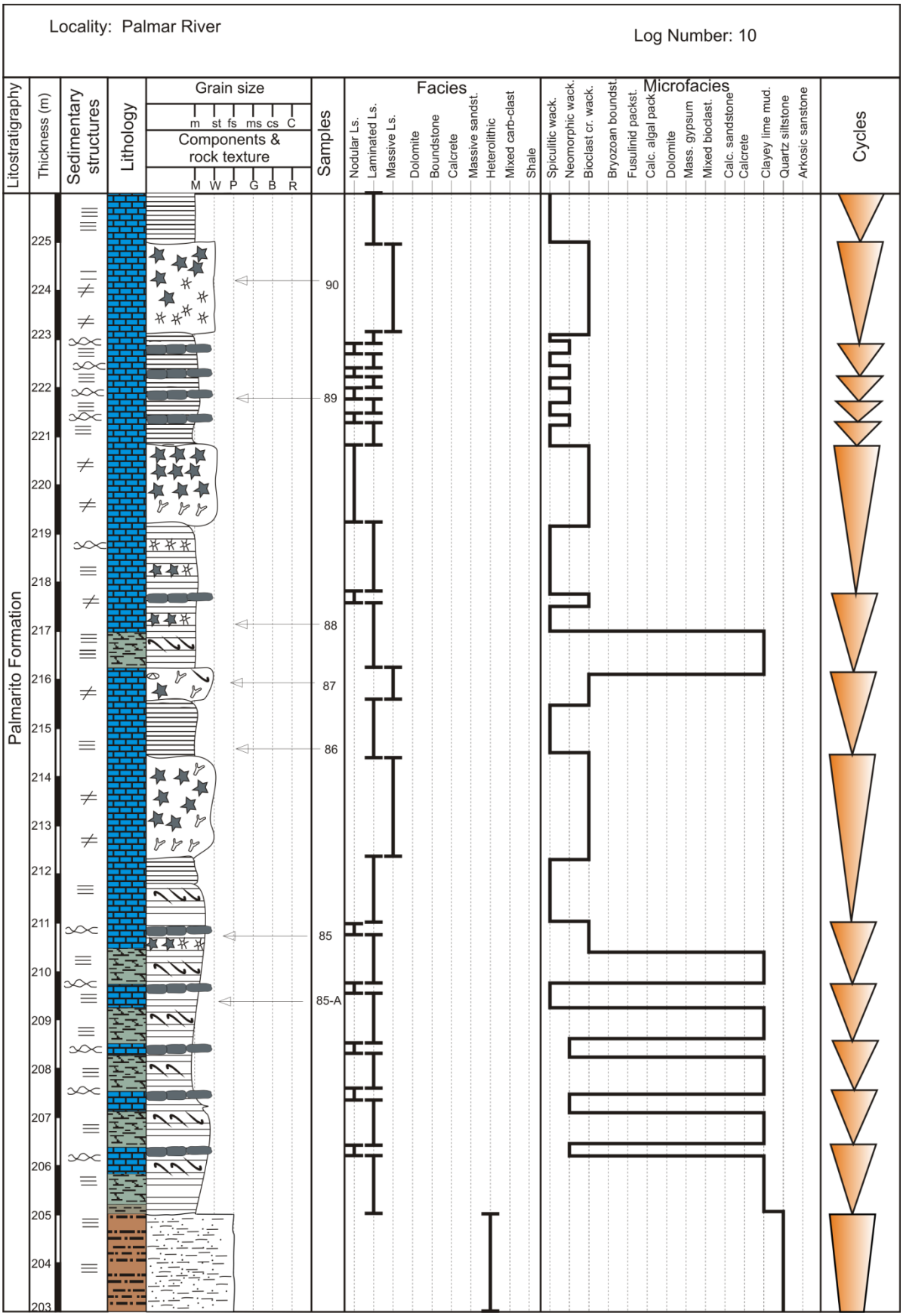
Locality: Palmar River
Log Number: 10
Litostratigraphy
Thickness (m)
Sedimentary structures
Lithology
Grain size
m st fs ms cs C
Components & rock texture
M W P G B R
Samples
Facies
Nodular Ls.
Laminated Ls.
Massive Ls.
Dolomite
Boundstone
Calcrete
Massive sandst.
Heterolithic
Mixed carb-clast
Shale
Microfacies
Spiculitic wack.
Neomorphic wack.
Bioclast cr. wack.
Bryozoan boundst.
Fusulinid packst.
Calc. algal pack.
Dolomite
Mass. gypsum
Mixed bioclast.
Calc. sandstone
Calcrete
Clayey lime mud.
Quartz siltstone
Arkosic sanstone
Cycles
Palmarito Formation
225
224
223
222
221
220
219
218
217
216
215
214
213
212
211
210
209
208
207
206
205
204
203
90
89
88
87
86
85
85-A

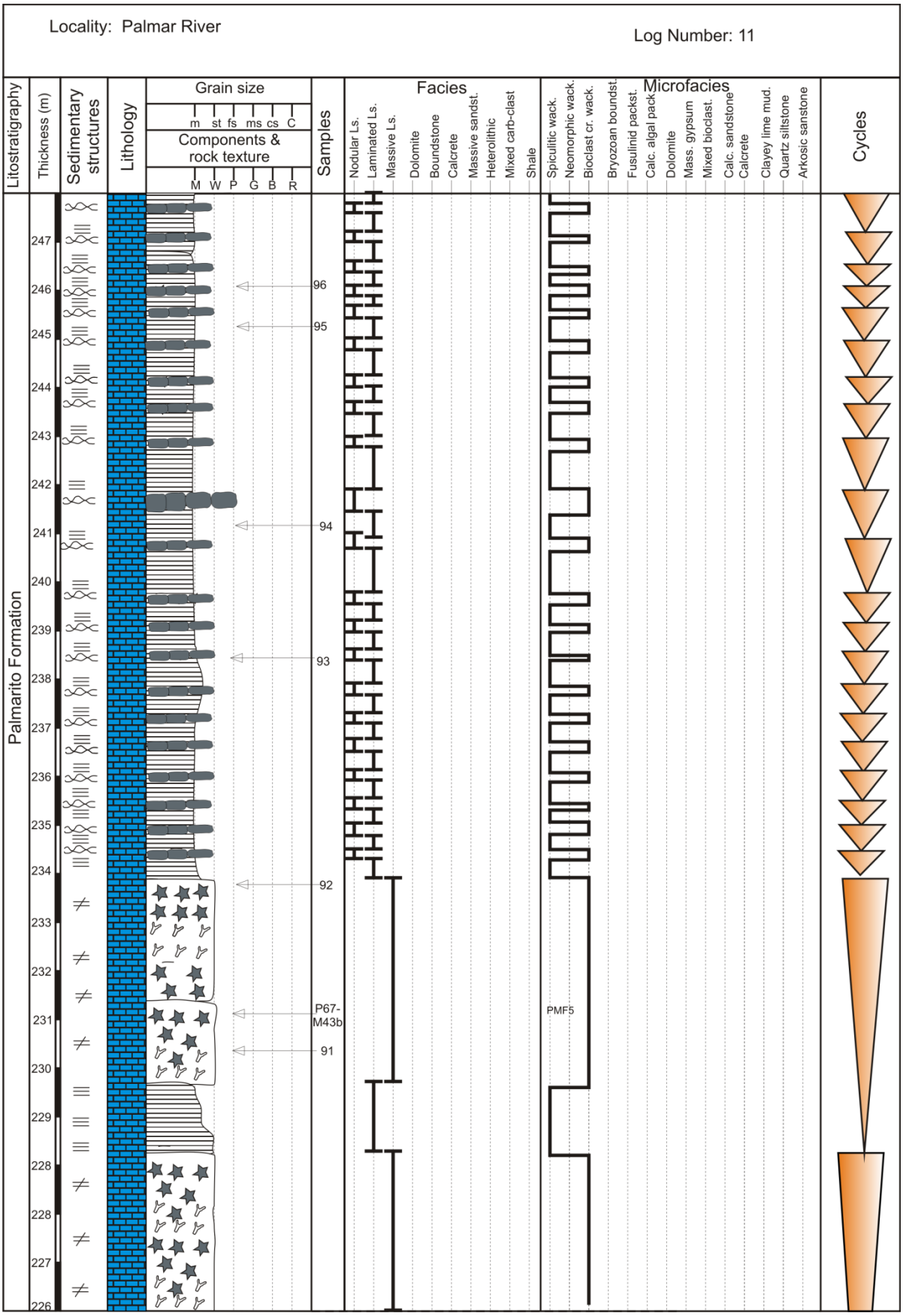
Locality: Palmar River
Log Number: 11
Litostratigraphy
Thickness (m)
Sedimentary structures
Lithology
Grain size
m st fs ms cs C
Components & rock texture
M W P G B R
Samples
Facies
Nodular Ls.
Laminated Ls.
Massive Ls.
Dolomite
Boundstone
Calcrete
Massive sandst.
Heterolithic
Mixed carb-clast
Shale
Microfacies
Spiculitic wack.
Neomorphic wack.
Bioclast cr. wack.
Bryozoan boundst.
Fusulinid packst.
Calc. algal pack.
Dolomite
Mass. gypsum
Mixed bioclast.
Calc. sandstone
Calcrete
Clayey lime mud.
Quartz siltstone
Arkosic sanstone
Cycles
Palmarito Formation
247
246
245
244
243
242
241
240
239
238
237
236
235
234
233
232
231
230
229
228
228
227
226
96
95
94
93
92
P67-M43b
91
PMF5

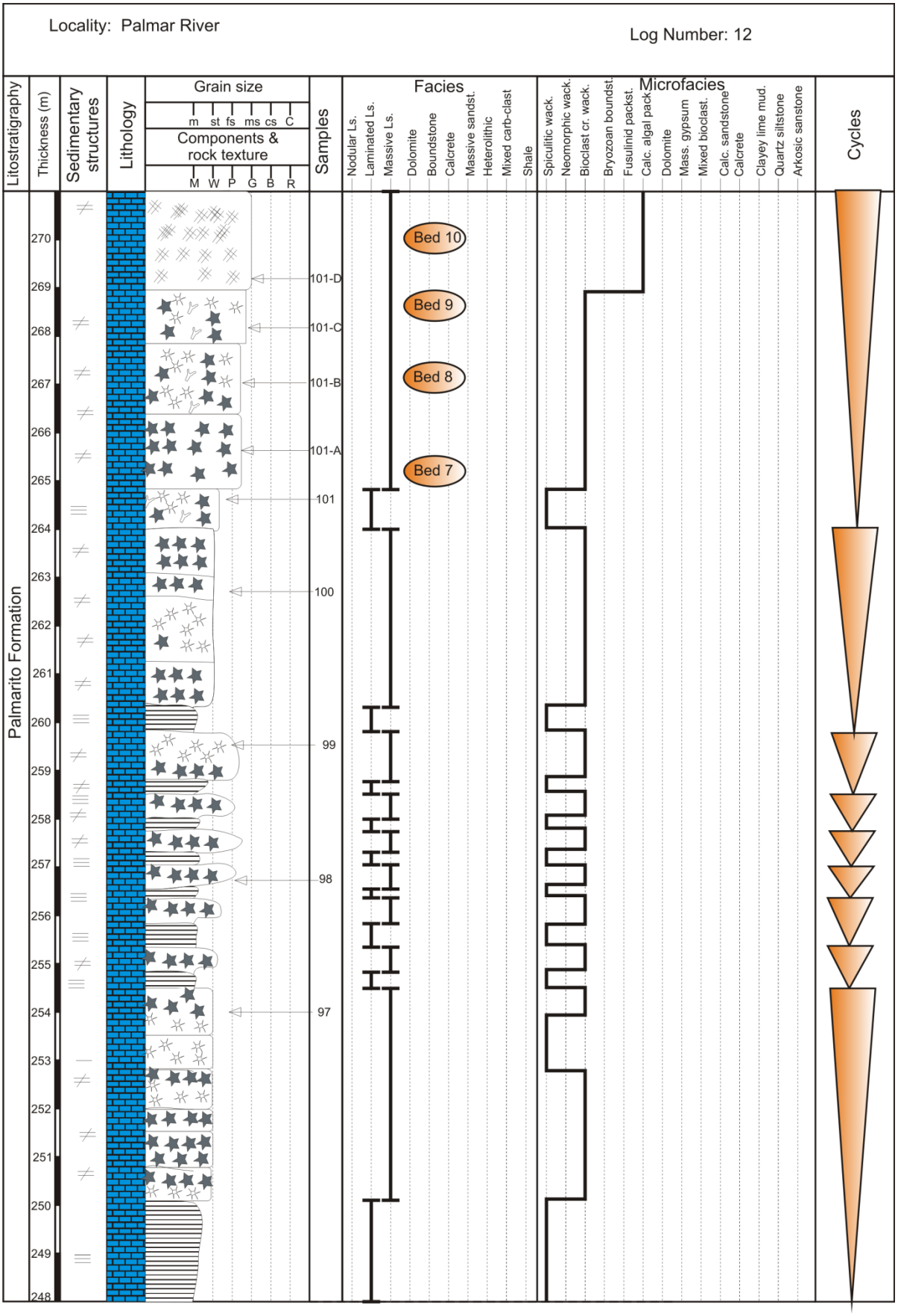
Locality: Palmar River
Log Number: 12
Litostratigraphy
Thickness (m)
Sedimentary structures
Lithology
Grain size
m st fs ms cs C
Components & rock texture
M W P G B R
Samples
Facies
Nodular Ls.
Laminated Ls.
Massive Ls.
Dolomite
Boundstone
Calcrete
Massive sandst.
Heterolithic
Mixed carb-clast
Shale
Microfacies
Spiculitic wack.
Neomorphic wack.
Bioclast cr. wack.
Bryozoan boundst.
Fusulinid packst.
Calc. algal pack.
Dolomite
Mass. gypsum
Mixed bioclast.
Calc. sandstone
Calcrete
Clayey lime mud.
Quartz siltstone
Arkosic sanstone
Cycles
Palmarito Formation
270
269
268
267
266
265
264
263
262
261
260
259
258
257
256
255
254
253
252
251
250
249
248
101-D
101-C
101-B
101-A
101
100
99
98
97
Bed 10
Bed 9
Bed 8
Bed 7

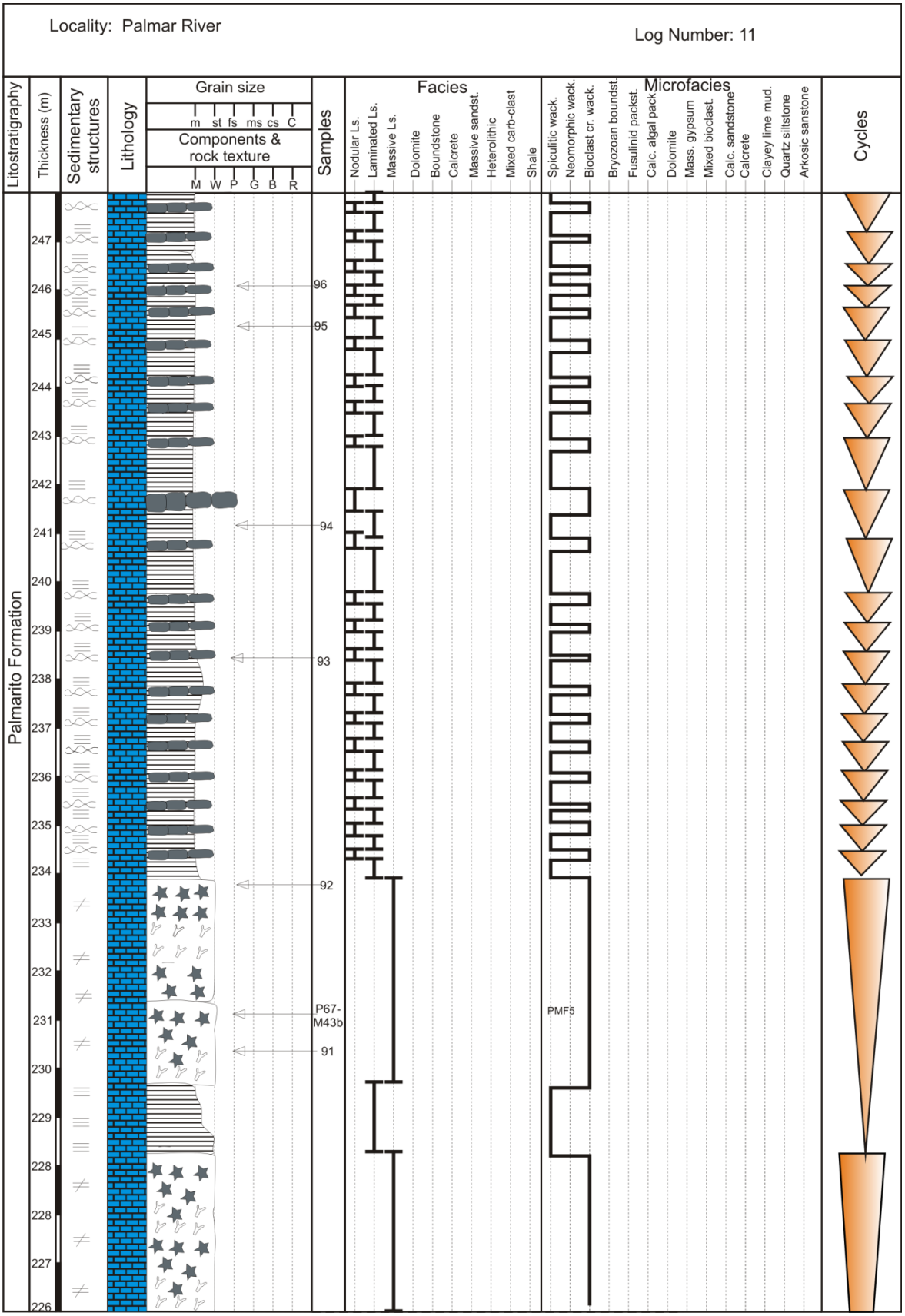
Locality: Palmar River
Log Number: 11
Litostratigraphy
Thickness (m)
Sedimentary structures
Lithology
Grain size
m st fs ms cs C
Components & rock texture
M W P G B R
Samples
Facies
Nodular Ls.
Laminated Ls.
Massive Ls.
Dolomite
Boundstone
Calcrete
Massive sandst.
Heterolithic
Mixed carb-clast
Shale
Microfacies
Spiculitic wack.
Neomorphic wack.
Bioclast cr. wack.
Bryozoan boundst.
Fusulinid packst.
Calc. algal pack
Dolomite
Mass. gypsum
Mixed bioclast.
Calc. sandstone
Calcrete
Clayey lime mud.
Quartz siltstone
Arkosic sanstone
Cycles
Palmarito Formation
247
246
245
244
243
242
241
240
239
238
237
236
235
234
233
232
231
230
229
228
228
227
226
96
95
94
93
92
P67-M43b
91
PMF5

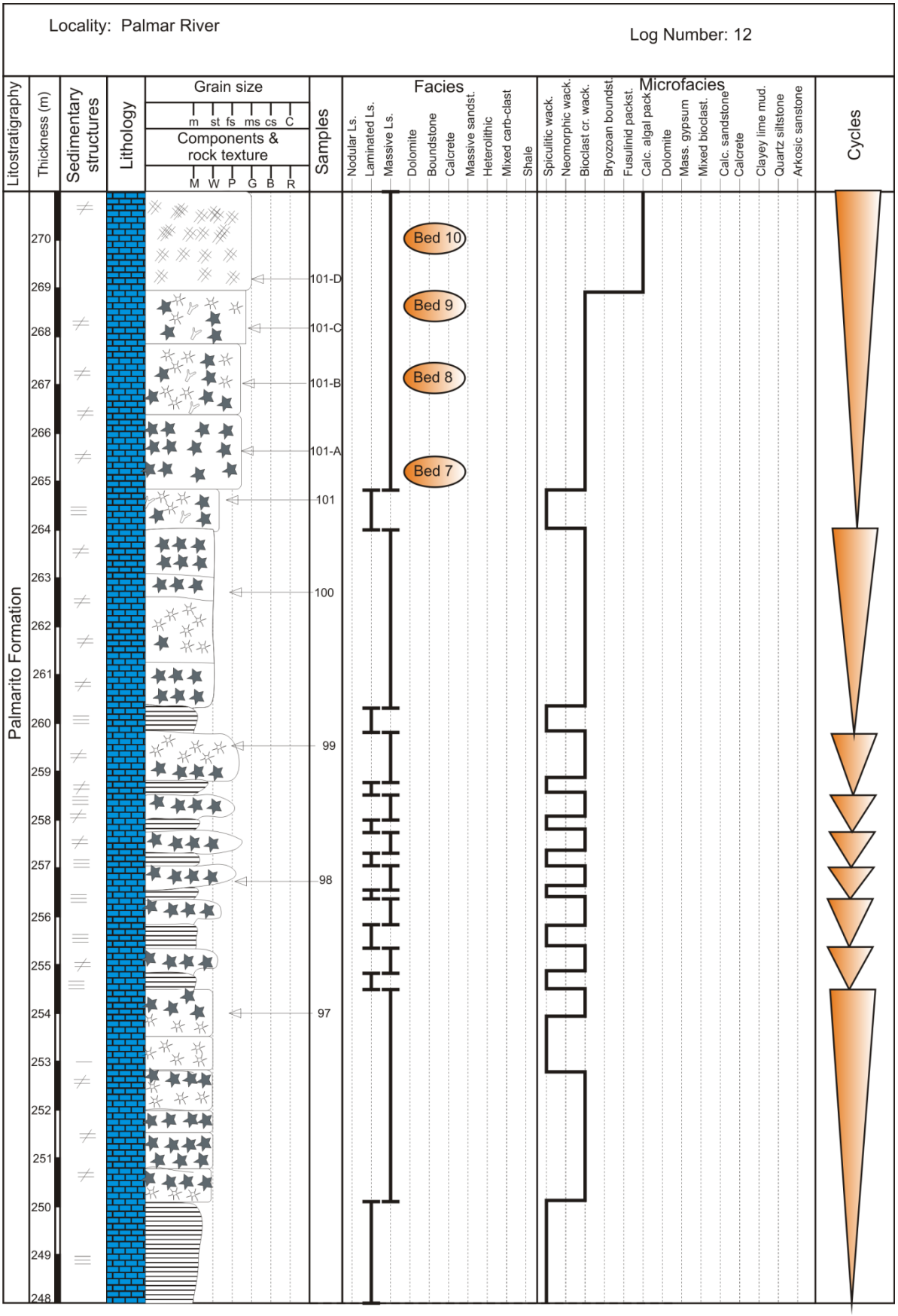
Locality: Palmar River
Log Number: 12
Litostratigraphy
Thickness (m)
Sedimentary structures
Lithology
Grain size
m st fs ms cs C
Components & rock texture
M W P G B R
Samples
Facies
Nodular Ls.
Laminated Ls.
Massive Ls.
Dolomite
Boundstone
Calcrete
Massive sandst.
Heterolithic
Mixed carb-clast
Shale
Microfacies
Spiculitic wack.
Neomorphic wack.
Bioclast cr. wack.
Bryozoan boundst.
Fusulinid packst.
Calc. algal pack
Dolomite
Mass. gypsum
Mixed bioclast.
Calc. sandstone
Calcrete
Clayey lime mud.
Quartz siltstone
Arkosic sanstone
Cycles
Palmarito Formation
270
269
268
267
266
265
264
263
262
261
260
259
258
257
256
255
254
253
252
251
250
249
248
101-D
101-C
101-B
101-A
101
100
99
98
97
Bed 10
Bed 9
Bed 8
Bed 7

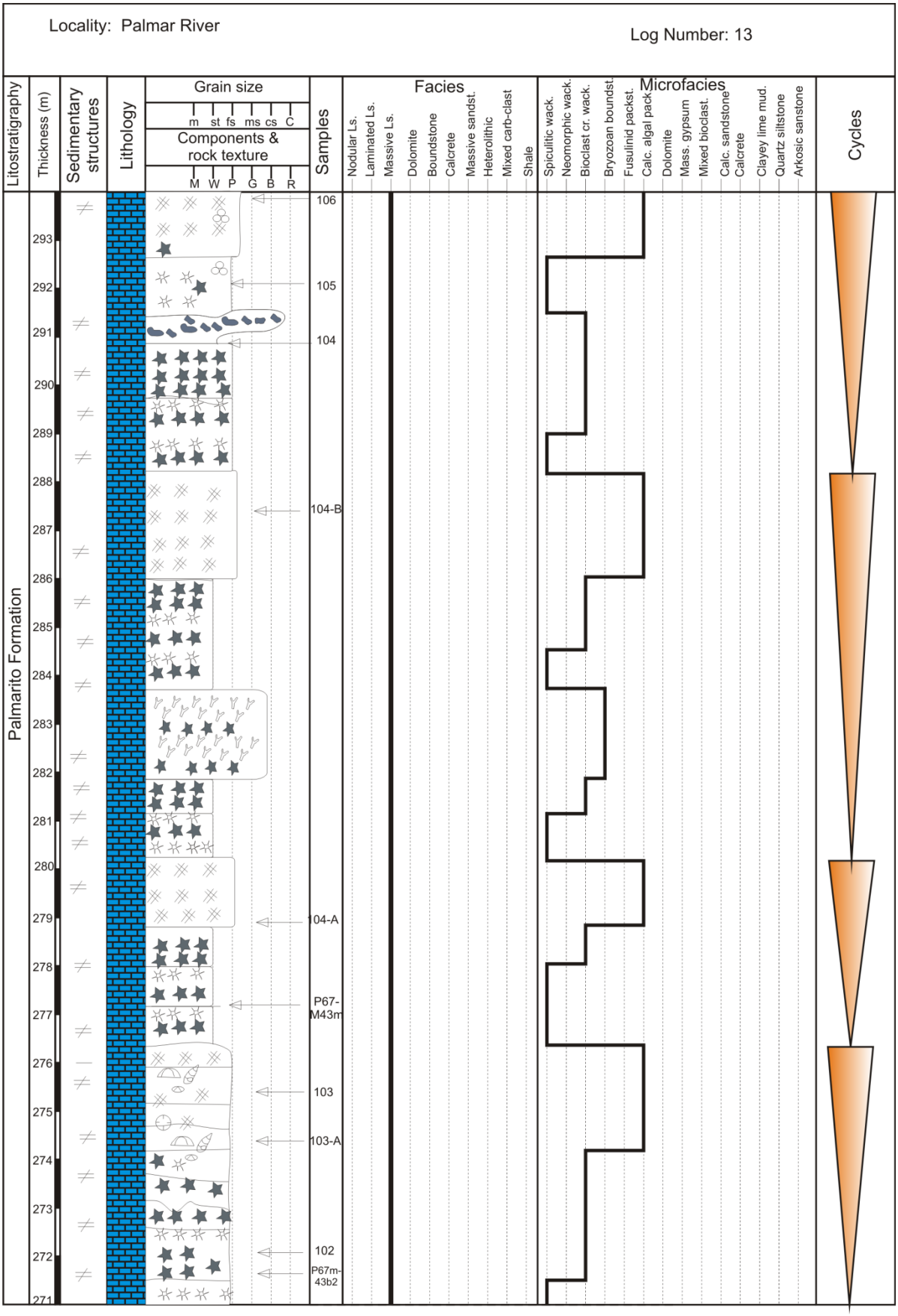
Locality: Palmar River
Log Number: 13
Litostratigraphy
Thickness (m)
Sedimentary structures
Lithology
Grain size
m st fs ms cs C
Components & rock texture
M W P G B R
Samples
Facies
Nodular Ls.
Laminated Ls.
Massive Ls.
Dolomite
Boundstone
Calcrete
Massive sandst.
Heterolithic
Mixed carb-clast
Shale
Microfacies
Spiculitic wack.
Neomorphic wack.
Bioclast cr. wack.
Bryozoan boundst.
Fusulinid packst.
Calc. algal pack
Dolomite
Mass. gypsum
Mixed bioclast.
Calc. sandstone
Calcrete
Clayey lime mud.
Quartz siltstone
Arkosic sanstone
Cycles
Palmarito Formation
293
292
291
290
289
288
287
286
285
284
283
282
281
280
279
278
277
276
275
274
273
272
271
106
105
104
104-B
104-A
P67-M43m
103
103-A
102
P67m-43b2

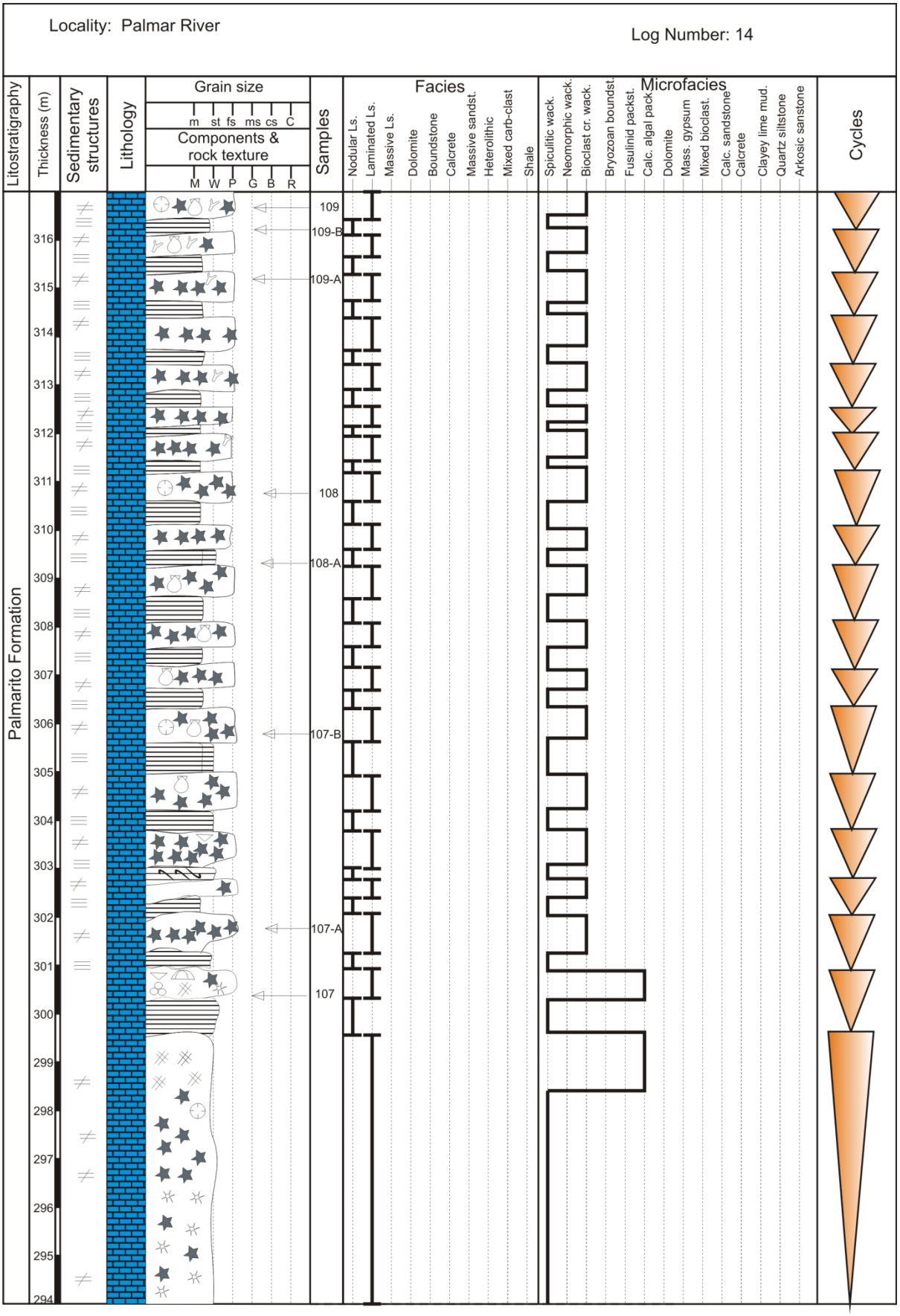
Locality: Palmar River
Log Number: 14
Litostratigraphy
Thickness (m)
Sedimentary structures
Lithology
Grain size
m st fs ms cs C
Components & rock texture
M W P G B R
Samples
Facies
Nodular Ls.
Laminated Ls.
Massive Ls.
Dolomite
Boundstone
Calcrete
Massive sandst.
Heterolithic
Mixed carb-clast
Shale
Microfacies
Spiculitic wack.
Neomorphic wack.
Bioclast cr. wack.
Bryozoan boundst.
Fusulinid packst.
Calc. algal pack.
Dolomite
Mass. gypsum
Mixed bioclast.
Calc. sandstone
Calcrete
Clayey lime mud.
Quartz siltstone
Arkosic sanstone
Cycles
Palmarito Formation
316
315
314
313
312
311
310
309
308
307
306
305
304
303
302
301
300
299
298
297
296
295
294
109
109-B
109-A
108
108-A
107-B
107-A
107

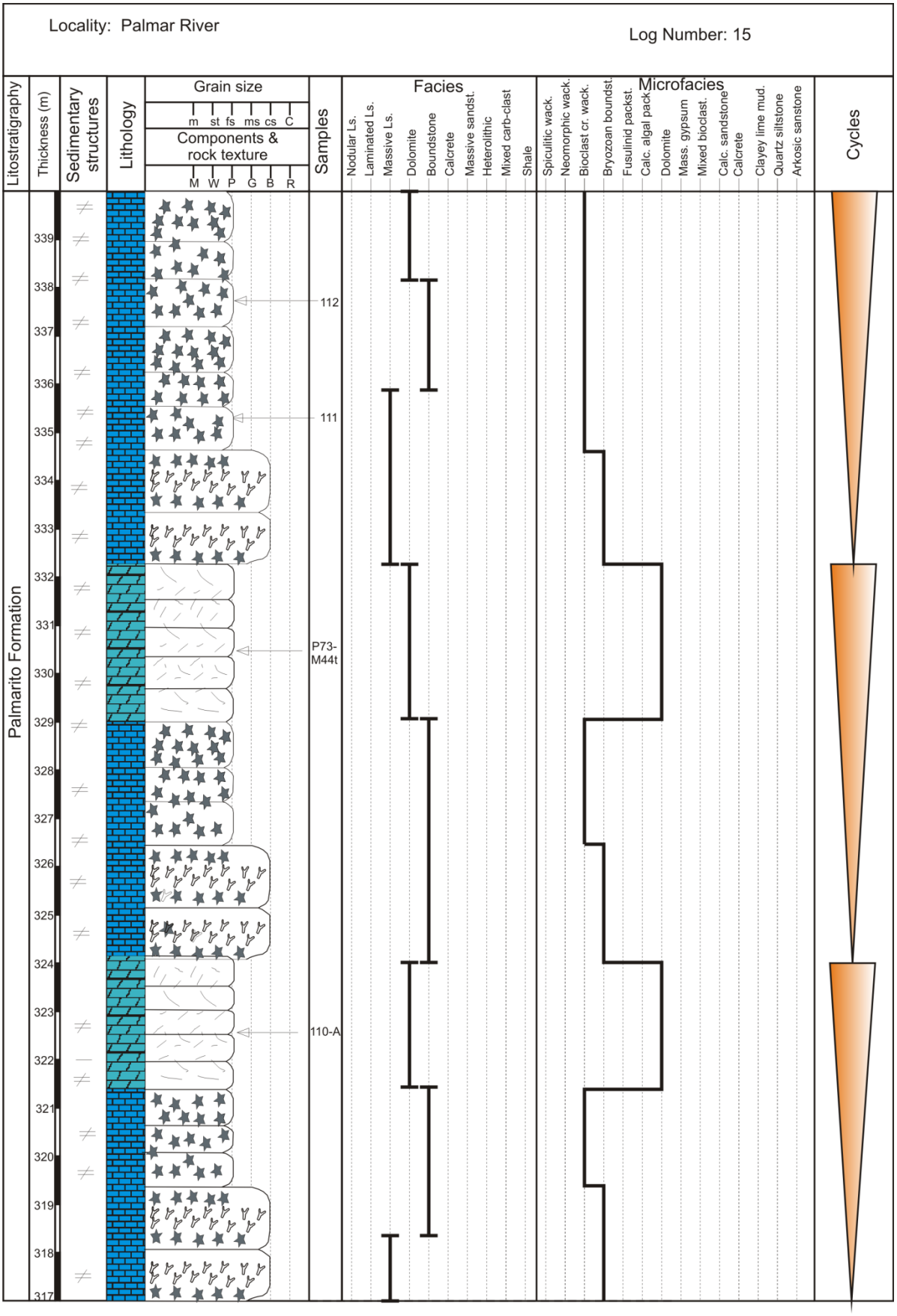
Locality: Palmar River
Log Number: 15
Litostratigraphy
Thickness (m)
Sedimentary structures
Lithology
Grain size
m st fs ms cs C
Components & rock texture
M W P G B R
Samples
Facies
Nodular Ls.
Laminated Ls.
Massive Ls.
Dolomite
Boundstone
Calcrete
Massive sandst.
Heterolithic
Mixed carb-clast
Shale
Microfacies
Spiculitic wack.
Neomorphic wack.
Bioclast cr. wack.
Bryozoan boundst.
Fusulinid packst.
Calc. algal pack
Dolomite
Mass. gypsum
Mixed bioclast.
Calc. sandstone
Calcrete
Clayey lime mud.
Quartz siltstone
Arkosic sanstone
Cycles
Palmarito Formation
339
338
337
336
335
334
333
332
331
330
329
328
327
326
325
324
323
322
321
320
319
318
317
112
111
P73-M44t
110-A

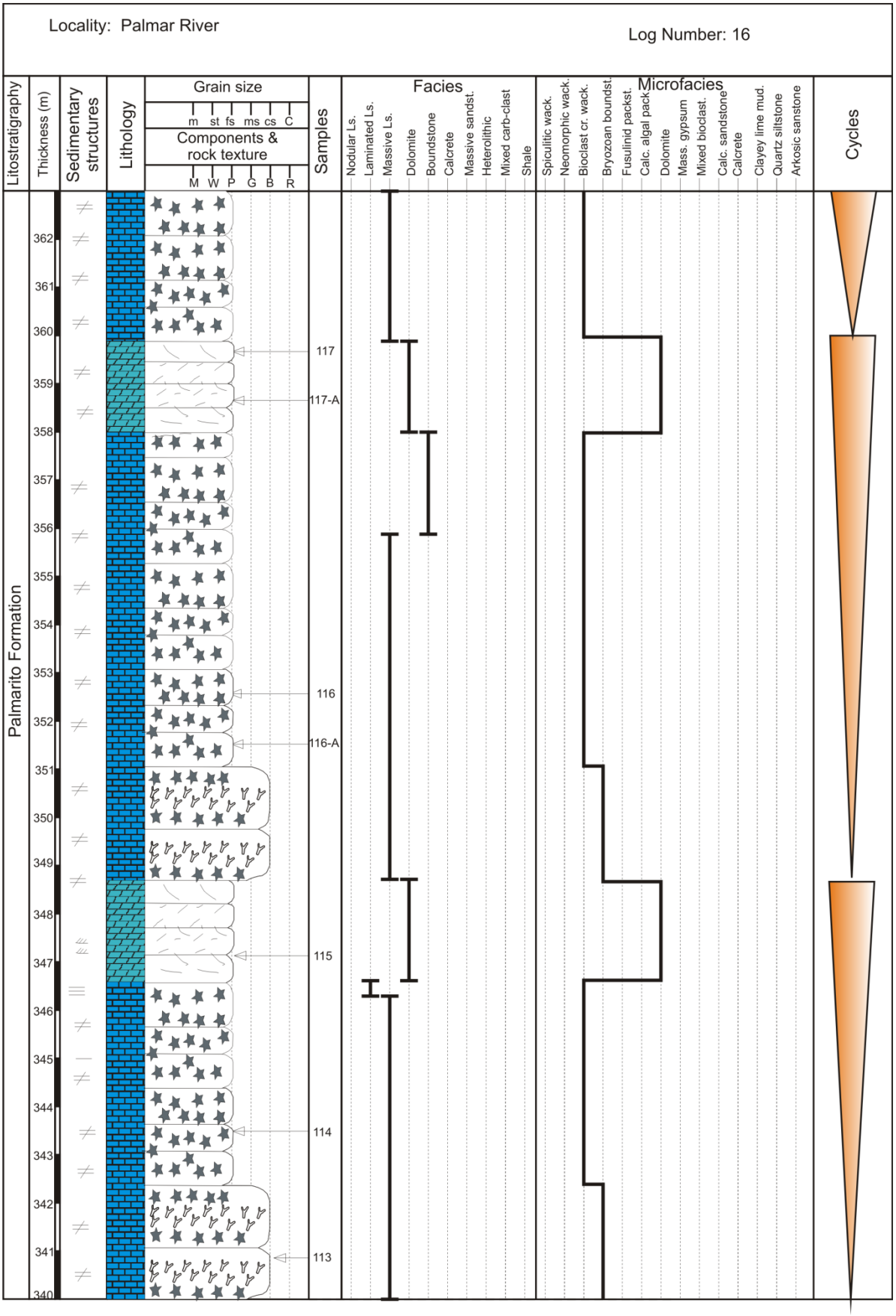
Locality: Palmar River
Log Number: 16
Litostratigraphy
Thickness (m)
Sedimentary structures
Lithology
Grain size
m st fs ms cs C
Components & rock texture
M W P G B R
Samples
Facies
Nodular Ls.
Laminated Ls.
Massive Ls.
Dolomite
Boundstone
Calcrete
Massive sandst.
Heterolithic
Mixed carb-clast
Shale
Microfacies
Spiculitic wack.
Neomorphic wack.
Bioclast cr. wack.
Bryozoan boundst.
Fusulinid packst.
Calc. algal pack.
Dolomite
Mass. gypsum
Mixed bioclast.
Calc. sandstone
Calcrete
Clayey lime mud.
Quartz siltstone
Arkosic sanstone
Cycles
Palmarito Formation
362
361
360
359
358
357
356
355
354
353
352
351
350
349
348
347
346
345
344
343
342
341
340
117
117-A
116
116-A
115
114
113

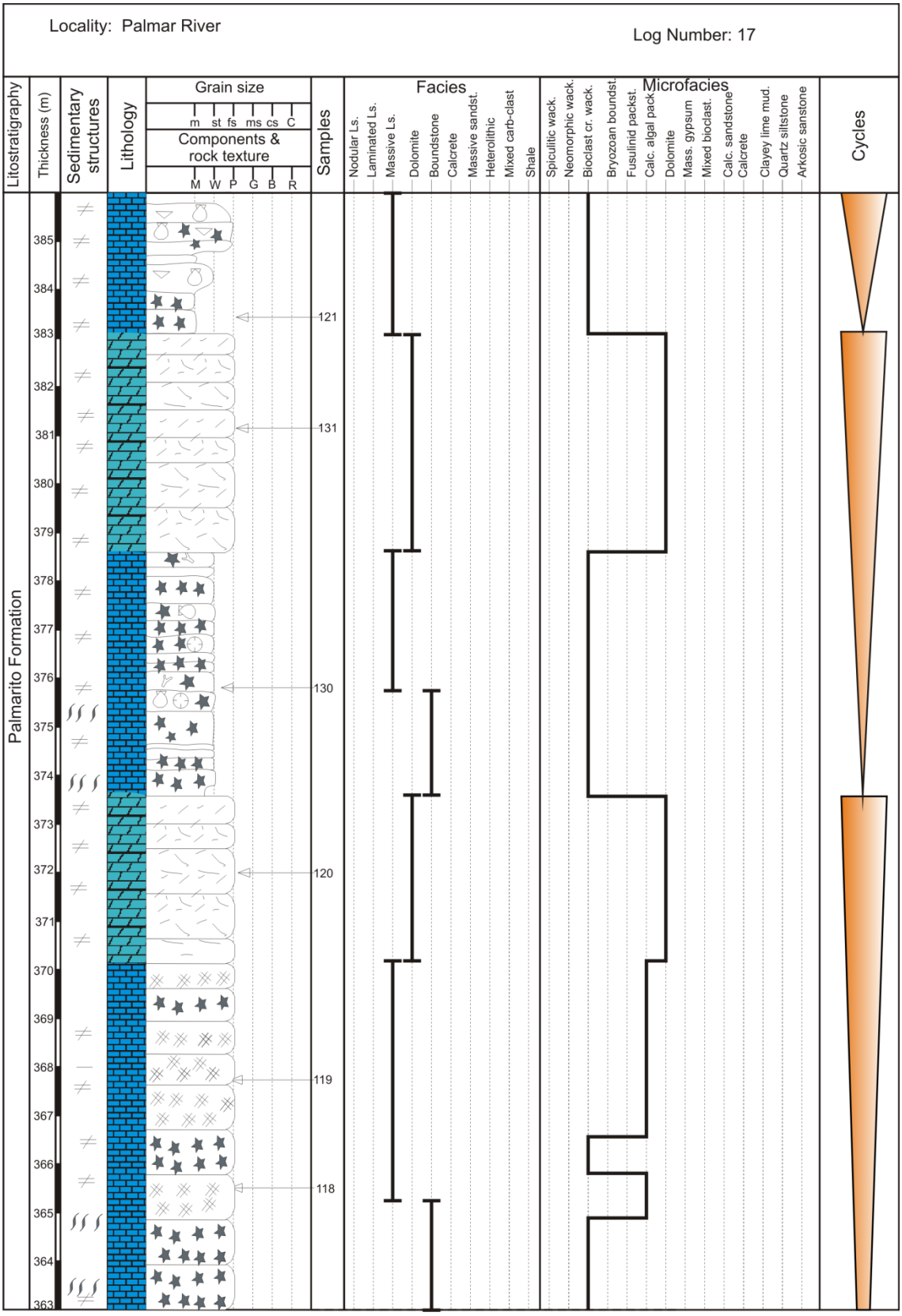
Locality: Palmar River
Log Number: 17
Litostratigraphy
Thickness (m)
Sedimentary structures
Lithology
Grain size
m st fs ms cs C
Components & rock texture
M W P G B R
Samples
Facies
Nodular Ls.
Laminated Ls.
Massive Ls.
Dolomite
Boundstone
Calcrete
Massive sandst.
Heterolithic
Mixed carb-clast
Shale
Microfacies
Spiculitic wack.
Neomorphic wack.
Bioclast cr. wack.
Bryozoan boundst.
Fusulinid packst.
Calc. algal pack.
Dolomite
Mass. gypsum
Mixed bioclast.
Calc. sandstone
Calcrete
Clayey lime mud.
Quartz siltstone
Arkosic sanstone
Cycles
Palmarito Formation
385
384
383
382
381
380
379
378
377
376
375
374
373
372
371
370
369
368
367
366
365
364
363
121
131
130
120
119
118

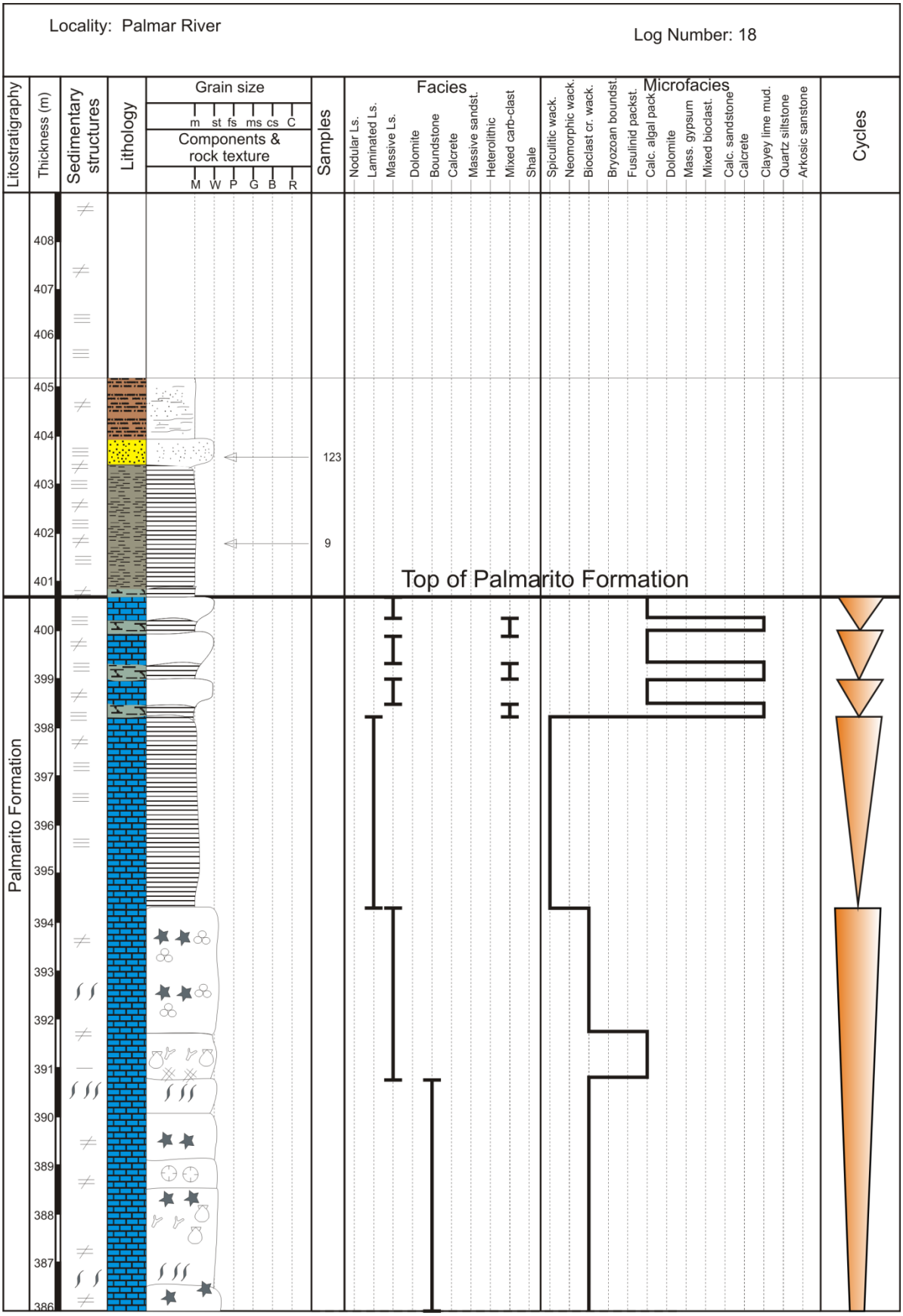
Locality: Palmar River
Log Number: 18
Litostratigraphy
Thickness (m)
Sedimentary structures
Lithology
Grain size
m st fs ms cs C
Components & rock texture
M W P G B R
Samples
Facies
Nodular Ls.
Laminated Ls.
Massive Ls.
Dolomite
Boundstone
Calcrete
Massive sandst.
Heterolithic
Mixed carb-clast
Shale
Microfacies
Spiculitic wack.
Neomorphic wack.
Bioclast cr. wack.
Bryozoan boundst.
Fusulinid packst.
Calc. algal pack
Dolomite
Mass. gypsum
Mixed bioclast.
Calc. sandstone
Calcrete
Clayey lime mud.
Quartz siltstone
Arkosic sanstone
Cycles
123
9
Top of Palmarito Formation
Palmarito Formation
408
407
406
405
404
403
402
401
400
399
398
397
396
395
394
393
392
391
390
389
388
387
386

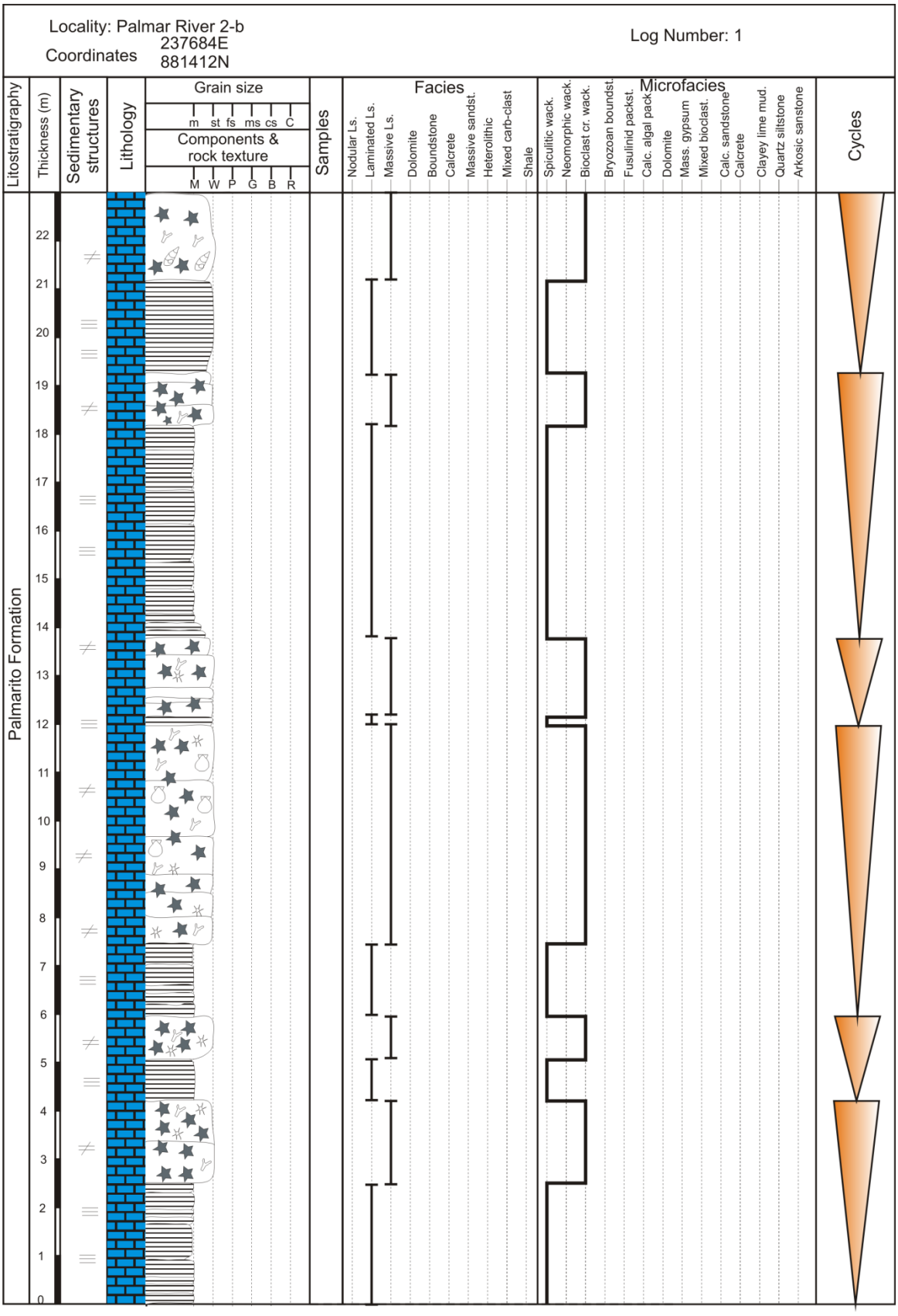
Locality: Palmar River 2-b
Coordinates 237684E 881412N
Log Number: 1
Litostratigraphy
Thickness (m)
Sedimentary structures
Lithology
Grain size
m st fs ms cs C
Components & rock texture
M W P G B R
Samples
Facies
Nodular Ls.
Laminated Ls.
Massive Ls.
Dolomite
Boundstone
Calcrete
Massive sandst.
Heterolithic
Mixed carb-clast
Shale
Microfacies
Spiculitic wack.
Neomorphic wack.
Bioclast cr. wack.
Bryozoan boundst.
Fusulinid packst.
Calc. algal pack.
Dolomite
Mass. gypsum
Mixed bioclast.
Calc. sandstone
Calcrete
Clayey lime mud.
Quartz siltstone
Arkosic sanstone
Cycles
Palmarito Formation
0
1
2
3
4
5
6
7
8
9
10
11
12
13
14
15
16
17
18
19
20
21
22

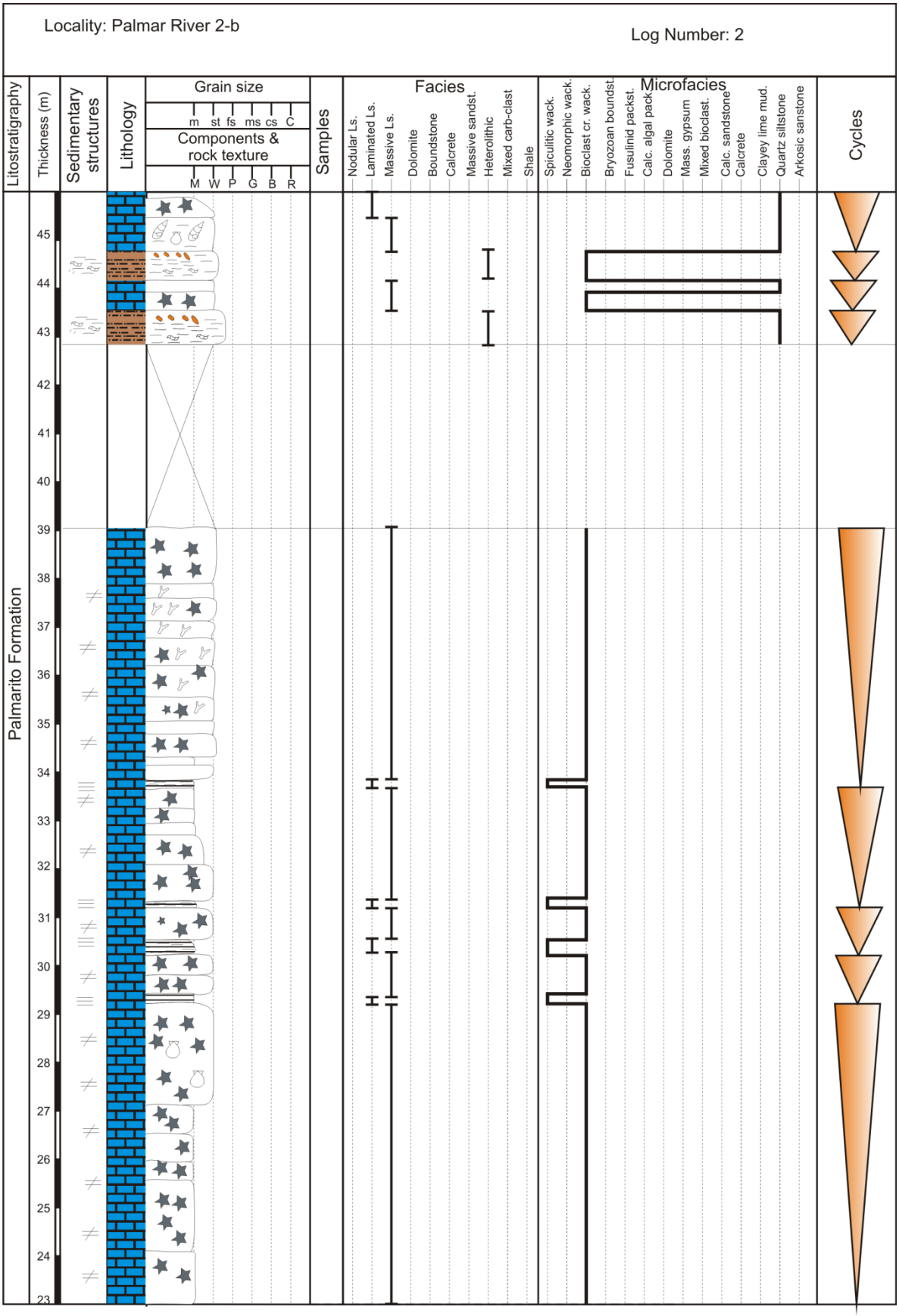
Locality: Palmar River 2-b
Log Number: 2
Litostratigraphy
Thickness (m)
Sedimentary structures
Lithology
Grain size
m st fs ms cs C
Components & rock texture
M W P G B R
Samples
Facies
Nodular Ls.
Laminated Ls.
Massive Ls.
Dolomite
Boundstone
Calcrete
Massive sandst.
Heterolithic
Mixed carb-clast
Shale
Microfacies
Spiculitic wack.
Neomorphic wack.
Bioclast cr. wack.
Bryozoan boundst.
Fusulinid packst.
Calc. algal pack.
Dolomite
Mass. gypsum
Mixed bioclast.
Calc. sandstone
Calcrete
Clayey lime mud.
Quartz siltstone
Arkosic sanstone
Cycles
Palmarito Formation
45
44
43
42
41
40
39
38
37
36
35
34
33
32
31
30
29
28
27
26
25
24
23

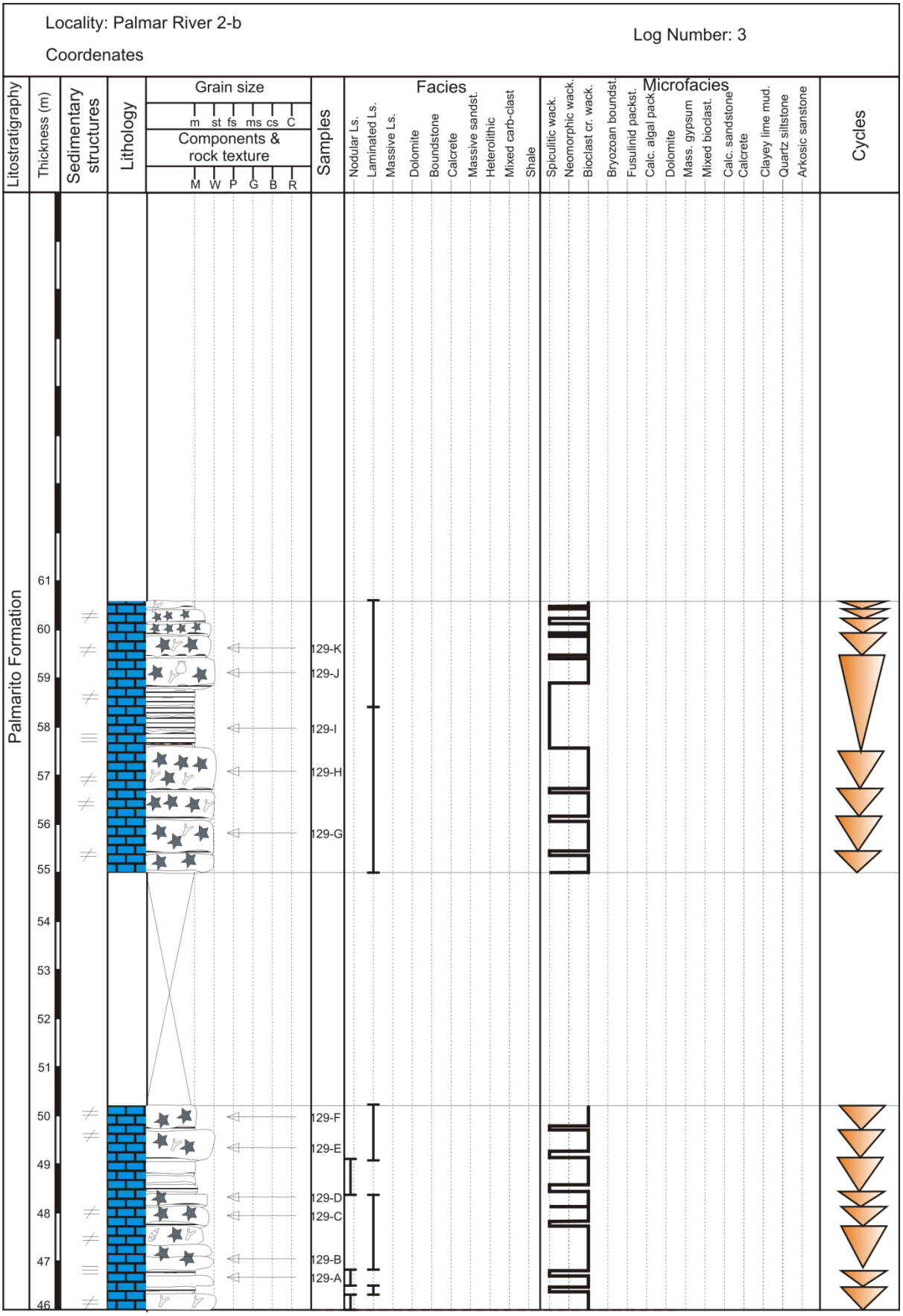
Locality: Palmar River 2-b
Coordenates
Log Number: 3
Litostratigraphy
Thickness (m)
Sedimentary structures
Lithology
Grain size
m st fs ms cs C
Components & rock texture
M W P G B R
Samples
Facies
Nodular Ls.
Laminated Ls.
Massive Ls.
Dolomite
Boundstone
Calcrete
Massive sandst.
Heterolithic
Mixed carb-clast
Shale
Microfacies
Spiculitic wack.
Neomorphic wack.
Bioclast cr. wack.
Bryozoan boundst.
Fusulinid packst.
Calc. algal pack.
Dolomite
Mass. gypsum
Mixed bioclast.
Calc. sandstone
Calcrete
Clayey lime mud.
Quartz siltstone
Arkosic sanstone
Cycles
Palmarito Formation
61
60
59
58
57
56
55
54
53
52
51
50
49
48
47
46
129-K
129-J
129-I
129-H
129-G
129-F
129-E
129-D
129-C
129-B
129-A

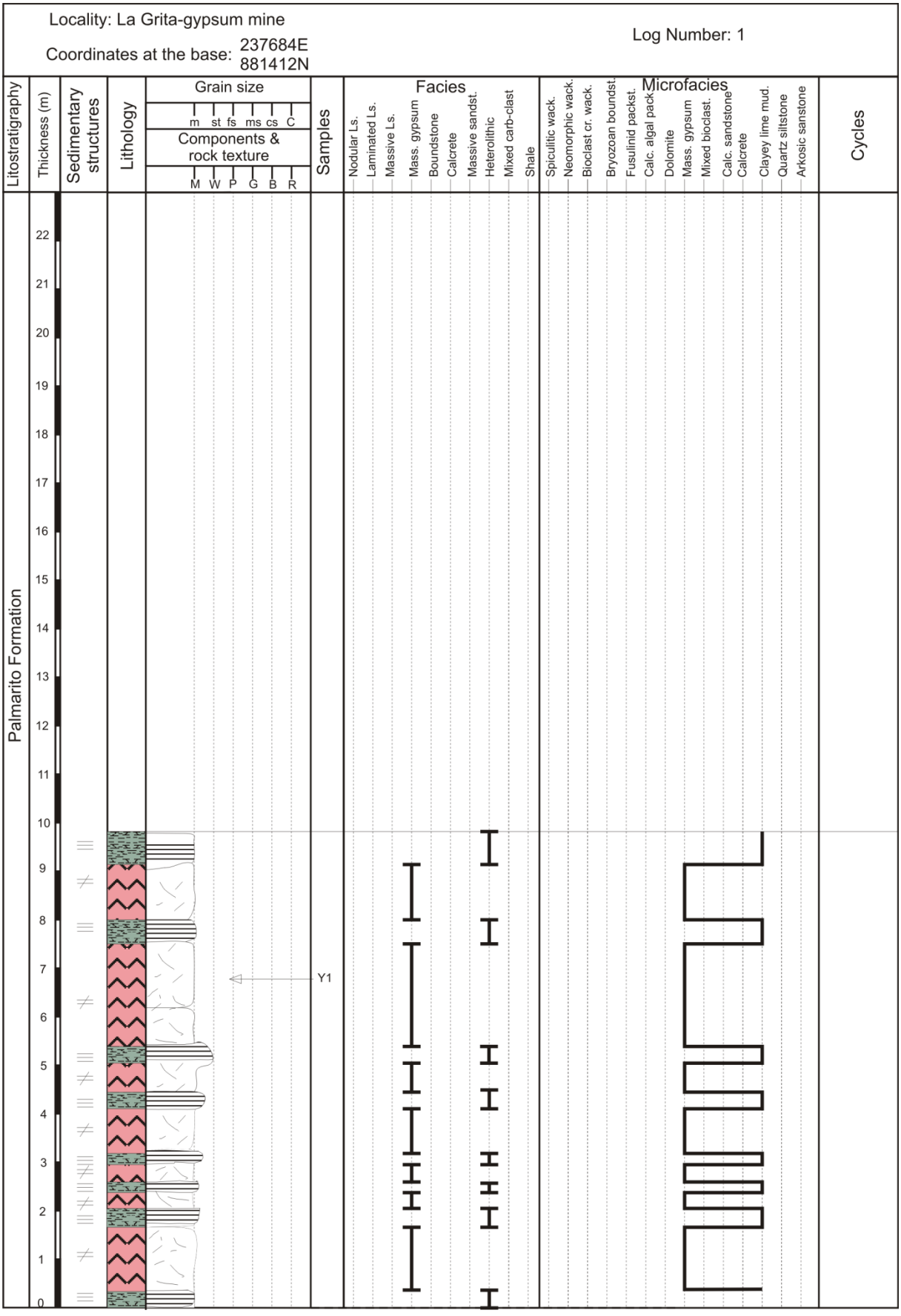
Locality: La Grita-gypsum mine
Coordinates at the base: 237684E 881412N
Log Number: 1
Litostratigraphy
Thickness (m)
Sedimentary structures
Lithology
Grain size
m st fs ms cs C
Components & rock texture
M W P G B R
Samples
Facies
Nodular Ls.
Laminated Ls.
Massive Ls.
Mass. gypsum
Boundstone
Calcrete
Massive sandst.
Heterolithic
Mixed carb-clast
Shale
Microfacies
Spiculitic wack.
Neomorphic wack.
Bioclast cr. wack.
Bryozoan boundst.
Fusulinid packst.
Calc. algal pack.
Dolomite
Mass. gypsum
Mixed bioclast.
Calc. sandstone
Calcrete
Clayey lime mud.
Quartz siltstone
Arkosic sanstone
Cycles
Palmarito Formation
Y1

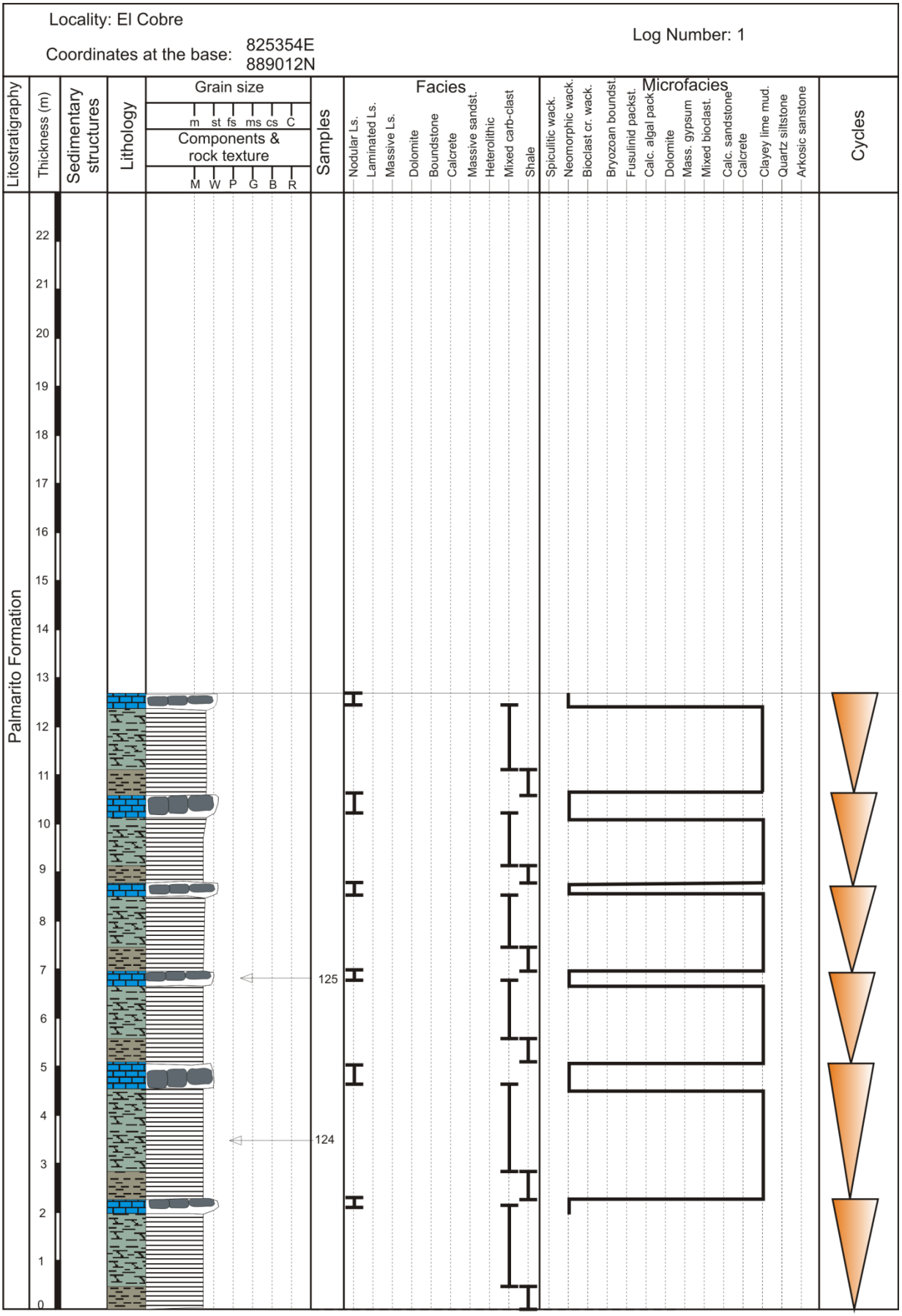
Locality: El Cobre
Coordinates at the base: 825354E 889012N
Log Number: 1
Litostratigraphy
Thickness (m)
Sedimentary structures
Lithology
Grain size
m st fs ms cs C
Components & rock texture
M W P G B R
Samples
Facies
Nodular Ls.
Laminated Ls.
Massive Ls.
Dolomite
Boundstone
Calcrete
Massive sandst.
Heterolithic
Mixed carb-clast
Shale
Microfacies
Spiculitic wack.
Neomorphic wack.
Bioclast cr. wack.
Bryozoan boundst.
Fusulinid packst.
Calc. algal pack.
Dolomite
Mass. gypsum
Mixed bioclast.
Calc. sandstone
Calcrete
Clayey lime mud.
Quartz siltstone
Arkosic sanstone
Cycles
Palmarito Formation
0
1
2
3
4
5
6
7
8
9
10
11
12
13
14
15
16
17
18
19
20
21
22
125
124

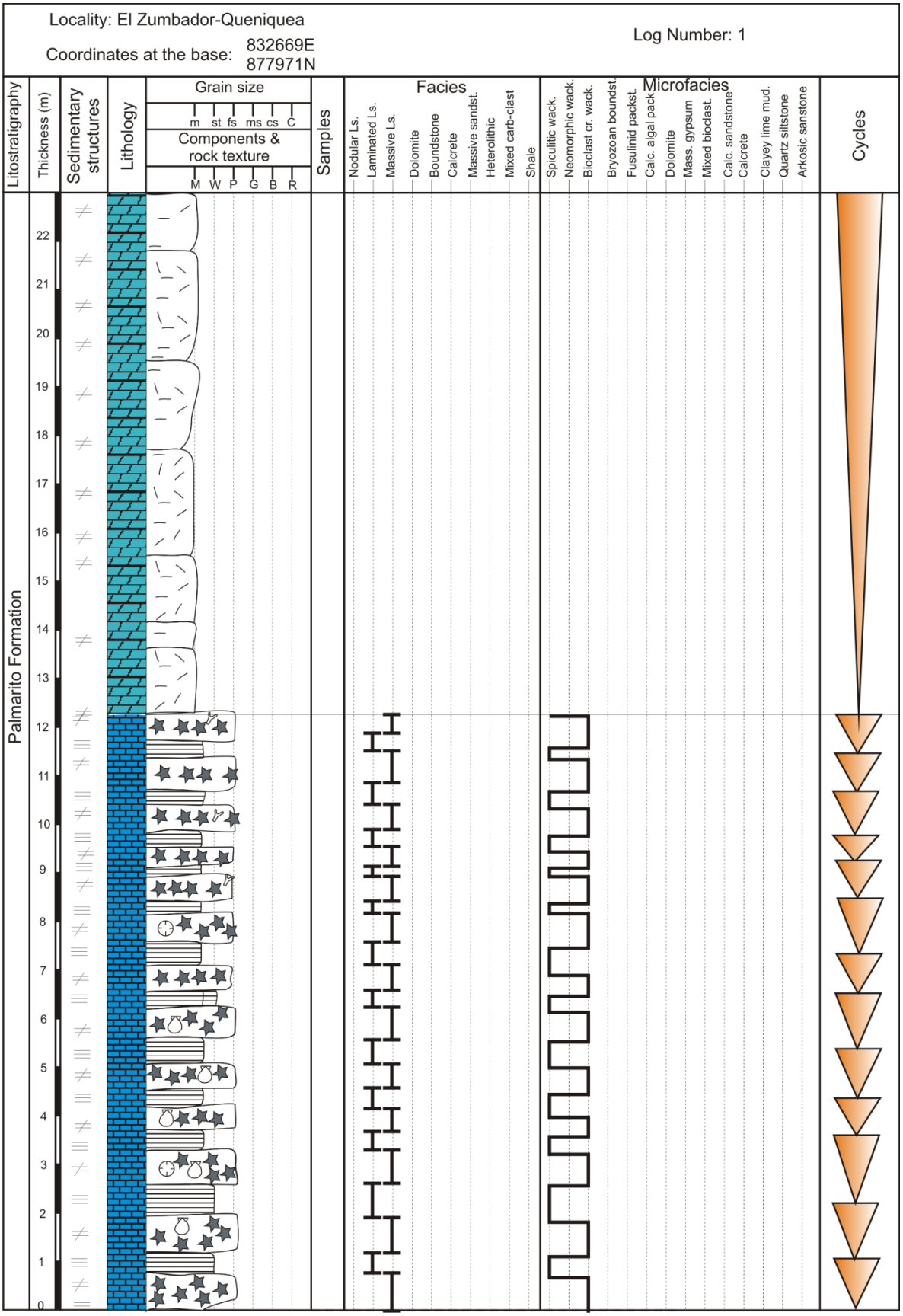
Locality: El Zumbador-Queniquea
Coordinates at the base: 832669E 877971N
Log Number: 1
Litostratigraphy
Thickness (m)
Sedimentary structures
Lithology
Grain size
m st fs ms cs C
Components & rock texture
M W P G B R
Samples
Facies
Nodular Ls.
Laminated Ls.
Massive Ls.
Dolomite
Boundstone
Calcrete
Massive sandst.
Heterolithic
Mixed carb-clast
Shale
Microfacies
Spiculitic wack.
Neomorphic wack.
Bioclast cr. wack.
Bryozoan boundst.
Fusulinid packst.
Calc. algal pack.
Dolomite
Mass. gypsum
Mixed bioclast.
Calc. sandstone
Calcrete
Clayey lime mud.
Quartz siltstone
Arkosic sanstone
Cycles
Palmarito Formation
0
1
2
3
4
5
6
7
8
9
10
11
12
13
14
15
16
17
18
19
20
21
22

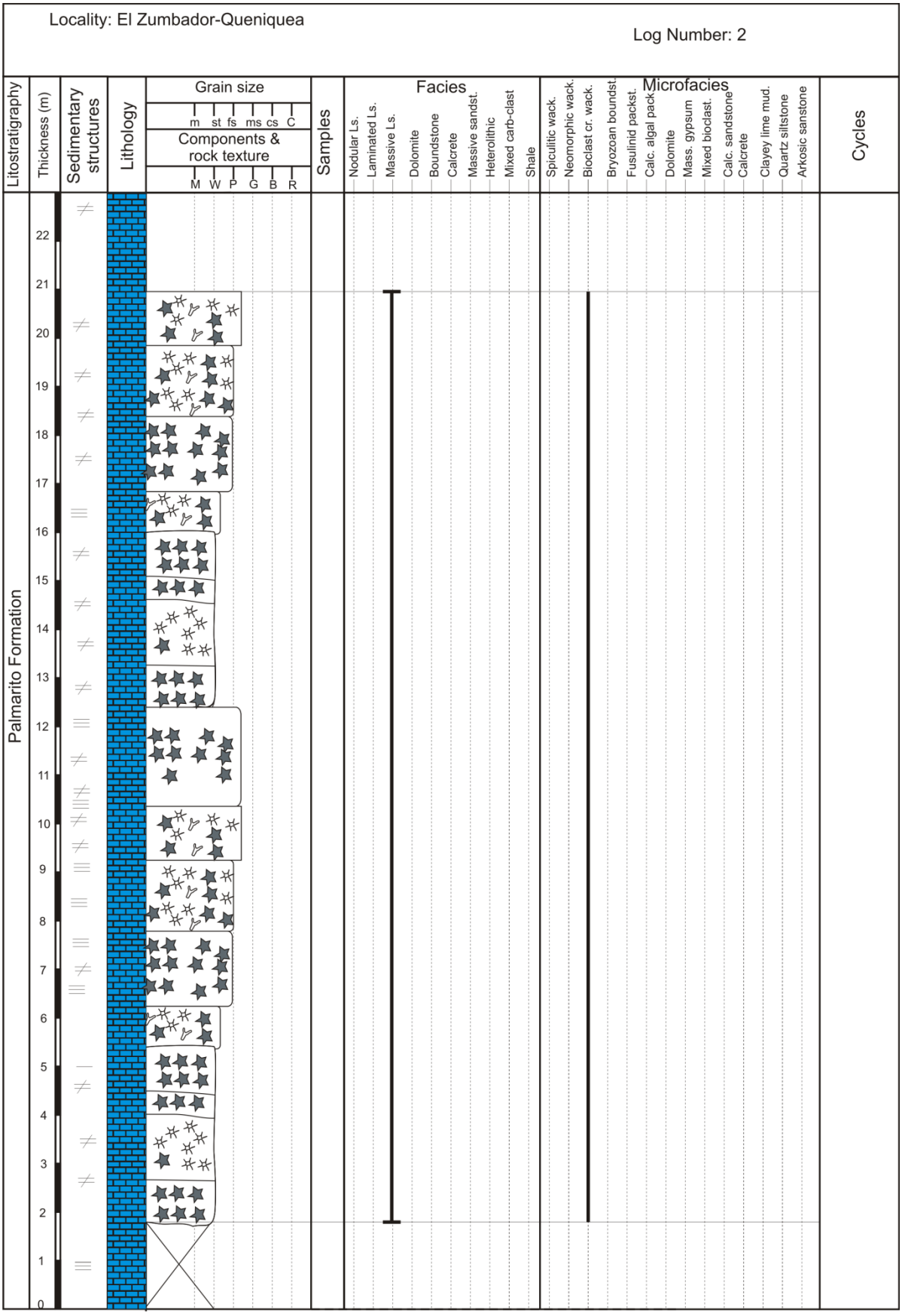
Locality: El Zumbador-Queniquea
Log Number: 2
Litostratigraphy
Thickness (m)
Sedimentary structures
Lithology
Grain size
m st fs ms cs C
Components & rock texture
M W P G B R
Samples
Facies
Nodular Ls.
Laminated Ls.
Massive Ls.
Dolomite
Boundstone
Calcrete
Massive sandst.
Heterolithic
Mixed carb-clast
Shale
Microfacies
Spiculitic wack.
Neomorphic wack.
Bioclast cr. wack.
Bryozoan boundst.
Fusulinid packst.
Calc. algal pack.
Dolomite
Mass. gypsum
Mixed bioclast.
Calc. sandstone
Calcrete
Clayey lime mud.
Quartz siltstone
Arkosic sanstone
Cycles
Palmarito Formation
0
1
2
3
4
5
6
7
8
9
10
11
12
13
14
15
16
17
18
19
20
21
22

Appendix 2. Petrography

The following appendix gives the guidelines that were used in the descriptions of the thin sections and presents a table of data collected from the thin-sections.

The thin-sections studied were mostly standard thin-section, 8 cm x 2 cm. A few samples were stained with alizarin Red S and potassium ferricyanide in the standard procedure to determine the dolomite content.

During the study a list of features observed was drawn up to help determine the microfacies scheme presented in the Chapter 3.

The list of characteristic features has been compiled from Flügel (2004) and Tucker and Wright (1990) and is noted here:

Grains

Systematic identification between different groups (skeletal or non-skeletal)

Detailed description of the grains.

Skeletal grains: Shape, Preservation (whole grain or fragment), Biogenic encrustation, Micrite rims, Diagenesis

Non-skeletal grains: Type, Shape and rounding, Size and sorting

Lithoclasts: Intraclast or extraclast, Abundance, Size

Terrigenous particles: Shape and sorting, Abundance

Matrix

Homogenous or inhomogeneous, Micrite/microspar/spar relative proportion.

Fabric

Durham classification, Microfacies assignation, Packing

Diagenesis

Micritization, Cements, Neomorphism, Compaction, Mineralization

Thin section tables

The Abraviation of the microfacies using in the table:

M1Spiculite wackestone-packstone

M2 Neomorphic wackestone

M3 Bioclastic crinoidal-bryozoan wackestone-packstone

M4 Bryozoan boundstone

M5 Fusulinid grainstone-packstone

M6 Calcareous green algal packstone

M7 Dolomite

M8 Massive gypsum

M9 Mixed bioclastic rudstone-packstone

M10 Calcareous sandstone

M11 Calcrete

M12 Clayey lime mudstone

M13 Quartz siltstone

M14 Arkosic sandstone

Texture used for tables

Silt: siltstone S: sandstone; M; Mudstone; W: wackestone; P: packstone; B: boundstone.

Values in the table are presented as %.

Palmar River section

Sample	**12**	**14**	**16**	**17**	**27**	**30**	**32**	**34**	**38**	**39**	**40**
Heigth above the base	10.2	14	14.8	17.2	36	47	49.1	55	55.5	63	63.5
Microfacies	M14	M11	M12	M11	M12	M9	M11	M11	M12	M13	M11
Texture	S	M	Silt	M	Silt	P	M	M	Silt	Silt	M
Grains:											
Peloids											
Lithoclast						5					
Bioclasts:											
Green algae											
Fusulinid											
Small foram											
Corals											
Bivalves				5				5			
Gasteropods											
Brachiopods						50					5
Crinoids											
Trilobites											
Bryozoan											
Ostracods						5	5		1		
Sponge spicules											
Sponges											
Matrix		60	60	55	40	25	60	90	9	30	90
Cements			20	40			30	4			2
Others	5	20			25	10	5			10	3
Quartz/silt	95	20	20		35	5			90	60	

Palmar River section

Sample	**42**	**43**	**47**	**48**	**49**	**49-a**	**53**	**56**	**57**	**59**	**60**
Heigth above the base	68.5	72	79.6	85.5	99.5	96.4	113.5	128.3	131.1	134.5	137.7
Microfacies	M11	M11	M11	M10	M3	M10	M1	M2	M3	M1	M2
Texture	M	M	M	S	W-P	S	W-P	W-M	W-P	W-M	W
Grains:											
Peloids											
Lithoclast											5
Bioclasts:											
Green algae									15		
Fusulinid											
Small foram											
Corals											
Bivalves							5				
Gasteropods									15		
Brachiopods				40	5			10		10	20
Crinoids				10	10	40	20		15	10	
Trilobites											
Bryozoan					5						
Ostracods		15			20						
Sponge spicules							40				
Sponges							30			10	
Matrix	75	50		20	40	15		80	35	70	50
Cements	20	35	90					5	20		25
Others	5		5	5			5				
Quartz/silt			5	25		5		5			

Palmar River section

Sample	61	65	67	67-a	68	71	73	75	78	79	80
Heigth above the base	140.8	146.2	151.5	150.4	153.6	156.7	163	169.5	179.5	180.4	189.1
Microfacies	M2	M2	M1	M9	M2	M2	M2	M1	M6	M3	M6
Texture	W	W	W	P-W	W-M	W-M	W	W	W-P	W	P
Grains:											
Peloids											
Lithoclast											
Bioclasts:											
Green algae									25		40
Fusulinid											
Small foram	10			5				5			
Corals											
Bivalves			5								
Gasteropods									5		15
Brachiopods	10			35		10	10	2		10	5
Crinoids		20		10	5			5	10		
Trilobites								1			
Bryozoan		5	10							10	
Ostracods											
Sponge spicules		5	10		5			1			
Sponges											
Matrix			50	50	90	90	80	80	60	60	30
Cements		60	25				5	7		20	10
Others							5				
Quartz/silt											

Palmar River section

Sample	80-a	80-b	80-c	80-d	80-e	80-f	81	83	85	85-a	93
Heigth above the base	188.6	189.5	190.1	190.3	190.5	190.8	191	196.5	209.4	210.5	238.5
Microfacies	M5	M5	M5	M5	M3	M3	M2	M3	M3	M3	M1
Texture	P	P	P	W	P	W		P-W	W	P-W	P-W
Grains:											
Peloids											
Lithoclast											
Bioclasts:											
Green algae	10	10	15	15	5						
Fusulinid	50	40	15	5	50						
Small foram		5				5		10			
Corals											
Bivalves											
Gasteropods		10									
Brachiopods	5			10	5				10	10	
Crinoids	20		15	15	20	10	30	20		20	10
Trilobites											
Bryozoan		10		15			10	10	10	30	15
Ostracods				5		5					
Sponge spicules			10			10			20		20
Sponges											10
Matrix	10	15	45	40	20	70	60	60	60	40	45
Cements	5										
Others											
Quartz/silt											

Palmar River section

Sample	97	99	100	101	101-a	101-b	101-c	101-d	102	103	103-a
Heigth above the base	254	259.4	262.3	264.5	265.5	267	268	269	272	275.3	274.5
Microfacies	M1	M3	M3	M3	M3	M3	M3	M6	M3	M3	M3
Texture	M	P-W	P-W	P-W	P-W	P	P	P	P	W	P
Grains:											
Peloids											
Lithoclast		10									
Bioclasts:											
Green algae								30		20	
Fusulinid											
Small foram											
Corals											
Bivalves											
Gasteropods											
Brachiopods			20	10		10	10	10	10		
Crinoids	10	25	15	30	30	20	30	20	30	5	40
Trilobites											
Bryozoan		20			10	10	20		20		10
Ostracods											
Sponge spicules	40	10	10	10	20	20	10		10	10	
Sponges			10								
Matrix	50	35	45	60	40	40	30	40	30	65	50
Cements											
Others											
Quartz/silt											

Palmar River section

Sample	103-b	104-a	104-b	107	107-a	107-b	108-a	109	109-a	109-b	110-a
Heigth above the base	275	279	287.4	300.4	301.8	305.5	309.5	316.4	315.2	315.8	322.5
Microfacies	M3	M6	M6	M3	M3	M4	M3	M3	M3	M3	M7
Texture	P	P	P	P-W	P-W	P-W	P	W-P	W	W-P	
Grains:											
Peloids											
Lithoclast											
Bioclasts:											
Green algae		30									
Fusulinid											
Small foram				5							
Corals											
Bivalves											
Gasteropods											
Brachiopods			10	5	20	10	10	10	10	5	
Crinoids	60			60	20	10	20	10	5	5	
Trilobites											
Bryozoan	10	10		5	20	30	30		10	10	
Ostracods											
Sponge spicules			40		10		10		10	5	
Sponges								10			
Matrix	40	60	50	25	30	60	30	65	65	75	
Cements											90
Others											10
Quartz/silt											

Palmar River section

Sample	114	115	116	118	119	128	129-c	129-e	129-f	129-g	129-k
Heigth above the base	343.5	347.1	352.5	365.2	367.4	359.7	362.7	363.7	364.5	365.7	366.7
Microfacies	M3	M7	M1	M6	M6	M6	M3	M3	M3	M3	M1
Texture	W-P		W-P	W-P	W-P	W-P	P	P-W	P-W	P-W	W
Grains:											
Peloids											
Lithoclast											
Bioclasts:											
Green algae				25	10	30					
Fusulinid	10										
Small foram			5		10		10	5			
Corals											
Bivalves				5							
Gasteropods					10						
Brachiopods	10		10			10	10	10	10	30	20
Crinoids						10	10	30	30		
Trilobites											
Bryozoan				5					10		
Ostracods	10										
Sponge spicules									10		
Sponges											
Matrix	70		70	65	60	50	70	55	40	60	80
Cements	9	90	15		10					10	
Others		10									
Quartz/silt											

Palmar River section

Sample	130	131	P55-m36b2	P55-m36m	P56-m36b2	P56-m37b	P56-m37b2	P56-m37b4	P56-m37b5	P61-m37m2
Heigth above the base	375.8	381	0.5	0.8	13.5	13.3	10.5	23.5	25.5	47
Microfacies	M4	M7	M14	M14	M11	M12	M13	M13	M10	M3
Texture	B		S	S	M	Silt	Silt	Silt	Silt	S
Grains:										
Peloids										
Lithoclast										
Bioclasts:										
Green algae										
Fusulinid										
Small foram										
Corals										
Bivalves										
Gasteropods										
Brachiopods										40
Crinoids										20
Trilobites										
Bryozoan	30									
Ostracods										
Sponge spicules	10									
Sponges										
Matrix	60		10	10	70	40	30	10	10	10
Cements		100			20					
Others										
Quartz/silt			90	90	10	60	70	90	90	30

Palmar River section

Sample	P62-m40b	P64-M41	P66-m42b	P66-m42b3	P67-m43b	P67-m43b2	P67-m43m	P73-m44t
Heigth above the base	131.5	135.5	152.3	157	231	271.5	277	330.5
Microfacies	M3	M3	M3	M1	M3	M3	M3	M7
Texture	W	W-P	W-P	W	M-W	P	W-P	
Grains:								
Peloids								
Lithoclast								
Bioclasts:								
Green algae								
Fusulinid								
Small foram	10		5					
Corals								
Bivalves								
Gasteropods								
Brachiopods			10	10	10	10	10	
Crinoids	10	20	20	10		40	10	
Trilobites							20	
Bryozoan		30		10	10			
Ostracods								
Sponge spicules						10		
Sponges		10						
Matrix	60	40	55	70	80	30	50	
Cements			10			10	10	90
Others								10
Quartz/silt								

Quebrada de Portachuelo 1

Sample	133	138	139	140	141	142	151	153	154	155	157
Heigth above the base	4	32.5		57.8	59	73.5	108.5	147	165.5	246	252.1
Microfacies	M11	M9	M3	M4	M3	M3	M5	M5	M3	M3	M3
Texture	M	P	P	B	P	P	P	P-W	W	P-W	P-W
Grains:											
Peloids											
Lithoclast											
Bioclasts:											
Green algae									10		
Fusulinid							30	60	5		
Small foram	10								5		
Corals											
Bivalves											
Gasteropods											
Brachiopods	10	60	20	20			10		10		20
Crinoids	10	10	20	10	30	40		10			40
Trilobites											
Bryozoan				40	20				5		
Ostracods											
Sponge spicules						10				10	
Sponges											
Matrix	70	30	60	30	40	50	60	30	65	10	40
Cements					10					80	
Others											
Quartz/silt											

Quebrada de Portachuelo 2

Sample	**160**	**161**	**162**	**163**	**164**	**165**	**165-a**	**166**	**166-a**	**166-b**	**167**
Heigth above the base	147.8	149.1	165.1	168.5	171	181.1	180	198.8	204.4	214	225.5
Microfacies	M6	M1	M7	M7	M7	M7	M7	M4	M3	M4	M3
Texture	P-W	P-W						B	P	B	P
Grains:											
Peloids											
Lithoclast											
Bioclasts:											
Green algae	20										
Fusulinid											
Small foram											
Corals								10			
Bivalves											
Gasteropods											
Brachiopods	10							20	10		10
Crinoids		10							40	10	20
Trilobites											
Bryozoan									5	60	30
Ostracods								30			
Sponge spicules	10	60									
Sponges											
Matrix	60	30	10	10	10	10	10	30	45	20	40
Cements			90	90	90	90	90	10		10	
Others											

Quebrada de Portachuelo 2

Sample	**167-a**	**167-b**	**168-a**	**169-a**	**170**	**170-a**	**170-b**	**170-c**	**171**
Heigth above the base	217.8	214	234.8	239.5	241.5	248	245.5	243.2	249.9
Microfacies	M3	M3	M6	M3	M3	M6	M4	M3	M6
Texture	P	P	P-W	W	W	P	B	P-W	P-W
Grains:									
Peloids									
Lithoclast									
Bioclasts:									
Green algae			30			40	5		30
Fusulinid									
Small foram		10							
Corals									
Bivalves									
Gasteropods			10						
Brachiopods			10	20		5		10	10
Crinoids	10			10	10	10			10
Trilobites									
Bryozoan	10				30		30	10	
Ostracods									
Sponge spicules	30	30		10	10	10	10	10	
Sponges								10	
Matrix	50	60	60	60	50	35	55	60	50
Cements									
Others									

Bócono River

Sample	**233**	**234**	**235**
Heigth above the base	192.5	194	19435
Microfacies	M5	M5	M5
Texture	P-W	P-W	P-W
Grains:			
Peloids			
Lithoclast			
Bioclasts:			
Green algae			
Fusulinid	10	20	10
Small foram			
Corals			
Bivalves			
Gasteropods			
Brachiopods			
Crinoids	10	10	10
Trilobites			
Bryozoan			
Ostracods			
Sponge spicules			
Sponges			
Matrix	70	70	80
Cements	10		
Others			

Santa Cruz de Palmarito

Sample	**236**	**237**	**238**	**239**	**240**	**241**	**243**	**245**	**246**	**248**	**249-a**
Heigth above the base	0.5	0.8	6.2	7	20.5	26	31.2	33.7	36.9	40.3	41.8
Microfacies	M6	M3	M1	M3	M3	M3	M3	M5	M3	M4	M5
Texture	P	P	M	W-P	W	P-W	P-W	P-W	P-W	B	P-W
Grains:											
Peloids											
Lithoclast											
Bioclasts:											
Green algae	10							20			
Fusulinid	10							20			30
Small foram											
Corals											
Bivalves											
Gasteropods											
Brachiopods					20		10		10	10	5
Crinoids		20	5	10		10	10		10	20	20
Trilobites											
Bryozoan	10	20			10		20	20	20	40	
Ostracods											
Sponge spicules	30	10	10	40	10	50	10	10	10	5	
Sponges											
Matrix	40	50	85	50	60	40	50	30	50	25	45
Cements											
Others											

Santa Cruz de Palmarito

Sample	**251**	**253**	**257**	**259**	**261**
Heigth above the base	43.5	49.5	59.3	71.2	80.5
Microfacies	M6	M6	M3	M3	M3
Texture	P	P	P	P-W	P
Grains:					
Peloids					
Lithoclast					
Bioclasts:					
Green algae	30	40			
Fusulinid	10				
Small foram					
Corals					
Bivalves					
Gasteropods					
Brachiopods				10	
Crinoids	10	10	10	20	40
Trilobites		20			
Bryozoan	10		20		10
Ostracods					
Sponge spicules			20	20	10
Sponges					
Matrix	40	20	50	50	40
Cements		10			
Others					

Santa Cruz de Palmarito

Sample	199	200	201	202	203	205	206	207	208	209	210	210-a
Heigth above the base	0.5	0.7	1	8.5	9.5	31	46	48.5	49.5	57.5	59	59.1
Microfacies	M5	M5	M3	M3	M3	M3	M5	M5	M5	M4	M5	M5
Texture	P	P	W-P	W-P	W	W	P-W	P-W	P-W	B	P-W	P-W
Grains:												
Peloids												
Lithoclast												
Bioclasts:												
Green algae			10									
Fusulinid	30	10	20				10	20	20	5	20	20
Small foram												
Corals												
Bivalves												
Gasteropods												
Brachiopods	5			10	5			10				
Crinoids	10			10		10	10	20	10	10	20	20
Trilobites												
Bryozoan		10			10		15			40		
Ostracods												
Sponge spicules			10						10			
Sponges												
Matrix	55	80	60	80	75	65	65	50	60	45	60	60
Cements						20						
Others												
Quartz/silt												

Appendix 3. Stable isotope (carbon, oxygen and strontium) and trace element data

The following tables present the stable isotope (carbon, oxygen and strontium) and trace element data that have been collected for this thesis.

Stable isotope $\delta^{13}C$ (‰) and $\delta^{18}O$ (‰) of four main sections.

Palmar River			
Samples	**m above base**	**$\delta^{13}C$ (‰)**	**$\delta^{18}O$ (‰)**
14	10.2	-9.2	-5.1
16	14	-5.3	-10.6
17	14.8	-8.0	-6.6
19	17.2	-3.0	-10.8
20	18.1	-3.2	-10.7
21	19	-2.7	-10.8
24	26.1	-1.0	-11.8
25	30.8	-0.6	-10.7
27	36	-1.1	-11.0
30	47	0.5	-9.1
31	48	-1.1	-9.9
32	49.1	-1.9	-10.0
33	50.5	-2.1	-11.5
34	55	-3.3	-7.7
35	55.5	-0.8	-11.5
38	61.2	-1.2	-9.9
39	63	-1.3	-10.2
40	63.5	0.6	-8.9
43	72	-0.3	-5.9
44	74.3	-0.7	-10.3
47	79.6	-2.2	-2.5
48	85.5	0.9	-9.0
49-A	96.4	2.1	-7.9
49	99.5	0.7	-9.4
51-A	106.2	0.8	-4.2
52	112	1.0	-7.5
53	113.5	1.0	-7.8
55	127.8	0.5	-7.0
56	128.3	3.8	-4.2
57	131.1	3.5	-5.2
58	132.8	1.7	-7.1
59	134.5	-0.2	-6.7
60	137.7	3.8	-5.8
61	140.8	2.9	-6.1
62	141.5	1.9	-7.4
Brach BQ-1	141.50	3.0	-5.7
Brach BQ-2	143.20	3.7	-7.2
63	143.4	1.6	-7.7
64	145	1.9	-7.4
Brach BQ-3	145.40	2.6	-6.9
65	146.2	3.5	-6.0
Brach BQ-4	147.50	2.5	-6.1
66	148	-1.4	-6.9
67-A	150.4	2.5	-6.8
67	151.5	2.1	-6.9
Brach BQ-5	152.20	2.5	-7.0
68	153.6	2.1	-6.4
Brach N1-A	154.4	4.1	-7.3
69	155	2.8	-6.3
70	155.5	2.2	-6.9
71	156.7	3.1	-6.3
Brach BQ-6	157.50	4.2	-5.9
Brach N1-B	159	4.1	-7.0
Brach BQ-7	159.50	4.1	-7.2
Brach BQ-8	160.00	4.5	-6.6
72-A	160.1	2.6	-6.7
72-B	160.3	3.0	-6.8
72-C	160.5	2.4	-6.6
72-D	160.7	2.3	-7.0
Brach BQ-9	161.00	2.6	-7.1
Brach BQ-10	161.50	4.0	-6.1
72	162.2	1.1	-7.4
73	163	3.6	-6.6
78	179.5	3.1	-5.0
79	180.4	4.2	-5.0
80-A	188.6	2.8	-4.6
80	189.1	3.3	-6.1
80-B	189.5	3.2	-7.5
80-C	190.1	3.2	-6.6
80-D	190.3	3.1	-6.2
80-E	190.5	3.3	-5.2
80-F	190.8	3.7	-4.5
81	191	3.2	-4.8
82	195	2.9	-2.9
83	196.5	3.5	-5.4

Palmar River			
Samples	**m above base**	**$\delta^{13}C$ (‰)**	**$\delta^{18}O$ (‰)**
85	209.4	4.7	-4.2
85A	210.5	2.8	-6.0
86	214.5	3.6	-5.6
87	215.8	3.6	-7.5
88	217.1	2.2	-6.4
89	221.5	1.2	-5.5
92	233.8	3.1	-5.3
94	241.2	1.2	-5.6
95	245.3	2.0	-6.5
96	245.8	2.8	-5.9
98	256.7	4.5	-4.7
101-A	265.5	4.8	-4.9
101-B	267	5.0	-5.1
101-C	268	4.9	-5.3
101-D	269	5.0	-5.0
103-A	274.5	4.7	-5.2
103-B	275	5.1	-5.1
104-A	279	4.5	-5.2
104-B	287.4	2.2	-6.0
105	292	4.1	-4.9
127-shell	300	4.4	-4.4
107-A	301.8	4.2	-5.0
107-B	305.5	3.9	-4.7
108-A	309.5	4.1	-4.9
108	310.5	4.4	-4.4
109-A	315.2	3.7	-4.9
109-B	315.8	3.6	-4.9
113	340.6	3.3	-7.5
114	343.5	3.1	-7.2
116-A	351.5	3.9	-5.8
116	352.5	4.1	-5.3
117-A	358.7	4.6	-6.2
128	359.7	4.2	-4.3
129	360.7	3.4	-5.0
129-A	361.7	4.1	-4.3
129-C	362.7	3.9	-4.6
129-E	363.7	3.5	-5.3
129-G	365.7	3.8	-5.6
129-K	366.7	4.5	-5.2
130	375.8	3.6	-6.1
131	381	4.3	-6.8

Quebrada de Portachuelo 1			
Samples	**m above base**	**$\delta^{13}C$ (‰)**	**$\delta^{18}O$ (‰)**
133	4	-2.3	-2.1
134	7.4	-0.3	-8.6
135	26	-3.6	-7.7
136	26.8	0.3	-2.9
138	33.5	0.4	-8.0
140	57.8	1.1	-5.6
141-brach	38.00	2.85	-4.50
141	59	0.9	-7.2
142	73.5	3.0	-7.5
143	77	0.7	-6.9
143-brach	77	2.30	-6.71
144	77.5	2.9	-7.1
147	84.5	1.1	-7.3
148	91.5	1.2	-7.4
149	99	1.6	-6.3
150	99.5	3.1	-5.5
151	107.5	0.7	-6.1
153	147	2.3	-6.2
154	165.5	2.9	-3.7
154-brach	165.5	4.18	-3.98
155	246	3.8	-5.8
156	249	4.3	-5.2
157	251	3.7	-5.2

Quebrada de Portachuelo 2			
Samples	**m above base**	**$\delta^{13}C$ (‰)**	**$\delta^{18}O$ (‰)**
265	3.5	2.4	-8.0
267	14.4	2.1	-7.7
268	18.2	2.5	-7.5
269	21.6	2.3	-8.1
270	24.2	2.5	-8.7
271	28.5	2.3	-7.9
272	32.4	2.8	-8.6
273	39.4	1.6	-7.8
276	52.6	2.1	-7.0
277	54.6	2.7	-7.0
278	61.7	2.3	-7.4
280	69.5	2.2	-7.8
285	88.7	2.1	-7.0
287	104.2	2.5	-6.3
288	108.5	2.2	-7.1
289	118.4	2.7	-6.0
158	140.1	4.4	-4.6
159	143.4	3.6	-4.0
162	165.1	4.7	-5.7
163	168.5	4.9	-5.1
164	171	5.0	-6.1
165	181.2	5.3	-5.6
166-B	196.4	5.6	-5.6
166	198.8	4.6	-5.8
166-A	204.4	4.6	-6.4

167-B	214	3.8	-5.6
167-A	217.8	5.0	-5.0
167	225.5	4.9	-5.6
168-A	234.8	4.7	-3.7
168	238.7	2.9	-4.5
169	239.5	3.9	-4.3
170	241.5	3.9	-3.7
171	249.9	3.9	-4.8

Santa Cruz de Palmarito			
Samples	**m above base**	**$\delta^{13}C$ (‰)**	**$\delta^{18}O$ (‰)**
236	0.5	4.0	-5.9
237	0.8	3.9	-5.0
238	6.2	2.5	-6.6
239	7	2.4	-6.2
240	20.5	4.2	-5.5
241	26	4.7	-5.9
243	31.2	4.2	-5.7
244	33.7	4.8	-5.2
245	35	4.8	-5.5
246	36.9	4.2	-6.0
248	40.3	5.0	-4.1
249	41.5	4.9	-5.1
251	43.5	4.4	-5.3
252	47.2	3.1	-6.6
253	49.5	4.3	-5.5
255	55.5	0.0	-6.1
256	57.3	2.7	-6.3
257	59.3	4.4	-5.6
258	69.3	3.2	-5.8
259	71.2	5.0	-4.2
260	71.8	5.0	-4.5
261	80.5	4.5	-4.6
262	85.5	4.5	-5.5
263	99	1.7	-7.2

$^{87}Sr/^{86}Sr$ values and ages in My based in GTS (2004)

Sample	**87Sr/86Sr**	**Age (My)**
67-A	0,707286	271
N1-B	0,707223	270,44
N1-A	0,707324	271,72
138-A	0,708537	-
109-B	0,707435	273,32
109-A	0,707331	271,88
152	0,707272	270,5
144	0,707319	271,6
143	0,707325	271,71
129	0,707366	272

Trace elements whole-rock of Palmar River section

Sample	CaCO3	Si	Na	Fe	Al	Mg	K	Ba	Sr	Mn	Zn	P	Ti	Cd	Cu	S	CaCO3%	m above base
25	520875	3963	3526	8151	2241	2870	841	0	421	1298	0	137	66	0	0	-	52	30.8
62	70992	17945	773	9867	11225	2578	2420	33	215	113	20	100	304	3	-	-	7	141.5
63	86850	20272	947	9936	11552	2177	2480	38	210	210	22	100	360	3	-	-	9	143.4
64	229036	18483	1013	9662	10593	2723	2167	37	437	218	38	153	407	7	-	-	23	145
65	869417	10808	700	7731	5017	3067	893	70	1005	457	33	100	264	7	-	-	87	146.2
66	197284	34138	1180	13191	15082	2440	3380	102	233	408	40	467	402	7	-	-	20	148
67-A	476878	23032	1493	9351	11770	3898	1807	67	903	287	24	33	451	7	-	-	48	150.4
67	333699	24922	933	8827	10198	3080	2280	35	673	170	36	80	282	7	-	-	33	151.5
68	366767	27430	1140	13009	11442	2720	2780	68	483	257	36	247	460	7	-	-	37	153.6
69	200400	22394	21353	15062	9703	6919	1981	654	294	200	188	156	19	0	0	-	20	155.5
70	173108	9899	7750	16946	9410	5267	1371	81	244	146	107	96	16	0	0	-	17	155.8
71	919714	4549	7482	2514	2724	4799	610	13	961	390	91	124	0	0	0	-	92	156.7
72-A	165307	20957	927	10802	9722	4368	2687	113	262	177	24	127	420	7	-	-	17	160.1
72-B	199334	20005	907	11611	8993	4462	2540	80	328	165	36	53	307	7	-	-	20	160.3
72-C	306936	15837	3388	8282	6861	1842	1541	0	377	126	0	222	295	0	0	-	31	160.5
72-D	402749	27782	860	10964	12508	2787	2287	73	423	253	31	360	407	7	-	-	40	160.7
72	36617	27399	20986	16795	12837	4411	2357	109	66	76	170	82	44	0	0	-	4	162.2
73	771331	13288	17146	5988	4238	3993	1192	126	1105	363	240	187	91	85	315	-	77	163
78	941748	3518	560	2849	1305	5522	27	15	1147	237	29	140	78	7	-	-	94	179.5
80-A	847824	23672	13896	22525	12032	20457	1605	366	1639	634	485	572	309	315	301	-	85	188.6
80	654443	20605	21784	9148	3842	10160	1212	172	1259	384	259	205	130	124	0	-	65	189.1
80-B	939024	4120	547	2262	845	3535	-	15	1505	187	24	0	31	7	-	-	94	189.5
80-C	949790	3190	467	2020	793	3362	-	15	1667	182	58	40	27	10	-	-	95	190.1
80-E	865320	7151	2743	2114	934	2870	0	0	1280	145	0	86	1	0	0	-	87	190.5
80-F	926098	7790	660	2627	2905	8420	427	18	1225	200	31	47	107	3	-	-	93	190.8

83	727788	11761	7516	22609	5531	9646	444	103	1270	878	202	283	75	60	0	-	73	196.5
84	15692	18999	7546	19076	13870	3548	1288	105	69	54	145	0	61	33	0	-	2	200
85	908707	10174	10451	2089	3247	5524	1127	128	1472	184	226	190	90	72	0	-	91	209.4
85A	459973	31648	24136	11241	9807	4386	2071	160	551	248	270	254	111	59	0	-	46	210.5
89	333166	25120	1020	8480	10357	3672	3387	45	172	182	20	413	473	7	-	-	33	221.5
98	780115	13215	260	4222	3978	8342	1553	33	1127	418	36	173	140	7	-	-	78	256.7
101-A	834660	1278	353	2042	867	5362	427	43	1240	120	27	147	0	7	-	-	83	265.5
101-B	899036	1383	347	2084	442	5395	0	17	1417	85	27	113	0	7	-	-	90	267
101-C	694704	1427	393	5171	865	17638	180	22	1047	115	29	500	0	7	-	-	69	268
101-D	935644	7063	413	1322	677	4232	0	15	1525	65	22	0	13	3	-	-	94	269
107-B	474714	21922	633	6196	6482	4153	2667	78	567	130	16	213	164	7	-	-	47	305.5
113	999570	1697	453	1800	807	11453	0	30	553	258	29	0	7	7	-	-	100	340.6
117-A	991850	468	393	916	285	3495	0	18	848	112	78	267	4	7	-	-	99	358.7
128	838432	22517	19995	3575	5164	5758	1024	84	944	180	235	243	63	43	0	-	84	359.7
129-A	633667	1755	133	5816	844	21987	474	5	197	75	37	63	19	0	0	577	63	361.7
129-C	894341	1453	162	926	847	4369	205	0	536	58	47	16	26	0	0	892	89	362.7
129-E	533927	554	103	6601	688	18718	549	9	274	163	34	105	7	0	0	538	53	363.7
129-E	566075	9131	5896	5053	3699	4596	1218	0	288	137	0	82	130	0	0	-	57	364.7
129-G	459906	16040	349	15300	8548	13870	3275	28	232	221	52	826	267	0	0	865	46	365.7
129-K	671209	14234	240	5252	7554	4568	2789	7	243	159	45	241	275	0	0	825	67	366.7
130	592066	5615	413	1053	738	2628	187	27	603	87	20	287	2	7	-	-	59	375.8

Trace elements whole-rock of Quebrada de Portachuelo 1 section.

Sample	CaCO3	Si	Na	Fe	Al	Mg	K	Ba	Sr	Mn	Zn	P	Ti	Cd	Cu	S	CaCO3%	m above base
151	237510.6	35251.5	19950.2	15755.7	14356.7	4702.4	2177.2	121.5	227.3	307.9	175.4	0.0	66.6	0.0	0.0	0.0	23.8	107.5
153	363510.9	39155.9	31525.5	36496.2	18134.3	8653.2	1813.2	70.2	820.8	697.4	162.5	897.4	48.8	0.0	0.0	0.0	36.4	147.0

Trace elements whole-rock of Santa Cruz de Palmarito section

Sample	CaCO3	Si	Na	Fe	Al	Mg	K	Ba	Sr	Mn	Zn	P	Ti	Cd	CaCO3%	m above base
240	561314	14843	183	9361	8899	4118	902	4	465	180	51	665	221	724	56	20.5
241	890487	0	68	1641	305	2761	0	0	1055	74	51	175	5	695	89	26
242	15223	9324	652	6077	7242	2084	1490	6	23	89	0	383	59	146	2	29.8
243	692650	3817	112	7663	3904	4534	66	0	587	160	46	1520	10	642	69	31.2
244	559750	4596	415	4765	4042	2729	661	0	661	160	33	199	16	433	56	33.7
245	581294	1303	93	8598	1780	12315	214	0	633	124	38	573	9	340	58	35
246	823197	9762	159	2624	1262	1996	130	0	694	145	52	308	22	786	82	36.9
247	98260	14053	892	5505	6475	1187	1625	6	74	100	12	709	138	228	10	39.8
248	809350	340	132	2297	817	3516	169	0	1087	124	47	410	7	828	81	40.3
249	858349	346	91	1849	616	2748	21	0	1068	85	49	151	7	667	86	41.5
250	133797	4030	421	5019	3953	1263	829	0	63	133	3	533	9	139	13	43
251	789514	935	114	3352	1320	2565	0	0	872	117	45	110	4	629	79	43.5
252	174494	16089	273	17078	10420	3966	1653	4	133	103	16	451	212	425	17	47.2
253	864806	1216	79	3718	1489	2670	0	0	845	145	49	499	6	506	86	49.5
254	115771	9395	307	8404	8263	3153	1059	4	81	139	4	258	15	4	12	52.5
255	197659	7138	665	7584	6076	2620	1159	5	75	94	13	556	23	218	20	55.5
256	211691	25370	350	11308	13382	4332	2125	6	149	137	9	437	259	452	21	57.3
257	868663	62	63	2033	502	1954	0	0	660	101	48	145	5	689	87	59.3

Trace elements of brachiopods from Palmarito Formation.

Sample	CaCO3	Si	Na	Fe	Al	Mg	K	Ba	Sr	Mn	Zn	P	Ti	Cd	Cu	S	m above base
BQ-1	970625	0	597	967	296	2696	0	19	927	130	51	19	3	0	0	745	141.50
BQ-2	614370	5945	418	26154	5843	4330	252	113	869	323	37	116	14	0	0	760	143.20

BQ-3	785423	1660	701	12398	1892	2462	13	68	867	212	46	61	7	0	0	747	145.40
BQ-4	784543	2117	420	5080	1880	2127	49	7	874	526	41	65	18	0	0	677	147.50
BQ-5	552960	13823	474	25633	12402	6555	730	12	896	386	63	134	17	0	0	506	152.20
N1-A	711569	11745	1727	13120	6283	3857	760	77	978	405	44	127	127	7	0	0	154.4
BQ-6	834271	984	739	3361	2837	2355	75	1	750	116	49	44	0	0	0	576	157.50
N1-B	941838	1957	2180	7322	1243	3503	-220	52	1423	578	42	0	7	7	0	0	159
BQ-7	631958	5516	466	9129	5033	3119	638	17	747	118	44	72	0	0	0	673	159.50
BQ-8	492976	4649	494	16902	4239	5377	562	42	532	130	35	158	12	0	0	642	160.00
BQ-9	801614	1790	732	9746	2010	2781	250	22	826	92	57	94	10	0	0	718	161.00
BQ-10	800415	944	872	4050	1334	3084	68	478	1704	110	34	72	8	0	0	715	161.50
141-shell	928525	2477	1513	3171	1535	2673	-33	45	740	610	33	20	20	3	-18	0	60.00
143-shell	1008543	6700	1040	6442	4035	3913	913	32	1085	488	29	87	62	7	-5	0	78.00
154-shell	1024921	82	1807	367	168	1042	-407	23	970	22	56	27	0	10	0	0	167.2

Trace elements of cements from Palmarito Formation.

Sample	CaCO3	Si	Na	Fe	Al	Mg	K	Ba	Sr	Mn	Zn	P	Ti	Cd	Cu	S
14-CEM	408841	12757	354	26530	10499	38671	2369	34	99	12692	27	101	48	0	0	149
57-CEM	927206	0	79	3097	1938	2729	0	0	717	334	47	25	6	0	0	606
80-CEM	919540	0	46	1657	213	2336	0	0	1177	134	47	20	4	0	0	813
130-CEM	697085	351	169	271	333	9601	0	0	1387	75	38	50	5	0	0	533
160-CEM	918810	0	51	2843	186	2404	0	0	254	225	47	19	3	0	0	679
165-CEM	518620	0	127	7759	393	110208	0	0	55	802	32	73	4	0	0	18
166-CEM	913719	0	19436	147	287	4801	0	0	2014	22	3095	33	4	0	0	1178
167-CEM	685349	0	87	1658	301	71134	0	0	246	344	37	13	3	0	0	359
236-CEM	915343	163	69	3928	263	1456	0	0	1092	171	47	47	4	0	0	772
241-CEM	886880	153	32	1916	449	1612	0	0	504	84	49	110	5	0	0	742
246-CEM	920615	0	48	3539	359	2603	0	0	518	150	47	38	4	0	0	844

Appendix 4. Cycle thickness data

The following tables provide the measurements of cycle thickness that have been collected for Chapter 5 of this thesis.

Palmar River section			
Cycle number	**Cycle type**	**Thickness (m)**	**Cumulative thickness (m)**
1	A2	2,2	2,2
2	A2	3,7	5,9
3	A2	4,6	10,5
4	A1	2,9	13,4
5	A1	1,4	14,8
6	A1	2,5	17,3
7	A1	6,5	23,8
8	A2	7	30,8
9	A2	5	35,8
10	A1	5	40,8
11	A1	4,7	45,5
12	A1	4,5	50
13	A1	3,5	53,5
14	A1	2	55,5
15	A1	1,7	57,2
16	A1	1,3	58,5
17	A1	2	60,5
18	A1	1,5	62
19	A1	2,5	64,5
20	A1	1	65,5
21	A1	3,5	69
22	A1	2,2	71,2
23	A1	1,5	72,7
24	A1	3,8	76,5
25	A1	1,9	78,4
26	A2	2	80,4
27	B4	6	86,4
28	B4	3,6	90
29	B4	2,5	92,5
30	B4	1,5	94
31	B4	2,4	96,4
32	B4	2	98,4
33	B4	1,5	99,9
34	B4	4,1	104
35	B4	3,9	107,9
36	B4	3,3	111,2
37	C2	3	114,2
38	C1	1,5	115,7
39	C1	2,2	117,9
40	C1	1,5	119,4
41	A3	1	120,4
GAP	GAP	5	125,4
42	C1	2,5	127,9
43	C1	1,3	129,2
44	B1	2	131,2
45	B1	1,8	133
46	C1	3,7	136,7
47	C1	0,9	137,6
48	C1	1,4	139
49	C1	1,7	140,7
50	C1	5,5	146,2
51	C1	0,8	147
52	C1	1,4	148,4
53	C1	1	149,4
54	C1	0,9	150,3
55	C1	1,9	152,2
56	C1	1,4	153,6
57	C1	1,5	155,1
58	C1	1,7	156,8
59	C1	3,3	160,1
60	C1	0,6	160,7
61	C1	2,2	162,9
62	C1	2,6	165,5
63	C1	1,9	167,4
64	C1	1,7	169,1
65	C1	1,9	171
66	C1	2,4	173,4
67	C2	1,4	174,8
68	C2	2	176,8
69	B1	2,9	179,7
70	C1	1	180,7
71	C1	0,9	181,6
72	B1	4,2	185,8
73	B1	1,4	187,2
74	B1	3,3	190,5
75	B2	3,8	194,3
76	C2	3	197,3
77	A3	7,3	204,6
78	C1	1,4	206
79	C1	1,2	207,2
80	C1	0,9	208,1

Palmar River section (cont.)

Cycle number	Cycle type	Thickness (m)	Cumulative thickness (m)
81	C1	1,2	209,3
82	C1	1,2	210,5
83	C2	3,5	214
84	C2	1,8	215,8
85	C1	1,6	217,4
86	C2	2,9	220,3
87	C1	0,7	221
88	C1	0,6	221,6
89	C1	0,4	222
90	C1	0,5	222,5
91	C2	2	224,5
92	C2	4,3	228,8
93	C2	5,6	234,4
94	C1	0,6	235
95	C1	0,5	235,5
96	C1	0,5	236
97	C1	0,6	236,6
98	C1	0,7	237,3
99	C1	0,5	237,8
100	C1	0,6	238,4
101	C1	0,7	239,1
102	C1	0,6	239,7
103	C1	0,6	240,3
104	C1	1,1	241,4
105	C1	1	242,4
106	C1	1,1	243,5
107	C1	0,7	244,2
108	C1	0,5	244,7
109	C1	0,7	245,4
110	C1	0,7	246,1
111	C1	0,5	246,6
112	C1	0,5	247,1
113	C1	0,6	247,7
114	C1	0,5	248,2
115	C2	6,6	254,8
116	C2	0,9	255,7
117	C2	1	256,7
118	C2	0,7	257,4
119	C2	0,8	258,2
120	C2	1,1	259,3
121	C2	1,7	261
122	C2	4,2	265,2
123	B2	7	272,2
124	B2	5,3	277,5
125	B2	4	281,5
126	B2	8	289,5
127	B2	5,8	295,3
128	B3	5,5	300,8
129	B1	1,3	302,1
130	C2	1,1	303,2
131	C2	0,6	303,8
132	C2	1	304,8
133	C2	1,1	305,9
134	C2	1,3	307,2
135	C2	0,8	308
136	C2	1	309
137	C2	1,2	310,2
138	C2	0,9	311,1
139	C2	1	312,1
140	C2	0,8	312,9
141	C2	0,5	313,4
142	C2	0,8	314,2
143	C2	0,9	315,1
144	C2	0,9	316
145	C2	0,9	316,9
146	C2	0,8	317,7
147	B3	7,2	324,9
148	B3	8	332,9
149	B3	7,2	340,1
150	B3	8,7	348,8
151	B3	11,2	360
152	B3	13,6	373,6
153	B3	9,4	383
154	B3	11,2	394,2
155	B3	5	399,2
156	B1	0,9	400,1
157	B1	0,6	400,7
158	B1	0,8	401,5

Quebrada de Portachuelo 1 section

Cycle number	Cycle type	Thickness (m)	Cumulative thickness (m)
1	A2	4.1	4.1
2	A2	4	8.1
GAP	GAP	4.7	12.8
3	A1	2	14.8
4	A1	7.4	22.2
5	A1	1.1	23.3
6	A1	1.4	24.7
7	A1	1	25.7
8	A1	1.1	26.8
9	A1	1.4	28.2
10	A1	1.1	29.3

11	A1	1	30.3
12	A1	0.8	31.1

Quebrada de Portachuelo 1 section (cont.)

Cycle number	Cycle type	Thickness (m)	Cumulative thickness (m)
13	A1	1	32.1
14	A1	0.8	32.9
15	A1	0.5	33.4
16	A1	0.5	33.9
17	A1	7.6	41.5
18	A1	1	42.5
19	A1	1	43.5
GAP	GAP	4.4	47.9
20	C1	1.1	49.0
21	C1	0.7	49.7
22	C1	0.3	50.0
GAP	GAP	2.9	52.9
23	C2	4.1	57.0
24	C2	0.75	57.8
25	C2	1.4	59.2
GAP	GAP	6	65.2
26	C2	0.8	66.0
27	A3	5.35	71.3
28	C2	2	73.3
GAP	GAP	1.7	75.0
29	C2	4	79.0
30	C2	3.7	82.7
31	C2	4.3	87.0
GAP	GAP	3.7	90.7
32	C2	0.5	91.2
33	C1	3.8	95.0
34	C1	2.7	97.7
35	C2	2.2	99.9
GAP	GAP	4.5	104.4
36	B1	3.5	107.9
37	C1	4	111.9
38	C1	4.3	116.2
39	C1	6.1	122.3
40	C1	3.1	125.4
41	C1	1.1	126.5
42	C1	3	129.5
43	C1	1	130.5
44	C1	0.6	131.1
45	C1	0.7	131.8
46	C1	0.7	132.5
47	C1	5.2	137.7
48	B1	1.8	139.5
49	C1	1.95	141.5
50	C1	0.7	142.2
51	C1	0.55	142.7
52	B1	5.9	148.6
53	C1	0.9	149.5
54	C1	0.5	150.0
55	C1	0.9	150.9
56	C1	0.8	151.7
57	C1	1.5	153.2
58	C1	1.75	155.0
59	C1	0.9	155.9
GAP	GAP	2.95	158.8
60	C2	0.4	159.2
61	C2	0.4	159.6
62	C2	0.3	159.9
63	C2	0.35	160.3
64	C1	3.05	163.3
65	C1	1.05	164.4
66	B1	0.9	165.3
67	C1	0.25	165.5
68	C1	0.5	166.0
69	C1	0.35	166.4
70	C1	2.45	168.8
GAP	GAP	2.85	171.7
71	B1	2.18	173.8
72	B1	0.92	174.8
GAP	GAP	55	229.8
73	B3	5	234.8
74	B3	11.32	246.1
GAP	GAP	1.55	247.6
75	B3	5	252.6

Quebrada de Portachuelo 2 section

Cycle number	Cycle type	Thickness (m)	Cumulative thickness (m)
1	C1	3.8	3.8
2	C1	4.0	7.8
GAP	GAP	2.0	9.8
3	C1	5.0	14.8
4	C1	2.3	17.1
GAP	GAP	1.0	18.1
5	C1	10.0	28.1
6	C1	5.5	33.6
GAP	GAP	2.0	35.6
7	C1	1.0	36.6
8	C1	15.0	51.6
9	C1	2.4	54.0
10	C1	0.6	54.6
11	C1	3.5	58.1

GAP	GAP	3.1	61.2
12	C1	3.5	64.6
13	A3	6.0	70.6
14	C1	0.6	71.2

Quebrada de Portachuelo 2 section

Cycle number	Cycle type	Thickness (m)	Cumulative thickness (m)
15	C1	0.8	72.1
16	C1	0.5	72.6
17	C1	0.6	73.2
18	C1	0.4	73.6
GAP	GAP	5.0	78.6
19	C1	1.2	79.9
GAP	GAP	1.5	81.4
20	C1	8.7	90.1
21	C1	0.6	90.6
22	C1	3.1	93.8
23	C1	11.4	105.2
24	C1	0.4	105.6
25	C1	3.0	108.6
26	C1	0.6	109.2
27	C1	1.5	110.6
28	C1	1.0	111.6
29	C1	0.8	112.4
30	C1	0.4	112.8
31	C1	0.3	113.1
32	C1	4.0	117.1
33	C1	1.3	118.4
34	C1	1.0	119.3
35	C1	3.0	122.3
GAP	GAP	9.9	132.2
36	C1	1.0	133.2
37	C1	0.6	133.8
38	C1	0.8	134.5
39	C1	0.5	135.0
40	C1	0.5	135.5
41	C1	0.4	135.9
42	C1	0.2	136.1
GAP	GAP	3.5	139.6
43	C2	0.5	140.1
44	C2	0.5	140.6
45	C2	0.3	140.8
46	C2	0.3	141.1
47	C2	0.6	141.7
48	C2	0.3	142.0
49	C2	0.7	142.7
50	C2	0.4	143.0
51	C2	0.8	143.8
52	C2	0.2	144.0
53	C2	0.3	144.3
GAP	GAP	3.9	148.2
54	B1	0.3	148.5
55	B1	0.4	148.8
56	B1	0.5	149.3
57	C2	0.3	149.6
58	C2	0.3	149.9
59	C2	0.7	150.6
60	C2	0.7	151.3
61	C2	0.6	151.9
62	C2	0.5	152.4
63	C2	0.7	153.1
64	C2	0.5	153.6
65	C2	0.5	154.1
66	C2	0.5	154.5
GAP	GAP	2.7	157.3
67	C1	4.2	161.5
GAP	GAP	4.0	165.5
68	B3	3.4	168.9
69	B3	14.4	183.3
70	B3	2.0	185.3
GAP	GAP	10.4	195.7
71	B3	9.2	204.8
GAP	GAP	7.8	212.6
72	B3	6.7	219.3
GAP	GAP	5.0	224.3
73	B3	2.3	226.7
GAP	GAP	5.0	231.7
74	B2	3.5	235.2
75	B2	1.7	236.9
GAP	GAP	1.7	238.5
76	C2	1.0	239.5
77	C2	0.3	239.7
78	C2	1.0	240.7
79	C2	0.2	240.9
80	C2	0.3	241.1
81	C2	0.3	241.5
82	C2	0.2	241.7
83	B2	10.5	252.1

Santa Cruz de Palmarito section

Cycle number	Cycle type	Thickness (m)	Cumulative thickness (m)
1	B2	0.6	0.6
2	B2	0.6	1.2
GAP	GAP	4.0	5.2

3	C1	2.0	7.2
4	C1	0.5	7.7
GAP	GAP	11.8	19.5
5	C2	1.6	21.1
6	C1	1.9	23.0
7	C2	1.1	24.1

Santa Cruz de Palmarito section

Cycle number	Cycle type	Thickness (m)	Cumulative thickness (m)
8	C2	0.6	24.7
9	C2	4.4	29.1
10	C2	2.9	32.0
11	B1	3.8	35.8
12	C2	3.6	39.3
13	B1	1.3	40.6
14	B1	2.3	42.9
15	B1	2.3	45.2
16	B1	2.4	47.6
17	B1	2.8	50.4
18	B1	3.3	53.6
19	C2	2.3	55.9
20	C2	4.6	60.5
GAP	GAP	8.5	69.0
21	C2	0.9	69.9
22	C2	1.6	71.5
23	C2	0.6	72.1
24	C2	0.3	72.4
GAP	GAP	8.0	80.4
25	C2	0.8	81.2
26	C2	4.5	85.7
27	C2	1.6	87.3
28	C2	2.3	89.6
29	C2	2.4	91.9
GAP	GAP	5.0	96.9
30	C2	3.2	100.1

Palmar River 2-a section

Cycle number	Cycle type	Thickness (m)	Cumulative thickness (m)
1	C1	0.8	0.8
2	C1	1.3	2.0
3	C1	0.6	2.6
4	C1	0.9	3.5
5	C1	1.0	4.5
6	C1	1.0	5.5
7	B1	2.1	7.6
8	C1	1.0	8.6
9	C1	4.5	13.1
10	C1	2.1	15.1
11	C1	0.8	15.9
12	C1	1.1	17.0
13	C1	0.4	17.4
14	C1	0.4	17.8
15	C1	0.5	18.3
16	C1	0.5	18.8
17	C1	0.5	19.2
18	C1	0.5	19.7

Palmar River 2-b section

Cycle number	Cycle type	Thickness (m)	Cumulative thickness (m)
1	C2	4.2	4.2
2	C2	1.9	6.0
3	C2	6.1	12.1
4	C2	1.9	14.0
5	C2	5.3	19.3
6	C2	3.9	23.2
7	C2	6.2	29.3
8	C2	1.1	30.4
9	C2	1.0	31.4
10	C2	2.5	33.9
11	C2	5.4	39.2
GAP	GAP	3.8	43.0
12	A3	0.6	43.6
13	C2	0.6	44.2
14	A3	0.6	44.8
15	C2	0.7	45.5
16	C2	0.6	46.1
17	C2	0.3	46.4
18	C2	0.5	46.9
19	C2	1.0	47.8
20	C2	0.4	48.2
21	C2	0.3	48.5
22	C2	0.7	49.2
23	C2	0.6	49.8
24	C2	0.5	50.3
GAP	GAP	5.2	55.5
25	C2	0.7	56.2
26	C2	0.6	56.8
27	C2	0.9	57.7
28	C2	1.8	59.4
29	C2	0.6	60.0
30	C2	0.2	60.2
31	C2	0.3	60.5
32	C2	0.2	60.7